DOE/ER--0045/11

DE84 007335

ALLOY DEVELOPMENT FOR IRRADIATION PERFORMANCE
SEMIANNUAL PROGRESS REPORT FOR PERIOD ENDING SEPTEMBER 30, 1983

ARGONNE NATIONAL LABORATORY

GA TECHNOLOGIES, INC.

McDONNELL DOUGLAS ASTRONAUTICS COMPANY

MASSACHUSETTS INSTITUTE OF TECHNOLOGY

NAVAL RESEARCH LABORATORY

OAK RIDGE NATIONAL LABORATORY

SANDIA NATIONAL LABORATORIES

WESTINGHOUSE ADVANCED ENERGY SYSTEMS DIVISION

WESTINGHOUSE HANFORD COMPANY

Date Published: March 1984

Prepared by
OAK RIDGE NATIONAL LABORATORY
Oak Ridge, Tennessee 37831
operated by
UNION CARBIDE CORPORATION
for the
U. S. DEPARTMENT OF ENERGY
Under Contract No. W-7405-eng-26

Reports previously issued in this series are as follows:

DOE/ET-0058/1	Period Ending March 31, 1978
DOE/ET-0058/2	Period Ending June 30, 1978
DOE/ET-0058/3	Period Ending September 30, 1978
DOE/ET-0058/4	Period Ending December 31, 1978
DOE/ET-0058/5	Period Ending March 31, 1979
DOE/ET-0058/6	Period Ending June 30, 1979
DOE/ET-0058/7	Period Ending September 30, 1979
DOE/ER-0045/1	Period Ending December 31, 1979
DOE/ER-0045/2	Period Ending March 31, 1980
DOE/ER-0045/3	Period Ending June 30, 1980
DOE/ER-0045/4	Period Ending September 30, 1980
DOE/ER-0045/5	Period Ending December 31, 1980
DOE/ER-0045/6	Period Ending March 31, 1981
DOE/ER-0045/7	Period Ending September 30, 1981
DOE/ER-0045/8	Period Ending March 31, 1982
DOE/ER-0045/9	Period Ending September 30, 1982
DOE/ER-0045/10	Period Ending March 31, 1983

FOREWORD

This report is the eighteenth in a series of Technical Progress Reports on *"Alloy Development for Irradiation Performance"* (ADIP), which is one element of the Fusion Reactor Materials Program, conducted in support of the Magnetic Fusion Energy Program of the U.S. Department of Energy. Other elements of the Materials Program are

- *Damage Analysis and Fundamental Studies (DAFS)*
- *Plasma-Materials Interaction (PMI)*
- *Special-Purpose Materials (SPM)*
- *High Heat Flux Components*

The first seven reports in this series are numbered DOE/ET-0058/1 through 7. This report is the eleventh in a new numbering sequence that begins with DOE/ER-0045/1.

The ADIP program element is a national effort composed of contributions from a number of National Laboratories and other government laboratories, universities, and industrial laboratories. It was organized by the Materials and Radiation Effects Branch, Office of Fusion Energy, DOE, and a Task Group on *Alloy Development for Irradiation Performance,* which now operates under the auspices of the Reactor Technologies Branch. The purpose of this series of reports is to provide a working technical record of that effort for the use of the program participants, for the fusion energy program in general, and for the Department of Energy.

This report is organized along topical lines in parallel to a Program Plan of the same title so that activities and accomplishments may be followed readily relative to that Program Plan. Thus, the work of a given laboratory may appear throughout the report. Chapters 1, 2, 8, and 9 review activities on analysis and evaluation, test methods development, status of irradiation experiments, and corrosion testing and hydrogen permeation studies, respectively. These activities relate to each of the alloy development paths. Chapters 3, 4, 5, 6, and 7 present the ongoing work on each alloy development path. The Table of Contents is annotated for the convenience of the reader.

This report has been compiled and edited under the guidance of the Secretary of the Task Group on *Alloy Development for Irradiation Performance.* F. W. Wiffen, Oak Ridge National Laboratory, and his efforts and those of the supporting staff of ORNL and the many persons who made technical contributions are gratefully acknowledged. T. C. Reuther, Reactor Technologies Branch, is the Department of Energy Counterpart to the Task Group Chairman and has responsibility for the ADIP Program within DOE.

G. M. Haas, Chief
Reactor Technologies Branch
Office of Fusion Energy

CONTENTS

1. ANALYSIS AND EVALUATION STUDIES

1.1 MATERIALS HANDBOOK FOR FUSION ENERGY SYSTEMS - J. W. Davis (McDonnell Douglas Astronautics Company - St. Louis Division) and T. K. Bierlein (Westinghouse Hanford Company)

1.1.1 ADIP Task

Task Number 1.A.1 - Define material property requirements and make structural life predictions.

1.1.2 Objective

To provide a consistent and authoritative source of material property data for use by the fusion community in concept evaluation, design, safety analysis, and performance/verification studies of various fusion energy systems. A secondary objective is the early identification of areas in the materials data base where insufficient information or voids exist.

1.1.3 Summary

During the past six months the handbook effort has been towards developing data sheets. For this period the effort has been to establish a continuous flow of data sheets into the handbook. Substantial progress has been made towards the achievement of this goal with the publication of 7 new data pages covering the properties of HT-9 and 316 stainless steel as well as the establishment of a backlog of new data sheets in various stages of preparation.

1.1.4 Progress and Status

While the Materials Handbook for Fusion Energy Systems (MHFES) still has a long way to go, it is beginning to look like a materials handbook. With the addition of publication package No. 8, the MHFES now contains information on materials for five of its eight major chapters. The latest additions to the handbook consist of data pages on the properties of a ferritic steel designated HT-9 prepared by D. S. Gelles of HEDL and properties of 316 stainless steel prepared by N. J. Simon of NBS. The inclusion of HT-9 in the handbook represents the first step in expanding the information in each handbook chapter to include more than one material. These data sheets cover materials used in two important areas in reactor design: 1st wall structure and magnet structural materials. The HT-9 data consists of density, thermal expansion coefficient and linear thermal expansion all as a function of temperature. The 316 stainless data adds Poisson's Ratio, Young's Modulus, Shear Modulus, Bulk Modulus and magnetic permeability all as a function of temperature.

In addition to the data sheets that have been incorporated into the handbook during this reporting period there are a number of data sheets in various stages of incorporation into the handbook. Several data sheets on HT-9 and 316 steels are awaiting publication or in the review cycle. The HT-9 data sheets, prepared by D. S. Gelles of HEDL, provide mechanical property information on Poisson's Ratio, Young's Modulus, and Shear Modulus, and thermal property information on specific heat, thermal diffusivity, thermal emissivity (in vacuum and stably oxidized), and thermal conductivity. The 316 stainless data sheets prepared by N. J. Simon of NBS provide mechanical property information showing the effect of temperature on ultimate tensile and yield strengths, elongation, reduction of area and engineering stress stain. Data sheets currently in preparation or planned will cover structural materials (vanadium alloys and copper alloys), superconducting magnet case materials, and neutron multipliers/breeders (beryllium and lithium lead). In addition, effort is underway to develop data sheets on specific design related issues such as irradiation creep and its treatment in structural design, swelling, and magnetic effects when magnetic materials are used (e.g. ferritic steels). HT-9 data sheets are being prepared by D. S. Gelles of HEDL on irradiation induced stress free swelling.

In addition to the data pages contained in the MHFES, we are currently in the process of producing a supporting documentation volume which contains information regarding the assumptions with respect to the treatment of the data, the uncertainty in the analysis, and the sources of the data used to develop the data pages. The supporting documentation volume distribution will be limited to one individual at each organization currently on the distribution list for the handbook.

The handbook is currently distributed to more than 100 individuals at over 30 organizations in the United States. Because of the continually changing nature of these organizations, a verification of the handbook distribution list was recently made. In addition to an updating of names, addresses and phone numbers numerous comments and suggestions were received which will be considered for improvement of the handbook. One comment from several individuals indicated some data sheets are inadvertently missing from some of the handbooks. To correct this problem the next publication package will contain a complete listing of all data pages. The listing will be used to verify that all handbooks are either currently complete or identify missing pages which will then be sent to complete those handbooks. The comment received from most handbook holders expressed the general thought that the handbook is very useful and is actively being used by the many others in the organizations in addition to the custodians.

1.1.5 Conclusions

Substantial progress has been made with regard to putting information in the handbook during this period. Additional work is needed on the part of everyone, especially reviewers and page preparers. There are still a number of data pages in the review cycle awaiting approval, however, once these data pages are included in the handbook additional new data pages will be needed if the current momentum is to be sustained. Researchers in ADIP and other task groups can help by turning their experimental results into data sheets.

1.2 CONTROL OF ACTIVATION LEVELS TO SIMPLIFY WASTE MANAGEMENT OF FUSION REACTOR FERRITIC STEEL COMPONENTS — F. W. Wiffen and R. T. Santoro (Oak Ridge National Laboratory)

1.2.1 ADIP Task

ADIP Task I.A.1, Define Material Property Requirements and Make Structural Life Predictions.

1.2.2 Objective

The objective of this work is to examine the restrictions placed on the composition of steels to allow simplified waste management after service in a fusion reactor first wall.

1.2.3 Summary

Decay of steel activity within tens of years could simplify waste disposal or even permit recycle. For material recycle, N, Al, Ni, Cu, Nb, and Mo must be excluded. For shallow land burial, initial concentration limits include (in at. ppm) Ni, <20,000; Mo, <3650; N, <3650; Cu, <2400; and Nb, <1.0. Other constituents of steels will not be limited.

1.2.4 Progress and Status

1.2.4.1 Introduction

Disposal of materials and components from nuclear power systems is complicated by the radioactivity induced by neutron reactions. This disposal has attracted unfavorable publicity and lack of public acceptance of the fission power options. To counter this public attitude, it is incumbent on those developing the fusion power source to examine the potential for the same problem in a fusion power economy and to evaluate the feasibility of mitigating the material disposal problem for fusion reactor components.

The fusion fuel cycle most likely to be commercialized is the D-T-Li cycle. In this system deuterium (D) and tritium (T) are the fuels. Since tritium does not occur in nature, it must be bred in the two isotopes of lithium in the reactions

$$n + {}^{6}Li \rightarrow T + {}^{4}He$$

and

$$n + {}^{7}Li \rightarrow n' + T + {}^{4}He \ .$$

The neutrons that drive this reaction and that carry the greatest fraction of the energy are produced in the fusion reaction

$$D + T \rightarrow n + {}^{4}He + 17.6 \text{ MeV} \ .$$

The radioactivity concerns in a fusion reactor all derive from this reaction. Both the deuterium fuel component and the helium reaction product are stable and thus pose no handling problem. The tritium fuel component is radioactive and decays by electron emission with a half-life of 12.33 years. This requires that the tritium be contained and recovered with a high level of efficiency. The other component of radioactivity, and the one that is being treated in this paper, is the activity produced in all plant materials from reactions with the fusion neutrons.

The flux of neutrons on the various components of a fusion power plant will decrease approximately exponentionally with increasing distance from the plasma chamber. The highest neutron flux is at the components of the first wall and blanket zone of the reactor, and it is this zone on which we will focus. Consideration will further be restricted to steels, the most probable structural materials for use in the first wall and blanket.

The ideal fate for materials from fusion reactor components that have failed or have reached the end of their service life is recycle for reuse in the same or a new application. If recycle is not feasible, the simplest disposal system that is acceptable will be preferred. These two options for used material will be examined in this paper.

The question of recycle of fusion reactor components has been discussed by Jarvis.[1] The subject of low-activation materials for fusion reactor components was reviewed and discussed by the DOE panel chaired by Conn.[2] The material presented in those two reports forms the basis of this paper. The goal here is to establish limits that would be imposed on the composition of steels by the requirements for recycle or for simplified disposal as waste at the end of useful component service.

Conn, Okula, and Johnson[3] have examined the control of activity, especially at long times after shutdown, by elementally or isotopically tailoring the composition of structural alloys. They showed the advantages to be obtained by selecting alloys free of nickel and molybdenum and also showed advantages of using only selected isotopes of these elements if alloys containing nickel or molybdenum were to be used. The results were not evaluated against any regulated limits on recycle or waste disposal.

All earlier evaluations of reduced activation steels, as for example by Conn et al.[3] and in the Mirror Advanced Reactor Study project[4], are deficient in considering only the nominal compositions of the alloys. These studies did not include the effects of impurities routinely contained in steels; these impurities will in some cases dominate the long term radioactivity characteristics of the steel.

1.2.4.2 Levels of Activation and Rates of Decay

Neutrons emitted from the plasma will undergo reactions with all elements in the reactor structure and produce nuclei in excited states. These activated isotopes undergo radioactive decay; however, some have intolerably long half-lives. The cross sections for neutron reactions and the radioactive states that result are dependent on the parent element and the neutron energy. More than one isotope species can result from a single parent isotope, and more than one decay route may be possible from a single activated isotope. Calculation of the activation products and subsequent decay first requires the calculation of the neutron flux at the component of interest. The products of the energy-dependent neutron flux and the energy-dependent reaction cross sections yields the radioactive isotope inventory. The decay characteristics of this inventory give the measure of activity or radiation field.

The neutron-induced activation of various elements calculated for the first wall of a fusion reactor is given in Fig. 1.2.1. The neutron spectrum was determined for a reactor blanket consisting of a stainless steel structure, a liquid-lithium breeding medium, and a helium coolant. The data given in Fig. 1.2.1 were obtained by convoluting this neutron spectrum for the first wall zone with activation cross-section data for the separate elements. It was assumed that the neutron flux would not be significantly different if the actual element were used in place of the stainless steel in the initial flux calculation. The calculations used the density of the elements at about 20°C except for gaseous elements, where the density of the liquid state at the boiling point was used.

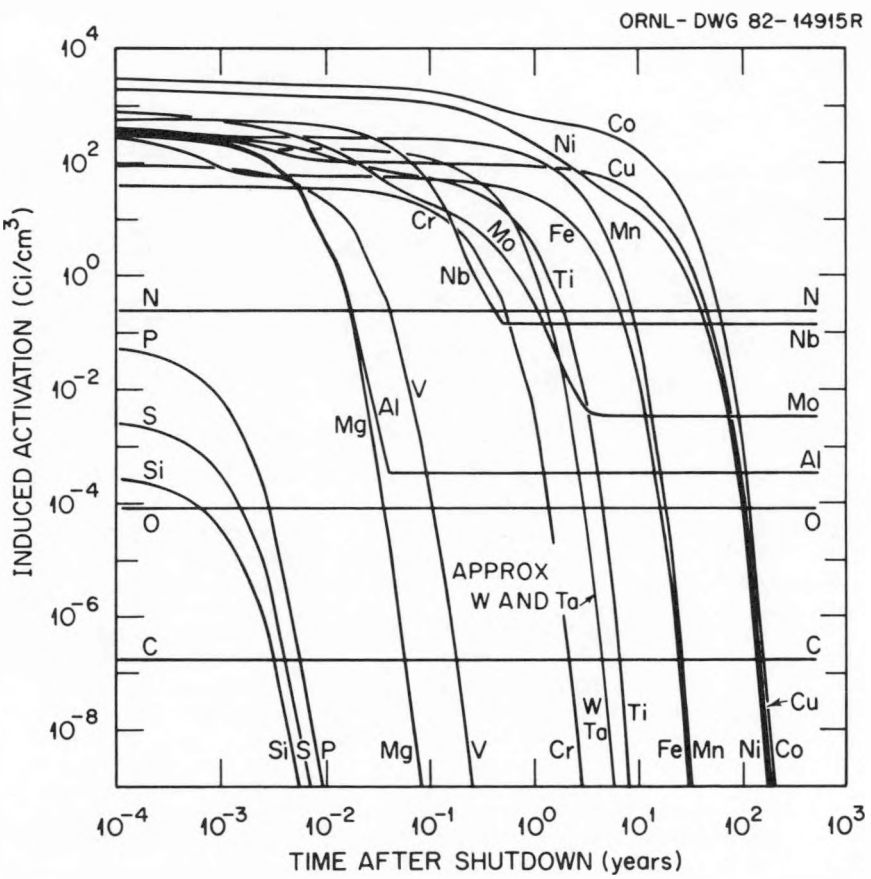

Fig. 1.2.1. Activation level and rate of decay for elements exposed for 9 MW·years/m^2 in the neutron flux at the first wall of a fusion reactor.

The data presented in Fig. 1.2.1 were calculated for a total reactor operation to 9 MW·years/m^2 accumulated in three years of continuous operation. This lifetime corresponds to a total neutron fluence of approximately 1.0×10^{27} neutrons/m^2 and would produce 100 dpa in an iron alloy first wall. This is probably a minimum acceptable lifetime for an economically viable reactor.

Note that for almost all elements treated, and certainly for all those that are major constituents of candidate fusion reactor structural materials, the range of activity soon after shutdown is only two orders of magnitude. The range is from about 2800 Ci/cm^3 for Co to 40 Ci/cm^3 for Cr. For most steels, the activity will be slightly above the activation level for unalloyed iron, about 1000 Ci/cm^3.

These activation levels can be put into perspective by comparing them with materials activated in fission reactors. Kazimi[5] has provided such a comparison (Table 1.2.1). At 1 and 10 years after discharge from reactor service, the total activities per unit volume are quite similar for STARFIRE (a fusion reactor with stainless steel structure), a light-water (thermal) fission reactor, and an LMFBR (fast) fission reactor. One hundred years after shutdown, the fusion system material has an advantage of approximately 100, since the activation products in stainless steel decay more rapidly than do the actinide fuel and fission products in the two fission reactors. The relative hazards of the materials in the system, which give fusion a decided advantage, will be discussed later.

Table 1.2.1. Comparison of the radioactivity in high-activity wastes from fusion and fission reactors [for a 1200-MW(e) plant at 80% capacity factor and 33% thermal efficiency]

(from Kazimi[5])

	Years after discharge	Total activity (Ci/cm^3)	Biological hazard potential [per GW(e)-year]	
			10^6 km^3_{air}	km^3_{water}
STARFIRE[a]	1	26.36	42	620
fusion	10	2.34	6.3	86.5
reactor	100	7.6×10^{-3}	0.2	5.2
PWR light	1	25.3	7,600[b]	26,900[b]
water fission	10	3.94	6,080	13,300
reactor	100	0.41	3,800	2,090
LMFBR fast	1	27.0	1,600[c]	16,400[c]
fission	10	3.4	1,120	3,800
reactor	100	0.41	740	570

[a]This represents half the blanket structural material of STARFIRE, but the radioactivity of the other half is at least an order of magnitude less.

[b]With recycle. Inhalation BHP is actinide dominated, but ingestion is fission product dominated.

[c]Only high level waste and fuel assembly waste are considered here.

The decay of induced activity in individual elements for times up to 1000 years after reactor shutdown is also shown in Fig. 1.2.1. While shutdown activities showed little range, a much greater separation of elements results if they are compared on the basis of the rate of decay of this total induced activity.

1.2.4.3 Criteria, Goals, and Regulations on Activity

A number of criteria have been used to judge the "hazard" of radioactive waste and to measure the rate of decay as a function of elapsed time. The simplest of these is the specific activity (in curies per unit mass or per unit volume), which is a measure of the radioactive decay rate only. (These units are used in Fig. 1.2.1.) Representing the activity in these units does not distinguish between decay processes, so a decay event that emits a high-energy gamma ray is counted equally with a low-energy electron emission, internal electron capture, etc. Another useful measure of activity in determining occupational hazard is the rem, which accounts for the energy deposition of the different types of radiation. Two other units are used to evaluate the potential for harm after ingestion or inhalation. These are the biological hazard potential (BHP) for water or air, given as the volume of water or air needed to dilute the waste to the maximum permissible concentration (MPC) permitted by law. The MPC, and hence the BHP, is specific to each radioactive isotope and is determined by the decay mode and the rate of decay for the isotope and by the biological activity of the chemical species.

The difference in the relative hazards of structural materials after service in a fusion reactor and of the structure, fuel, and fission products of a fission reactor is shown in Table 1.2.1. While the total activity was comparable for fusion and fission at 1 and 10 years after shutdown, the BHP for the three systems shows fusion to have an advantage of 30 to 970. The advantage increases with time because of the long-lived actinide isotopes in the fission reactor wastes.

The treatment of recycle given by Jarvis[1] uses the specific activity and the radiation field, in rem, on which to base judgments. The U.S. Federal Regulation governing waste disposal considers the activity of specific radionuclides, selected on the basis of their long-lived hazard potential.

Rules governing the handling and disposal of radioactive materials are relatively new, and the processes of setting these rules and issuing licenses under them are still in the formative stages. In particular, large quantities of a "new" type of spent material, such as will be generated in a fusion economy, can be expected to attract close scrutiny. It is likely that the rules and standards will be altered and adapted to meet the requirements of fusion. It is very speculative to attempt to judge the fate of materials discharged from a future fusion reactor on the basis of regulations available today. However, such an analysis is attempted here to provide guidance on measures that can be taken to achieve control of the radioactivity in steel structures at long times after reactor shutdown.

1.2.4.4 The Recycle Option

Jarvis has treated the question of recycling discharged fusion reactor component materials 100 years after removal from the reactor.[1] He calculated the level of activation in a first wall operated for two years at 10MW(th)/m^2. The calculation was performed for 39 elements, including all of those normally found as constituents of common alloy systems. The decay of this induced activity was also calculated in order to determine activity for 100 years after shutdown.

Recycle is the most desirable option for used reactor component materials. In STARFIRE, the blanket zone will contain 450 metric tons of stainless steel. With random failures and scheduled replacements, the blanket zone will "use" 3400 metric tons of steel during the reactor lifetime.[6] In a full fusion power economy, the quantities of material become very large, and recycle could reduce the pressures on the mineral extraction and primary metal production industries.

If recycle does become possible, economic issues will determine if it is practical. The costs of recycle and of possible restricted use of recovered material must be traded against the values in the material and in reduced material storage costs.

Jarvis made a number of assumptions to estimate the potential for material recycle. Among the most important were the recycle scenario and the criteria used to judge if a recycled alloy was acceptable for reuse. The assumption on recycling was that the reprocessing (melting, casting, forging, rolling, etc.) would be fully remote, without any emissions, and that limits on use of the material would be set by radiation levels encountered by workers during machining and assembly operations. Two limits were used to judge the acceptable activity levels of the reprocessed alloys: first, that the activity be not greater than that of newly refined uranium metal, which is 12 $\mu Ci/cm^3$, and second, that the occupational exposure due to the gamma dose rate from an infinite-area thick sheet be no more than 2.5 mrem/h.

The above assumptions and acceptability criteria are reasonable bases for analysis, and we have no better criteria to propose. However, it must be recognized that they would likely be unacceptable under U.S. licensing procedures. Licensing of a recycle operation would require a detailed calculation of effluents expected during reprocessing and would impose isotope-specific limits on both reprocessing effluents and on activity of the recycled product. While the limits will not be anticipated here, it seems likely that the greatest restrictions will be on those gamma-emitting isotopes with long half-lives. The limit on exposure of occupational workers can also be expected to be lower than assumed by Jarvis. In the United States, the ALARA concept (As Low As Reasonably Achievable) is generally interpreted as restricting exposures to approximately 1 rem/year instead of the 5 rem/year that was assumed by Jarvis to arrive at the 2.5 mrem/h criterion. A more likely limit on occupational exposure for the work force, under the ALARA concept, is then about 0.5 mrem/h.

Based on the assumptions discussed, the analysis of the potential for recycle results in a classification of the 39 elements considered. The classification is in terms of allowed initial concentration of these elements to allow recycle 100 years after service. The results presented by Jarvis[1] are summarized in Table 1.2.2. Note that the limitations on Fe, Ni, and Mo would rule out recycle of any of the steels in the 100 year scenario.

Table 1.2.2. Limits on constituents of a fusion reactor first wall to allow recycle 100 years after service

(Adapted from Jarvis[1])

Function in alloy	Composition range	Limited elements
Alloy base	Not limited	C, Mg, P, S, V, Cr, Y, Ta, W, Tl
Major alloy constituent	20 to 50%	O, F, Si, Mn, Fe, Pb
Minor alloy addition	0.1 to 20%	Li, Be, B, Na, Cl, Ca, Ti, Co, Zr, In
Acceptable impurity	10 to 500 ppm	N, Al, Ar, K, Sc, Ni, Cu, Zn, Mo, Cd, Sn
Unacceptable impurity	< 10 ppm	Nb, Ag

1.2.4.5 Simplified Waste Disposal

While the technology exists for the permanent disposal of long-lived radioactive wastes under several geologic storage options, it would be economically and politically more acceptable to use a simpler disposal system. The favored approach is to generate only wastes that could be emplaced in land disposal sites (shallow land burial). Institutional control of the facility would be required only for such times that the activity presents a hazard. At time beyond about 100 years, only engineered barriers will be required.

United States regulations covering the licensing and operation of land disposal facilities for radioactive waste disposal were finalized in late 1982 and published in the Federal Register.[7] These rules form part of the Code of Federal Regulations for Energy, and are referred to hereafter as 10CFR61. The performance objectives used in deriving these regulations were

- protect the general public,
- protect individuals from inadvertent intrusion,
- protect individuals during operation, and
- ensure stability of site after closure.

In establishing procedures to meet these objectives, waste was classified into three categories, depending on the stability and activity level of the waste. The highest permissible level is for Class C wastes, and it is only this category that can apply to steel components from the blanket zone of fusion reactors. Class A and B wastes, with more restrictive limits on activity, will not be considered here.

The general rules governing the disposal of Class C wastes are designed to meet the performance objectives. These requirements include

- waste or container stable for 300 years,
- burial 5 m below surface or intruder barriers with 500-year life,
- institutional control of access for up to 100 years, and
- activity at 500 years not unacceptable hazard to intruder.

While these performance objectives and waste requirements are general, they must be translated to specific measurable quantities that can be used in judging the acceptability of material for disposal. This has been done by examining the isotopes expected in discharged fission reactor materials, evaluating the decay life and the potential biological hazard of each isotope, and then establishing a concentration limit for each isotope. Table 1.2.3 gives the limits for long-lived radionuclides allowed in Class C waste. (If concentrations do not exceed 0.1 times the value in Table 1.2.3, the waste may qualify for a less restricted disposal class, Class A.) Limits are also set for some of the shorter-lived radionuclides, and these limits, given in Table 1.2.4, are for all three classes of waste qualifying for land disposal.

The only limits on concentrations of radionuclides are those specifically listed in these two tables. Draft versions of 10CFR61 had proposed setting limits by similarity to listed isotopes, but this blanket rule was rejected in setting the final regulations. It must be recognized, however, that other regulations covering exposure of the occupational work force (that would apply during waste emplacement) and limits covering transportation may also set practical restrictions on the material that can be disposed of at landfill sites. The removal of decay heat may also set practical limitations on the concentration of radioactivity in storage containers.

In evaluating radionuclide concentrations, the activity is averaged over the container volume. Dilution with inert filler material can be used to reduce the activity per unit volume. Wastes containing more than one of the isotopes restricted in Tables 1.2.3 and 1.2.4 are evaluated by the "sum of fractions" rule.

Table 1.2.3. Limitations on long-lived radionuclides for land disposal

Radionuclide	Concentration (Ci/m^3)
^{14}C	8
^{14}C in activated metal	80
^{59}Ni in activated metal	220
^{94}Nb in activated metal	0.2
^{99}Tc	3
^{129}I	0.08
Alpha-emitting transuranic nuclides with half-life greater than 5 years	100[a]
^{241}Pu	3,500[a]
^{242}Cm	20,000[a]

[a]Units are nanocuries per gram.

Table 1.2.4. Limits on short-lived radionuclides for land disposal

Radionuclide	Concentration (Ci/m^3)		
	Class A	Class B	Class C
Total of all nuclides with less than 5-year half-life	700	NL[a]	NL
^{3}H	40	NL	NL
^{60}Co	700	NL	NL
^{63}Ni	3.5	70	700
^{63}Ni in activated metal	35	700	7000
^{90}Sr	0.04	150	7000
^{137}Cs	1	44	4600

[a]Not limited. Practical limits on personnel dose rates or heat generation during handling may set limits.

That is, the concentration of each nuclide must be divided by the regulated limit for that nuclide, and the fractions obtained for all limited nuclides are summed. To be acceptable for land disposal, the sum of fractions must not exceed 1.0.

Further details in 10CFR61 establish how activities can be calculated or estimated, methods of packaging wastes, placement of wastes at the site, and other particulars not pertinent to the discussion here. However, these rules are new and they have not yet been tested through judicial challenge nor have they been tested in the licensing process for which they are designed. It is also important to note that the rules were evolved for wastes from the light-water fission reactor industry, and the focus was on the isotopes normally encountered in these wastes. Many changes can be expected before regulations are needed to control the wastes of fusion power reactors, and there is no firm basis for anticipating these changes. Inasmuch as the most stringent limits are on the longest lived, gamma-emitting radionuclides, prediction of any relaxation on these limits does not appear to be justified.

1.2.4.6 Disposal Limits Applied to Steels

The calculated activity levels in the separate elements included in Fig. 1.2.1 can now be used with the limits discussed in the previous section to establish allowed concentrations of alloy and impurity elements in steels. For material that has been in service in the reactor first wall and has been held 10 years after service, the limits given in Tables 1.2.3 and 1.2.4 impose limits on the initial concentration of elements that are activated to produce the restricted isotopes. Only three of the restricted radionuclides impose restrictions on the composition of steels. These are ^{94}Nb, ^{63}Ni, and ^{14}C. The limitations these impose on initial concentrations of Mo, Nb, Ni, Cu, and N are given in Table 1.2.5. These limits, however, are mutually exclusive. Allowing any one of these elements to reach the concentration limit would meet the limit for waste disposal and would then allow no contribution to the waste radioactivity from the other four elements. These limits are given without taking any credit for dilution in packaging the waste. They also assume the natural isotopic distribution in each of the elements considered.

In practice, the "sum of fractions" rule must be used in counting all restricted radionuclides for evaluating the suitability for disposal. The limits on radionuclides are divided in this way for two hypothetical steels in Table 1.2.6. In the first steel, one-half of the allowed limit fraction is assigned to niobium, to allow 0.9 wt ppm residual niobium in the steel. In the second case, a less realistic assumption of niobium-free steel was made, and a relatively low limit was set for impurity Ni, Cu, and N to allow the concentration of molybdenum to be as high as possible. This treatment allows just over 0.5 wt % Mo in the steel

The alloying and impurity concentration limits derived are "worst case" assumptions for a service life of 9 MW·years/m^2. Since these limits are all set by relatively long-lived isotopes, the allowed initial concentrations will vary inversely with the service life. The limits were derived for first-wall service, and the attenuation of neutron flux deeper in the blanket will result in lower production rates of the restricted isotopes in most of the blanket structure. It will also be impossible to pack steel drums or other containers with first-wall material without either leaving void space or adding inert filler material. A more likely scenario is for first-wall steel to be carefully mixed with material from deeper in the blanket to relax the restriction on initial concentration limits. The combination of material mixing and some dilution with filler material should result in relaxation of at least a factor of 3 to 10 in impurity content limitations.

Table 1.2.5. Initial concentration limits for first-wall material 10 years after shutdown, following 9 MW·years/m^2 service

(from ref. 2)

Alloying element	Limiting radionuclide	Limit on alloying element[a]	
		(at. ppm)	(wt % in steel)
Mo	^{94}Nb	3,650	0.63
Nb	^{94}Nb	1	0.00017
Ni	^{63}Ni	20,000	2.1
Cu	^{63}Ni	2,400	0.27
N	^{14}C	3,650	0.092

[a]These limits are mutually exclusive.

Table 1.2.6. Examples of two acceptable steels, for 9 MW·years/m^2 service, then held 10 years before disposal

(The "sum of fractions" rule is used)

Element	Individual maximum (wt %)	Steel A		Steel B	
		(wt %)	(f)[a]	(wt %)	(f)
Mo	0.63	0.13	0.2	0.54	0.85
Nb	0.00017	0.00009	0.5	0	0
Ni	2.1	0.42	0.2	0.11	0.05
Cu	0.27	0.014	0.05	0.014	0.05
N	0.092	0.0046	0.05	0.0046	0.05
Total			1.00		1.00

[a]f is the fraction of the allowed concentration in Class C waste.

Further mitigation would be possible through the use of isotopic tailoring or layered construction, but both would increase the cost of a fusion reactor blanket. If isotopic tailoring were used, some of the isotopes of Ni, Cu, and Mo would be reduced to low levels by separation to avoid the production of restricted radionuclides. Isotopic tailoring is not possible with niobium, with only a single naturally occurring isotope, and is unlikely with nitrogen, where the problem isotope ^{14}N is 99.6% of naturally occurring nitrogen. Construction of a reactor blanket structure in separable layers might also be possible. High-activity first-wall material could then be separated for geologic disposal. Material from deeper in the blanket would qualify for land disposal. An alternative method of layer construction would be to use steel with tightly controlled specifications at the first wall and less rigidly controlled material deeper in the blanket, so that all material would qualify for landfill disposal.

1.2.4.7 Prospects for Controlled Activation Steels

The limits established for the concentration of Ni, Mo, N, Cu, and Nb to meet Class C land disposal requirements after service in a fusion reactor are very stringent. The restrictions on nickel and molybdenum will require the selection of alternative alloy additions for strengthening and phase control. Among the unrestricted elements, Mn, W, Ta, Ti, V, and Si may be attractive substitutes for achieving desired properties. The elements N, Cu, and Nb can be present only as impurities, but only niobium should prove a problem for control to the required level. Discussions with steelmakers suggest that, while control of niobium below 1 wt ppm can be achieved, it will be expensive.[8]

Two factors can affect the prospects of developing steels to meet the low activation goal of land disposal. A possible adverse effect could be on the further restriction of activity levels acceptable for land disposal. This could result from more complete examination of the anticipated characteristics of fusion reactor waste material or from a general reduction in acceptable activity levels due to the reluctance of the general public to accept the perceived hazards of radioactive material. The other major factor is the relaxation of impurity control because of dilution of the activated metal components in storage containers and because of lower activation levels for material more remote from the first-wall zone.

1.2.5 References

1. O. N. Jarvis, "Selection of Low-Activity Elements for Inclusion in Structural Materials for Fusion Reactors," AERE-R 10496 Atomic Energy Research Establishment, Harwell, Oxon, England, (June 1982).

2. R. W. Conn et al., *Report of the DOE Panel on Low Activation Materials for Fusion Applications*, PPG-728, University of California at Los Angeles, June 1983.

3. R. W. Conn, K. Okula, and A. W. Johnson, "Minimizing Radioactivity and Other Features of Elemental and Isotopic Tailoring of Materials for Fusion Reactors," *Nucl. Technol.* **41**, 389–400 (1978).

4. B. G. Logan et al., *Mirror Advanced Reactor Study Interim Design Report*, UCRL-53333, Lawrence Berkeley Laboratory, Berkeley, Calif., April 1983.

5. M. S. Kazimi, "Risk Considerations for Fusion Energy," *Nucl. Technol./Fusion* 4, 527–32 (1983).

6. C. C. Baker et al., *STARFIRE — A Commercial Tokamak Fusion Power Plant Study*, ANL/FPP-80-1, Argonne National Laboratory, Argonne, Ill., September 1980.

7. Nuclear Regulatory Commission, "Licensing Requirements for Land Disposal of Radioactive Waste," 10 CFR Part 61, *Federal Register* 47(248), 57446–82 (Dec. 27, 1982).

8. D. A. Canonico, Combustion Engineering Company, Chattanooga, Tenn., personal communication to F. W. Wiffen, June 1983.

1.3 ALLOY DEVELOPMENT FOR FAST INDUCED RADIOACTIVITY DECAY FOR FUSION REACTOR APPLICATIONS — R. L. Klueh and E. E. Bloom (Oak Ridge National Laboratory)

1.3.1 ADIP Task

ADIP Task I.A.1, Define Material Property Requirements and Make Structural Life Predictions.

1.3.2 Objective

During the operation of a fusion reactor, the structural material of the first wall and blanket structure will become highly radioactive from activation by the high-energy fusion neutrons. A difficult radioactive waste management problem will be involved in the disposal of this material after the service lifetime is complete. One way to minimize the management problem is the use of structural materials where the radioactive isotopes in the irradiated material decay to levels that allow for simplified disposal techniques. We are exploring how ferritic and austenitic steels could be developed to meet this objective.

1.3.3 Summary

Waste management could be simplified by developing steels that contain only elements that produce radioactive isotopes that decay to low levels in a reasonable time. The development of such steels by elemental substitutions for molybdenum in Cr–Mo steels and nickel and molybdenum in austenitic stainless steels is discussed.

1.3.4 Introduction

Serious safety and environmental concerns for fusion reactors involve the induced radioactivity in the first wall and blanket structure. Public safety could be jeopardized by the accidental release of this induced radioactivity, and the biological hazard posed for plant personnel would eliminate the possibility of contact maintenance and repair. Another problem involves the special waste storage problems that will be faced with the highly radioactive blanket and first-wall structures after service. All of these problems would be alleviated by the use of a low-activation structural material. However, as pointed out in a recent report by a U.S. Department of Energy (DOE) panel set up to study this subject, the technology for commercially producing and fabricating material that would meet the low-activation criteria is not presently available and is unlikely to be available soon.[1] (High-purity silicon carbide was the only material considered to meet the requirements, if purity could be adequately maintained.) Even though other solutions must be sought for the safety and maintenance problems, it appears possible that the storage of radioactive reactor components can be simplified by developing materials in which the induced radioactivity decays in a reasonable time to such levels that the waste no longer requires maintenance.

Guidelines (10CFR61) for the classification of nuclear wastes have been issued by the U.S. Nuclear Regulatory Commission;[2] these guidelines are summarized in Table 1.3.1. The DOE panel on low-activation materials set as a goal the development of reactor materials that fall within Class C, but with the hope to meet Class B criteria.[1]. It should be noted that the 10CFR61 guidelines will undoubtedly be extensively revised by the time the first components are discharged from an operating fusion reactor and are ready for disposal. Nevertheless, these guidelines offer a standard to which alloys can be developed.

The 10CFR61 guidelines were examined by the DOE panel[1] and more recently by Wiffen and Santoro.[3] Based on the guidelines, initial concentration limits have been calculated for various common alloying elements or the three waste classes for

Table 1.3.1. Nuclear waste classification and storage under proposed 10CFR61 rules

Waste class	Definition	Disposal
Class A — Segregated	Decays to acceptable levels during site occupancy	
Class B — Stable	Stabilized; decays within 100 years to levels that are not a danger to public health and safety	Covered to reduce surface radiation to a few percent of background
Class C — Intruder	Decays to acceptably safe levels in times greater than 100 years but less than 500 years	At least 5 m below the surface with natural or engineered barriers
Waste that does not meet Class C intruder waste definition	Decay times greater than 500 years	Does not qualify for near-surface disposal; proposed methods will be considered on a case-by-case basis

first-wall and blanket structures 10 years after the shutdown of a reactor operated for 9 MW·years/m^2. Those elements for which a limit exists for Class B and Class C waste are given in Table 1.3.2. No limits are anticipated for elements not shown. The possibility of a material that results in Class A waste is quite remote; vanadium alloys offer the possibility for Class B waste. It appears that steels, the subject of this report, will have to be handled as Class C waste.[1,3]

From Table 1.3.2 it is seen that for the induced radioactivity of a steel to decay rapidly enough to qualify for Class C treatment, certain common steel alloying elements must be restricted. In particular, niobium must be eliminated. (It is this restriction on niobium that will probably make it impossible to ever meet the Class C criteria for any steel.) Nickel, molybdenum, and nitrogen must be severely restricted relative to the concentration of these elements in steels presently being considered for first wall and blanket structure applications. Copper, generally present as an impurity element, will also have to be controlled.

In this paper the development of steels with "fast" induced-radioactivity decay (FIRD) characteristics will be discussed. Fast is a relative term, which for this discussion is taken to mean steels with radioactive decay rapid enough to at least meet Class C waste disposal criteria. The term low-activation material is often used to describe such alloys that minimize waste disposal as well as those that would allow hands-on maintenance. Materials that would allow hands-on maintenance would not only have to be low activating but would also have to decay to low levels very rapidly (e.g. pure SiC). The steels under discussion here will have much higher initial activation, and for that reason we will not call them low-activation alloys.

The limits on the initial concentrations of Ni, Mo, Cu, Nb, and N (Table 1.3.2) established by the 10CFR61 guidelines are mutually exclusive.[3] That is, if any one of the elements is present at the concentration limit, the other elements must not be present. The 1 at. ppm limit for niobium will be the most difficult to meet. Wiffen and Santoro indicated that steelmakers will probably be able to meet the limit, although doing so will be expensive. Because of the restrictiveness on the niobium, the alloys discussed below will be those for which Mo, Ni, Cu, and N will be kept to a minimum.

Table 1.3.2. Initial concentration level restrictions from 10CFR61 waste disposal rules ten years after shutdown, 9-MW·years/m^2 exposure

Element	Initial concentration limit[a] (at. ppm)	
	Class B	Class C
N	365	3,650
Cu	240	2,400
Fe	35,000	—10^6
Ni	2,000	20,000
Mo	*b*	3,650
Nb	*b*	1

Source: R. W. Conn et al., *Panel Report on Low Activation Materials for Fusion Applications*, UCLA Report PPG-728, University of California at Los Angeles, June 1983.

[a]Limits apply to first wall region.

[b]These elements do not qualify for Class B disposal.

For various technological reasons, austenitic stainless steels and the Cr-Mo ferritic (and martensitic) steels are presently the leading candidate alloys for fusion reactor structures. The effect of irradiation on such steels has been extensively studied in the fusion reactor development program and in the breeder reactor program. Furthermore, there is an extensive background of experience available to draw upon for fabricating large and complicated steel structures for elevated-temperature service. Because of this background of experience with such steels, these materials are the logical choices for modification to develop FIRD alloys.

Common steel alloying elements that can be used in FIRD steels include Mn, Ti, Cr, Si, W, V, Ta, Co, and C. The most important of the elements not available are nickel and molybdenum. Both elements are present in the austenitic stainless steels, and molybdenum is used in the Cr-Mo ferritic steels. If these two types of steels are to be used, substitutions must be found for these two elements. In the following we will discuss possibilities for developing FIRD ferritic steels similar to the Cr-Mo steels and FIRD austenitic stainless steels similar to type 316 stainless steel.

1.3.5 Ferritic Steels

The Cr-Mo ferritic steels are of two types: (1) those that basically contain only Cr, Mo, and C, and (2) those that contain these elements plus one or more of the strong carbide formers* Nb, V, Ti, and W (ref. 4). As an example of the first type, we can consider 2 1/4 Cr-1 Mo steel. This steel was an outgrowth of the C-Mo steels, with the chromium added to improve ductility, decrease the tendency toward graphitization, and provide oxidation and corrosion resistance at elevated temperature. Much of

*These are the elements that give strength to the Cr-Mo steels through the formation of carbides. The commercial steels generally also contain up to 0.5% Mn, 0.4% Si, 0.5% Ni, plus small amounts of impurity elements.

the elevated-temperature strength in this alloy is provided by a dispersion of Mo_2C;[5] molybdenum also provides solid solution strengthening. Several other carbides also form,[6] including M_3C, M_7C_3, $M_{23}C_6$, and M_6C. After prolonged exposure at elevated temperature, only $M_{23}C_6$ and M_6C remain. The addition of 0.25% V to 2 1/4 Cr-1 Mo steel has a pronounced effect on the precipitate formed and thus on the elevated-temperature properties.[7] In addition to the Mo- and Cr-rich carbides, V_4C_3 appears. The fine dispersion of this precipitate provides improved creep strength.

The high-chromium Cr-Mo steels have attracted attention for fusion reactor applications.[8,9] Steels with 9 or 12% Cr and 1% Mo are presently being investigated. Without the addition of a strong carbide-forming element, $M_{23}C_6$ precipitate forms in these high-chromium steels.[9] When vanadium is added, $M_{23}C_6$ is still the predominant precipitate and the only precipitate present at equilibrium.[10] However, the addition of vanadium leads to a finer, more stable $M_{23}C_6$, which increases the elevated-temperature strength. Small amounts of niobium and titanium added to these steels lead to the formation of niobium- and titanium-rich MC-type carbides, in addition to $M_{23}C_6$ (refs. 10 and 11). Evidently these alloying elements are not as readily absorbed in the $M_{23}C_6$ as is vanadium. The formation of a fine dispersion of these precipitates at the service temperature can lead to improved strength, although a reduced ductility can also result. A small amount of tungsten (~0.5 wt. %) added to the high-chromium Cr-Mo steels has a minor effect on strength, probably caused by solid-solution effects.[12,13]

1.3.5.1 Alloy Composition Selection

If the objective in developing a FIRD alloy is the replacement of molybdenum in the Cr-Mo steels with an element that will lead to dispersion strengthening, vanadium would appear to be a logical choice. Just as the Cr-Mo steels evolved from the Fe-Mo-C steels, which develop their strength from molybdenum carbides, a similar progression from Fe-V-C would seem possible. Indeed, a 2 1/4 Cr-1.5 V steel has been proposed as a FIRD alloy.[14]

Considerable research has been conducted on Fe-V-C steels, which develop their elevated-temperature strength by the formation of V_4C_3 (refs. 15–17). Two types of heat treatment have been considered for these steels. First, a conventional quench-and-temper or normalize-and-temper heat treatment procedure can be used to form a tempered martensite that contains the V_4C_3. A second possibility that has been studied in recent years is the use of a direct transformation. In this process, a ferrite and fine carbide microstructure can be developed with superior properties to a quenched-and-tempered product. By the direct transformation, which is most easily obtained by an isothermal treatment, a fine interphase precipitate of V_4C_3 is formed rather uniformly throughout the ferrite. (An interphase precipitate is one that forms in conjunction with the movement of the austenite-ferrite boundary during transformation.) There have been studies to determine how an interphase precipitate could be developed in a continuous cool (as opposed to an isothermal transformation) from the austenitizing temperature — a probable necessity for a commercial steel. One way to accomplish this is by the addition of nickel or manganese to the steel (however, nickel should be avoided for a FIRD alloy).

Because any ferritic steel developed for fusion reactor applications should have properties that allow it to be used to 500–550°C, the alloy will undoubtedly need to contain chromium for oxidation and corrosion resistance. Little information is presently available on the effect of chromium on the Fe-V-C steels. The major effect of chromium is the appearance of the chromium-rich carbides in the precipitation sequence. Which carbides form will depend on the vanadium and chromium concentrations; an equilibrium structure of either V_4C_3 and M_7C_3 or V_4C_3 and $M_{23}C_6$ would be expected for vanadium and chromium concentrations of probable interest (0–1% V and 2–12% Cr) (refs. 18 and 19). Chromium could also change the precipitate morphology that results in a direct transformation. Instead of a fine interphase precipitate distributed uniformly throughout the microstructure, chromium may promote the formation of a fibrous precipitate, usually consisting of carbide fibers 30–50 nm in diameter spaced about 30–50 nm apart.[16] (The precipitation sequence for such carbides appears similar to the process by which pearlite forms.) The effect of such a precipitate morphology on mechanical properties is not known, although the properties are not expected to be as favorable as those of a fine interphase precipitate.

Any alloy development program should concentrate on alloys in a normalized-and-tempered or quenched-and-tempered condition (i.e., avoid the direct transformation route, at least initially). If vanadium is to replace molybdenum in Cr-Mo a start should be made with 0.25 and 0.5 wt % V in steels with 2–2.5% Cr (less vanadium is required because the molecular weight of vanadium is about one-half that of molybdenum). Vanadium is sometimes thought to make a steel less weldable. For that reason less than 0.15% C should be used; it may also be of interest to investigate the effect of carbon (say 0.1 and 0.15% C alloys).

Because of the large uncertainty with the development of Cr-V steels, the Cr-W steels may offer a better possibility for the development of a replacement for Cr-Mo steels. Tungsten is in the same group of the periodic table and displays several similarities to molybdenum when it is used as an alloying element. All indications are that Fe-W-C alloys develop analogous precipitates with similar precipitation sequences to Fe-Mo-C alloys (i.e., both form M_2C and M_6C of similar morphology, etc.).[16] Tungsten and molybdenum also show similar solid-solution hardening characteristics.[16] One important difference involves the diffusion of the two atoms: the tungsten diffusivity is substantially less than that of molybdenum. This results in a slower developing secondary hardening peak for a tungsten steel; however, the tungsten steel does not overage as rapidly. (It should be noted that the secondary hardening peak for a tungsten steel is not as large as that for a comparable molybdenum steel.) This similarity of tungsten and molybdenum suggests an initial composition of 2–2.5% Cr–2% W steel (2 wt % W is required to obtain an atomic concentration similar to that for 1 wt % Mo).

Table 1.3.3 lists ferritic and martensitic steels for a "first cut" in a FIRD alloy development program. These include the Cr-V, Cr-W, and Cr-W-V steels discussed above. The 9% Cr–2% W–0.25% V and 12% Cr–2% W–0.25% V steels are added for comparison with the modified 9 Cr-1 MoVNb and 12 Cr-1 MoVW (HT9) steels currently under study in the fusion reactor alloy development program. A suitable substitute for the 0.06% Nb in the 9 Cr-1 MoVNb steel may be 0.12% Ta in the 9% Cr–2% W–0.25% V steel. Tantalum is in the same group of the periodic table as niobium and often displays analogous properties to niobium.

Table 1.3.3. Possible ferritic steels for Fast Induced Radioactivity Decay (FIRD) Alloy Development Program

Alloy	Chemical composition (wt %)[a]			
	Cr	V	W	C
2 1/4 Cr-1/4 V	2–2.5	0.25		0.1–0.15
2 1/4 Cr-1/2 V[b]	2–2.5	0.5		0.1–0.15
2 1/4 Cr-2 W	2–2.5		2	0.1–0.15
2 1/4 Cr-1 W-1/4 V	2–2.5	0.25	1	0.1–0.15
2 1/4 Cr-2 W-1/4 V	2–2.5	0.25	2	0.1–0.15
5 Cr–2 W-1/4 V	5	0.25	2	0.1–0.15
9 Cr–2 W-1/4 C[c]	9	0.25	2	0.1–0.15
12 Cr–2 W-1/4 C	12	0.2	2	0.1–0.15

[a]Balance iron.

[b]Alloys with 0.08 and 0.15% C should be tested.

[c]An alloy with 0.12% Ta should be considered to complete the analogy with 9 Cr-1 MoVNb steel.

We propose to develop the FIRD ferritic steels based on 2 1/4% Cr instead of the 9 and 12% Cr used in the alloys presently of primary interest to the fusion program. This choice of 2 1/4% Cr is based on an analysis of our present understanding of Cr-Mo steels. The 9 and 12% Cr steels were chosen because of their excellent swelling resistance in the breeder reactor program. However, the proposed breeder reactor applications involve service conditions considerably different from those presently envisioned for fusion reactors. Because of these differences, we previously recommended that 2 1/4 Cr-1 Mo steel should be strongly considered for fusion reactor applications.[4] The reasons for this recommendation included the operating temperatures of proposed fusion reactor designs, possible advantages in welding the low-chromium steel, and conservation of a strategic material.[4] The swelling resistance of 2 1/4 Cr-1 Mo steel has been found to be equivalent to that of high-chromium steels when they have been compared in ion-irradiation studies.[4]

Chromium in excess of about 2% does not affect the elevated-temperature strength,[10] and with this amount of chromium, oxidation resistance is adequate for service to about 600°C. Chromium content will affect the hardenability, but for fusion reactor applications where relatively thin sections are to be used, this effect should not prove important. One of the reasons the 9 and 12% Cr steels are often assumed to be superior to 2 1/4 Cr-1 Mo steel is that the long-time elevated-temperature strength of the high-chromium Cr-Mo steels containing V, Na, or Ti are compared with 2 1/4 Cr-1 Mo without any of these strong carbide formers added. Whenever the elevated-temperature strength of 9 Cr-1 Mo and 12 Cr-1 Mo without vanadium or niobium are compared with 2 1/4 Cr-1 Mo (all with similar microstructures), little difference is observed.[10] At higher temperatures, above 600°C, adequate oxidation resistance will be possible only with the higher chromium steels.

There might well be an advantage for a low-chromium Cr-Mo-V steel, for when the Cr-Mo-V-C diagrams of Smith[18] are consulted for a 1% Mo–0.25% V–0.1% C steel with 2 1/4% Cr and for the 9 and 12% Cr steels, different carbides are predicted for equilibrium at 700°C. The M_4C_3 (V_4C_3) and M_7C_3 carbides are present in the 2 1/4% Cr steel, and only $M_{23}C_6$ is present for the two high-chromium steels. The $M_{23}C_6$ carbide is generally a coarser carbide than M_4C_3 and M_7C_3, although as noted above, vanadium stabilizes a finer precipitate. This possible difference in carbides that occurs with varying chromium concentration does not seem to have been systematically investigated, even though the Japanese Steel Works has recently introduced a modified 2 1/4 Cr-1 Mo steel in which 0.25% V and 0.02% Ti have been added.[7]

Although the proposed alloy development scheme summarized in Table 1.3.3 emphasizes 2 1/4 Cr, we also propose to investigate the effect of chromium. These studies are necessary because the above arguments relative to chromium will only apply if molybdenum and tungsten behave in a completely analogous manner.

Comparative studies on the 9 Cr-1 MoVNb and 12 Cr-1 MoVW steels that are presently being considered for fusion reactor applications have indicated differences in the long-time elevated-temperature strength, with the 9 Cr-1 MoVNb steel the stronger.[20] This difference may be due to the niobium in the 9% Cr steel, because at equilibrium fine MC carbides are observed in this steel, in addition to $M_{23}C_6$ (ref. 10). Only the $M_{23}C_6$ is observed in the 12 Cr-1 MoVW steel.[10,18,19] Although niobium must be eliminated in a FIRD steel, tantalum is often analogous to niobium. This is the basis for suggesting a tantalum addition (Table 1.3.3).

As noted above, the Japanese Steel Works added titanium to its modified 2 1/4 Cr-1 Mo steel. Titanium in steels at about 0.02% is known to prevent grain coarsening in the weld heat-affected zone during high-heat-input welding, thus assuring good notch toughness. Such titanium additions may be useful in the FIRD alloy development program. There is also evidence that a low-carbon 2 1/4 Cr-1 Mo steel with about 0.14% Ti has creep properties superior to those of commercial 2 1/4 Cr-1 Mo steel. If the 2 1/4 Cr-2 W and/or the 2 1/4 Cr-2 W-0.25 V steels should have favorable properties, the addition of titanium to one or both of these compositions should be considered.

1.3.5.2 Alloy Development Strategy

Any alloy developed for fusion reactor applications must be thoroughly tested in a suitable irradiation environment. However, before any detailed irradiation studies are conducted, it is necessary to understand the unirradiated behavior and to compare that behavior with the reference alloys that are presently candidates for fusion reactor applications (i.e., the developmental steel must be compared with 2 1/4 Cr-1 Mo, 9 Cr-1 MoVNb, and 12 Cr-1 MoVW steels). Information will be required on the physical metallurgy (e.g., precipitate type, precipitation kinetics), fabricability, weldability, elevated-temperature strength, impact properties, compatibility, and other properties. Once alloys with satisfactory unirradiated properties are obtained, detailed irradiation effects studies will be required.

Information on the physical metallurgy of the new steels will come from heat-treatment studies to determine the phases developed when quenched, normalized, tempered, and aged. Hardness measurements and optical- and electron-microscopy studies will be used to study phase stability. Analysis of carbide extractions may also prove useful.

Fabricability will be determined in the normal melting, casting, and rolling operations necessary to obtain the sheet that will be used to make TEM and mechanical-property specimens. A simple weldability test should also be performed; perhaps Varistraint and/or guide-bend tests could be used for early qualifications.

Elevated-temperature tensile properties of prospective FIRD ferritic steels will be required. Creep properties will also be needed to define upper temperature limits for the alloys. Comparison with results on presently available steels will provide a relative assessment of the elevated-temperature behavior.

Ferritic steel may be useful only in a temperature window with a lower temperature limit determined by the toughness and impact properties and an upper limit governed by compatibility limits or elevated-temperature strength. The impact properties are known to be affected by irradiation. For example, the ductile-brittle transition temperature (DBTT) of 12 Cr-1 MoVW steel was found to increase by 108°C during irradiation in EBR-II at 419°C to 1.1×10^{26} neutrons/m^2 (ref. 21); this was accompanied by a decrease in the upper-shelf energy. There is a question about whether the magnitude of the shift is fixed and whether the final value depends on the value of the unirradiated steel. Any FIRD alloy development program will need to consider the impact properties of the proposed alloys. These properties will need to be determined, and the properties should be at least as good as those of present candidate ferritic steels.

Finally, it will be necessary to determine the compatibility of these steels with potential coolant and breeding materials (i.e., water, helium, lithium, lead-lithium alloys, and solid lithium ceramics). Because there is no change in the chromium concentration between these steels and the Cr-Mo steels, little difference in compatibility is expected. Nevertheless, comparative tests will be necessary.

1.3.6 Austenitic Stainless Steels

Type 316 stainless steel and modifications of that basic alloy composition (e.g., by the adjustment of chromium and nickel contents and the addition of titanium) are presently the primary austenitic stainless steels under consideration for fusion reactor structural applications.[22] The alloy development approach to be followed here will be similar to that followed for the ferritic steels. An attempt will be made to develop an austenitic steel patterned on type 316 stainless steel, which is presently a candidate alloy. Once a base alloy is developed, improvements will be sought in the manner presently being used to develop a prime candidate austenitic alloy (PCA), which is being developed as a variation on type 316 stainless steel.[22] Of the elements that are contained in those alloys, nickel and molybdenum are not acceptable in a FIRD alloy. Manganese, like nickel, is an austenite-forming element and has often been used as a replacement for nickel.[23-27] However, the austenite-forming tendency of manganese is considerably less than that of nickel, and the development of an Fe-Cr-Mn stainless steel does not follow simply by replacing nickel with manganese.

Other common austenite-forming alloying elements include C, N, Cu, and Co. The carbon concentration will be maintained at 0.05 to 0.1% to minimize corrosion problems. To meet the 10CFR61 waste-storage criteria for Class C waste,[2] the nitrogen concentration cannot exceed 3650 at. ppm (~0.09 wt. %). Thus, small nitrogen additions may be possible. The decay of radioactive daughter elements produced by the irradiation of copper in a fusion reactor makes it unsuitable for FIRD alloys (Table 1.3.2).

Cobalt presents an interesting possibility. As an austenite stabilizer, it is as strong as nickel.[28] Its radioactive decay characteristics are such that it is not forbidden in Class B or Class C waste by 10CFR61 (ref. 2). However, immediately after irradiation, steels containing cobalt emit high-energy gamma rays that make the steels difficult to handle. Thus, even though cobalt could improve the possibility of developing a FIRD stainless steel, it would make irradiation studies extremely difficult or impossible. For that reason, cobalt will be considered an unsuitable alloy addition for this discussion.

1.3.6.1 Alloy Composition Selection

The idea of using the less expensive manganese to replace nickel in austenitic stainless steels has appeal and has been investigated quite extensively,[23-27] mainly in the 1930s and 1940s. Although manganese is used to replace some nickel in the 200-series stainless steels, the lower austenite-forming capability of

manganese is offset by the addition of up to 0.25% N. The only Cr-Mn stainless steels that appear to have been used commercially were used in Germany.[24] These were an 8 Cr-18 Mn and an 18 Cr-8 Mn alloy, both containing 0.1% C. The first alloy was entirely austenite (because of the low chromium concentration), while the second contained ~40% ferrite. The low chromium concentration of the first means it has relatively low oxidation and corrosion resistance, while the high ferrite content of the second means it will be prone to sigma-phase formation, both reasons making the alloys unsuitable for elevated-temperature service. In addition to these two reasons why the development of manganese-stabilized (nickel-free and low-nitrogen) stainless steels has never been actively pursued, another reason is that the increased manganese leads to decreased corrosion resistance by sulfuric, hydrochloric, and nitric acids.[29,30]

There have been more-recent studies on the effect of manganese on properties and as an austenite stabilizer.[29-33] Manganese lowers the stacking-fault energy and therefore increases the rate of work hardening.[30] This could lead to problems in fabrication. It also lowers the thermal conductivity relative to nickel,[31] a disadvantage for fusion-reactor applications. The reduced oxidation resistance of Cr-Mn steels at elevated temperatures should not prove limiting if the maximum temperature is limited to about 600°C.

Recently, Desforges and Dancoisne[33] investigated a large number of manganese-containing ferrous alloys. Because of the low austenite-stabilizing capacity of manganese, most of the alloys proved to be magnetic (i.e., they contained some ferrite or martensite), including an Fe–14% Cr–15% Mn steel. Of the 18 manganese-containing alloys melted and cast, only three were nonmagnetic. One of these contained 5% Ni, another 2% Cu. Because copper is generally considered a weaker austenite stabilizer than manganese, the copper could presumably be replaced by manganese and retain the austenite microstructure. However, this Fe–11% Cr–15% Mn–2 Cu alloy suffered from hot shortness when worked. The only other nonmagnetic alloy was an Fe–8% Cr–2% Al–15% Mn steel. This steel had reasonably good oxidation resistance to 600°C. The steel had excellent tensile properties relative to the other steels when tested in the cold-rolled condition. After a solution anneal at 900 or 1100°C, it was one of the weakest as measured by the 0.2% offset yield stress; the ultimate tensile strength was similar to that for most of the other steels.

Although the early work on the ternary phase diagrams for Fe-Cr-Mn would indicate that a steel containing 15% Cr and 15% Mn would be entirely austenite but near the α-γ phase boundary, there is little guidance available when other elements such as carbon are added. A common method used to represent the phases present in Cr-Ni stainless steels is a Schaeffler diagram[28] (Fig. 1.3.1), in which the phase fields expected at room temperature are shown in terms of nickel and chromium equivalents. The nickel and chromium equivalents have been determined empirically for the most common alloying elements, including manganese.[28] The equations that apply to Fig. 1.3.1 are given by

$$\text{Cr Equiv} = (\text{Cr}) + 2(\text{Si}) + 1.5(\text{Mo}) + 5(\text{V}) + 5.5(\text{Al}) + 1.75(\text{Nb}) + 1.5(\text{Ti}) + 0.75(\text{W}) \quad (1)$$

$$\text{Ni Equiv} = (\text{Ni}) + (\text{Co}) + 0.5(\text{Mn}) + 0.3(\text{Cu}) + 2.5(\text{N}) + 30(\text{C}) \quad (2)$$

where ( ) is the concentration expressed in weight percent. According to Eq. (2), manganese is only half as effective as nickel in stabilizing austenite.

The Cr and Ni equivalents were calculated for several alloy compositions (Table 1.3.4), and the positions of these steels are shown in Fig. 1.3.1. Of interest is the fact that the 15-15 steel (15% Cr, 15% Mn, 0.1% C) and the 12-15 steel (12% Cr, 15% Mn, 0.1% C) are in the austenite-plus-martensite field. The phase diagram indicates that such alloys should be entirely austenite.[25-27] A 12-20 steel falls in the austenite-plus martensite region while a 15-20 steel lies just outside this field in the austenite field. Contrary to expectations, the diagram indicates that an increase in chromium from 12 to 15% (with 20% Mn) leads to an austenitic steel.

Also shown in Table 1.3.4 and Fig. 1.3.1 are data for type 316 stainless steel and two experimental steels. The EP-838 is a Russian steel in which much of the nickel from a Cr-Ni-type stainless steel such as type 316 was replaced by manganese. To help maintain austenite, the chromium and molybdenum were reduced from the amounts of these elements in type 316 stainless steel. This steel is in the austenite region. The Cr-Mn steel

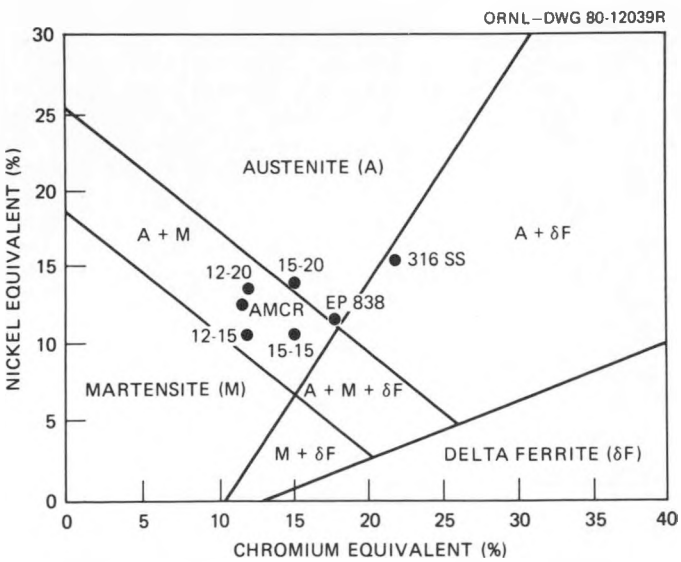

Fig. 1.3.1. Schaeffler diagram with points for various steels superimposed. For the double numbers the first number is the weight percent chromium, the second weight percent manganese (e.g., 12–15 is 12% Cr and 15 Mn); all are assumed to have 0.1% C. AMCR is 10% Cr–17.5% Mn–0.11% C, EP-838 is 11.6% Cr–13.5% Mn–4.2% Ni–0.9% Mo–0.02% C, and 316 SS is 17.3% Cr–1.7% Mn–12.5% Ni–2.1% Mo–0.06% C.

designated ACMR is a steel being studied by the European Communities fusion program as a possible FIRD steel.[34] Although no information is presently available for this material, we would expect it to be austenitic, while the Schaeffler diagram predicts otherwise. Further difficulties with the diagram are found when the three nonmagnetic steels of Desforges and Dancoisne are referred to the diagram.[33] None of them was found to fall in the austenite region (or near a boundary).

Table 1.3.4. Chromium and nickel equivalents for several commercial and experimental steels

Alloy	Composition (wt %)							Equivalent	
	Cr	Mn	Ni	Mo	Si	Al	C	Ni	Cr
316 SS	17.3	1.7	12.4	2.1	0.7		0.06	15.0	21.9
15-15	15	15					0.10	18.0	15.0
12-15	12	15					0.10	18.0	12.0
15-20	15	20					0.10	23.0	15.0
EP-838	11.6	13.5	4.2	0.9	0.4	0.7	0.02	11.6	17.6
AMCR	10.1	17.5	0.10		0.55		0.11	12.2	11.2

These inconsistencies between phase diagrams and experimental results with the Schaeffler diagram indicate that the words of Desforges and Dancoisne are appropriate. They wrote:[33]

> A Schaeffler constitution diagram for manganese-containing steels would be of great value in providing designers and welding engineers with the necessary information on weld metal microstructure.

And, it might be added, base metal microstructure.

There have been various studies that indicate that the 0.5 multiplier for manganese in Eq. (2) may be an overestimate of manganese's austenite-stabilizing effect.[35] One study indicated that the effect of manganese may be a constant with a value of 0.35 (ref. 35). However, such a low value does not seem reasonable in light of the above discussion. Thus, it appears that much still needs to be learned about the effect of manganese in austenitic steels. The Schaeffler diagram, as now constituted, would appear to be of little help in developing manganese-stabilized austenitic steels.

Molybdenum is present in type 316 stainless steel to enhance the corrosion resistance against chlorides and pitting as well as improving the high-temperature mechanical properties. It is not known whether tungsten, which is analogous to molybdenum in ferritic steels, would achieve the same effect as molybdenum in these steels. However, tungsten is a ferrite former, and in a Cr-Mo steel would probably have to replace chromium if a duplex structure was to be avoided.

The strength of the Fe-Cr-Mn steels is of some concern. We have recently determined the strength of the Russian steel designated EP-838.[36] (The composition is given in Table 1.3.4). The tensile properties of this steel in the 20%-cold-worked condition at room temperature and 300°C are similar to those of

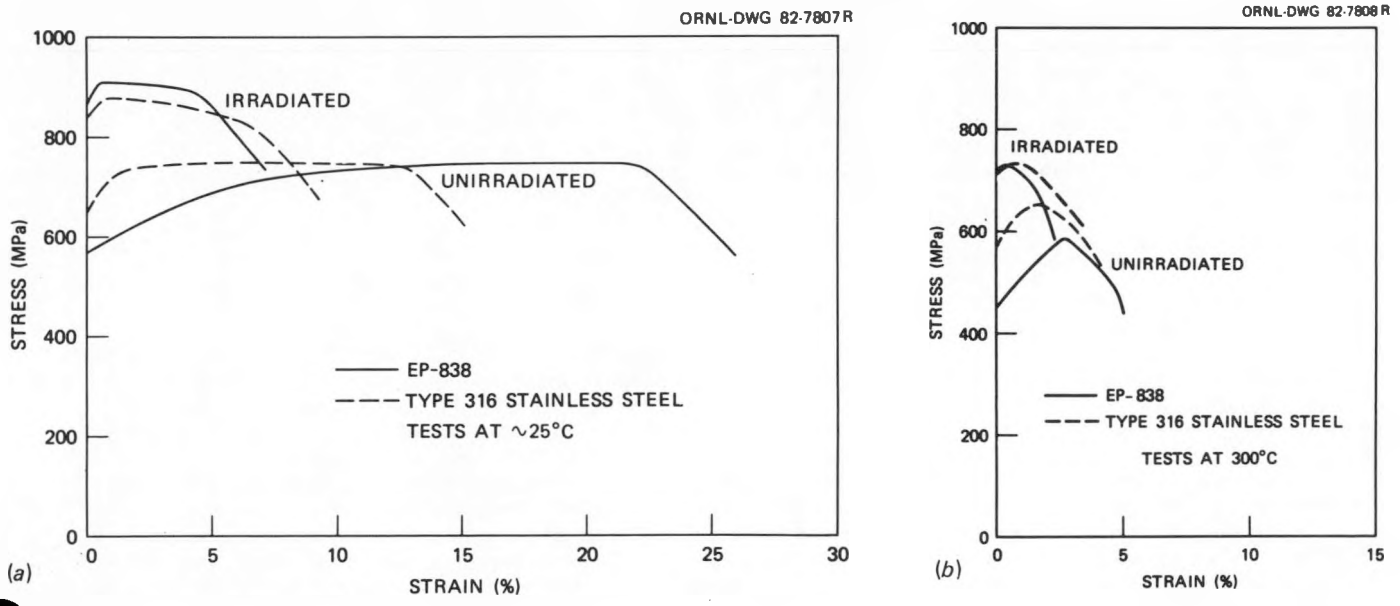

Fig. 1.3.2. Engineering stress-strain curves at (*a*) room temperature and (*b*) 300°C for unirradiated and irradiated 20%-cold-worked EP-838 and type 316 stainless steels. Irradiation was in HFIR at ~50°C to ~5 to 8 dpa.

20%-cold-worked type 316 stainless steel (Fig. 1.3.2). The effect of manganese on the work-hardening capacity is evident, especially in the room-temperature tests. After irradiation to a displacement-damage level of 5-8 dpa, the properties of the two steels were also similar. These two steels also have similar tensile properties in the solution-annealed condition before and after irradiation.[37] From these results it appears that manganese could be used to replace a large portion of the nickel and at the same time the chromium and molybdenum concentrations could be reduced without affecting the strength. No information is available on the effect of the reduced amounts of chromium and molybdenum on corrosion resistance.

The major concerns with austenitic steels for fusion-reactor applications involve void swelling,[38] helium embrittlement,[39] and compatibility with coolants. The void and dislocation structure that develops during irradiation in the temperature range 0.35 to 0.6 times the absolute melting point of the steel can lead to large volume increases, which could not be tolerated in a structural component. The large amounts of transmutation helium that will be generated in a fusion reactor first-wall structure are known to affect void nucleation and growth.[38] In addition, above half the absolute melting point, small amounts of helium at grain boundaries lead to embrittlement.[39]

Methods being tested for the suppression of void swelling are to use a high dislocation density (cold work) and/or a high density of fine titanium carbide precipitates (MC precipitates) in the microstructures.[40] The dislocations and precipitates act as helium-collection sites, giving rise to a high density of fine cavities that subsequently act as preferential sinks for the vacancies and interstitials produced during irradiation. The MC carbides on grain boundaries also impart resistance to helium embrittlement at elevated temperatures. The application of these principles has led to an austenitic prime candidate alloy (PCA) for fusion reactors;[40] this alloy with 14% Cr, 16% Ni, 2% Mo, and 0.25% Ti is presently being irradiated and tested. In addition to helping control the helium and minimize the swelling, the MC also strengthens by precipitate hardening. The similar use of titanium in a manganese-stabilized austenitic steel would appear appropriate to provide swelling resistance and additional strength. It should be noted, however, that titanium is a ferrite stabilizer, and the formation of TiC would eliminate carbon from solution and thus negate its role as an austenite stabilizer.

The above considerations indicate that the development of a FIRD austenitic steel will be more complicated than that of a ferritic steel. The first step in a developmental program must be the determination of a stable composition for a Cr-Mn steel. In order to obtain an indication of the limits of austenitic phase stability, small heats with the compositions given in Table 1.3.5 are proposed. The phase stability of the proposed steels will be determined by optical microscopy following solution-anneal and thermal-aging treatments.

After a stable composition is determined, it will be necessary to adjust the composition for swelling resistance, strength, and compatibility with possible breeding and cooling media. Experience with type 316 stainless steel and improvements made when the PCA was developed suggests the addition of Ti, Si, and W (as a substitute for Mo). The development of PCA was aided by the knowledge previously obtained on processes such as solute segregation during cavity growth and the effect of different precipitates on nucleation and growth of cavities (e.g., the difference between MC and $M_{23}C_6$).[40] The substitution of manganese for nickel could well alter these processes, thus making necessary detailed studies of the new alloy system. Note also that Ti, W, and Si are ferrite stabilizers. Even if a phase-stable quaternary alloy is obtained from the initial studies, that stability may be jeopardized by the addition of these elements, and further compositional adjustments and stability studies will be required.

Table 1.3.5. Possible austenitic stainless steels for Fast Induced Radioactivity Decay (FIRD) Alloy Development Program

Alloy	Chemical Composition, wt %[a]			
	Cr	Mn	C	N
15 Cr–15 Mn	15	15	0.05–0.1	<0.01
15 Cr–20 Mn	15	20	0.05–0.1	<0.01
10 Cr–15 Mn	10	15	0.05–0.1	<0.01
10 Cr–20 Mn	10	20	0.05–0.1	<0.01

[a]Balance iron.

1.3.6.2 Alloy Development Strategy

Once an austenitic-stable alloy composition is identified, the strength of the alloys will have to be determined in the cold-worked and solution-annealed conditions in an effort to get alloys with strengths comparable to those of type 316 stainless steel. Tensile properties should be adequate for the initial comparisons. Because the life limitation on the austenitic stainless steels is their propensity to swell during irradiation, samples of these alloys should be irradiated to high fluences. Swelling measurements can be used to compare the behavior of the new alloy with type 316 stainless steel and PCA.

Information on fabricability will be obtained during the melting, casting, and rolling operations necessary to obtain test material. Simple weldability tests can be conducted on the steels that evolve from the first series of alloys. Compatibility tests with potential cooling and breeding media (e.g., Li, Pb-Li, and solid lithium ceramics) may prove extremely important for this class of alloys. A large reduction of chromium and the elimination of molybdenum may well have a large effect on the compatibility of this class of steel.

1.3.6.3 Other Austenitic Alloys

Several Japanese steel companies have developed high-manganese, low-chromium austenitic steels. However, most of these either contain nickel and/or nitrogen content above the limits given by 10CFR61 and thus do not qualify as FIRD alloys. An exception is a steel by Nippon Kokan designated NM-1, which contains 20% Mn, 2% Cr, 0.5% C, and 0.5% Si. Of course, this steel is not "stainless" and as such does not fit the criteria established above when the types of alloys to be developed were discussed. Nevertheless, this alloy might be used to define another class (low-Cr, Cr-Mn steel) of FIRD steels to be considered should those discussed above not prove adequate. Indeed, in the alloy development approach suggested above, this class of steels is one of the limits being approached.

1.3.7 Conclusions

If a future fusion reactor could be constructed from a material that develops little or no induced radioactivity during service, a reactor more acceptable to the public and the utility industry would result, one that would allow for hands-on maintenance and would minimize radioactive waste-disposal problems. No structural materials are presently available to construct such a reactor. However, it appears possible to develop alloys that have relatively fast induced-radioactivity decay (FIRD), which would simplify the radioactive waste-disposal problem. An approach to developing such alloys has been presented.

The Cr-Mo ferritic (martensitic) steels and the austenitic stainless steels (primarily type 316) are presently leading candidate structural materials for fusion reactors. These steels do not qualify as FIRD alloys primarily because of the molybdenum and nickel contents (nitrogen and niobium must be kept to extremely low concentrations). An alloy development approach has been outlined where substitutions could be made for these elements in the Cr-Mo steels and austenitic steels and yet maintain properties similar to the parent steels. For steels with properties analogous to the Cr-Mo steels, the substitution of tungsten for molybdenum appears straightforward. To induce dispersion strengthening, the addition of vanadium is also possible, and titanium and tantalum additions may also be valuable. The production of austenitic steels in which nickel is replaced by manganese may be possible, although this may prove much more difficult than the development of a FIRD ferritic steel. This difficulty arises because manganese is not as strong an austenite stabilizer as nickel.

1.3.8 References

1. R. W. Conn et al., *Panel Report on Low Activation Materials for Fusion Applications*, UCLA Report PPG-728, University of California at Los Angeles, June 1983.
2. Nuclear Regulatory Commission, "Licensing Requirements for Land Disposal of Radioactive Waste," 10CFR Part 61, *Fed. Regist.* 47(248), 57446–82 (Dec. 27, 1982).
3. F. W. Wiffen and R. T. Santoro, "Control of Activation Levels to Simplify Waste Management of Fusion Reactor Ferritic Steel Components," in *Ferritic Alloys for Use in Nuclear Technologies*, to be published.
4. R. L. Klueh, "Chromium-Molybdenum Steels for Fusion Reactor First Walls — A Review," *Nucl. Eng. Design* 72, 329–44 (1982).
5. K. J. Irvine, J. D. Murray, and F. B. Pickering, "Structural Aspects of Creep-Resisting Steel," pp. 246–75 in *Structural Processes in Creep*, Iron and Steel Institute, London, 1961.
6. R. G. Baker and J. Nutting, "The Tempering of 2 1/4 Cr–1 Mo Steel After Quenching and Normalizing," *J. Iron Steel Inst., London* 192, 257–68 (1959).
7. T. Ishiguro et al., "A 2 1/4 Cr-1 Mo Pressure Vessel Steel with Improved Creep Rupture Strength," pp. 129–47 in *Application of 2 1/4 Cr-1 Mo Steel for Thick-Wall Pressure Vessels*, ASTM STP 755, ed. G. S. Sangdahl and M. Semchyshen, American Society for Testing and Materials, Philadelphia, 1982.
8. S. N. Rosenwasser et al., "The Application of Martensitic Steels in Long Lifetime Fusion First Wall/Blankets," *J. Nucl. Mater.* 85&86, 177–82 (1979).
9. S. D. Harkness and B. Cramer, "A Review of Lifetime Analyses for Tokamaks," *J. Nucl. Mater.* 85&86, 135–45 (1979).
10. J. Orr, F. R. Beckitt, and G. D. Fawkes, "The Physical Metallurgy of Chromium-Molybdenum Steels for Fast Reactor Boilers," pp. 91–109 in *Ferritic Steels for Fast Reactor Steam Generators*, vol. 1, British Nuclear Energy Society, London, 1978.
11. J. M. Vitek and R. L. Klueh, "Precipitation Reactions During the Heat Treatment of Ferritic Steels," *Metall. Trans.* 14A, 1047–55 (1983).
12. L. Egnell and N. G. Persson, "On the Creep Properties of Sandvik HT7 and HT9," pp. 212–16 in *Ferritic Steels for Fast Reactor Steam Generators*, vol. 1, British Nuclear Energy Society, London, 1978.
13. G. Oakes, J. Orr, and P. W. Taylor, "The Effect of Tungsten on the Tensile and Creep Rupture Strength of 12CrMoV Steels," pp. 222–27 in *Ferritic Steels for Fast Reactor Steam Generators*, vol. 1, British Nuclear Energy Society, London, 1978.
14. N. M. Ghoniem, A. Shabiak, and M. Y. Youssef, "Development of a 'Low-Activation' Vanadium Steel for Fusion Applications," in *Ferritic Alloys for Use in Nuclear Energy Technologies*, to be published.
15. A. D. Batte and R. W. K. Honeycombe, "Precipitation of Vanadium Carbide in Ferrite," *J. Iron Steel Inst., London* 211, 284–95 (1973).
16. R. W. K. Honeycombe, *Structure and Strength of Alloy Steels*, Climax Molybdenum Company, London, 1974.

17. P. R. Wilyman and R. W. K. Honeycombe, "Relation Between γ-α Transformation Kinetics and Mechanical Properties of Vanadium Steels," *Met. Sci.* 16, 295–303 (1982).
18. R. Smith, "Fe-Cr-Mo-V Constitution Diagrams," pp. 307–11 in *Precipitation Processes in Steels*, Special Report 64, Iron and Steel Institute, London, 1959.
19. K. W. Andrews, H. Hughes, and D. J. Dyson, "Constitution Diagrams for Cr-Mo-V Steels," *J. Iron Steel Inst., London* 210, 337–50 (1972).
20. V. K. Sikka, C. T. Ward, and K. C. Thomas, "Modified 9 Cr-1 Mo Steel – An Improved Alloy for Steam Generator Application," pp. 65–84 in *Ferritic Steels for High-Temperature Applications*, American Society for Metals, Metals Park, Ohio, 1983.
21. F. A. Smidt, J. R. Hawthorne, and V. Provenzano, "Fracture Resistance of HT-9 After Irradiation at Elevated Temperature," pp. 269–84 in *Effects of Irradiation on Materials*, ASTM STP 725, American Society for Testing and Materials, Philadelphia, 1981.
22. P. J. Maziasz et al., "Progress in Alloy Development in the Fusion Materials Program," *J. Nucl. Mater.* 108&109, 296–98 (1982).
23. J. H. G. Monypenny, *Stainless Iron and Steel*, vol. 2, Chapman & Hall, London, 1954, pp. 261–99.
24. S. Gunzberg, N. A. Aleksandrova, and L. S. Geldermann, "Eigenschaften von Nichtrostenden Chrom-Mangan und Chrom-Nickel-Mangan Stahlen," *Arch. Eisenhüttenwes.* 8, 121–27 (1934).
25. M. Schmidt and H. Legat, "Hitzebestandige Chrom-Mangan Stahle," *Arch. Eisenhüttenwes.* 10, 297–303 (1936).
26. F. Brühl, "Gefuge und Eigenschaften von Chrom-Mangan Stahlen mit Gehalten bis 1% C, 15% Mn, und 30% Cr," *Arch. Eisenhüttenwes.* 10, 243–55 (1936).
27. C. O. Burgess and W. D. Forgeng, "Constitution of Iron-Chromium-Manganese Alloys," *Trans. AIME* 131, 277–302 (1938).
28. H. Schneider, "Investment Casting of High-Hot-Strength 12-Percent Chrome Steel," *Foundry Trade J.* 108, 562–63 (1960).
29. C. D. Desforges, W. E. Duckworth, and T. F. J. N. Ryan, *Manganese in Ferrous Metallurgy*, The Manganese Centre, Paris, 1976, pp. 67–70.
30. R. A. Lula and W. G. Renshaw, "Corrosion Resistance and Mechanical Properties of Cr-Ni-Mn Stainless Steels," *Met. Prog.* 69, 73–77 (1956).
31. S. J. Carlisle, J. W. Christian, and W. Hume-Rothery, "The Equilibrium Diagram of the System Cr-Mn," *J. Inst. Met.* 76, 195–208 (1949).
32. F. Nair and M. Semchyshen, "Corrosion Resistance of Molybdenum Modified Cr-Ni-Mn Austenitic Stainless Steels," *Corrosion (Houston)* 19, 210–16 (1963).
33. C. D. Desforges and P. L. Dancoisne, "The High Temperature Properties of Manganese Containing Ferrous Alloys," pp. 522–37 in *Environmental Degradation of High Temperature Materials*, vol. 2, Institution of Metallurgists, Northway House, Whetstone, London, 1981.
34. M. L. Grossbeck, Oak Ridge National Laboratory, personal communication to R. L. Klueh, July 1983.
35. E. R. Szmachowski and D. J. Kotecki, "Manganese Effect on Stainless Steel Weld Metal Ferrite," *Weld. J. (Miami)* to be published.
36. R. L. Klueh and M. L. Grossbeck, "Irradiated Tensile Properties of a High-Manganese Austenitic Steel," *J. Nucl. Mater.*, to be published.
37. S. N. Votinov et al., "Effects of Neutron Irradiation on Mechanical Properties of EP-838 and 316 Steels," *Fiz. Khim. Obrab. Mater.* 1981(1) 50–52; also ORNL-TR-4812, 1982.
38. P. J. Maziasz and M. L. Grossbeck, "Swelling, Microstructural Development, and Helium Effects in Type 316 Stainless Steel Irradiated in HFIR and EBR-II," *J. Nucl. Mater.* 103&104, 987–92 (1981).
39. E. E. Bloom, "Irradiation Strengthening and Embrittlement," pp. 295–329 in *Radiation Damage in Metals*, American Society for Metals, Metals Park, Ohio, 1976.
40. P. J. Maziasz and T. K. Roche, "Preirradiation Microstructural Development Designed to Minimize Properties Degradation During Irradiation in Austenitic Steels," *J. Nucl. Mater.* 103&104, 797–802 (1981).

1.4 MAGNETIC FORCES ON A FERROMAGNETIC HT-9 FIRST WALL/BLANKET AND COOLANT PIPE - T. A. Lechtenberg, C. Dahms (GA Technologies Inc.) and H. Attaya (University of Wisconsin)

1.4.1 Task #1.A.1

Define material property requirements and make structural life predictions.

1.4.2 Objective

To calculate the magnetic loads induced on typical fusion reactor first wall components and coolant pipes fabricated at ferrogmagnetic HT-9.

1.4.3 Summary

The GFUN 3D code was used to model the toroidal fields and determine the magnetic body forces on the STARFIRE design for coolant pipes exiting the first wall sector and first wall/blanket modules. The HT-9 coolant pipes were modeled on the basis of a square bar having the same length and material volume as the coolant pipes. The stress analysis was performed using these magnetic forces applied to a pipe of 4 meters length, 8.25 cm O.D., and 0.75 cm thickness by the MODSAP stress analysis code. For the first wall/blanket module, GFUN 3D does not allow full modeling of the complex thin-walled structure or numerous small tubes because of the element aspect ratio limitations. Therefore, to obtain three dimensional loads, a solid homogenous equivalent structure was used.

Results on the coolant pipe show that magnetic stresses are increased if the pipe is moved closer to the TF magnet into the region of higher field gradient. Maximum effective stresses at a pipe distance of 1.4 meter from the center of the TF magnet were calculated to be 33 MPa. This is considered to be at the level in which magnetic forces must be accounted for in design, yet not so high as to be unmanageable. By placing the pipe 0.54 meters closer to the magnet, the maximum of stresses increased to about 107 MPa. However, these can be reduced significantly by simply supporting the pipe in the center or at the location of the largest force. Maximum effect of stresses in the former case are less than 80 MPa. By placing the simple support nearer the end with the maximum force at a distance on the pipe between 1.10 and 1.15 meters, the stresses are estimated to be reduced to even smaller levels of about 27 MPa.

Load calculations for the FW/B modules were performed using the STARFIRE design consisting of 24 blanket sectors each composed of nine individual modules. All sectors were assumed to be equal in size and placed in symmetry with the strong magnetic field planes under the TF coils. The calculations determined that three types of magnetic force would be induced on the blanket sector of the STARFIRE design if HT-9 were used as the first wall/blanket module material. Due to the placement of the sector with respect to the magnetic field gradients, a small force would be pulling the sector upward. The forces less than 0.3 times the weight of the material. A second force would be in the toroidal direction resulting in a self-cancelling system of forces being generated in each module. This force would produce low internal loads in the modules. The third type of force is directed radially inward toward the reactor center and results in equivalent pressures exerted on the internals of the blanket modules. The stresses resulting from these forces can be controlled to the same levels as for other loads such as dead weight. While the supports internal to the breeding blanket were not intended to support a magnetic force such that either a thickening of the walls or the addition of internal walls would decrease the stresses on the structure. Slight design changes, therefore, could accommodate any extra magnetic forces generated.

1.4.4 Progress and Status

1.4.4.1 Introduction

An issue for Path E is the effect of using a ferromagnetic alloy in a device with a high magnetic field. Previous work by Rosenwasser et al[1] and a recent review by Lechtenberg and co-workers[2] showed that the effects of HT-9 on plasma engineering and reactor stability are manageable. This contribution contains the results of an analysis and evaluation of the forces induced on a coolant pipe and a FW/B module made of HT-9 using the STARFIRE tokamak model.

1.4.4.2 Analysis

In order to understand the stresses that might be expected in a tokamak ferromagnetic engineering structure, studies were initiated using the GFUN3D code[3] for magnetic force calculations, and MODSAP[4] for stress calculations. STARFIRE was selected as the functional model, although in this study all material previously assigned as austentic PCA was replaced by HT-9. Thus the magnetic forces due to HT-9 near and within the toroidal field coils could be calculated, and the body forces used to compute the stress.

Coolant Pipe

An analysis was performed on a typical coolant manifold pipe exiting a blanket module on STARFIRE and passing through the toroidal magnetic field. Magnetizations (M) were computed by GFUN throughout a solid

square bar of equal length and volume to that of the actual pipe. Figure 1.4.1 shows the location of the pipe relative to the rest of the reactor components. For the purpose of calculating magnetization, M, the pipe was modeled in GFUN3D as a solid square bar or having equal length and volume to that of the pipe. The magnetic force was calculated by using

$$F = \int_V \frac{Mo \cdot B}{\mu_o} \, dV$$

where F, M , B, μ_0, and V are the total force, the magnetization, gradient of the field, permeability, and material volume respectively. Details of the calculation are described elsewhere[15].

SCHEMATIC SHOWING THE POSITION OF THE MODULE AND PIPE WITH RESPECT TO THE MAGNETS

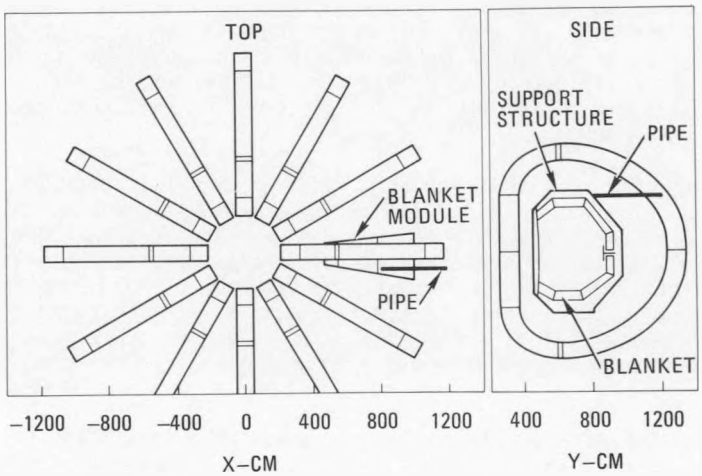

Fig. 1.4.1 Schematic of the location of module and coolant pipe with respect to the toroidal field magnets in (a) top view and (b) side view

The gradient of B, or its equivalent partial derivatives was calculated from GFUN3D by modeling the square bar such that there would be two integration points in directions perpendicular to the bar axis. Thus, at each axial location there were four integration points in a plane perpendicular to the bar axis. This allowed a gradient to be calculated in all three directions of space, thus utilizing the 3-D capabilities of GFUN3D. By taking finite differences between elements and using the equations previously mentioned, approximate force vectors (F_x, F_y, F_z) were calculated at each specified node point. The derived point loads were distributed over the length of pipe. The load distribution was then used in an analysis performed with the computer code MODSAP on a beam having the approximate cross sectional dimensions of the pipe. The pipe's end conditions were assumed fixed and the resultant loads were then used to calculate the effective stresses.

The analysis was performed using a new addendum to the GFUN3D code for calculating magnetostatic forces. Details of the addendum are reported elsewhere.[6] GFUN does not allow full modeling of a complex thin-wall structure, or numerous small tubes, because of element aspect ratio limitations. Therefore, to obtain three dimensional loads a solid homogeneous equivalent structure was used.

First Wall/Blanket Model

The load calculations for the FW/B modules were performed using the STARFIRE design consisting of 24 blanket sectors, each composed of nine individual modules[7]. All sectors were assumed to be equal in size at 15 degrees each for the purpose of utilizing the symmetry capabilities of GFUN, although there are actually two sizes of sectors, one with an arc of 16.2 degrees and the other 13.8 degrees with respect to the center of the torus. Twelve blanket sectors were placed in symmetry with the strong field planes under the TF coils and twelve sectors were placed in symmetry with the weak field planes between the TF coils. Fig. 1.4.2 shows the blanket location relative to the magnet. Field contour lines from a recent tokamak study[7] have been included to show the relative position of the module with respect to magnetic field contours for a reactor of similar size and field strength.

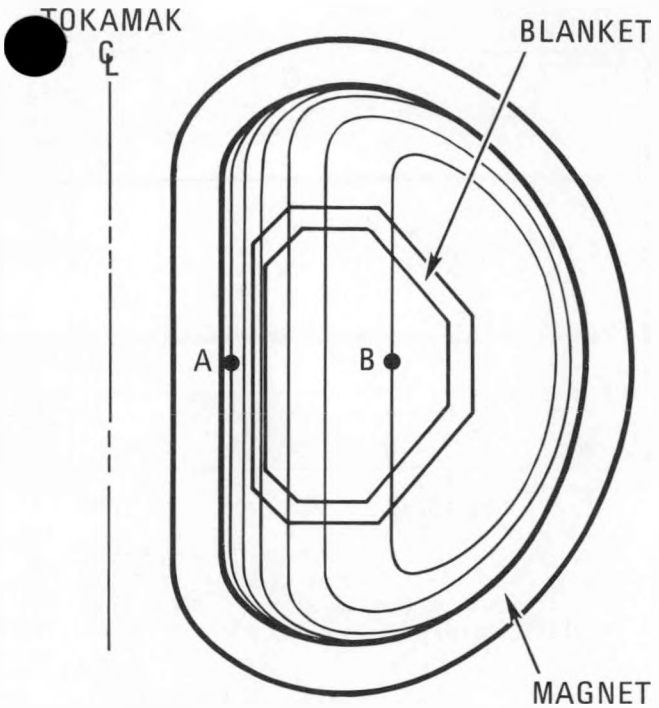

Fig. 1.4.2. Schematic showing position of blanket module relative to the toroidal field magnets with field lines added which were calculated for a similar tokamak, GA-TNS.

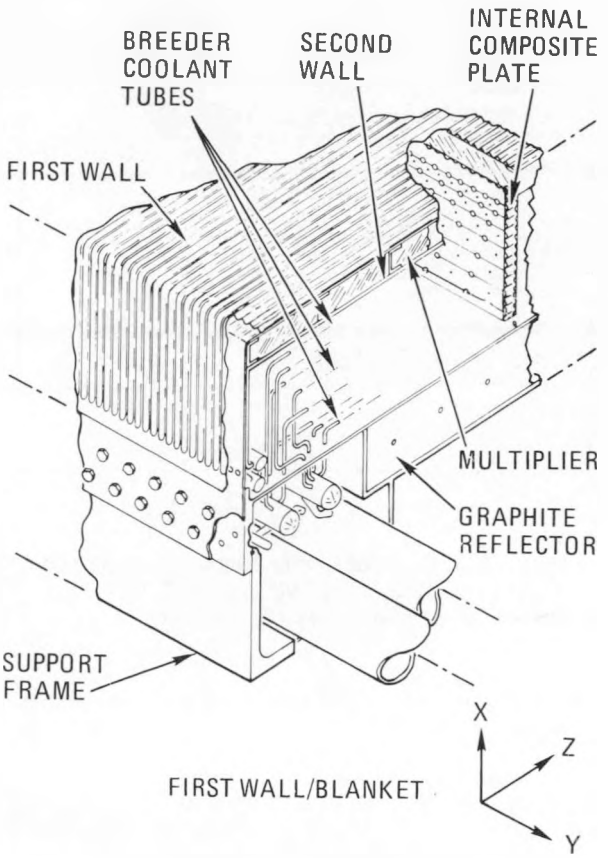

Fig. 1.4.3. Schematic of STARFIRE first wall/blanket module

The blanket module consists of a corrugated first wall, a neutron multiplier, a corrugated second wall, a tritium breeder and a reflector. Fig. 1.4.3 shows a sketch of the internal structure of the modules. The total volume percent of structural material in these regions is 8.8%[7] not including the side walls of the blanket module, internal composite plates acting as supports, headers, manifolds or support frame. The reflector, manifolds and support frame are not considered in this calculation because the fluence level is much lower at these locations and it is assumed that a non-magnetic material can be used. For magnetic force calculations, the HT-9 side walls and support plates must also be included. For calculational simplicity it was assumed that the ferritic material was contained solely within the breeder region and second wall. A total conservative estimate of 15% volume HT-9 was used in the finite element computation.

Within each module are support plates that are spaced a maximum of 60cm apart. The plates themselves consist of two corrugated walls providing cooling with about 5cm spacing between, and are very similar in design to the first wall/multiplier/second wall region of the blanket modules. For the GFUN calculation, modules were segmented into 16 elements appropriately sized to reflect the internal support structure.

1.4.4.3 Magnetic Forces on Coolant Pipe

Figure 1.4.4 shows the component forces distribution, axial, shear, and bending stresses resulting from the load distribution on the modeled pipe. These forces were translated into an effective stress and the results are shown in Figure 1.4.5 for pipes at two horizontal distances from the TF magnet. The magnetic field gradient increases sharply close to the magnets resulting in significantly higher magnetic forces at that location. This clearly results in an increase in the magnetically induced stress. At a distance of 1.40m from the magnet center, the maximum magnetic stress occurs at the end of the pipe exiting the shield access door, and is 33 MPa. If the pipe were moved closer to the magnet center by 0.54m, the stress increases to approximately 170 MPa.

Although in judicious design using HT-9 critical components would be kept away from magnets as far as possible, it is possible that complicated machines containing HT-9 may require some components to be close

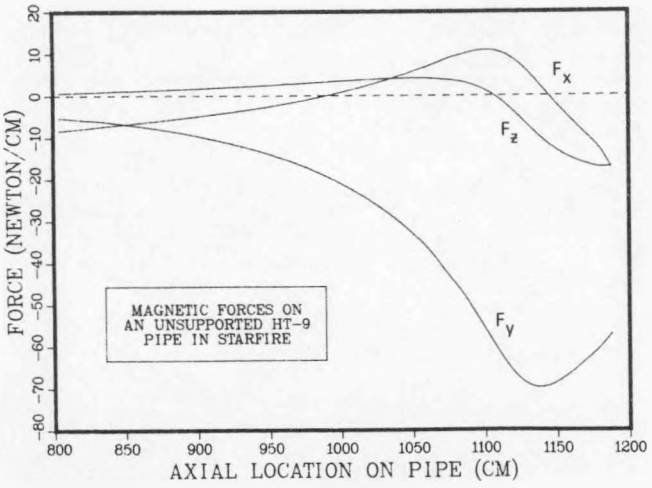

Fig. 1.4.4. Magnetic force distribution for a coolant pipe in STARFIRE at 0.86 m from the center of the TF magnet

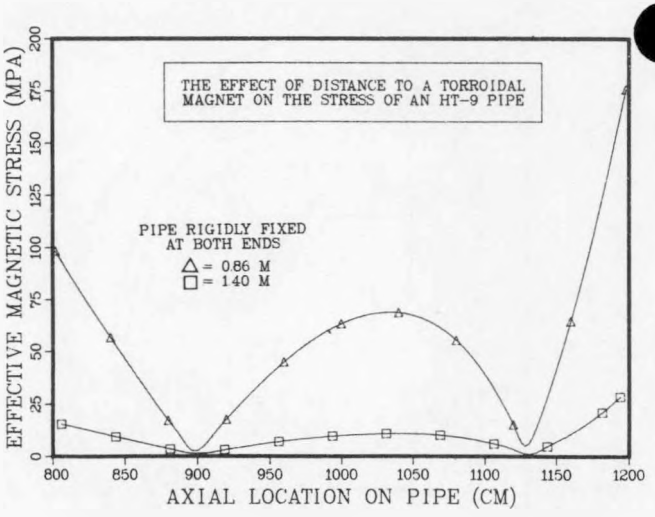

Fig. 1.4.5. Effective magnetic stresses on a rigidly-fixed-at-both-ends coolant pipe in STARFIRE located at 0.86 m and at 1.40 m from the toroidal field magnet center

to the magnets. In this case appropriate supports would be added to control magnetically induced stresses to acceptable low levels.

In order to demonstrate the control available to the designer, two further cases were run for the pipe located at 0.86 m from the center of the TF coil. In these two cases a simple support was located in the middle and at an optimized location to minimize the stress. The results are shown in Figure 1.4.6. As previously discussed, the pipe with no intermediate supports would develop a maximum effective stress of 170 MPa. However, by simply supporting the pipe in the middle, the stresses can be reduced to less than 80 MPa. As is seen in Figure 1.4.4, the largest forces are developed away from the magnet and in the y-direction very near the end of the pipe. If the simple support were moved to between 1.10 and 1.15m on the pipe, these stresses would be reduced even further to a maximum stress of less than 27 MPa. As a result, even if a design required a pipe to be in a large field gradient, the stresses could be reduced to handleable or insignificant levels by stiffening the structure such as with a simple support. A scrutiny of the STARFIRE schematic shows that there is room for such added support structures, although their exact nature and location was not a part of this study.

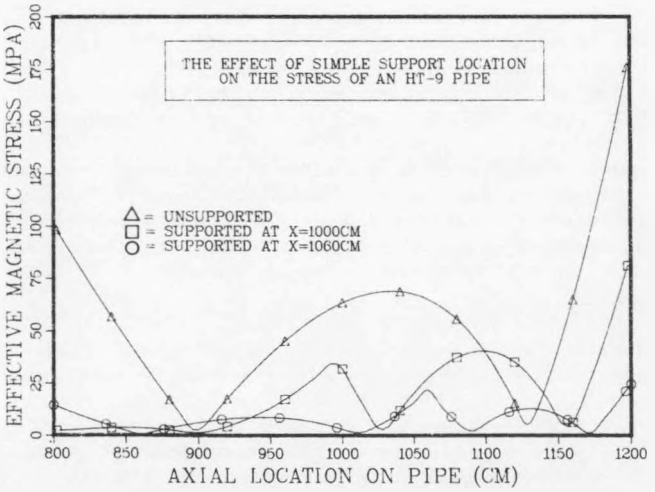

Fig. 1.4.6. Effective magnetic stresses on a pipe at 0.86 m from the TF magnet center rigidly fixed at both ends and then supported at two locations

Magnetic Forces on Modules

The force calculations resulted in magnetic loads which are illustrated schematically in Fig. 1.4.7. The computation of the magnetic loads included the entire tokamak blanket structure such that any effect of magnetization from neighboring elements was taken into account. Magnetic loads on the structures of interest were compared with loads from other sources such as pressure and weight.

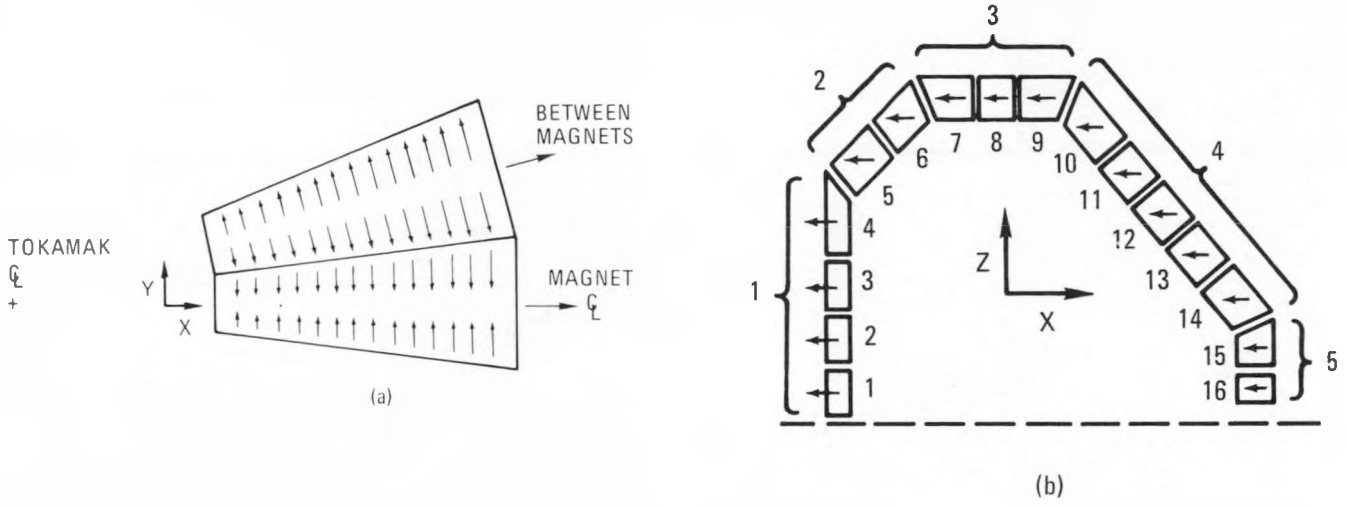

Fig. 1.4.7 Schematic showing position and forces on blanket modules: (a) shows forces in Y-direction, and (b) shows forces in X-direction. Brackets indicate full blanket modules while small numbers refer to elements used in GFUN calculation

In the plane of the magnet with symmetry of about Y = 0, equal and opposite loads in the Y-direction resulted in a compressive force in the blanket modules located under the magnet and a tensile force in the modules located between the magnets. This is shown in Fig. 3a where two sectors side by side have internally generated tensile and compressive forces which have no net effect on a module. The stress in the side walls, resulting from the tensile and compressive forces, are small since the loads are relatively small and the HT-9 breeder tubes, which generate the majority of the magnetic force, are stiff in the Y-direction because of their parallel orientation to this axis, thus enabling them to take a large proportion of the load. The magnitude of the magnetic body forces generated were between 3 and 6 times the weight of the ferromagnetic material.

Loads in the X-direction are shown in Fig. 1.4.7. All modules experience a negative force, pulling the frame towards the center of the tokamak. The greatest load is generated in the highest field gradient nearest the center of the tokamak. In this case, the magnetic body forces generated were between 5 and 25 times the structure weight depending on the distance of the material from the reactor centerline. This distribution is shown in Fig. 1.4.8. The order of magnitude of these loads is consistent with the results of analyses performed on other reactors. In elements 15 and 16 the force is completely transferred to the multiplier zone. At the top of the torus, in elements 7, 8, and 9, the force is supported by the internal composite plates because of its lateral direction. In elements 1 to 4, the force is at its maximum, but is transferred to the inner structure which in these inside modules takes the place of the reflector.

Equal and opposite vertical forces on the upper and lower halves of a blanket sector tend to pull the C-shaped blanket sector frame apart. However, these body forces are all less than 0.3 times the weight of material and can be considered insignificant relative to those in the X-direction.

Module Internal Loads

The only forces reported for the PCA STARFIRE modules were those for gravity and internal pressure. The magnetic forces generated in this study are not necessarily in the same direction as those due to pressure and gravity. But, although the PCA STARFIRE modules were not designed specifically to support loads in the directions commensurate with a magnetic material being used, the magnetic forces can be compared to those calculated for the PCA design. (For example, the PCA module 5 in Fig. 1.4.7 will have a shearing force due to gravity, and the forces placed on the internal supports have been calculated. In the

magnetic calculation, a similar shearing force would be placed on module 3 but due to magnetism instead. So, forces for these two cases can be compared even though they are in different locations. Comparisons in the form of pressure loads are made for the two materials.

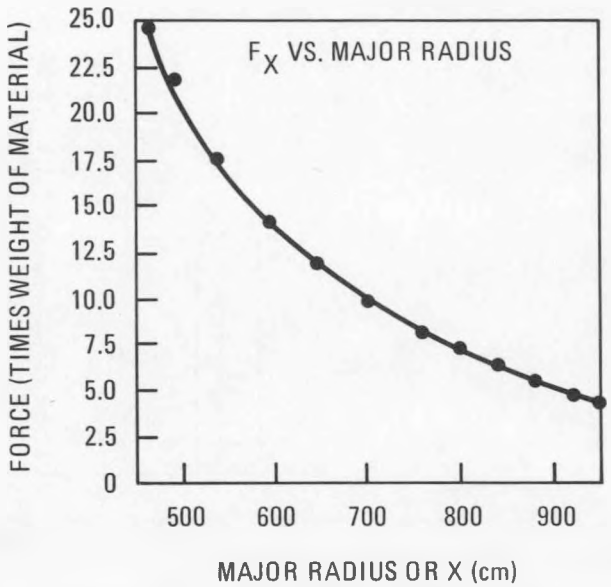

Fig. 1.4.8. The force distribution in the direction of major radius on the blanket module

As indicated above, examples of the critically loaded elements (and therefore modules) are those designated 16, 8, and 1. For element 16, the inward acting magnetic force 25kPa and internal pressure 101kPa apply a total pressure of 126kPa to the multiplier zone. For comparison, the force direction is indicated in Figure 2 as +x, and it is seen to act on the inside of the second wall. In STARFIRE, the force of gravity 9kPa and pressure would have placed a 110kPA load in that same direction for a module located at the top of the torus. So, it appears the added magnetic force is small compared to those for which the module was designed. A schematic showing the internal pressure due to magnetic loading as P_1 is in Figure 1.4.9 for element no. 16.

For element 8, the magnetic loads are shearing the module in a similar loading direction to that for gravity which was the only force on the side of the support frame (for example, element 16). For element 8, the inward magnetic force in the direction shown in Figure 1.4.7 is 62kPa. This is also shown as P_2 in Figure 1.4.9. For a PCA module, the structure was designed to support a gravitational load of 16kPa in that direction. A simple calculation can show that by increasing the thicknesses of the plates by less than a factor of two, the stresses can be reduced to those for which the module was designed. It is not expected that this change would significantly affect the neutronics of the systems in this region. As an alternate, the number of support plates might be increased to support the increased load.

For element 1, the magnetic loads generated within the module would be supported directly by the reflector and the support frame structure. Thus the structural components of the module would not experience significant loads. However, a support frame would have to be provided for these elements. Although a load analysis of the module support frame was not part of this study, it is anticipated that adequate support structure can be provided in the space between the frame and the center part of the torus.

Three types of magnetic force would be induced on a blanket sector of the STARFIRE design if HT-9 were to be used as a first wall/blanket module material. Due to the placement of the sector with respect to the magnetic field gradients, a small force would be pulling the sector upward. The force is less than 0.3 times the weight of the material. The force appears negligible although no detailed design work has been performed on the pedestal support upon which the torus rests.

The second force will be in the toroidal direction. A large amount of computer time would be required to perform a non-symmetric analysis with the modules slightly off-center under the TF magnets as was in the STARFIRE design. A symmetric design was therefore used in this study resulting in a self-cancelling system of forces being generated in each module. If the sectors were off-center, as described for STARFIRE, the forces would not balance but it is doubtful they would increase significantly because the field gradients in the toroidal direction cannot change more than $\sim$4% in order to maintain appropriate levels of field ripple. This force would produce low internal loads in the modules.

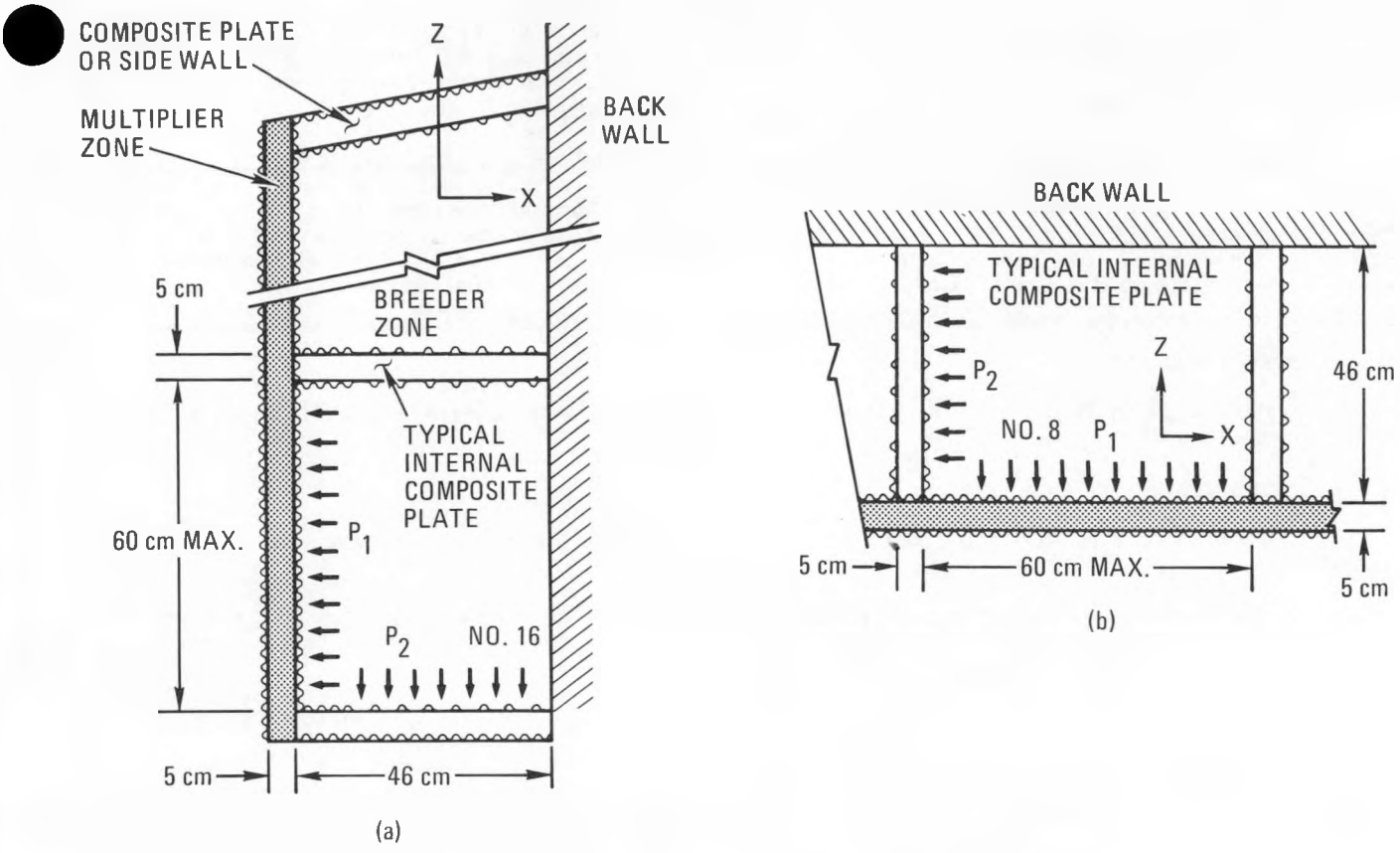

Fig. 1.4.9 Schematic showing the two types of blanket modules analyzed: (a) shows a module referring to elements 15 and 16 while (b) shows a module referring to element 8 in Fig. 1.4.7

The third type of force is directed radially inward toward the reactor center and results in equivalent pressures exerted on the internals of the blanket modules. However, stresses resulting from these forces can be controlled to the same levels as for other loads such as dead weight. The main concern is in the module at the top of the sector where a shearing force is pulling the structure radially inward toward the center of the tokamak. The supports internal to the breeding blanket were not intended to support a magnetic force over and above that of gravity. However, the fractional part of the breeder region that the internal composite plate consumes is very small and either a thickening of walls or the addition of walls would not greatly increase this fractional volume. This slight design change could accommodate any extra magnetic forces generated.

The computer code GFUN does not allow modeling of thin-walled structures because the number of finite elements with the required aspect ratio would be prohibitive with respect to computer time. A detailed model more closely representing the real structure would be desirable for accurately computing the magnetic forces. In addition, an analysis should be performed on the first wall/blanket support frame and pedestal in order to assess the total inward load the magnetic field produced on the individual modules which transfers to the support frame.

1.4.4.4 Summary

An analysis of a ferromagnetic HT-9 pipe in the STARFIRE tokamak model was made to determine the effective magnetic stresses caused by the interaction with the TF magnets. The location of the pipe was determined based on the dimensions of the cryogenic casing on the TF magnets. The GFUN3D code was used to model the toroidal fields and determine the magnetic body forces on a square bar having the same length and material volume as the pipe. The stress analysis was performed using these magnetic forces placed applied to a pipe of 4m length, 8.25 cm o.d., and 0.75 cm thickness by the MODSAP stress analysis code. Results show that magnetic stresses are increased if the pipe is moved closer to the TF magnet into the region of higher field gradient. Maximum effective stresses at a pipe distance of 1.4m from the center of the TF magnet were calculated to be 33 MPa. This is considered to be at the level in which magnetic forces must be accounted for in design, yet not so high as to be unmanageable.

By placing the pipe 0.54m closer to the magnet, the maximum effective stresses increase to about 170 MPa. However, these can be reduced significantly by simply supporting the pipe in the center or at the location of largest force. Maximum effective stresses in the former case are less than 80 MPa. By placing the simple support nearer the end with the maximum force at a distance on the pipe between 1.10 and 1.15m, the stresses are estimated to be reduced to even smaller levels of about 27 MPa.

The magnetic forces induced on an HT-9 Starfire blanket module are of the same order as those due to weight or pressure. The maximum magnetic force applied to the first wall/multiplier/second wall region is approximately one-fourth of that generated from other sources. The maximum magnetic force applied to the internal composite plate support is approximately four times that generated by other sources. The stress produced in this second case can be kept to low values by proper design of the internal supports in the breeding zone. Although the Starfire design with austenitic PCA did not consider magnetic forces in designing the blanket, this analysis shows that with HT-9 the same basic design may be used with small changes.

1.4.4.5 Acknowledgements

The authors wish to thank Prof. W. Wolfer at the University of Wisconsin and R. Ryder at GA for many helpful discussions and suggestions.

1.4.4.6 References

1. S. Rosenwasser, P. Miller, J. Dellessandro, J. Rawls, W. Toffalo, W. Chen, J. Nuclear Mat, 85 and 86 (1979) 177.

2. T. Lechtenberg, C. Dahms, and H. Attaya, "An Assessment of Ferromagnetic Martensitic Stainless Steels for Fusion Machines," Topical Conference on Ferritic Alloys for use in Nuclear Energy Technology, ed. J. Davis and J. Michel, ASME, 1983.

3. "GFUN3D User Guide." A. G. Armstrong, J. Simkin, and C. W. Trowbridge, Rutherford Laboratory, RL-76-029/A, (November, 1976).

4. "MODSAP - A Modified Version of the Structural Analysis Program SAP4 for the Static and Dynamic Response of Linear and Localized Nonlinear Structures," J. J. Johnson, GA-A14006, UC-77 (January, 1980).

5. A. Armstrong, et al, "New Developments in the Magnetic Design Computer Program GFUN3D," Proc. 5th Intl. Conf. of Magnet Technology, Rome, Italy, April 1975.

6. H. Attaya, K. Yuan, G. Kulcinski, and W. Wolfer, "Implications of Using Ferromagnetic Steels in Tandem Mirror Fusion Reactors," Topical Conference on Ferritic Alloys For Use in Nuclear Energy Technology, ed. J. Davis and J. Michel, ASME, 1983.

7. C. Baker (ed.), "STARFIRE - A Commercial Tokamak Fusion Power Plant Study," Argonne National Laboratory, ANL/FPP-80-1, Sept. 1980.

5. "GA TNS Project, Status Report for FY-78," General Atomic Report GA-A15100 (1978).

2.1 NEUTRON SOURCE CHARACTERIZATION FOR MATERIALS EXPERIMENTS - L. R. Greenwood (Argonne National Laboratory)

2.1.1 ADIP/DAFS Tasks

ADIP - Task I.A.2 - Define Test Matrices and Procedures
DAFS - Task II.A.1 - Fission Reactor Dosimetry

2.1.2 Objective

To characterize neutron irradiation facilities in terms of neutron flux, spectra, and damage parameters (DPA, gas production, transmutation) and to measure these exposure parameters during fusion materials irradiations.

2.1.3 Summary

Damage and gas production calculations are summarized for the CTR 31, 32, 35, and 35 irradiations in HFIR. Neutron dosimetry measurements and damage calculations are also presented for the T2 and RB1 irradiations in HFIR. The helium production from nickel has been revised according to new cross section evaluations for ^{59}Ni. The status of all other experiments is summarized.

2.1.4 Progress and Status

The status of all fission reactor dosimetry is summarized in Table 2.1.1.

Table 2.1.1. Status of Dosimetry Experiments

	Facility/Experiment	Status/Comments
ORR	- MFE 1	Completed 12/79
	- MFE 2	Completed 06/81
	- MFE 4A1	Completed 12/81
	- MFE 4A2	Completed 11/82
	- MFE 4B	Samples Expected 07/83
	- MFE 4C	Irradiation in Progress
	- TBC 07	Completed 07/80
	- TRIO-Test	Completed 07/82
	- TRIO-1	Irradiation in Progress
HFIR	- CTR 32	Completed 04/82
	- CTR 31, 34, 35	Completed 04/83
	- CTR 30	Irradiation in Progress
	- T1, T2, RB1, CTR39	Samples Counted 06/83
	- T3	Irradiations in Progress
	- RB2, RB3	Irradiations in Progress
	- CTR 40-49	Irradiations in Progress
Omega West	- Spectral Analysis	Completed 10/80
	- HEDL1	Completed 05/81
	- HEDL2	Samples Sent 05/83
EBR II	- X287	Completed 09/81
IPNS	- Spectral Analysis	Completed 01/82
	- LANL1 (Hurley)	Completed 06/82
	- Hurley	Completed 02/83
	- Coltman	Samples Received 05/83

2.1.4.1 Damage Calculations for HFIR-CTR-31, 32, 34, and 35

Neutron activation and fluence measurements for the HFIR-CTR 31, 32, 34, and 35 irradiations were reported in the previous semiannual report.[1] Gas production and damage rates for these experiments are reported in the present report. Damage calculations were reported earlier[2] for the CTR 32 experiment; however, helium values have been revised for nickel-bearing materials according to a new evaluation of cross sections for ^{59}Ni by F. M. Mann.[3]

In the past, helium generation in nickel has been calculated and measured in various reactors using a semi-empirical technique. Although neutron energy spectra have been known for these reactors, the energy-dependent cross sections for ^{59}Ni were not previously available. As a result, equations developed for HFIR could not be readily used in other reactors such as ORR. In particular, it is not clear how corrections should be made for epithermal neutrons, a problem which we pointed out recently for ORR.[4]

With the newly evaluated cross sections it is now a straightforward calculation to obtain spectral-averaged reaction rates for any specified neutron energy spectrum. The $^{58}Ni(n,\gamma)$ cross section can be obtained from the ENDF/B-V activation file. The ^{58}Ni and ^{59}Ni cross sections were averaged for the four experiments in HFIR using the flux spectra adjusted by STAYSL. The results were then averaged and the standard deviation was only ~0.7%. The recommended reaction rates for the HFIR-PTP are given in Table 2.1.2. It should be noted that these values are only valid for the PTP position and are averages over the total neutron spectrum. Thermal (2200 m/s) values are also given and compared to previous work in HFIR.[5] As can be seen, the new values are not significantly different from earlier estimates. Furthermore, since about 36% of the flux in HFIR consists of thermal neutrons, neglecting epithermal and fast neutron effects will not cause a serious error. This is not the case, however, in other less thermalized reactors (e.g., ORR) as we will show in future reports.

Table 2.1.2. Cross Sections for ^{58}Ni and ^{59}Ni and Helium Calculation

Symbol	Reaction	Cross Section, b		
		HFIR-PTP	Thermal (2200 m/s)	
		(Total)	ENDF/B-V	Ref. 5
$\sigma\gamma$	$^{58}Ni(n,\gamma)^{59}Ni$	1.615	4.81	4.6
--	$^{59}Ni(n,\gamma)^{60}Ni$	28.979	81.04	--
--	$^{59}Ni(n,p)^{59}Co$	0.731	1.96	--
$\sigma\alpha$	$^{59}Ni(n,\alpha)^{56}Fe$	4.292	11.99	11.6
σT	^{59}Ni ABS	34.00	94.99	92.0

The production of helium from $^{58}Ni(n,\gamma)^{59}Ni(n,\alpha)^{56}Fe$ is calculated as follows:

$$\frac{He}{^{58}Ni} = \frac{\sigma_a \left[\sigma_T \left(1 - e^{-\sigma_\gamma \phi t}\right) - \sigma_\gamma \left(1 - e^{-\sigma_T \phi t}\right)\right]}{\sigma_T \left(\sigma_T - \sigma_\gamma\right)}$$

where ϕt is the neutron fluence in n/cm^2.

Using the values above:

$$\frac{He}{^{58}Ni} = 0.1325305 \left(1 - e^{-1.615\ \phi t}\right) - 0.0062952 \left(1 - e^{-34\ \phi t}\right)$$

For production in natrual nickel, multiply the above result by 0.683.

The ^{56}Fe recoils also add extra DPA in the ratio of 1 DPA for 567 appm He (see Ref. 6).

Helium concentrations in nickel and stainless steel as a function of fluence in the HFIR-PTP are listed in Table 2.1.3. Displacement damage, helium production and fluences are listed at midplane for the four irradiations in Table 2.1.4.

All of these parameters obey the same functional dependence on height above midplane, as follows:

$$f(z) = a[1 + bz + cz^2],\ z = \text{height (cm)} \qquad (1)$$

where $b = 0.195 \times 10^{-3}$ and $c = -0.975 \times 10^{-3}$. The b term is negligible and the gradients are quite symmetric about midplane. The helium values listed in Tables 2.1.4-2.1.5 for CTR32 differ slightly from our previous results[2] for two reasons. First of all, we have now adopted the ENDF/B-V gas production file (533) and some elements include reactions not contained in the general files which we used previously. Secondly, the nickel reactions are computed directly from the cross sections, as discussed earlier.

In order to find the helium production in nickel, and stainless steel, at a given height in one of the four experiments, one can first determine the fluence using Table 2.1.4 and Eq. (1) and then either interpolate the helium value from Table 2.1.2 or use the accompanying equations. Due to the complexity of this procedure, the helium and fluence gradients are illustrated in Figs. 2.1.1 and 2.1.2 and helium and DPA gradients for nickel are listed in Table 2.1.5.

Table 2.1.3. Helium Generation in Nickel and Stainless Steel in the HFIR-PTP

	Helium, appm			
	Nickel		Stainless Steel[a]	
Fluence, n/cm^2	^{59}Ni(n,α)	Fast	^{59}Ni(n,α)	Fast
1 x 10^{20}	0.024	0.092	0.003	0.017
2 x 10^{20}	0.094	0.184	0.012	0.034
5 x 10^{20}	0.59	0.46	0.077	0.086
1 x 10^{21}	2.34	0.92	0.30	0.17
2 x 10^{21}	9.25	1.84	1.20	0.34
5 x 10^{21}	55.8	4.6	7.25	0.86
1 x 10^{22}	211.	9.2	27.4	1.7
2 x 10^{22}	756.	18.4	98.3	3.4
5 x 10^{22}	3508.	46.	456.0	8.6
1 x 10^{23}	9343.	92.	1215.	17.
2 x 10^{23}	20691.	184.	2690.	34.

[a]316 ss: Ni (0.13), Fe (0.645), Cr (0.18), Mn (0.019), Mo (0.026)

Table 2.1.4. Fluence and Damage Parameters for HFIR-CTR 31, 32, 34, 35

Values are listed at midplane; for gradients use Eq. (1) in text

	CTR31	CTR32	CTR34	CTR35
Neutron Fluence, x 10^{22} n/cm^2				
Total	9.34	4.78	4.47	4.38
Thermal (<.5 eV)	3.84	1.98	1.82	1.78
>0.11 MeV	2.45	1.26	1.19	1.17

DPA and He (appm)	CTR31		CTR32		CTR34		CTR35	
Element	DPA	He	DPA	He	DPA	He	DPA	He
Al	31.9	16.9	16.5	8.20	15.6	7.70	15.5	7.64
Ti	20.2	10.5	10.5	5.38	9.97	5.15	9.86	5.11
V	22.7	0.57	11.7	0.28	11.1	0.26	11.0	0.26
Cr	20.0	3.80	10.3	1.87	9.84	1.75	9.74	1.76
Mn[a]	22.0	3.41	11.4	1.66	10.8	1.56	10.7	1.55
Fe	17.7	6.84	9.14	3.34	8.72	3.15	8.63	3.12
Co[a]	22.4	3.38	11.5	1.64	10.9	1.55	10.8	1.53
Ni[b] Fast	19.1	88.3	9.84	43.95	9.36	41.94	9.25	41.55
Ni[b] ^{59}Ni	15.1	8554.	5.77	3272.	5.19	2945.	5.03	2852.
Ni[b] Total	34.2	8642.	15.61	3316.	14.55	2987.	14.28	2894.
Cu	17.3	6.13	8.92	2.98	8.49	2.80	8.40	2.78
Nb	17.1	1.25	8.84	0.61	8.41	0.58	8.32	0.57
Mo	12.8	--	6.58	--	6.25	--	6.17	--
316 ss[c]	20.2	11.29	14.1	4.34	9.65	3.91	9.54	3.79

[a](n,γ) damage is 8.4% for Mn and 27.6% for Co; however, neutron self-shielding effects must be considered for samples

[b]Ni values include thermal helium and extra DPA (see text)

[c]316 ss: Fe (0.645), Ni (0.13), Cr (0.18), Mn (0.019), Mo (0.026)

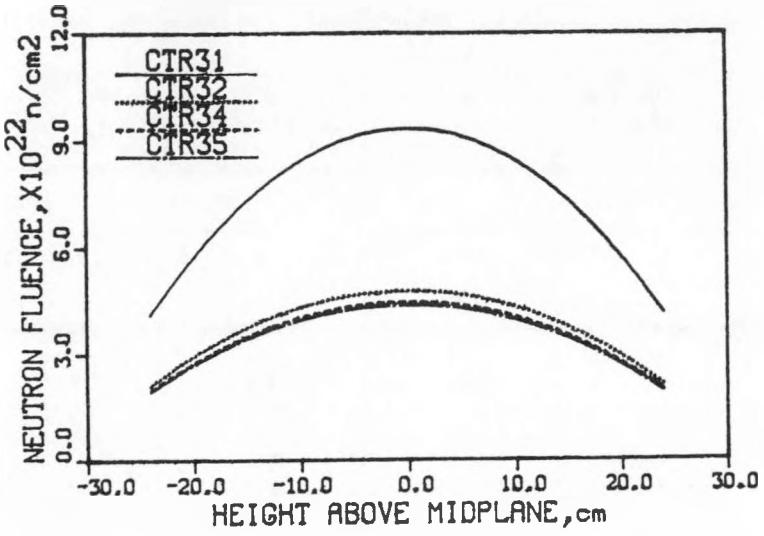

Fig. 2.1.1. Neutron fluence gradients for irradiations in the HFIR-PTP.

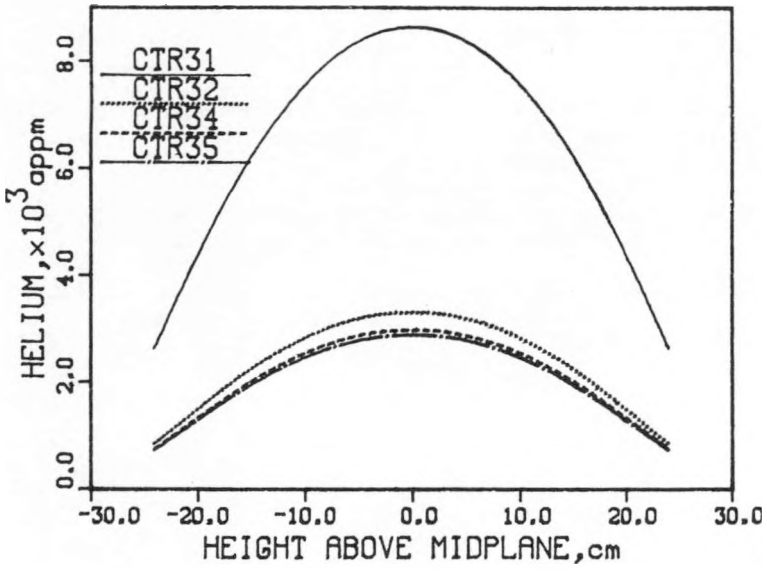

Fig. 2.1.2. Helium gradients in nickel for irradiations in the HFIR-PTP. The ^{59}Ni and fast neutron reactions are combined.

Table 2.1.5. Helium (appm) and DPA Gradients for Nickel in the HFIR-PTP

Helium values include $^{59}Ni(n,\alpha)$ and fast effects.
DPA values include thermal effects (He/567)
Gradients are symmetric about midplane

	CTR31		CTR32		CTR34		CTR35	
Height, cm	He	DPA	He	DPA	He	DPA	He	DPA
0	8642	34.2	3316	15.6	2987	14.6	2894	14.3
3	8553	33.9	3275	15.5	2950	14.4	2857	14.1
6	8259	32.9	3143	15.0	2829	14.0	2739	13.7
9	7776	31.2	2926	14.2	2632	13.2	2547	13.0
12	7091	28.8	2625	13.0	2358	12.2	2282	11.9
15	6222	25.8	2254	11.6	2020	10.8	1954	10.6
18	5168	22.2	1818	9.92	1627	9.26	1573	9.08
21	3954	17.8	1340	7.97	1196	7.44	1155	7.30
24	2643	13.1	857	5.84	761	5.46	734	5.36

2.1.4.2 Dosimetry Measurements and Damage Calculations for HFIR - RB1 and T2

Neutron activation dosimetry measurements and damage parameter calculations have been completed for the T2 and RB1 experiments in the High Flux Isotopes Reactor (HFIR) at Oak Ridge National Laboratory. The irradiation histories are, as follows:

Irradiation	Reactor Position	Dates	Exposure, MWD
T2	Target	2/81 to 5/81	6,616
RB1	Be	11/81 to 7/82	23,386

Dosimetry capsules were placed at two heights in T2 and five heights in the RB1 subassembly. The T2 capsules contained Fe, Co, Ti, Mn-Cu, and Cu wires. The RB1 capsules did not have the Mn-Cu and Cu samples. The measured activation rates are listed in Table 2.1.6.

Table 2.1.6. Activation Rates Measured in HFIR-T2, RB1
(Values Normalized to 100 MW Power Level)

Reaction	Activation Rate, atom/atom-s					
	Height, cm:	7.22		16.95		
T2 Experiment						
$^{58}Fe(n,\gamma)^{59}Fe$	(10^{-9})	--		2.08		
$^{59}Co(n,\gamma)^{60}Co$	(10^{-8})	--		6.32		
$^{54}Fe(n,p)^{54}Mn$	(10^{-11})	5.83		4.50		
$^{46}Ti(n,p)^{46}Sc$	(10^{-12})	8.58		6.31		
$^{55}Mn(n,2n)^{54}Mn$	(10^{-13})	1.79		1.43		
$^{63}Cu(n,\alpha)^{60}Co$	(10^{-13})	4.87		3.04		
RB1 Experiment						
	Height, cm:	-23.02	-5.40	+2.02	+10.72	+21.15
$^{59}Co(n,\gamma)^{60}Co$	(10^{-8})	1.27	3.51	3.68	2.80	1.67
$^{58}Fe(n,\gamma)^{59}Fe$	(10^{-10})	--	--	10.12	7.69	4.77
$^{54}Fe(n,p)^{54}Mn$	(10^{-11})	--	--	1.38	1.21	0.81
$^{46}Ti(n,p)^{46}Sc$	(10^{-12})	--	--	2.17	1.86	1.20

The T2 data in the target position close to the PTP is similar to our previous measurements in the PTP. Consequently, we assume that the flux gradients are also described by our previous equations, namely:

$$f(z) = a(1 + bz + cz^2) \qquad (2)$$

where z is the height above midplane (cm), $b = 0.195 \times 10^{-3}$, $c = -0.975 \times 10^{-3}$, and a is the flux or damage rate at midplane. The midplane fluence and damage rates are listed in Table 2.1.7. In order to find a given

fluence or damage rate at any other height, the user should simply take the midplane value in Table 2.1.7 for and use Eq. (2) for the desired value of z.

Table 2.1.7. Fluence and Damage Parameters for HFIR-T2, RB1
Values are listed at midplane; for gradients use Eq. (2) in text where for T2: $b = 1.95 \times 10^{-4}$, $c = -9.75 \times 10^{-4}$, and for RB1: $b = -9.18 \times 10^{-5}$, $c = -1.175 \times 10^{-3}$

Neutron Fluence, x 10^{22} n/cm^2	T2	RB1
Total	3.20	3.89
Thermal (<.5 eV)[a]	1.55	2.21
Fast (>.11 MeV)	0.722	0.685

		T2		RB1	
Element		DPA	He	DPA	He
Al		9.37	4.37	8.66	4.12
Ti		5.95	2.87	5.49	2.43
V		6.68	0.15	6.20	0.15
Cr		5.84	1.00	5.35	0.91
Mn[b]		6.59	0.88	6.32	0.83
Fe		5.15	1.76	4.68	1.61
Co[b]		6.97	0.87	7.27	0.81
Ni[c]	Fast	5.61	22.84	5.24	19.40
	^{59}Ni	3.89	2206.	6.82	3865.
	Total	9.50	2230.	12.06	3884.
Cu		5.06	1.58	4.67	1.48
Nb		4.99	0.32	4.56	0.29
Mo		3.73	--	3.45	--
316 ss		5.83	291.	5.64	506.

[a]The 2200 m/s value is equal to 0.886 times the total <.5 eV.

[b]The thermal (n,α) damage is 8% for Mn and 28% for Co; however, self-shielding effects must be considered.

[c]Nickel gradients for He must be done differently; see Table 2.1.8 and Ref. 3.

[d]316 ss: Fe (0.645), Ni (0.13), Cr (0.18), Mn (0.019), Mo (0.026)

The spectral and gradient differences between the PTP, target, and Be positions are illustrated in Fig. 2.1.3. As can be seen the spectra become considerably softer as we move out from the core, as expected. The gradients are only slightly steeper in the Be position.

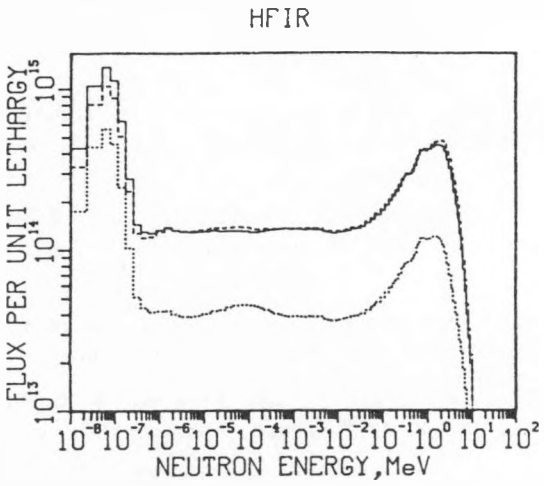

Fig. 2.1.3. Neutron flux spectra are compared at different locations in HFIR. The dashed line is the PTP (CTR 32), the solid line is for the target position (T2), and the dotted line is for the removable beryllium position (RB1).

The helium production and damage in nickel and stainless steel requires a more detailed calculation, as discussed in recent publications.[6,8] Due to the complexity of this calculation, detailed gradients are listed in Table 2.1.8. The thermal two-step reaction and fast reactions are summed in the table and the extra DPA from the ^{56}Fe recoils (He/567) is also included.[6]

Table 2.1.8. HELIUM (appm) AND DPA GRADIENTS FOR NICKEL IN HFIR-T2, RB1
Helium values include $^{59}Ni(n,\alpha)$ and fast reactions.
DPA values include thermal effects (He/567).
Gradients are nearly symmetric about midplane.

	T2		RB1	
Height, cm	He	DPA	He	DPA
0	2230.	9.50	3884	12.06
3	2195.	9.39	3823.	11.90
6	2105.	9.09	3628.	11.38
9	1950.	8.57	3330.	10.58
12	1746.	7.88	2909.	9.45
15	1488.	6.99	2393.	8.05
18	1188.	5.93	1793.	6.37
21	869.	4.74	1172.	4.57
24	547.	3.44	574.	2.68

Helium calculations were made using newly evaluated cross sections for ^{59}Ni[3] averaged over our adjusted neutron spectra. This procedure appears to agree quite closely with helium measurements made at Rockwell International, as discussed elsewhere.[8] With over 45 separate measurements in HFIR, ORR, and EBR II, the measurements and calculations have an average ratio of 0.982 ± 0.064 and the maximum difference was only ±11%.

2.1.5 Conclusions

Samples have been gamma counted from the CTR39 and T1 irradiations in HFIR and analysis is now in progress. Samples have been received from the MFE4B irradiation in ORR. Data in the present report is being added to our DOSFILE program on the NMFECC computer for rapid access by experimenters. Selected samples have been sent to Rockwell International for helium analysis.

The following papers have been accepted for publication in the proceedings of the Third Topical Meeting of Fusion Reactor Materials in Albuquerque, New Mexico, on September 19-22, 1983.

1. L. R. Greenwood, D. W. Kneff, R. P. Skowronski, and F. M. Mann, Comparison of Measured and Calculated Helium Production in Nickel Using Newly Evaluated Neutron Cross Sections for ^{59}Ni.

2. L. R. Greenwood, Recent Developments in Neutron Dosimetry and Radiation Damage Calculations for Fusion Materials Studies.

2.1.6 References

1. L. R. Greenwood, Neutron Source Characterization for Materials Experiments, Alloy Development for Irradiation Performance, Semiannual Progress Report, DOE/ER-0045/10, pp. 12-18, March 1983.

2. L. R. Greenwood and R. K. Smither, Neutron Dosimetry Measurements for the HRIF-CTR32 Irradiation, Damage Analysis and Fundamental Studies Quarterly Progress Report, DOE/ER-0046/9, pp. 32-40, May 1982.

3. F. M. Mann, ^{59}Ni + n Cross Section Evaluation, Damage Analysis and Fundamental Studies Quarterly Progress Report, DOE/ER-0046/12, pp. 35-36, February 1983.

4. L. R. Greenwood, Dosimetry and Damage Analysis for the MFE4A Spectral Tailoring Experiment in ORR, Alloy Development for Irradiation Performance, Semiannual Progress Report, DOE/ER-0045/9, February 1983.

5. F. W. Wiffen, E. J. Allen, H. Farrar IV, E. E. Bloom, T. A. Gabriel, H. T. Kerr, and F. G. Perey, The Production Rate of Helium During Irradiation of Nickel in Thermal Spectrum Fission Reactors, to be published in J. Nucl. Mater.

6. L. R. Greenwood, A New Calculation of Thermal Neutron Damage and Helium Production in Nickel, J. Nucl. Mater. 115, 137-142 (1983).

7. F. B. K. Kam and J. H. Swanks, "Neutron Flux Spectrum in the HFIR Target Region," ORNL-TM-3322, 1971.

8. D. W. Kneff and L. R. Greenwood, "Comparison of Measured and Calculated Helium Production in Nickel," Damage Analysis and Fundamental Studies Progress Report, to be published.

2.2 NEUTRONICS CALCULATIONS IN SUPPORT OF THE ORR-MFE-4A AND -4B SPECTRAL TAILORING EXPERIMENTS — R. A. Lillie (Oak Ridge National Laboratory)

2.2.1 ADIP Task

ADIP Task 1.A.2, Define Test Matrices and Test Procedures.

2.2.2 Objective

The objective of this work is to provide the neutronic design for materials irradiation experiments in the Oak Ridge Research Reactor (ORR). Spectral tailoring to control the fast and thermal fluxes is required to provide the desired displacement and helium production rates in alloys containing nickel.

2.2.3 Summary

The calculated fluences from the ongoing three-dimensional neutronics calculations are being scaled to agree with experimental data. As of September 30, 1983, this treatment yields 121.6 at. ppm He (not including 2.0 at. ppm He from ^{10}B) and 8.25 dpa for type 316 stainless steel in ORR-MFE-4A and 69.3 at. ppm He and 5.19 dpa in ORR-MFE-4B.

2.2.4 Progress and Status

The operating and current calculated data based on the fluence scaling factors[1] are summarized in Table 2.2.1 for the ORR-MFE-4A and -4B experiments.

The real-time projections of the helium-to-displacement ratios based on current calculated data as of September 30, 1983 are presented in Figs. 2.2.1 and 2.2.2 for the ORR-MFE-4A and -4B experiments, respectively. The projected dates were obtained by assuming an ORR duty factor of 0.86. As noted, the solid aluminum core pieces were inserted in the ORR-MFE-4A experiment on December 7, 1982 and in the ORR-MFE-4B experiment on August 5, 1983. The current target dates for removal of specimens and for insertion of the 1.0-mm-thick hafnium core pieces at the 10 dpa level are March 1, 1984, and December 10, 1984, for the ORR-MFE-4A and -4B experiments, respectively.

The effect of LEU (low-enriched uranium) fuel in the ORR reactor on the helium and displacement damage levels in the ORR-MFE-4A and -4B experiments has been estimated and found to be minimal. At present, an LEU fuel experiment is planned for the ORR beginning on or about January 1, 1985. The experiment consists of gradually replacing the existing highly enriched fuel with low-enriched fuel over a nine-month period. After approximately six months of full power use of the low-enriched fuel, it will be gradually replaced with highly enriched fuel, again over a nine month period. At the 30 dpa level in both the ORR-MFE-4A and -4B experiments, the only noticeable effect will be a 6% drop in the calculated helium level in both MFE experiments.

Table 2.2.1. Operating and calculated data for experiments ORR-MFE-4A and -4B as of September 30, 1983

	ORR-MFE-4A	ORR-MFE-4B
ORR Cycles	59	37
Operation (MWh)	488,346	344,937
Equivalent full-power days[a]	680	480
Thermal fluence (neutrons/m^2)	1.09×10^{26}	7.93×10^{25}
Total fluence (neutrons/m^2)	3.37×10^{26}	2.13×10^{26}
He (at. ppm)[b]	121.6	69.3
dpa[b]	8.25	5.19

[a]Full power for ORR is 30 MW.

[b]Helium and dpa values are for type 316 stainless steel.

2.2.5 Future Work

The three-dimensional neutronics calculations that monitor the radiation environment in the ORR-MFE-4A and -4B experiments will continue with each ORR cycle. The scale factors used to scale the fluences obtained from these calculations will be updated as new experimental data become available.

2.2.6 Reference

1. R. A. Lillie and T. A. Gabriel, "Neutronics Calculations in Support of the ORR-MFE-4A and -4B Spectral Tailoring Experiments," pp. 19–20 in *ADIP Semiannu. Prog. Rept. Mar. 31, 1983*, DOE/ER-0045/10, U.S. DOE Office of Fusion Energy.

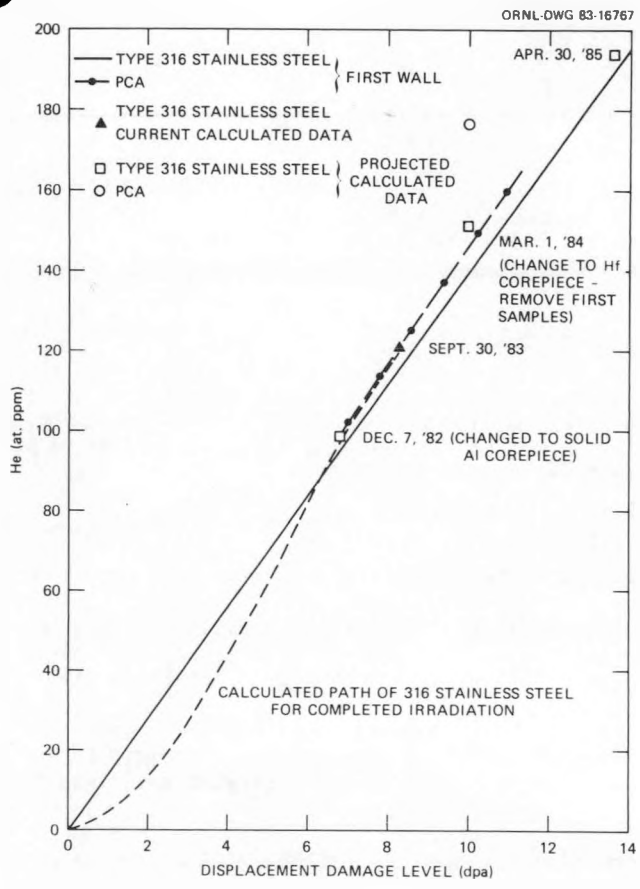

Fig. 2.2.1. Current and projected helium and displacement damage levels in the ORR-MFE-4A experiment.

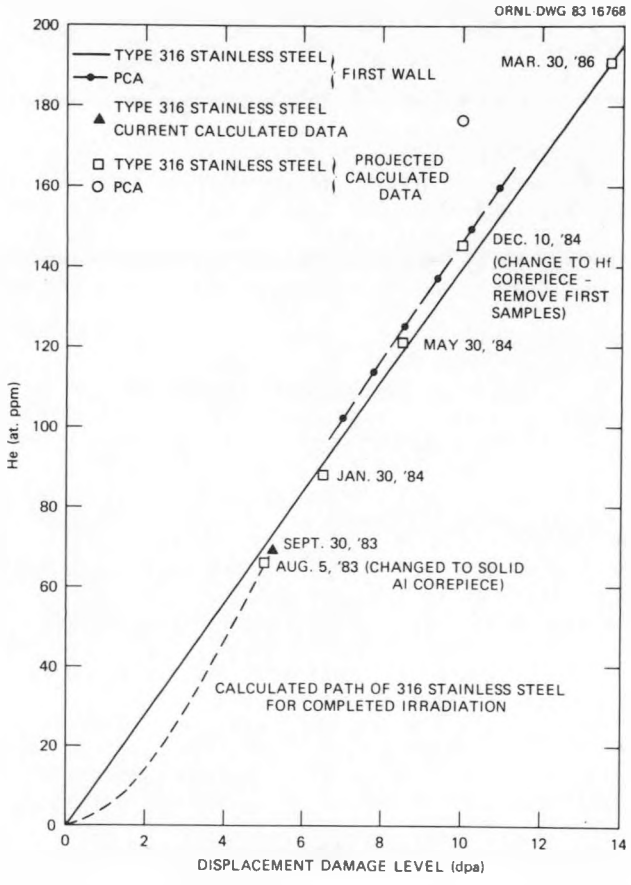

Fig. 2.2.2. Current and projected helium and displacement damage levels in the ORR-MFE-4B experiment.

2.3 OPERATION OF THE ORR SPECTRAL TAILORING EXPERIMENTS ORR-MFE-4A AND ORR-MFE-4B — J. A. Conlin, I. T. Dudley, and E. M. Lees (Oak Ridge National Laboratory)

2.3.1 ADIP Task

ADIP Task I.A.2, Define Test Matrices and Test Procedures.

2.3.2 Objectives

Experiments ORR-MFE-4A and -4B, which irradiate austenitic stainless steel, use neutron spectral tailoring to achieve the same helium-to-displacement-per-atom (He/dpa) ratio as predicted for fusion reactor first-wall service. Experiment ORR-MFE-4A contains mainly type 316 stainless steel and Path A Prime Candidate Alloy (PCA) at irradiation temperatures of 330 and 400°C. Experiment ORR-MFE-4B contains similar materials at irradiation temperatures of 500 and 600°C.

2.3.3 Summary

The specimens contained in the ORR-MFE-4A experiment have operated for an equivalent of 680 d at 30 MW reactor power, with temperatures of 400 and 330°C. The ORR-MFE-4B capsule was disassembled; the test specimen were transferred to a new capsule assembly and reinstalled in the ORR on July 19, 1983. It has operated for an equivalent of 480 d at 30 MW reactor power with temperatures of 500 and 600°C.

2.3.4 Progress and Status

The details of the Oak Ridge Research Reactor (ORR) Spectral Tailoring Experiments have been described previously.[1-6]

The ORR-MFE-4A capsule experiment continues to operate. Temperature fluctuations indicated by thermocouple 4 continue to occur. These fluctuations are believed to be caused by bubbles of helium in the NaK collecting in the annulus containing the thermocouples. Movements of the bubbles produced shifts in the temperature indicated by thermocouple number 4.

On July 7, 1983 the helium blanket gas pressure above the NaK in the primary containment was increased from 103 kPa (15 psig) to 241 kPa (35 psig) in an effort to reduce the bubble size and thereby minimize its effect on the thermocouple 4 temperature indication. There was no significant improvement as a result of this pressure change.

During the ORR refueling shutdown on September 29, 1983, it was found that the capsule helium blanket gas inlet line was partially plugged at a point between the capsule bulkhead and instrumentation in the shielded valve box. The capsule blanket gas outlet line proved to be clear. The alarms and reactor setback circuits, which were activated by pressure switches on the capsule inlet gas line, were transferred to pressure switches on the capsule outlet line. This provided the necessary double tracking of the capsule primary gas high- and low pressure reactor safety circuits. The capsule primary system pressurization and venting operations are now accomplished by use of the outlet line.

During this reporting period there have been no thermocouple failures. Through September 30, 1983, the ORR-MFE-4A experiment specimens have accumulated an equivalent of 680 d at 30 MW reactor power with specimen temperatures of 400 and 330°C.

The ORR-MFE-4B experiment test specimens were removed from the capsule, inspected, and transferred to a new capsule assembly. The capsule assembly was reinstalled in the ORR on July 29, 1983. At that time the water-filled aluminum core piece was removed and replaced with a solid aluminum core piece. The core piece change was made on schedule to adjust the neutron spectrum so as to continue to provide the proper helium production to displacement level ratios within the test specimens.

During the operation of this capsule the temperature indicated by thermocouple 4 has periodically increased 10 to 15°C and a few hours later dropped an equal amount. This change occurs two or three times every 24 h. The temperature indicated by thermocouple 5 showed similar irregularities at the same time as those of thermocouple 4; however, the temperature changes were much smaller. The temperature fluctuations are believed to be caused by gas bubbles similar to those in the ORR-MFE-4A experiment. The bubbles are believed to be produced by helium cover gas absorbed in the NaK. On September 29, 1983, the NaK cover gas was changed from helium to argon because argon does not absorb as readily in NaK. This change in cover gas made no significant change in the temperature fluctuations.

Through September 30, 1983, the ORR-MFE-4B experiment specimens have accumulated an equivalent of 480 d at 30 MW reactor power with temperatures of 500 and 600°C.

2.3.5 References

1. K. R. Thoms and M. L. Grossbeck, "Operation of the ORR Spectral Tailoring Experiment ORR-MFE-4A," pp. 20–24 in *ADIP Quart. Prog. Rep. Sept. 30, 1980*, DOE/ER-0045/4, U.S. DOE, Office of Fusion Energy.

2. K. R. Thoms, "Operation of the ORR Spectral Tailoring Experiment ORR-MFE-4A," pp. 18–21 in *ADIP Quart. Prog. Rep. March 31, 1981*, DOE/ER-0045/6, U.S. DOE, Office of Fusion Energy.

3. I. T. Dudley, "Operation of the ORR Spectral Tailoring Experiments ORR-MFE-4A and ORR-MFE-4B," pp. 24–29 in *ADIP Semiannu. Prog. Rep. Sept. 30, 1981*, DOE/ER-0045/7, U.S. DOE, Office of Fusion Energy.

4. I. T. Dudley and J. A. Conlin, "Operation of the ORR Spectral Tailoring Experiments ORR-MFE-4A and ORR-MFE-4B," pp. 10–12 in *ADIP Semiannu. Prog. Rep. March 31, 1982*, DOE/ER-0045/8, U.S. DOE, Office of Fusion Energy.

5. J. A. Conlin, I. T. Dudley, and E. M. Lees, "Operation of the ORR Spectral Tailoring Experiments ORR-MFE-4A and ORR-MFE-4B," pp. 17–20 in *ADIP Semiannu. Prog. Rep. Sept. 30, 1982*, DOE/ER-0045/9, U.S. DOE, Office of Fusion Energy.

6. J. A. Conlin, I. T. Dudley, and E. M. Lees, "Operation of the ORR Spectral Tailoring Experiments ORR-MFE-4A and B," pp. 21–22 in *ADIP Semiannu. Prog. Rep. March 31, 1983*, DOE/ER-0045/10, U.S. DOE, Office of Fusion Energy.

2.4 Summary of EBR-II AD-2 Ferritic Irradiation Experiment — Westinghouse Hanford Company

No contribution.

2.5 DISK-BEND DUCTILITY TESTS FOR IRRADIATED MATERIALS — R. L. Klueh and D. N. Braski (Oak Ridge National Laboratory)

2.5.1 ADIP Task

ADIP Task I.A.2, Define test matrices and test procedures.

2.5.2 Objective

The objective of this work is to develop a miniature mechanical-property test capability for irradiated specimens in support of Fusion Reactor Materials Testing. The ability to test small specimens allows a large number of specimens to be irradiated simultaneously in the limited irradiation volume available in most test reactors.

2.5.3 Summary

We modified the HEDL disk-bend test machine and are using it to qualitatively screen alloys that are susceptible to embrittlement caused by irradiation. Tests designed to understand the disk-bend test in relation to a uniaxial test are discussed. Selected results of tests of neutron-irradiated material are also presented.

2.5.4 Progress and Status

2.5.4.1 Introduction

Because of space limitations in nuclear irradiation facilities, many attempts have been made to reduce the size of mechanical property test specimens used to determine the effect of irradiation on mechanical properties. The ductility of many structural alloys is decreased by neutron irradiation, and such embrittlement may limit the use of the material. It would therefore be useful to have a simple test on small specimens that could be used to detect embrittlement due to irradiation. Such a test could be used as a simple screening test in a program to develop alloys for resistance to irradiation damage.

Hanford Engineering Development Laboratory (HEDL) has developed a mechanical test technique to determine changes in ductility by bending transmission electron microscopy (TEM) disks (3 mm diameter by 0.25 mm thick) in a hemispherical punch and die.[1] The test apparatus was designed to operate on the crosshead of a standard Instron tensile test machine, where the punch load and displacement can be monitored during testing.

We have built a modified version of the HEDL test apparatus for screening candidate structural alloys for fusion reactor applications. Studies designed to understand the test technique will be discussed along with examples of preliminary results of disk-bend tests on candidate first-wall alloys.

2.5.4.2 Experimental

A modified version of the HEDL test apparatus was constructed. The size of the hemispherical punch and die was the same as that used in the HEDL test, but the overall size of the test fixture was reduced to fit into the vacuum chamber used for hot-cell tensile tests. A similar fixture was fabricated for the out-of-cell tests in a similar vacuum chamber.

The test apparatus is shown in Fig. 2.5.1. The main parts of the apparatus include the hemispherical punch with a 1.59-mm (0.0625-in.) radius, die (same radius as punch), and the 2.4-mm-diam (0.093-in.) guide rods, which were welded into place to maintain alignment of the system during testing. The punch, die, and guide rods were constructed of hardened Inconel 718;* the remainder of the apparatus

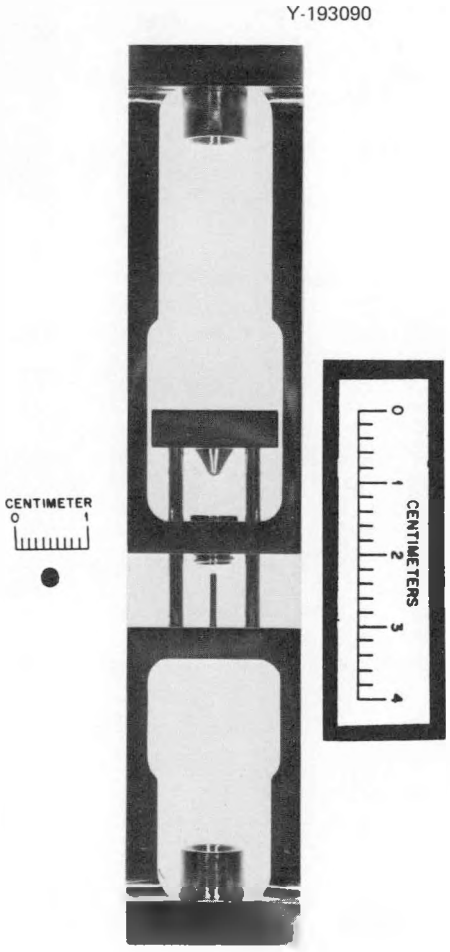

Fig. 2.5.1. Disk-bend test apparatus; TEM disk is also shown

*Inconel is a registered trademark of International Nickel Company, Inc.

was made from type 304 stainless steel. Figure 2.5.2 shows the apparatus installed in the tensile machine. The test apparatus was installed in a vacuum chamber fitted to a 40 kN capacity Instron universal testing machine. The apparatus was adapted to the load train with a simple ball-and-socket arrangement, used to provide alignment.

To allow the disk to be easily centered above the die, a 0.05-mm-wide by 0.254-mm-deep (0.002-in. by 0.01-in.) recessed lip was machined around the top of the die. The outer diameter of the recessed lip is slightly larger than the diameter of the test disk. To conduct a test, a disk (3-mm diameter by 0.25 mm thick) is first placed on the recessed lip above the hemispherical cavity. The punch is then drawn into the specimen, and the load and displacement are monitored.

Y-193089

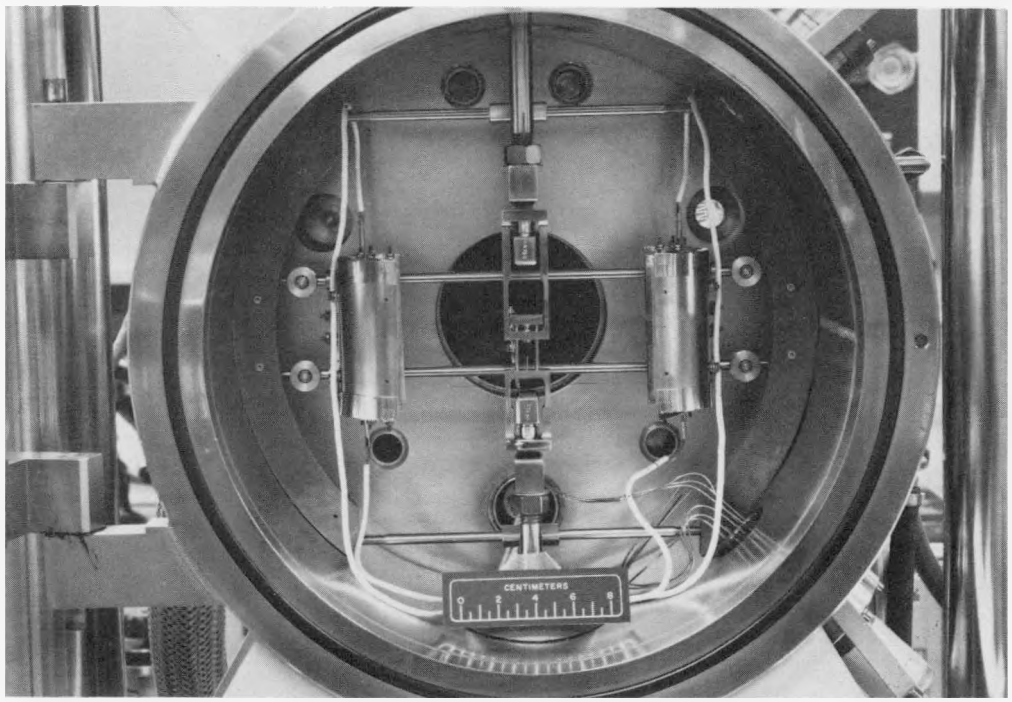

Fig. 2.5.2. Disk-bend test apparatus installed on the load train of the tensile test machine. The apparatus is installed inside a vacuum test chamber.

Our objective is to describe the operation of the disk-bend apparatus and to develop an understanding of the relationship between the ductility determined in a biaxial disk-bend test and that determined in a uniaxial tensile test. To make the ductility comparisons, the ferritic stainless steel type 446 was chosen; the nominal chemical composition for this steel in wt. % is: 23.7 Cr, 0.46 Ni, 0.46 Mn, 0.29 Si, 0.046 C, and 0.13 N. After a solution anneal of 1 h at 1050°C, the steel was quite ductile (total elongation exceeded 20%). The solution-annealed steel can be embrittled by aging for various times at 475°C. (Aging 100 h reduces the total elongation to less than 0.5%.)

Miniature tensile specimens 31.8 mm long (1.25 in.) with a reduced gage section 12.7 mm (0.5 in.) long by 1.0 mm (0.040 in.) wide were used for comparative tests. The tensile specimens were punched from the same 0.25-mm-thick sheet from which the TEM specimens were punched.

2.5.4.3 Results and Discussion

A large number of alloys are embrittled when irradiated with neutrons.[2] When the Cr-Mo ferritic steels and austenitic stainless steels are irradiated and tensile tested at low temperatures, considerable hardening is observed; the hardening is accompanied by a decrease in ductility. At elevated temperatures (above about 600°C), several alloys, including the austenitic stainless steels and nickel-base alloys, are embrittled by small amounts of helium.[2] The disk-bend apparatus is to be used to detect large changes in ductility caused by irradiation. In an alloy development program containing a large number of alloys, it may be possible to use the disk-bend test as a screening technique to eliminate alloys with a tendency toward excessive embrittlement.

Before a test technique can be profitably used, it is necessary to understand its operation. Figure 2.5.3 shows a typical room-temperature disk-bend load-deflection curve for type 446 stainless steel in a ductile condition. The shape of the disk-bend curve shown in Fig. 2.5.3 is the same for all ductile materials tested to date, including the ferritic stainless steel type 446, several austenitic stainless steels, several Cr-Mo steels, and the $(Fe,Ni)_3V$ long-range-ordered alloys.

The disk-bend test in Fig. 2.5.3 was conducted to a punch displacement of 0.51 mm (0.02 in.). All disk-bend tests were arbitrarily stopped at or before this displacement was reached in order to avoid damaging the test fixture. Any irradiated specimen that deformed to this displacement would be assumed to have sufficient ductility for further evaluation in a test program. Also shown in Fig. 2.5.3 is a load-deflection curve for a uniaxial test on the same material. Although the test was run to fracture at a total elongation of 8.4% [a displacement of 1.07 mm (0.042 in.)], only the early portion is shown.

The shape of the load-deflection curve for a disk-bend test is complicated and differs significantly from that for a uniaxial tensile test (Fig. 2.5.3). The initial portions are similar: both are linear, indicating elastic behavior. When a disk-bend or a tensile specimen is reloaded after being deformed into this region, the same loading curve is reproduced. After the linear portion of the curve ends, the rate of loading decreases, which is similar to the yield behavior observed for a uniaxial tensile test. Beyond this point, however, the two types of curves begin to differ. Whereas the slope of the tensile curve remains constant or decreases slightly between the yield stress and the ultimate tensile strength, the slope of the disk-bend curve goes through an inflection point (point A of Fig. 2.5.3) and begins to increase.

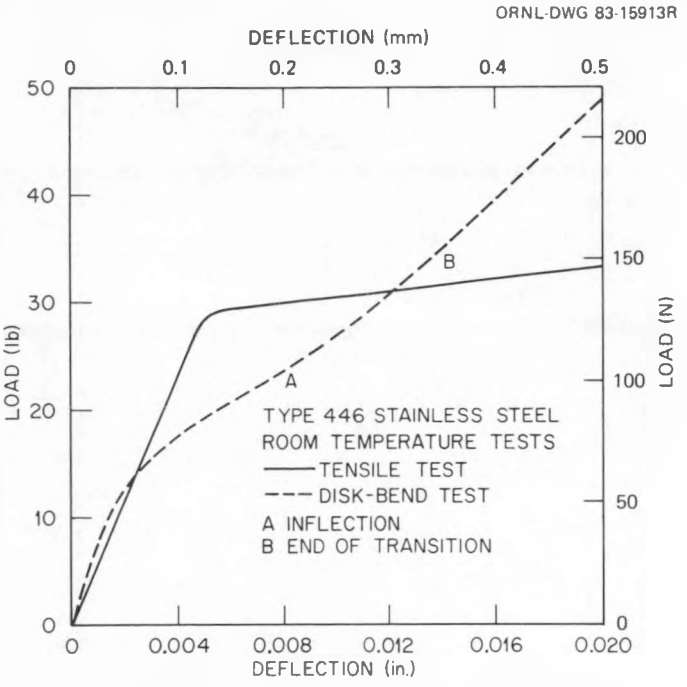

Fig. 2.5.3. Room-temperature disk-bend and uniaxial tensile load-displacement curves for solution-annealed type 446 stainless steel. The disk-bend test was discontinued after a displacement of 0.51 mm (0.02 in.).

Manahan has analyzed the deformation behavior during a disk-bend test.[3] In the region of the curve immediately following the elastic portion, deformation was concluded to be bending that is controlled by the "radial propagation of the yield surface from the region of contact with the punch," and "is governed primarily by the yield stress."[3] The region of the curve where the slope again begins to increase is a transition region to the region where the slope is again relatively constant. This latter region is where the "membrane stretching regime is dominant in most regions of the plate [disk]."[3] This analysis gives an indication of the complexity of the deformation sequence. We have noted that for essentially all of our ductile test specimens, the start of the transition from the bending deformation mode to the membrane stretching deformation mode occurs at a deflection that is approximately equal to the specimen thickness (0.25 mm). A similar observation is made when the curves published by Manahan et al. are examined.[4] If the deformation for a ductile material is continued beyond that shown in Fig. 2.5.3, the load eventually begins to decrease in coincidence with the specimen thinning or fracture.[3,4]

From disk-bend tests on brittle materials, we have been able to show that disk fracture is accompanied by a load drop (an exception will be discussed later). This was determined by discontinuing tests immediately after a load drop and examining the specimens by optical and/or scanning electron microscopy (SEM). A crack was detected in all instances.

The disk-bend curves for room-temperature tests on molybdenum in a brittle condition are shown in Fig. 2.5.4, along with a photomicrograph of a fractured specimen. Figure 2.5.5 shows similar curves along with an SEM photomicrograph for brittle type 446 stainless steel. Fracture occurred with little plastic deformation; the test was discontinued immediately after fracture. If the test of a brittle material is not discontinued immediately after the initial load drop, the load can continue to increase — sometimes up to the 0.51-mm (0.02-in.) stop (Fig. 2.5.6). The load increase is accompanied by further sharp drops in the curve, and the specimen contains cracks (Fig. 2.5.6) that have been opened by the continued deformation.

It would be extremely useful to have a correlation between the ductility determined in a biaxial disk-bend test and a uniaxial tensile test. Huang, Hamilton, and Wire[1] derived the following equation for the strain in a disk-bend test:

$$\varepsilon = \omega t/(a^2 + \omega^2) \ , \qquad (1)$$

where ε is the strain at the center of the disk, t the thickness, a the disk radius, and ω the deflection at the center of the disk. Because this equation is based on elastic behavior, it can be used only as an estimate, good only for small plastic strains. It was shown to give reasonably good agreement with the tensile measurements to approximately 1% strain.[1] It is not useful in the membrane-stretching regime.

To obtain the ductility from the disk-bend load-deflection curve, the same technique is used as is used for a tensile curve. Namely, the displacement measurement at fracture is made from the modulus line; the strain is then calculated from Eq. (1).

One of the objectives for this work was the development of a correlation of the disk-bend and tensile ductility beyond the limit of Eq. (1). One way to accomplish this would be to test disk-bend and tensile

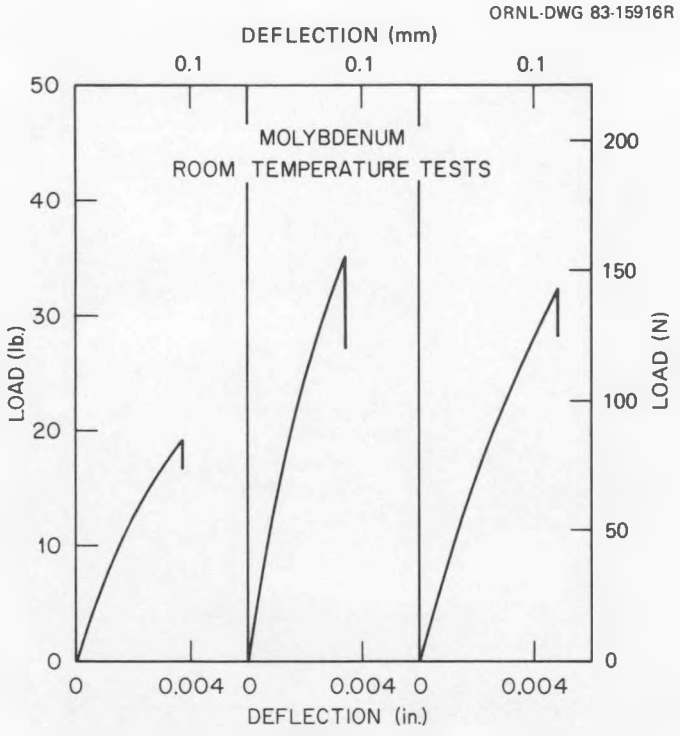

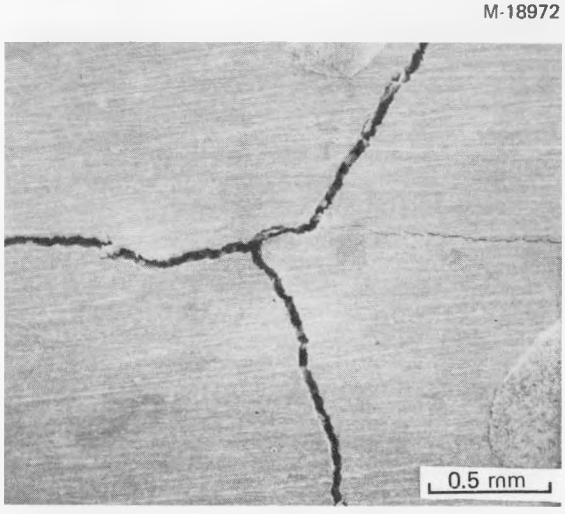

Fig. 2.5.4. Disk-bend load-deflection curve for brittle molybdenum specimens tested at room temperature. A photomicrograph of a fractured specimen is also shown.

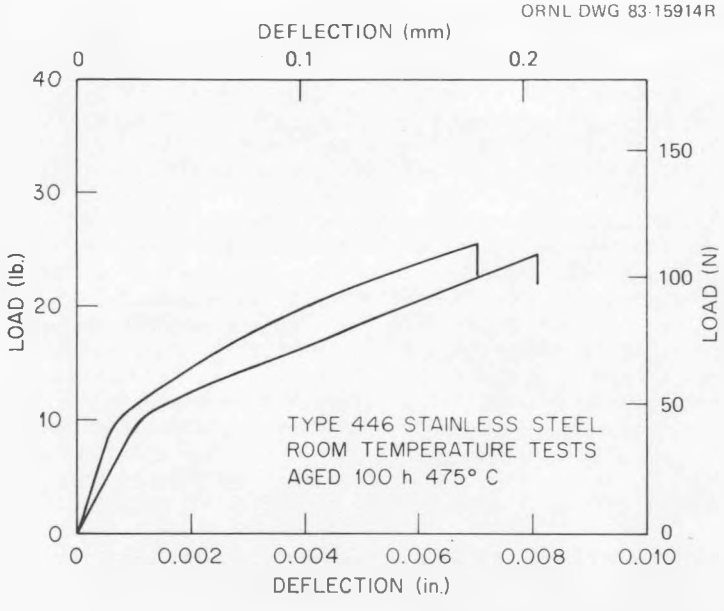

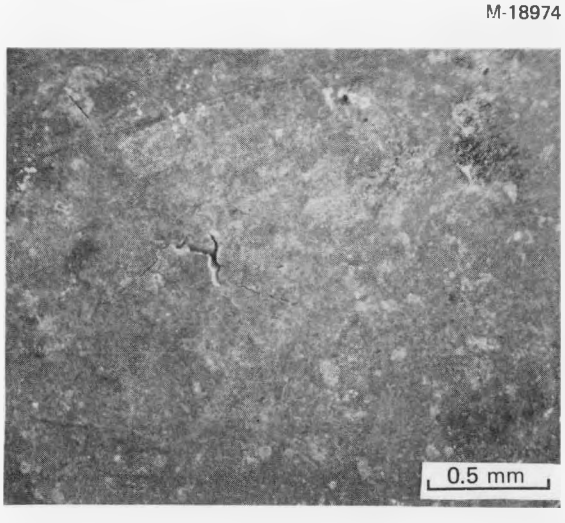

Fig. 2.5.5. Disk-bend load-deflection curve for embrittled type 446 stainless steel specimens tested at room temperature. The test was discontinued immediately after a load drop. A photomicrograph of one of the specimens is also shown.

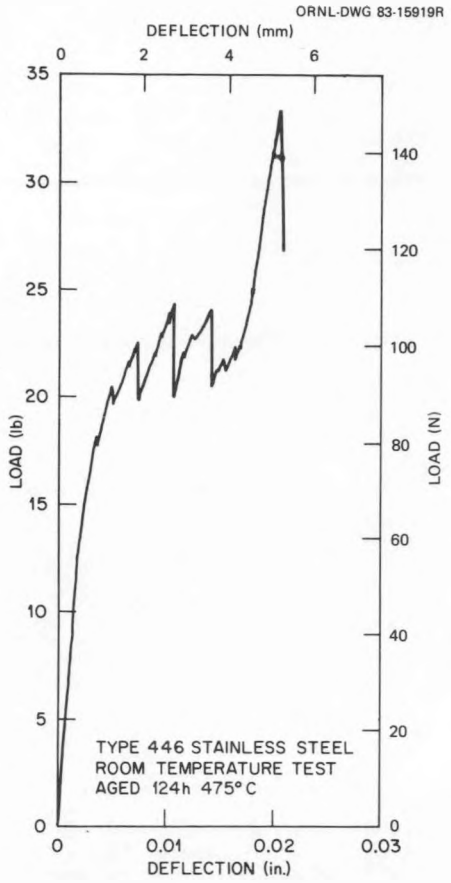

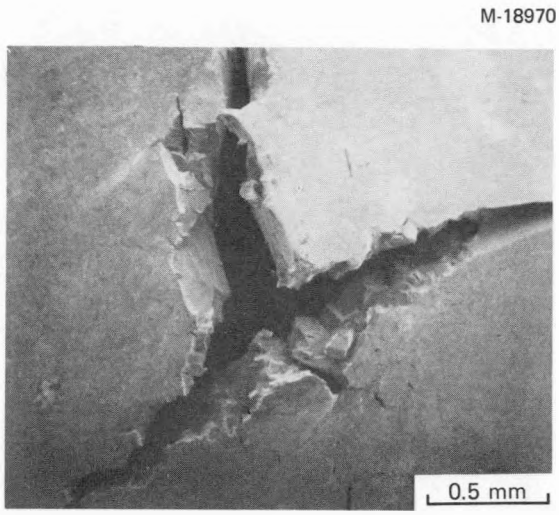

Fig. 2.5.6. Disk-bend load-deflection curve for brittle type 446 stainless steel specimen tested at room temperature; the test was continued after the initial load drop (a load drop indicates fracture). A photomicrograph of the test specimen is also shown.

specimens that have been similarly irradiated to produce various amounts of embrittlement. Unfortunately, no such irradiated specimens were available. For that reason, we have attempted to experimentally correlate disk-bend and tensile ductility for the ferritic stainless steel type 446 after it was embrittled by a thermal aging treatment. This work is still in progress. To date we have determined that the 0.51-mm deformation limit used in the present studies corresponds to about a 4% uniaxial tensile strain.

The sharpness of the load drop when fracture occurs depends on the material as well as on the test temperature. (The tests discussed above were conducted at room temperature.) The disk-bend test was used to investigate the embrittlement of the $(Fe,Ni)_3V$ long-range-ordered alloys between 400 and 600°C after irradiation at the same temperature in HFIR (ref. 5). In the unirradiated condition, the load-deflection curves at 400 to 600°C for this material were similar to those of the other materials tested at room temperature [Fig. 2.5.7(*a*)]. Several alloy compositions were investigated after irradiation to fluences producing 12 dpa and up to 1000 at. ppm of transmutation helium. For the irradiated $(Fe,Ni)_3V$ a slightly different load-deflection curve was obtained for the brittle materials [Fig. 2.5.7(*b*) and (*c*). The abrupt decrease in load was not detected. Rather, a maximum was reached after which the load decreased rather gradually with further deformation.

Scanning electron microscopy studies of fractured specimens (two of which are shown in Fig. 2.5.8) showed that the material was extremely brittle and failed intergranularly. We believe that the cracks initiated at the point in the curve where the load began to decrease.

The disk-bend tests on the $(Fe,Ni)_3V$ long-range-ordered alloys irradiated and tested at temperatures between 400 and 600°C were used to scope the extent of embrittlement with dpa and helium concentration.[5] Data were assessed on a pass-fail criterion (Fig. 2.5.9) or based on the strain as evaluated by Eq. (1) (Fig. 2.5.10). The pass-fail criterion was determined by noting whether specimens could be deformed to a 0.51-mm (0.02-in.) deflection without fracture. In Fig. 2.5.9 the filled symbols represent those that fractured, open symbols those that deformed 0.51 mm. The curve shown indicates that embrittlement becomes more severe with increasing temperature and increasing neutron fluence. These same results are shown more quantitatively when disk-bend ductility values estimated with Eq. (1) are plotted as a function of damage

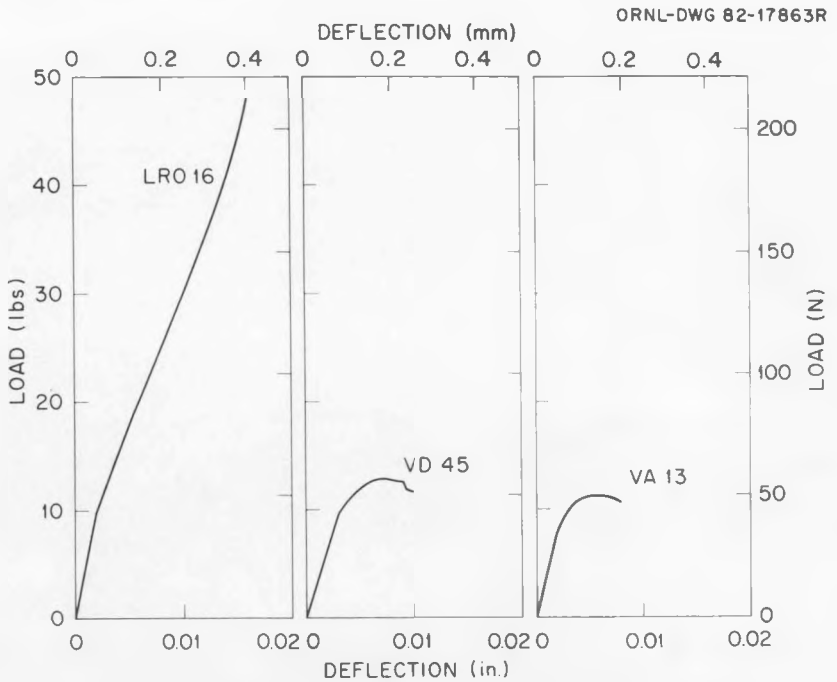

Fig. 2.5.7. Disk-bend curves for $(Fe,Ni)_3V$ long-range-ordered alloys tested at 600°C. (*a*) Unirradiated control. (*b*) and (*c*) Specimens irradiated at 600°C in HFIR to 12 dpa and 1000 at. ppm He.

level (Fig. 2.5.10). The disk-bend test has proved valuable for such scoping studies.[5] Microstructural studies are presently in progress to determine the cause of the embrittlement in the $(Fe,Ni)_3V$ alloys.

Manahan, Argon, and Harling[3,4] of Massachusetts Institute of Technology (MIT) have designed a somewhat different disk-bend apparatus from that used in the present tests and that developed by HEDL.[1] One of the principal differences is that the punch used in the MIT bend test has a tip radius that is approximately one-third of that used in the HEDL-designed apparatus.

Manahan et al.[4] tested 10 specimens of 20%-cold-worked type 316 stainless steel and found the scatter band shown in Fig. 2.5.11. We have superimposed two other tests conducted in the present investigation on this scatter band. These two tests were discontinued after a 0.51-mm (0.02-in.) deflection. The agreement is excellent, despite the fact that different heats of type 316 stainless steel were tested. We also found very good reproducibility for our machine on ductile materials, as shown in Fig. 2.5.12 for multiple tests on type 446 stainless steel.

The above discussion relating changes in the disk-bend curves to the fracture of the disk indicated that a drop in load accompanied the start of fracture. However, recent observations on the Path A Prime Candidate Alloy (PCA) austenitic stainless steel have shown that this is not always the case.[6] Tests at 400, 500, and 600°C were made on several microstructural variations of PCA that had been irradiated at the same temperature in HFIR to produce 22 dpa and up to 1700 at. ppm He. In the most embrittled condition, the load-drop behavior was similar to that of the long-range-ordered alloy at 600°C (Fig. 2.5.7), and a brittle fracture was observed by SEM. However, several tests were run on PCA where no load drop was detected, but the SEM examination showed that fracture had occurred. The disk-bend curves in this case contained a "waviness" not present in the curves for ductile material. This waviness may have been an indication that there was a decrease in the rate at which the load was increasing (i.e., a difference in slope from the curve of an unirradiated specimen). Although an intergranular fracture was observed, the initial conclusion was that the alloy was more ductile than those that were accompanied by a pronounced load drop.[6] This "more ductile" behavior appears to be characterized by cracks that propagate more slowly and are accompanied by tearing (as opposed to rapid propagation through the specimen thickness for an extremely brittle material). Work is in progress to understand this behavior; this work will eventually include the comparison of tensile tests and disk-bend tests.[6]

2.5.5 Summary and Conclusions

A modified version of the disk-bend apparatus originally developed by HEDL was fabricated and tests were conducted to understand the the test technique and to use the test on irradiated materials. The apparatus consists of a punch and die that are used to bend a TEM disk. To conduct a test, the apparatus is installed in a tensile test machine, and a load-deflection curve is recorded as the punch bends the disk into the die. The following summarizes our observations and conclusions.

M-14998

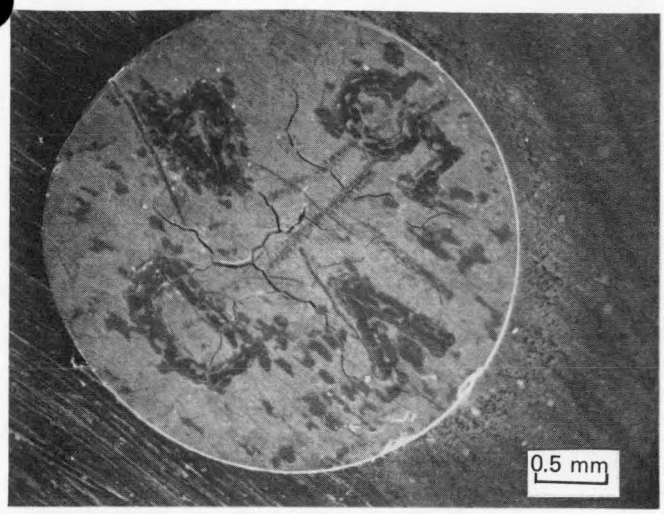

(*a*)

M-15002

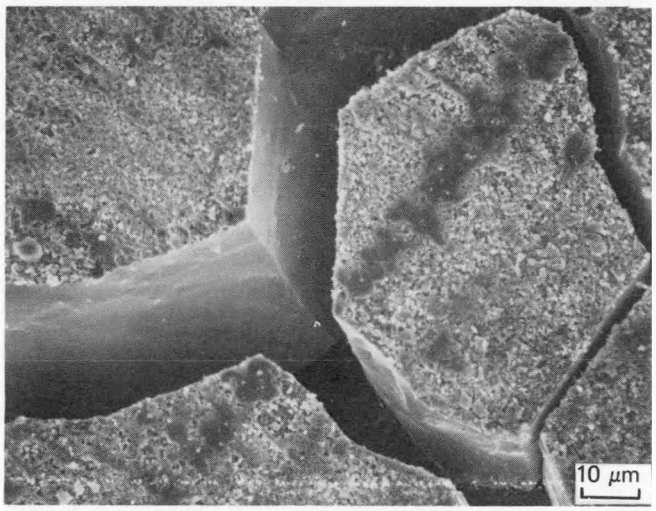

(*b*)

M-14983

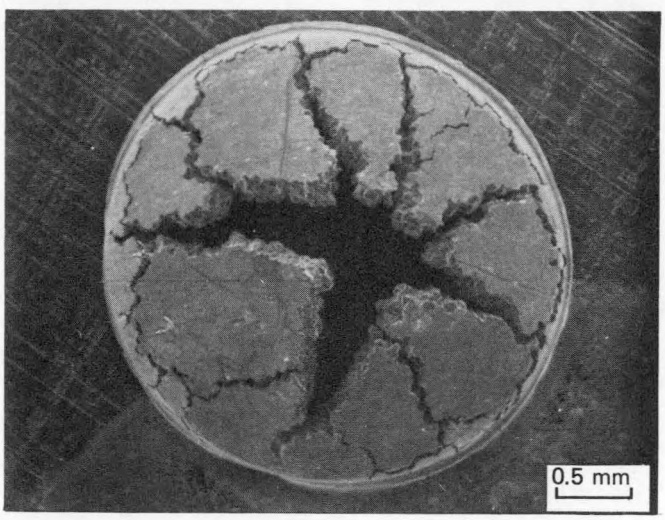

(*c*)

M-14987

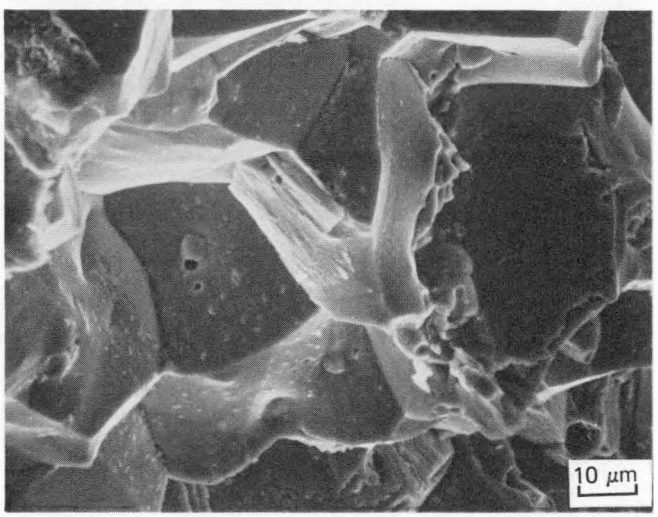

(*d*)

Fig. 2.5.8. Photomicrographs of brittle long-range-ordered alloy specimens fractured at 600°C. The disk-bend curve for the upper specimen was shown in Fig. 2.5.7(*b*), the curve for the lower specimen in Fig. 2.5.7(*c*).

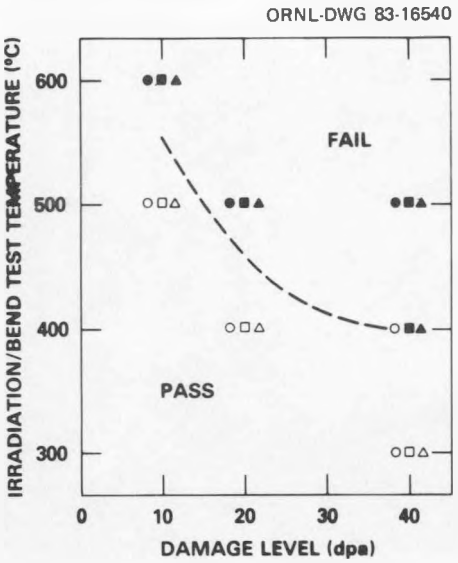

Fig. 2.5.9. Graph of irradiation and disk-bend test temperature against displacement-damage level on which three long-range-order alloys have been plotted. Filled symbols are for disk-bend specimens that failed in a brittle manner; open symbols are for specimens that deformed to the 0.51-mm displacement limit of the apparatus.

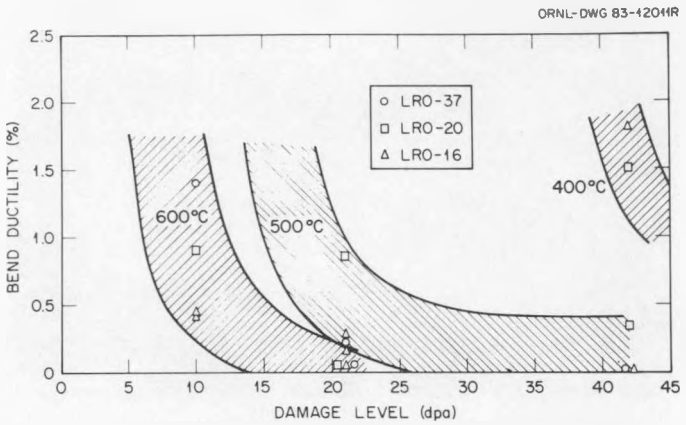

Fig. 2.5.10. Bend ductility as a function of displacement-damage level for three long-range-order alloys irradiated and tested at 400, 500, and 600°C that shows the effect of temperature and displacement damage on ductility.

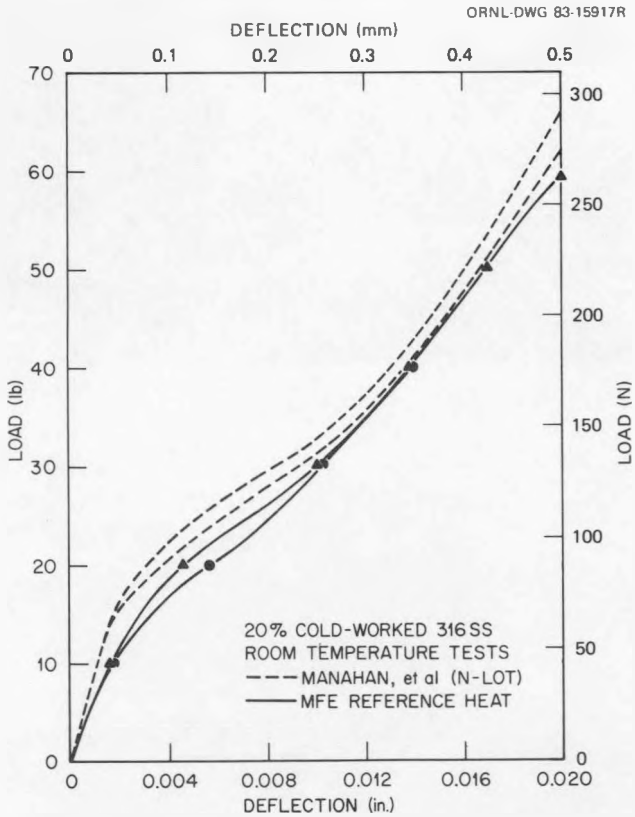

Fig. 2.5.11. Comparison of data points taken from two disk-bend tests conducted on 20%-cold-worked type 316 stainless steel (heat X15893, the MFE reference heat) with scatter band for ten tests (N-lot heat) taken from ref. 4.

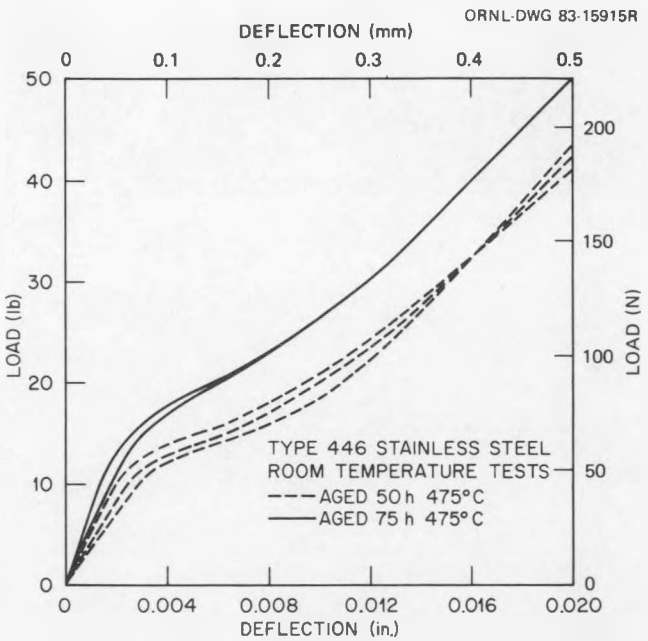

Fig. 2.5.12. Disk-bend tests on aged type 446 stainless steel that show the reproducibility of disk-bend tests. Different aging times at 475°C led to different strength levels.

1. The bend test is convenient, gives reproducible results on small test specimens, and provides a useful method for qualitatively screening materials that are susceptible to irradiation embrittlement.
2. The deformation behavior of a disk during the bend test is complex and not easily analyzed.
3. Disk fracture is normally easily detected because it is accompanied by a drop in load. An exception to this behavior was noted in an austenitic stainless steel.

2.5.6. References

1. F. H. Huang, M. L. Hamilton, and G. L. Wire, "Bend Testing for Miniature Disks," *Nucl. Technol.* 57, 234–42 (1982).
2. E. E. Bloom, "Irradiation Strengthening and Embrittlement," *Radiation Damage in Metals*, ed. N. L. Peterson and S. D. Harkness, American Society for Metals, Metals Park, Ohio, 1976, pp. 295–329.
3. M. P. Manahan, *The Development of a Miniaturized Disk Bend Test for the Determination of Post-Irradiation Mechanical Behavior*, Ph.D. Thesis, Massachusetts Institute of Technology, May 1982.
4. M. P. Manahan, A. S. Argon, and O. K. Harling, "The Development of a Miniaturized Disk Bend Test for the Determination of Postirradiation Mechanical Properties," *J. Nucl. Mater.* 103&104, 1545–49 (1981).
5. D. N. Braski, "Microstructure and Bend Ductility of a $(Fe,Ni)_3V$ Ordered Alloy Irradiated in HFIR," *J. Nucl. Mater.*, to be published.
6. P. J. Maziasz, Private Communication to R. L. Klueh, August 1983.

3.1 IMPROVED SWELLING RESISTANCE FOR PCA AUSTENITIC STAINLESS STEEL UNDER HFIR IRRADIATION THROUGH MICROSTRUCTURAL CONTROL — P. J. Maziasz and D. N. Braski (Oak Ridge National Laboratory)

3.1.1 ADIP Tasks

ADIP Tasks I.C.1, Microstructural Stability, and I.C.2, Microstructure and Swelling in Austenitic Alloys.

3.1.2 Objective

This work is intended to evaluate the effect of preirradiation microstructural variation on swelling of the Path A PCA irradiated in the HFIR. These results are compared with results on several heats of type 316 and 316 + Ti stainless steel similarly irradiated.

3.1.3 Summary

Swelling evaluation of PCA variants and 20%-cold-worked (N-Lot) type 316 stainless steel (CW 316) at 300–600°C was extended to 44 dpa. Swelling was negligible in all the steels at 300°C after ~44 dpa. At 500 to 600°C 25%-cold-worked PCA showed better void swelling resistance than type 316 at ~44 dpa. There was less swelling variation among alloys at 400°C, but again 25%-cold-worked PCA was the best.

3.1.4 Progress and Status

Compositions of the PCA alloy and three other comparison materials designated DO-heat and N-lot 316s, and the R1-heat of 316 + Ti are given in Table 3.1.1. Designations, descriptions, and thermo-mechanical pretreatments for the preirradiation microstructural variants of the PCA are given in Table 3.1.2. Standard 3-mm-diam disks were punched from 0.254-mm-thick sheet stock. The PCA and 20%-cold-worked (CW) 316 (N-lot) disks were irradiated in experiments HFIR-CTR-30, -31, and -32, at 300, 400, 500, and 600°C, with temperatures verified by temperature monitors. More detail is available elsewhere.[1,2] Cavity volume fraction (cvf) swelling was measured by transmission electron microscopy (TEM), described elsewhere.[3] Data are also included on solution-annealed (SA) and CW 316 (DO-heat) and CW 316 + Ti (R1-heat) from previous experiments,[3,4] with irradiation temperatures ranging from 325 to 755°C and fluence from ~3 to 69 dpa. (These experiments were designated HFIR-SS-2 through -6 and HFIR-CTR-9 through -13.) Calculated irradiation temperatures from the older HFIR experiments have been corrected[5] upward by 50 to 75°C. All displacement damage (dpa) calculations in this work include the recent correction (increase) due to helium production from nickel transmutations reported by Greenwood.[2] The dpa values for HFIR-CTR-30, -31, and -32 ranged from ~10.5 dpa (calculated from dosimetry[2]) to ~44 dpa (estimated, pending dosimetry). Helium levels range up to about 3000 at. ppm for the type 316 and up to ~3600 at. ppm for the PCA at ~44 dpa.

Table 3.1.1. Alloy compositions

Element	Content (wt. %)			
	DO-heat 316	N-lot 316	R1-heat 316 + Ti	PCA
Fe	Bal	Bal	Bal	Bal
Ni	13.0	13.5	12.0	16.2
Cr	18.0	16.5	17.0	14.0
Ti	0.05		0.23	0.24
Mo	2.6	2.5	2.5	2.3
Mn	1.9	1.6	0.5	1.8
C	0.05	0.05	0.06	0.05
Si	0.8	0.5	0.4	0.4
P	0.01	0.09	0.01	0.01
S	0.016	0.006	0.013	0.003
N	0.05	0.006	0.006	0.01

3.1.4.1 Temperature and Fluence-Dependence of Swelling

Of the six PCA variants examined, PCA-A2, -B1, and -C were eliminated from further consideration because of poor swelling resistance identified at ~10.5 dpa at 500 and 600°C. The data are plotted as functions of temperature in Fig. 3.1.1 and are tabulated elsewhere.[6] The PCA variants and CW 316 (N-lot) show increased swelling with increased irradiation temperature. Study of PCA-A1 was continued as a higher swelling base line against which to gage swelling resistance at higher fluence. A trend band for the CW 316 (DO-heat) and CW 316 + Ti (R1-heat) data in this temperature and fluence range is also included in Fig. 3.1.1. At temperatures above 500°C, these alloys show better swelling resistance than the PCA variants or CW 316 (N-lot). However, below 450 to 500°C, the situation is reversed.

The swelling values for PCA-A1, -B2, and -A3 and CW 316 (N-lot) are shown as functions of temperature in Fig. 3.1.2(*a*) and fluence in Fig. 3.1.2(*b*). Trend bands for data on SA and CW 316 (DO-heat) are included for comparison. The swelling of the PCA variants and CW 316 (N-lot) is low at 400°C and negligible at 300°C, even at ~44 dpa. The temperature dependence of swelling in PCA-A1 and CW 316 (N-lot) is weak and the level of swelling low at ~22 dpa; these are roughly parallel to the dependence found at ~10 dpa. The PCA-A3

Table 2. Alloy microstructural variants and thermomechanical pretreatments of PCA

Designation	Microstructure	Treatment
PCA-A1	Very low dislocation density	50%-CW + SA for 15 min at 1175°C
PCA-A2	Moderately high dislocation density	SA (A1 treatment) + 10% CW
PCA-A3	Very high dislocation density	SA (A1 treatment) + 25% CW
PCA-B1	Low dislocation density; medium-g.b. and coarse matrix MC	SA (A1 treatment) + 8 h at 800°C + 8 h at 900°C
PCA-B2	Very high dislocation density; medium-coarse g.b. and fine matrix MC	SA (A1 treatment) + 8 h at 800°C + 25% CW + 2 h at 750°C
PCA-C	Very high dislocation density; fine g.b. and matrix MC	SA (A1 treatment) + 25% CW + 2 h at 750°C

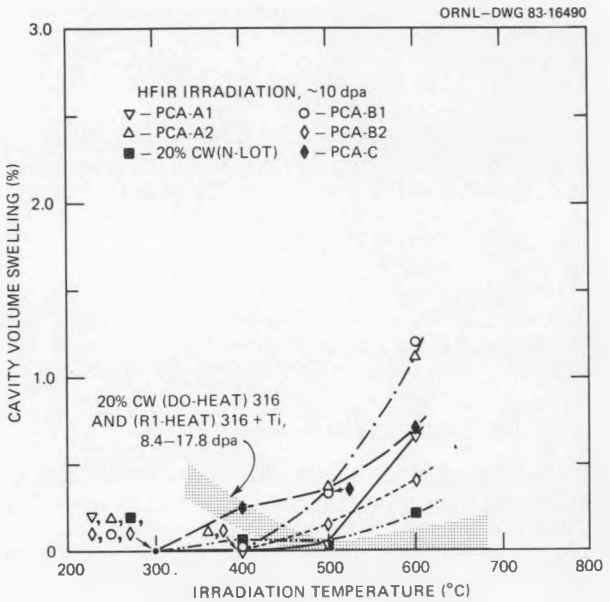

Fig. 3.1.1. Swelling as functions of temperature for PCA variants and several 20%-cold-worked stainless steels irradiated to lower fluences in HFIR.

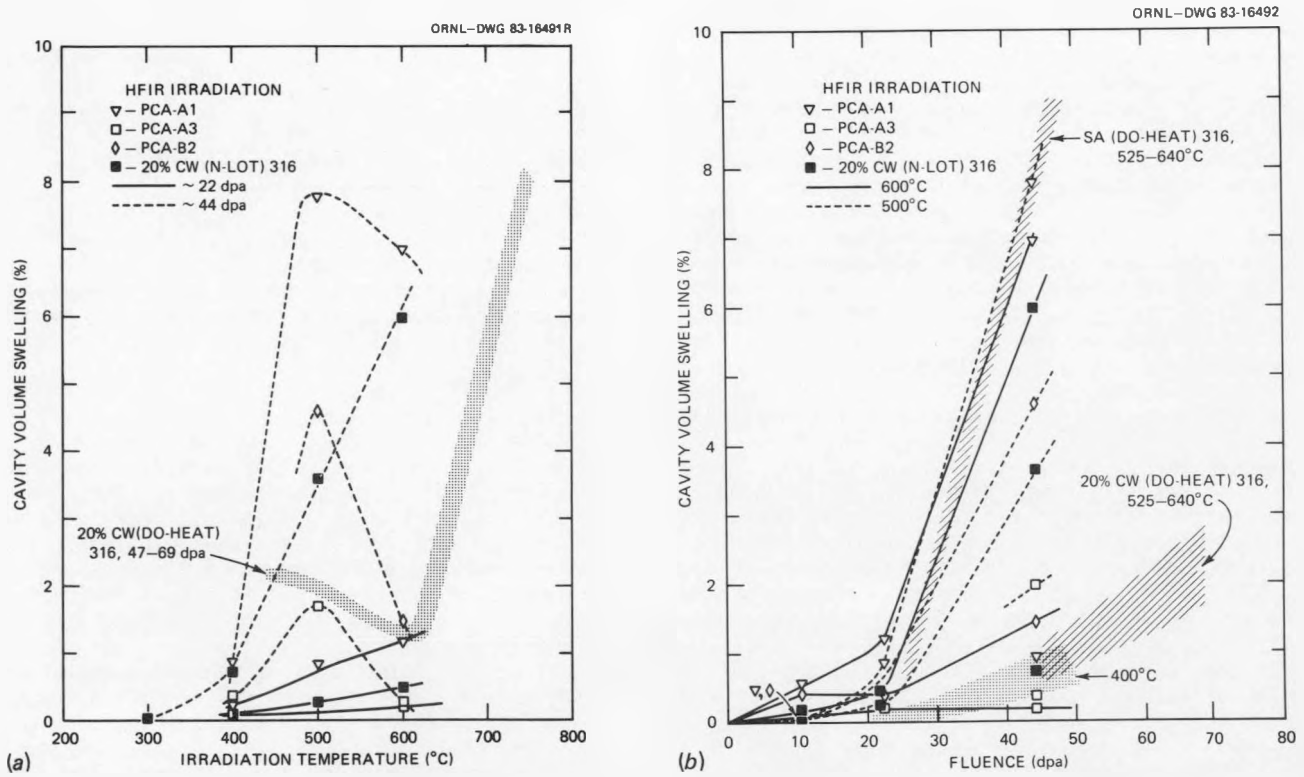

Fig. 3.1.2. Swelling of several HFIR-irradiated PCA variants and type 316s (*a*) as functions of temperature at 22 and 44 dpa and (*b*) as functions of fluence at 400 to 640°C.

has the lowest swelling, with the least temperature dependence at ~22 dpa. All of these alloys develop much stronger temperature dependence at ~44 dpa. Swelling of the PCA variants peaks at 500°C, whereas that of CW 316 (N-lot) increases monotonically from 400 to 600°C. Of the PCA variants, the swelling resistance of PCA-A3 is by far the best from 400 to 600°C. Also, PCA-A3 is considerably better than CW 316 (N-lot) at 500 to 600°C at 44 dpa, and PCA-A1, -B2, and CW 316 (N-lot) are clearly less resistant than CW 316 (DO-heat) at higher fluences for temperatures below 600°C.

At 400°C, PCA-A1, -A3, and CW 316 (N-lot) all swell at less than 0.04%-dpa, with the latter two showing the lowest rates. With increasing fluence, swelling rates increase rapidly after a low-swelling transient of about 20 to 25 dpa at both 500 and 600°C for PCA-A1 and CW 316 (N-lot) but only at 500°C for PCA-B2. These alloys roughly follow the high swelling behavior of SA 316 (DO-heat) irradiated at 525 to 640°C, with swelling rates after the transient region ranging from 0.16 to 0.37%-dpa. The PCA-A3 at 500°C and PCA-B2 at 600°C simply extend their lower fluence behavior with no additional rate increase, similar to CW 316 (DO-heat) irradiated at 525 to 640°C. For irradiation at 600°C, PCA-A3 shows virtually no increase in swelling from ~22 to ~44 dpa.

3.1.4.2 Microstructural Development

Over 50 TEM disks were examined, and the total microstructure (i.e., dislocation, precipitate, cavity, and grain boundary components) of each was observed in detail. Only a brief summary of these results appears in this paper; more details can be found elsewhere[6,7] and will be published later.

In these samples, swelling greater than about 0.5 to 1.0% appears to be due to formation of large voids (or bias-driven cavities[8]) initiated at small helium bubbles (or stable cavities), particularly at higher fluences at 400 to 600°C. An experimental basis for distinguishing between voids and bubbles has been suggested previously,[9] even though both can be described by the more general term of cavity. For example, at 600°C CW 316 (N-lot) and PCA-A1 begin forming voids at ~10.5 dpa[6,7] which then lead to the high-swelling void microstructures found at ~44 dpa and shown in Fig. 3.1.3(*a*) and (*b*), respectively. In contrast, large voids do not develop in PCA-A3 after similar exposure, as shown in Fig. 3.1.3(*c*). Although many fine bubbles can be found at lower fluences in the PCA-A1 and CW 316 (N-lot), they do not remain stable but coarsen with increasing fluence and convert to a combination of large matrix voids and precipitate-associated voids. Many more (up to a factor of 50) fine bubbles develop early in PCA-A3; these appear to be stable and do not coarsen appreciably or convert to voids. The microstructure of PCA-A3 at ~22 dpa is nearly identical with that shown at ~44 dpa in Fig. 3.1.3(*c*).

The temperature dependence of microstructural development between 300 and 600°C, is shown in Fig. 3.1.4 for PCA-A3 irradiated to ~44 dpa. At 300°C, bubbles are barely resolvable (<2 nm in diameter). High concentrations ($>10^{23}$ m^{-3}) of fine (4 to 5 nm in diameter) bubbles remain stable at 400 and 600°C [Fig. 3.1.4(*b*,*d*), respectively]. At 500°C, both matrix and precipitate-associated voids form.

Void swelling differences shown in Fig. 3.1.3 at 600°C correlate with differences observed in the evolution of the precipitate and dislocation components among these alloys. Both PCA-A1 and CW 316 (N-lot) develop higher dislocation concentrations, many more Frank interstitial loops, and radiation-induced phases [γ' (Ni_3Si) in this case] earlier in the irradiation than does PCA-A3. These in turn correlate with the onset of early bimodal cavity distributions in the matrix. The Frank loops remain in the microstructure to ~22 dpa at 600°C in CW 316 (N-lot) and to ~44 dpa in PCA-A1. In both of these steels, the γ' forms early and then dissolves, giving way at higher fluence to coarse η (M_6C) in the CW 316 (N-lot) and to coarse η and/or G phase in the PCA-A1. Fairly large voids then develop in association with these coarse precipitates. By contrast, a considerable amount of fine MC, very few Frank loops, and considerable dislocation recovery develop in PCA-A3 at ~22 dpa, and these then remain unchanged with increasing fluence. The one-to-one spatial correspondence between rafts of fine bubbles and clusters of fine MC particles can be seen in Fig. 3.1.5. Comparing PCA-A1 and -A3 at 600°C and ~44 dpa shows that the absence of voids correlates with maximum fine MC precipitation and minimum formation of coarse, radiation-induced solute segregation (RIS)-induced or -modified phases. Fine, stable MC is evident at both 400 and 600°C after ~44 dpa, but at 500°C MC is minimal and is mixed with coarser phases associated with voids. These correlations are consistent among the other PCA variants considered only at low fluence.[6,7]

3.1.4.3 Discussion

The comprehensive microstructural data reveal at least several expected and unexpected mechanisms influencing swelling resistance. It is expected that large differences in point defect sink strengths between alloys should influence both the critical radius for conversion of bubbles (or stable cavities) to voids and the bifurcation of possible cavity evolution to high- or low-swelling paths.[8,10] Furthermore, it is also expected that such large differences in cavity evolution can affect precipitation, leading to enhanced thermal precipitation (like MC) when RIS is suppressed or diluted in a refined, cavity sink-dominated system.[9] Similar correlations between void formation and phase evolution are also observed in a large body of data on PCA by Imeson et al.[11] It seems unexpected, at least from previous neutron irradiation data, that Frank loop formation should be so variable under the same irradiation conditions and so strongly correlate with void development and especially RIS-induced γ' formation at higher temperatures. What yet remains to be understood about the effects of helium on overall microstructural and microchemical evolution.

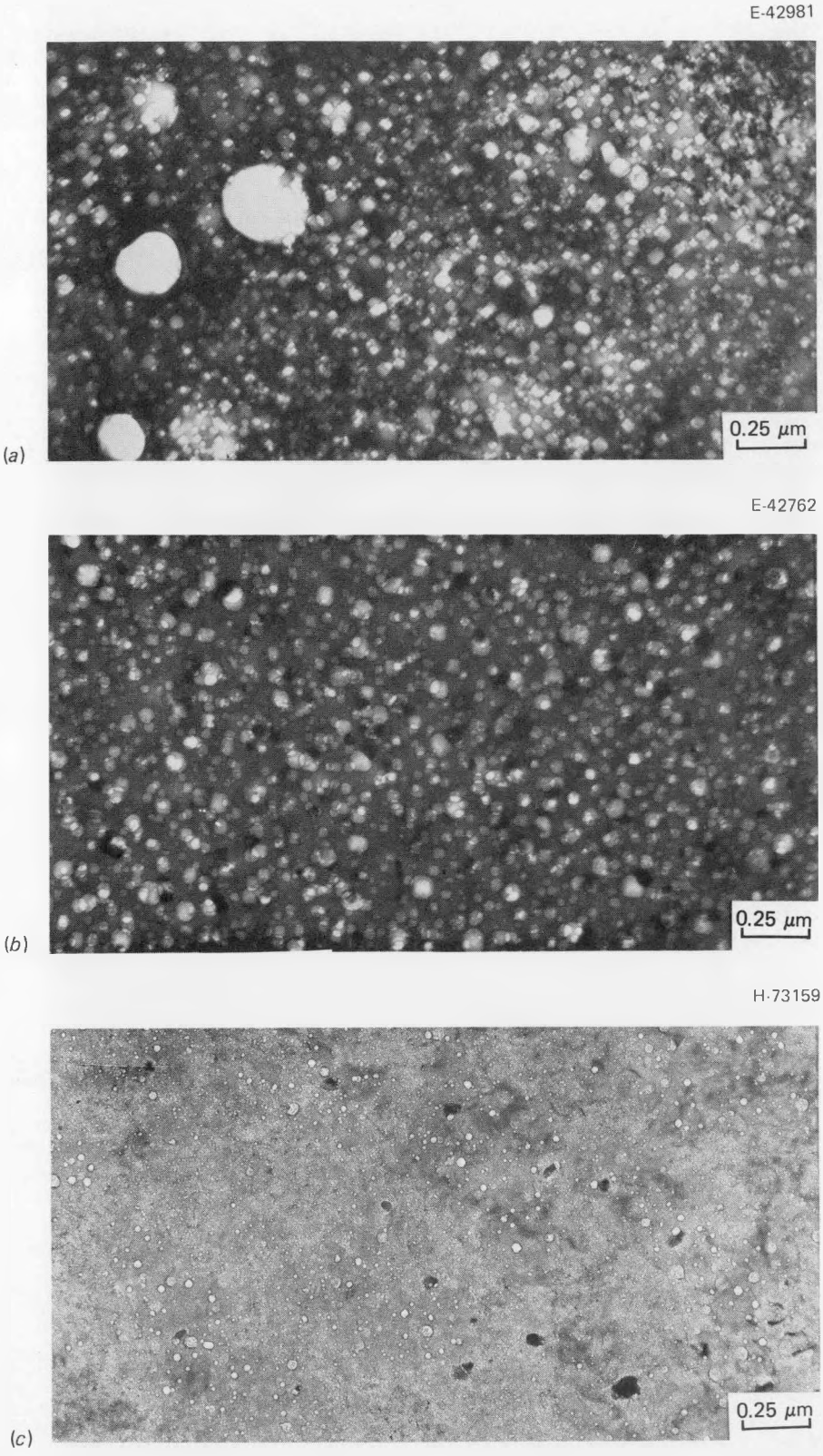

Fig. 3.1.3. Cavity microstructures of stainless steels irradiated in HFIR at 600°C to ~44 dpa. (*a*) CW 316 (N-lot). (*b*) PCA-A1. (*c*) PCA-A3.

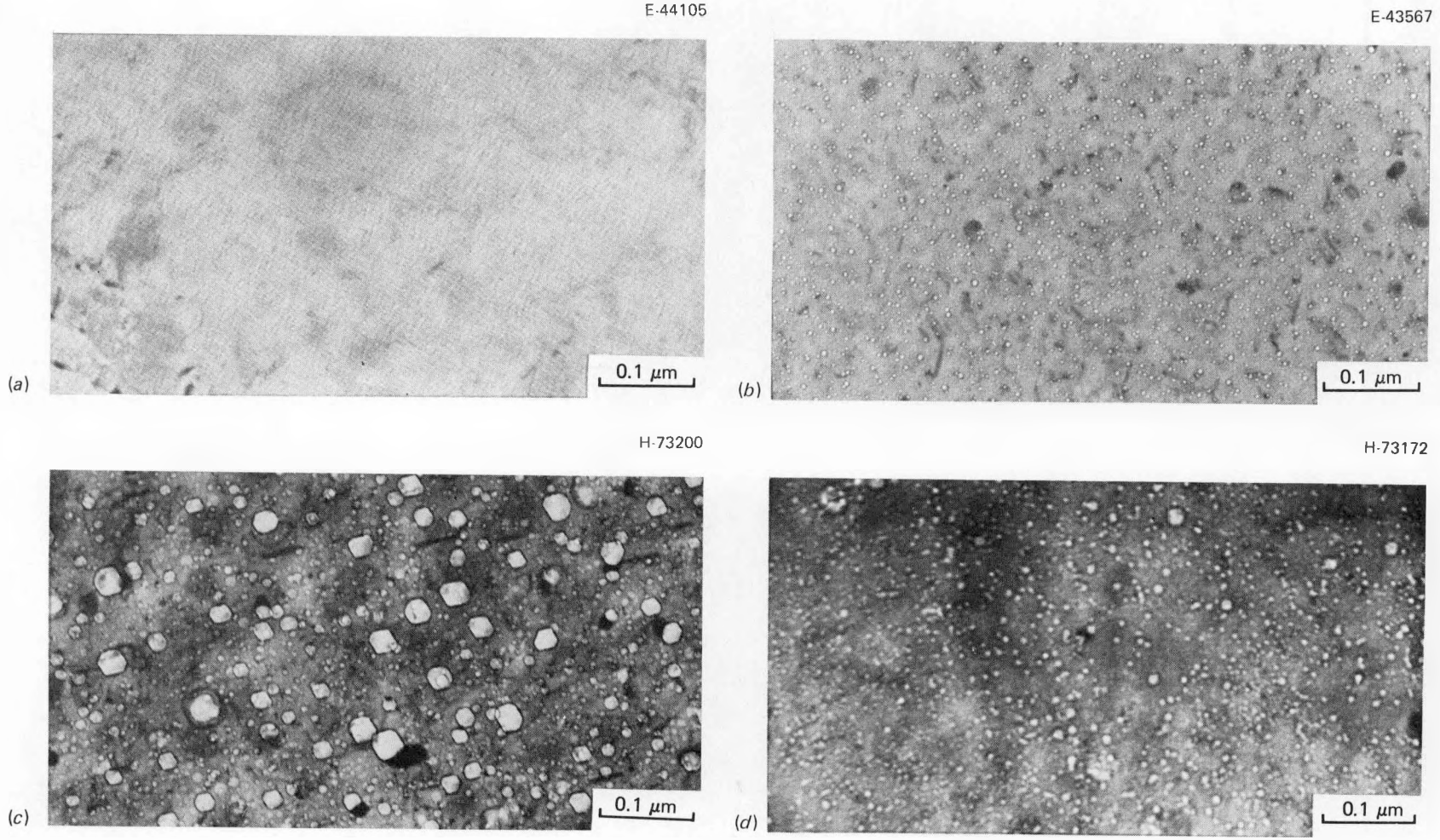

Fig. 3.1.4. Cavity microstructures of PCA-A3 irradiated in HFIR to ~44 dpa at (*a*) 300°C, (*b*) 400°C, (*c*) 500°C, and (*d*) 600°C. Note the void formation at 500°C.

H-73174

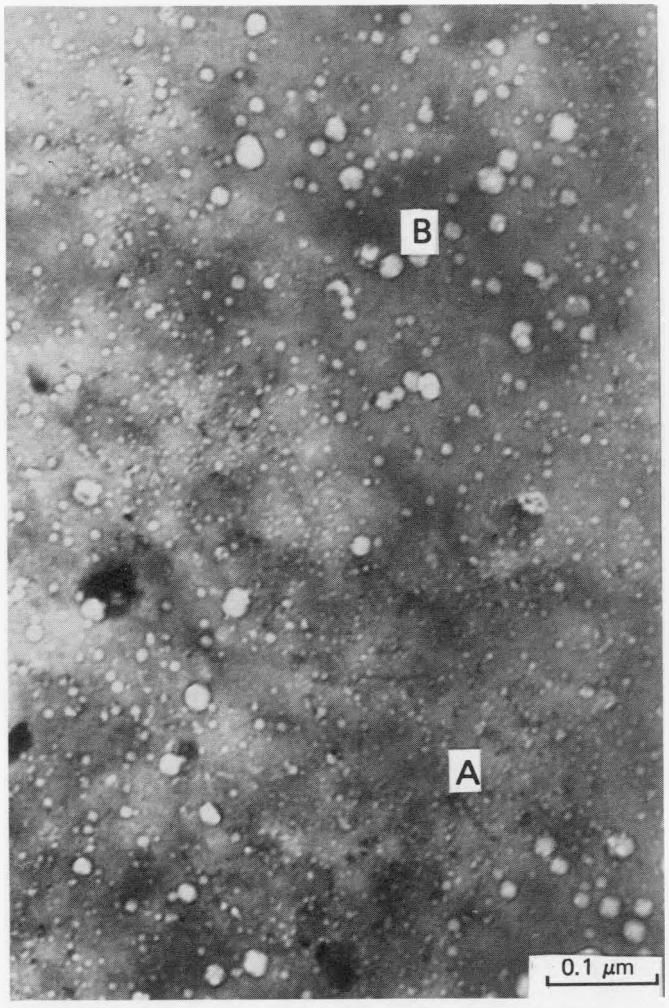

(a)

H-73177

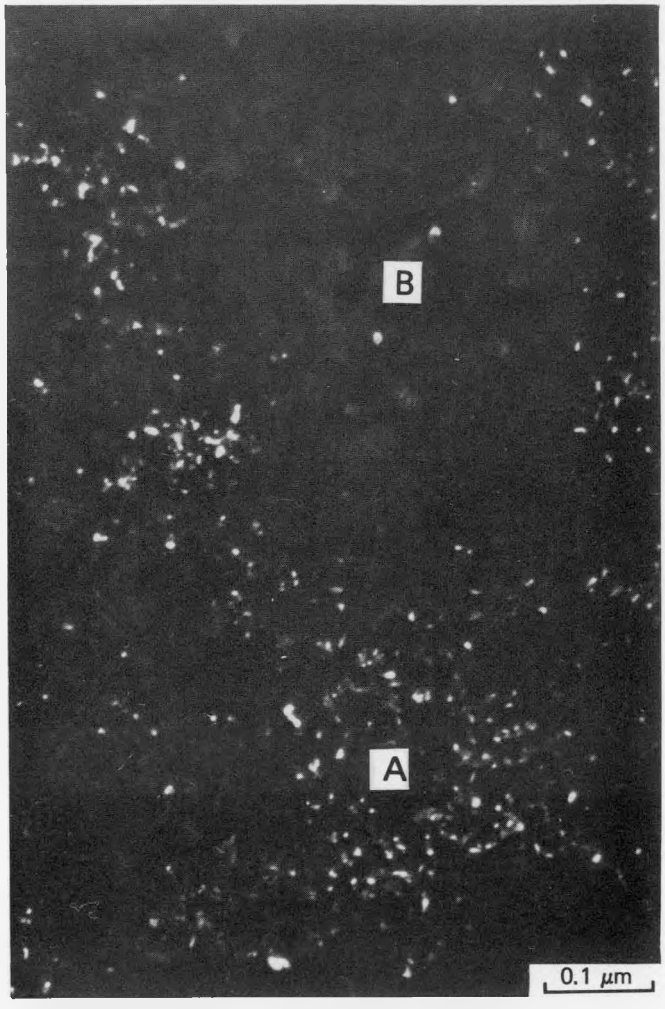

(b)

Fig. 3.1.5. Microstructural correlation of (*a*) patches of fine bubbles in bright field and (*b*) clusters of fine MC particles in precipitate dark field in PCA-A3 irradiated in HFIR at600°C to ~44 dpa.

3.1.5. Conclusions

1. The microstructural variations of the Path A Prime Candidate Alloy PCA-A2 (10% CW), -B1 (SA plus double aged), and -C (25% CW plus aged) were eliminated from further consideration because of rapid swelling for irradiation to ~10 dpa at 500 to 600°C. After irradiation to ~44 dpa, PCA-A1 (SA) exhibited the highest swelling between 400 and 600°C, nearly as high as swelling in SA 316 (DO-heat).
2. At higher fluences in HFIR, the void swelling resistance of PCA-A3 is similar to or better than that of CW 316 (DO-heat) and better than that of CW 316 (N-lot) between 500 and 600°C. The PCA-A3 is more resistant to swelling than is CW 316 (DO-heat) below 500°C.
3. Swelling resistance under high helium generation correlates directly with the formation of high concentrations of stable, fine bubbles that resist conversion to voids. Other microstructural factors that correlate with good swelling resistance are: stable MC precipitate particles, lower concentrations of network dislocations, fewer Frank loops, and a suppression of RIS effects.
4. Swelling was negligible at 300°C and low at 400°C in all steels examined, for fluences producing up to ~44 dpa.

3.1.6 References

1. M. L. Grossbeck, J. W. Woods, and G. A. Potter, "Experiments HFIR-CTR-30, -31, and -32 for Irradiation of Transmission Electron Microscopy Disk Specimens," pp. 36–44 in *ADIP Quart. Prog. Rep. Sept. 30, 1980*, DOE/ER-0045/4, U.S. DOE, Office of Fusion Energy.

2. L. R. Greenwood, "Neutron Source Characterization for Materials Experiments," pp. 66–86 in *ADIP Semiannu. Prog. Rep. Mar. 31, 1982*, DOE/ER-0045/8, U.S. DOE, Office of Fusion Energy.

3. P. J. Maziasz and M. L. Grossbeck, "Swelling and Microstructure of HFIR-Irradiated 20%-Cold-Worked Type 316 Stainless Steel and 316 + 0.23 wt. % Ti," pp. 43–69 in *ADIP Quart. Prog. Rep. Dec. 31, 1980*, DOE/ER-0045/5, U.S. DOE, Office of Fusion Energy.

4. P. J. Maziasz, F. W. Wiffen, and E. E. Bloom, "Swelling and Microstructure Changes in Type 316 Stainless Steel Irradiated under Simulated CTR Conditions," pp. 259–88 in *Radiation Effects and Tritium Technology for Fusion Reactors*, CONF-750989, Vol. 1, 1976.

5. P. J. Maziasz, "Microstructural Development on 20%-Cold-Worked Types 316 and 316 + Ti Stainless Steels Irradiated in HFIR: Temperature and Fluence Dependence of the Dislocation Component," pp. 54–97 in *ADIP Quart. Prog. Rep. Sept. 30, 1981*, DOE/ER-0045/7, U.S. DOE, Office of Fusion Energy.

6. P. J. Maziasz and D. N. Braski, "Swelling and Microstructural Development in Path A PCA and Type 316 Stainless Steel Irradiated in HFIR to About 22 dpa," pp. 44–62 in *ADIP Semiannu. Prog. Rep. Sept. 30, 1982*, DOE/ER-0045/9, U.S. DOE, Office of Fusion Energy.

7. P. J. Maziasz and D. N. Braski, in "Swelling and Microstructural Development of Path A PCA and Type 316 Stainless Steel Irradiated in HFIR," pp. 28–38 in *ADIP Semiannu. Prog. Rep. Mar. 31, 1983*, DOE/ER-0045/10.

8. L. K. Mansur and W. A. Coghlan, "Mechanisms of Helium Interaction with Radiation Effects in Metals and Alloys," to be published in *Journal of Nuclear Materials*, 118, (1983).

9. P. J. Maziasz, "Some Effects of Increased Helium Content on Void Formation and Solute Segregation in Neutron-Irradiated Type 316 Stainless Steel," *J. Nucl. Mater.* 108&109, 359–84 (1982).

10. R. E. Stoller and G. R. Odette, "The Effect of Helium on Swelling in Stainless Steel: Influence of Cavity Density and Morphology," in *Effects of Radiation on Materials: Eleventh Conf.*, ASTM-STP-782, eds., H. R. Brager and J. S. Perrin, 1982, pp. 275–94.

11. D. Imeson et al., "Irradiation Response of Rapidly Solidified Path A Type Prime Candidate Alloys," pp. 141–68 in *ADIP Semiannu. Prog. Rep. Mar. 31, 1982*, DOE/ER-0045/8, U.S. DOE, Office of Fusion Energy.

3.2 MICROSTRUCTURAL DESIGN OF PCA AUSTENITIC STAINLESS STEEL FOR IMPROVED RESISTANCE TO HELIUM EMBRITTLEMENT UNDER HFIR IRRADIATION — P. J. Maziasz and D. N. Braski (Oak Ridge National Laboratory)

3.2.1 ADIP Task

ADIP Tasks I.B.13, Tensile Properties of Austenitic Alloys, and I.C.1, Microstructural Stability.

3.2.2 Objective

The purpose of this work is to examine and evaluate the effect of thermal-mechanical pretreatments that vary preirradiation grain boundary precipitate structure on grain boundary microstructural development during irradiation in HFIR and on post-irradiation disk-bend ductility. The goal is to refine grain boundary cavity structures and thus reduce helium embrittlement.

3.2.3 Summary

Microstructural variants of PCA and two heats of 20%-cold-worked type 316 stainless steel were irradiated in HFIR and tested for embrittlement resistance with the disk-bend test. No embrittlement was observed for irradiation to ~44 dpa and 3000 to 3600 at. ppm He at 300 and 400°C. All materials were brittle after similar irradiation at 600°C. The best embrittlement resistance for irradiation to 44 dpa at 500°C and to 22 dpa at 600°C was found in PCA variants that contained grain boundary MC particles produced prior to irradiation.

3.2.4 Progress and Status

3.2.4.1 Introduction

Titanium and niobium modifications are known to improve the helium embrittlement resistance of austenitic stainless steels under neutron irradiation.[1-3] In 1967, Rowcliffe et al.[1] and Martin and Weir[2] conjectured that the reason for such resistance was interfacial helium bubble trapping by grain boundary MC carbides. Kesternich and Rothaut[4] recently demonstrated embrittlement resistance resulting from helium trapping at fine matrix MC particles in helium-preinjected and creep-tested DIN 1.4970 stainless steel (a 15 wt % Ni—15 Cr—0.1 C—1.3 Mo— 0.3 Ti alloy, otherwise similar to PCA).

Helium embrittlement resistance at the higher helium generation rates expected for fusion (12 to 15 at. ppm He/dpa) is an important concern for first-wall lifetime at higher temperatures. In 1981, preirradiation microstructural variants of PCA were designed and produced, with optimized distributions of grain boundary titanium carbide (MC), intended for better helium embrittlement resistance in fusion reactor service.[5] An important feature was incorporation of the understanding of phase stability under neutron irradiation.[6,7] The present work is intended to evaluate relative embrittlement resistance through bend testing of various specimens irradiated in HFIR at the high helium generation rates of 20 to 80 at. ppm/dpa.

3.2.4.2 Experimental

The compositions of N-lot type 316 stainless steel and the PCA are given in Sect. 3.1 of this report, as are the designations and descriptions of the PCA pretreatment variants.[8] The fusion reference heat (ref.-heat) of CW 316 (20%-cold-worked type 316 stainless steel) was also included and has the composition 12.4 Ni—17.3 Cr—2.2 Mo—1.7 Mn— 0.7 Si—0.05 C—0.03 P—bal Fe (all in weight percent). Standard 3-mm-diam disks were punched from 0.254-mm-thick sheet stock. Four disks of each of these were irradiated in HFIR at 300, 400, 500, and 600°C to fluences producing 10.5 to ~44 dpa (Sect. 3.1).[8] After irradiation, selected disks were bend tested at the irradiation temperature. Details of the disk bend testing and calculation of bend ductilities can be found elsewhere.[8-10] Scanning electron microscopy (SEM) and optical stereomicroscopy were used to examine cracks or fractures on tested disks. Transmission electron microscopy (TEM) was used to characterize grain boundary microstructures in identically irradiated but untested disks.

3.2.4.3 Disk Bend Test Results

Disk bend ductilities as functions of irradiation temperature (equal to test temperature) and fluence for the various alloy and pretreatment variants (47 disks) are shown in Fig. 3.2.1. The data symbols also indicate fracture behavior (opened symbols — no cracks; filled symbols — intergranular cracking). The data are separated into general trend bands indicating relatively better or worse behavior. Figure 3.2.2 shows SEM of typical examples of the fracture extremes for specimens judged better or worse. In general, PCA-B1 and -B2 as well as CW 316 (ref.-heat) exhibited better behavior at higher temperatures and fluences than did the other materials.

The temperature dependence of the bend ductilities indicated virtually no embrittlement due to irradiations of ~22 and 44 dpa at 300 and 400°C [Fig. 3.2.1(*c*,*d*)]. Consistent with this, optical stereomicroscopy indicated considerable cupping of the disks to conform to the punch during testing, and SEM

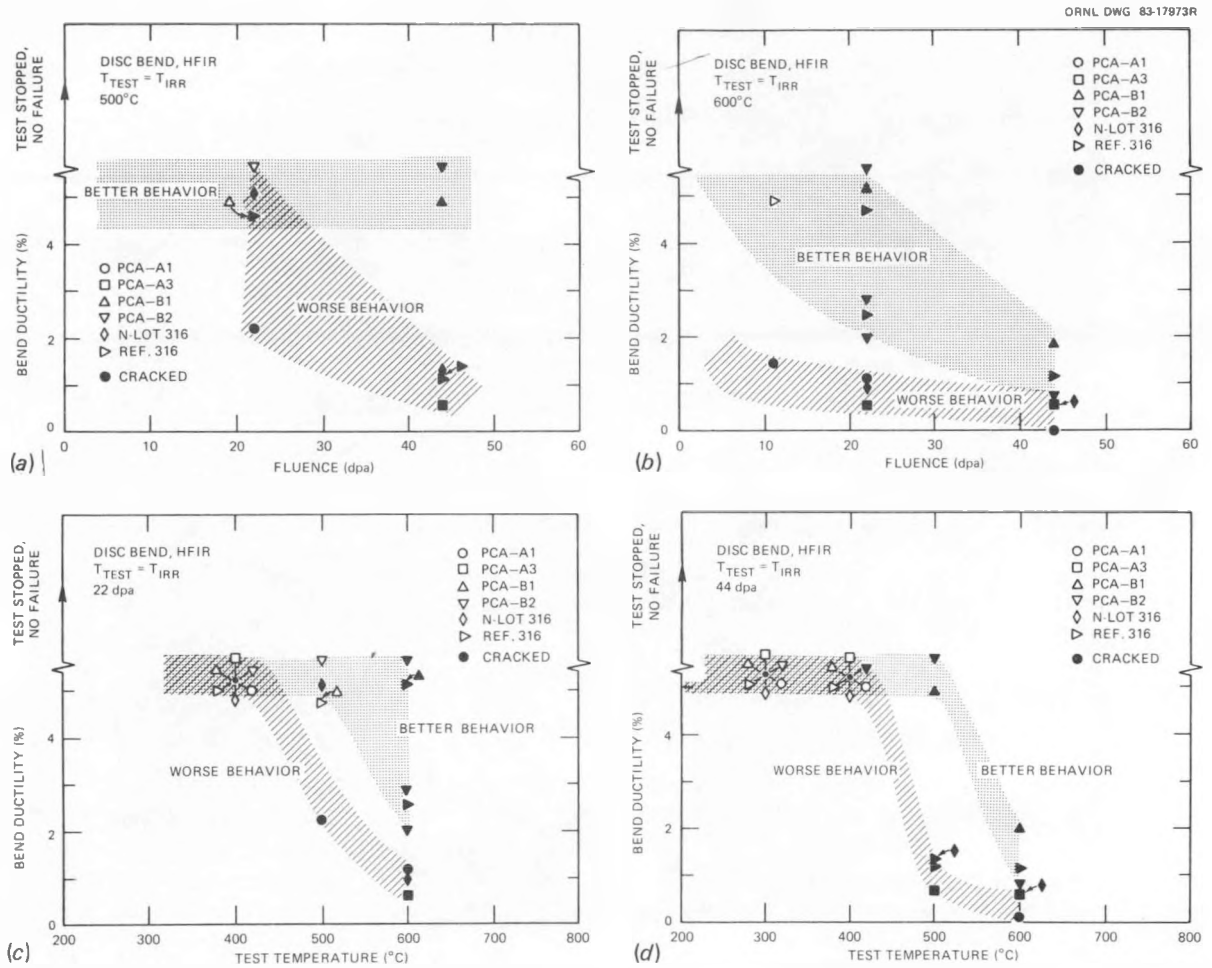

Fig. 3.2.1. Bend ductility as a function of fluence at (*a*) 500°C and (*b*) 600°C and as a function of irradiation temperature at (*c*) ~22 dpa and (*d*) 44 dpa for the alloys indicated after irradiation in HFIR. Note that the helium content (because of higher nickel content) is higher in PCA (~3600 at. ppm) than in the CW 316 (~3000 at. ppm) after exposure to ~44 dpa. Scatter bands indicate relatively better or worse behavior as judged from both fracture behavior and bend ductility.

showed no cracking. At 500 and 600°C, embrittlement increased with increased temperature and fluence but varied among the specimens. The PCA-B1 (solution annealed plus 8 h at 800°C plus 8 h at 900°C) and -B2 (solution annealed plus 8 h at 800°C plus 25% cold work plus 2 h at 750°C) consistently show better ductility and embrittlement resistance than does PCA-A3 (25% cold worked), -A1 (solution annealed), or CW 316 at 500 and 600°C. This is particularly true at 500°C after ~44 dpa (see for instance, PCA-B1 in Fig. 3.2.2). At 500°C and ~22 dpa, CW 316 (ref. heat) behaves similar to PCA-B1 and -B2, and this is also the case for 600°C at both ~22 dpa (with multiple specimen testing) and ~44 dpa. However, two points should be noted. First, the CW 316 (ref. heat) has the lowest nickel content of the steels investigated (~12.4 wt % Ni) and hence experienced the lowest helium production in HFIR, about 20 to 25% less than the PCA, which has the highest nickel content (16.2 wt % Ni). Second, the CW 316 (ref.-heat) appears to be less prone to embrittlement shown by postirradiation tensile testing than are other heats of type 316 (primarily the DO-heat) irradiated in HFIR.[11] The heat-to-heat embrittlement variation may be due to differences in residual impurity concentrations.

The fluence dependence of the bend ductility shows that all the alloys are eventually embrittled by irradiation at 600°C. However, continued embrittlement resistance was achieved in PCA-B1 and -B2 at 500°C [Fig. 3.2.1(*a*,*b*)]. At 600°C, severe embrittlement occurred in PCA-A1 after irradiation to only ~11 dpa and ~550 at. ppm He. At ~22 dpa, PCA-A1, -A3, and CW 316 (N-lot) are all similarly embrittled at 600°C and grow only slightly worse as fluence increases [see Fig. 3.2.1(*b*)]. These disks show very little bulging and very large, opened intergranular cracks when examined by SEM [see CW 316 (N-lot) in Fig. 3.2.2]. They also showed clearly defined and sharp drops in their load-versus-displacement curves.[9] By comparison, PCA-B1, -B2, and CW 316 (ref.-heat) show less embrittlement at 22 dpa as judged by higher ductilities before

ORNL-PHOTO 4902-83

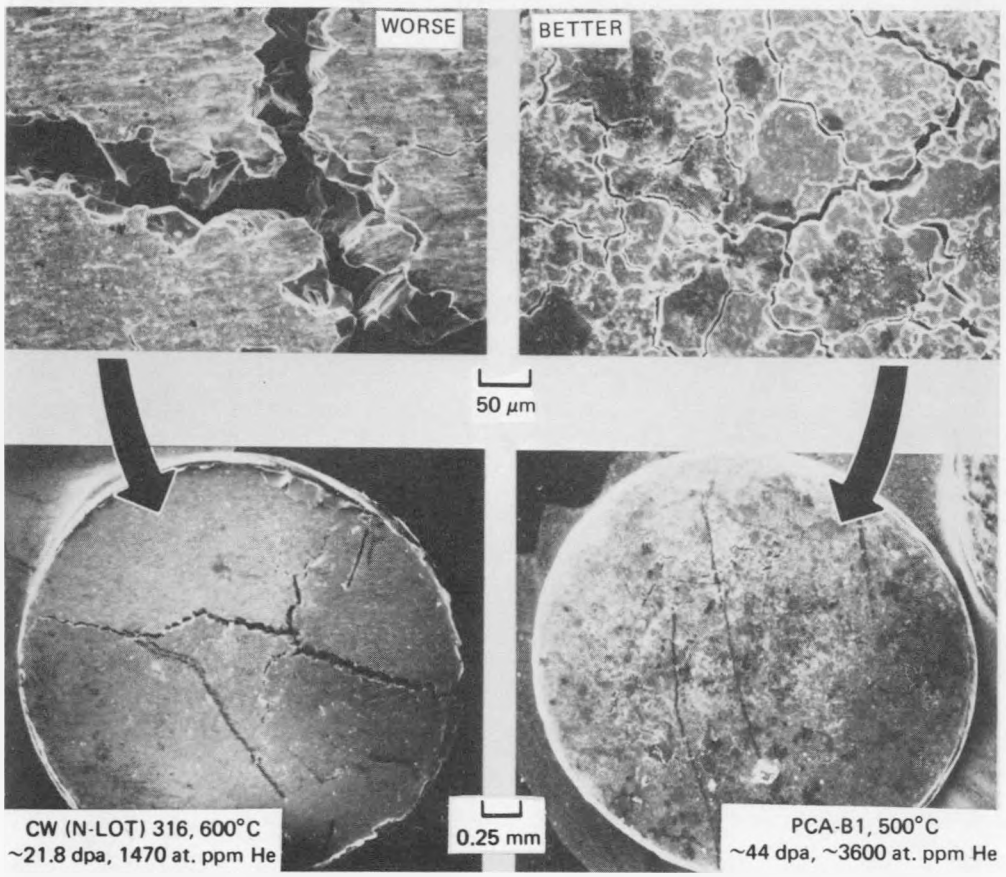

Fig. 3.2.2. Scanning electron microscope fractography of HFIR-irradiated and bend-tested ($T_{test} = T_{irr}$) disks and that failed (i.e., CW 316 N-lot, designated worse) and passed (i.e., PCA-B1, designated better). Irradiation conditions are indicated.

catastrophic cracking than do the other disks. Both PCA-B1 and -B2 show only small intergranular cracks in SEM (see Fig. 3.2.2), and they exhibit no sharp load drop (load versus displacement curve), even after ~44 dpa, at 500°C. Their ability to resist intergranular cracking is a sign that some ductility was retained, especially compared with the other alloys.

3.2.4.4 Grain Boundary Microstructural Observations

Grain boundary TEM was obtained on irradiated, untested disks. All alloys irradiated at 300 and 400°C showed similar tiny bubbles. However, at 500 and 600°C, both grain boundary bubble and precipitation development varied significantly with alloy and pretreatment variations. Figure 3.2.3 shows that increased helium generation under neutron irradiation increases bubble nucleation at the grain boundaries for CW 316 (DO-heat) irradiated at 525 to 550°C in EBR-II and HFIR. The fact that irradiated steels in EBR-II show no evidence of embrittlement for irradiation to very high fluences at temperatures below about 650°C helps illustrate the embrittling effect of these bubbles.[12] However, the variation in embrittlement among the alloys irradiated in HFIR indicated that differences in bubble and precipitate development also strongly influence embrittlement.

In this work, only PCA-B1 and -B2 contained grain boundary precipitates (MC) before irradiation. These precipitates were produced by aging for 8 h at 800°C after solution annealing.[5] The as-fabricated grain boundary MC precipitate microstructure can be seen in PCA-B1 in Fig. 3.2.4(*a*,*c*). During irradiation the medium-coarse grain boundary MC developed via pretreatments in PCA-B1 and -B2 remained stable and virtually unchanged up to 44 dpa at 300 to 500°C and up to ~22 dpa at 600°C. The latter case is shown in

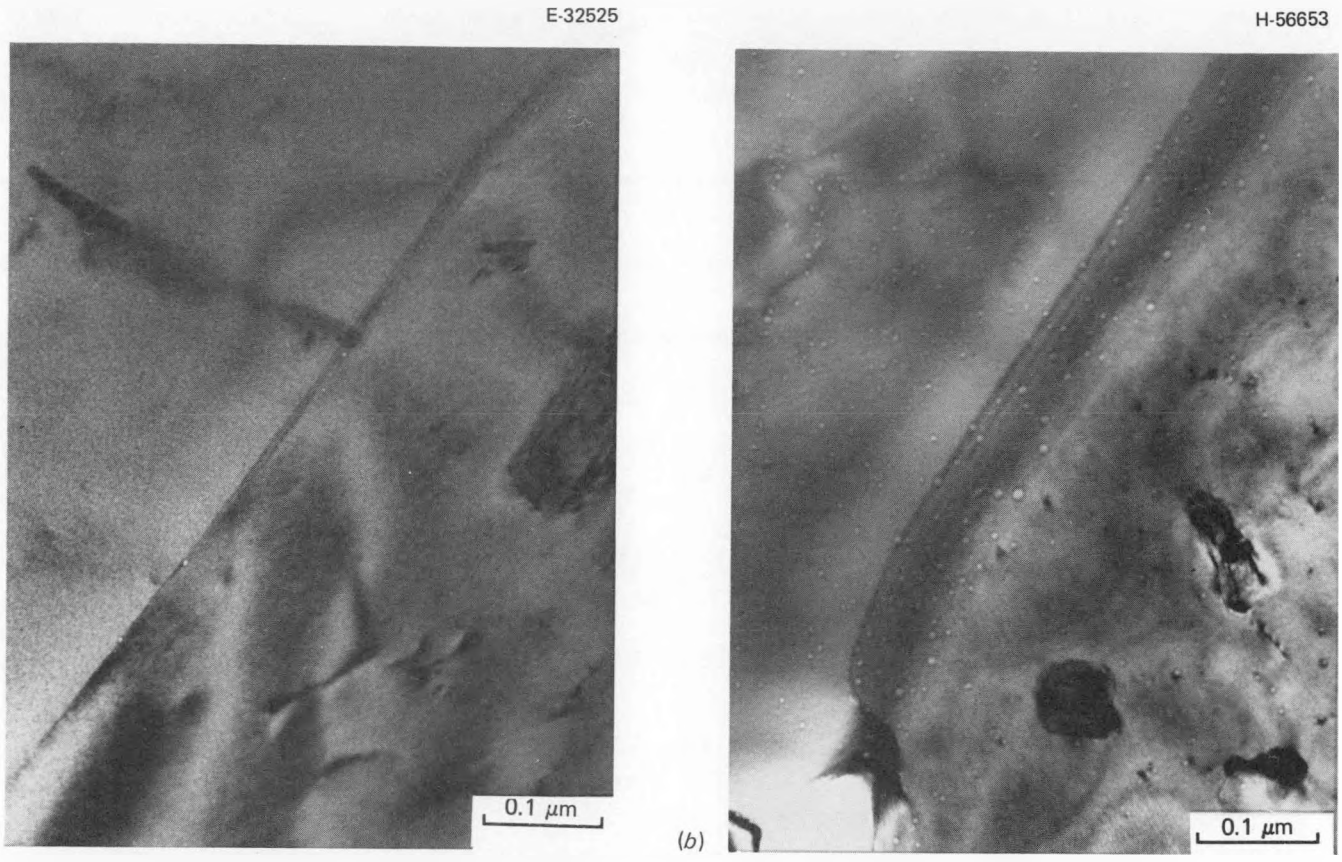

Fig. 3.2.3. Grain boundary bubbles in 20%-cold-worked type 316 stainless steel (DO-heat) irradiated at 525 to 550°C in (*a*) EBR-II to produce 36 dpa and 22 at. ppm He and (*b*) HFIR to produce 17.8 dpa and 1020 at. ppm He.

Fig. 3.2.4(*b*,*d*). This stability was unique to the coarser MC in the PCA because fine MC developed via pretreatments in PCA-C (25%-cold-worked plus 2 h at 750°C) dissolved in irradiation to only 11 dpa at 600°C. In contrast, neither PCA-A1 nor -A3 develop any grain boundary MC under similar irradiations. The grain boundary MC stability was also fairly independent of matrix microstructural development, since at 600°C up to 22 dpa PCA-B1 develops high void swelling and radiation-induced precipitation, whereas PCA-B2 develops much less swelling and enhanced thermal precipitation (MC) under irradiation. The medium-coarse MC in both PCA-B1 and -B2 dissolved on irradiation to ~44 dpa at 600°C, but this may be due to grain boundary migration resulting from differential void swelling in adjacent grains. When the grain boundary MC was stable, it caused much finer grain boundary helium bubble distributions because of trapping at the interphase boundaries, particularly when compared with grain boundaries without MC (see PCA-A1 and -B2 in Fig. 3.2.5). Bubbles are almost unresolvable at these MC particles at lower fluence.

In comparison with PCA-B1 or -B2, CW 316 (N-lot) developed bubbles and little grain boundary precipitation at 500°C, and bubble and M_6C precipitate structures that coarsened considerably with fluence at 600°C. By contrast, grain boundaries in CW 316 (ref.-heat) have fairly uniform and stable dispersions of medium-coarse M_6C particles[12] after ~10 dpa in HFIR at 400 to 550°C. This may explain why this heat of CW 316 resists embrittlement more than do the other heats of CW 316 (N-lot).

3.2.4.5 Bend Test — Microstructural Correlation

This work emphasizes that embrittlement resistance was predicted and correlates with the stability and beneficial bubble refinement of grain boundary MC in the PCA alloys irradiated at 500 and 600°C. Despite their higher helium content, PCA-B1 and -B2 also show consistently better embrittlement resistance than the CW 316, especially N-lot. The CW 316 (ref.-heat) may also benefit from better stability of grain boundary M_6C. At 400°C and below, helium embrittlement does not appear to be a problem for any of these alloys. Precipitate-free grain boundaries covered with many bubbles consistently appear quite brittle and prone to cracking for all alloys irradiated and tested at 500 and 600°C. Stable grain boundary MC, and hence embrittlement resistance, does not naturally develop under irradiation, but must be produced by appropriate thermal mechanical treatments before irradiation. Because the MC instability appears to correlate with

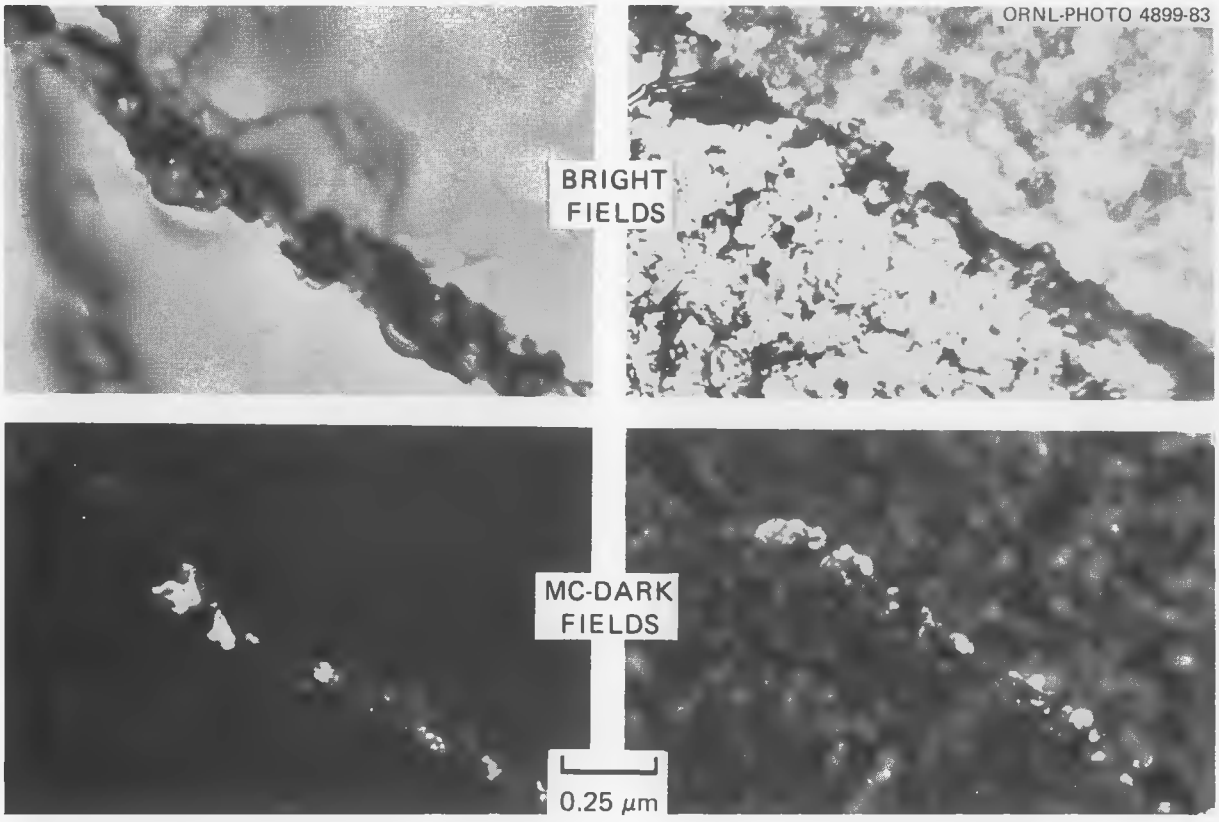

Fig. 3.2.4. A comparison of grain boundary MC in PCA-B1 (*left*) as fabricated and (*right*) after HFIR irradiation to 22 dpa at 600° to demonstrate its stability under irradiation.

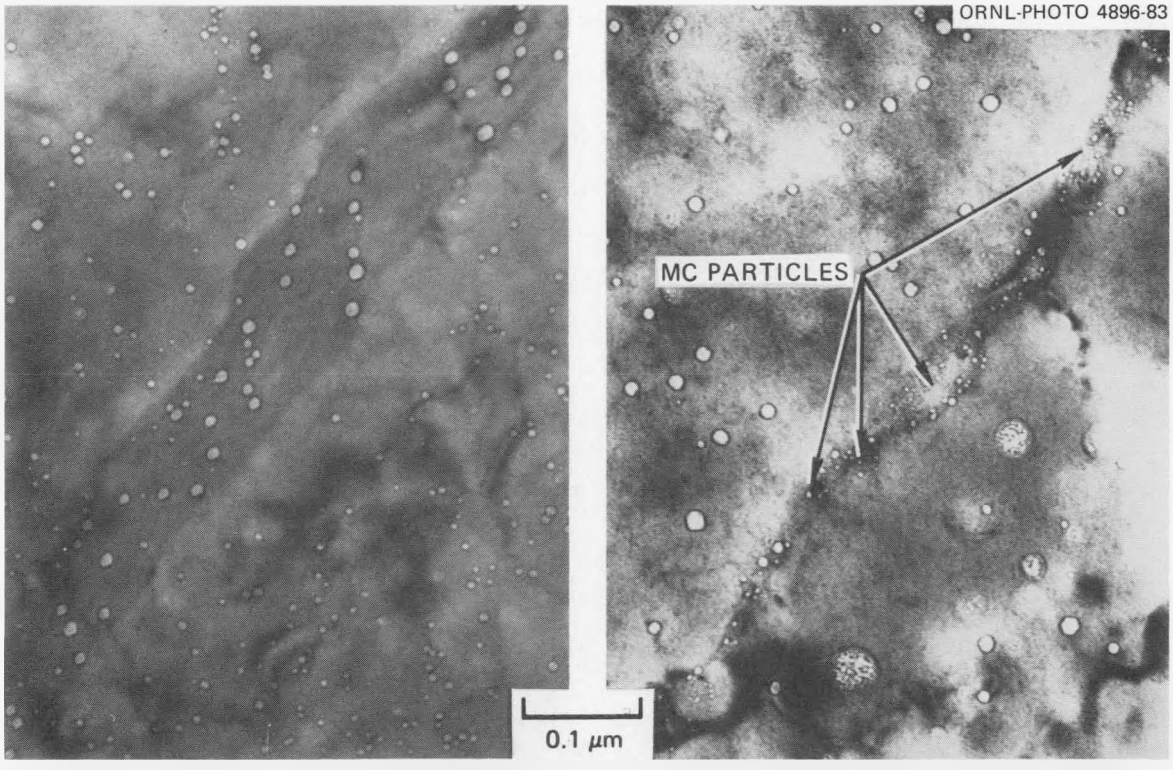

Fig. 3.2.5. A comparison of grain boundary bubble structures in (*left*) PCA-A1 with no MC and (*right*) PCA-B2, irradiated in HFIR at 600°C to ~22 dpa (~1760 at. ppm He) with prior grain boundary MC.

grain boundary migration under irradiation, grain boundary MC stability should be improved with more swelling-resistant grains. Therefore, a new PCA microstructure, PCA-B3, has been developed to combine the void swelling resistance of PCA-A3 (Sect. 3.1 of this report) with the grain boundary MC structures of PCA-B1 and -B2. The PCA-B3 is produced by aging solution-annealed material (PCA-A1) for 8 h at 800°C and then cold working 25%.

3.2.5 Conclusions

The bend test results demonstrate qualitatively that embrittlement can be diminished by suitable design and control of the microstructure. These results must be supported by more engineering-relevant mechanical testing to verify the embrittlement resistance and to qualify these alloy conditions for fusion reactor applications.

3.2.6 References

1. A. F. Rowcliffe et al., "An Electron Microscope Investigation of High Temperature Embrittlement of Irradiated Stainless Steels," pp. 161–99 in *Effects of Radiation on Structural Metals*, ASTM-STP-426 American Society for Testing and Materials, 1967.

2. W. R. Martin and J. R. Weir, "Solutions to the Problems of High-Temperature Irradiation Embrittlement," pp. 440–57 in *Effects of Radiation on Structural Metals*, ASTM-STP-426 American Society for Testing and Materials, 1967.

3. P. J. Maziasz and E. E. Bloom, "Comparison of 316 + Ti with 316 Stainless Steel Irradiated in a Simulated Fusion Environment," pp. 268–69 in *Trans. Am. Nucl. Soc.* 27, 1977.

4. W. Kesternich and J. Rothaut, "Reduction of Helium Embrittlement in Stainless Steel by Finely Dispersed TiC Precipitates," pp. 845–52 in *J. Nucl. Mater.* 103&104, (1981).

5. P. J. Maziasz and T. K. Roche, "Preirradiation Microstructural Development Designed to Minimize Properties Degradation During Irradiation in Austenitic Alloys," pp. 797–802 in *J. Nucl. Mater.* 103&104, 1981.

6. E. H. Lee, P. J. Maziasz, and A. F. Rowcliffe, "The Structure and Composition of Phases Occurring in Austenitic Stainless Steels in Thermal and Irradiation Environments," pp. 191–218 in *Phase Stability During Irradiation*, ed. J. R. Holland, L. K. Mansur, and D. I. Potter The Metallurgical Society of AIME, Warrendale, Pa., 1981.

7. P. J. Maziasz, pp. 75–129 in *ADIP Quart. Prog. Rep. June 30, 1980*, DOE/ER/0045/3, U.S. DOE, Office of Fusion Energy.

8. R. L. Klueh and D. N. Braski, "The Use of Nonstandard Subsized Specimens for Irradiation Testing," presented at Symposium on Use of Non-Standard Subsized Specimens in Irradiated Testing, Albuquerque, N. Mexi., Sept. 23, 1983; to be published by American Society for Testing and Materials, see also Sect. 2.5 of this report.

9. F. H. Huang, M. L. Hamilton, and G. L. Wire, "Bend Testing for Miniature Disks," *Nucl. Technol.* 57, 234–42 (1982).

10. M. Manahan et al., "The Use of Nonstandard Subsized Specimens for Irradiation Testing," presented at Symp. Use of Non-Standard Subsized Specimens in Irradiated Testing, Albuquerque, N. Mexi., Sept. 23, 1983; to be published by American Society for Testing and Materials.

11. A. F. Rowcliffe and M. L. Grossbeck, "Radiation Effects in Austenitic Steels," to be published.

12. P. J. Maziasz, Oak Ridge National Laboratory, unpublished data, 1981–82.

4. PATH B ALLOY DEVELOPMENT — HIGHER STRENGTH Fe-Ni-Cr ALLOYS

4.1 AN EVALUATION OF FATIGUE PROPERTIES OF HFIR-IRRADIATED NIMONIC PE-16 AT 430°C — M. L. Grossbeck and K. C. Liu (Oak Ridge National Laboratory)

4.1.1 ADIP Task

ADIP Task I.B.6, Stress/Strain Controlled Fatigue in High Strength/High Temperature Fe-Ni-Cr Alloys.

4.1.2 Objective

The goal of this experiment is to scope the fatigue behavior of Nimonic PE-16 irradiated in a helium-producing environment.

4.1.3 Summary

Nimonic PE-16 was irradiated in the HFIR to 6 to 9 dpa and 560 to 1000 at. ppm He at 430°C. Post-irradiation fatigue tests revealed a reduction in fatigue life by about a factor of 10 at 430°C. In contrast with AISI type 316 stainless steel, no endurance limit was observed. All irradiated specimens exhibited some intergranular fracture with an increasing tendency toward "cleavage like" intragranular fracture for low strain ranges.

4.1.4 Progress and Status

4.1.4.1 Introduction

Most conceptual designs of tokamak fusion reactors involve a cyclic mode of operation, where fatigue in the structural materials is of prime concern. However, even if steady-state tokamak machines can be built, plasma disruptions and shutdown cycles will still result in fatigue of first wall and blanket structures. Primarily because of their higher strength, high nickel alloys such as Nimonic PE-16 have been considered for first wall structural material.

In addition to atomic displacements, the fusion environment produces hydrogen by (n,p) reactions and helium by (n,α) reactions. The hydrogen is not normally a concern in iron and nickel alloys, but helium is insoluble and has been observed to segregate to sinks such as grain boundaries, where it might affect mechanical behavior. For this reason, a radiation environment that produces helium simultaneously with atomic displacements has been chosen for this study.

4.1.4.2 Experimental Procedure

Specimen Preparation

Specimens were prepared from 7.11-mm rod of heat TC-1747, the composition of which is shown in Table 4.1.1. The specimens are of the hourglass configuration with a 3.18-mm minimum diameter, as used previously for studies of irradiated type 316 stainless steel.[1,2] The specimen geometry and irradiation capsule are shown in Fig. 4.1.1. Following machining, the specimens were heat treated in an argon atmosphere to achieve a precipitation-hardened condition. The specimens were solution annealed at 1080°C for 4 h, then aged at 900°C for 1 h and 750°C for 8 h.

Table 4.1.1. Composition of Nimonic PE-16 used in experiment (wt %)

C	0.062	Cr	16.93	Mo	3.35
Si	0.29	Ti	1.12	Ni	43.94
Cu	0.098	Al	1.15	S	0.001
Mn	0.098	Co	0.42	Zr	0.008
				Fe	bal

Irradiation

Helium is produced in nickel-containing alloys through irradiation in a mixed-spectrum reactor, such as the High Flux Isotope Reactor (HFIR). The strong fast-neutron component of the flux causes considerable atomic displacement damage. Helium formation results from a series of two thermal neutron absorption reactions beginning with ^{58}Ni: $^{58}Ni(n,\gamma)^{59}Ni$ and $^{59}Ni(n,\alpha)^{56}Fe$, which deposit helium homogeneously throughout the alloy. In the HFIR, which was used for the irradiation, both the fast and thermal fluxes exceed 10^{19} neutrons/(m^2·s) at the irradiation sites.

Specimens were arranged ten per irradiation capsule along the longitudinal axis of the reactor. The desired elevated temperature was achieved through nuclear heating, using helium gas gaps between each specimen and its support to control radial heat conduction (Fig. 4.1.1). Low-melting metals and alloys and silicarbide were used as temperature indicators.[1] The melt wire materials used were Cu—30.7% Mg, Mg—23.5% Zn—5 % Al, and Zn. The irradiation temperature was determined to be 430 ± 25°C.

Irradiation and test parameters are given in Table 4.1.2. Damage levels were calculated by the method recommended by the IAEA working group[3] from previous dosimetry measurements, with the addition of the displacements produced by recoiling iron nuclei in the $^{59}Ni(n,\alpha)^{56}Fe$ reactions.[4] Helium levels were calculated from a relation based on experimental data.[5]

Fatigue testing

The tests were performed on a servo-hydraulic closed-loop-controlled testing system installed in a radiation hot cell. The system has a four-column load frame capable of 220 kN. It is equipped with an ultrahigh vacuum system pumped by a turbomolecular pump capable of pressures of 10^{-6} to 10^{-4} Pa during elevated-temperature testing. Specimen heating is accomplished by induction with a load coil surrounding the specimen. Strain is measured by a diametral extensometer which fits between two windings of the load coil.

Tests were performed at the irradiation temperature of 430°C. Specimens were subjected to a fully reversed triangular strain versus time program beginning with compression at a strain rate of 4×10^{-3} s^{-1}. For low-cycle fatigue ($\Delta\varepsilon_T > 0.5\%$), tests were controlled on the basis of axial strain computed by a strain computer from diametral strain, measured directly at the minimum gage section. For high-cycle tests, the same strain control was used until a stable hysteresis loop was achieved, at which time control was shifted to load. At the same time the frequency was increased by a factor of 10 to reduce the test duration. Specimens were cycled to complete separation in order to perform fractography, except in cases where an apparent endurance limit was observed. All specimens, both irradiated and unirradiated, were loaded remotely in the hot cell by the same procedure in order to avoid differences in alignment. Specimens aged at 430°C for the duration of the irradiation were not tested.

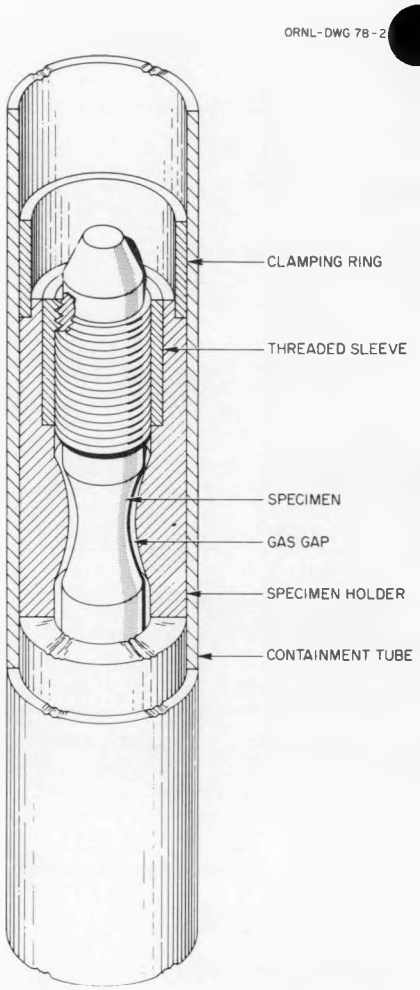

Fig. 4.1.1. Fatigue specimen positioned in an irradiation capsule.

4.1.4.3 Results

Nimonic PE-16 initially exhibited slight cyclic hardening followed by very slight softening prior to establishing a steady-state hysteresis loop. The irradiated specimens were observed to have significantly higher cyclic strengths than the unirradiated ones above a strain range of 0.5% (Fig. 4.1.2). This behavior was also observed at 430°C in 20%-cold-worked type 316 stainless steel.[1] However, the Nimonic PE-16 is a stronger alloy and appears to exhibit higher cyclic work hardening than does type 316 stainless steel.

The results of the fatigue tests are presented in Table 4.1.2 and appear in graphical form in Fig. 4.1.3. The curves in Fig. 4.1.3 were established by a least-squares fit to a power law equation commonly used for fatigue data. For unirradiated material the following equation was derived:

$$\Delta\varepsilon_T = 0.023N_f^{-0.12} + 0.39N_f^{-0.46} .$$

For the Nimonic PE-16 irradiated to 6 to 9 dpa containing 560–1000 at. ppm He, the following equation was found to fit the data:

$$\Delta\varepsilon_T = 0.015N_f^{-0.12} + 0.49N_f^{-0.60} ,$$

where $\Delta\varepsilon_T$ = total strain range, N_f = cycles to failure.

For the unirradiated alloy, the test was discontinued at 10^7 cycles, where no failure was observed at a total strain range of 0.35%. However such an apparent endurance limit was not observed in the irradiated material, where even at a total strain of 0.30%, failure was observed in 1.5×10^6 cycles.

The fracture surfaces were examined by scanning electron microscopy (SEM) to aid in determining the fracture mechanism, and typical fractographs are shown in Fig. 4.1.4. The unirradiated specimens displayed primarily intragranular ductile rupture. However, the primary mode of fracture in the irradiated specimens appeared to be intergranular. In addition to intergranular fracture, some "cleavagelike" intragranular fracture was observed. Decreasing the strain range and therefore increasing the length of the test appeared to increase the tendency toward "cleavage like" fracture.

Table 4.1.2. Irradiation and test parameters

Specimen	Temperature (°C)		Fluence E > 0.1 MeV (neutrons/m^2 × 10^{26})	dpa	Helium (at. ppm)	Total strain range (%)	Cycles to failure	Cycles to crack N_f	Maximum stress $\Delta\sigma/2$ at $N_f/2$ (MPa)
	Irradiation	Test							
PS3		430	0			2.0	2,294		790
PX3		430	0			1.0	45,463	43,000	630
PX2		430	0			0.6	316,057	303,600	550
PX4		430	0			0.35	>10,043,048		310
PX6	430	430	0.96	8.8	940	2.0	727	650	830
PS4	430	430	0.96	9.1	1000	1.0	1,297	790	800
PS5	430	430	0.96	8.8	940	0.6	22,134		550
PS6	430	430	0.80	7.4	730	0.35	142,264		320
PX1	430	430	0.68	6.3	560	0.30	1,534,755		276

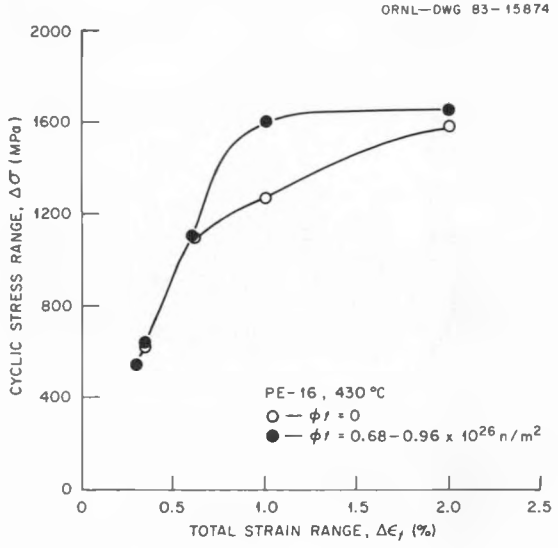

Fig. 4.1.2. Cyclic stress-strain curves for HFIR-irradiated and unirradiated Nimonic PE-16. Each point represents an individual specimen. The stress range was measured at half the specimen life.

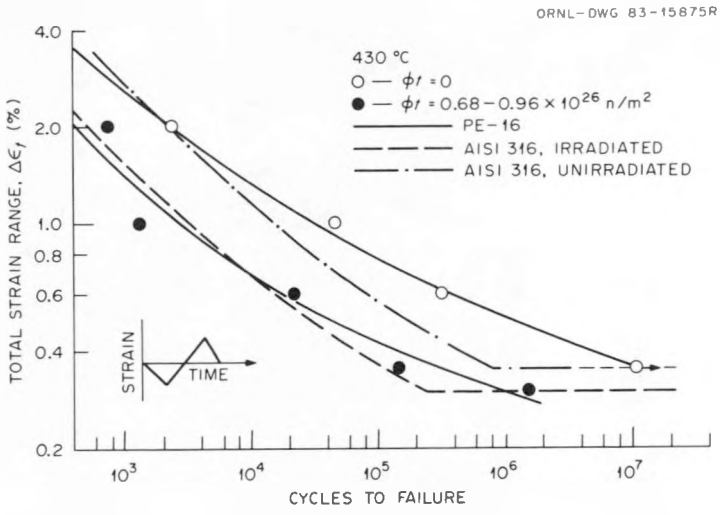

Fig. 4.1.3. Total strain range as a function of cycles to failure for HFIR-irradiated (6–9 dpa, 560–1000 at. ppm He) and unirradiated Nimonic PE-16. Dashed curves are for similarly irradiated and unirradiated 20%-cold-worked type 316 stainless steel.

4.1.4.4 Discussion

The cyclic hardening curves reflect the phenomenon of irradiation hardening, which was greater in the precipitation-hardened Nimonic PE-16 than in AISI type 316 stainless steel. The greater strength of Nimonic PE-16 is also evidenced in the fatigue life curves of Fig. 4.1.3. Here it is seen that Nimonic PE-16 has a slightly longer fatigue life in the high-cycle regime but a similar or possibly shorter life in the low-cycle regime, a characteristic of stronger alloys.

It is somewhat surprising that the fatigue behavior of the two alloys at 430°C was as similar as was observed, since the fracture modes were quite different. Figure 4.1.4 is an array of fractographs arranged according to fluence and strain range on a reverse scale; thus, length of test increases to the right. The unirradiated specimens are seen to have fractured by ductile rupture, but the irradiated specimens exhibited varying degrees of intergranular fracture. In AISI type 316 stainless steel, no intergranular fracture was

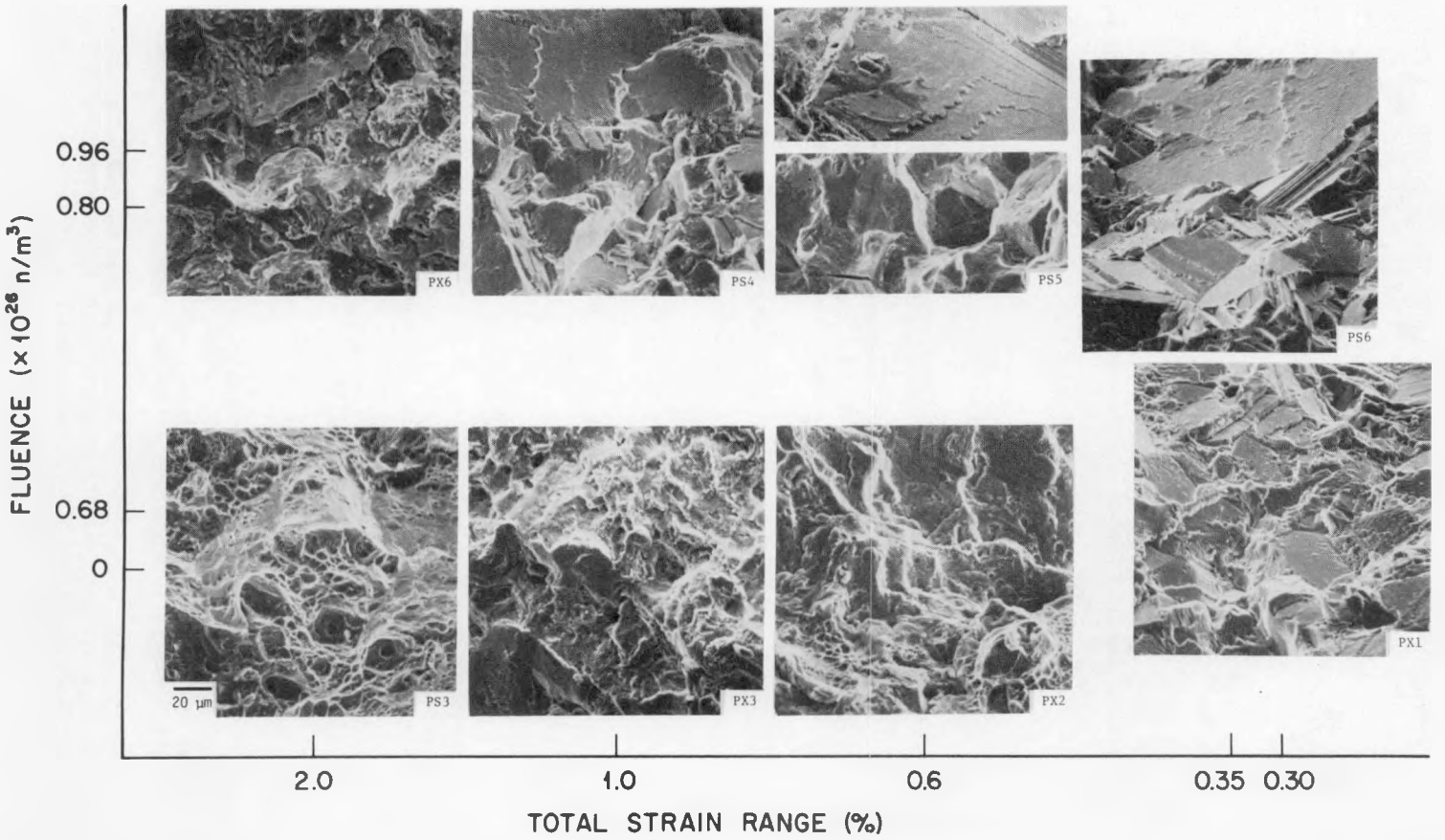

Fig. 4.1.4. An array of SEM fractographs arranged according to fluence and strain range for Nimonic PE-16 irradiated and tested at 430°C. Duration of test increases to the right. The scales are nonlinear, and numbers align with the center of corresponding fractographs.

served at 430°C. At lower strain range levels, flat cleavage like fracture is observed in both materials. Although the fracture mechanism remains to be determined by further study, it might involve separation along twin boundaries or possibly along persistent slip bands resulting from the cyclic stress.

The intergranular mode of fracture has been observed previously in tensile-tested high-nickel alloys such as Nimonic PE-16 following irradiation.[6] It is not clear that this is an effect of helium, but helium appears to be a significant factor in embrittlement in many cases.[7] The intergranular fracture observed in fatigue is believed to result from the same embrittling mechanism active in tensile testing of irradiated high-nickel alloys, which may involve segregation, precipitation, or helium.[6-7]

4.1.5 Conclusions

Significant intergranular fracture was observed in irradiated Nimonic PE-16. Nonetheless, fatigue life was not severely shortened by its presence. This mild reduction in life was observed even though the alloy contained helium levels as high as 1000 at. ppm, which might have aggravated the intergranular separation.

Although higher strength usually results in longer life in high-cycle fatigue, the absence of an endurance limit in Nimonic PE-16 following irradiation perhaps makes the overall high-cycle performance worse than that of type 316 stainless steel. Since the low-cycle fatigue behavior is similar in the two alloys, Nimonic PE-16 offers no advantage over type 316 in fusion reactor service.

4.1.6 References

1. M. L. Grossbeck and K. C. Liu, "Fatigue Behavior of Type 316 Stainless Steel Irradiated in a Mixed Spectrum Fission Reactor Forming Helium," *Nucl. Technol.* 58, 538–47 (1982).

2. M. L. Grossbeck and K. C. Liu, "High Temperature Fatigue Life of Type 316 Stainless Steel Containing Irradiation Induced Helium," *J. Nucl. Mater.* 103&104, 853–58 (1981).

3. "Recommendations for Displacement Calculations for Reactor/Accelerator Studies in Austenitic Steel," (Report of IAEC Specialists Meeting on Radiation Damage Units in Ferritic and Austenitic Steel) *Nucl. Eng. Des.* 33, 91 (1975).

4. L. R. Greenwood, "A New Calculation of Thermal Neutron Damage and Helium Production in Nickel," *J. Nucl. Mater.* 115, 137–42 (1983).

5. F. W. Wiffen et al., "The Production Rate of Helium During Irradiation of Nickel in Thermal Spectrum Fission Reactors," submitted to *Journal of Nuclear Materials.*

6. P. S. Sklad, R.E. Clausing, and E.E. Bloom, "Effects of Neutron Irradiation on Microstructure and Mechanical Properties of Nimonic PE-16," pp. 139–55 in *Irradiation Effects on the Microstructure and Properties of Metals*, ASTM STP 611, American Society for Testing and Materials, Philadelphia, 1976.

7. R. M. Boothby and D.R. Harries, "Irradiation-Induced Embrittlement and Precipitation in Nimonic PE-16," pp. 157–64 in *Mechanical Behavior and Nuclear Applications of Stainless Steel at Elevated Temperatures*, The Metals Society, London, 1982.

5. PATH C ALLOY DEVELOPMENT — REACTIVE AND REFRACTORY ALLOYS

No contributions.

6. INNOVATIVE MATERIAL CONCEPTS

No contributions.

7. PATH E ALLOY DEVELOPMENT — FERRITIC STEELS

7.1 SWELLING IN SEVERAL COMMERCIAL ALLOYS IRRADIATED TO VERY HIGH NEUTRON FLUENCE -

D. S. Gelles and J. S. Pintler (Westinghouse Hanford Company)

7.1.1 ADIP Task

The Department of Energy (DOE)/Office of Fusion Energy (OFE) has cited the need to investigate ferritic alloys under the ADIP program task, Ferritic Steels Development (Path E). The tasks involved are akin to task number 1.C.2, Microstructures and Swelling in Austenitic Alloys and task number 1.C.1, Microstructural Stability.

7.1.2 Objective

The objective of this work is to provide guidance on the applicability of martensitic stainless steels for fusion reactor structural components.

7.1.3 Summary

Swelling values have been obtained from a set of commercial alloys irradiated in EBR-II to a peak fluence of 2.5 x 10^{23} n/cm^2 (E > 0.1 MeV) or ~125 dpa covering the range 400 to 650°C. The alloys can be ranked for swelling resistance from highest to lowest as follows: the martensitic and ferritic alloys, the niobium based alloys, the precipitation strengthened iron and nickel based alloys, the molybdenum alloys and the austenitic alloys.

7.1.4 Progress and Status

7.1.4.1 Introduction

Irradiation induced swelling is an important materials property affecting the design of a fusion reactor. Swelling must be compensated for when determining design tolerances and is often found to be a limiting design factor. Unfortunately, generation of swelling information for very high fluence neutron irradiation requires long irradiation times and it is rarely possible to perform such experiments. As part of the National Cladding/Duct Materials Development Program (NCD) for Liquid Metal Fast Breeder Reactor development, a series of commercial alloys was included in the AA-I swelling test and irradiations were begun in December 1974 in the Experimental Breeder Reactor (EBR) II, at Idaho Falls, ID. As these materials are no longer being studied by the NCD program, they have been made available for fusion related studies. Results of density change measurements on specimens examined at earlier discharges of the AA-I test have been reported previously.[1,2] The purpose of the present effort is to provide results on specimens irradiated in the final irradiation of the AA-I test to a peak fluence of 2.53 x 10^{23} n/cm^2 (all fluences are reported as E > 0.1 MeV) or approximately 125 dpa.

The specimens which were included in the AAI test covered a large number of different types of commercial alloys. A listing of alloy compositions is provided in Table 7.1.1. Several alloy classes are represented. Six ferritic and martensitic alloys covered the composition range Fe-5Cr to Fe-22Cr and included carbide, yttria and copper precipitate strengthening. Three iron base solid solution strengthened alloys, one with high silicon additions, provided results for the Fe-(20 to 35) Ni - (20 to 25) Cr composition range. Nine precipitation strengthened alloys in the superalloy class were included covering both the iron-and nickel-base range. Both $Ni_3(Al,Ti)$ and Ni_3Nb precipitate strengtheners were included. Four nickel base solid solution strengthened alloys, most with high molybdenum contents, were irradiated as were two refractory alloys, one a niobium base alloy and the other a molybdenum base alloy. Therefore, the AAI test was able to provide results of irradiation induced swelling for a wide range of commercial structural alloys.

7.1.4.2 Experimental Procedure

Details of the AAI test design and configuration have been documented previously.[1,2] The present effort concerns capsule B116 following its removal from reactor for the fourth time. Examinations of AAI specimens generally involved measurements on specimens which had not been measured at a previous discharge. (One exception occurred in the case of specimens irradiated at 590°C to a fluence of 1.78 x 10^{23} n/cm^2.) This procedure was possible because the original AAI test involved side-by-side irradiation of four identical capsules, and only for one case was it necessary to measure specimens which had been measured previously and then reirradiated. Earlier removals were required in order to replace the stainless steel hardware (capsule and subcapsules) which were beginning to swell and thereby altering the operating temperatures. It was also found that the actual operating temperatures were lower than anticipated due to lower than expected gamma heating in EBR-II throughout the life of the test. The temperatures reported in this paper as in references (1) and (2) are the design temperatures. The actual temperatures are as much as 20°C lower for the highest temperature subcapsules and proportionately less for the remainder.

The compositions of the specimens examined from the AAI test are listed in Table 7.1.2 and the heat treatment given these specimens are provided in Table 7.1.2. Composition overchecks by Lukens Steel Company are in good agreement with the values in Table 7.1.1. It was apparent that a great deal of effort would be required to measure the density change of every specimen in capsule B116 of the AAI test and therefore only a limited number of specimens was selected for density change measurements. Those specimens of major interest to the Fusion materials community, namely those ferritic alloys and refractory alloys

Table 7.1.1 Compositions of the alloys as supplied by the vendors (weight percent)

Type	Alloy	Fe	Ni	Cr	C	Mo	Mn	Nb	Al	Ti	Si	Other
Ferritic	H11	bal.	0.12	4.97	0.42	1.31	0.37	--	--	--	0.88	V = 0.49
	EM-12	bal.	--	9.42	0.09	2.02	1.00	0.40	--	--	0.28	V = 0.27
	AISI 416	bal.	0.27	13.36	0.11	0.26	0.42	--	--	--	0.48	--
	430 F	bal.	--	17.64	0.04	0.04	0.40	--	--	--	0.50	--
	FeCrAlY	bal.	--	22.5	0.009	--	--	--	5.04	--	--	Y = 0.68
	Carpenter Custom 455	bal.	8.4	11.7	0.008	--	0.10	0.24+	00	1.2	0.08	Cu = 2.14
Austenitic	AISI 310	bal.	19.7	24.7	0.06	0.30	1.52	--	--	--	0.56	Cu = 0.33
	RA-330	bal.	36.05	19.1	0.05	--	1.58	--	--	--	1.27	Cu = 0.25
	Incoloy 800*	bal.	33.7	20.5	0.07	--	0.91		0.38	0.44	0.45	Cu = 0.54
Precipitation Strengthened	A286	bal.	24.6	14.2	0.05	1.21	1.22	--	0.17	2.20	0.54	V = 0.25
	M813	bal.	34.1	18.35	0.34	4.26	--	--	1.59	2.38	--	Co = 0.020, Zr = 0.12
	D979	bal.	44.8	14.9	0.04	4.15	0.10	--	1.16	3.07	1.10	W = 4.03, Zr = 0.04
	Incoloy 901*	bal.	42.2	13.7	0.04	5.50	0.10	--	0.26	2,85	0.10	B = 0.16
	Inconel 718*	18.5	bal.	18.6	0.04	2.83	0.10	5.28+	0.50	0.92	0.23	
	Inconel X-750*	7.81	bal.	15.4	0.045	--	0.09	1.06+	0.68	2.45	0.07	
	Nimonic 80A*	0.17	bal.	19.5	0.07	00	0.03	00	1.42	2.57	0.14	
	Nimonic 115*	0.48	bal.	14.5	0.16	3.23	0.03	--	4.94	3.78	0.20	Zr = 0.04, Cu = 0.04
	Inconel 625*	4.36	bal.	21.9	0.02	9.17	0.09	3.35	0.29	0.28	0.15	
Nickel Base	Hastelloy X*	18.8	bal.	21.2	0.11	8.84	0.46	--	--	--	0.45	W = 0.5, Co = 1.96
	Hastelloy S*	0.73	bal.	16.6	0.006	15.3	0.21	--	0.21	--	0.05	W = 0.07, Co = 0.11
	Hastelloy C-4*	0.45	bal.	15.3	0.002	14.3	--	--	--	0.42	0.04	
	Inconel 600*	8.03	bal.	15.8	0.08	--	0.24	--	0.18	0.25	0.21	Cu = 0.32
Refractory	Nb-1Zr	<0.005	<0.002	--	0.003	0.002	<0.002	bal.	--	<0.004	<0.005	Zr = 0.96, Ta = 0.095
	TZM	0.003	0.001	--	0.013	bal.	--	--	--	0.45	0.002	Zr = 0.09

*Incoloy and Inconel are registered trademarks of the International Nickel Company, Nimonic is a registered trademark of Henry Wiggin & Co., U.K., and Hastelloy is a registered trademark of the Cabot Corporation.
+Includes Ta.

which were previously examined,[2] were measured for density following irradiation at each irradiation temperature where available. The remainder was only measured after irradiation at two temperatures, 425°C and 540°C. These two were selected because they corresponded to high flux conditions. The 425°C condition was intended to identify materials which develop a swelling maximum at low temperatures. The 540° condition was intended to provide data at a moderately high temperature, close to the peak swelling temperature for AISI 316 stainless steel.[3] Details regarding density measurement procedures have been described previously.[1,2]

Table 7.1.2 Swelling measurements for specimens irradiated in B116 of the AA-I test

			Swelling ($\Delta V/V_o$, %)							
		Temperature (°C)	400	425	450	480	510	540	590	650
Alloy	Heat Treatment	Fluence (10^{23}n/cm^2)	1.60	2.07	1.55	1.98	2.41	2.32	2.53	2.50
H11	1010/1/W.Q.+570/2/W.Q.		0.16	0.14	0.18	-0.11	-0.05	0.04		
EM12	1050/0.5/A.C.+750/1.5/A.C.		0.57	0.56	-0.02	-0.28	-0.38	-0.29		0.08
AISI 416	870/F.C. AT 13°C Per Hour to 590/A.C.		0.35	0.25	0.08	0.08	0.20	0.05		0.21
430 F	1070/1/W.Q.		0.23	0.20	0.09	0.17	0.24	0.05		0.11
FeCrAlY	Consolidated at 1150°C			0.12				-0.18		
C.C. 455	1070/1/W.Q. + 510/4/A.C.			-0.36				1.78		
AISI 310	1070/1/W.Q.			49.79				17.92		
RA-330	1070/1/W.Q.			12.36				2.04		
INC. 800	1070/1/W.Q.			41.08				11.95		
A-286	1070/1/W.Q.			31.60				0.51		
A-286	980/1/O.Q. + 720/16/A.C.			N.M.				0.81		
M813	1080/4/A.C. + 900/1/A.C. + 750/8/A.C.			1.75				1.84		
D979	1020/2/W.Q. + 840/6/A.C. + 705/16/A.C.			-1.91				-2.45		
INC. 901	1100/3/W.Q. + 790/4/A.C. + 720/24/A.C.			0.15				-0.07		
INC. 718	750/1/W.Q. + 720/8/F.C. to 620/18 total A.C.			0.60				0.25		
INC. X-750	1150/2/A.C.			1.06				-0.06		
INC. X-750	1150/2/A.C. + 840/24/A.C. + 700/20/A.C.			4.18				0.46		
INC. X-750	1150/2/A.C. + 840/0.5/A.C.			1.47				-0.05		
NIM. 80A	1080/8/A.C. + 705/16/A.C.			1.16				0.33		
NIM115	1190/1.5/A.C. + 1100/6/A.C.			2.05				7.17		
INC 625	1150/1/W.Q.			1.01				-0.06		
HAST X	1190/1/W.Q.			-2.30				38.00	79.90	
HAST S	1070/1/A.C.			-0.30				0.06		
HAST C-4	1070/1.5/W.Q.			-0.09				4.79		
INC 600	1120/1.5/A.C.			12.70				1.60		
INC 600	20% cold worked			7.92				0.07		
Nb-1Zr	1200/1/V.C.		0.43	0.53	0.25	0.16	0.43	0.31	0.39	0.56
TZM	1300/2.5/V.C.		0.35	0.03	0.03	0.02	0.36	0.05	3.77	2.86

Heat Treatment Code: temperature (°C)/time (hour)/W. Q. = water quench, A.C. = air cooled, F.C. = furnace cool, O.Q. = oil quench, V.C. = cool under vacuum.

7.1.4.3 Results

The swelling results are presented in Table 7.1.2. Results in Table 7.1.2 for several of the ferritic alloys and for the refractory alloys which were measured over the full range of irradiation temperature show that these materials are low swelling alloys. Only TZM developed swelling in excess of one percent. Results shown for the remaining alloys indicate that most of the alloys investigated are low swelling alloys, but several notable exceptions occur. In interpreting these results, it should be noted that swelling and density change are not equal at high values. Volumetric swelling in percent, $\Delta V/V_o$, must be computed according to the relationship:

$$S(\%) = \frac{(\Delta\rho/\rho_o)}{1 - (\Delta\rho/\rho_o)} \times 100$$

where $\frac{\Delta\rho}{\rho_o}$ is the fractional density change.

For example, the density change value of 33.24 percent for AISI 310 irradiated at 425°C corresponds to 49.8 percent swelling. The remainder of this section will be a description of each alloy and its swelling response.

Ferritic/Martensitic Alloys

H11 is a corrosion resistant 5 percent chromium martensitic steel used in heat exchanger applications. It is found to be highly swelling resistant, with peak swelling of 0.18 percent found for the 450°C irradiation condition. Values of this magnitude generally arise from precipitation rather than void development. EM-12 is a French heat exchanger material with a duplex (ferrite and martensite) microstructure. The density change measurements show peak swelling of 0.6 percent at 400 to 425°C and densification on the order of -0.10 to -0.30 percent for the temperature range 480 to 540°C. These results are very similar to those found for lower fluences[2] and indicate this alloy may be stable at high fluences. Such a response was not expected.[4] The alloy AISI 416, a martensitic stainless steel with low molybdenum, is also foundto be highly swelling resistant. However, in comparison with lower fluence results,[2] minor increases of 0.1 percent are found for 400 and 425°C. Therefore, it is possible that AISI 416 begins to swell at fluences on the order of 1.6 to 2.0 x 10^{23} n/cm^2 or 90 dpa. The alloy 430F, which contains 17 percent chromium and is fully ferritic, was developed for corrosion resistance. It is found to be very swelling resistant and gives results very similar to those found at a lower fluence.[2] The alloy FeCrAlY is an yttria strengthened fully ferritic alloy which provides high temperature corrosion resistance. It is found to behave like other ferritic/martensitic alloys and is very swelling resistant. Carpenter Custom 455 is a martensitic alloy designed to be strengthened by precipitation of copper. It was found to be very swelling resistant at low temperatures, but developed moderate swelling, 1.78% at 540°C. As this alloy contains almost ten percent nickel which promotes austenite and as it is uncharacteristic for ferritic alloys to swell at 540°C, the observed high temperature response could be attributed to swelling in austenite which forms in-reactor. However, a magnetic susceptibility check indicates that this specimen is strongly magnetic and so another explanation may be required. In summary, the ferritic/martensitic alloy class of commercial alloys appears to be highly swelling resistant. Even when voids develop at a low fluence, the swelling rate remains very low.

Austenitic Alloys

AISI 310 stainless steel in the solution treated condition was expected to show high swelling. It swelled 49.8 percent at 425°C and 17.9 percent at 540°C. R.A. 330 stainless steel in the solution treated condition also swelled, but the swelling was not as large. It swelled 12.4 percent at 425°C and 2.04 percent at 540°C. Incoloy 800, an alloy very similar to RA 330, but with minor aluminum and titanium additions and lower silicon swelled about the same as AISI 310 stainless steel, 41 percent at 425°C and 11.9 percent at 540°C. Austenitic stainless steels are therefore found to be some of the highest swelling alloys in this test. Swelling is systematically higher at the lower irradiation temperature and additions of silicon reduce swelling at both temperatures.

Precipitation Strengthened Alloys

Alloy A-286 is a gamma prime $Ni_3(Al,Ti)$ precipitation strengthened alloy in the 25 percent nickel composition range. Following irradiation at 425°C, the solution treated condition developed high swelling, 31.6 percent, whereas at 540°C, swelling was negligible at 0.51 percent. The high swelling at 425°C can be attributed to a change in the precipitation strengthening phase. Gamma prime transformed to eta (Ni_3Ti) in the form of large thin sheets in this condition following neutron irradiation at 425°C and low fluences (R. W. Powell of Westinghouse Hanford Company, private communication.) A similar observation is reported in reference 5 for the aged condition. Unfortunately, the 425°C condition for aged A-286 was not available, but at 540°C, aged A-286 developed negligible swelling, 0.81 percent. M813 is also a gamma prime strengthened alloy in the 35 percent nickel range. This alloy is found to develop moderate swelling, 1.72 percent at 425°C and 1.81 percent at 540°C. D979 is similar to M813 but with a higher nickel content of 42 percent, with a high titanium to aluminum ratio and with tungsten additions of 4 percent. Its swelling response is quite different. D979 densified approximately 2 percent at both irradiation temperatures. An explanation for the densification is not yet available. Incoloy 901 is very similar to D979 but has an even higher titanium to aluminum ratio and no tungsten additions. It is found to be a very low swelling alloy, 0.15 percent at 425°C, and to densify slightly, only -0.07 percent at 540°C. Inconel 718 is a somewhat different alloy. It contains 53 percent nickel and uses a 5 percent addition of niobium in order to promote the gamma double prime phase (Ni_3Nb) for strength. The consequence is low swelling, 0.60 percent, at 425°C and negligible swelling, 0.25 percent, at 540°C. Inconel X-750 is a nickel base gamma prime strengthened alloy. It was irradiated in three heat treatment conditions and provides an interesting example of the effect of heat treatment on swelling. Inconel X-750 develops a little over one percent swelling at 425°C in both the solution treated and the aged conditions, but develops 4 percent under identical conditions in the overaged condition. For irradiation at 540°C, the same behavior occurs but the swelling is low, 0.46 percent for the overaged condition and -0.05 percent for the other two. Nimonic 80A, an alloy similar in composition to X-750, develops swelling of similar magnitude, 1.15 percent at 425°C and 0.33 percent at 540°C. Nimonic 115 differs from Nimonic 80A primarily as a result of a higher volume fraction of gamma prime precipitate, a lower titanium to aluminum ratio and 3 percent molybdenum additions. However, these changes result in significantly more swelling, 2.96 percent at 420°C and 6.69 percent at 540°C. Nimonic 115 therefore provides an unusual case where swelling is higher at the higher irradiation temperature. A possible explanation for the higher swelling response can be ascribed to the pre-irradiation microstructure. The heat treatment given this alloy provides a triplex precipitate particle size distribution with the largest particles being on the order of one micron in size. The alloy may therefore be behaving as if it had an overaged microstructure in reactor. The final alloy in the precipitation strengthened series was

Inconel 625, a nickel base gamma double prime strengthened alloy. The swelling response of Inconel 625 was similar to that of X-750 and Nimonic 80A. The swelling was 1.00 percent at 425°C and -0.06 percent at 540°C. In summary, iron and nickel base precipitation strengthened superalloys are generally low swelling materials. The exceptions either involved a situation where a phase change promoted high swelling or where an overaged microstructure was used and moderate swelling developed.

Nickel Base Solid Solution Strengthened Alloys

Hastelloy X is a high-temperature corrosion resistant alloy with approximately 20 percent chromium and 20 percent iron. Hastelloy X was found to densify, -2.36 percent, following irradiation at 425°C and swell 38.0 percent at 540°C. Density change measurements on Hastelloy X showed 44.4 percent density change at 590°C following irradiation to 2.47 x 10^{23} n/cm^2. This corresponds to 79.9 percent swelling. Therefore, solid solution hardened alloys in the 50 percent nickel range can develop very high swelling and the peak swelling temperature is high. In comparison, Hastelloy S, a similar alloy with negligible iron and higher levels of molybdenum and nickel, was highly swelling resistant. The swelling was -0.30 percent at 425°C and 0.06 percent at 540°C. Hastelloy C-4 a similar alloy gave intermediate results. At 425°C, -0.09 percent swelling was found but at 540°C, 4.79 percent swelling developed. Inconel 600, an alloy intermediate in composition between Hastelloy X and Hastelloy S or C-4 but without molybedenum and with minor additions of gamma prime forming elements, developed moderate swelling. A value of 12.7 percent swelling was found at 425°C and 1.60 percent for 540°C in the case of solution annealed Inconel 600. Inconel 600 in the 20% cold worked condition developed 7.92 percent swelling at 425°C and 0.07 percent swelling at 540°C. In summary, nickel based solid solution hardened alloys developed a wide range of swelling responses. Low swelling, moderate swelling and high swelling alloys were found and the temperature dependence of swelling varied from peak swelling at low temperatures to peak swelling at high temperatures. An explanation for this wide variation in response is not yet available.

Refractory Alloys

Nb-1Zr is a commercial niobium base alloy used in the body centered cubic state for high temperature applications. It is found to be highly swelling resistant, at least over the temperature range studied in the experiment, 400 to 630°C. Comparison with lower fluence data[2] appears to show that a larger scatter in the data occurs at higher fluence and that swelling in this alloy has saturated. TZM is a commercial molybdenum base body centered cubic alloy used for high temperature applications. It is found to develop moderate swelling over the available range of irradiation temperature with peak swelling of 3.77 percent measured for the 590°C irradiation condition.

This represents a low swelling rate, 0.07 percent increase over 7.5 x 10^{22} n/cm^2 (Ref. 2) or .002 percent per dpa, and indicates that the swelling of this alloy is approaching saturation. A similar comparison for the 630°C case shows that TZM is densifying at high fluence. A specimen to specimen variation might explain the difference but certainly initial predictions based on lower fluence response[6] cannot be justified. In summary, refractory commercial alloys are moderately to highly swelling resistant with peak swelling occurring at 590°C. Saturation is apparent in both alloys examined at fluence levels on the order of 2.0 x 10^{23} n/cm^2 or 100 dpa.

Discussion

Based on this study of density change in a series of commercial alloys irradiated to fluences as high as 2.5 x 10^{23} n/cm^2 or 125 dpa, it is possible to draw several generalizations regarding swelling in commercial structural alloys at high fluence in a fast neutron environment. This section is intended to provide recommendations regarding the more swelling resistant alloy classes, a basis for understanding the response by comparison with the response of simple experimental alloys, and a commentary on effects which arise due to overaging in precipitation strengthened alloys and minor element additions.

The Low Swelling Alloy Classes

The present work identifies three classes of commercial alloys which remain either low swelling (less than 1 percent) or moderate swelling (less than 5 percent) at high fluence. Ferritic/Martensitic alloys are found to be the most swelling resistant as a group of alloys. Apart from the case where austenite formation is expected to have influenced behavior, swelling remains well below one percent and the highest swelling alloy maintains a very low swelling rate: 0.05 percent per 10^{22} n/cm^2 or 0.01 percent per dpa. In comparison, refractory alloys are less swelling resistant but still low swelling. However, the refractory alloy class of commercial alloys does develop significant differences in swelling level from one alloy to another: 0.6 percent for Nb-1Zr versus 3.6 percent for TZM. The alloy class does appear to develop swelling saturation at doses on the order of 100 dpa and therefore further increases in swelling are not expected at even higher doses. Precipitation strengthened iron and nickel base superalloys are also found to be low or moderate swelling except in the exceptional cases where a phase transformation or overaging is involved. However, saturation cannot be generally demonstrated in this alloy class and therefore higher swelling can be anticipated at still higher doses.

Comparison With Simple Alloys

The swelling response in simple alloys can provide a basis for understanding the swelling behavior found in the present study on commercial alloys. For example, simple ferritic alloys develop void swelling only at irradiation temperatures below 500°C in fast reactors, the peak swelling temperature is 425°C, and the swelling rate which is obtained is low compared to simple austenitic allows.[7] Such results are in good agreement with the present results except that in the present case several alloys do not appear to develop void swelling even at high fluence, and when they do, the swelling rates obtained are not as large as in simple alloys. It can therefore be concluded the swelling behavior of the ferritic/martensitic commercial alloys may be overpredicted by simple alloy response. Minor element additions increase the incubation period prior to swelling and may reduce the steady state swelling rate.

Austenitic alloy swelling response can also be successfully predicted by simple alloy behavior. For example, in Fe-Cr-Ni pure ternary alloys[8] it has been shown that swelling rates of 5 percent per 10^{22} n/cm^2 or 1 percent per dpa are independent of chromium and/or nickel content for alloys with 35 percent nickel or less. However, the duration of the transient regime of swelling is not. It increases with increasing nickel or temperature and with decreasing chromium content. Higher accumulated swelling is therefore found at 425°C than at 540°C. For alloys with greater than 35 percent nickel,[9] similar response is obtained except that a peak swelling rate is difficult to define due to the large duration of the transient regime. The results of the present test follow several of these trends. For example, the peak swelling rate for AISI 310 at 425°C estimated using the present data and data at 4.3 x 10^{22} n/cm^2 (Ref. 1) can be shown to be 3.1 percent per 10^{22} n/cm^2 or 0.6 percent per dpa. This is probably a low estimate because it assumes 4.0 x 10^{22} n/cm^2 for the swelling incubation fluence. Therefore, the peak swelling rate in these commercial alloys approaches that of ternary alloys. In most cases where moderate or high swelling is found in commercial alloys, swelling is higher at 425 than at 540°C, a trend which is very clear in the ternary data. Three exceptions exist however. Nimonic 115, Hastelloy X and Hastelloy S each swell significantly more at 540°C than at 425°C. An explanation for these exceptions is not yet available. Finally, it is possible to interpret the swelling response of those austenitic and precipitation strengthened alloys which develop low or moderate swelling as having swelling responses controlled by a very high swelling incubation fluence. Unfortunately, in order to prove that this interpretation is correct, fluences beyond those provided by the present experiment are needed.

Effects of Microstructure

As an alloy class, precipitation strengthened alloys are found to be more swelling resistant than austenitic or nickel base solid solution strengthened alloys. The results for X-750 and Nimonic 115 provide a possible explanation. It appears that precipitates can influence the evolution of irradiation induced microstructure so as to reduce void swelling. When the precipitate structure is overaged, higher swelling results. It is likely that this reduced swelling behavior is only due to an increase in the transient regime of swelling. Nonetheless, fully aged precipitate structures as opposed to overaged structures should be employed for improved swelling resistance in precipitation strengthened alloys.

Effects of Minor Alloying Additions

Effects of minor alloying additions on swelling can be demonstrated in this data set but it does not appear possible to generalize those effects over the entire data set. For example, silicon additions to RA-330 provide the most reasonable explanation for the reduced swelling observed in that alloy compared to Incoloy 800. All other differences in composition should either have made Incoloy 800 a lower swelling alloy or should have had no effect. Silicon additions have been identified previously for promoting swelling resistance.[10-13] However, this trend is not applicable to the Hastelloy alloys where the reverse trend is found. Additions of carbon may be responsible for the higher swelling found in M813, Nimonic 115, Hastelloy X and Inconel 600 in comparison with similar alloys. (This is in contradiction to low fluence observations by Bates[10] but in better agreement with intermediate fluence response.[11] However, the response is not universal: austenitic alloys which are high swelling contain low carbon contents. A better correlation of swelling is obtained as a function of copper content, but such a correlation is not expected to be meaningful. It is therefore concluded that effects of minor alloying additions are complex. Trends found in one composition range do not apply to other composition ranges. But the effects must be present based on the range of response found in this data set. It is therefore concluded that extrapolation of simple alloy behavior to complex commercial alloys can easily lead to incorrect predictions.

7.1.5 Conclusions

A series of 24 commercial alloys covering a wide range of alloy types has been examined following irradiation in EBR-II to fluences as high as 2.53 x 10^{23} n/cm^2 or 125 dpa. The swelling resistance of these alloy classes (from best to worst) may be rated as follows:

Ferritic/Martensitic Alloys
Refractory Alloys
Precipitation Strengthened Superalloys
Nickel Base Alloys
Austenitic Stainless Steels

The results tend to follow predictions based on the response of simple alloys but many exceptions are found which demonstrate that minor element additions and microstructure can play an important role in the control of swelling.

7.1.6 Further Work

Microstructural examinations on selected specimens will be performed in the next reporting period.

7.1.7 References

1. J. F. Bates and R. W. Powell, "Irradiation-Induced Swelling in Commercial Alloys," *J. Nuc. Mat.* 102 (1981) 200.
2. R. W. Powell, D. T. Peterson, M. I. Zimmerscheid and J. F. Bates, "Swelling in Several Commercial Alloys Following High Fluence Neutron Irradiation," Ibid, 103 & 104 (1981) 969.
3. J. F. Bates and M. K. Korenko, "Empirical Development of Irradiation-Induced Swelling Design Equations," *Nuc. Tech.* 48 (1980) 303.
4. D. S. Gelles, "Microstructural Examination of Several Commercial Ferritic Alloys Irradiated to High Fluence," *J. Nuc. Mat.* 103 & 104, (1981) 975.
5. D. S. Gelles, L. E. Thomas and J. J. Laidler, "Swelling in Previously Neutron Irradiated Commercial Fe-Cr-Ni Based Alloys Under Electron Irradiation," *J. Nuc. Mat.* 108 & 109 (1982) 504.
6. D. S. Gelles, D. T. Peterson and J. F. Bates, "Void Swelling in the Molybdenum Alloy TZM Irradiated to High Fluence," *J. Nuc. Mat.* 103 & 104 (1981) 1141.
7. D. S. Gelles and L. E. Thomas, "Effects of Neutron Irradiation on Microstructure in Experimental and Commercial Ferritic Alloys," HEDL-SA-2772FP, to be published in the *Proceedings of the AIME Topical Conference on Ferritic Alloys for Use in Nuclear Energy Technologies*.
8. F. A. Garner, "Dependence of Swelling on Nickel and Chromium Content in Fe-Ni-Cr Ternary Alloys," *Damage Analysis and Fundamental Studies Quarterly Progress Report*, DOE/ER-0046/14 (July 1983) 133.
9. H. R. Brager, "Swelling of High Nickel Fe-Ni-Cr Alloys in EBR-II," Ibid.
10. J. F. Bates, "Irradiation-Induced Swelling Variations Resulting from Compositional Modifications of Type 316 Stainless Steel," *Properties of Reactor Structural Alloys after Neutron or Particle Irradiation*, ASTM STP 570 (1975) 369.
11. J. F. Bates, R. W. Powell and E. R. Gilbert, "Reduction of Irradiation-Induced Creep and Swelling in AISI 316 by Compositional Modifications," in *Effects of Radiation on Materials: Tenth Conference*, ASTM STP 725 (1981) 713.
12. H. R. Brager and F. A. Garner, "Radiation-Induced Evolution of the Austenitic Matrix in Silicon - Modified AISI 316 Alloys," in *Phase Stability During Irradiation*, AIME (1981) 219.
13. F. A. Garner, "The Microchemical Evolution of Irradiated Stainless Steels," Ibid, 165.

7.2 EVALUATION OF FERRITIC ALLOY Fe-2-1/4Cr-1Mo AFTER NEUTRON IRRADIATION - IRRADIATION CREEP AND SWELLING - D. S. Gelles and R. J. Puigh (Westinghouse Hanford Company)

7.2.1 ADIP Task

The Department of Energy (DOE) Office of Fusion Energy (OFE) has cited the need to investigate ferritic alloys under the ADIP program task, Ferritic Steels Development (Path E). The tasks involved are akin to task number 1.C.2, Microstructures and Swelling in Austenitic Alloys and task number 1.C.1, Microstructural Stability.

7.2.2 Objective

The objective of this work is to provide guidance on the applicability of martensitic stainless steels for fusion reactor structural components.

7.2.3 Summary

Irradiation creep and swelling measurements are reported for Fe-2-1/4Cr-1Mo after irradiation by fast neutrons over the temperature range 390 to 560°C. Diameter change measurements on thin walled pressurized tubes in a bainitic condition and density change measurements on rods in a nonstandard condition were made following irradiation in the Experimental Breeder Reactor II. The irradiation creep specimens were irradiated to a fluence of 5.7 x 10^{22} n/cm^2 (E > 0.1 MeV) or 30 dpa and the swelling specimens were irradiated to a peak fluence of 2.4 x 10^{23} n/cm^2 or 115 dpa. These results have been used as a basis to establish in-reactor creep and swelling correlations for 2-1/4Cr-1Mo in a bainitic condition. The correlations predict moderate swelling and moderate irradiation enhanced creep at 390°C.

7.2.4 Progress and Status

7.2.4.1 Introduction

The Electric Power Research Institute of Palo Alto, CA has funded a program entitled Evaluation of Irradiation Metal Samples for Use in Fusion Components under contract RP-1597-1 with McDonnell Douglas Astronautics Company. Westinghouse Hanford Company has been a participant in that program under contract Y3E052R entitled Evaluation of Ferritic Alloy Fe-2-1/4Cr-1Mo After Neutron Irradiation - Irradiation Creep and Swelling. The first phase of that effort has now been completed. In order to disseminate the results of that effort to the fusion materials community in the shortest possible time, a version of the summary report is being included in the Alloy Development for Irradiation Performance Semiannual Progress Report. This report provides results of in-reactor creep and swelling measurements, and proposed swelling and creep MHFES design equations for 2-1/4Cr-1Mo steel.

7.2.4.2 Objectives and Technical Approach

The objectives of this ferritic steel study are to develop an understanding of the response of the 2-1/4Cr-1Mo steel to neutron irradiation and to present the results of the mechanical property evaluations and swelling studies in a format consistent with its inclusion in the Materials Handbook for Fusion Energy Systems (MHFES). The results of these evaluations will be interpreted in terms of their impact on future studies of this alloy and its suitability for use in fusion reactor components.

7.2.4.3 Experimental Procedures

Materials for irradiation creep and swelling experiments were obtained from different sources. The creep specimens were fabricated from a Mannesmann heat #38649 provided by Climax Molybdenum Company and swelling specimens were fabricated from a Lukens Steel Company sample, heat number C4337-14S (also identified as alloy A-387-D). The compositions, as supplied by the vendors, are provided in Table 7.2.1. The Mannesmann heat was received in the form of a 12.7 cm long section of 7 cm wall pipe. The section was cut radially in 2 cm thick slices, which were subsequently rolled and machined into tubes according to the rolling schedule diagrammed in Figure 7.2.1. Tube dimensions were 0.457 cm OD x 0.417 cm ID. The specimens were heat treated according to the schedule given in Table 7.2.2. Endcaps of HT-9, a martensitic stainless steel, were electron beam welded to tubing segments 1.981 cm in length. This geometry was chosen to ensure an adequate wall thickness of 0.02 cm and yet optimize the use of the limited irradiation volume. One endcap had a capillary hole for pressurizaton. Each specimen was filled with He to the desired pressure and the closure weld for gas containment was made with a laser beam which passed through the glass port of the pressure vessel and sealed the capillary fill hole in the endcap. Specimen diameters were measured both before and after irradiation using a non-contacting laser system which has an accuracy of $\pm 2.5 \times 10^{-5}$ cm and has repeatability in the hoop strain measurement of 0.05 percent. The Lukens Steel Company heat was sectioned into random cross sections approximately 1 cm in diameter and heat treated according to the schedule given in Table 7.2.2. The somewhat unusual heat treatment was based on information from reference 1. Specimens 0.3 cm diameter by 1.3 cm long were then machined from the stock. Swelling was determined from density measurements based on the Archimedian principle. Multiple measurements were made on each specimen with a typical measurement uncertainty of $\pm$0.05 percent.

Table 7.2.1. Chemical analysis of 2-1/4Cr-1Mo heats as supplied by the vendors (in weight percent)

Element	Creep Tubes[a]	Swelling Rods[b]
C	0.093	0.12
Mn	0.52	0.42
P	0.011	
S	0.011	
Si	0.17	0.21
Ni	0.40	0.16
Cr	2.15	2.17
Mo	0.95	0.93
Cu	0.16	
Al	0.003	
Fe	bal	bal

[a] Mannesmann Company heat #38649
[b] Lukens Steel Company heat #C4337-14S

Table 7.2.2. Heat treatments given creep tubes and swelling specimens prior to irradiation

Specimen Type	Heat #	Heat Treatment*
Creep Tubes	38649	900°C/30 min./AC +700°C/1 hr/AC
Swelling specimens	C4337-14S	1010°C/1 hr/WQ + 843°C/2 hr/WQ

*Temperature/time at temperature/cooling procedure where AC = air cooled, WQ = water quenched

Specimens were irradiated in the Experimental Breeder Reactor (EBR-II) located in Idaho Falls. The irradiation vehicle for the creep specimens identified as capsule B 329 which was part of the AAXIV experiment was a cylindrical tube 1.5 m in length and 2.0 cm in diameter. Inside were three subcapsules which were connected to the Na coolant flow by a capillary tube with an inlet at the bottom of the capsule and an outlet at the top of the capsule. The Na flow was necessary to achieve the desired lowest temperature in the capsule and permit gas release from the subcapsule should a creep specimen rupture. The dimensions of the insulating gas gap between the subcapsule and the outer capsule was designed to control the heat transferred from the gamma heated subcapsule to the reactor coolant which was flowing past the outer capsule wall. Calculations were performed to optimize the Na flow rate through the capsules so as to minimize the thermal gradient within a given subcapsule. The nominal design temperatures for each subcapsule was 400, 450, and 550°C. The capsule B329 was loaded into subassembly X359 which was irradiated in position 4C2 in EBR-II for cycles 109 through 111 and 113. The specimens were in the reactor for a period of 10680 MWD which corresponds to 4477 hours at temperature and a peak fluence exposure 2.8×10^{22} n/cm^2 (E > 0.1 MeV). The reconstitution of the AAXIV experiment which contained the ferritic creep specimens consisted of three separate B7 capsules. The capsules B331, B333 and B334 contained the ferritic pressurized tube specimens reconstituted from the AAXIV three temperature capsule (B329) and were designed for the irradiation temperatures of 550, 450 and 400°C, respectively. Capsule B334 was a weeper design and, therefore, the specimens were dirctly exposed to the sodium coolant. These B7 capsules werepart of subassembly X359a which was irradiated in position 4C2 in EBR-II for cycles 116 through 119. The specimens were in the reactor for a period corresponding to 10979 MWD which corresponds to 4603 hours at temperature and a peak fluence exposure of 2.9×10^{22} n/cm^2 (E > 0.1 MeV).

The irradiation temperatures were determined with thermal expansion devices (TED).[2] TEDs were located at the top and bottom of each subcapsule and were used to indicate the maximum temperature to which the specimens were exposed during irradiation. The results of the analysis of the TED's are summarized in Table 7.2.3. The TED's indicate the peak temperature to which the specimens were exposed. The TED temperatures reported in Table 7.2.3 have been corrected for measured volume changes in the cladding material. The nominal irradiation temperature assumes that the average irradiation temperature is the midplane coolant temperature plus 90% of the temperature difference between the coolant and peak (TED) temperatures. In other words, the γ-heating at the specimen locations is assumed to vary $\pm$10% during the coarse of an irradiation.

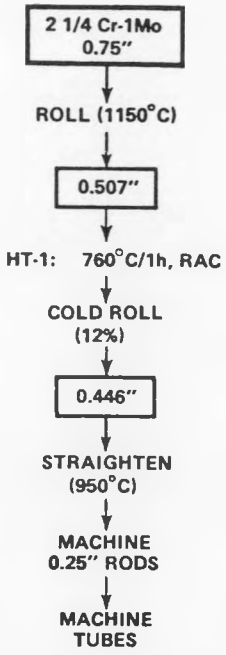

Fig. 7.2.1. Rolling schedule, alloy 2-1/4Cr-1Mo.

Table 7.2.3. Irradiation temperatures for in-Reactor creep specimens

Capsule	Design Temperature (°C)	Peak Irradiaton Temperature (°C)
B329[+]	400	392
	450	480
	550	560
B334	400	383
B333	450	475 ± 10
B331[++]	550	570 ± 9

[+]Inconel 600 TED in same level as specimens.
[++]Average peak temperatures for TEDs above and below level containing specimens.

The irradiation vehicle for the swelling specimens identified as the AAI test was of similar outer dimensions. Inside were eight subcapsules, each of which contained identical specimen loadings immersed in sodium. The subcapsule temperatures were obtained by controlled gamma heat losses through an inert gas gap between the subcapsules and the capsule. Design temperatures were 400, 425, 455, 480, 510, 540, 595 and 650°C. A low fluence experimental test of this design used thermal expansion devices (TEDs) to check operating temperatures and the temperature uncertainties are estimated at ±25°C for the higher subcapsule temperatures. The major factor controlling this uncertainty was found to be variations in the reactor gamma heating rate. Heat transfer calculations based on those gamma heating values indicate that the actual operating temperatures were lower than the design temperatures by as much as 20°C. Reactor fluences given for both experiments are the product of the EBR-II flux for the appropriate reactor positions and the residence time of the vehicle in-reactor. The fluence uncertainty is estimated to be ±10%.

7.2.4.4 Results

The results of in-reactor creep measurements are presented in Table 7.2.4 and the results of swelling measurements are presented in Table 7.2.5. In each case, results of a lower fluence discharge are also given.[3,4] The creep results are plotted in Figures 7.2.2 through 7.2.7. Figures 7.2.2, 7.2.3 and 7.2.4 show diameter change as a function of fluence for each of the irradiation temperatures 390, 480 and

Table 7.2.4. Diameter change measurements for 2-1/4Cr-1Mo pressurized tube specimens contained in the AAXIV experiment[3]

Specimen Number	Temperature (°C)	Fluence (x 10^{22} n/cm^2)	Midwall Hoop Stress (MPa)	Diameter Change (%)
PJ54	392	2.0	0	0.002
PJ54	383	5.0	0	0.09
PJ61	392	2.0	50	0.038
PJ61	383	5.0	50	0.20
PJ64	392	2.0	75	0.033
PJ64	383	5.0	75	0.22
PJ67	392	2.0	100	0.041
PJ67	383	5.0	100	0.27
PJ53	480	2.6	0	0.023
PJ53	475	5.7	0	0.01
PJ60	480	2.6	50	0.037
PJ60	475	5.7	50	0.05
PJ63	480	2.6	75	0.090
PJ63	475	5.7	75	0.12
PJ66	480	2.6	100	0.102
PJ66	475	5.7	100	0.15
PJ52	560	2.3	0	-0.016
PJ52	570	5.4	0	-0.06
PJ58	560	2.3	50	0.308
PJ58	570	5.4	50	0.69
PJ62	560	2.3	75	0.483
PJ62	570	5.4	75	1.85
PJ65	560	2.3	100	2.290 (failed)
PJ65	570	5.4	100	2.33 (failed)

570°C. The diametral changes shown in these figures have been corrected for volumetric changes in the specimen by subtracting the diameter change for the unstressed specimen from the stressed specimen diametral strain at each temperature. In all but one case, diameter change increases with stress (the exception being at 390°C and low fluence where the variations are within the uncertainty of the measurement technique.) The high stress specimen (100 MPa) tested at 570°C had apparently failed prior to the lower fluence measurement (2.3 x 10^{22} n/cm^2) at a diameter strain of 2.3%. The stress dependence of the corrected diameter changes at 390, 480 and 570°C is shown in Figures 7.2.5, 7.2.6 and 7.2.7. Response at 390°C and at 480° (Figures 7.2.5 and 7.2.6) can be adequately represented by a linear fit given the data scatter, but the onset of tertiary creep prevents such an analysis in Figure 7.2.7. It can also be shown by comparison of Figures 7.2.2 and 7.2.3 or 7.2.5 and 7.2.6, that in-reactor creep at the higher fluence is greater for the 380°C case than for the 460°C case. Such a response can occur when irradition creep is enhanced by swelling.

The pressurized tube data base can also provide swelling information. The diameter change for the unstressed conditions can be interpreted from equation 1 to give fractional swelling values. If one assumes isotropic swelling, then

$$S = \Delta V/V_o \approx 3\ \Delta D/D_o \qquad (1)$$

Therefore, swelling at 390°C to 5 x 10^{22} n/cm^2 can be estimated at 0.27% whereas at 480°C and 560, the swelling is negligible and densification of 0.18% occurs at 570°C. The swelling values from Table 7.2.5 are plotted in Figure 7.2.8. Figure 7.2.8 also shows the results of the unstressed pressurized tubes for comparison. From Figure 7.2.8 it can be demonstrated that swelling is low in 2-1/4 Cr-1Mo to fluences as high as 2.4 x 10^{23} n/cm^2. Peak swelling occurs at the lowest temperature of 400°C but a secondary swelling peak is found at 540°C. This secondary peak is expected to arise as a result of precipitation rather than void swelling. However, the 400°C peak can be expected to be due to void swelling. A swelling rate of 0.08%/10^{22} n•cm^{-2} or 0.016%/dpa is predicted from the AAI results at 400°C. In comparison, the pressurized tubes produced comparable swelling values at a much lower fluence. This may be an effect due to heat-to-heat, fabrication or heat treatment variations. It may also be noted that densification is occuring at 510°C, an indication that precipitation is continuing at high fluence.

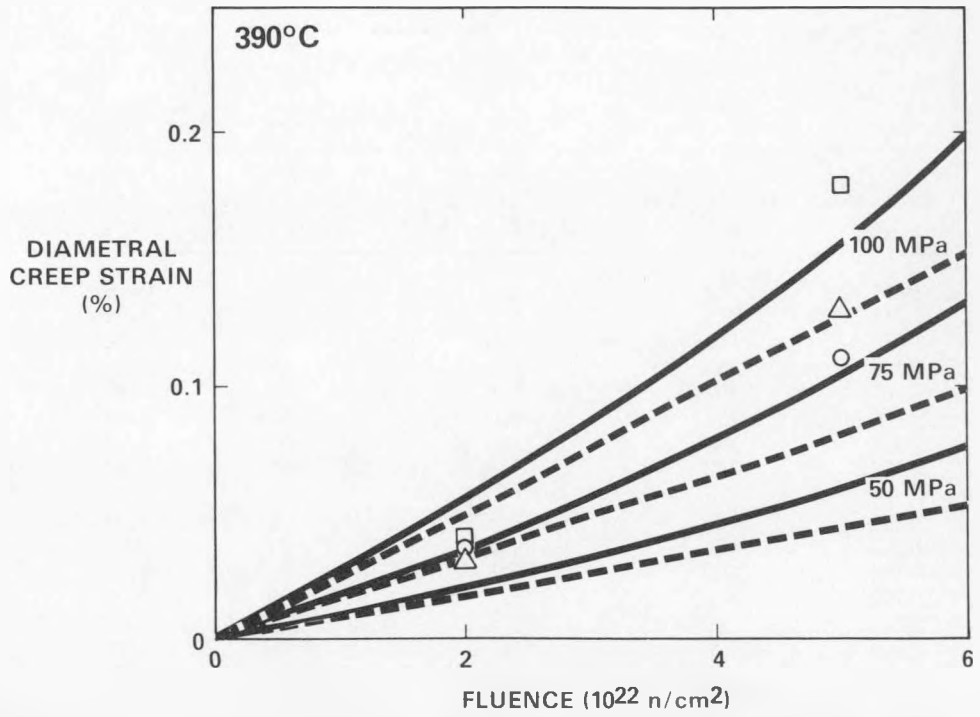

Fig. 7.2.2. Diameter change corrected for swelling as a function of fluence at 390°C for midwall hoop stress levels as high as 100 MPa. The solid curves define the in-reactor creep correlation prediction for the stress indicate. The dashed curves define the irradiation creep contribution without swelling enhanced creep.

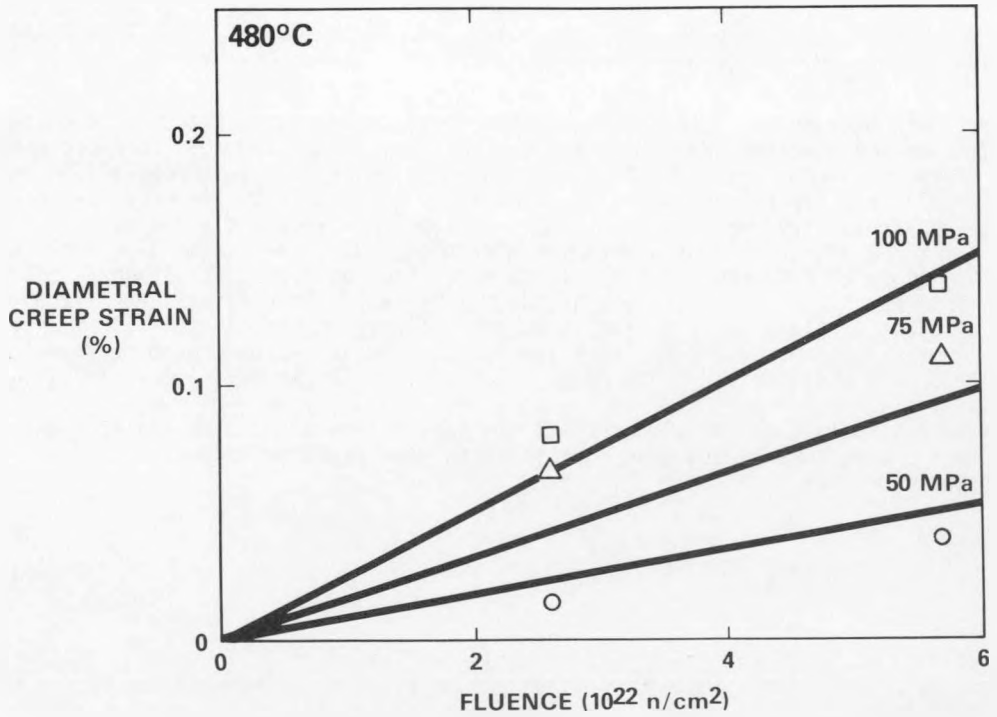

Fig. 7.2.3. Diameter change corrected for swelling as a function of fluence at 480°C for midwall hoop stress levels as high as 100 MPa. The curves define the in-reactor creep correlation prediction with thermal creep neglected for the stress values indicated.

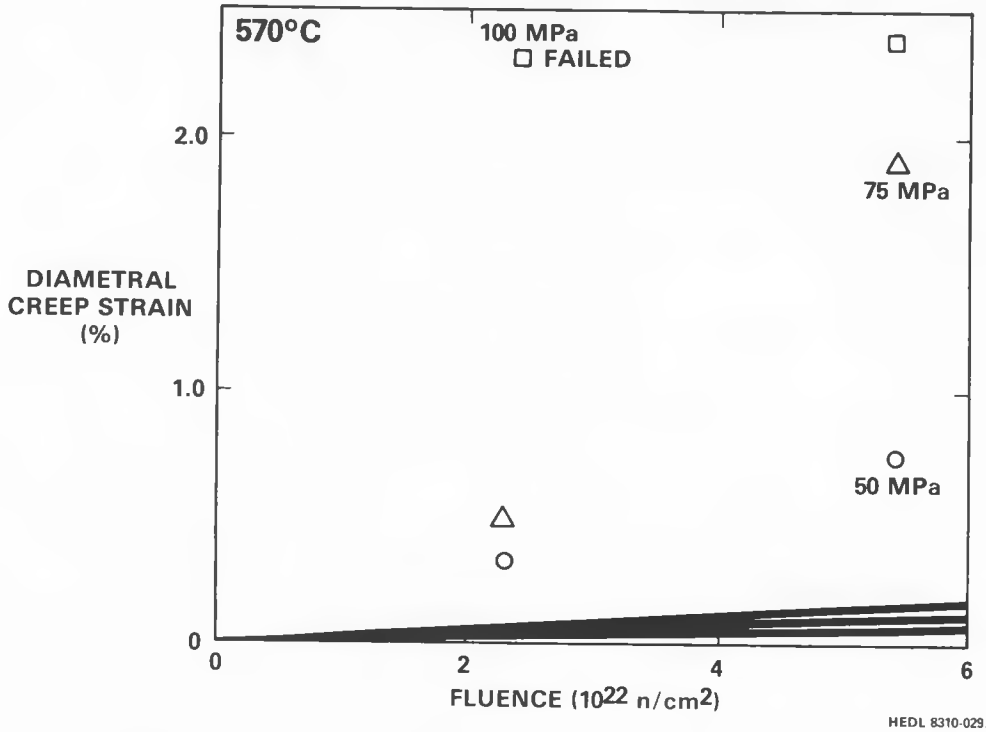

Fig. 7.2.4. Diameter change corrected for swelling as a function of fluence at 570°C for midwall hoop stress sevels as high as 100 MPa. Note that the 100 MPa specimen failed prior to 2.3×10^{22} n/cm^2. The curves define the in-reactor creep correlation prediction with thermal creep neglected.

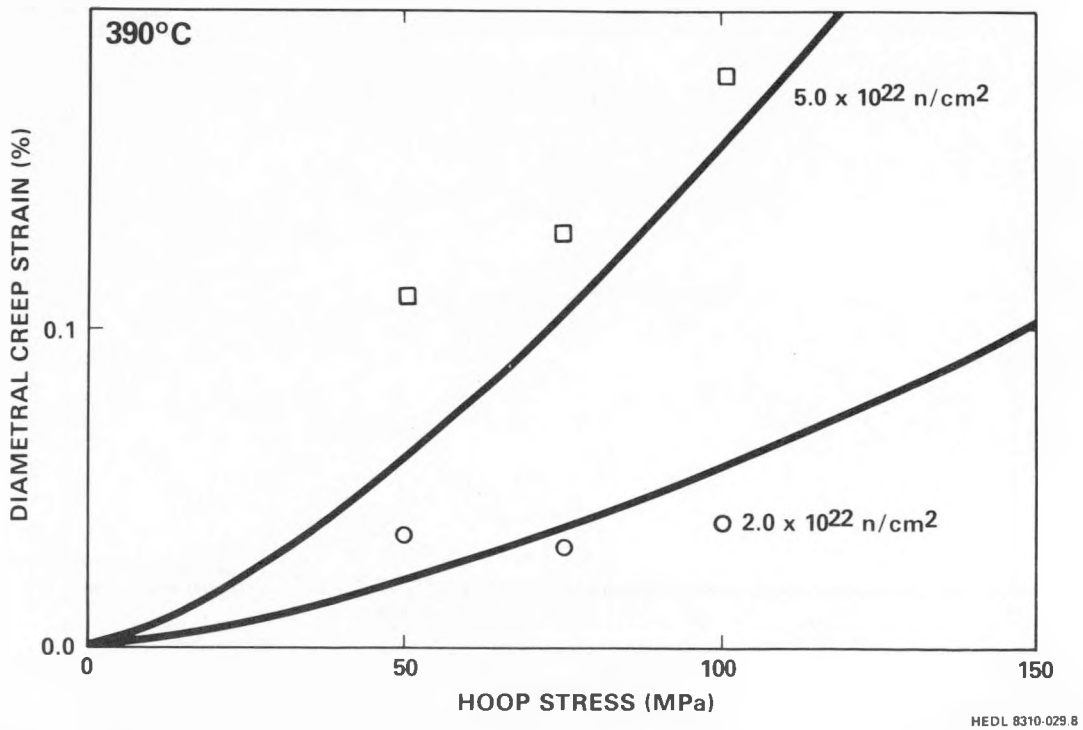

Fig. 7.2.5. Diameter change at 390°C corrected for swelling as a function of hoop stress. The curves define the in-reactor creep correlation predictions.

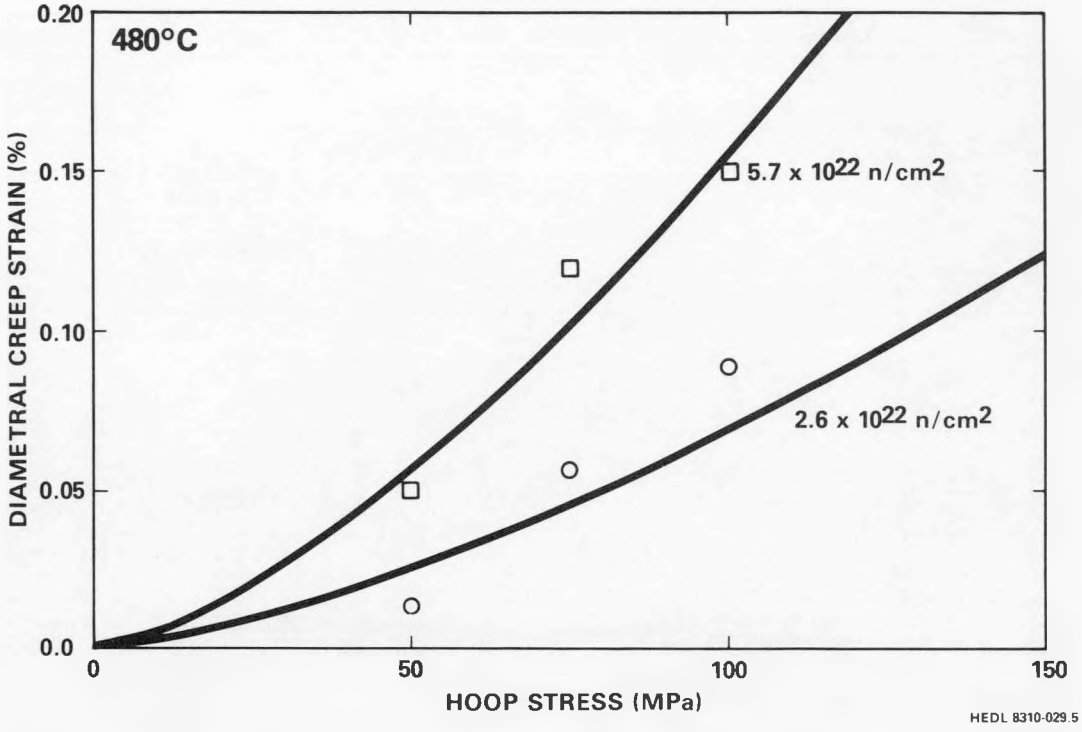

Fig. 7.2.6. Diameter change at 480°C corrected for swelling as a function of hoop stress. The curves define the in-reactor creep correlation prediction with thermal creep neglected.

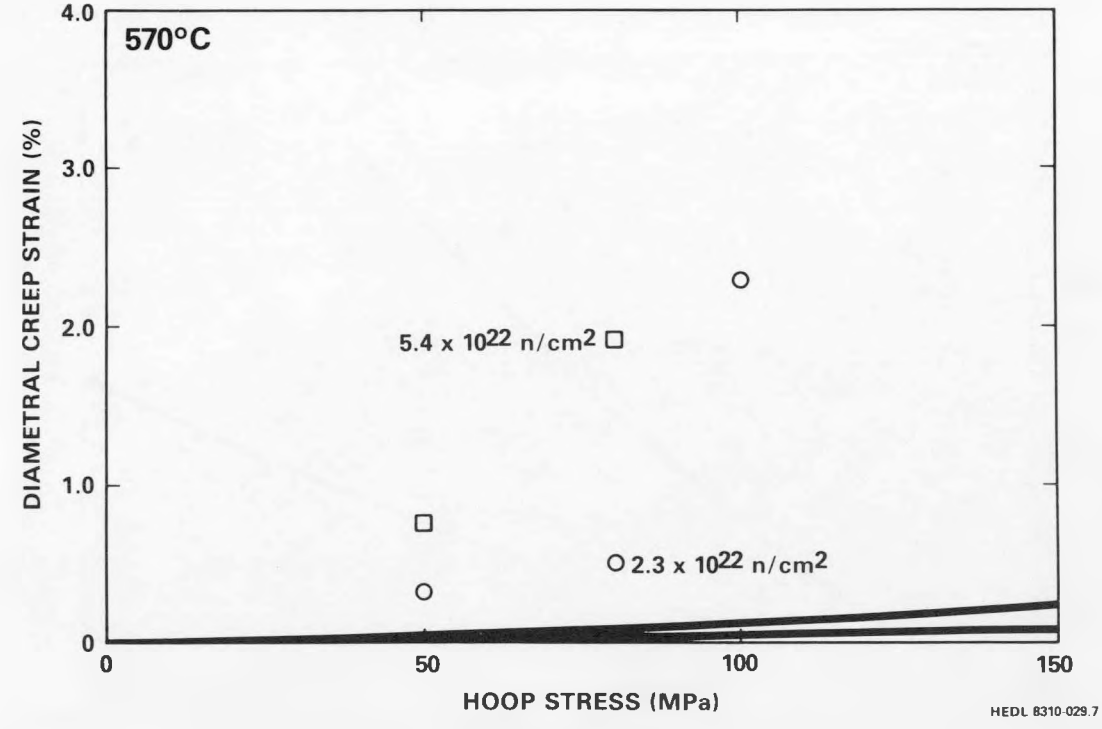

Fig. 7.2.7. Diameter change at 570°C corrected for swelling as a function of hoop stress. The curves define the in-reactor creep correlation prediction with thermal creep neglected.

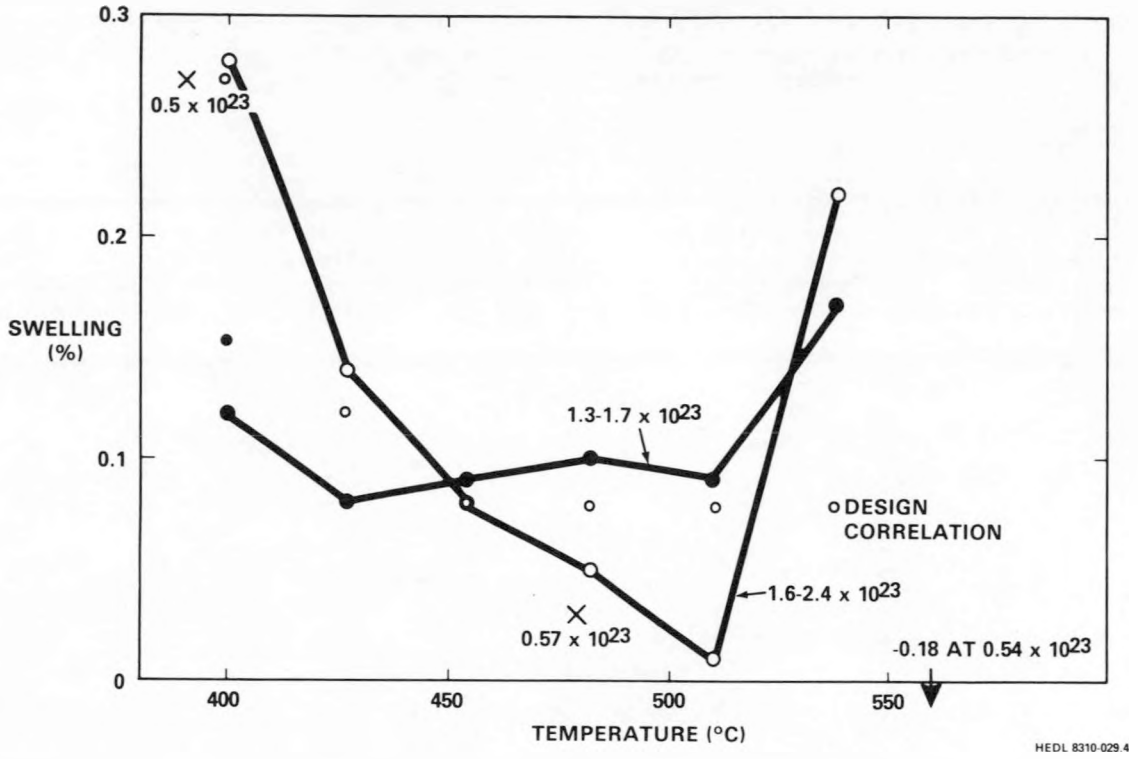

Fig. 7.2.8. Swelling results as a function of irradiation temperature. Both density change and unstressed pressurized tube data are shown. The smaller open and closed data points define the swelling correlation prediction for the fluences corresponding to the swelling results shown.

Table 7.2.5. Swelling Measurements ($-\Delta\rho/\rho_0$) for 2-1/4Cr-1Mo Specimens Contained in the AAI Test[4], ρ_0 = 7.8414

Specimen Number	Temperature (°C)	Fluence (x 10^{23} n/cm^2)	Density (gm/cm^3)	Swelling (%)
94M6	400	1.40		0.12
94M7	400	1.60	7.8204	0.28
94L6	427	1.58		0.08
94L7	427	2.07	7.8315	0.14
94E6	454	1.32		0.09
94E7	454	1.55	7.8368	0.08
94F6	482	1.53		0.10
94F7	482	1.98	7.8384	0.05
94K6	510	1.72		0.09
94K7	510	2.41	7.8422	0.01
94G6	538	1.67		0.17
94G7	538	2.32	7.8237	0.22

7.2.4.5 Discussion

The intent of this work is to develop an understanding of the in-reactor creep and swelling response of 2 1/4 Cr 1 Mo steel and to present the results in a format consistent for its inclusion in the Materials Handbook for Fusion Energy Systems. The latter objective requires that the results be provided in a design equation format. However, it is not within the scope of this project to provide a complete and defendable design equation. Nor is the data set sufficient by itself to provide a clear indication of the functional dependence required for such equations. Therefore, the approach which will be taken will be to assume the necessary functional dependence based on other martensitic steels and expermental ferritic alloys and then to establish the values of the necessary parameters in order to obtain an acceptable fit to the present

data sets. Of considerable concern was the establishment of an in-reactor creep equation which was compatible at high temperature with out-of-reactor thermal creep data. This required that the thermal creep dependence of 2-1/4 Cr-1Mo be obtained from the literature.

Swelling Equation

The swelling equational form used is standard and consists of two functional relationships. Void swelling (S_o) is modeled using a bi-linear functional relationship with three adjustable parameters: a swelling rate, R, a swelling incubation parameter, τ, and a transition parameter, α. Each of these parameters can be specified as a function of temperature.[5] Concurrently, densification (D) is modeled using a functional relationship with two adjustable parameters: a steady state density, D* and a transition paremeter, λ, and again each of these parameters can be specified as a function of temperature. The equations are as follows.

$$\text{Swelling} = \frac{\Delta V}{V_o}(\%) = S_o - D, \tag{3}$$

where

$$S_o = R\left[\phi t + \frac{1}{\alpha}\ln\left\{\frac{1 + \exp[\alpha(\tau - \phi t)]}{1 + \exp(\alpha\tau)}\right\}\right], \tag{3a}$$

$$D = D^*[1 - \exp(-\lambda\phi t)],$$

where

R = steady-state swelling rate parameter, % per 10^{22} n.cm^{-2}
ϕt = fluence in units of 10^{22} n.cm^{-2} (E > 0.1 MeV)
α = transition parameter (10^{22} n.cm^{-2})$^{-1}$
τ = incubation fluence in units of 10^{22} n.cm^{-2} (E > 0.1 MeV),

and τ will be given by

$$\tau = C_1 \exp[C_2 (T - C_3)^2]$$

T = temperature, °K.

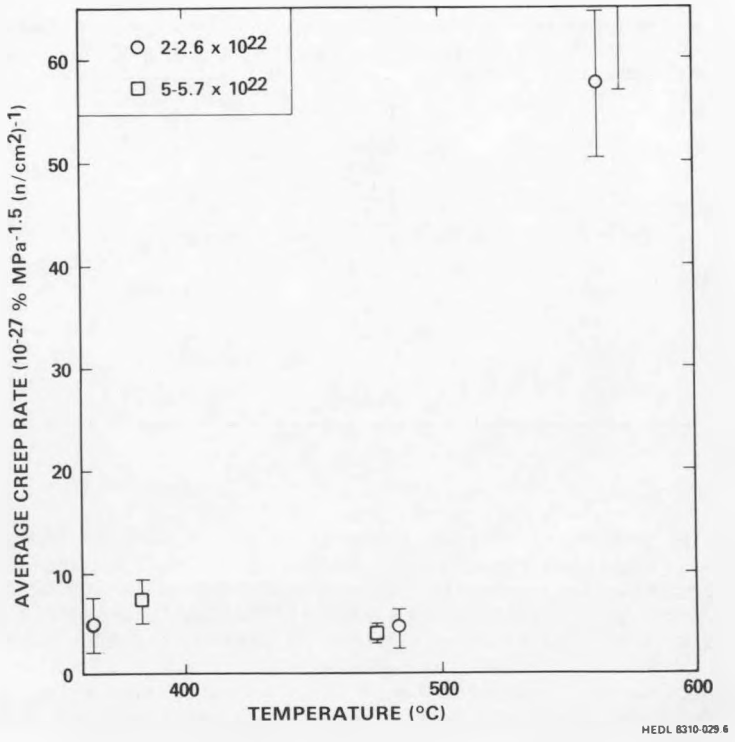

Fig. 7.2.9. Average creep rate as a function of irradiation temperature using a stress exponent of 1.5

In-Reactor Creep Equation

In order to emphasize the need for three terms to describe in-reactor creep in 2-1/4Cr-1Mo, the average creep rates are plotted in Figure 7.2.9 assuming that $\varepsilon = B\,\sigma^{1.5}\,\phi t$. A minimum value of B = 0.4 is found at 480°C whereas the higher value obtained at 392°C can most easily be interpreted as swelling enhanced creep. Void swelling at 5 x 10^{22} n/cm^2 in 2-1/4Cr-1Mo is established by the present results and by reference 6. Higher values for B are also obtained at 550 and 560°C and are interpreted as thermal creep response.

The in-reactor creep is therefore expected to consist of three terms, irradiation creep, swelling enhanced irradiation creep and thermal creep. The functional dependence which has been selected to describe the in-reactor creep of 2-1/4Cr-1Mo is based largely on results for HT-9.[3,7-8] Those results recommend a stress exponent (n) of 1.5 which is somewhat different from the linear response observed in Figures 7.2.5 and 7.2.6. Due to the data uncertainties in Figures 7.2.5 and 7.2.6, the stress exponent of 1.5 is still consistent with the data. Therefore effective in-reactor creep (ε) is defined as

$$\varepsilon = \varepsilon_I + \varepsilon_T \qquad (2)$$

where the irradiation dominated behavior can be described by

$$\varepsilon_I = \overline{B}\,\sigma^n\,\phi t + DS\sigma \qquad (2a)$$

and the thermal behavior is defined by ε_T.

The parameters of interest are

ε = effective creep strain, cm • cm^{-1}
σ = effective stress, MPa
n = stress exponent
t = time, hr
ϕt = neutron fluence in units of 10^{22}, n•cm^{-2} (E > 0.1 MeV)
B = average creep coefficient
D = swelling enhanced creep coefficient
S = fractional swelling rate, % per 10^{22} n•cm^{-2}
T = temperature, °K
R = gas constant, 1.987 cal•mole^{-1}•k^{-1}

Evaluation of Design Equation Parameters

Insufficient data is available from the AAI test to establish a steady state swelling rate from the present data set. Instead, three data sets for Fe-Cr binary alloys have been used[10-12] which demonstrate a steady state swelling rate of 0.25%/10^{22} n•cm^2. This steady state swelling rate does not appear to be sensitive to irradiation temperature over the range 400 to 450°C[12] and therefore the temperature dependence of swelling found in the AAI test will be modeled by a temperature dependent incubation parameter, τ. The α parameter has been set at 0.5 based on recent results[13] on other commercial ferritic alloys in the AAI test where it is found that voids form at fluences on the order of 10^{23} n/cm^2 but steady state swelling is not achieved even at fluences on the order of 2 x 10^{23} n/cm^2. The peak swelling temperature was selected based on Fe-Cr binary alloy data[10-12] where peak swelling for Fe-3Cr is found to be in the range 400-425°C, but it was decided to shift the peak swelling temperature slightly downward for 2-1/4Cr-1Mo to 390°C (C_3 = 663°K) based on the present results for pressurized tube and AAI rod specimens from this study. A best fit of the AAI results given the above values for R, α and C_3 established C_1 = 20 x 10^{22} n/cm^2 and C_2 = 5 x 10^{-5} (°K)$^{-2}$.

D* was set at 0.08% based on the AAI results at 450°C which are in agreement with the pressurized tube results at 480°C. This densification is expected to be due to Mo_2C precipitation which develops rapidly and therefore λ was arbitrarily set at 3 (10^{22} n/cm^2)$^{-1}$. Attempts at defining the complex temperature dependence for densification found at high fluence must await completion of the next phase of this study, microstructural examination of the AAI specimens. The above correlation for swelling in AAI specimens can be altered straightforwardly to describe swelling in the pressurized tubes and therefore account for heat-to-heat and heat treatment effects which arise in the comparison with the AAXIV test. All parameters were held constant except for C_1 and a fit was made for the 390°C pressurized tube results. A best fit was found with C_1 = 7.5 x 10^{22} n/cm^2. A tabulation of the design correlation parameters is given in Table 7.2.6. Table 7.2.6 separates the correlation parameters into AAI and AAXIV values. This is intended to emphasize the differences in heat treatment and heat-to-heat variations between specimens in the two experiment.

In determining the parameters for the in-reactor creep correlation for 2-1/4Cr-1Mo the following assumptions were made. At 475°C the average creep rate was 4 x 10^{-27}%•MPa$^{-1.5}$(n/cm^2)$^{-1}$. We assumed that this rate was an upper bound for the irradiation induced creep in this material and have set B in equation

Table 7.2.6. Assignment of design correlation parameters for swelling and in-Reactor creep in 2-1/4CR-1MO

	AAI	AAXIV
Swelling:		
	$R = 0.25\%/10^{22} n \cdot cm^{-2}$	
	$\alpha = 0.5\ (10^{22} n \cdot cm^{-2})$	
	$C_1 = 20 \times 10^{22} n/cm^2$	$C_1 = 7.5 \times 10^{22} n/cm^2$
	$C_2 = 5.0 \times 10^{-5}\ (°K)^{-2}$	
	$C_3 = 663°K$	
	$D^* = -0.08\%$	
	$\lambda = 3\ (10^{22} n \cdot cm^{-2})^{-1}$	
Creep:		
		$B = 0.4 \times 10^{-6}\%(MPa)^{-1.5}$
		$D = 2.7 \times 10^{-5}\%/MPa\text{-}10^{22} n \cdot cm^{-2}$

2a equal to this rate. The value for D in equation 2a was taken from reference 14. This value for D is typical of results from fitting in-reactor creep in several austenitic stainless steels. The swelling equation for this particular heat of 2-1/4Cr-1Mo has already been described in this report.

Evaluation of the thermal creep contribution ε_T has proven to be too large a problem for the scope of the present work. It has been shown that thermal creep response is very sensitive to the carbon content in 2-1/4Cr-1Mo.[15] Several models have been reported in the literature for describing thermal creep in 2-1/4Cr-1Mo. We chose for investigation the model for tertiary creep given in Reference 16. However, our analysis has not proven to be sufficiently reliable for extensive application. The approach taken[16] was as follows:

$$\varepsilon'_T = \frac{1}{B} \ln (1 - AB^*) \tag{4a}$$

or

$$\dot{\varepsilon}'_T = A \exp (B\, \varepsilon) \tag{4b}$$

where ε'_T and ε'_T are the true strain and strain rate and where A defines the minimum thermal creep rate and B is a constant which defines the strain at which the creep rate begins to increase significantly. The functional dependence for A and B to best fit the thermal creep data for the bainitic alloy with 0.12%[10] was

$$A = \text{maximum of} \begin{cases} 1.56 \times 10^{-6} \exp \dfrac{-121700}{RT}\ \sigma^{14} \\ 1.46 \times 10^{-5} \exp \dfrac{-33950}{RT}\ \sigma^{4} \end{cases} \tag{4c}$$

$$B = 0.206 - 1.17 \times 10^{-3}\ (T\text{-}273) + 6.3 \times 10^{-5}\ \sigma + 1.4 \times 10^{-6}\ (T\text{-}273)^2 \tag{4d}$$

However, this representation did not satisfactorily fit the AAXIV results at 560°C, nor did it provide a reasonable estimate for the activation energy which controls steady state creep, 121,7 kcal/mole. These results are not unexpected since the carbon content for our pressurized tubes is only 0.04%. The data in reference 10 clearly show that the rupture times decrease and the minimum creep rates increase with

decreasing carbon content in this steel. Therefore, we expect to underpredict the observed creep stains at 465°C for our data. It can be used however, to predict the thermal creep which might be observed at 460°C in comparison to thermal creep at 560°C. Equations 4a and 4b predict thermal creep of 0.1% diameter change at 480°C for a 100 MPa hoop stress with a value for the stress exponent of 4. However, this calculation represents a significant extrapolation beyond the data base used in the development of the model. Therefore the calculated strains for this condition have large uncertainties. For this reason it is difficult to assess what fraction of the creep strains observed at 480°C are due to thermal creep mechanisms. In the development of the in-reactor creep equation we have assumed that all the m easured strain at 480°C can be attributed to irradiation induced creep mechanisms. Therefore our equation is necessarily an upper bound for this component of the in-reactor creep strain.

It may be noted that the swelling correlation parameters α and τ can be defined completely, based on the AAI results at 400°C. Density change values at fluences of 0, 1.4 x 10^{23} n/cm^2 and 1.6 x 10^{23} n/cm^2 give values of α = 1.06 and τ = 15.5 x 10^{22} n/cm^2 if R and D* are fixed as in Table 7.2.6. This corresponds at very high fluences to a swelling prediction which is no more than 0.4 percent higher than the correlation defined in Table 7.2.6. It is recommended that the values in Table 7.2.6 be used based on observed behavior in other commercial ferritic alloys,[13] i.e., α = 0.5.

7.2.5 Conclusions

Diameter change has been measured for a series of pressurized tubes of 2-1/4Cr-1Mo steel in a bainitic condition following irradiation at 390, 480 and 570°C to ~5.5 x 10^{22}n/cm^2 (E > 0.1 MeV). The maximum applied hoop stress was 100 MPa in each case. In-reactor creep was found to be lowest at 480°C, and somewhat higher at 390°C. At 570°C failure occurred within the first irradiation period under a 100 MPa hoop stress and evidence for tertiary creep was observed in the 75 MPa hoop stress specimen. These results are interpreted as swelling enhanced creep at 390°C and significant thermal creep contributions at 570°C.

Swelling has been measured for a series of 2-1/4Cr-1Mo steel specimens in a non-standard bainite/tempered-bainite condition following irradiation over the temperature range 400 to 540°C to fluences as high as 2.4 x 10^{23}n/cm^2 (E > 0.1 MeV). Swelling remained below 0.3 percent for all conditions examined and therefore this material is highly swelling resistant. A maximum swelling value of 0.28 percent at 400°C for a fluence of 1.6 x 10^{22}n/cm^2 (E > 0.1 MeV) is interpreted as void swelling whereas a value of 0.22 percent at 540°C and 2.4 x 10^{23}n/cm^2 (E > 0.1 MeV) is believed to be due to in-reactor precipitation.

Diameter change increases measured on unstressed pressurized tubes irradiated at 390°C to 5.0 x 10^{22} n/cm^2 (E > 0.1 MeV) indicate 0.27 percent swelling. This is interpreted as an effect of other heat treatment or composition variations on void swelling in 2-1/4Cr-1Mo steel.

Correlations have been developed to describe the in-reactor creep and swelling of 2-1/4Cr-1Mo steel based on these results.

7.2.6 References

1. Figure 17, *Metals Handbook VI*, "Properties and Selection of Metals," 8th Edition, ASM, Metals Park, Novelty, Ohio, p. 481, 1961.

2. D. C. Franklin and D. S. Reuther, "A Reactor In-Core Temperature Monitor," *American Nuclear Society Transactions* 14, p. 632, November 1971.

3. R. J. Puigh and G. L. Wire, "In-Reactor Creep Behavior of Selected Ferritic Alloys," HEDL-SA-2786, submitted for publication in the Proceedings of the Topical Conference on Ferritic Alloys for Use in Nuclear Energy Technologies held June 19-23, 1983 in Snowbird, UT.

4. R. W. Powell, D. T. Peterson, M. K. Zimmerschied and J. F. Bates, "Swelling of Several Commercial Alloys Following High Fluece Neutron Irradiation," *J. Nuc. Mat.* 103&104, p. 969, 1981.

5. J. F. Bates and M. K. Korenko, "Emperical Development of Irradiation-Induced Swelling Design Equations," *Nuclear Tech* 48, p. 303, 1980.

6. D. S. Gelles, W. J. Mills and L. A. James, "Microstructural Examination of Postirradiation Deformation in 2-1/4Cr-1Mo," *Alloy Development for Irradiation Performance, Quarterly Progress Report for the Period Ending March 1981*, DOE/ER-0045/6, p. 165.

7. M. M. Paxton, B. A. Chin, E. R. Gilbert and R. E. Nygren, "Comparison of the In-Reactor Creep of Selected Ferritic, Solid Solution Strengthened and Precipitation Hardened Commercial Alloys," *J. Nucl. Mat.* 80, p. 144, 1979.

8. M. M. Paxton, B. A. Chin and E. R. Gilbert, "The In-Reactor Creep of Selected Ferritic, Solid Solution Strengthened and Precipitation Hardened Alloys," *J. Nucl. Mat.* 95, p. 185, 1980.

9. B. A. Chin, "An Analysis of the Creep Properties of a 12Cr-1Mo-W-V Steel," submitted for publication in the *Proceedings of the Topical Conference on Ferritic Alloys for Use in Nuclear Energy Technologies* held June 19-23, 1983 in Snowbird, UT.

10. E. A. Little and D. A. Stow, "Effects of Chromium Addition on Irradiation Induced Void Swelling in -Iron," *Met. Sci. J.* 14, p. 89, 1980.

11. D. S. Gelles, "Microstructural Examination of Neutron-Irradiation Simple Ferritic Alloys," *J. Nuc. Mat.* 108&109, p. 515, 1982.

12. D. S. Gelles and L. E. Thomas, "Effects of Neutron Irradiation on Microstructure in Experimental and Commercial Ferritic Alloys," HEDL-SA-2772, submitted for publication in the *Proceedings of the Topical Conference on Ferritic Alloys for Use in Nuclear Energy Technologies* held June 19-23, 1983 in Snowbird, UT.

13. D. S. Gelles, "Swelling in Several Commercial Alloys Irradiated to Very High Neutron Fluence," submitted for publication in the *Proceedings of the Third Topical Meeting on Fusion Reactor Materials* held September 19-22, 1983, in Albuquerque, NM.

14. R. A. Weiner, J. P. Foster and A. Boltax, "Irradiation Creep-Swelling Coupling: Microstructural Modeling and Data Analysis," *Radiation Effects in Breeder Reactor Structural Materials*, (AIME, NY, 1977) p. 865.

15. R. L. Klueh, "The Relationship Between Rupture Life and Creep Properties of 2-1/4Cr-1Mo Steel," *Nucl. Tech.* 26, p. 287, 1975.

16. R. Sandström and A. Kondyr, "Model for Tertiary-Creep in Mo and CrMo-Steels, *Mechanical Behavior of Materials*, 12, Pergamon Press, Oxford 1980, p. 275.

7.3 ELEVATED-TEMPERATURE TENSILE PROPERTIES OF 2 1/4 Cr-1 Mo STEEL IRRADIATED IN THE EBR-II, AD-2 EXPERIMENT* — R. L. Klueh and J. M. Vitek (Oak Ridge National Laboratory)

7.3.1 ADIP Task

ADIP Tasks are not defined for Path E, Ferritic Steels, in the 1978 program plan.

7.3.2 Objective

The goal of this project is to measure the tensile properties of 2 1/4 Cr-1 Mo steel irradiated at elevated temperatures in EBR-II. In the future, the results from this work will be compared with elevated-temperature irradiations of this steel in HFIR; comparisons will also be made between 2 1/4 Cr-1 Mo steel and the 9 Cr-1 MoVNb and 12 Cr-1 MoVW steels also irradiated in EBR-II, AD-2 experiment.

7.3.3 Summary

The effect of irradiation on the tensile properties of 2 1/4 Cr-1 Mo steel was determined for specimens irradiated in EBR-II at 390 to 550°C. Unirradiated control specimens and specimens aged for 5000 h at the irradiation temperatures were also tested. Irradiation to approximately 9 dpa at 390°C increased the strength and decreased the ductility compared with the unirradiated and aged specimens. Softening occurred in samples irradiated and tested at 450, 500, and 550°C.

7.3.4 Progress and Status

The tensile specimens described in this report were irradiated in EBR-II as part of the large AD-2 experiment conducted by HEDL.[1] The experiment included 12 Cr-1 MoVW, 9 Cr-1 MoVNb, and 2 1/4 Cr-1 Mo steels, with specimens for the determination of tensile properties, impact properties, fracture toughness, fatigue, and crack growth. Disks of each material were also included to determine microstructural effects of irradiation.

7.3.4.1 Experimental Procedure

The 2 1/4 Cr-1 Mo steel used in this experiment was obtained from a section of thick-walled pipe that was fabricated from Mannesman heat 38649 (ref. 1). The vendor-certified chemical composition and overcheck are given in Table 7.3.1. Tensile specimens were obtained from 0.76-mm-thick sheet that was produced by cold rolling 11.2-mm-thick sections of the pipe. The specimens were irradiated in the normalized-and-tempered condition: 0.5 h at 900°C, air cooled; 1 h at 700°C, air cooled.[1]

Sheet tensile specimens in this experiment were of the SS-1 type, with a reduced gage section 20.3 mm long by 1.52 mm wide by 0.76 mm thick (Fig. 7.3.1). All specimens were machined with their gage lengths perpendicular to the rolling direction of the sheet.[1]

Specimens were irradiated in capsules designed to maintain temperatures of 390, 450, 500, and 550°C; three specimens each were irradiated at 390 and 500°C, one each at 450 and 550°C. Irradiation was in

Table 7.3.1. Chemical composition of 2 1/4 Cr-1 Mo steel (heat 38649)

Element	Content (wt %)[a]		Element	Content (wt %)[a]	
	Vendor[b]	Overcheck[c]		Vendor[b]	Overcheck[c]
C	0.093	0.083	Mo	0.95	0.99
Mn	0.52	0.49	Cu	0.16	
P	0.011	0.011	Al	0.003	
S	0.011	0.016	As		0.017
Si	0.17	0.19	Sn		0.0088
Ni	0.40		N		0.010
Cr	2.15	2.17	Sb		0.0024

[a]Balance iron.

[b]Mannesmann Co.

[c]Climax Molybdenum Co., Ann Arbor, Mich.

*Research sponsored by Electric Power Research Institute, Palo Alto, California, under contract No. Y3E053R between McDonnell Douglas Astronautics Company, St. Louis, Missouri, and Union Carbide Corporation.

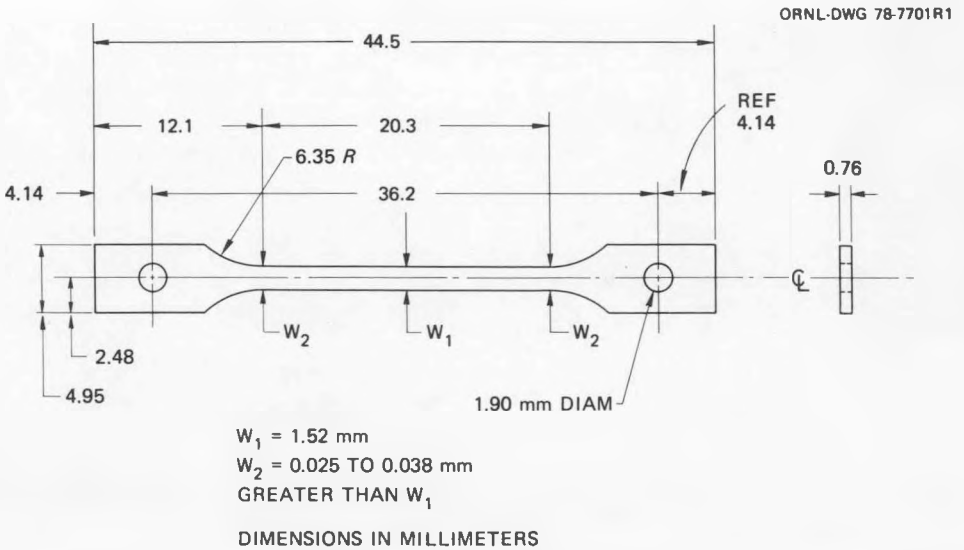

Fig. 7.3.1. Geometry of the SS-1 tensile specimen used in these experiments.

row 4 of EBR-II to a peak fluence of 2.8×10^{26} neutrons/m^2 ($E > 0.1$ MeV). The fluence on the specimens depended on their location relative to the horizontal midplane of the reactor. The 2 1/4 Cr-1 Mo steel specimens were in level No. 1 of the capsules[1] and were exposed to ~1.9×10^{26} neutrons/m^2, which produced a displacement damage of about 9 dpa. The uncertainty in fluence has been estimated as ±10% and the temperature uncertainities are 390 ± 10°C, 450 ± 15°C, 500 ± 20°C, 550 ± 30°C (ref. 2).

After irradiation, tensile tests were conducted at the irradiation temperature and, where specimens were available, at room temperature. As-heat-treated and thermally aged control samples were also tested to separate the effect of irradiation from thermal-aging effects. Thermal aging was at the irradiation temperatures for 5000 h — the approximate time of the irradiation. The tensile tests were made in a vacuum chamber on a 44-kN-capacity Instron universal testing machine at a crosshead speed of 8.5 μm/s, which results in a nominal strain rate of 4.2×10^{-4}/s.

7.3.4.2 Results

The microstructure of the normalized-and-tempered 2 1/4 Cr-1 Mo steel was tempered bainite [Fig. 7.3.2(*a*)]. The prior austenite grain size was estimated as being between ASTM number 8 and 9; the microhardness was 207 DPH (500-g load).[1] Thermal aging produced little change in the optical microstructure [Figs. 7.3.2(*b*) and (*c*)]. The microhardness was also unchanged; after aging at 400 and 550°C, the microhardness was 216 and 206 DPH (1000-g load), respectively.

The tensile results for the as-heat-treated, thermally aged, and irradiated 2 1/4 Cr-1 Mo steel are given in Tables 7.3.2 through 7.3.4. In Figs. 7.3.3 through 7.3.5 the tensile properties for these three different conditions are compared for tensile tests conducted at the irradiation temperature. Figures 7.3.6 and 7.3.7 compare results for room-temperature tests plotted against irradiation temperature. Fewer room-temperature tests were made because of the limited number of specimens available.

The behavior of the irradiated 2 1/4 Cr-1 Mo steel showed both hardening and softening, depending on the irradiation temperature. For tests at the irradiation temperature, the 0.2% yield strength and the ultimate tensile strength exceeded the as-heat-treated (unirradiated) values at 400°C, then fell below the unirradiated values at the three higher temperatures (Figs. 7.3.3 and 7.3.4). The difference in strength between unirradiated and irradiated values became larger as the temperature increased and was greatest at 550°C. Between 450 and 500°C, the strength decreased only slightly, remaining close to the values for the thermally aged steel, then dropped quite precipitously at the highest irradiation and test temperature. The ductility behavior reflected the strength behavior (Fig. 7.3.5). At 400°C, where the steel hardens, the uniform and total elongations of the irradiated steel fell below those of the unirradiated steel. As the test temperature increased, the ductility of the irradiated steel approached that of the unirradiated steel.

The room-temperature test results showed a similar relative behavior for the as-heat-treated and irradiated steels (Figs. 7.3.6 and 7.3.7). Because of the lack of irradiated specimens, a direct comparison was possible only for irradiation temperatures of 400 and 500°C, with interpolation and extrapolation necessary at the other temperatures. The major difference between the room-temperature tests and the elevated-temperature tests was that the curve for irradiated material was shifted to slightly higher values relative to the unirradiated values. There was major hardening at 400°C, a slight hardening at 450°C, relatively little difference at 500°C, and a large amount of softening at 550°C (extrapolated). Again, the relative ductility behavior reflected the strength changes.

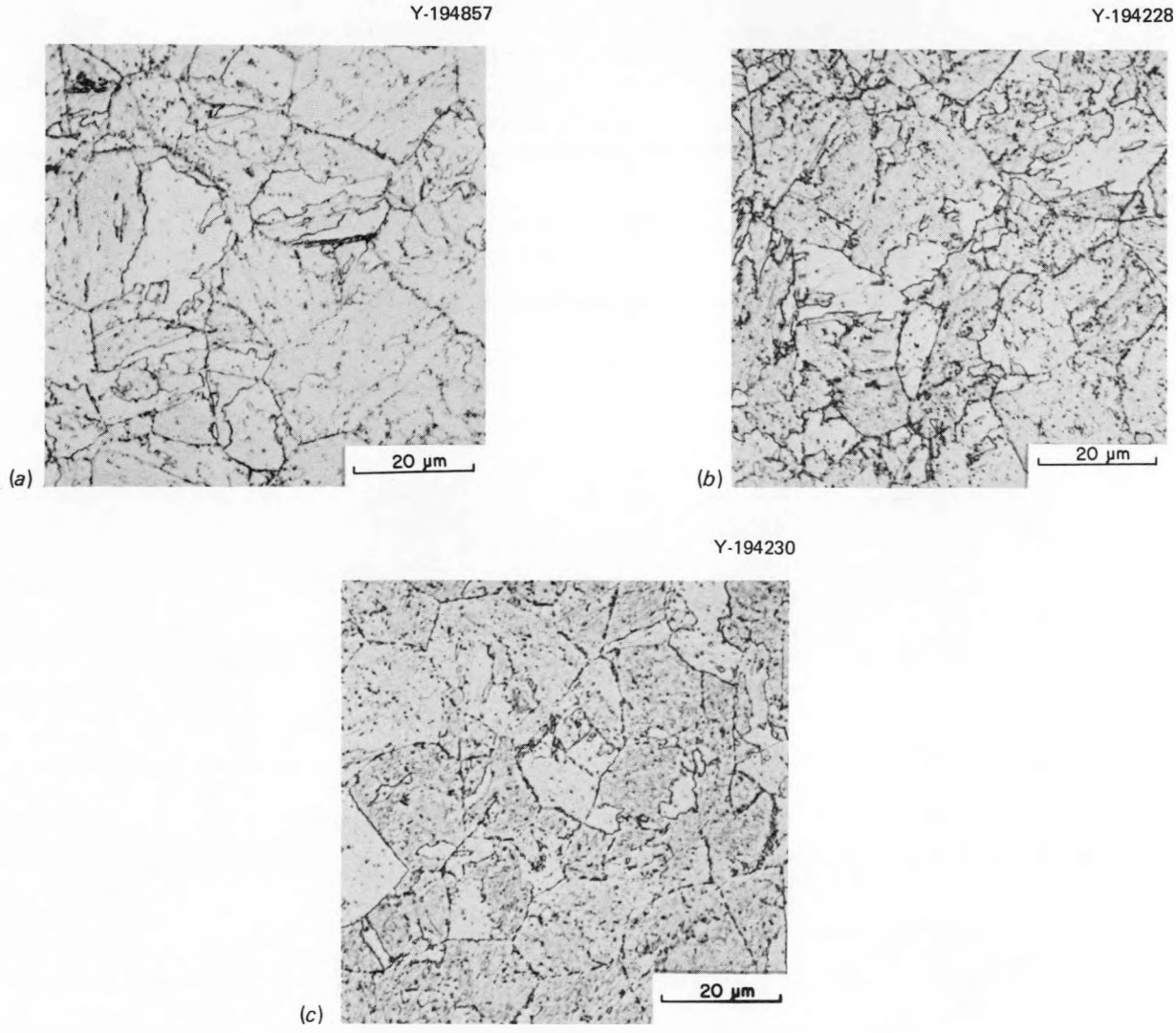

Fig. 7.3.2. Microstructure of 2 1/4 Cr-1 Mo steel (*a*) as heat treated (normalized and tempered), (*b*) after aging for 5000 h at 400°C, and (*c*) after aging for 5000 h at 550°C.

Table 7.3.2. Tensile properties of unirradiated 2 1/4 Cr-1 Mo steel in the normalized-and-tempered condition

Test temperature (°C)	Strength (MPa)		Elongation (%)	
	Yield	Ultimate	Uniform	Total
22	513	603	7.9	11.4
200	496	585	6.4	9.6
400	501	616	4.8	8.4
450	467	598	6.4	9.7
500	465	575	5.1	9.0
550	439	524	4.0	8.6

Table 7.3.3. Tensile properties of 2 1/4 Cr-1 Mo steel aged for 5000 h

Temperature (°C)		Strength (MPa)		Elongation (%)	
Aging	Test	Yield	Ultimate	Uniform	Total
400	22	519	635	7.8	10.9
400	400	456	570	5.3	7.8
450	22	498	611	8.1	12.3
450	450	404	510	5.0	7.5
500	500	409	485	3.6	7.4
550	22	349	460	6.9	10.5
550	550	365	407	2.9	7.1

Table 7.3.4. Tensile properties of 2 1/4 Cr-1 Mo steel irradiated in the AD-2 experiment in EBR-II. The irradiation produced a displacement damage level of approximately 9 dpa

Temperature (°C)		Strength (MPa)		Elongation (%)	
Irradiation	Test	Yield	Ultimate	Uniform	Total
390	22	728	791	4.1	6.9
390	400	636	716	2.3	5.4
450	450	440	510	3.6	6.2
500	22	506	584	7.8	12.4
500	500	402	465	3.5	7.8
550	550	258	289	2.1	7.5

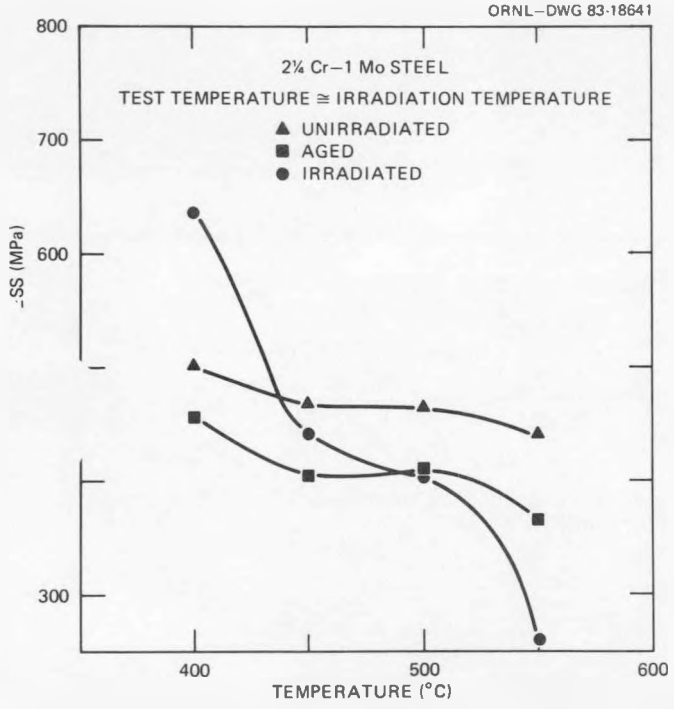

Fig. 7.3.3. The 0.2% yield stress of 2 1/4 Cr-1 Mo steel as a function of test temperature for irradiated specimens, unirradiated controls, and thermally aged controls. The test temperature equals the irradiation and aging temperatures; specimens were aged for 5000 h.

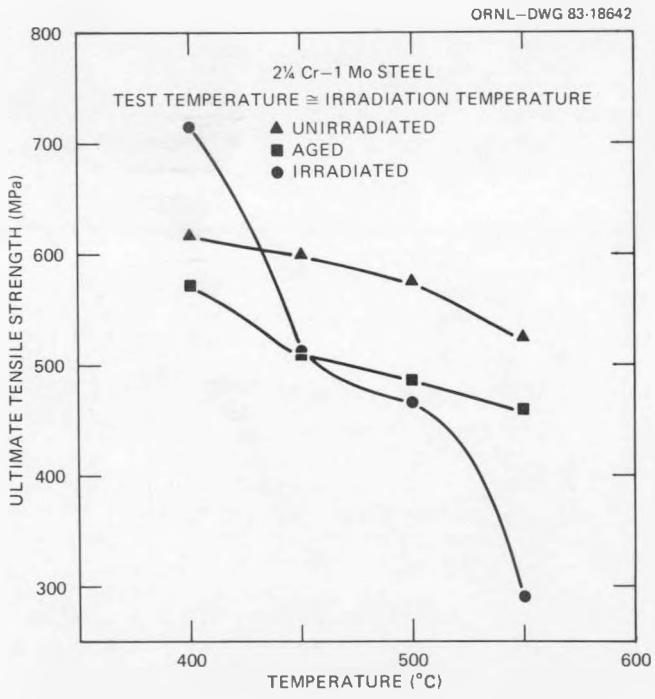

Fig. 7.3.4. The ultimate tensile strength of 2 1/4 Cr-1 Mo steel as a function of test temperature for irradiated specimens, unirradiated controls, and thermally aged controls. The test temperature equals the irradiation and aging temperatures; specimens were aged for 5000 h.

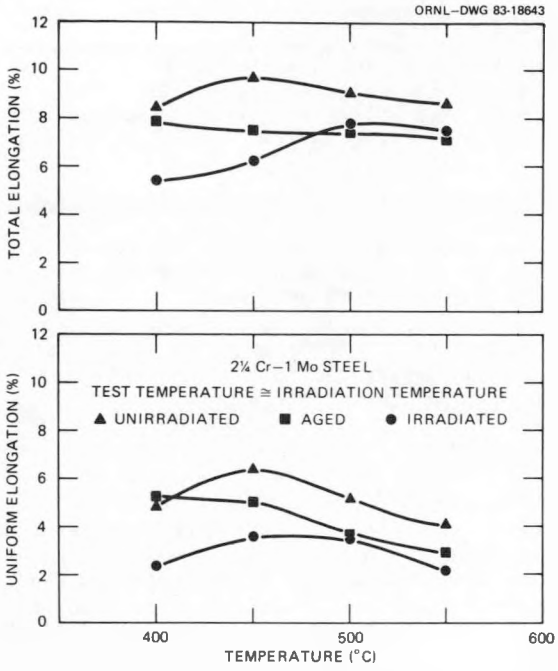

Fig. 7.3.5. The uniform and total elongation of 2 1/4 Cr-1 Mo steel as functions of test temperature for irradiated specimens, unirradiated controls, and thermally aged controls. The test temperatures equal the irradiation and aging temperatures; specimens were aged 5000 h.

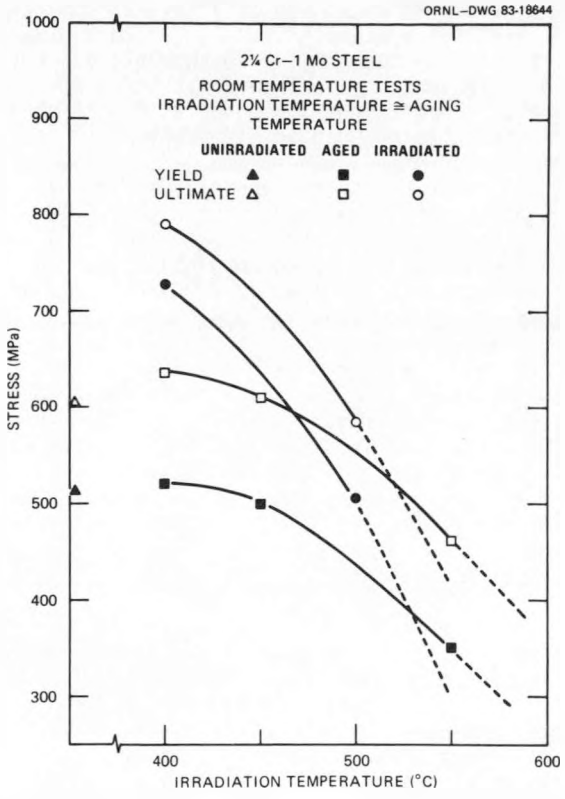

Fig. 7.3.6. The 0.2% yield stress and ultimate tensile strength of 2 1/4 Cr-1 Mo steel tested at room temperature plotted against irradiation (aging) temperature for irradiated and thermally aged specimens. Results for unirradiated control are also shown.

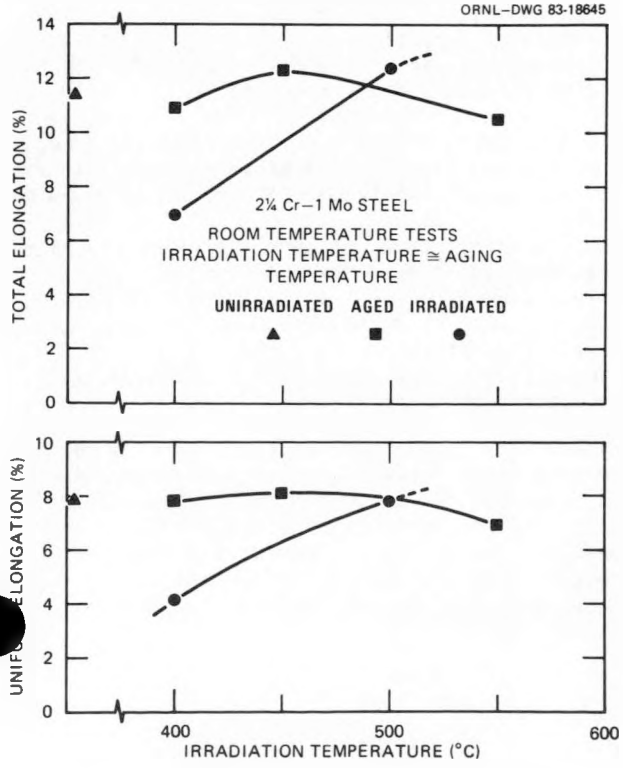

Fig. 7.3.7. The uniform and total elongations of 2 1/4 Cr-1 Mo steel tested at room temperature plotted against irradiation (aging) temperature for irradiated and thermally aged specimens. Results for unirradiated control are also shown.

Thermal aging at the irradiation temperatures had an effect on strength, reflected in tests at both the aging temperature (Figs. 7.3.2 and 7.3.3) and room temperature (Fig. 7.3.6). Aging gave rise to a relatively constant loss in both yield and ultimate tensile strength at all temperatures in tests at the aging (irradiation) temperature. For room-temperature tests, there was a gradual loss of strength caused by aging at temperatures above 450°C; little change was observed for specimens aged at 400 and 450°C. The uniform and total elongations generally followed the behavior of the as-heat-treated steel (Figs. 7.3.5 and 7.3.7).

A comparison of the aged and irradiated steels indicated that, for the elevated-temperature tests, the strength of the irradiated steel was essentially equal to that of the aged steel at 450 and 500°C. At 400°C, the strength of the irradiated steel was much higher than that of the aged steel, whereas at 550°C the strength of the irradiated steel was significantly below that of the aged steel (Figs. 7.2.3 and 7.3.4). For the room-temperature tests, where irradiation gave rise to a relatively larger amount of hardening over the irradiated control, the approach of aged and irradiated steels occurred at a higher temperature than for the elevated-temperature tests. Here the strengths became similar above 500°C.

As seen in Figs. 7.3.5 and 7.3.7, there was no severe loss of ductility due to irradiation for the range of conditions examined. Only those specimens irradiated at 390°C showed a large decrease in uniform and total elongation. However, even then the uniform elongation exceeded 2% and the total elongation exceeded 5%. Although no scanning electron microscopy observations were made, past experience indicates that such elongations are indicative of ductile-transgranular fractures. The elongation values reported here are considerably above those observed for 2 1/4 Cr-1 Mo steel irradiated in HFIR at ~50°C and tested at room temperature and 300°C; the fractures were also ductile-transgranular in those tests.[3]

7.3.4.3 Discussion

The elevated-temperature mechanical property behavior of the 2 1/4 Cr-1 Mo steel can be explained on the basis of the knowledge of the carbide precipitation reactions that occur at elevated temperatures.[4-6] Dispersion strengthening by carbide precipitates is important in determining the elevated-temperature strength of the steel. In bainite, which constitutes the microstructure of the steel tested in the normalized-and-tempered condition, Baker and Nutting found that M_3C and Mo_2C form quite early during elevated-temperature exposure — usually during the heat treatment.[4] During further elevated-temperature exposure, these carbides are replaced by M_7C_3, $M_{23}C_6$, and M_6C (eta-carbide). (Eta-carbide is usually referred to as M_6C, although studies have shown that the stoichiometry of eta-carbide in aged 2 1/4 Cr-1 Mo steel approximates M_4C.)[5] The M_7C_3 is unstable, and the final microstructure is a ferrite that contains $M_{23}C_6$ and M_6C.[4]

In addition to precipitation strengthening in 2 1/4 Cr-1 Mo steel, there is also a solid-solution strengthening effect.[6] This effect gives rise to dynamic strain-aging peaks in plots of flow stress against temperature in unaged steel. Baird and Jamieson studied the effect in Fe-Mo-C and Fe-Cr-C alloys and showed that the effect occurs in steels that contain in solution interstitial and substitutional solutes that have an affinity for each other.[7,8] They termed the effect interaction solid-solution hardening (ISSH) and concluded that it extended the effect of dynamic strain aging to temperatures of 400 to 600°C in the ternary alloys. This is well above the temperatures where dynamic strain aging is due to only carbon and/or nitrogen.[7] (This latter effect is confined to the range 100 to 300°C, the "blue brittleness" range.) Interaction solid-solution hardening was concluded to result from the formation of Mo-C and Cr-C atom pairs or atom clusters, which subsequently form dislocation atmospheres. Because such a dislocation atmosphere is much less mobile than an atmosphere that contains only interstitial atoms, the strengthening effect is extended to higher temperatures.

In mechanical property studies on 2 1/4 Cr-1 Mo steel, the effect of ISSH on this more complicated steel was examined.[6,9] For a normalized-and-tempered steel with a tempered-bainite microstructure, it was concluded that ISSH was due to Cr-C interactions.[6,9,10] Interaction solid-solution hardening had a dominant effect on tensile properties between about 250 and 450°C.

During thermal aging of the normalized-and-tempered steel, precipitation relieves the supersaturation that causes ISSH. Hardening then becomes due to dispersion strengthening by carbide precipitates. With prolonged exposure at elevated temperatures, the strength will decrease further as the finer precipitates formed during the heat treatment are replaced by the stable $M_{23}C_6$ and M_6C. With prolonged elevated-temperature exposure, these precipitates will coarsen by Ostwald ripening.

The loss of strength due to thermal aging at 400 and 450°C (Figs. 7.3.3 and 7.3.4) is attributed to the loss of ISSH caused by the loss of the supersaturation that causes ISSH. At the two highest temperatures, both the loss of ISSH and changes in dispersion strengthening caused by precipitate changes are expected to play a role in the strength loss. The higher the temperature, the larger will be the effect on the precipitate changes that lead to a coarser precipitate and thus to a lower strength. Also, the higher the temperature, the less effect ISSH has on strength. Little effect of ISSH is expected at 550°C (ref. 9). The above conclusions are confirmed by the room-temperature tests. The specimens aged at 400 and 450°C showed little change due to the aging treatment. A slight decrease was noted at 500°C (interpolated) and a large decrease at 550°C. The nature of these strength changes reflect the fact that ISSH has a minor effect on strength at room temperature, and strength is determined primarily by the precipitate structure.

The above discussion helps rationalize the observed effects of irradiation. The increase in strength the lowest irradiation temperature (390°C) is primarily attributed to the development of the dislocation-loop structure that forms as a result of irradiation damage. At 450 and 500°C, dislocation recovery processes are rapid enough to prevent the formation of a dislocation structure that can increase strength. The loss of strength, which is similar to that observed for the aged steels, is attributed to the loss of the ISSH effect at 450°C and a combination of the loss of ISSH and dispersion-strengthening at 500°C. Finally, the large decrease in strength at 550°C relative to the unaged and aged controls is concluded to be due to the acceleration of the precipitation-coarsening reactions during irradiation. That is, the vacancies and interstitials generated during irradiation accelerate diffusion and increase the rate at which the equilibrium precipitate structure of coarse $M_{23}C_6$ and M_6C is developed.

The hardening at 400°C is similar to the irradiation response noted by Gelles et al.[11] on fully annealed 2 1/4 Cr-1 Mo steel irradiated in EBR-II. A steel is annealed by slowly cooling (in a furnace) from the austenitizing temperature; 2 1/4 Cr-1 Mo steel in this condition has a much different microstructure from the tempered bainite irradiated and tested in the present study. The annealed steel contained primarily polygonal ferrite with small amounts of pearlite.[10] (Annealed steel also generally contains some bainite.[12]) The carbide precipitation sequence in polygonal ferrite begins with the formation of a high density of small Mo_2C particles, which eventually transform to M_6C (ref. 4).

In the irradiation study on the annealed steel, one specimen that was irradiated to 6.1×10^{26} neutrons/m^2 (>0.1 MeV) (compared with 1.9×10^{26} neutrons/m^2 in this study) was examined by TEM. Yield stress data were presented for this specimen along with results for several specimens that had been irradiated between ~0.2 and 0.7×10^{26} neutrons/m^2. A plot of the 0.2% yield stress and ultimate tensile strength against fluence indicated a saturation-type curve, where the strength values increasing with fluence up to $\sim 1 \times 10^{26}$ neutrons/m^2 and then leveled off. For the specimen irradiated to 6.1×10^{26} neutrons/m^2, the yield stress and ultimate tensile strength were 624 and 627 MPa, respectively; the before-test values were ~230 and 460 MPa, respectively.[11] The final yield stress and ultimate tensile strength values in the present study of 636 and 716 MPa are quite similar to those of the annealed steel, even though the starting strengths were quite different.

Gelles et al. reported large amounts of fine Mo_2C precipitate in the irradiated steel but not in the as-annealed microstructure.[11] A high density of small dislocation loops and ~0.5% void swelling was also observed. The large increase in strength was attributed to the formation of the Mo_2C, rather than the irradiation-generated dislocation loops, because it was felt that point defect agglomeration would not saturate with increasing fluence.[11]

The precipitate formed during irradiation of the annealed steel plays a role in the hardening, the high density of dislocation loops also appears to contribute to that hardening. Furthermore, irradiation-induced dislocation loop hardening is quite likely to play a dominate role in the hardening of the normalized-and-tempered steel of the present study. Although evaluating the relative contribution of precipitates and dislocations loops will require further TEM, several observations can be made.

The different precipitation sequence in the different microstructural constituents could be important. The formation of additional Mo_2C in the annealed steel is expected, as Mo_2C is the expected precipitate in polygonal ferrite.[4] (The irradiation presumably increases the precipitation rate at 400°C.) This is in contrast to the bainitic steel of the present study, where the Mo_2C precipitation sequence is probably complete after tempering and before irradiation. (The Mo_2C has been concluded to be the only precipitate in this steel to give substantial dispersion strengthening.[13]) Of course, it is possible that a new precipitation sequence occurs during irradiation of the normalized-and-tempered steel. (This would require a reversal of the sequence of the precipitation processes in comparison with the processes during thermal aging.) Differences in precipitation processes between irradiated and thermally aged austenitic stainless steels have been observed.

Irradiation-induced hardening due to dislocation loops formed during irradiation has been observed to play a major role in unalloyed metals[14] and alloys.[15] In type 316 stainless steel irradiated at temperatures above 370°C, precipitates and loops both contribute to the hardening; the network dislocations and the voids that form during irradiation also contribute.[15] Both the precipitate strengthening and loop strengthening gave rise to a saturation of strength with increasing fluence. If strengthening due to voids and network dislocations is ignored, the effect of loops became more pronounced and precipitates less pronounced as the irradiation temperature was lowered.[15]

We previously irradiated normalized-and-tempered and isothermally annealed 2 1/4 Cr-1 Mo steel at 50°C to about 1.2×10^{26} neutrons/m^2 (>0.1 MeV) (~8.5 dpa) in HFIR and found a much larger increase in hardening[3] than that observed in the present study. It is difficult to envision irradiation-enhanced diffusion such that precipitates can form at 50°C and cause the large strength increases observed (almost 200% for the isothermally annealed steel). If irradiation-enhanced precipitation were the cause, a slight strength increase might be expected after a 50°C irradiation, but a much larger increase would be expected at 400°C — opposite to the observed effect. The observed strength changes and the conclusion that irradiation-induced hardening must play a significant part in the hardening agree with the observations on stainless steel that loop hardening becomes a more significant contributor to total hardening as the irradiation temperature is decreased.[15]

The annealed steel studied by Gelles et al.[11] had a uniform elongation of 0.9% and total elongation of 1% for irradiation and testing at 400°C. In the TEM studies on the deformed specimen, indications of

channel deformation were observed. Although the polygonal ferrite was found to contain a high density of dislocation loops, Mo_2C precipitates, and cavities, the small amount of pearlite present was characterized by a higher density of larger voids, no Mo_2C, and, instead of a dislocation-loop structure, dislocation climb.[11] It was concluded that slip was probably localized in regions adjacent to the weaker pearlite, which led to the channel deformation. (This region is expected to be weaker because of the lack of Mo_2C and the coarser dislocation structure.[11]) The uniform elongation of 2.3% for the normalized-and-tempered steel tested in the present study is not indicative of channel deformation, even though the irradiated strength of this steel is the same as that of the annealed steel. If the channel deformation of the annealed steel is due to the localized deformation in the small amount of pearlite, then the lack of such deformation in the normalized-and-tempered structure may be the result of a uniform tempered-bainite microstructure.

The large decrease in strength in the irradiated 2 1/4 Cr-1 Mo steel relative to the unirradiated steel at 550°C does not imply that the steel should not be considered for fusion reactor applications. Ferritic steels were initially proposed for this application for use below 520°C.[16] (The proposal of a 520°C limit was made for the 12 Cr-1 MoVW steel.) The present results indicate that normalized-and-tempered 2 1/4 Cr-1 Mo steel has good stability for the 9 dpa irradiation to 500°C. Further tests are required to determine if the irradiation-enhanced softening observed at 550°C becomes important at lower temperatures. It was previously pointed out that 2 1/4 Cr-1 Mo steel can be modified with vanadium, niobium, and titanium in the same way as the 9 and 12 Cr steels have been modified.[17] This would give increased precipitate stability and allow the steels to be used at still higher temperatures. Such a steel has been proposed for pressure vessel applications.[18]

Finally, it should be kept in mind that only one specimen was tested for each test condition. Although trends are noted and reasons given for observations, the extent of experimental error has not been accounted for. It would be extremely useful to have more data to verify the observations.

7.3.5 References

1. R. J. Puigh and N. F. Panayotou, "Specimen Preparation and Loading for the AD-2 Ferritics Experiment," pp. 260–93 in *ADIP Quart. Prog. Rep. June 30, 1980*, DOE/ER-0045/3, U.S. DOE, Office of Fusion Energy.
2. R. J. Puigh, HEDL, private communication to R. L. Klueh, Oct. 19, 1983.
3. R. L. Klueh and J. M. Vitek, "Tensile Behavior of Three Commercial Ferritic Steels After Low-Temperature Irradiation," to be published in *Ferritic Alloys fur Use in Nuclear Technologies*, by AIME.
4. R. G. Baker and J. Nutting, "The Tempering of 2 1/4 Cr-1 Mo Steel After Quenching and Normalizing," *J. Iron Steel Inst. London* 192, 257–68 (1959).
5. J. M. Leitnaker, R. L. Klueh, and W. R. Laing, "The Composition of Eta-Carbide Phase in 2 1/4 Cr-1 Mo Steel," *Metall. Trans.* 6A, 1949–55 (1975).
6. R. L. Klueh, "Interaction Solid Solution Hardening in 2.25 Cr-1 Mo Steel," *Mater. Sci. Eng.* 35, 239–53 (1978).
7. J. D. Baird and A. Jamieson, "High-Temperature Tensile Properties of Some Synthesized Iron Alloys Containing Molybdenum and Chromium," *J. Iron Steel Inst. London* 210, 841–46 (1972).
8. J. D. Baird and A. Jamieson, "Creep Strength of Some Synthesized Iron Alloys Containing Manganese, Molybdenum, and Chromium," *J. Iron Steel Inst. London* 210, 847–56 (1972).
9. R. L. Klueh and R. E. Oakes, Jr., "Strain Rate Effects on the Elevated-Temperature Tensile Behavior of a Bainitic 2 1/4 Cr-1 Mo Steel," *J. Eng. Mater.* 99, 350–58 (1977).
10. R. L. Klueh, "Heat Treatment Effects on the Tensile Properties of Annealed 2.25 Cr-1 Mo Steel," *J. Nucl. Mater.* 68, 294–307 (1977).
11. D. S. Gelles, W. J. Mills, and L. A. James, "Microstructural Examination of Postirradiation Deformation in 2 1/4 Cr-1 Mo," pp. 165–73 in *ADIP Quart. Prog. Rep. March 31, 1981*, DOE/ER-0045/6, U.S. DOE, Office of Fusion Energy.
12. T. Kunitake, "Continuous Cooling Transformation Structures in a Low Carbon 2 1/4 Cr-1 Mo Steel," *Sumitomo Kinzoku* 12, 17–26 (1960).
13. K. J. Irvine, J. D. Murray, and F. B. Pickering, "Structural Aspects of Creep-Resisting Steel," pp. 246–75 in *Structural Processes in Metals*, Iron and Steel Institute, London, 1961.
14. J. Moteff, D. J. Michel, and V. K. Sikka, "The Influence of Irradiation Temperature on the Hardening Behavior of the Refractory BCC Metals and Alloys," pp. 198–215 in *Defects and Defect Clusters in B.C.C. Metals and Their Alloys*, National Bureau of Standards, Gaithersburg, Md., 1973.
15. G. D. Johnson et al., "The Microstructural Interpretation of the Fluence and Temperature Dependence of the Mechanical Properties of Irradiated AISI 316," pp. 393–412 in *Effects of Radiation on Materials: Tenth Conference*, ASTM STP 725, American Society for Testing and Materials, Philadelphia, 1981.
16. S. N. Rosenwasser et al., "The Application of Martensitic Stainless Steels in Long Lifetime Fusion First Wall/Blankets," *J. Nucl. Mater.* 85&86, 177–82 (1979).
17. R. L. Klueh, "Chromium-Molybdenum Steels for Fusion Reactor First Walls — A Review," *Nucl. Eng. Design* 72, 329–44 (1982).
18. T. Ishiguro et al., "A 2 1/4 Cr-1 Mo Pressure Vessel Steel With Improved Creep Rupture Strength," pp. 129–47 in *Application of 2 1/4 Cr-1 Mo Steel for Thick-Wall Pressure Vessels*, ASTM STP 755, American Society for Testing and Materials, Philadelphia, 1982.

7.4 SWELLING IN SIMPLE FERRITIC ALLOYS IRRADIATED TO HIGH FLUENCE - D. S. Gelles and R. L. Meinecke (Westinghouse Hanford Company)

7.4.1 ADIP Task

The Department of Energy (DOE)/Office of Fusion Energy (OFE) has cited the need to investigate ferritic alloys under the ADIP program task, Ferritic Steels Development (Path E). The task involved is akin to task number 1.C.2, Microstructures and Swelling in Austenitic Alloys.

7.4.2 Objective

The objective of this work is to provide guidance on the applicability of martensitic stainless steels for fusion reactor structural components.

7.4.3 Summary

A series of Fe-Cr-C-Mo simple alloys has been measured for density change as a function of irradiation in EBR-II over the temperature range 400 to 650°C to fluences as high as 2.13 x 10^{23} n/cm^2 (E > 0.1 MeV) or 105 dpa. The highest swelling was found in a Fe-12Cr binary alloy, 4.72 percent, after 1.87 x 10^{23} n/cm^2 or 95 dpa at 425°C, which corresponds to a swelling rate of 0.06%/dpa. This peak swelling rate value can be used to define swelling predictions for commercial ferritic alloys to 40 MWy/m^2.

7.4.4 Progress and Status

7.4.4.1 Introduction

Ferritic and martensitic alloys appear to be very attractive for fusion reactor structural applications due to their high swelling resistance.[1-3] A primary objective of the ADIP program is to develop materials capable of operating in a fusion reactor up to a time-integrated neutron exposure of 40 MWy/m^2 or approximately 500 dpa. This corresponds to a fast reactor fluence on the order of 10^{24} n/cm^2 (all fluences given as E > 0.1 MeV). Irradiation experiments to neutron exposures of this magnitude require excessively long times and so procedures must be found which will allow extrapolation of materials properties beyond the available exposure range. An example can be provided by swelling measurements on martensitic alloys. The highest exposure thus far achieved is 125 dpa.[1] This exposure required 9 years of irradiation in EBR-II and the experiment has now been stopped. To reach goal fluence, an additional 36 years of irradiation time would have been required. Therefore, demonstration that ferritic and martensitic alloys will remain swelling resistant to a goal exposure of 40 MWy/^{2} will not be possible for some time to come. Extrapolation of available data must be considered.

Swelling as a function of fluence is generally modelled by a bilinear equation. The necessary parameters are R, the steady state swelling rate, τ, the fluence corresponding to the intersection of the linear extrapolation of steady state swelling with the zero swelling axis and α, a measure of the curvature of the swelling curve in the vicinity of τ. Modeling swelling in ferritic or martensitic alloys is difficult because a value for steady state swelling has not been established.

The present effort is intended to establish a steady state swelling estimate for ferritic and martensitic alloys. A series of simple ferritic alloys based on the martensitic stainless steel base composition Fe-12Cr-1Mo-0.1C and including binary Fe-Cr alloys covering the range 3 to 18 Cr has been irradiated as part of the National Cladding/Duct (NCD) Materials Development Program for LMFBR development. These specimens are no longer of interest to the NCD program so they have been made available to the MFE program. This report describes density change measurements on several of these specimens as a function of irradiation in EBR-II to fluences as high as 2.0 x 10^{23} n/cm^2.

7.4.4.2 Experimental Procedures

Specimens of the "simple ferritic alloy series" were included as ballast in very limited numbers to fill unused space in each of four capsules which were irradiated side-by-side in EBR-II. Details of the alloy series prior to irradiation and following irradiation to 4.3 x 10^{22} n/cm^2 and 1.38 x 10^{23} n/cm^2 have been reported previously.[4,5] Each reactor discharge including the fluence obtained for the present study involved a separate set of specimens. In general, only one TEM dish for each condition of fluence and temperature was available and density measurements included at least three repeated determinations for each specimen. Following density measurements, the specimens irradiated to the highest fluence were reinserted into EBR-II in order to provide results to still higher fluences.

7.4.4.3 Results

It has already been noted[5] and must be reemphasized here, that there is now reason to believe that the Fe-3Cr binary alloy contained a significant amount of impurities. A chemistry overcheck on this material indicates a comparison of Fe-3.27Cr-0.50Ni-0.005P-0.03Mn-0.0005C-0.00013N-0.0147 O with no analysis for silicon. Also, precipitation following irradiation to ~4.3 x 10^{23} n/cm^2 was characteristic of G-phase. Fig. 7.4.1 is provided to further emphasize this point. It shows the preirradiation density found for the Fe-Cr binary alloys (and the value for pure iron[6]) as a function of chromium content.

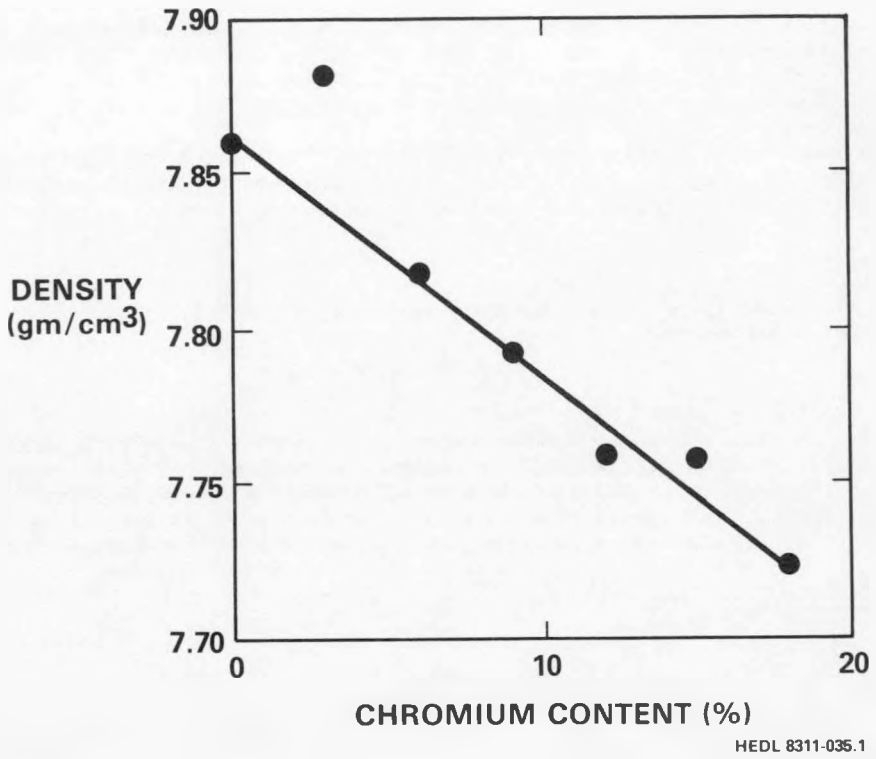

Fig. 7.4.1. Density for Fe-Cr binary alloys as a function of chromium content. The value for pure iron is from reference (6).

The Fe-3Cr specimen does not fit the trend, being 0.05 gm/cm^3 too dense. The results for this material should therefore be interpreted as an example of a more complicated alloy in the Fe-3Cr composition range.

Table 7.4.1 is provided to summarize all results of swelling and density change measurements on the simple ferritic alloy series. This includes preirradiation density values, estimates for void swelling at low fluence based on transmission electron microscopy (TEM),[4] results of density measurements at intermediate fluences[5] and the results of the present effort. Examination of the information in this table reveals that the simple ferritic alloys remain swelling resistant even at fluences on the order of 2.0 x 10^{23} n/cm^2. The highest swelling observed was 4.72% for Fe-12Cr at 425°C for a fluence of 1.9 x 10^{23} n/cm^2. Somewhat lower swelling was found for Fe-6Cr and 9Cr at 425°C for this fluence level. The peak swelling temperature is in the vicinity of 425°C, and is a slight function of chromium content; higher chromium contents result in slightly higher peak swelling temperature. Additions of carbon and molybdenum (and in the case of Fe-3Cr, various impurity additions) have the effect of reducing the peak swelling temperature to 400°C or below. Finally, examples can be found where swelling saturation may have occurred. See for example, Fe-3Cr at 400°C, Fe-6Cr at 400°C, and Fe-12Cr-0.1C-2Mo at 400°C.

Table 7.4.1. Results of swelling measurements of simple ferritic alloy specimens contained in the AA-VII test[4,5]

Alloy	I.D. Code	Cold Density	Temp.[c]: Flu.[c]:	400 3.4	400 10.3	400 16.3	425 4.3	425 18.7	450 2.8	450 10.7	450 11.5	482[b] 11.8	510 20.4	540 20.0	650 21.3
Fe-3Cr	65	7.8826		---	1.76	0.70	0.09[b]	1.65	0.0[b]	0.62	0.36	0.83			
Fe-6Cr	66	7.8185		0.28[b]	1.91	1.43	0.63[b]	3.51	0.10[b]		1.91	1.32		0.55	0.11
Fe-9Cr	67	7.7933			1.82	2.22	0.68[b]	4.14	0.24[b]	1.79	2.11	1.29		0.42	0.03
Fe-12Cr	6A	7.7596		0.25[b]	1.05	1.36	0.63[b]	4.72	0.29[b]	2.18	2.27	1.17		-0.21	-0.08
Fe-12Cr-0.1C	6B	7.7774			-0.46			1.60							
Fe-12Cr-0.1C[a]	6C	7.7952			-0.07										
Fe-12Cr-0.2C	6E	7.7680			0.28						-0.19				
Fe-12Cr-0.1C-0.5Mo	6F	7.7933			1.65			1.12	0.10[b]						
Fe-12Cr-1Mo	6H	7.7911			2.41			0.01	0.05[b]		-0.09				
Fe-12Cr-0.1C-1Mo	6J	7.7953			0.75	1.08		0.54							
Fe-12Cr-0.1C-2Mo	6K	7.8046			2.88	2.62		0.63	0.06[b]		0.16				
Fe-12Cr-0.1C-3Mo	6L	7.8231			1.40	1.59		0.94	0.07[b]		0.10				
Fe-15Cr	6N	7.7461			0.17	0.53		0.83	0.0[b]	0.66	0.06	0.18	0.14	0.80	0.01
Fe-18Cr	6R	7.7233								0.32	0.0[b]	-0.23		-0.01	

[a]Heat treatment was 1038°C/1 hour/air cooled whereas all other conditions received 1038°C/1 hour/air cool + 760°C/2 hours/air cool.
[b]TEM measurement whereas all other values are by density measurement.
[c]Temp. - Irradiation temperature (°C), Flu - Irradiation fluence (10^{22} n/cm^2).

These swelling measurements can be used to estimate a peak steady state swelling rate for ferritic alloys. Fig. 7.4.2 shows the results for swelling in Fe-6, 9 and 12Cr specimens at 400, 425 and 450°C. The 400°C points are connected by dashed lines, the 425°C points by solid lines and the 450°C points by short dashed lines. The peak swelling rate occurs for the 12Cr specimen for which a rate of 0.057%/dpa is found between 4.3 x 10^{22} n/cm^2 and 1.87 x 10^{23} n/cm^2. A rate of 0.06%/dpa appears to approximate the swelling rate observed at 400 and 450°C as can be perceived by comparison with the line for 0.06%/dpa inset in the figure. Therefore, a value of 0.06%/dpa is recommended as an estimate for the peak steady state swelling rate to be expected in ferritic alloys. This rate appears to apply over the temperature range 400 to 450°C and the temperature dependency of swelling in ferritic alloys is likely a consequence of differences in swelling incubation response. Effects of swelling saturation may also play a role at lower temperatures.

7.4.4.4 Discussion

Comparison with other materials

It is constructive to compare the present results with those of other materials of high technological impact, i.e., Path A. Such a comparison allows one to extend the present results so as to provide swelling predictions for commercial Path E alloys. Therefore, swelling values at 425°C for simple Fe-Cr-Ni ternary austenitic alloys,[7] commercial austenitic alloys,[1] Fe-12Cr and commercial ferritic alloys[1,2] are presented in Fig. 7.4.3. From Fig. 7.4.3 it can be shown that swelling in simple alloys is generally higher than in the commercial counterpart of the given alloy, that swelling in austenitic alloys is higher than in ferritic alloys and that a wide-range of commercial ferritic alloys show only a small variation in swelling response whereas a wide range of swelling response is found for a relatively narrow range of commercial austenitic alloys.

Swelling equation development

An approach to predict swelling in austenitic stainless steels has been proposed by Garner based on results for simple Fe-Ni-Cr ternary alloys.[7] The ternary alloy results can be interpreted to establish that the steady state swelling rate is 1%/dpa and that swelling differences among alloys and conditions arise from differences in the onset of swelling. Swelling incubation is increased with increases in nickel content or temperature and with decreases in chromium content. This behavior is expected to apply for commercial austenitic alloys in various heat treatment conditions, as well.[8] Fig. 7.4.3 has been prepared in this manner. Swelling for the commercial austenitic alloys has been drawn to predict a steady state swelling rate of 1%/dpa.

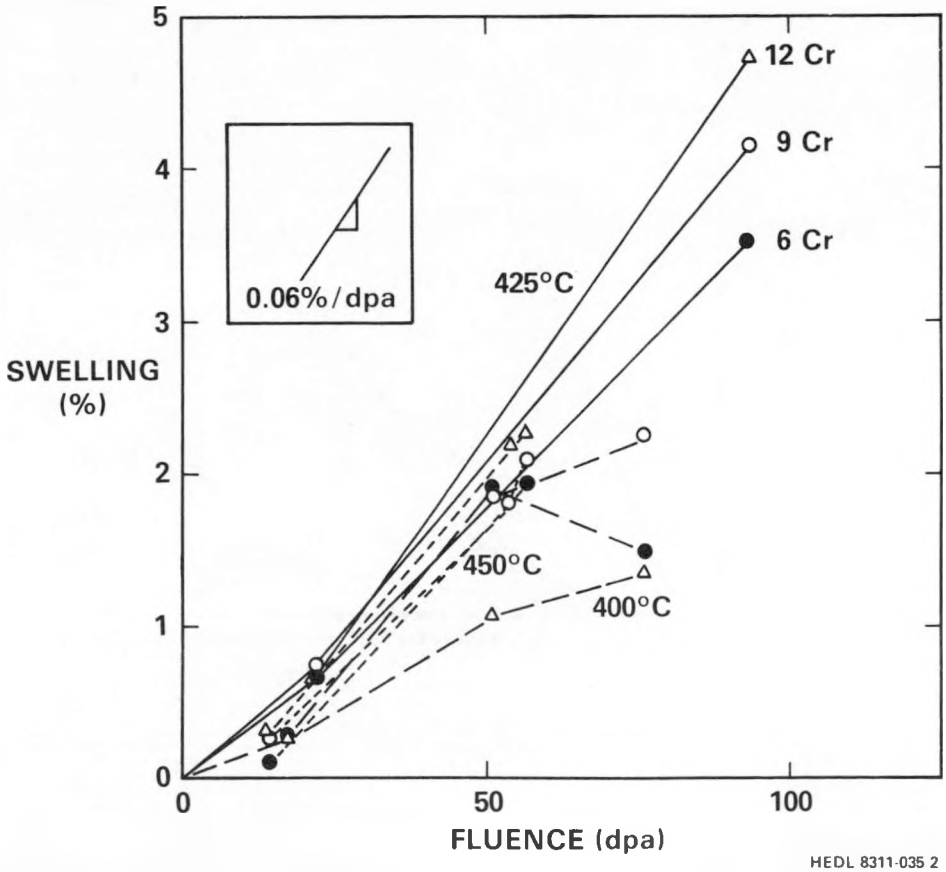

Fig. 7.4.2. Swelling in Fe-6Cr, 9Cr and 12Cr binary alloys at 400, 425 and 450°C demonstrating a peak swelling rate of 0.06%/dpa.

Swelling response in ferritic alloys may be analyzed in the same way. For example, the peak swelling rate could be set at 0.06%/dpa based on the present results. This swelling rate appears to be satisfactory over the temperature range 400 to 450°C. Swelling differences from alloy to alloy can be ascribed to differences in the onset of swelling. (An exception must be made for the 400°C results at fluences above 50 dpa and this will be discussed presently.) Such an approach has been used in an accompanying report on 2-1/4Cr-1Mo.[9] In order to predict swelling in commercial ferritic alloys such as EM12 and AISI 416, one must set a value for the incubation parameter and Fig. 7.4.3 indicates that a value of 100 dpa is probably conservative. A conservative estimate for swelling in commercial ferritic alloys at 500 dpa is then predicted to be 24 percent.

The appearance of void swelling in ferritic alloys does not necessarily mean that steady state swelling will immediately follow. Voids were found in both 2-1/4Cr-1Mo and EM12 after irradiation at 425°C to 1.6 x 10^{23} n/cm^2.[10] However, comparison of density change results for these materials at 425°C to 1.6 x 10^{23} [2] and to 2.1 x 10^{23} (Refs. 1-9) reveals only moderate increases in swelling, 0.06 percent for 2-1/4Cr-1Mo and 0.24 percent for EM12. A swelling rate of 0.06%/dpa yields a value of 1.5 percent for swelling. This means either that the transition to steady state swelling for commercial ferritic alloys is very gradual or that steady state swelling rates for simple ferritic alloys do not apply to commercial ferritic alloys. In either case, the prediction of 24 percent swelling in commercial ferritic alloys at 500 dpa is an overestimate.

Saturation

The results in Fig. 7.4.2 which are most difficult to explain are those for the 400°C irradiation temperature. The deviation from steady state swelling which is observed for the 400°C condition might be a consequence of specimen to specimen variations or experimental difficulties such as temperature control problems. However, the most likely explanation is that swelling saturation may have occurred. The condition required for saturation is that the void structure becomes the dominate sink for point defects.[11] Such a situation is most likely to occur when the void density is very high (as is the case at lower temperature) and when the material is unable to maintain a high dislocation density (as is the case for soft, pure materials). Therefore, it is concluded that the results for the 400°C irradiation condition do not discredit the approach recommended for swelling equation development for commercial ferritic alloys.

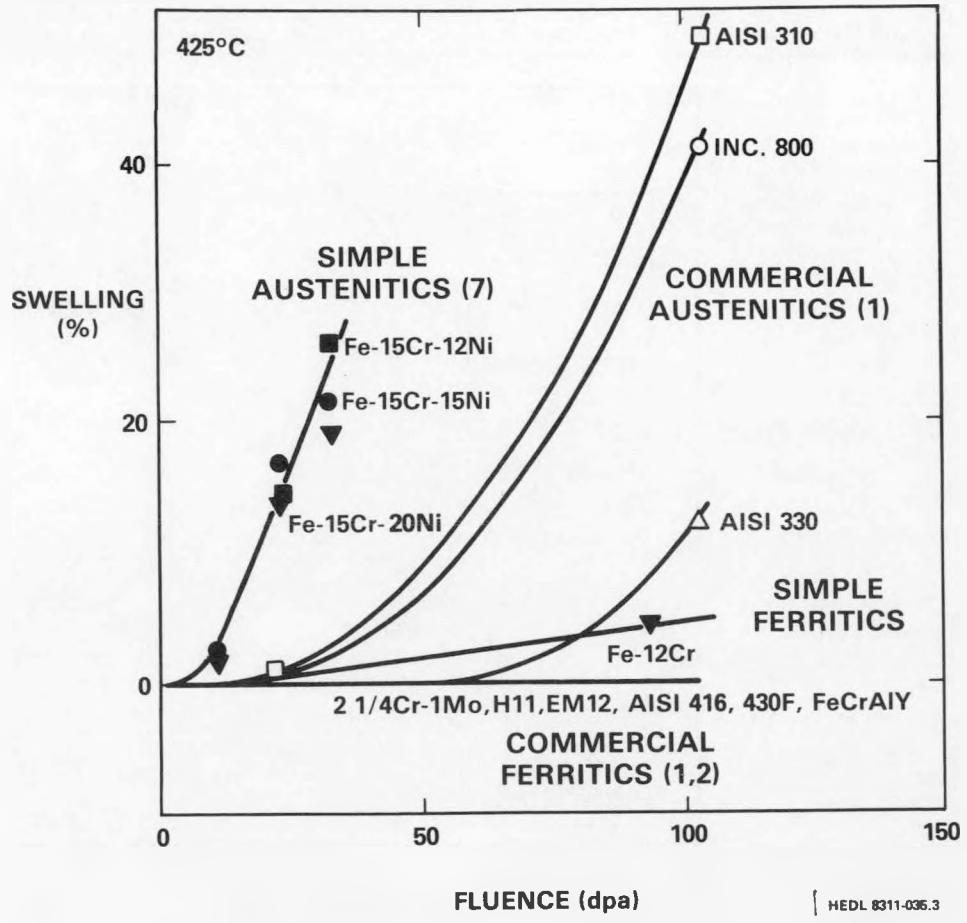

Fig. 7.4.3. Comparison of swelling at 425°C in austenitic[1,7] and ferritic alloys.[1,2]

7.4.5 Conclusions

Swelling is moderate in Fe-Cr-C-Mo simple alloys irradiated to fluences on the order of 100 dpa. The peak swelling observed was 4.72 percent in an Fe-12Cr specimen irradiated at 425°C to 95 dpa. This corresponds to a swelling rate of 0.06%/dpa.

It is shown that this peak swelling rate of 0.06%/dpa may be used as a basis for developing swelling design equations for commercial ferritic alloys. Such equations, which are considered conservative estimate, that swelling in commercial ferritic alloys will be less than 24 percent after neutron exposures of 40 MWy/m^2.

7.4.6 Future Work

An MHFES swelling equation for HT-9 will be developed in the next reporting period.

7.4.7 References

1. D. S. Gelles, "Swelling in Several Commercial Alloys Irradiated to Very High Neutron Fluence," this report.
2. R. W. Powell, D. T. Peterson, M. I. Zimmerscheid and J. F. Bates, "Swelling in Several Commercial Alloys Following High Fluence Neutron Irradiation," *J. Nucl. Mat.* 103 & 104 (1981) 969.
3. E. A. Little and D. A. Stow, "Void Swelling in Irons and Ferritic Steels, Part II," Ibid 87 (1979) 25.
4. D. S. Gelles, "Microstructural Examination of Neutron-Irradiated Simple Ferritic Alloys," Ibid, 108 & 109 (1982) 515.
5. D. S. Gelles and L. E. Thomas, "Effects of Neutron Irradiation on Microstructure in Experimental and Commercial Ferritic Alloys," HEDL-SA-2772, submitted to AIME for publication in the *Proceedings of the Topical Conference on Ferritic Alloys for Use in Nuclear Energy Technologies* held at Snowbird, UT on June 19-23, 1983.
6. *Handbook of Chemistry and Physics*.
7. F. A. Garner, "Dependence of Swelling on Nickel and Chromium in Fe-Ni-Cr Ternary Alloys," *Damage Analysis and Fundamental Studies Quarterly Progress Report* 4-6/1983, DOE/ER-0046/14, pg. 133.
8. F. A. Garner, "Recent Insights on the Swelling and Creep of Irradiated Austenitic Alloys," presented at the Third Topical Meeting on Fusion Reactor Materials in Albuquerque, NM on September 19-22, 1983. To be published in *J. Nucl. Mat.*
9. D. S. Gelles and R. J. Puigh, "Evaluation of Ferritic Alloy Fe-2-1/4Cr-1Mo After Neutron Irradiation - Irradiation Creep and Swelling," this document.
10. D. S. Gelles, "Microstructural Examination of Several Commercial Ferritic Alloys Irradiated to High Fluence," *J. Nuc. Mat.* 103 & 104 (1981) 975.
11. see for example L. K. Mansur, Void Swelling in Metals and Alloy Under Irradiation: An Assessment of the Theory," *Nucl. Tech.* 40 (1978) 5.

7.5 MICROSTRUCTURE OF 9 Cr-1 MoVNb AND 12 Cr-1 MoVW FERRITIC STEELS AFTER IRRADIATION AT ELEVATED TEMPERATURES IN HFIR — J. M. Vitek and R. L. Klueh (Oak Ridge National Laboratory)

7.5.1 ADIP Task

ADIP tasks are not defined for Path E, ferritic steels, in the 1978 program plan.

7.5.2 Objective

The objective of this work is to evaluate the microstructural response of two ferritic steels, 9 Cr-1 MoVNb and 12 Cr-1 MoVW, to irradiation at elevated temperatures. The steels were subjected to simultaneous displacement damage and limited helium production from a transmutation reaction of nickel during HFIR irradiation. Thus, the effect of helium as well as displacement damage on the microstructure can be ascertained.

7.5.3 Summary

Microstructures of 9 Cr-1 MoVNb and 12 Cr-1 MoVW were examined following irradiation in HFIR to 36 dpa at 300 to 600°C. Maximum cavity development in the form of voids occurred at 400°C with only small helium bubble formation at 500 and 600°C. Swelling was greater in 9 Cr-1 MoVNb than in 12 Cr-1 MoVW. The cavity development is attributed in part to the production of helium during irradiation.

7.5.4 Progress and Status

7.5.4.1 Introduction

Three ferritic steels, 2 1/4 Cr-1 Mo, 9 Cr-1 MoVNb, and 12 Cr-1 MoVW, were irradiated in HFIR in the form of TEM disks in experiments HFIR-CTR-30, -31, and -32 (ref. 1). These experiments were conducted at 300, 400, 500, and 600°C to nominal displacement damage levels (at the reactor horizontal midplane) of 40, 20, and 10 dpa, respectively. These experiments were designed to evaluate the microstructural response of these steels to neutron irradiation.

During HFIR irradiation, any nickel-bearing alloy undergoes transmutation reactions with the thermal portion of the neutron spectrum, producing helium. Thus, helium is generated simultaneously with the displacement damage produced by the fast portion of the spectrum. A series of nickel-doped ferritic steels[2] were included in the HFIR-CTR-30, -31, and -32 experiments in order to achieve higher helium concentrations than those produced in the standard alloys. This report presents results on the standard 9 Cr-1 MoVNb and 12 Cr-1 MoVW alloys irradiated in HFIR-CTR-30 to a nominal dose of 40 dpa.

7.5.4.2 Specimen Preparation and Experimental Conditions

The alloys investigated were from heats produced by Combustion Engineering, Chattanooga, Tennessee; chemical compositions are given in Table 7.5.1. The TEM disks were normalized and tempered as follows:

9 Cr-1 MoVNb: 1040°C/0.5 h/AC + 760°C/1 h/AC
12 Cr-1 MoVW: 1050°C/ 0.5 h/AC + 780°C/2.5 h/AC.

These heat treatments yielded a tempered lath martensite microstructure in both alloys. Most of the precipitates formed were chromium-rich $M_{23}C_6$, with some additional vanadium or vanadium-niobium precipitates also found. These structures have been evaluated in detail elsewhere.[2,3] The $M_{23}C_6$ carbides were preferentially located at lath boundaries and prior austenite grain boundaries. However, a larger percentage of carbides was located at prior austenite grain boundaries in the 9 Cr-1 MoVNb steel than in the 12 Cr-1 MoVW steel.

Table 7.5.1. Composition of 9 Cr-1 MoVNb (Heat XA 3590) and 12 Cr-1 MoVW (Heat XAA 3587)

Element	Content (wt. %)[a]	
	9 Cr-1 MoVNb	12 Cr-1 MoVW
Cr	8.62	11.99
Mo	0.98	0.93
Mn	0.36	0.50
Ni	0.11	0.43
V	0.21	0.27
W	0.01	0.54
Nb	0.063	0.018
C	0.090	0.21
N	0.050	0.02

[a]Balance iron.

Evaluation of temperature and flux monitors is currently under way to confirm the irradiation conditions. Based on the evaluation of flux monitors from similar experiments irradiated to a lower fluence,[4,5] the fluence achieved was 4.9×10^{26} neutrons/m^2 ($E > 0.1$ MeV), corresponding to a damage level of 36 dpa (nominally 40 dpa). The helium concentrations were 30 at. ppm in 9 Cr-1 MoVNb and 99 at. ppm in 12 Cr-1 MoVW.

The disks were electropolished remotely in a hot cell with a twin-jet polisher. A 7:1 methanol: sulfuric acid electrolyte was used at −12°C with a current of 140 mA and a voltage of approximately 20 V. The specimens were examined within 24 h of electropolishing. A JEM 100C transmission electron microscope equipped with a low magnetic field objective lens polepiece was used.

7.5.4.3 Irradiated Microstructures

Few cavities were found in either alloy irradiated at 300°C. The cavities were small, approximately 4 nm in diameter, and appeared to be homogeneously distributed through the structure. They were often difficult to distinguish from polishing artifacts. The swelling resulting from these cavities is negligible. Although extraction replicas were not examined, there was no apparent change in the precipitate structure in either alloy, according to examination of the precipitate morphology and distribution in the foil. In the case of 12 Cr-1 MoVW, where the initial microstructure was tempered to a greater degree and thus contained a lower density of dislocations in the martensite laths, the dislocation density increased during irradiation. This increase was not evaluated quantitatively.

Following irradiation at 400°C, the greatest degree of cavity formation and subsequent swelling was found. This was true for both alloys. Typical microstructures are shown in Figure 7.5.1. The cavities ranged in size from 4 nm to over 30 nm in diameter. Size distributions for both alloys are given in Figure 7.5.2. Since the cavity microstructure was most developed by the irradiation at 400°C, these microstructures were analyzed in detail. Volume-averaged cavity diameters, cavity concentrations, and cavity swelling values are given in Table 7.5.2. The cavity sizes were comparable in both alloys, but the higher cavity concentration in 9 Cr-1 MoVNb led to a nearly three-fold greater value of the swelling. In both alloys, the cavities were uniformly distributed throughout the structure, with no preferential formation of cavities at lath boundaries, precipitate interfaces, or prior austenite grain boundaries. As was the case for the 300°C irradiation, no apparent change in the nature of the precipitation was noticed. The dislocation density increased somewhat during irradiation of the 12 Cr-1 MoVW alloy.

Table 7.5.2. Cavity parameters for 9 Cr-1 MoVNb and 12 Cr-1 MoVW following irradiation at 400°C to 9.9×10^{26} neutrons/m^2

	9 Cr-1 MoVNb	12 Cr-1 MoVW
Volume-averaged diameter, nm	15	16
Cavity concentration, m^{-3}	11×10^{20}	3×10^{20}
Cavity swelling, %	0.19	0.07

The cavity microstructures in both alloys irradiated at 500 and 600°C were similar. No large cavities were found. Instead, smaller cavities were observed, and these were preferentially located at lath boundaries and dislocations. This is illustrated for the 600°C irradiation in Figure 7.5.3. The density of cavities was significantly higher in the 12 Cr-1 MoVW alloy. Cavity sizes ranged from 2.5 to 9 nm in diameter and a size distribution for 12 Cr-1 MoVW is given in Figure 7.5.4. The lath networks contained relatively low dislocation densities. Once again, no change in the precipitate density, distribution or morphology was found for 12 Cr-1 MoVW. However, some additional unidentified precipitation was observed in 9 Cr-1 MoVNb irradiated at 500°C, as shown in Figure 7.5.5.

7.5.5 Discussion

Ferritic steels, as a class of alloys, are known to be resistant to cavity swelling. Studies on several different alloys irradiated to fluences up to 17.6×10^{26} neutrons/m^2 have shown only minimal swelling values.[6] A few investigations have been carried out on alloys comparable to those examined in the present study.[7-10] All these irradiations were in fast spectrum reactors, thus helium contents produced by these irradiations were lower than in the present work. Work on 9 Cr-1 MoVNb irradiated to a fluence of 2.5×10^{26} neutrons/m^2 revealed only a small number of voids, up to 20 nm in diameter, after irradiation at 400°C (ref. 7). No voids at all were found in several 12-Cr steels, including 12 Cr-1 MoVW, irradiated to doses of up to ~23 dpa at temperatures of 380 to 615°C (refs. 7–10). Thus, the present study indicates significantly more cavities formed during HFIR irradiations. Although the fluence levels were not exactly the same, it is felt that the greater degree of cavity formation is due to a large extent to the greater amount of helium produced during HFIR irradiation. This conclusion is supported by recent ion irradiation work in which cavity formation in 12 Cr-1 MoVW was found only after ion irradiation with simultaneous helium injection.[11] No cavities were observed when only nickel ions were used for irradiation.

Some comments can be made on the nature of the cavities observed after HFIR irradiation. For both 9 Cr-1 MoVNb and 12 Cr-1 MoVW irradiated at 500 and 600°C, small cavities were found to be preferentially distributed along lath boundaries and dislocations. The fact that only small cavities were found at these temperatures, and that they were located at structural defects, suggests that they are helium bubbles. This is supported by the observation that the cavity (bubble) density is significantly greater in 12 Cr-1 MoVW, where the higher nickel content led to more than three times as much helium produced during irradiation. Furthermore, the observation of cavities after 500 and 600°C irradiation is unique. All previous neutron irradiation studies,[6–10] in which very little helium was present, revealed cavities to a maximum temperature of only 425°C. The large cavities found at 400°C, homogeneously distributed throughout the matrix, are

E-42654

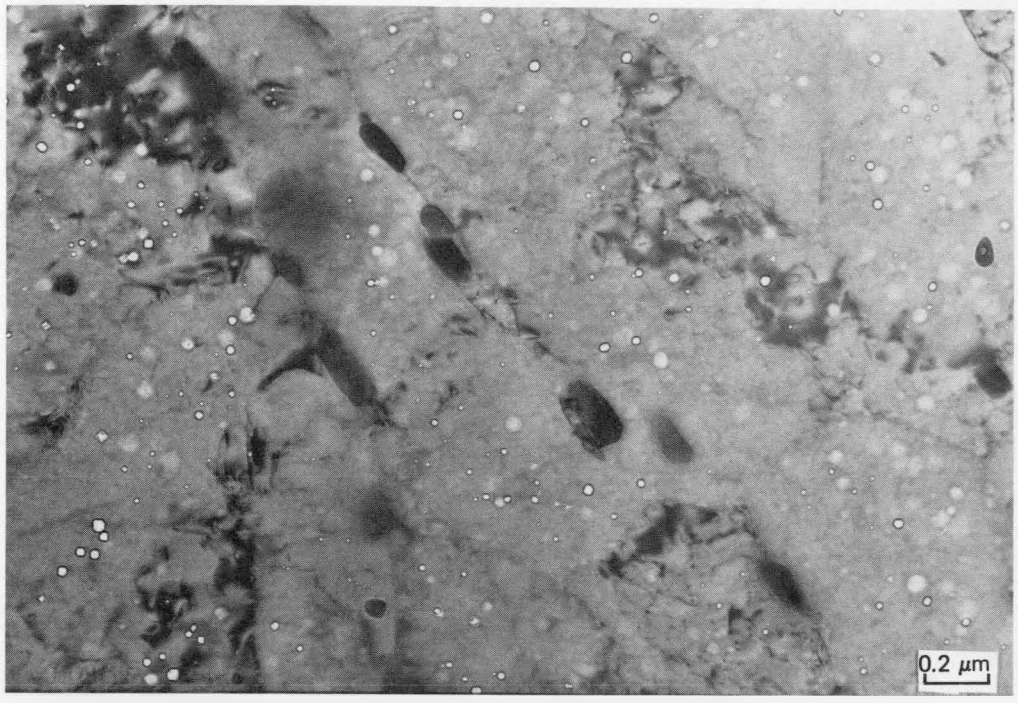

(*a*)

E-39552

(*b*)

Fig. 7.5.1. Microstructures following HFIR irradiation at 400°C to 4.9 × 10^{26} neutrons/m^2 in (*a*) 9 Cr-1 MoVNb and (*b*) 12 Cr-1 MoVW.

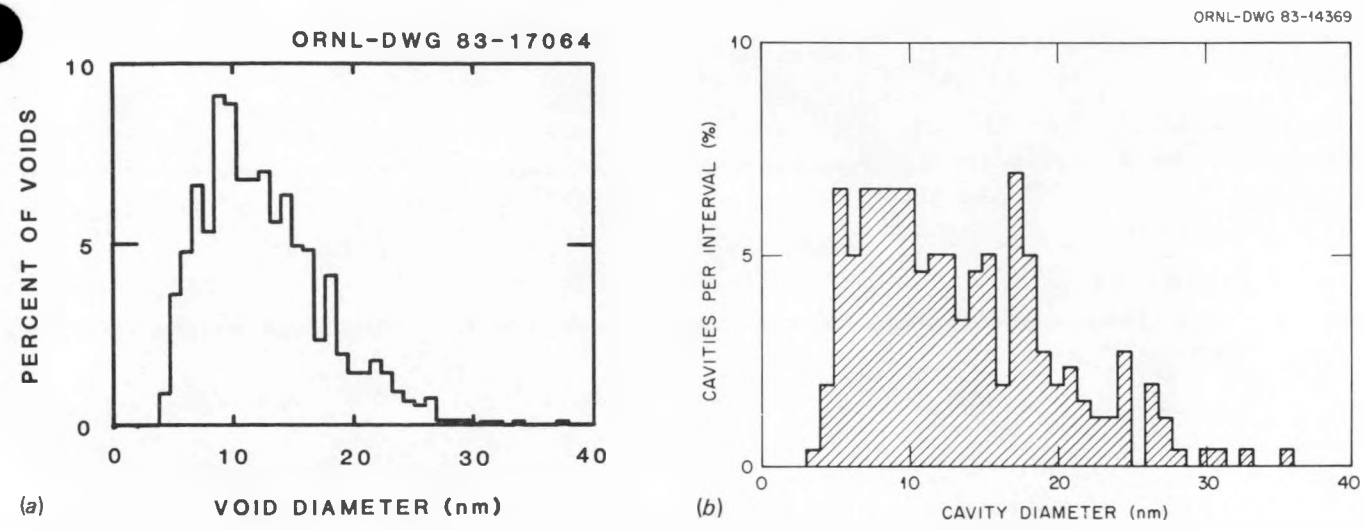

Fig. 7.5.2. Cavity size distributions following HFIR irradiation at 400°C to 4.9 × 10^{26} neutrons/m^2 in (*a*) 9 Cr-1 MoVNb and (*b*) 12 Cr-1 MoVW.

assumed to be voidlike in character. Since cavities were not observed previously in 12-Cr steels following irradiation, it is also concluded that the helium present in HFIR results in helium-assisted void growth. This same mechanism is assumed to operate in the 9 Cr-1 MoVNb alloy irradiated in HFIR.

In comparison with 12 Cr-1 MoVW, the amount of swelling at 400°C is noticeably greater in 9 Cr-1 MoVNb (0.19% vs 0.07%). The fact that 9 Cr-1 MoVNb swells more readily than 12 Cr-1 MoVW agrees with earlier observations by Gelles and Thomas.[7] However, in the present case, this increased swelling occurs in spite of the higher helium concentration in the HFIR-irradiated 12 Cr-1 MoVW. Thus, although helium is assumed to play a role in the cavity development in 9 Cr-1 MoVNb, other effects such as microstructural differences must be instrumental in producing the greater swelling in 9 Cr-1 MoVNb. It was suggested by Gelles and Thomas[7] that G-phase formation in 12 Cr-1 MoVW inhibits void swelling. However, G phase was not found in the HFIR-irradiated 12 Cr-1 MoVW, and another explanation is needed. Although the preirradiated microstructures of the two steels are quite similar, differences do exist. More than twice as much carbide precipitates in 12 Cr-1 MoVW during tempering, and the distribution of $M_{23}C_6$ carbide is more uniform through the matrix. In 9 Cr-1 MoVNb, the large $M_{23}C_6$ carbides are more concentrated on prior-austenite grain boundaries. In addition, the tempering treatments prior to irradiation differed somewhat, resulting in the irradiation of a slightly overtempered microstructure for the 12 Cr-1 MoVW alloy. Finally, minor compositional differences may play a role, such as the higher nickel and carbon levels or lower niobium concentration in 12 Cr-1 MoVW. The question of which of these factors are important needs to be addressed in future work.

Extensive evaluation of the precipitation response to irradiation of 9 Cr-1 MoVNb and 12 Cr-1 MoVW steels cannot be made at present. Such an evaluation requires TEM examination of extraction replicas; such work is planned. However, some observations can be made. Qualitatively, no change due to irradiation was observed in the morphology, distribution, or amount of precipitate in 12 Cr-1 MoVW. A quantitative evaluation of the amount of precipitation would require electrolytic extractions of irradiated specimens. On the other hand, the 9 Cr-1 MoVNb alloy showed some sign of precipitate instability. After irradiation at 500°C, the elongated rod or platelike precipitates shown in Figure 7.5.5 were found. These were not observed prior to irradiation. Although they have not been identified, similar precipitates have been found in furnace-cooled, unirradiated 9 Cr-1 MoVNb (ref. 3) and also after irradiation in EBR-II at 400°C (ref. 7). These precipitates were identified as Cr_2N and Cr_2C, respectively. The significantly greater nitrogen concentration in 9 Cr-1 MoVNb may be a contributing factor to the precipitate development.

The present results, in conjunction with the ion irradiation work of Ayrault,[11] indicate that helium plays a significant role in promoting cavity formation in 12 Cr-1 MoVW. Because of the similar structures, it is also likely that helium enhances cavity formation in 9 Cr-1 MoVNb. However, the observation of swelling at 36 dpa at 400°C does not allow for a determination of the steady state swelling rate. Projections of swelling at higher fluence levels, 100 or 200 dpa, is not yet possible. Furthermore, the steels in the present investigation were subjected to helium production rates significantly below those expected in fusion reactors (1–3 at. ppm He/dpa vs 10–15 at. ppm/dpa in a reactor). Thus, another factor that must be considered in trying to relate these results to fusion reactor conditions is the effect of higher helium concentrations on swelling.

E-44512

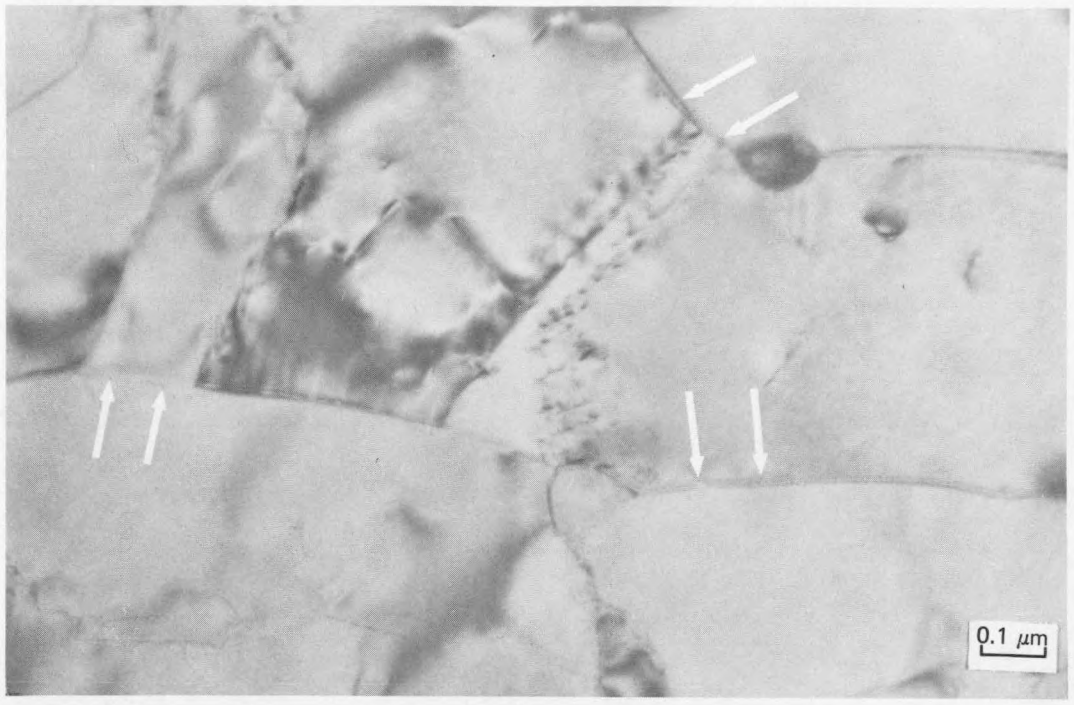

(a)

E-41561

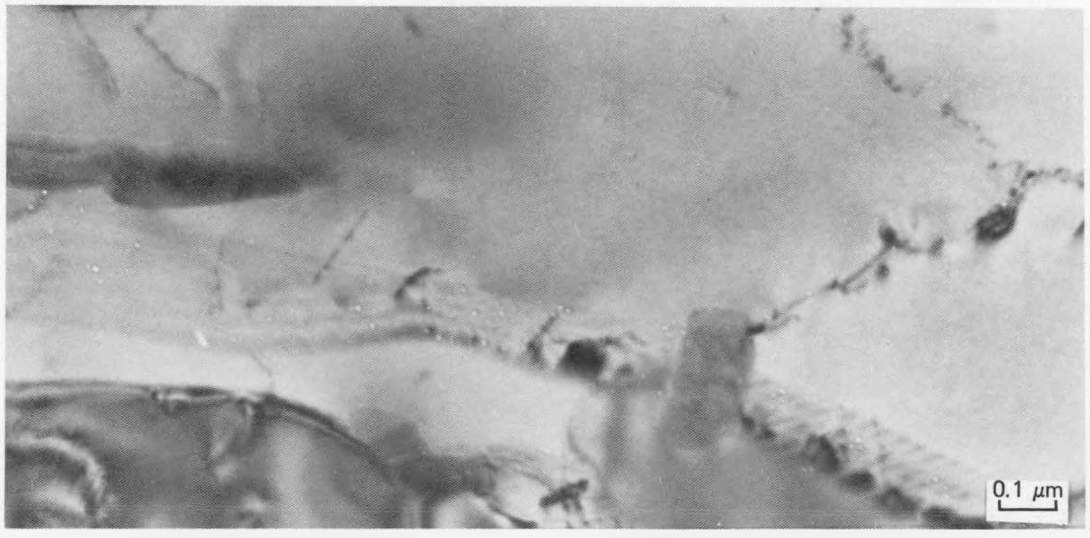

(b)

Fig. 7.5.3. Microstructures following HFIR irradiation at 600°C to 4.9×10^{26} neutrons/m^2 in (*a*) 9 Cr-1 MoVNb and (*b*) 12 Cr-1 MoVW. Arrows indicate helium bubbles.

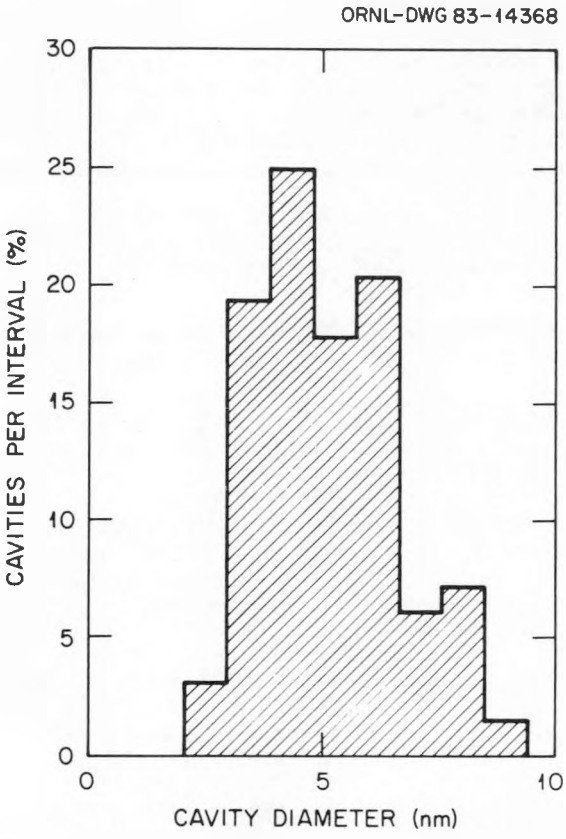

Fig. 7.5.4. Cavity size distribution in 12 Cr-1 MoVW irradiated to 4.9×10^{26} neutrons/m^2 in HFIR at 600°C.

Fig. 7.5.5. Elongated precipitates found in 9 Cr-1 MoVNb after HFIR irradiation at 500°C.

A comparison of the present results with comparably irradiated austenitic PCA is inevitable, and some important points should be noted. Austenitic stainless steel PCA irradiated in the same HFIR experiment to the same dose exhibits a maximum swelling at 600°C of ~0.2 to 0.5% (ref. 12). These values are somewhat greater than the 0.07 to 0.19% found for ferritic steels, but the helium concentration produced during irradiation of the austenitic stainless steel is considerably greater. A comparison of the two classes of steels at similar helium levels is not possible. The temperatures of maximum swelling for the austenitic and ferritic steels are quite different. Austenitics show maximum swelling at 600°C, whereas maximum swelling in ferritics is found for irradiation at 400°C.

Both the LRO alloys and austenitic stainless steels show elevated temperature embrittlement following HFIR irradiation. Significant He embrittlement is observed in austenitic stainless steels at levels of He as low as 30 at. ppm. The ferritic steels do not show the same sensitivity to helium embrittlement in tensile tests.[13] However, the fact that the helium bubbles accumulate at lath boundaries and other structural defects may signal potential embrittlement at significantly greater levels of helium.

7.5.6 References

1. M. L. Grossbeck, J. W. Woods, and G. A. Potter, "Experiments HFIR-CTR-30, -31, and -32 for Irradiation of Transmission Electron Microscopy Disk Specimens," pp. 36– 44 in *ADIP Quart. Prog. Rep. Sept. 30, 1980*, DOE/ER-0045/4, U.S. DOE, Office of Fusion Energy.

2. R. L. Klueh and J. M. Vitek, "Characterization of Ferritic Steels for HFIR Irradiation," pp. 294–308 in *ADIP Quart. Prog. Rep. June 30, 1980*, DOE/ER-0045/3, U.S. DOE, Office of Fusion Energy.

3. J. M. Vitek and R. L. Klueh, "Precipitation Reactions During the Heat Treatment of Ferritic Steels," *Metall. Trans.* **14A**, 1047–55 (1983).

4. L. R. Greenwood and A. K. Smither, "Neutron Dosimetry Measurements for the HFIR-CTR-32 Irradiation," pp. 32–40 in *DAFS Quart. Prog. Rep. May 1982*, DOE/ER-0046/9, U.S. DOE, Office of Fusion Energy.

5. L. R. Greenwood, Argonne National Laboratory, personal communication to J. M. Vitek, ORNL, 1983.

6. D. S. Gelles, "Microstructural Examination of Several Commercial Ferritic Alloys Irradiated to High Fluence," *J. Nucl. Mater.* 103&104, 975–80 (1981).

7. D. S. Gelles and L. E. Thomas, "Microstructural Examination of HT-9 and 9 Cr-1 Mo Contained in the AD-2 Experiment," pp. 343–61 in *ADIP Semiannu. Prog. Rep. March 31, 1982*, DOE/ER-0045/8, U.S. DOE, Office of Fusion Energy.

8. E. A. Little and L. P. Stoter, "Microstructural Stability of Fast Reactor Irradiated 10–12 Cr Ferritic-Martensitic Stainless Steels," pp. 207–33 in *Effects of Radiation on Materials: Eleventh Conference*, ed. H. R. Brager and J. S. Perrin, American Society for Testing and Materials, ASTM-STP-782, Philadelphia, 1982.

9. E. A. Little and D. A. Stow, "Void Swelling in Irons and Ferritic Steels II. An Experimental Survey of Materials Irradiated in a Fast Reactor," *J. Nucl. Mater.* 87, 25–39 (1979).

10. D. S. Gelles and L. E. Thomas, "Microstructural Examination of HT-9 Irradiated in the HFIR/CTR-32 Experiment," pp. 162–77 in *ADIP Semiann. Prog. Rep. Sept. 30, 1982*, DOE/ER-0045/9, U.S. DOE, Office of Fusion Energy.

11. G. Ayrault, "Cavity Formation in Single- and Dual-Ion Irradiated HT-9 and HT-9 + 2Ni Ferritic Alloys," pp. 182–190 in *DAFS Quart. Prog. Rep. Feb. 1982*, DOE/ER-0046/8, U.S. DOE, Office of Fusion Energy.

12. P. J. Maziasz, Oak Ridge National Laboratory, personal communication to J. M. Vitek, ORNL, 1983.

13. R. L. Klueh and J. M. Vitek, "The Resistance of 9 Cr-1 MoVNb and 12 Cr-1 MoVW Steels to Helium Embrittlement," *J. Nucl. Mater.* 117: 295–302 (1983).

7.6 EFFECTS OF HFIR IRRADIATION AT 55°C ON THE MICROSTRUCTURE AND TOUGHNESS OF HT-9 AND 9Cr-1Mo - D. S. Gelles, W. L. Hu, F. H. Huang and G. D. Johnson (Westinghouse Hanford Company)

7.6.1 ADIP Task

The Department of Energy/Office of Fusion Energy (DOE/OFE) has cited the need to investigate ferritic alloys under the ADIP program task Ferritic Steels Development (Path E). The task involved is akin to Task Number 1.B.13, Tensile Properties of Austenitic Alloys, Task Number 1.C.2, Microstructure and Swelling in Austenitic Alloys and Task Number 1.C.1, Microstructural Stability.

7.6.2 Objective

The objective of this work is to determine the effect of low temperature irradiation in HFIR on the properties of Path E alloys in order to determine the applicability of these alloys as first wall materials.

7.6.3 Summary

Results are reported for base metal and weld metal specimens of HT-9 and Modified 9Cr-1Mo following irradiation in HFIR at 55°C to 5 dpa. The DBTT shifts in irradiated base metal specimens were 30°C for HT-9 and 90°C for 9Cr-1Mo with further shifts of 20°C for weld metal. Concurrently, strength as measured by hardness increased 15 percent for HT-9 and 25 percent for 9Cr-1Mo. The hardness increases can be attributed in part to defect clusters 1.5 to 3.0 nm in diameter at densities approaching 10^{17} cm^{-3} and also to lower rates of cavity nucleation ahead of the propagating crack.

7.6.4 Progress and Status

7.6.4.1 Introduction

Postirradiation fracture toughness is one of the properties which may limit Path E alloys for fusion reactor first wall applications. Large shifts in ductile brittle transition temperature (DBTT) occur in Charpy specimens of Path E alloys following fast neutron irradiation to moderate fluence. Shifts of 120°C in HT-9[1,2] and 50°C in Modified 9Cr-1Mo[1] have been measured after irradiation to ~10 dpa at 400°C. In comparison, irradiation at higher temperature has less effect. (Miniature compact tension specimens have not yet shown this effect).[3] However, information on behavior at lower irradiation temperatures is limited because most experimental results have been obtained from the Experimental Breeder Reactor (EBR)-II which has a low temperature limit of ~370°C.

The purpose of the present effort is to investigate the effects of irradiation at ~55°C to 10 dpa on HT-9 and Modified 9Cr-1Mo. Specimens were irradiated in the High Flux Isotope Reactor (HFIR). As HFIR causes nickel to transmute rapidly and to produce helium in the process, effects due to the production of helium could also be investigated. Tests on miniature compact tension specimens have been completed and are reported in a companion report.[4] Charpy specimen tests are almost complete but a few specimens remain to be tested. Fracture surfaces of specimens from both series of tests have been examined and microstructural examinations based on transmission electron microscopy of Charpy specimens and TEM disks have been performed. However, it is not yet possible to provide a straightforward explanation for the mechanical property results and therefore this report is intended as a progress report.

7.6.4.2 Experimental Procedures

Details of the construction of the HFIR-MFE-RBI experiment have been previously documented.[5-7] The experiment was removed from the reactor in July 1982 after an estimated peak fluence of 10 dpa at 55°C.[8] Compact tension specimens, Charpy specimens, fatigue crack growth specimens and TEM disks were received from ORNL in January 1983. Many of the Charpy specimens were found to be rusted presumably because the encapsulating aluminium tubes leaked during the test thereby exposing the specimens to the water coolant.

Tests on miniature compact tension specimens are described in a companion paper in this document.[4] The Charpy impact specimen test maxtrix is given in Table 7.6.1. Table 7.6.1 includes fluence estimates calculated from reference 9, identification of rusted specimens, identification of specimens selected for fractographic examination by SEM and a number identifying the tube in which each specimen was irradiated. It may be noted that tube #2 does not appear to have leaked. Also, fluence estimates are approximately a factor of two lower than expected. Specimens selected for microstructural examinations are listed in Table 7.6.2. These specimens were irradiated in the same TEM disk tube (holder #1). Miniature compact tension specimens selected for fractographic examination were of HT-9 in a standard condition (1038°C/10 min/Ac + 760°C/30 min/AC). Two specimens[4] were examined following irradiation to ~5 dpa at 55°C. The first, specimen BA09, was tested at 25°C and gave a J_{IC} of 63.5 kJ/m^2 and the second, specimen BA07, was tested at 205°C and gave a J_{IC} of 56.7 kJ/m^2.

7.6.4.3 Results

Charpy Impact Tests -- The results of Charpy impact tests are included in Table 7.6.1. From Table 7.6.1, it can be shown that upper shelf energies are on the order of 50 to 60 J/cm^2 and that all conditions are behaving in a similar manner. Figure 7.6.1 provides a plot of fracture energy per unit area as a function of test temperature for all conditions. From Figure 7.6.1, it is apparent that weld metal

Table 7.6.1. Charpy specimen conditions irradiated in the HFIR-MFE-RBI experiment with test results

Material	Specimen	Fluence* (dpa)	Test Temp. (°C)	P_{max} (knt)	E_{total} (J)	E_{total} (J/cm^2)	Tube No.	Comments	
HT-9	AA01	4.8	27	2.3393	1.9855	17.150	#2		SEM
Base Metal	02	4.8	50	2.3374	5.0323	45.438	#1	Rusted	SEM
(HT.91353)	05	4.7	80	2.3805	6.7950	59.679	#1	Rusted	SEM
	14	4.8	110	2.5996	5.4760	46.992	#3	Rusted	
	18	4.8	NT				#2		
	19	4.8	NT				#3	Rusted	
9Cr-1Mo	FA03	4.6	34	1.2155	0.5080	4.4616	#2		
Base Metal	17	4.6	50	1.7193	2.1231	16.875	#1	Rusted	SEM
(HT.30176)	05	4.6	70	1.6369	1.8579	17.466	#1	Rusted	
	09	4.7	100	2.0752	5.3470	46.646	#1	Rusted	
	11	4.6	120	1.7437	5.1124	45.051	#3	Rusted	
	27	4.6	85	2.6558	7.5245	58.946	#3	Rusted	SEM
HT-9	AK00	4.7	34	1.6032	1.2509	10.433	#3	Rusted	
Weld Metal	03	4.7	65	2.7120	4.4277	38.246	#3	Rusted	SEM
	08	4.7	80	2.6165	7.0064	56.810	#2		
	09	4.7	NT				#2		
9Cr-1Mo	FJ04	4.4	65	2.2850	1.5425	12.851	#2		
Weld Metal	05	4.4	85	1.9104	2.0404	17.321	#2		SEM
	06	4.4	140	2.2943	7.2924	60.183	#3	Rusted	
	07	4.4	105	2.4524	5.7514	47.992	#3	Rusted	SEM

*Calculated from Reference 9.
NT = not tested.

Table 7.6.2. Specimens selected for microstructural examination

Material	Specimen ID	Condition
HT-9 HT 91353	HIJ4	40%CW+1038°C/5 min/AC + 760°C/30 min/AC
9Cr-1Mo HT 30176	JBJ4	40%CW+1038°C/5 min/AC + 760°C/60 min/AC
HT-9 HT 91353	HTJ4	Weld fusion zone + 760°C/2 hr/AC
HT-9	AA01	Charpy specimen
9Cr-1Mo	FA17	Charpy specimen

specimens are behaving like the base metal but with a DBTT 20°C higher and that Modified 9Cr-1Mo has a higher DBTT than HT-9 by about 30°C. In the preirradiation condition, it has been shown that HT-9 has a DBTT of 5°C with an upper shelf of 47 J/cm^2 and Modified 9Cr-1Mo has a DBTT of -25°C and an upper shelf energy of 80 J/cm^2.[1] Therefore, irradiation of HT-9 in HFIR at 55°C to 5 dpa has little effect on Charpy impact test response. The DBTT is increased to 35°C (as defined by the temperature at which the fracture energy is one half the peak value) and therefore the shift in DBTT is 30°C. The upper shelf energy is unchanged. However, Modified 9Cr-1Mo response is altered considerably by HFIR irradiation at 55°C. The DBTT is shifted to 65°C and therefore irradiation has increased the DBTT by 90°C and has lowered the upper shelf energy by 25 percent. These results indicate that HT-9 and Modified 9Cr-1Mo are behaving quite differently following HFIR irradiation at 55°C. Furthermore, it is unlikely that this is due to helium production because HT-9 contains 0.5% nickel and 9Cr-1Mo contains 0.1% nickel.

Compact Tension Tests -- The results of J_{IC} measurements on precracked miniature compact tension specimens of HT-9 and Modified 9Cr-1Mo specimens which were irradiated in HFIR at 55°C to 5 dpa[4] are plotted in Figure 7.6.2. Figure 7.6.2 shows that the toughness of HT-9 remains in the range of 60 kJ/m^2

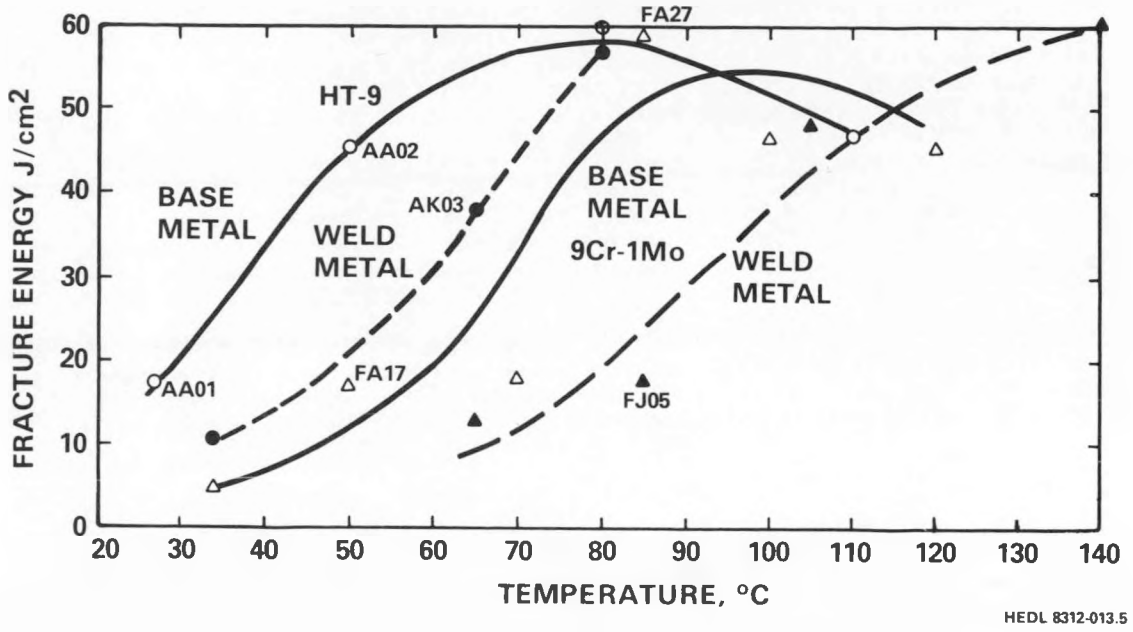

Fig. 7.6.1. Results of charpy impact tests on HT-9 and 9Cr-1Mo precracked miniature specimens irradiated at 55°C to 10 dpa in HFIR.

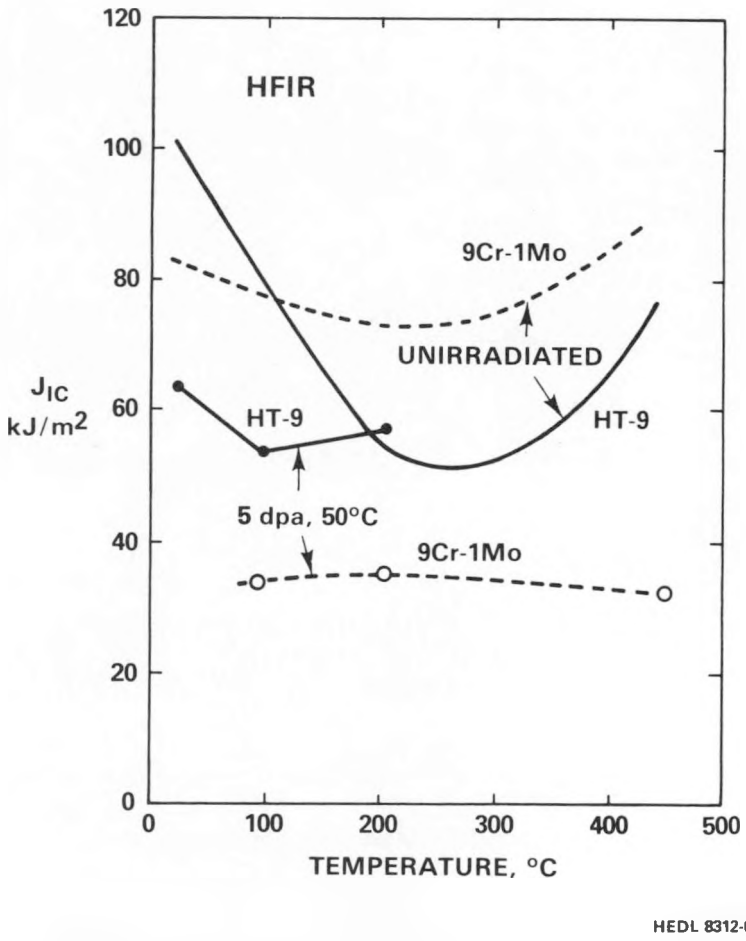

Fig. 7.6.2. Effect of irradiation at 55°C to 10 dpa in HFIR on the fracture toughness of HT-9 and 9Cr-1Mo base metal.

for test temperatures from 25°C to 205°C. This represents a significant reduction in toughness for test temperatures near 25°C but is very similar to values for unirradiated specimen tested at 200°C. However, the toughness of Modified 9Cr-1Mo is reduced by more than 50 percent following HFIR irradiation at 55°C. This behavior is observed for all test temperatures between 100 and 450°C. Concern is therefore raised with regard to fracture toughness degradation as measured with compact tension samples in Modified 9Cr-1Mo following irradiation in HFIR at 55°C.

Hardness -- In order to determine if the cause of the DBTT response of HFIR-irradiated specimens was a result of strength changes, Rockwell C hardness measurements were made on Charpy specimens of HT-9 base metal (AA01 and AA02) and Modified 9Cr-1Mo base metal (FA17). The results were R_C = 29.5 + 0.5 for AA01, R_C = 24.7 + 0.4 for FA17. These results are shown in Figure 7.6.3 in comparison with results for specimens irradiated in EBR-II.[11] From Figure 7.6.2, it can be shown that the hardness values for HT-9 and Modified 9Cr-1Mo increase due to irradiation to 5 dpa in HFIR at 55°C, but the increase in hardness is comparable to but no higher than that observed at 390°C. The increases in DBTT observed in these conditions do not directly correlate with increases in hardness because at 390°C, the shift for HT-9 was 124°C and for modified 9Cr-1Mo it was 55°C.[1] When the hardness values are converted to tensile strength results as shown on the right hand scale[12] it is found that for HT-9 irradiation in HFIR at 55°C has resulted in a 15 percent increase in tensile strength whereas for Modified 9Cr-1Mo the increase is 25 percent.

Microstructure

Microstructural examinations were undertaken in order to account for hardness increases and to determine if a temperature excursion could have occurred. Specimens HIJ4, HBJ4, HTJ4 and FA17 have been examined but a suitable foil of AA01 has not yet been prepared. Examinations revealed small defects in all specimen conditions. Under imaging conditions approaching weak beam, the defect images varied in size from 1.5 to 3.0 nm. Examples of weak beam images for specimen HIJ4 and HBJ4 are shown in Figure 7.6.4. The defects (generally defined as black spot damage) appear as white spots on a dark background and several dislocations can also be seen. The defect density was at 6.7 x 10^{16} cm^{-3} for specimen HBJ4. This was based on a measurement of 35 nm for the foil thickness in Figure 4b. Defect densities of this magnitude

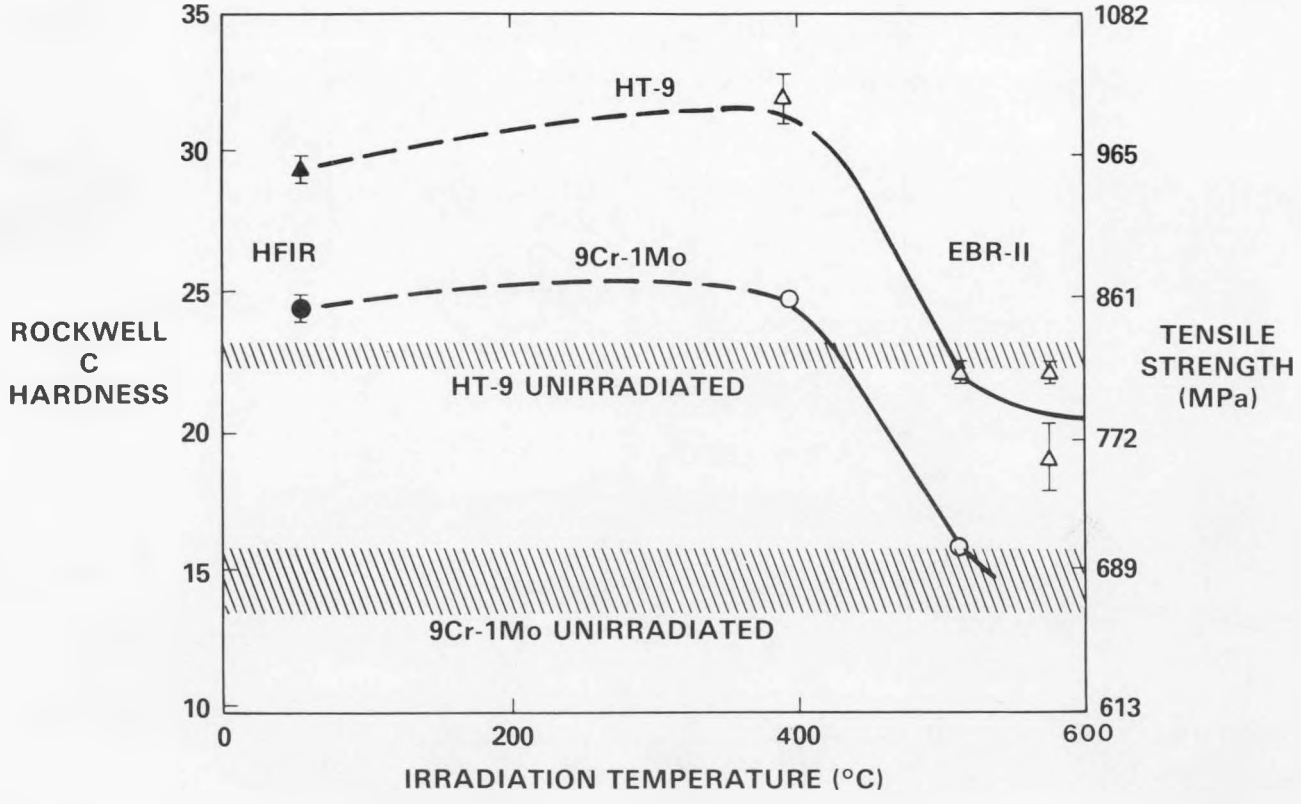

Fig. 7.6.3. Results of Rockwell hardness measurements on irradiated miniature charpy specimens estimates for tensile strength are based on results for carbon and alloy steels.[12]

[redacted]n account for the observed 15 to 25 percent increases in yield strength. Analysis of two and a half D [redacted]ges showed only one defect type but no attempt was made to determine if the defects were of vacancy or interstitial type.

Apart from the small defects, no other effects of HFIR irradiation at 55°C could be identified. Distributions of $M_{23}C_6$ carbides were normal and martensite lath structure were retained. Examples of the HT-9 weld metal at low magnification and Modified 9Cr-1Mo base metal at moderate magnification are provided in Figure 7.6.5. Specimen FA17 gave similar results. Therefore, no evidence for a large temperature excursion has been found.

Fractography

Fractographic examinations showed that irradiation in HFIR at 55°C to 5 dpa did alter fracture behavior in several detectable ways. The fracture modes did not appear to be affected. For example, Charpy specimens which gave fracture energies below 20 J/cm^2 failed by transgranular cleavage whereas Charpy specimens which gave fracture energies of 40 to 60 J/cm^2 and miniature compact tension specimens in both conditions examined gave dimple rupture fracture surfaces. Examples are provided in Figures 7.6.6 through 7.6.13. Figures 7.6.6 and 7.6.7 show examples of fracture behavior in irradiated Charpy specimens of HT-9 basemetal. Each fracture surface is shown as stereo pairs in (a) at low magnification with the fatigue crack at the left and in (b) at higher magnification immediately adjacent to the fatigue crack. Typical brittle cleavage facets can be seen on specimen AA01 tested at 25°C in Figure 7.6.6 whereas specimen AA02 which was tested at 50°C contains only ductile failure features as evidenced by large and small dimples as

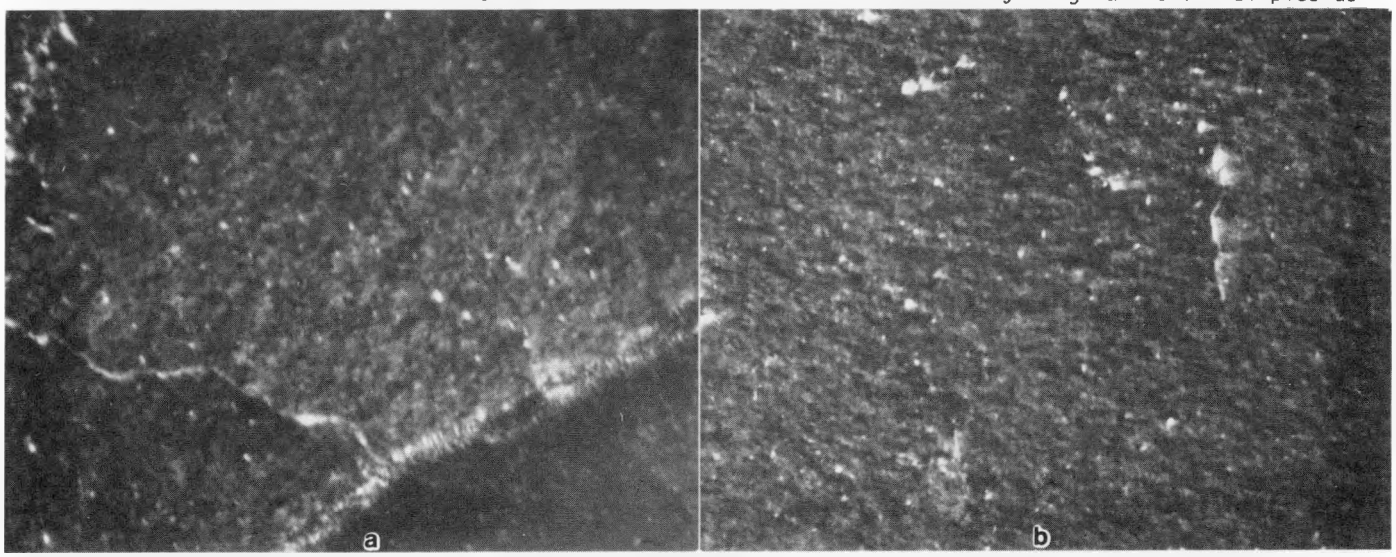

Fig. 7.6.4. Weak beam dark field images of specimens of (a) HT-9 and (b) modified 9Cr-1Mo specimens irradiated to 5 dpa at 55°C in HFIR.

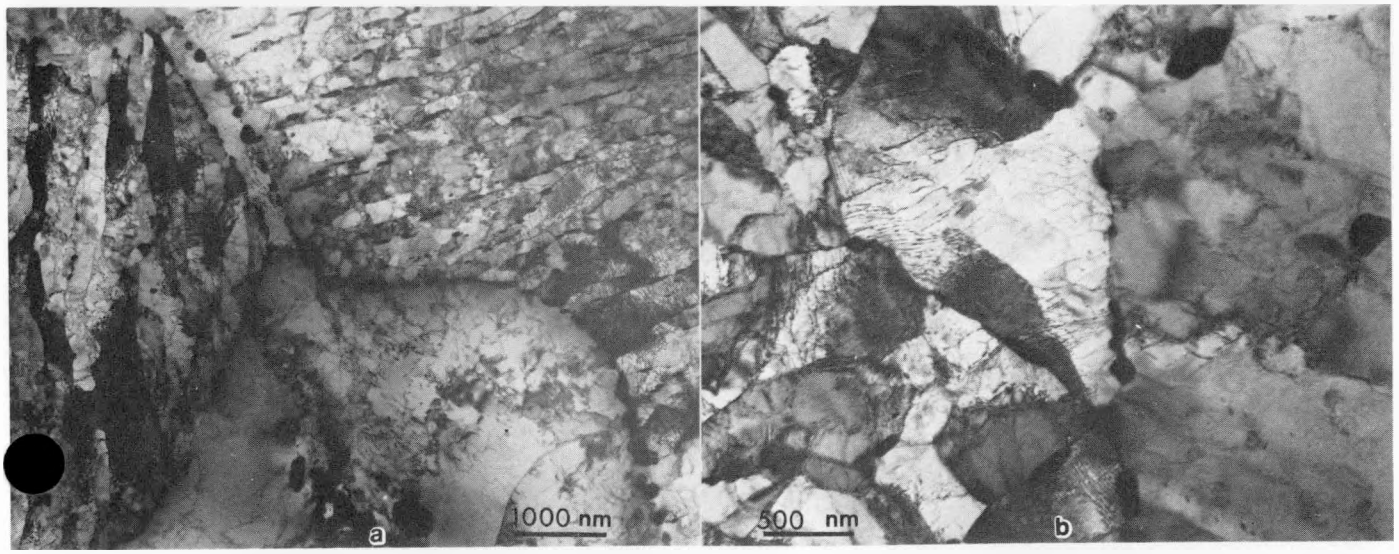

Fig. 7.6.5. Low magnification micrographs of HT-9 weld metal and 9Cr-1Mo base metal specimens irradiated to 5 dpa at 55°C in HFIR.

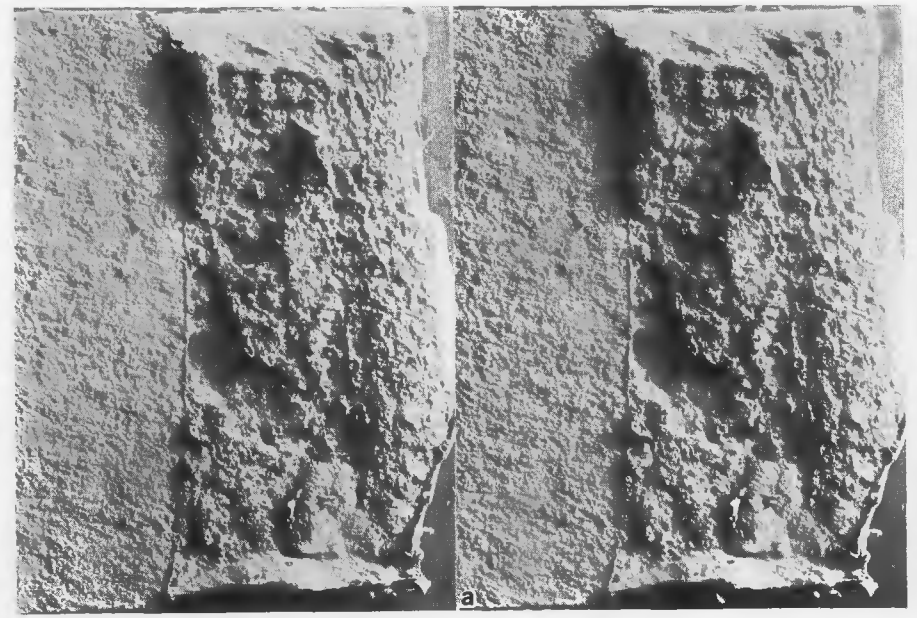

Fig. 7.6.6. Stereo pair fractographs of charpy specimen AA01, HT-9 base metal, irradiated to 5 dpa at 55°C in HFIR and tested at 27°C (a) a[redacted] and (b) intermediate magnification.

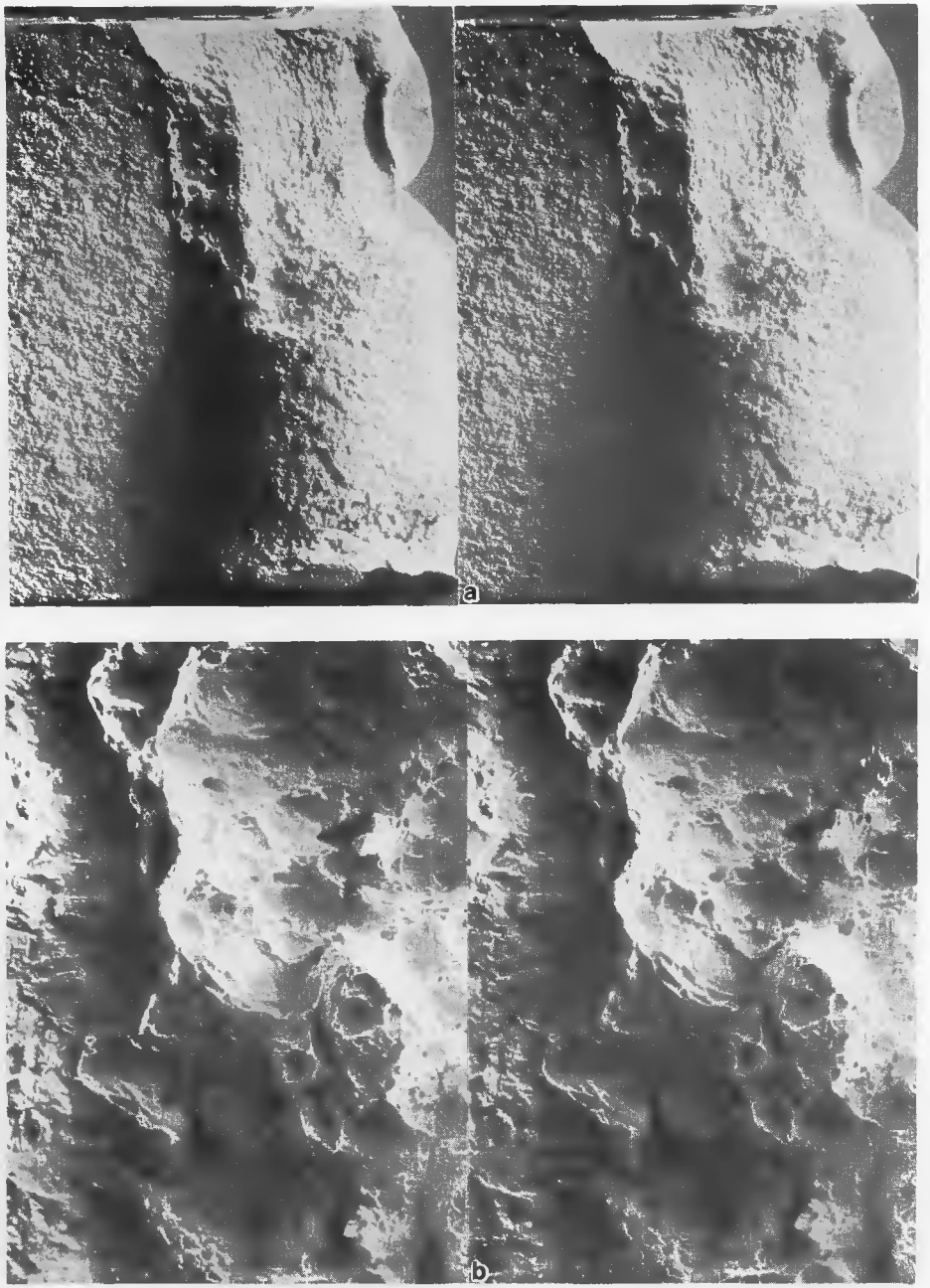

Fig. 7.6.7. Stereo pair fractographs of charpy specimen AA02, HT-9 base metal, irradiated to 5 dpa at 55°C in HFIR and tested at 50°C at (a) low and (b) intermediate magnification.

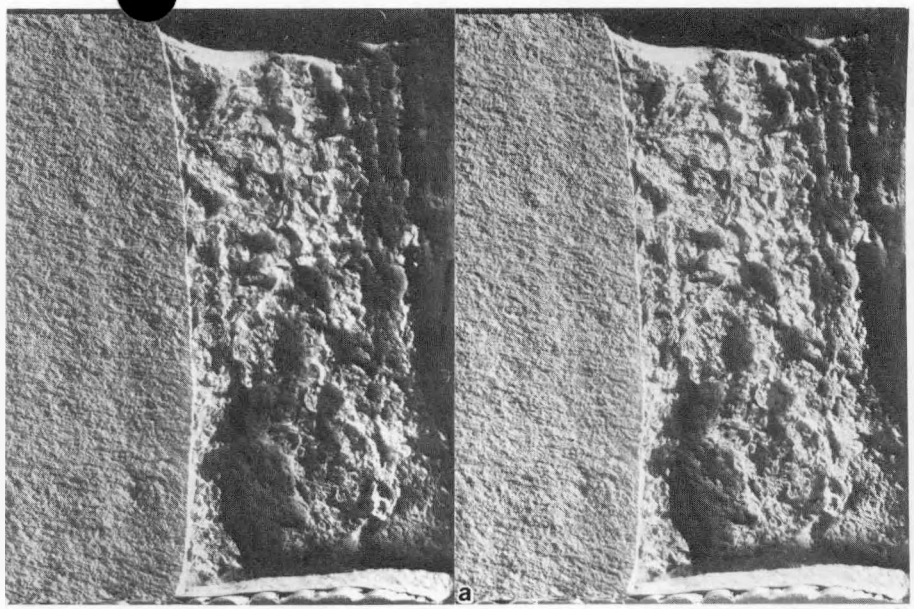

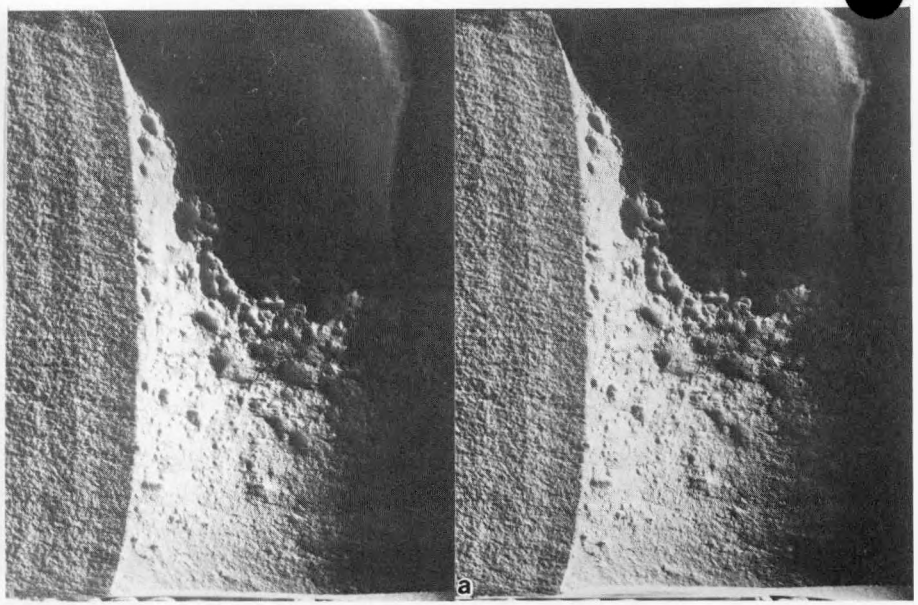

1 mm

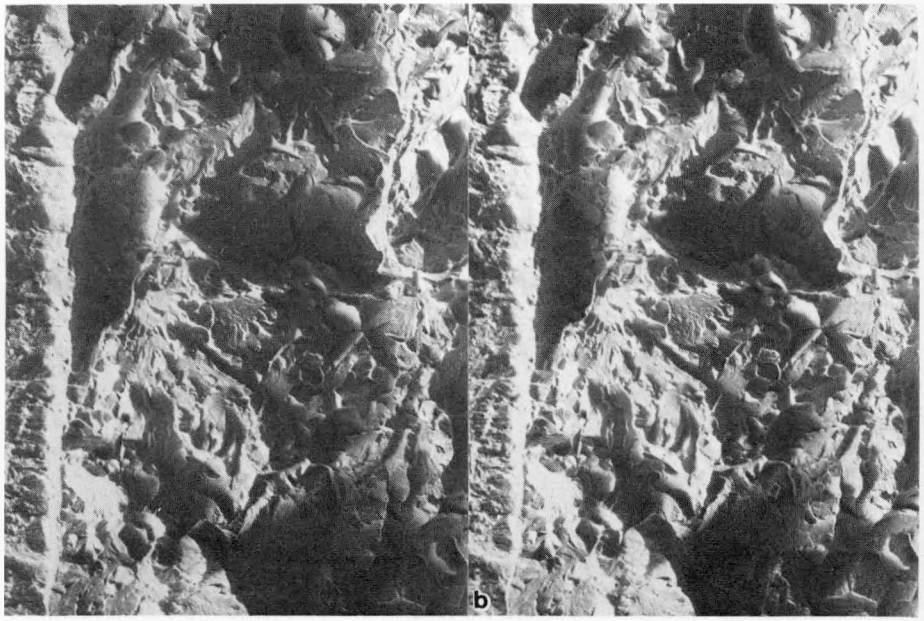

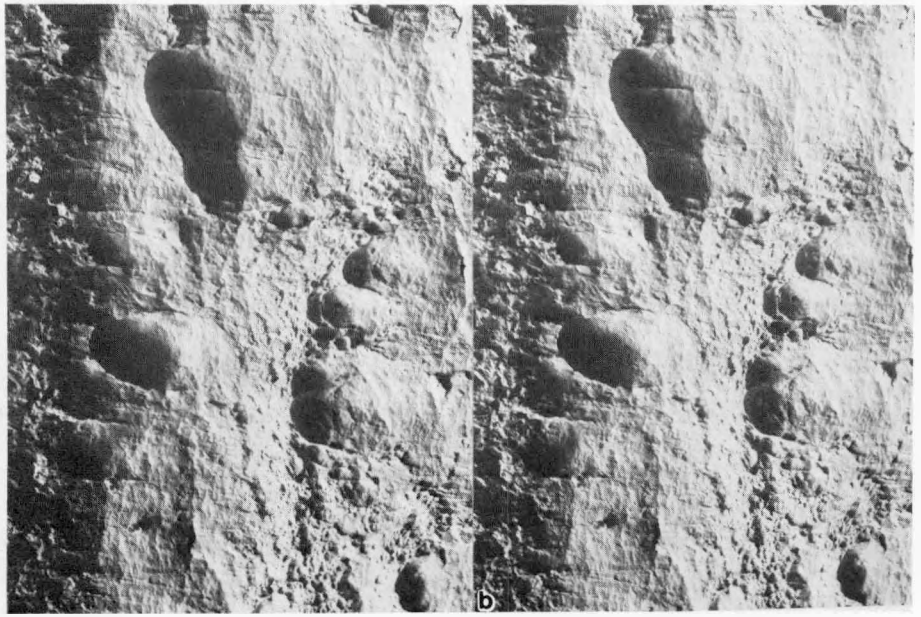

0.1 mm

Fig. 7.6.8. Stereo pair fractographs of charpy specimen FA17, 9Cr-1Mo base metal, irradiated to 5 dpa at 55°C in HFIR and tested at 50°C (a) at low and (b) intermediate magnification.

Fig. 7.6.9. Stereo pair fractographs of charpy specimen FA27, 9Cr-1Mo base metal, irradiated to 5 dpa at 55°C in HFIR and tested at 85°C (a) at low and (b) intermediate magnification.

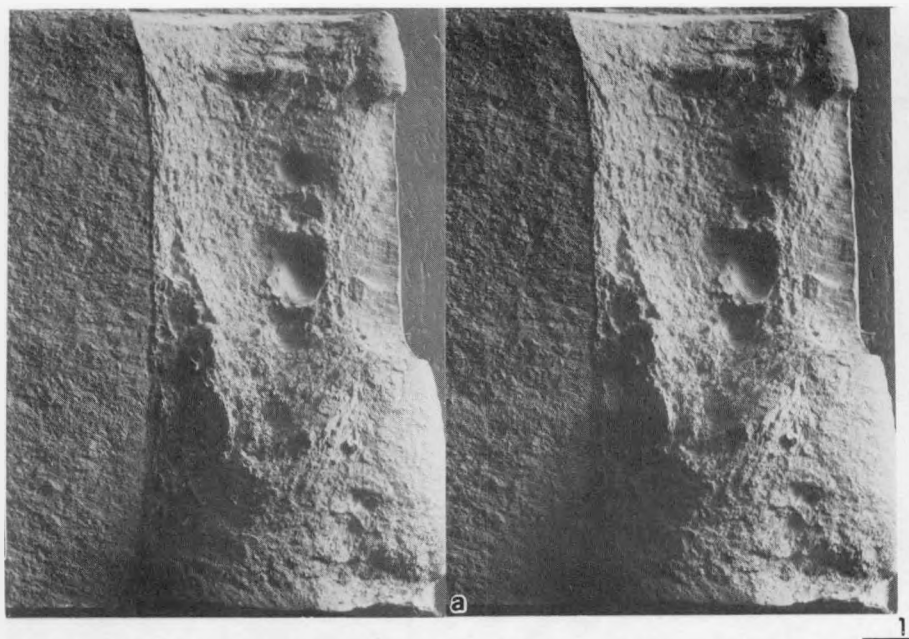

Fig. 7.6.10. Stereo pair fractographs of charpy specimen AK03, HT-9 weld metal, irradiated to 5 dpa at 55°C in HFIR and tested at 65°C (a) at low and (b) intermediate magnification.

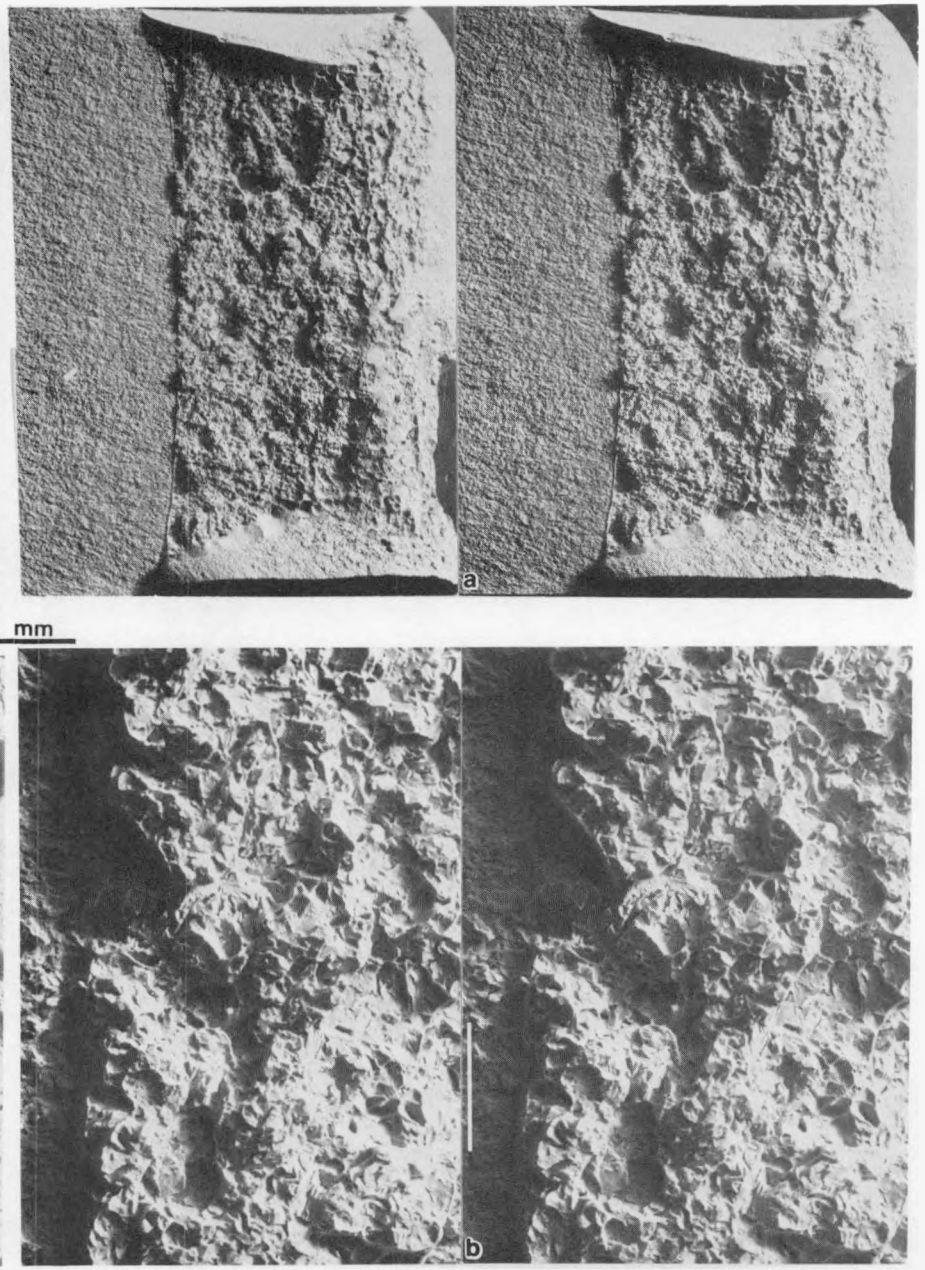

Fig. 7.6.11. Stereo pair fractographs of charpy specimen FJ05, 9Cr-1Mo weld metal, irradiated to 5 dpa at 55°C in HFIR and tested at 85°C (a) at low and (b) intermediate magnification.

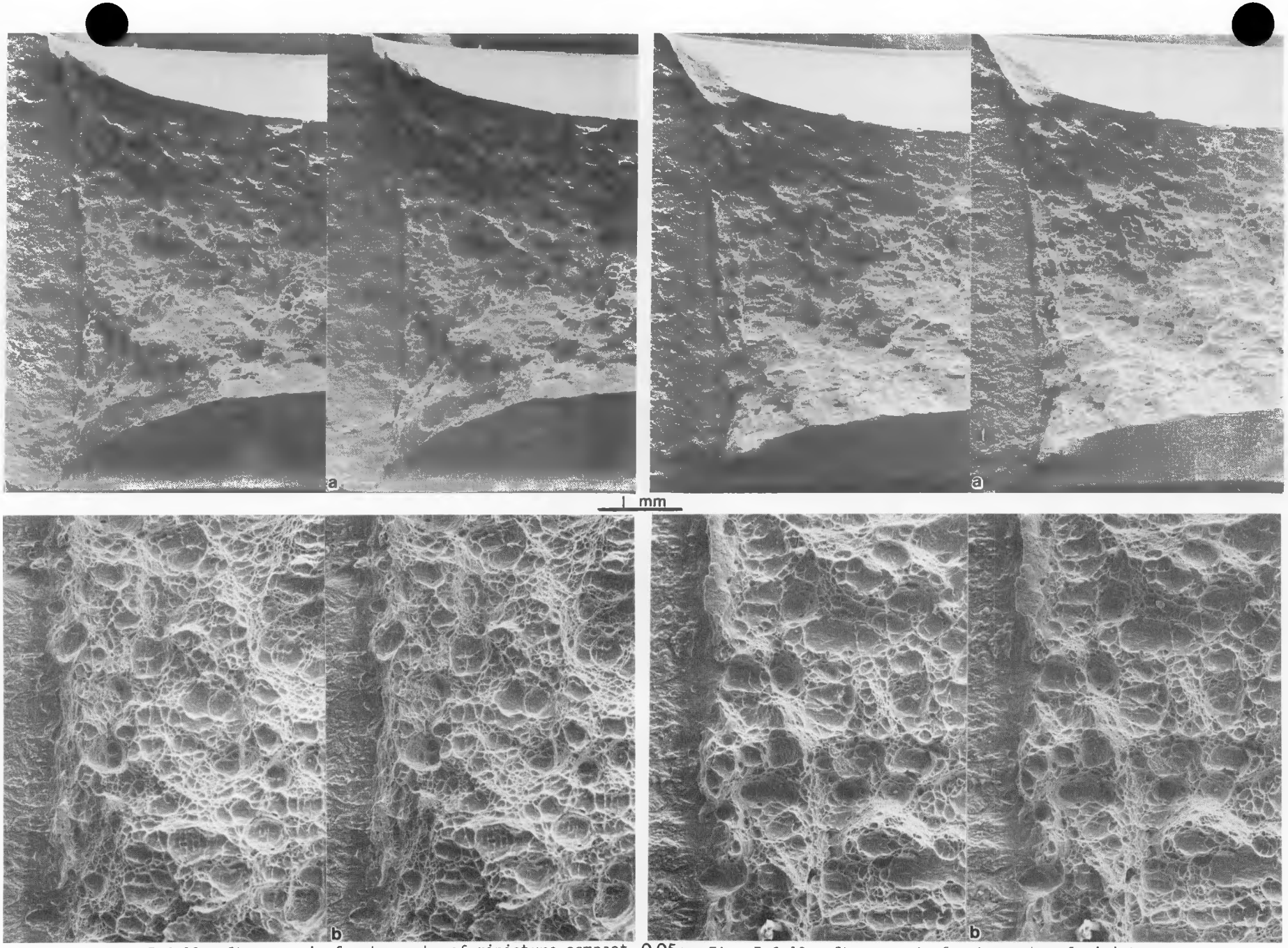

Fig. 7.6.12. Stereo pair fractographs of miniature compact tension specimen BA09, HT-9 basemetal, irradiated to 5 dpa at 55°C in HFIR and tested at 25°C (a) at low and (b) at intermediate magnification.

Fig. 7.6.13. Stereo pair fractographs of miniature compact tension specimen BA07, HT-9 base metal, irradiated to 5 dpa at 55°C in HFIR and tested at 205°C (a) at low and (b) at intermediate magnification.

shown in Figure 7.6.7. However, two observations are of particular note. First, the scale of the fracture surface contours appears to be quite rough both for cleavage facets and dimples. Examples can be found where cleavage facets or dimples are separated from adjacent features by large differences in height. Secondly, no example of delta ferrite stringers can be identified in either set of fractographs. In order to demonstrate that these results are unusual, the reader should refer to reference 11, Figures 7.2.4 and 7.2.5 showing unirradiated HT-9 tested at 0°C and 73°C. (Note that reproduction of the present report has reduced magnifications so that Figures 7.6.4 and 7.6.5 are approximately 25 percent smaller.
Similar behavior is found for Modified 9Cr-1Mo basemetal as shown in Figures 7.6.8 and 7.6.9. Cleavage facets control fracture behavior in specimen FA17 which was tested at 50°C as shown in Figure 7.6.8 and dimple rupture with large amounts of tearing between dimples controls fracture behavior in specimen FA27 which was tested at 85°C as shown in Figure 7.6.9. Again large differences in fracture surface contour can be found for the brittle failure condition. A clue to the controlling behavior is identified in Figure 7.6.9; cavity nucleation is reduced. With reduced cavity nucleation, the fracture surface tends to be more contorted unless only a few cavities control fracture (as in the case of specimen FA27 in Figure 7.6.9.

The weld metal specimens provide similar results. Figure 7.6.10 shows specimen AK03, irradiated HT-9 weld metal which was tested at 65°C and gave upper shelf behavior. Several dimples are seen but they are often very large with surface structure that generally arises from shear or tearing. No evidence of delta ferrite stringers is found. Figure 7.6.11 shows specimen FJ05, irradiated Modified 9Cr-1Mo weld metal which was tested at 85°C and failed by cleavage fracture. The surface is quite contorted and is similar to that in Figure 7.6.8. Therefore, cavity nucleation appears to be quite limited in weld metal specimens as well.

Miniature compact tension fracture surfaces provided similar results. Specimens of irradiated HT-9 base metal which were tested at 25°C and 205°C are shown in Figures 7.6.12 and 7.6.13. In both cases, failure is by dimple rupture but the dimple size is large, the surface is contorted and effects due to delta ferrite stringers cannot be identified. Comparison can best be made with unirradiated specimens tested at 25°C shown in reference 13.

The fracture surfaces shown in Figures 7.6.12 and 7.6.13 are very atypical for HT-9. It is apparent that irradiation in HFIR at 55°C to 5 dpa has caused large changes in fracture behavior.

7.6.4.4 Discussion

Consequences of HFIR Irradiation at 55°C -- Irradiation at 55°C in HFIR has produced changes in mechanical properties. DBTT shifts of 30°C for HT-9 base metal and 90°C for Modified 9Cr-1Mo and reductions in J_{IC} of over 50 percent for Modified 9Cr-1Mo have been measured. This is in part due to increases in hardness corresponding to yield strength increases of 15 percent for HT-9 and 25 percent for Modified 9Cr-1Mo. The hardness increases are believed to be due to damage by black spot defects on the order of 1.5 to 3.0 nm in diameter. However, fractographic examination reveals unrelated significant changes in fracture behavior. Fracture surfaces tend to be rougher on a fine scale and evidence could not be found for delta ferrite stringers controlling crack propagation. The reason for such behavior is believed to be due to reduced crack nucleation at carbide particles ahead of the propagating crack but the reason for reduced crack nucleation has not been determined.

Comparison With Previous Results -- A series of tensile tests have been performed on several ferritic steels after irradiation in HFIR at about 50°C to 9.3 dpa.[14-16] The steels included compositions meeting specifications for HT-9 and Modified 9Cr-1Mo but were not the same heats used in the present study. The intent of the experiment was to determine the effect of nickel variations on postirradiation properties in order to establish the effect of helium production levels relevant to fusion reactor service.
It was found that HFIR irradiation at 50°C produced large increases in strength and corresponding decreases in elongation. For 12 Cr steels such as HT-9 yield stengths measured at room temperature increased by 70 to 90 percent and ultimate tensile strengths increased by 30 to 40 percent. For 9Cr steels such as Modified 9Cr-1Mo the strength increases were similar, 60 to 80 percent for room temperature strengths and 30 to 50 percent for ultimate tensile stengths. The study concluded that hardening resulted from the displacement damage and was not affected by the transmutation helium formed during irradiation.

The results of these tests are in reasonable agreement with the results of the present work. Both experiments demonstrated that large increases in yield strength occurred following HFIR irradiation at 50°C and that helium effects were unimportant. The major differences which can be identified are those due to the magnitudes of the increases. The earlier experiments gave increases twice as large as those found in the present experiment. Also, the earlier experiments gave similar results for 9Cr and 12Cr steels whereas the present results show larger changes in Modified 9Cr-1Mo properties. A possible explanation is that the differences are due to differences in fluence. The earlier experiment appears to have attained approximately twice the fluence of the present experiment. Tests on specimens irradiated in the HFIR-MFE-RB2 experiment to twice the fluence of RB1 will be available shortly to clarify this possibility.

The Issue -- As postirradiation fracture toughness is one of the properties which may limit Path E alloys for fusion reactor first walls, it is necessary to characterize fracture toughness properties. A key issue is "What irradiation condition will give the largest property degradation?" Once the answer to this question is known, limits on the applicability of ferritic steels can be assessed. An example can be given using DBTT. Figure 7.6.14 shows measured DBTT response in HT-9 and Modified 9CR-1Mo as a function of irradiation temperature. For HT-9, DBTT is shown as a function of irradiation temperature in three reactor experiments EBR-II,[1] UBR[17] and HFIR and for Modified 9Cr-1Mo, the shift in DBTT is shown as a function of irradiation temperature in EBR-II[1] and HFIR.

The EBR-II results indicate that at temperatures below 400°C large effects of irradiation can be expected. This is confirmed by HFIR results on modified 9Cr-1Mo, but is not demonstrated for HT-9 by UBR

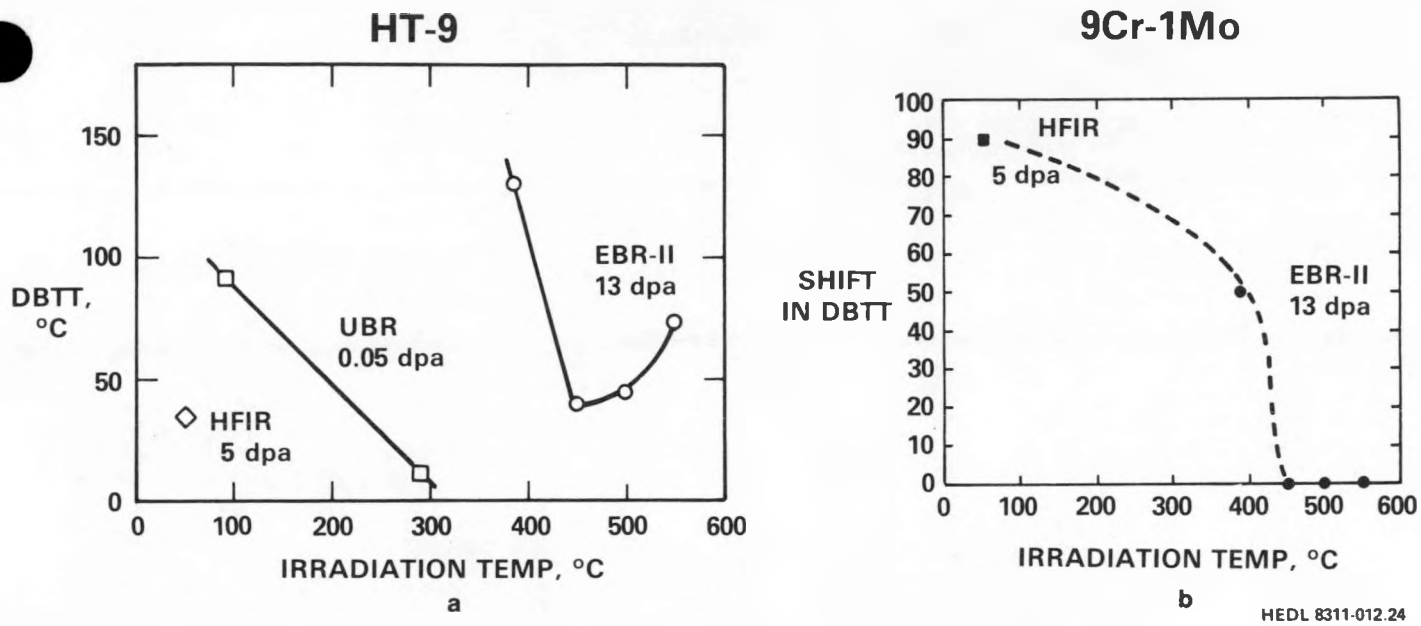

Fig. 7.6.14. DBTT response as a function of irradiation temperature for (a) HT-9 and (b) 9Cr-1Mo.

or HFIR experiments. These differences may be due to fluence effects. Certainly more results are needed to investigate this question. However, using strength and hardness increases for a measure of DBTT degradation, the worst case can be expected at low temperatures. This can be seen in Figure 7.6.15 where the increase in properties compared to the unirradiated condition is shown as a function of irradiation temperature. The trend is for the largest effect to be found at the lowest irradiation temperature. The present hardness results (interpreted as yield strength values) are the major exceptions and the most likely explanation for this exception is that higher fluences will produce larger effects. Similar behavior as a function of irradiation temperature has been observed in pressure vessel steels. This is shown in Figure 7.6.16 which provides results of shift in DBTT for pressure vessel steels as a function of irradiation temperature following irradiation to low fluence.[18] The peak shift in DBTT of 140°C is found following irradiation at 50°C. It may be noted that the issue or saturation in DBTT shift has not been settled for pressure vessel steels, that the lowest irradiation temperature conditions shoud saturate most slowly and therefore even higher shifts in DBTT can be anticipated for higher fluence and low temperature.

Controlling Mechanisms -- The present results provide two unexpected insights into mechanisms controlling toughness in martensitic stainless steels. An example has been obtained where shifts in DBTT due to irradiation do not correlate with increases in strength as measured by hardness. Figure 7.6.13 shows that similar hardness values are obtained following irradiation in EBR-II and HFIR. HT-9 gave values of R_C between 29 and 32 and modified 9CR-1Mo gave values of R_C around 25. However, the DBTT shifts did not follow these trends. In one case (HT-9), a small shift was obtained in HFIR irradiated specimens and a large shift in EBR-II irradiated specimens whereas in the other case, the reverse was true. Apparently, another factor was controlllng. The second insight came from fractographic examination. Irradiation at 55°C in HFIR resulted in less cavity nucleation ahead of propagating cracks in comparison with the unirradiated condition or after irradition in EBR-II at 400°C. Concurrently, fracture in association with delta ferrite stringers was prevented following HFIR irradiation. Both observations suggest that the carbides which are the most likely crack nucleation sites are being altered. As the carbides are still present following HFIR irradiation (see Figure 7.6.5), the most likely possibility is that the carbide crystal structure may have been altered by a process such as recoil dissolution. A change in crystal structure of carbide particles with consequent changes in their fracture behavior accompanied by increased matrix strength may be able to account for the observed fracture toughness response. Further efforts will investigate this possibility along with other explanations such as specimen misidentifications or heat treatment errors.

7.6.5 Conclusions

Irradiation at 55°C to ~5 dpa has produced significant changes in toughness properties for HT-9 and modified 9Cr-1Mo specimens. The DBTT for is increased 30°C and 90°C for HT-9 and 9Cr-1Mo, respectively, strength as measured by hardness is increased by 15 and 25 percent, respectively, and the toughess of ified 9Cr-1Mo is reduced by more than 50 percent. The hardness increases are ascribed to defect clusters 1.5 to 3.0 nm in diameter at number densities of about 10^{17} cm^{-3} but the toughness degradation may in fact be due to a reduction in cavity nucleation ahead of the propagating crack.

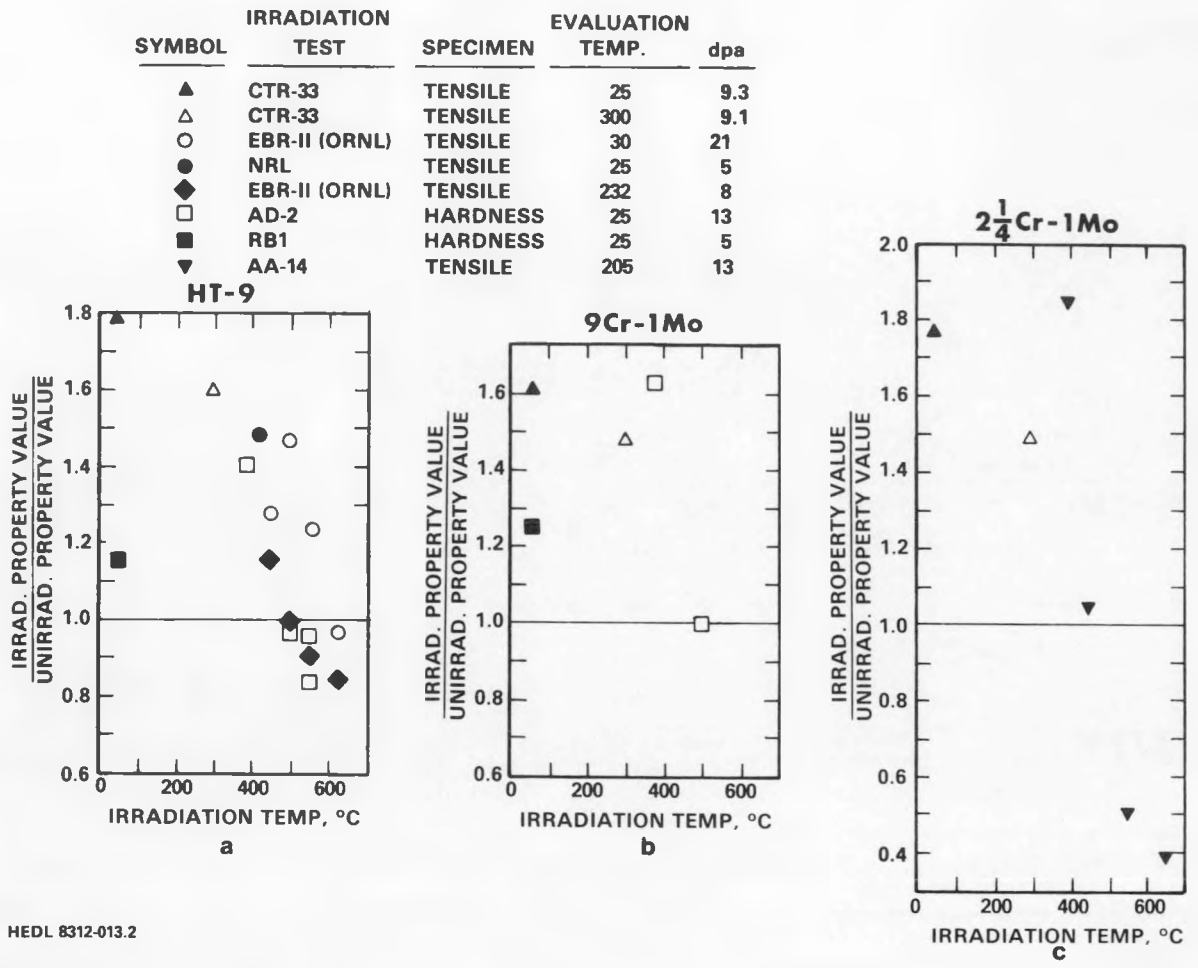

Fig. 7.6.15. Effect of irridiation on strength (hardness) as a function of irradiation temperature for HT-9, 9Cr-1Mo and 2 1/4 Cr-1Mo.

7.6.6 Future Work

Testing of RB1 Charpy specimens will be completed and microstructural examinations of specimens irradiated in RB1 will be continued.

7.6.7 References

1. W. L. Hu, "Miniature Charpy Impact Test Results for Irradiated Ferritic Alloys," DOE/ER-0045/9, p. 255.
2. F. A. Smidt, Fr., J. R. Hawthorne and V. Proverrzano, "Fracture Resistance of HT-9 After Irradiation at Elevated Temperature," *Effects of Radiation on Materials*, ASTM STP 725 (1981) p. 269.
3. F. H. Huang and D. S. Gelles, "Fracture Toughness of Irradiated HT-9 Weld Metal," DOE/ER-0045/10, p. 125.
4. F. H. Huang, "The Fracture Toughness of Ferritic Alloys Irradiated in HFIR," this document, (DOE/ER-0045/11).
5. J. M. Vitek, R. L. Kleuh, M. L. Grossbeck and J. W. Woods, "HFIR-MFE-T1, -T2 and -RB1: Experiments to Evaluate the Effects of Low-Temperature Irradiation on Ferritic Steels," DOE/ER-0045/4, p. 26.
6. R. L. Puigh and R. D. Stevenson, "Fabrication of Mateials for the RB-1 Experiment in HFIR," DOE/ER-0045/5, p. 170.
7. J. M. Vitek and J. W. Woods, "Experiments HFIR-MFE-RB1, -RB2, and -RB3 for Low Temperature Irradiation of Path E Ferritic Steels," DOE/ER-0045/7, p. 30.
8. M. L. Grossbeck, "Irradiation Experiment Status and Schedule," DOE/ER-0045/9, p. 274.
9. L. R. Greenwood, "Fission reactor Dosimeter-HFIR-T2 and RB1," *Damage Analysis and Fundamental Studies Quarterly Progress Report*, DOE/ER-0046/15, for period ending September 30, 1983.
10. D. S. Gelles and W. L. Hu, "Fractographic Examination of HT-9 and 9Cr-1Mo Charpy Specimens Irradiated in the AD-2 Test," DOE/ER-0045/9, p. 178.

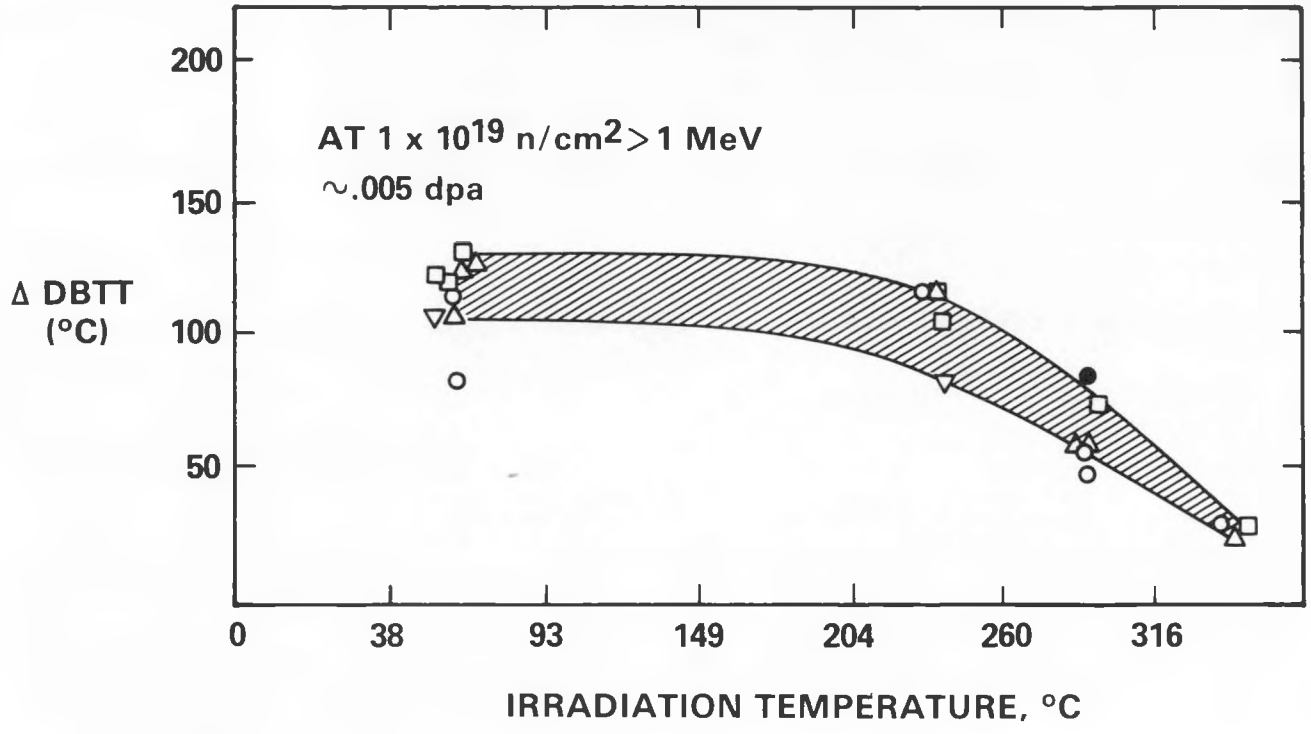

Fig. 7.6.16. Shift in DBTT for pressure vessel steels as a function of irradiation temperature.[18]

11. See for example the *1966 SAE Handbook or the Nickel Alloy Steels Data Book*, Section 8, Appendix B.
12. D. S. Gelles and F. H. Huang, "Fractographic Examination of HT-9 Miniature Compact Tension Specimens Tested at Low Temperatures," this document, (DOE/ER-0045/11).
13. R. L. Klueh and J. M. Vitek, "Tensile Properties of Ferritic Steels After Low Temperature HFIR Irradiation," DOE/ER-0045/5, p. 218.
14. R. L. Klueh and J. M. Vitek, "Tensile Properties of Ferritic Steels After Low Temperature HFIR Irradiation," DOE/ER-0045/6, p. 139.
15. R. L. Klueh and J. M. Vitek, "Tensile Properties of Ferritic Steels After Low Temperature HFIR Irradiation," DOE/ER-0045/7, p. 275.
16. J. R. Hawthorne, "Postirradiation Notch Ductility and Fracture Toughness Behavior of AOD Heat of Alloy HT-9," DOE/ER-0045/8, p. 336.
17. R. W. Wullaert, J. W. Sheckherd and R. W. Smith, "Evaluation of the Maine Yankee Reactor Beltlime Materials," *Irradition Effects on the Microstructure and Properties of Metals*, ASTM STP 611, 1976. p. 400.

7.7 FRACTOGRAPHIC EXAMINATION OF HT-9 MINIATURE COMPACT TENSION SPECIMENS TESTED AT LOW TEMPERATURES - D. S. Gelles and F. H. Huang (Westinghouse Hanford Company)

7.7.1 ADIP Task

The Department of Energy/Office of Fusion Energy (DOE/OFE) has cited the need to investigate ferritic alloys under the ADIP program task Ferritic Steels Development (Path E). The tasks involved are akin to Task Number 1.B.13, Tensile Properties of Austenitic Alloys, and Task Number 1.C.2, Microstructure and Swelling in Austenitic Alloys.

7.7.2 Objective

The objective of this effort is to provide baseline (preirradiation) fractographic data for comparison with irradiated specimens to be examined at a later date.

7.7.3 Summary

Fractographic examinations have been performed on a series of miniature compact tension specimens of HT-9 tested at room temperature and below. Reductions in toughness found for these specimens are shown to be associated with transgranular cleavage fracture and are a function of the plastic deformation which occurs prior to the onset of brittle fracture.

7.7.4 Progress and Status

7.7.4.1 Introduction

Postirradiation fracture toughness properties of Path E alloys has been assessed using both Charpy and miniature compact tension test techniques. Results to date[1-5] have indicated that irradiation can shift the ductile brittle transition temperature (DBTT) and can lower the upper shelf energy as determined from Charpy tests and can lower the fracture toughness as measured from J_{IC} tests. However, it has been difficult to compare the DBTT behavior with the J_{IC} behavior because compact tension specimen tests have never demonstrated brittle failure. The intent of the present examination is to demonstrate the type of response which occurs when brittle failure controls in a compact tension test. A series of miniature tension specimens of HT-9 has been tested at temperatures well below room temperature. The results of fractographic examinations of those specimens are described in order to provide a description of brittle behavior in miniature compact tension specimens under brittle cleavage fracture.

7.7.4.2 Experimental Procedure

Miniature compact tension specimens of HT-9 which had been fabricated but were not used for irradiation experiments were tested to determine J_{IC} at temperatures below room temperature.[6] A limited number of specimens of heat 91354 were tested at a high strain rate of 3.2×10^{-2} m/s, and in order to determine the effect of strain rate, a similar experiment was performed on specimens of another heat of material both at 3.2×10^{-2} m/s and 2.1×10^{-5} m/s. Details regarding composition and heat treatment are given in Table 7.7.1. Results of tests on heat 91354 in this heat treatment condition tested at room temperature and above have been previously reported.[8] Details of the J_{IC} fracture toughness tests performed below room temperature are described in another report in this document.[6] The specimens selected for fractographic examination are listed in Table 7.7.2 along with test conditions and J_{IC} determinations. Figure 7.7.1 shows these results along with results of other tests. The specimens selected for examination are identified by specimen number. Examinations followed routine procedures. An 8° specimen tilt was always used to provide stereo fractographic pairs.

Table 7.7.1. Alloy compositions and heat treatment conditions

Alloy	C	Mn	Si	P	S	Cr	Ni	Mo	Cu	Co	V	Ti	Al	N
91354	0.21	0.50	0.21	0.008	0.003	12.11	0.58	1.03	0.04	0.01	0.33	0.002	0.034	0.004
84425	0.20	0.58	0.27	0.003	0.004	11.87	0.53	1.02	0.013	0.011	0.30	>0.01	0.002	0.0017

(Cont'd)	B	Cb	Ta	W	As	Fe	Heat Treatment
	0.0007	--	0.01	0.53	<0.005	balance	1150°C/1 hr/hot worked/AC + 750°/1 hr./AC[a]
	<0.0010	<0.010	<0.010	0.55	<0.005	balance	1040°C/5 min/AC + 760°/30 min/AC

[a]This condition has been described as mill annealed, but the material was cooled to room temperature (and therefore transformed to martensite) prior to tempering.[7]

Table 7.7.2. Results of J_{IC} cod and estimates of σy for the specimens selected for fractographic examination

Specimen ID	Heat Number	Test Temperature (°C)	Loading Rate (m/s)	J_{IC} (KJ/m^2)	Estimated[6] sy (MPa)	COD (mm)
T411	91354	25	3.2×10^{-2}	95.4	852	0.050 ± 0.015
T406	91354	-58	3.2×10^{-2}	17.1	1064	0.015 ± 0.05
D6	84425	-42	2.1×10^{-5}	77.4	894	0.050 ± 0.015
D2	84425	-74	2.1×10^{-5}	32.1	962	0.012 ± .001
D7	84425	-74	3.2×10^{-2}	27.3	1072	0.0055 ± .0015
D8	84425	-191	2.1×10^{-5}	5.0	1943	~0.001 ± 0.0015

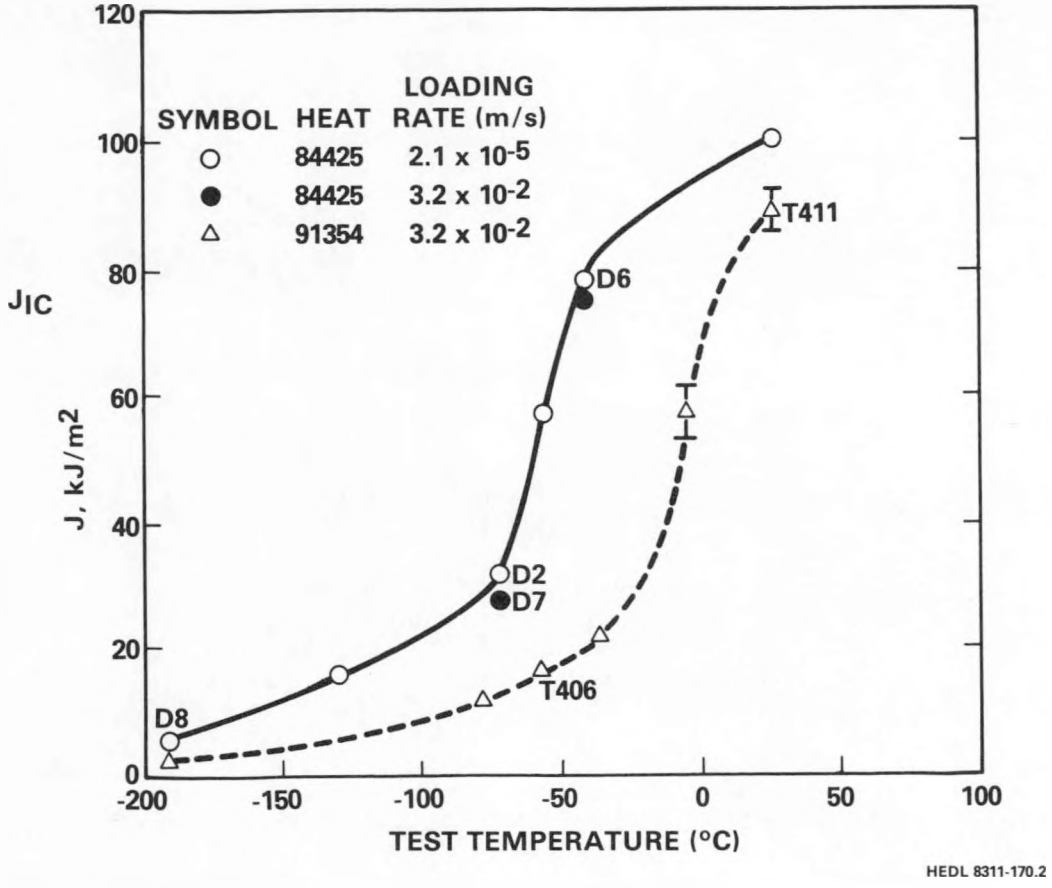

Fig. 7.7.1. J_{IC} measurements for miniature compact tension specimens of HT-9 at low temperatures.

Results

The fracture surfaces of unirradiated miniature compact tension specimens tested at low temperatures contained cleavage fracture areas typical of response in Charpy specimens tested on the lower shelf. The fracture surfaces are displayed as stereo pairs in Figures 7.7.2 through 7.7.7. In each case, a low and a higher magnification series of micrographs is provided to allow examination of both halves of the fracture region immediately adjacent to the fatigue precrack. The viewer should be able to envision the fracture surface folded open along a vertical centerline so that if it were folded closed along that line, the two surfaces would match up.

Figures 7.7.2 and 7.7.3 provide comparison of heat 91354 in the mill annealed condition following testing at room temperature and at -58°C. Specimen T411 tested at room temperature had a fracture surface typical of fracture in HT-9 tested at room temperature and above. A fairly flat triangular region was created during the J_{IC} test whereas the steeply inclined sheat surfaces were produced after the toughness test was completed and the specimen had been heat tinted. The triangular region is therefore the region of interest. It contains many depressions and protrusions and it can be shown that in most cases, a depression on one fracture surface corresponds to a protrusion on the matching surface. Such features are therefore a

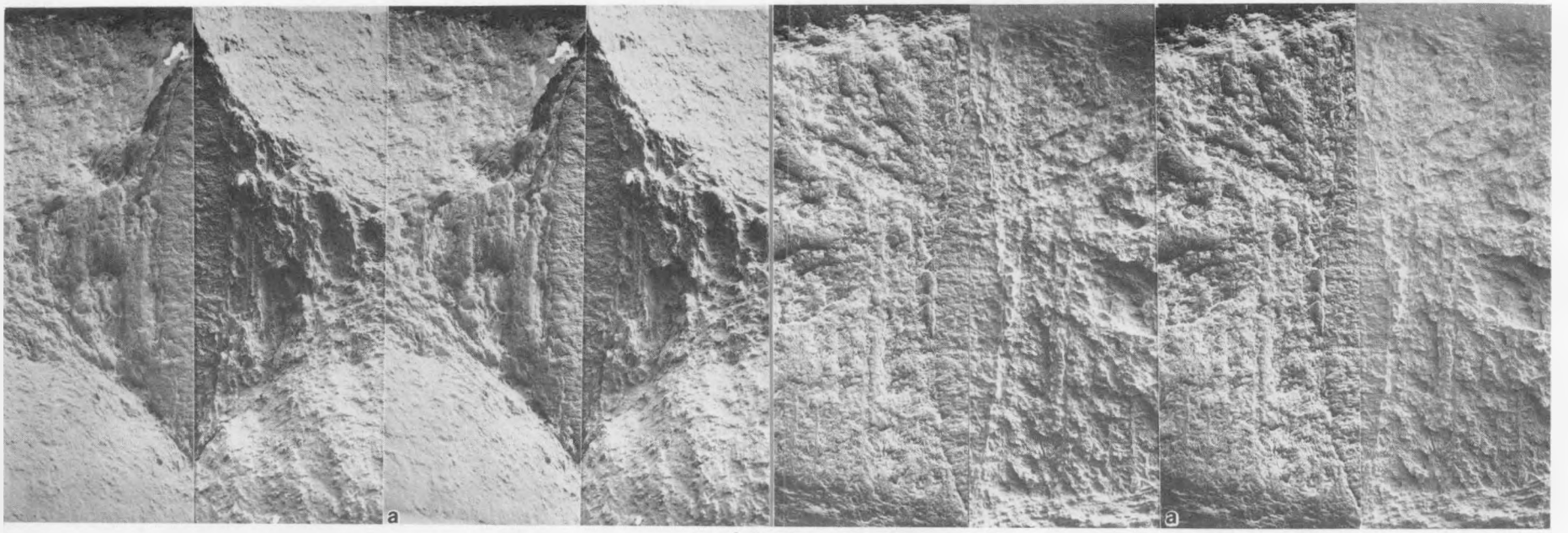

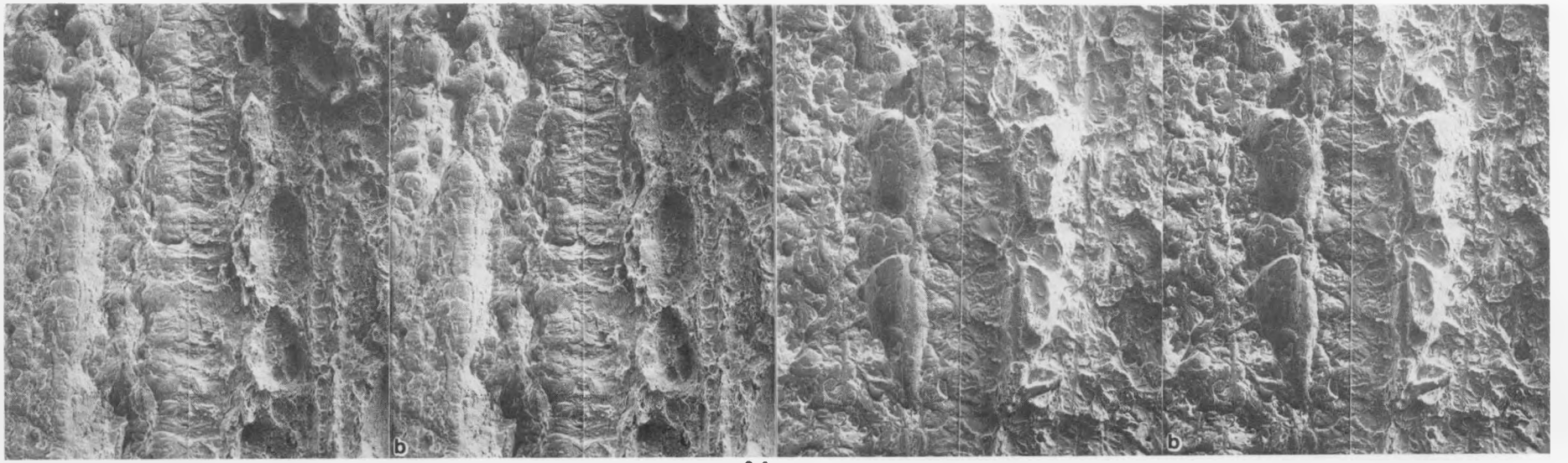

Fig. 7.7.2. Both fracture surfaces of specimen T411, heat 91354, tested at 25°C at fast loading rate, displayed as stereo pairs a) at low and b) higher magnifications.

Fig. 7.7.3. Both fracture surfaces of specimen T406, heat 91354, tested at -58°C at a fast loading rate, displayed as stereo pairs a) at low and b) higher magnifications.

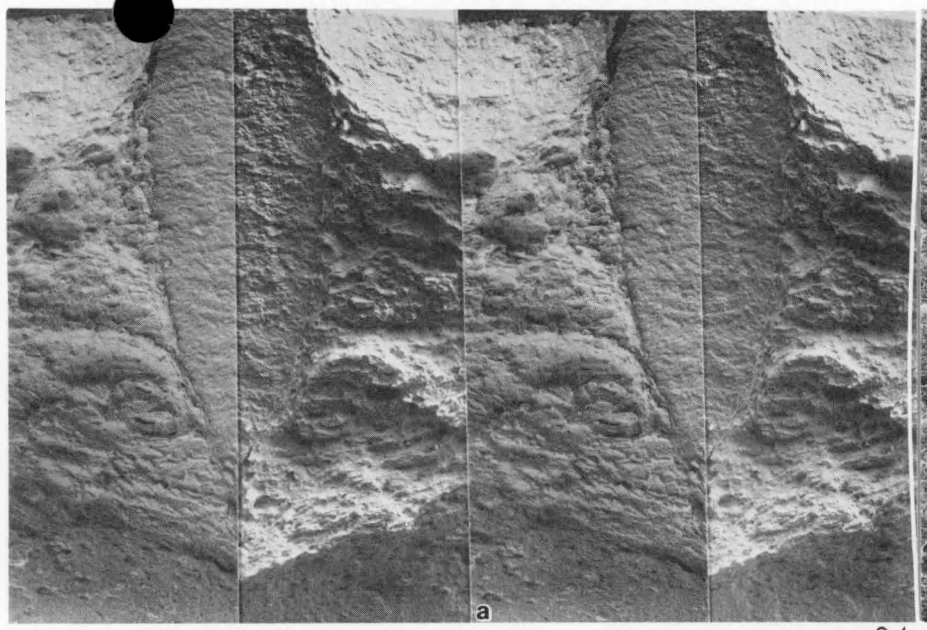

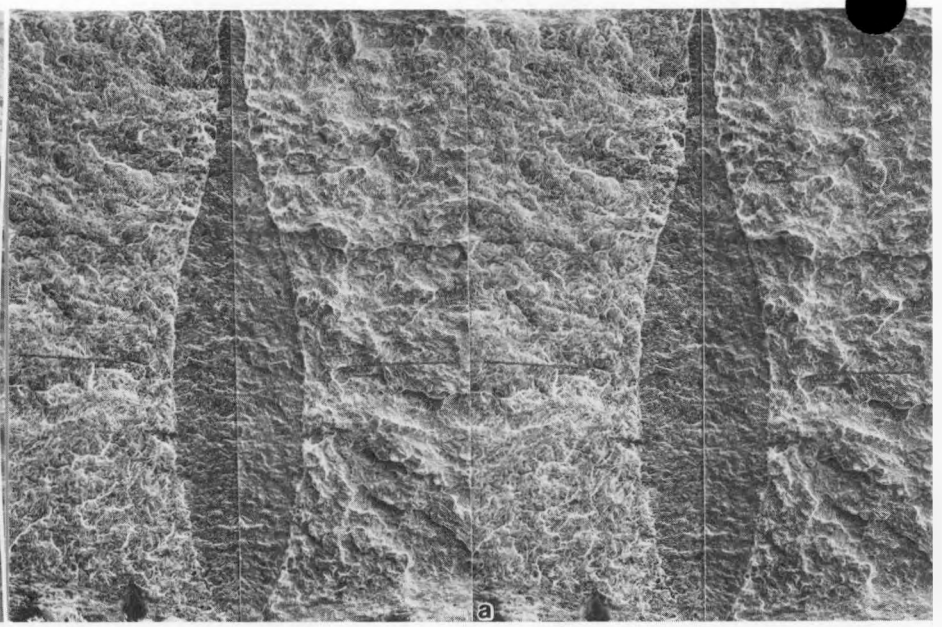

0.4 mm

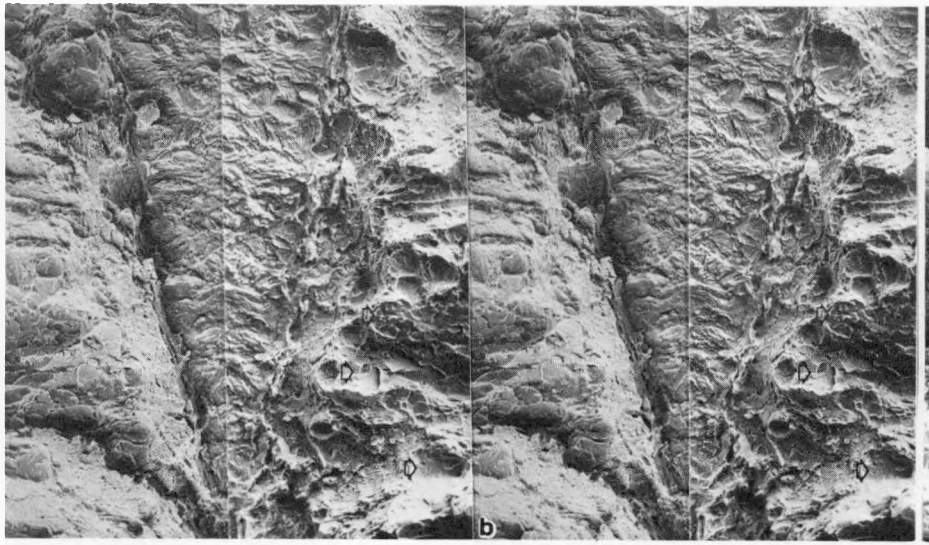

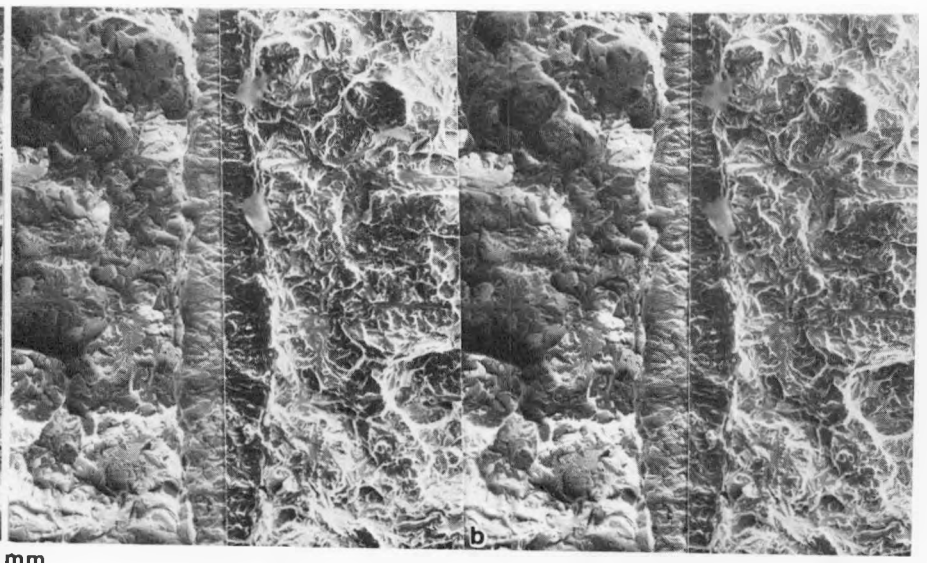

0.1 mm

Fig. 7.7.4. Both fracture surfaces of specimen D6, heat 84425, tested at -42°C at a slow loading rate, displayed as stereo pairs a) at low and b) higher magnifications.

Fig. 7.7.5. Both fracture surfaces of specimen D2, heat 84425, tested at -74°C at a slow loading rate, displayed as stereo pairs a) at low and b) higher magnifications.

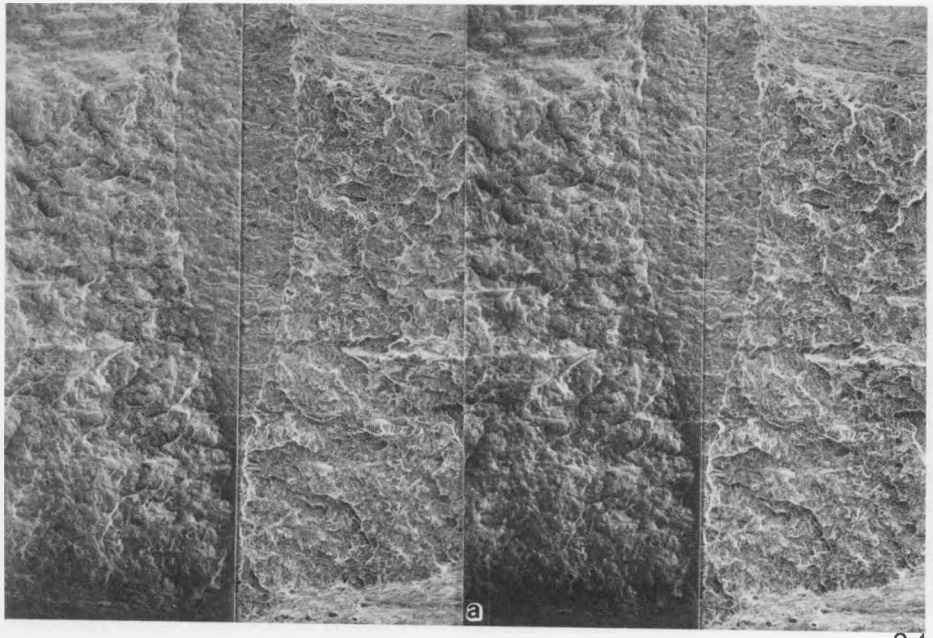

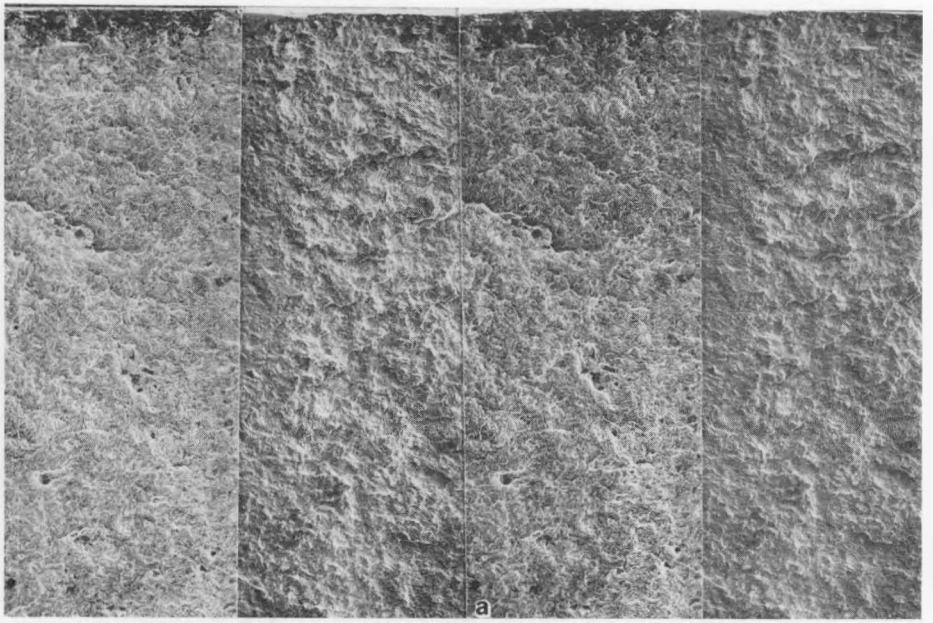

0.4 mm

0.1 mm

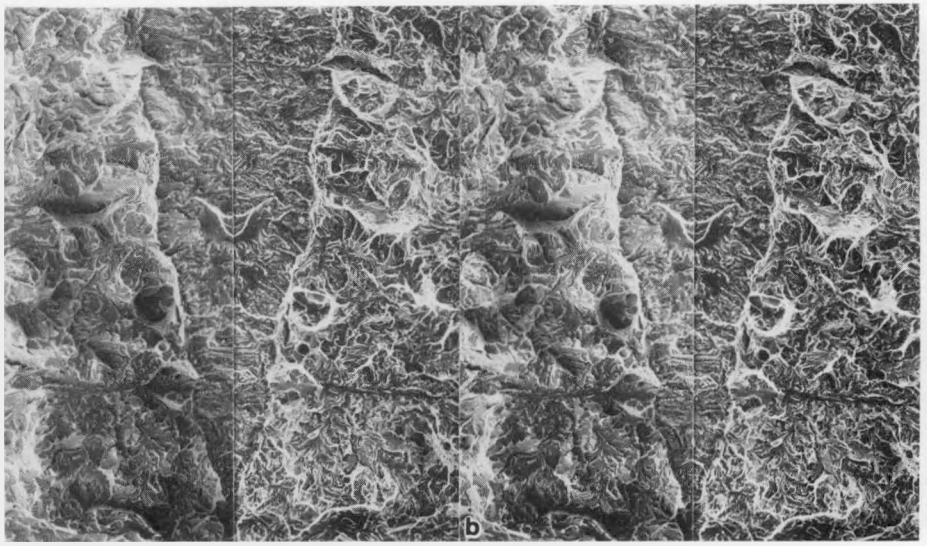

Fig. 7.7.6. Both fracture surfaces of specimen D7, heat 84425, tested at -74°C at a slow loading rate, displayed as stereo pairs a) at low and b) higher magnifications.

0.02 mm

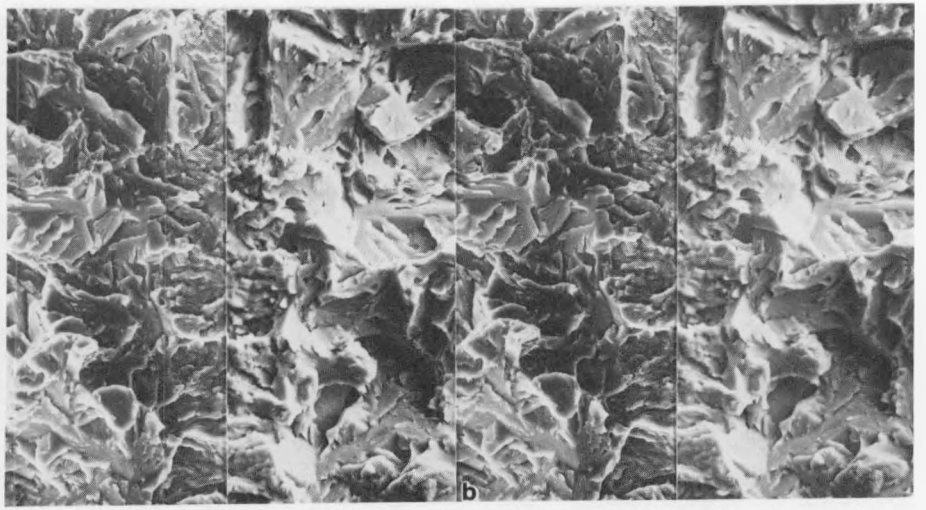

Fig. 7.7.7. Both fracture surfaces of specimen D7, heat 84425, tested at -191°C at a slow loading rate, displayed as stereo pairs a) at low and b) high magnifications.

consequence of nonplanar crack propagation and not due to gross cavitation. Several examples of linear structure parallel to the fatigue crack can be seen. These are due to the presence of delta ferrite stringers and the orientation defines the rolling direction for the material. On a fine scale, many examples of cups created during dimple rupture can be identified (whereas no example of cleavage fracture can be found). In several cases, particles 1000 to 5000 nm in diameter can be observed in the center of the larger dimples. Therefore, failure during toughness testing of specimen T411 at room temperature is entirely ductile.

Testing at -58°C as shown in Figure 7.7.3 for specimen T406 produced quite a different fracture surface. The triangular region of interest has broadened so that most of the fracture surface is fairly flat and the steeply inclined shear surfaces are very narrow. Protrusion and depressions again match up and examples of linear structure due to delta ferrite strings can still be identified. However, the fracture appearance is very different. It is typical of cleavage fracture as found in Charpy specimens of HT-9. Quite flat regions separated by steeply inclined surfaces can be seen both at low and at higher magnifications. The flat regions contain features typical of river pattern steps created during brittle fracture. Therefore, tests on this mill annealed condition tested at -56°C using rapid loading conditions produces brittle failure. However, careful examination of the region immediately adjacent to the fatigue crack reveals a stretch zone approximately 500 nm on both halves of the fracture surface. Therefore, the J_{IC} value of 1.71 KJ/m^2 is a consequence of plastic yielding at the crack tip prior to the onset of brittle transgranular failure.

Figures 7.7.4 through 7.7.7 show the fracture surfaces for specimens of heat 84425. Figure 7.7.4 provides the example of specimens D6 for a test at -42°C and a slow loading rate of 2.1 x 10^{-5} m/s. The fracture surface at low magnification contains a fairly flat triangular region and large shear surfaces typical of ductile failure. Linear features although poorly defined indicate a delta ferrite stringer orientation parallel to the direction of crack propagation. (The starting stock for these specimens was heavily deformed plate whereas the starting stock for heat 91354 specimens was rod sectioned normal to the rolling direction.) Failure in the triangular region is again by non-planar crack propagation which produces protrusions and depressions in corresponding locations on the two halves of the fracture surface. Dimple rupture is the general failure mechanism but a few regions can be found which may have failed by brittle cleavage. Examples have been marked with arrows in Figure 7.7.4b. Therefore it is possible that a small percentage of the fracture surface is a result of brittle fracture.

Specimen D2 shown in Figure 7.7.5 was tested at -74°C at the slow loading rate of 2.1 x 10^{-5} m/s. The specimen has a fracture appearance similar in many ways to specimen T406 (see Figure 7.7.3). Failure is predominantly by cleavage. Observable differences are associated with delta ferrite stringers and stretch zone configuration. The delta ferrite stringers in specimen D2 are oriented in the direction of crack propagation and appear to be less numerous than in specimen T406. The stretch zone in D2 appears to be larger (on the order of 1000 nm) and is better defined in Figure 7.7.5b than is the case for specimen R406 but this is in part due to the difficulty in interpretation created by the large depression in the center of the field of view in Figure 7.7.3b.

Specimen D7 shown in Figure 7.7.6 was also tested at -74°C but at a loading rate three orders of magnitude faster. Comparisons with results for specimen D2 in Figure 7.7.5 reveal that the fracture surfaces are very similar. Small stretch zones adjacent to the fatigue cracks can be identified but almost all failure is a consequence of brittle cleavage.

Specimen D8, tested at -191°C at the slow loading rate is shown in Figure 7.7.7. The fracture surface is very flat in comparison with the other specimens examined. No evidence was found for shear surfaces at specimen surfaces (the edge of the specimen is shown at the top of Figure 7.7.7a) and it is very difficult to differentiate between the fatigue surface and the fracture surface. This transition is shown in Figure 7.7.7b at high magnification (5 times higher than in the other figures); no evidence for plastic deformation (stretch zone formation) can be identified.

The fractograph series taken for each specimen allows estimates to be made for crack opening displacement (COD) by procedures developed previously.[9] COD measurements were made and the values obtained are given in Table 7.7.2 along with estimates for yield strength (σ_y) taken from reference 6. The COD results follow the trends expected. Specimens displaying high toughness, D6 and T411, gave COD values on the order of 0.05 mm. Specimens with moderate toughness, D2, D7 and T406 gave values between 0.005 and 0.015 mm and the specimen with low toughness gave a barely measurable value of 0.001 mm. Also, a difference of a factor of 2 in COD was measured for identical specimens D2 and D7 tested at different strain rates. These results are plotted in Figure 7.7.8. Figure 7.7.8 provides a comparison of toughness as a function of test temperature giving results similar but not as well behaved as those shown in Figure 7.7.1. It may also be noted that from comparison of values for J_{IC}, σ_y and COD, values of m as defined by the relationship

$$J_{IC} = m\,\sigma_y\,COD \qquad (1)$$

are found to vary between 1 and 4.5. As m is expected to be on the order of 2, it can be inferred that the COD measurements may be in error by more than the uncertainty given for COD values.

Discussion

This effort was intended to demonstrate that brittle failure can occur in miniature compact tension specimens and toughness measurements can be obtained under those conditions. It is apparent from

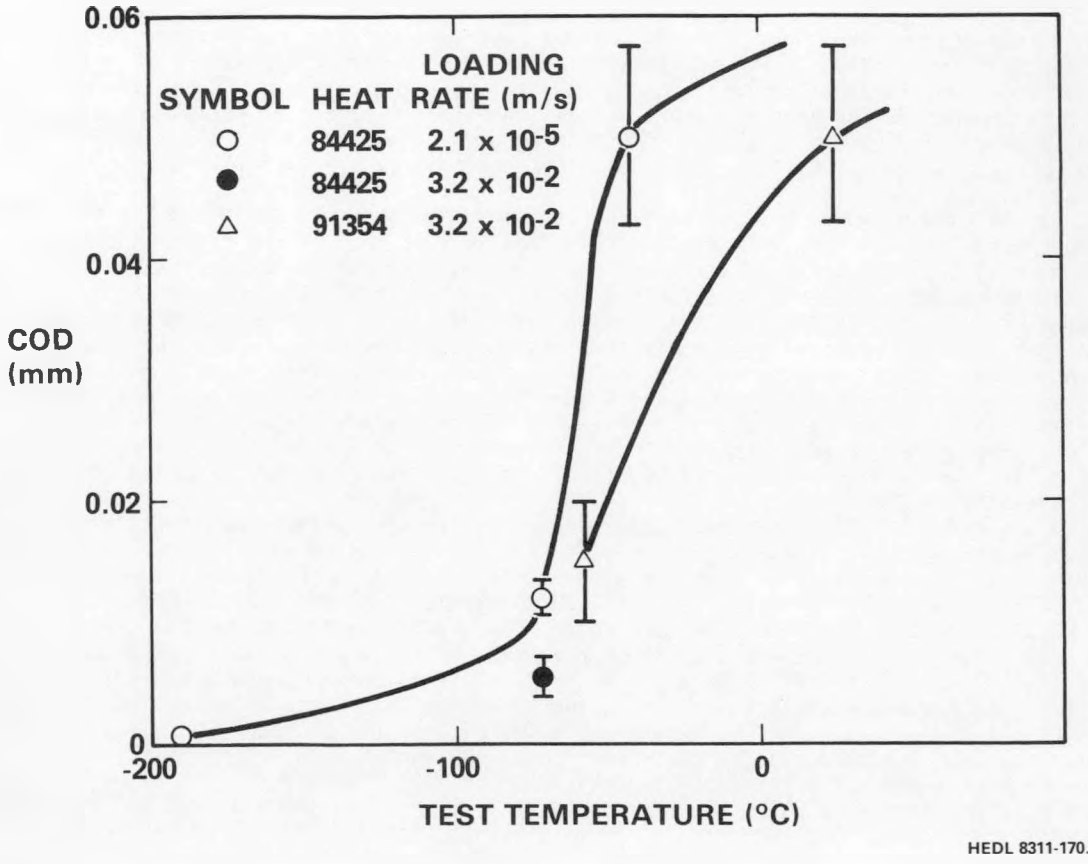

Fig. 7.7.8. COD measurements based on fractographic analysis as a function of test temperature for miniature compact tension specimens of HT-9 tested at low temperatures.

Figures 7.7.2 through 7.7.7 that as the test temperature is reduced, HT-9 does undergo a ductile-to-brittle transition in miniature compact tension specimens. Concurrently, the stress state well away from the crack is altered so that plane strain controls over a much greater range of crack propagation. Therefore, it can be expected that a shift in DBTT due to irradiation as measured using Charpy specimens should also be measurable using miniature compact tension specimens.

An increasing tendency for brittle failure is manifested in the fracture surface as follows, based on the present results where failure is due to transgranular cleavage. If cleavage failure is very limited, only a few isolated regions with a size on the order of a prior austenitic grain fail by brittle cleavage. These regions are often widely separated. When cleavage failure becomes the dominant failure mode, plastic deformation still preceeds cleavage fracture. Crack tip blunting occurs creating a stretch zone immediately adjacent to the crack tip. Once cleavage begins, evidence for plastic strain is difficult to recognize even when delta ferrite stringers are present. The fracture appearance during cleavage consists of flat cleavage steps containing river pattern-like features joined by steeply inclined shear surfaces. However, when toughness is further decreased by testing at still lower temperatures, the variation in cleavage step height is reduced and the fracture surface becomes much flatter. Therefore, nucleation of cleavage cracks ahead of the propagating crack occurs closer and closer to the crack tip as specimen toughness is reduced.

The toughness of a specimen can be estimated from a fracture surface (albeit crudely) by measurement of COD, and this is probably the best way to obtain such information after testing has been completed. However, the present effort also suggests that the degree of roughness of the fracture surface can be used as a crude measure of toughness at least for HT-9. An explanation is proposed as follows. The COD is a measure of how extensive plastic deformation must be before crack propagation can occur. Crack propagation in HT-9 is not continuous. It takes place in a jerky manner being dependent on crack nucleation ahead of the propagating crack. Crack nucleation probably occurs at discrete sites in the structure (carbide particles) after a finite amount of plastic deformation, and therefore the surface roughness is a measure of the extent of significant plastic deformation away from the crack tip. The concept of plastic zone size applies to COD, to stretch zone size, and to surface roughness. It is plastic zone size which provides the basis for correlations of fracture appearance with J_{IC}.

The above description for brittle crack propagation indicates that toughness will be dependent on microstructure. The size and distribution of crack nucleation sites, the amount of plastic strain needed to nucleate the crack and the stress needed for plastic strain all can be expected to play a role in the transition from ductile to brittle failure.

Comparison of miniature compact tension specimen behavior with Charpy test response now provides some unexpected results. Charpy tests have shown that DBTT shifts as large as 120°C can occur in HT-9 following

irradiation at 400°C. Miniature compact tension results now show that a DBTT for unirradiated HT-9 should be in the range of -60 to -10°C (using as a definition for DBTT half the upper shelf energy). However, a DBTT has never been observed in miniature compact tension specimens of HT-9 following irradiation at 400°C. The difference is not simply ascribable to loading rate because a three order of magnitude shift in rate does not significantly change miniature toughness test results. Therefore, it must be concluded that measurements of DBTT shifts due to irradiation are dependent on test technique. The question must be asked: "Which results are more relevant to fission reactor design?"

7.7.5 Conclusion

Fractographic examination of unirradiated miniature compact tension specimens of HT-9, which were tested at temperatures below room temperature and which had shown reduced toughness, are found to have failed by transgranular cleavage fracture. Therefore the concept of a DBTT as measured by miniature compact tension specimens is applicable. The specimen toughness measured in each specimen is shown to be due to plastic deformation prior to the onset of brittle cleavage. A description of the processes which control brittle crack propagation can be generated based in this work.

7.7.6 Future Work

Efforts to define the microstructural features which control fracture behavior in Path E alloys will continue when specimens become available.

7.7.7 References

1. W. L. Hu, "Miniature Charpy Impact Test Results for Irradiated Ferritic Alloys," DOE/ER-0045/9, p. 255.
2. J. R. Hawthorne, "Postirradiation Notch Ductility and Fracture Toughness Behavior of AOD Heat of Alloy HT-9," DOE/ER-0045/8, p. 336.
3. F. A. Smidt, Jr, J. R. Hawthorne and V. Provenzano, "Fracture Resistance of HT-9 After Irradiation at Elevated Temperature," *Effects of Radiation on Materials*, ASTM STP 725 (1982) p. 269.
4. F. H. Huang and D. S. Gelles, "Fracture Toughness of Irradiated HT-9 Weld Metal," DOE/ER-0045/10, p. 125.
5. D. S. Gelles, W. L. Hu, F. H. Huang and G. D. Johnson, "Effects of HFIR Irradiation at 60°C on Microstructure and Toughness in HT-9 and 9Cr-1Mo," this document.
6. F. H. Huang, "The J_{IC} Fracture Toughness Transition Behavior of Alloy HT-9," this document.
7. R. J. Puigh and N. F. Panayotou, "Specimen Preparation and Loading for the AD-2 Ferritics Experiment," DOE/ER-0045/3, p. 261.
8. F. H. Huang and G. L. Wire, "Analysis of Single Specimen Tests on HT-9 for J_{IC} Determination," DOE/ER-0045/3, p. 236.
9. D. S. Gelles, F. H. Huang and N. F. Panayotou, "Fractographic Examination of Compact Tension Specimen of Unirradiated HT-9 and Modified 9Cr-1Mo Welds," DOE/ER-0045/8, p. 442.

7.8 POSTIRRADIATION NOTCH DUCTILITY TESTS OF ESR ALLOY HT-9 AND MODIFIED 9Cr-1Mo ALLOY FROM UBR REACTOR EXPERIMENTS - J. R. Hawthorne (Naval Research Laboratory)

7.8.1 ADIP Task

The Department of Energy (DOE)/Office of Fusion Energy (OFE) has stated the need to investigate ferritic alloys under the ADIP program task. Ferritic Steels Development (Path E)

7.8.2 Objectives

Alloy HT-9 and Alloy 9Cr-1Mo(Mod.) are being evaluated for a potential application as a first wall material in magnetic fusion reactors. Objectives of the current research task were to postirradiation test Charpy-V (C_V) specimens from ESR plates irradiated in the UBR reactor at 150°C and at 300°C and to analyze the results in terms of melt processing and plate composition effects.

7.8.3 Summary

During this period, irradiation exposures at 300°C and 150°C to ~8×10^{19} n/cm^2, E>0.1MeV, were completed for the Alloy HT-9 plate and the modified Alloy 9Cr-1Mo plates, respectively. Postirradiation tests of Charpy-V (C_V) specimens were completed for both alloys; other specimen types included in the reactor assemblies were fatigue precracked Charpy-V (PCC_V), half-size Charpy-V, and in the case of the modified 9Cr-1Mo, 2.54 mm thick compact tension specimens.

7.8.4 Progress and Status

7.8.4.1 Introduction

The ferritic stainless steel compositions, HT-9 and 9Cr-1Mo(Mod.), are being assessed for possible first wall applications in magnetic fusion reactors by the Magnetic Fusion Materials Program and for duct applications in liquid metal fast breeder reactors by the Cladding/Duct Alloy Development Program of the Department of Energy. For these proposed uses, fracture resistance properties before and after elevated temperature irradiation are being investigated. Specimen types include C_V specimens for notch ductility determinations, PCC_V specimens for dynamic fracture toughness (K_J) determinations and compact tension (CT) specimens for static fracture toughness determinations. Tensile property changes with irradiation are also being established for use in fracture resistance assessments.

Previous studies[1] evaluated an HT-9 plate representing AOD melt processing after irradiation at 93°C and 288°C. The current study on the HT-9 composition is evaluating ESR processing vs AOD processing and, through a joint program with ORNL (J. Vitek), the relative effects of a low vs. a high fluence level. For the latter, a set of half size C_V specimens from the NRL plate are being irradiated in HIFR at 300°C. The 150°C irradiation of the 9Cr-1Mo(Mod.) alloy on the other hand, was undertaken to investigate the low temperature service capabilities of the composition and to permit a test of the postirradiation correlation of dynamic vs. static fracture toughness.

7.8.4.2 Materials

The HT-9 plate, NRL code ES9, was 15.2 mm (0.6-in.) thick and was produced from the electroslag remelted heat no. 9607R2[2]. The 9Cr-1Mo(Mod.) plate, NRL code VS, was 25.4 mm (1.0-in) thick and was produced from the electroslag remelted heat no. 30176-1. Plate compositions and heat treatments are listed in Tables 7.8.1 and 7.8.2[3,4]. The code ES9 plate was heat treated by Armco Steel Company under contract to NRL; the code VS plate was received from ORNL in the fully heat treated condition. Note that the ES9 plate was cut into four sections prior to heat treatment and that the two sections providing specimens for the reactor irradiations were heat treated separately. C_V specimens were oriented in the plates to represent the longitudinal (LT, strong) test direction.

Included in the 300°C irradiation assembly were a very limited number of C_V specimens (LT orientation) from the AOD melted plate of HT-9. These specimens permitted a direct spot comparison of the relative radiation embrittlement sensitivity of ESR vs. AOD melt products. The composition and heat treatment of the AOD plate, NRL code 9TH, are included in the tables[1]. Particulars for a VIM-ESR HT-9 rod studied earlier[5] are also included in the tables for reference.

Table 7.8.1 Composition (wt-%) of HT-9 and 9Cr-1Mo(Mod.) plates

Material	C	Si	Mn	P	S	Cr	Mo	Ni
ESR HT-9[a] (Code ES)	0.20	0.17	0.57	0.016	0.003	12.1	1.04	0.51
AOD HT-9[b] (Code 9TH)	0.20	0.24	0.57	0.018	0.007	11.64	1.01	0.52
9Cr-1Mo(Mod.) (Code VS)[c]	0.081	0.11	0.37	0.010	0.003	8.61	0.89	0.09
HT-9 Rod (Code HT9)[d]	0.21	0.21	0.50	0.008	0.003	12.09	1.02	0.58
Material	**V**	**W**	**N**	**Al**	**Ti**	**Cu**	**Cb/Ta**	**B**
ESR HT-9 (Code ES)	0.28	0.45	0.027	0.006	0.001	0.07	<0.001	<0.001
AOD HT-9 (Code 9TH)	0.30	0.57	0.044	0.009	<0.01	0.04	0.01	0.001
9Cr-1Mo(Mod.) (Code VS)	0.33	0.54	0.004	0.035	—[e]	0.04	—[e]	—[e]
HT-9 Rod (Code HT9)	0.209	<0.01	0.055	0.007	0.004	0.04	0.072	<0.001

[a]INCO analysis [b]Avg. GA and CE analyses [c]CE analysis

[d]NRL stock (Ref. 5, melt 91354) [e]Not determined

Table 7.8.2 Heat treatment of test materials

Material	Heat Treatment
ESR HT-9 (Code ESR)	1050°C ± 14°C - 0.5 h, air cool; 780°C - 4 h, air cool
AOD HT-9 (Code 9TH)	1050°C - 0.5 h, air cool; 780°C - 2.5 h, air cool
9Cr-1Mo(Mod.) (Code VS)	1038°C - 1 h, air cool; 760°C - 1 h, air cool
HT-9 Rod (Code HT9)	1050°C - 0.5 h, air cool; 780°C - 2.5 h, air cool

7.8.4.3 Material Irradiation

The materials were irradiated in the C2 fuel lattice position of the water cooled reactor (UBR) at the State University of New York at Buffalo. Two, individually temperature controlled assemblies were used with specimen temperatures being monitored continuously by means of thermocouples welded to the specimens. The neutron fluence is estimated at $8 \times 10^{19} n/cm^2 > 0.1MeV$ and will be verified from iron neutron dosimeter wires placed within each of the specimen arrays. A neutron energy spectrum calculation is available for the C2 position. The total irradiation time (reactor hours at power) was 848.0 hours which approximates closely the exposure condition of earlier NRL experiments in the UBR for the Magnetic Fusion Materials Program.

7.8.4.4 Preirradiation Notch Ductility Properties

As-heat treated C_V notch ductility properties of the ESR HT-9 plate and the ESR 9Cr-1Mo(Mod.) plate were developed during this reporting period and are illustrated in Figures 7.8.1 and 7.8.2. As-heat treated properties of the AOD HT-9 plate (and of the ESR HT-9 rod) were reported earlier[1,5].

A comparison of the data in Figures 7.8.1 and 7.8.2 (LT orientation) indicates about equal 41 J (30 ft-lb) transition temperatures (-40°C vs. -32° C) for the two compositions but significantly different upper shelf energy levels (157 vs. 229 J). TL (weak) orientation data for the 9Cr-1Mo(Mod) plate are not yet available for a full comparison of relative upper shelf toughness. Upper shelf toughness is governed, in part, by plate cross rolling practice. Figure 7.8.2 suggests that data scatter for the 9Cr-1Mo(Mod) plate is more pronounced than that for either the ESR HT-9 plate or the AOD HT-9 plate. The noted scatter places a degree of uncertainity on the exact brittle/ductile transition behavior of the material.

Figure 7.8.3 compares C_V trend curves for all three HT-9 materials. The 41 J transition temperatures (LT orientation) range from -40°C to -18°C; upper shelf values show a significant difference due to melt processing (ESR vs. AOD). TL orientation data are available for both plates to confirm the latter observation. The upper shelf of the ESR plate is about 70 per cent higher than that of the AOD plate (either test orientation); thus, ESR processing clearly is the superior method. The fracture surfaces of the AOD material showed the presence of delta ferrite stringers which contributed to its lower, upper shelf. The TL orientation, upper shelf of the AOD plate would be considered relatively low by many standards. The data sets, overall, demonstrate the validy of testing materials in both the strong and weak test orientations. C_V trend curves for the LT and TL orientations, however, do show a close similarity in the transition region (see Figures 7.8.1 and 7.8.2).

7.8.4.5 Postirradiation Notch Ductility: Modified 9Cr-1Mo Plate

Figure 7.8.2 includes data developed for the 149°C irradiated condition of the 9Cr-1Mo(Mod.) plate. The 41 J transition temperature elevation is only 83°C(150°F); the upper shelf energy reduction is essentially nil. Important to this capabilities study, the brittle/ductile transition of the plate after irradiation is well below the simulated irradiation service temperature of 149°C. The 41 J temperature, in fact, is only 52°C(125°F) and full shear fracture behavior develops at about 116°C(240°F). A tolerance for much higher fluences at 149°C, in terms of the transition, is thus evident.

The 41 J temperature elevation of 83°C is significantly less than that reported earlier for the AOD HT-9 plate irradiated at 93°C(200°F) to about the same fluence. Ignoring the exposure temperature difference, the 9Cr-1Mo(Mod.) material would appear to have a lower radiation sensitivity than HT-9. This could be a factor of relative alloying level, impurity content or general microstructure type, i.e., tempered lower bainite vs. tempered martensite.

In confirmation of the above comparison, a few specimens of the ESR HT-9 plate were inserted among the 9Cr-1Mo(Mod.) specimens in the 149°C irradiation assembly. Test results for these specimens (see Figure 7.8.1) likewise indicate that 9Cr-1Mo(Mod.) has better radiation resistance at 149°C than HT-9. Additional tests at a higher fluence and at higher exposure temperatures are recommended to define fully the low temperature service capabilities of the 9Cr material.

Dynamic fracture toughness (K_J) data for the unirradiated condition are superimposed on the C_V data in Figure 7.8.2. Significantly and in parallel with other (unreported) NRL observations for 9Cr-1Mo(Mod.) materials, the upswing in toughness begins at a higher temperature than the upswing in C_V energy absorption. As one result, C_V energy values of 120 J (80 ft-lb) are not indicative of a high toughness but correspond to a toughness level of ~33 MPa$\sqrt{m}$ (30 ksi $\sqrt{in}$). Applied load vs. time-to-fracture traces of those PCC_V specimens tested at -18°C and 4°C depicted elastic fracture behavior. The data trend suggests that high toughness can be expected for the postirradiation condition above 116°C(240°F). PCC_V tests to verify this projection are scheduled for the next reporting period.

7.8.4.6 Postirradiation Notch Ductility: ESR HT-9 Plate

Test results for the ESR plate following 300°C irradiation are given in Figure 7.8.4. The square and circle symbols refer, respectively, to plate sections 1 and 2 which were heat treated individually. Excellent agreement of as-heat treated properties is noted for the transition region; a small difference (~10 J) in upper shelf levels is discerned but may be simply data scatter.

The irradiation produced a 47°C elevation in 41 J temperature and a reduction in upper shelf to 136 J. A large toughness reserve against additional fluence at 300°C is thus demonstrated. The apparent radiation sensitivity, however, is significantly higher than that of A 302-B and A 533-B pressure vessel steels that have been specially tailored for elevated temperature radiation resistance. For example, A 302-B steel melts can be produced consistantly in the laboratory which will show essentially no transition temperature elevation after the same fluence at 300°C (Ref 6). The data of Figure 7.8.4 thus suggests considerable room for alloy improvement. Drawing on the pressure vessel steel technology, one goal should be the reduction of the phosphorus content to less than 0.010% [6]. Copper contents listed in Table 7.8.1, on the other hand, are below the level generally considered to be harmful to elevated temperature radiation embrittlement resistance.

7.8.4.7 Radiation Embrittlement Resistance of ESR vs. AOD Melt Products

Figures 7.8.5 and 7.8.6 compare the notch ductilities of the ESR HT-9 and AOD HT-9 plates in the 93° or 149°C and 288° or 300°C irradiated condition. Melt processing does not appear to be a factor in irradiation response in either figure. In Figure 7.8.5, the 114°C, transition temperature elevation of the ESR plate with 149°C irradiation agrees well with the 117°C elevation recorded for the AOD plate with 93°C irradiation. Likewise (Fig 7.8.6), the 47°C transition temperature elevation for the ESR plate with 300°C irradiated agrees closely with 36°C elevation for the AOD plate after 288°C irradiation. A few specimens of the AOD plate were irradiated at 300°C with the ESR plate specimens. The data (Fig 7.8.5) support the earlier determination for the AOD plate (288°C irradiation) and demonstrate the similarity of radiation sensitivities of the ESR vs. AOD materials.

Upper shelf reductions for the ESR plate are somewhat larger than those for the AOD plate; however, this tendency was expected as it is common among steels having high vs. low preirradiation upper shelf levels.

7.8.4.8 Postirradiation Evaluation of Half Size (Miniature) C_V Specimens

Tests of the miniature C_V specimens from the current irradiation experiments and from two previous NRL irradiation experiments are not to be conducted at NRL; rather, the DOE plans to have the specimen tests made at ORNL where the necessary equipment is already installed. The subject specimens have been shipped to ORNL and are awaiting testing.

7.8.4.9 Plans for the Next Reporting Period

Plans for the next reporting period are to complete the postirradiation PCC_V and tension tests of the materials and to initiate postirradiation CT tests using the single specimen unloading compliance method for R curve determinations.

7.8.4.10 References

[1] J. R. Hawthorne, "Postirradiation Notch Ductility and Fracture Toughness Behavior of AOD Heat of Alloy HT-9" in Alloy Development for Irradiation Performance, Semi-Annual Progress Report for period ending March 31, 1982, DOE/ER-0045/8, Sept. 1982.

[2] J. R. Hawthorne, "Irradiation of ESR Alloy HT-9 and Alloy 9Cr-1Mo(Mod.) Plates for Fracture Toughness Assessment," in Alloy Development for Irradiation Performance, Semi-Annual Progress Report for Period ending September 30, 1983, DOE/ER-0045/12, Sept 1983.

[3] Communication to ADIP and DAFS Participants from T. Lechtenberg (General Atomic Co) March 18, 1982.

[4] Private communication, V. K. Sikka (ORNL) to J. R. Hawthorne (NRL) dated April 2, 1981.

[5] F. A. Smidt, Jr., J. R. Hawthorne, and V. Provenzano, "The Fracture Resistance of HT-9 After Irradiation at Elevated Temperature," Proceedings of the Symposium on Effects of Radiation on Structural Materials, ASTM STP 725, Feb 1980.

[6] U. Potapovs and J. R. Hawthorne, "The Effect of Residual Elements on the Response of Selected Pressure-Vessel Steels and Weldments to Irradiation at 550°F," Nuclear Applications, Vol. 6, Jan 1969, p. 27.

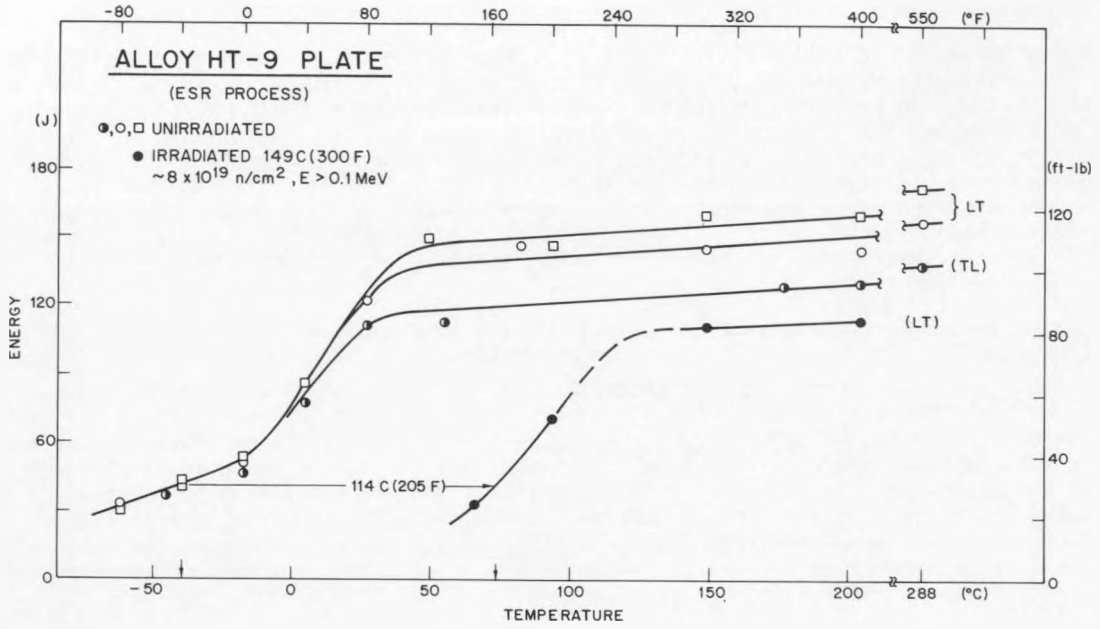

7.8.1 Notch ductility of the Alloy HT-9 plate (ESR reference melt) before and after irradiation at 149°C. The neutron fluence of 8 x 10^{19}n/cm^2 (E > 0.1MeV) is a preliminary estimate. LT and TL refer to longitudinal and transverse test orientations, respectively. Square symbols identify plate section 1 data; circle symbols identify plate section 2 data.

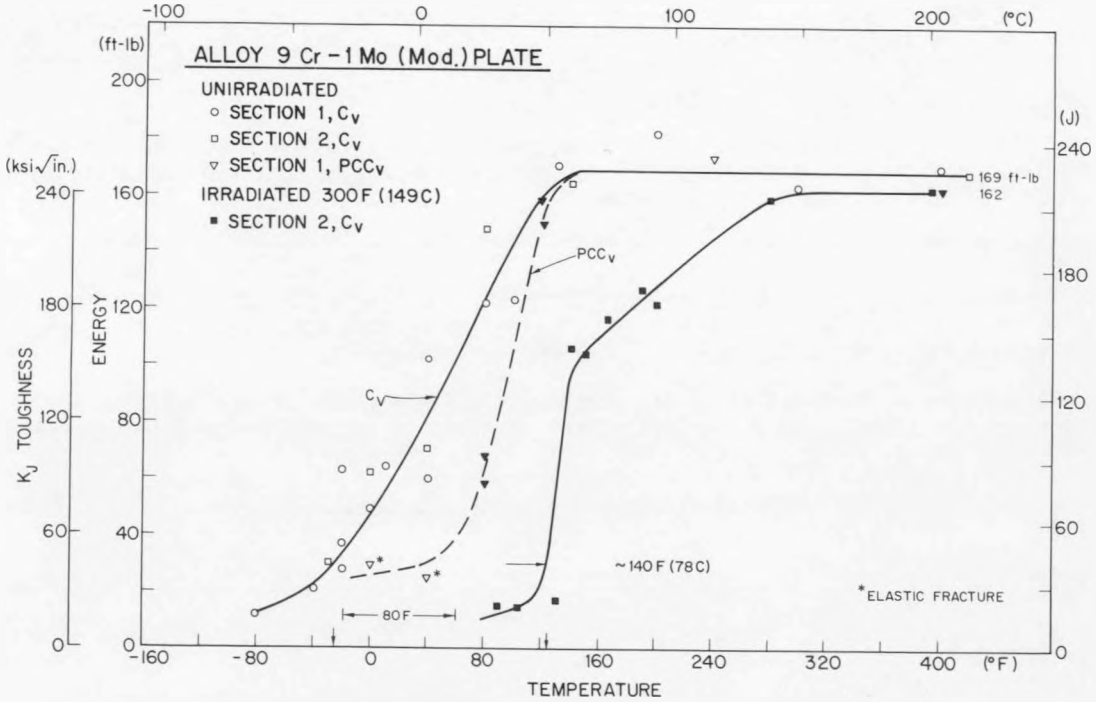

7.8.2 Notch ductility of the Modified 9Cr-1Mo Alloy plate (ESR melt) before and after irradiation at 149°C. The neutron fluence is estimated at 8 x 10^{19}n/cm^2 (E > 0.1MeV). Dynamic fracture toughness data for the unirradiated condition from PCC_V tests are also shown.

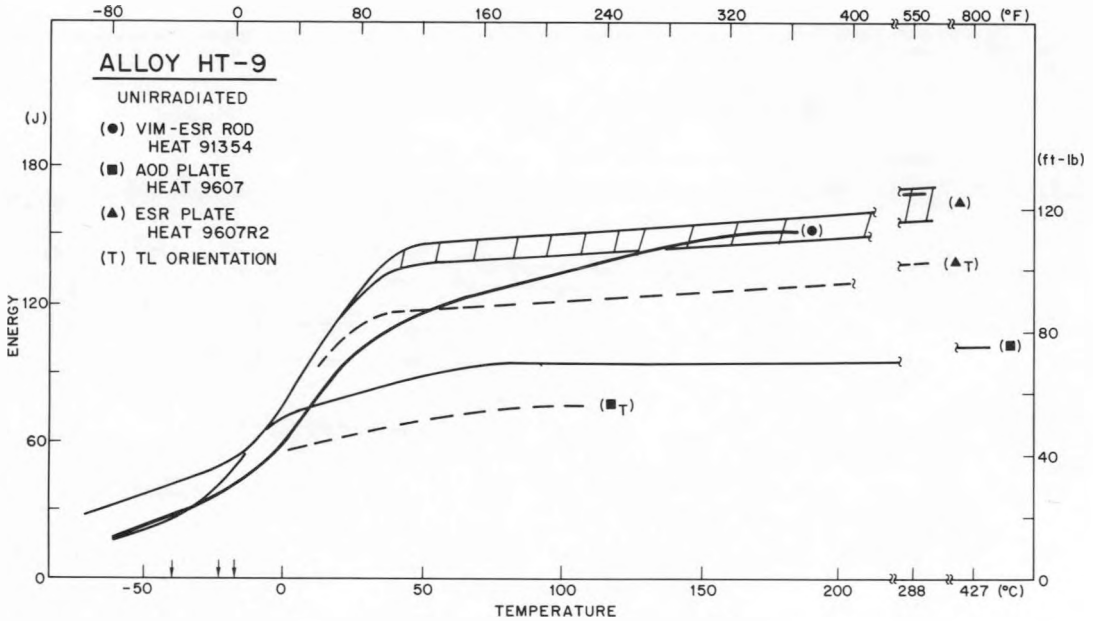

7.8.3 Comparison of as-heat treated notch ductility for three Alloy HT-9 materials. Note the similarity of 41 J transition temperatures (marked by the vertical arrows).

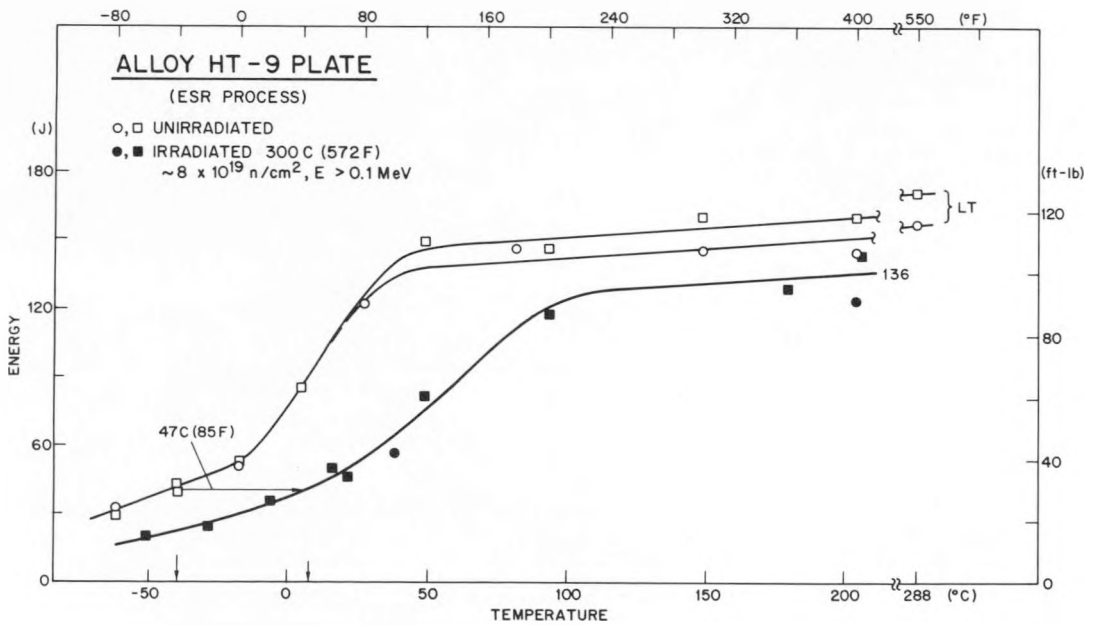

7.8.4 Notch ductility of the Alloy HT-9 plate (ESR reference melt) before and after irradiation at 300°C.

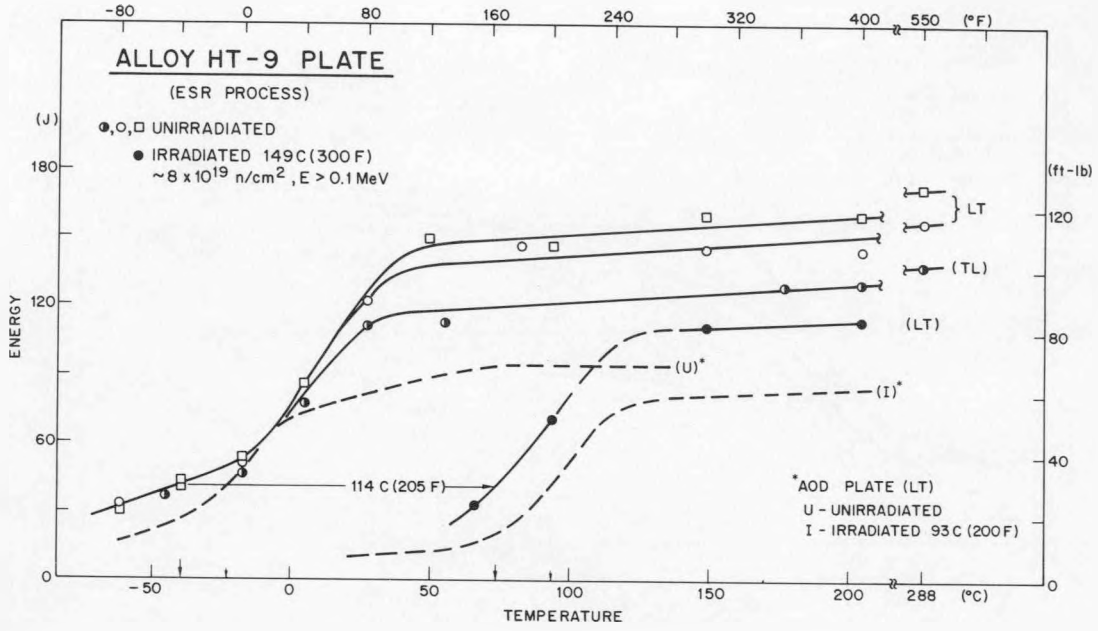

7.8.5 Comparison of radiation embrittlement resistances of ESR vs. AOD Alloy HT-9 plates for neutron exposure in the range 93°C to 149°C.

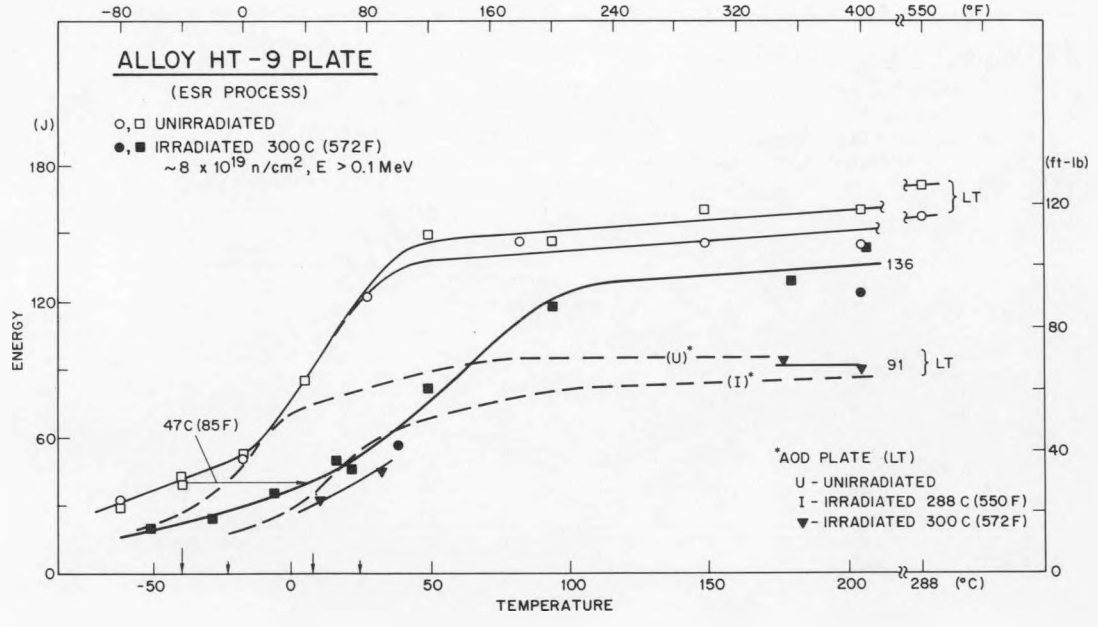

7.8.6 Comparison of radiation embrittlement resistances of ESR vs. AOD Alloy HT-9 plates for neutron exposure in the range 288°C to 300°C.

7.9 EFFECT OF SPECIMEN SIZE AND NICKEL CONTENT ON THE IMPACT PROPERTIES OF 12 Cr-1 MoVW FERRITIC STEEL — W. R. Corwin, R. L. Klueh, and J. M. Vitek (Oak Ridge National Laboratory)

7.9.1 ADIP Task

ADIP tasks are not defined for Path E, ferritic steels in the 1978 program plan.

7.9.2 Objective

The objective of this study is to provide baseline impact property data (unirradiated) on several heats of 12 Cr-1 MoVW steel with varying nickel contents. These data on full- and subsize impact specimens are designed to qualify the subsequent irradiation effects testing that will be conducted with subsize specimens.

7.9.3 Summary

Charpy impact properties were developed on six heats of 12 Cr-1 MoVW steel with full- and subsize specimens to examine effects of nickel and chromium adjustments. These data provide a baseline for comparison of effects of irradiation on the impact properties of these alloys.

7.9.4 Progress and Status

7.9.4.1. Introduction

The irradiation-resistant properties of ferritic (martensitic) steels, such as those based on 12 Cr-1 Mo and 9 Cr-1 Mo, have led to consideration of these alloys for use as fusion reactor first-wall and blanket structural components. Under the high-energy (up to 14.1 MeV) neutron flux from the deuterium-tritium fusion reaction, not only would a large number of atomic displacements occur, but also large amounts of helium would be generated in transmutation reactions. A major concern under these conditions is reduction of the fracture resistance. The relationship between helium concentration and displacement damage for austenitic and ferritic steels for various test reactors and a tokamak neutron spectrum has been established.[1] Because no adequate source of deuterium-tritium fusion neutrons exists, an alternative method for simulating 14-MeV neutron irradiation effects must be used. In alloys containing nickel, such effects can be simulated in mixed-spectrum fission reactors, in which the two-step transmutation reaction of ^{58}Ni with thermal neutrons produces helium. This technique has been widely used to study helium effects in austenitic stainless steels containing high nickel concentrations. However, the commercial steels based on 12 Cr-1 Mo generally contain less than 0.5% Ni, which is not adequate for this helium simulation. If these alloys contained about 2% Ni, irradiation in the High Flux Isotope Reactor (HFIR) would produce about the same ratio of helium to displacements per atom as the original alloys would develop during service in a fusion reactor.[1]

Impact testing is planned to assess the effects of simultaneous helium and displacement damage on the degradation in fracture resistance of 12 Cr-1 Mo–base steels. This will be done by irradiating nickel-doped 12 Cr-1 MoVW steels in HFIR.[2] However, because of irradiation volume limitations it will be possible to irradiate only subsize Charpy-type impact specimens. Therefore, to characterize the effects of the nickel doping on the 12 Cr-1 Mo steels more fully before irradiation and to evaluate the capabilities of the subsize impact specimen, both full- and subsize Charpy V-notch impact specimens were tested.

7.9.4.2 Experimental

Four electroslag-remelted (ESR) heats of 12 Cr-1 MoVW ferritic steels with varying nickel contents were prepared by Combustion Engineering, Inc., Chattanooga, Tennessee (C-E). The compositions of the alloys were based on the commercial Sandvik alloy HT9. This alloy, containing about 0.2% C and including the carbide-forming elements vanadium (~0.3%) and tungsten (~0.5%), is referred to here by its generic designation, 12 Cr-1 MoVW; it contains nominally 0.5% Ni.

In addition to preparing the basic alloy (heat XAA-3587), steels were also prepared with the same basic composition, but with 1 and 2% Ni (heats XAA-3588 and XAA-3589, respectively). Finally, a 12 Cr-1 MoVW-type alloy with 2% Ni was prepared (heat XAA-3592) in which the ferrite-forming element concentrations were increased to give the steel a net chromium equivalent similar to that of the low-nickel base alloy.[1,3] To adjust the net chromium equivalent to account for the nickel additions, the ferrite-forming elements Cr, Mo, and W were added but were kept within the Sandvik HT9 composition range specified for them.

Two additional commercial ESR heats were also tested (9607-R2 and 91354). Heat 9607-R2 is the national fusion program heat, and 91354 is a heat from the fast breeder reactor program. The chemical compositions of the alloys tested and their tensile properties have been reported.[1,4]

The steels were tested in the normalized-and-tempered condition. The steel plates from which the specimens were taken were austenitized for 0.5 h at 1050°C in an argon atmosphere, and then gas cooled. Tempering treatments were also carried out in argon, followed by gas cooling. The three 12 Cr-1 MoVW heats of the steel with 1% Ni were tempered 2.5 h at 780°C, the 2% Ni alloy was tempered 5 h at 700°C, and the 2% Ni (adjusted) alloy was tempered 8 h at 700°C. This resulted in a completely tempered martensitic microstructure for all heats except the 2% Ni (adjusted) heat. The adjusted heat contained about 25% δ-ferrite. The reason for the different tempering temperatures is discussed elsewhere.[1]

Two types of impact specimens were tested for each heat. Full-size specimens were used according to ASTM specification E 23 with dimensions of 10 by 10 by 55 mm containing a 2-mm-deep 45° V-notch with a 0.25 mm root radius. Subsize specimens were 5 by 5 by 25.4 mm in overall dimensions containing a 0.76-mm-deep 30° V-notch with a 0.05 to 0.08 mm root radius. All specimens were in the L-T orientation.[5]

Both types of specimens were tested on a specially modified pendulum-type instrumented impact machine. For testing the full-size specimens, the impact machine was configured and calibrated in exact accordance with ASTM E 23. To test the subsize specimens, the machine was modified by replacing the standard anvils and tup. The modified anvils supported the subsize specimen so that its relative position with respect to the pendulum was the same as that for the full-size specimen; i.e., the center of percussion of the pendulum is maintained at the point of impact while the specimen is kept just touching the striker with the pendulum hanging free. The 4:1 ratio of span-to-specimen width was maintained, and the minimum distance between the anvil radii was 20 mm. This follows the E 23 definition of span in contrast with the practice of previous researchers.[6] The tup thickness for the subsize specimen was reduced to 4 mm to allow clearance of the specimen halves between the anvils. Specimen temperature conditioning for both size specimens was by means of a hot air-cold nitrogen gas chamber in conjunction with a rotary positioning arm.[7] Temperatures were maintained within ±2°C.

Each individual Charpy data set was fitted to a hyperbolic tangent function for obtaining transition temperature and upper-shelf energy.

7.9.4.3 Results and Discussion

To establish baseline impact notch toughness for 12 Cr-1 MoVW, the three standard HT9 heats were compared. The upper-shelf data from full-size specimens of the C-E heat fell between the breeder and fusion ESR heats, and all had similar transition temperatures (Fig. 7.9.1). The results from the breeder and fusion heats compare quite well with reported information.[6] The test results of the subsize Charpy specimens for the same three heats (Fig. 7.9.2) agree qualitatively with those of full-size specimens. The transition temperatures of the subsize specimen data sets are all about equal to each other, but the lower energy of the upper shelf of the fusion ESR heat was not reflected in the subsize specimens. In an absolute comparison, the transition temperatures as measured with the subsize specimens were about 20°C lower than those measured with the full-size specimens. This is consistent with previous work on subsize V-notched impact specimens whose orientation, product form, heat treatment, and other parameters were held constant.[8-9] Note that the transition temperature reported here is arbitrarily defined as the temperature corresponding to one-half the upper-shelf energy. Although this does not agree with more conventional definitions (e.g., absolute energy levels or fracture appearance), it is self-consistent and is useful in comparing different sizes of Charpy-type impact specimens.

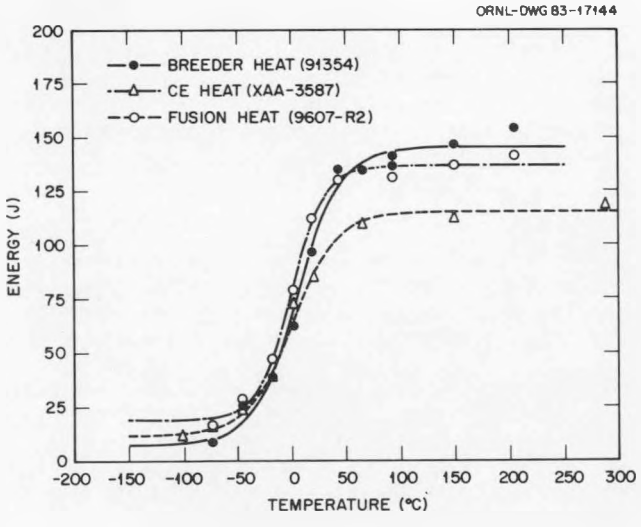

Fig. 7.9.1. Impact energy of full-size Charpy specimens for three heats of 12 Cr-1 MoVW steel.

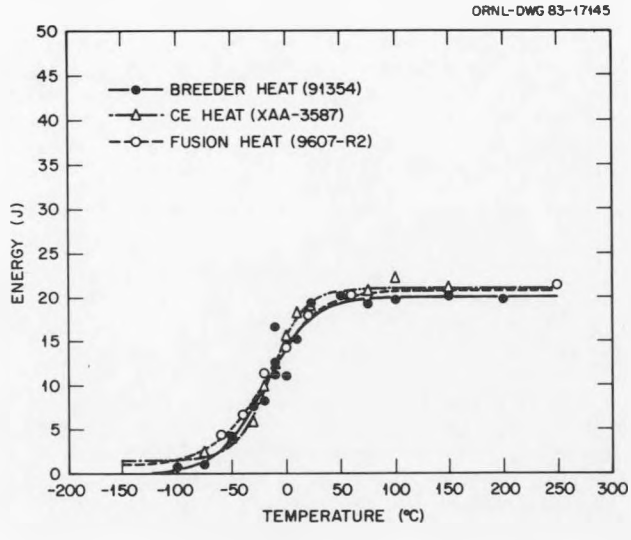

Fig. 7.9.2. Impact energy of subsize Charpy specimens for three heats of 12 Cr-1 MoVW steel.

The effect of nickel additions and chromium-equivalent adjustments on the full-size Charpy impact properties (Fig. 7.9.3) of 12 Cr-1MoVW agree well with typical effects in lower alloy pearlitic steels.[10] Additions of nickel tend to decrease both the transition temperature and upper-shelf energy. Additions of Cr, Mo, and W and the resultant two-phase microstructure tended to raise the transition temperature. The results for the subsize specimens (Fig. 7.9.4) again agree qualitatively with those of the full-size Charpys, although their transition temperatures are also about 15 to 20°C lower than those of the corresponding larger specimens.

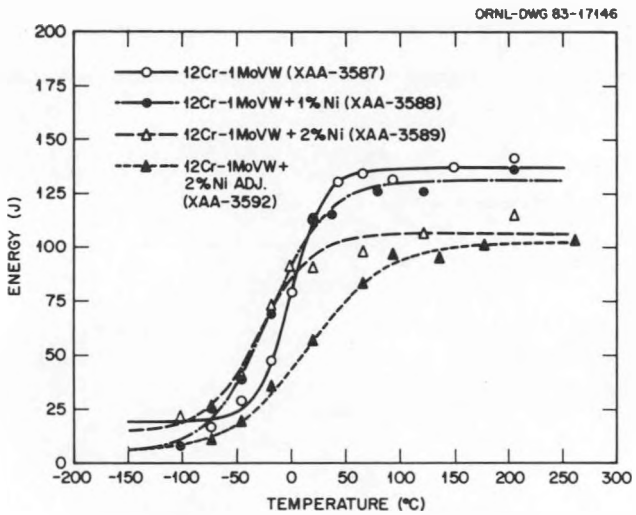

Fig. 7.9.3. Effect of nickel additions and chromium equivalent adjustment on the full-size Charpy specimen impact energy of 12 Cr-1 MoVW steel.

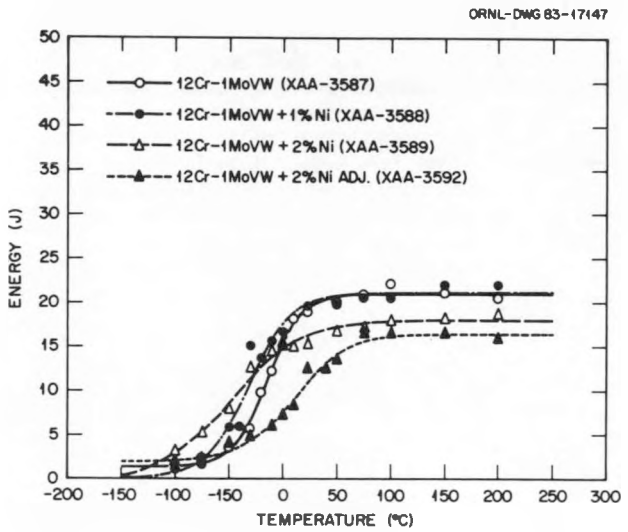

Fig. 7.9.4. Effect of nickel additions and chromium equivalent adjustment on the subsize Charpy specimen impact energy of 12 Cr-1 MoVW steel.

To improve the correspondence of the full-size and subsize data sets, the data were normalized by a nominal fracture area and fracture volume. The impact energies of the specimens were normalized by dividing by the nominal fracture area Bb (80 and 21 mm^2 for full- and subsize specimens, respectively) or the nominal fracture volume $(Bb)^{3/2}$, (720 and 98 mm^3 for full- and subsize specimens, respectively), where B is the specimen width and b is the depth of the ligament.

At lower energy levels, at which flat fracture is predominant, an area normalization would be expected to correlate the data better. At higher energy levels, at which more material is plastically deformed and shear lips develop, a volume-based normalization should yield better results.

The better correspondence between the full- and subsize data sets was for upper-shelf energies normalized to nominal fracture volume. However, agreement was still only fair, with the energy per unit volume being consistently greater for the subsize specimens. The undoped heat XAA-3587, for example, shows that the volume-normalized upper-shelf energy for the subsize specimens exceeds that of the full-size by about 10% (Fig. 7.9.5). Normalization on an area basis produced no agreement between the different specimen sizes. The transition temperatures and upper-shelf energies for all six heats are summarized in Table 7.9.1.

The primary use of the subsize specimens in the fusion reactor materials research program is to measure the changes of fracture resistance due to irradiation embrittlement; the results of the subsize specimen will be useful as comparative baseline data. However, if direct comparisons with full-size Charpy results and the use of existing correlation methods for such data are required, development of a more sophisitcated analysis or testing method will be necessary.

7.9.5 Conclusions

Six heats of 12 Cr-1 MoVW steels were impact tested to examine the effect of nickel and chromium equivalent variations on the fracture resistance. Nickel, added intentionally to more accurately simulate irradiation damage in future experiments, lowered both the upper-shelf energy and the transition temperature of the steels. Adjusting the net chromium equivalent of the nickel-doped steel to equal that of the undoped steel lowered the upper-shelf energy and raised its transition temperature.

Subsize impact specimens produced data qualitatively in agreement with full-size specimens but with lower transition temperatures. Normalization of the fracture energy of full- and subsize specimens by nominal fracture areas produced little agreement between the different size specimens. Use of the nominal fracture volume improved the data coincidence, but agreement was still within only about 20%.

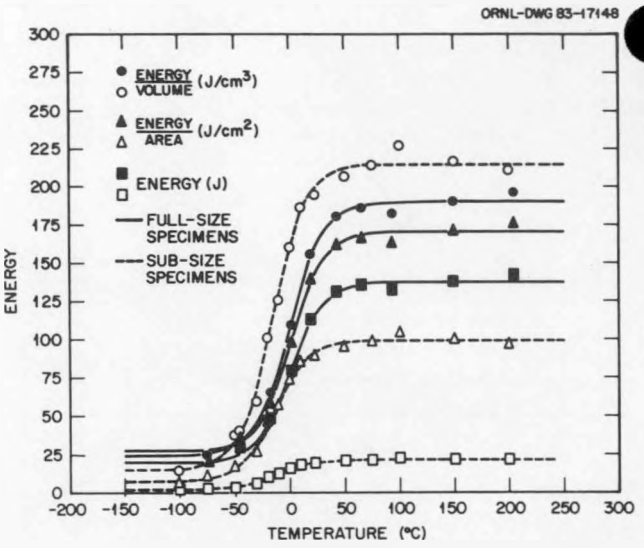

Fig. 7.9.5. Effects of area and volumetric normalization of the impact energy for full- and subsize specimens of the Combustion Engineering 12 Cr-1 Mo steel, heat XAA-3587.

Table 7.9.1. Transition temperature and upper-shelf energy of full- and subsize Charpy impact specimens at 12 Cr-1 MoVW steel

Heat	Transition temperature[a] (°C)		Upper shelf energy					
			Unadjusted (J)		Area normalized[b] (J/cm²)		Volume normalized[c] (J/cm³)	
	Full size	Sub-size	Full size	Sub-size	Full size	Sub-size	Full size	Sub-size
9607-R2	–2.4	–21.1	115	20.7	142	98	160	213
91354	3.9	–20.0	146	20.1	185	95	202	205
XAA-3587	–2.5	–16.1	137	21.0	170	99	189	215
XAA-3588	–13.0	–32.2	133	21.0	163	100	183	216
XAA-3589	–33.8	–49.5	106	18.0	132	85	147	184
XAA-3592	13.2	6.5	102	16.5	127	78	141	169

[a]Temperature at one-half the upper shelf energy.

[b]Test energy divided by Bb, where B is the specimen width and b is the ligament size.

[c]Test energy divided by $(Bb)^{3/2}$, where B is the specimen width and b is the ligament size.

7.9.6 References

1. R. L. Klueh, J. M. Vitek, and M. L. Grossbeck, "Nickel-Doped Ferritic (Martensitic) Steels for Fusion Reactor Irradiation Studies: Tempering Behavior and Unirradiated and Irradiated Tensile Properties," pp. 648–64 in *Effects of Radiation on Materials: Eleventh Conference*, eds. H. R. Brager and J. S. Perrin, ASTM STP 782 American Society for Testing and Materials, Philadelphia, 1982.

2. J. M. Vitek et al., "HFIR-MFE-T1, -T2 and -RB1: Experiments to Evaluate the Effects of Low-Temperature Irradiation on Ferritic Steels," pp. 26–35 in *ADIP Quart. Prog. Rep. Sept. 30, 1980*, DOE/ER-0045/4, U.S. DOE, Office of Fusion Energy.

3. C. J. Boyle and D. L. Newhouse, *Met. Prog.* 87, 61–62 (1965).
4. T. A. Lechtenberg, "The Procurement and Characterization of the Electroslag Remelted National Fusion Program Heat of 12 Cr-1 Mo Steel," pp. 363–69 in *ADIP Semiannu. Prog. Rept. March 31, 1982*, DOE/ER-0045/8, U.S.DOE, Office of Fusion Energy.
5. "Standard Test Method for Plane-Strain Fracture Toughness of Metallic Materialsm"E 399-83, pp. 518–53 in *1983 Annu. Book ASTM Stand.* Vol. 03.01 (1983).
6. W. L. Hu, "Miniature Charpy Impact Test Results for Irradiated Ferritic Alloys," pp. 255–71 in *ADIP Semiannu. Prog. Rept. September 30, 1982*, DOE/ER-0045/8, U.S. DOE, Office of Fusion Energy.
7. E. O. Fromm, M. P. Ludlow, and J. S. Perrin, "Remote Charpy V-Notch Impact Testing of Pressure Vessel Steels," pp. 116–20 in *Transactions of American Nuclear Society International Conference on World Energy Accomplishments and Perspectives.*
8. G. E. Lucas, J. W. Sheckland, and G. R. Odette, "Developments in Small Scale Strength and Impact Testing," p. 43 in *DAFS Quart. Prog. Report. Sept. 30, 1983*, DOE/ER-0046/11, U.S. DOE, Office of Fusion Energy.
9. W. R. Corwin and A. G. Hougland, "Effect of Specimen Size and Material Condition on Charpy Impact Properties of 9 Cr-1 MoVW," pp. 131–37 in *ADIP Semiannu. Prog. Rept. March 31, 1983*, DOE/ER-0045/10 U.S. DOE, Office of Fusion Energy.
10. J. A. Rinebolt and W. J. Harris, Jr., *Trans. Am. Soc. Met.* 43, 1175–1214 (1951).

7.10 GRAIN BOUNDARY SEGREGATION AND EMBRITTLEMENT IN A 12CR-1MO STEEL RESULTING FROM COOLING RATE VARIATIONS - J. M. Hyzak and W. M. Garrison, (Sandia National Laboratories, Livermore, CA)

7.10.1 ADIP Task

The Department of Energy (DOE) Office of Fusion Energy (OFE) has cited the need for these data under the ADIP Program Task, Ferritic Alloy Development (Path E).

7.10.2 Objective

The goal of this work was to determine the influence of cooling rate from both the austenitization and tempering temperature on grain boundary segregation and tensile fracture.

7.10.3 Summary

Segregation of embrittling elements, especially phosphorous, to the prior austenite grain boundaries in this 12Cr-1Mo steel has been shown to reduce tensile ductility, increase grain boundary fracture, and affect hydrogen compatibility. Tests were performed to determine the influence of variations in cooling rate during heat treatment on the tensile properties. The non-hydrogen exposed tensile ductility increased and the occurence of intergranular rupture decreased as the cooling rates were increased. Phosphorous segregation at the prior austenite grain boundaries also decreased as the cooling rates were increased.

7.10.4 Progress and Status

7.10.4.1 Introduction

The 12% chromium martensitic/ferritic steel, HT-9, is being evaluated as a first wall blanket material for fusion reactors. In this application, the compatibility of the alloy with hydrogen is of importance. Previous research at Sandia, Livermore has shown that an internal concentration of 2 wppm hydrogen reduced the tensile ductility (reduction in area) of quenched-and-tempered HT-9 from 54% to 36%. Charging to a hydrogen concentration of 4 wppm further reduced the ductility to 10% RA and changed the fracture mode from dimpled rupture to brittle intergranular fracture.[1]

It has also been shown that HT-9 is susceptible to intergranular embrittlement even in the uncharged condition.[1]. Tensile specimens with the commercial heat treatment (1050°C for 1/2 hour and air cooled followed by a 1 hour temper at 750°C then again air cooled) failed by a dimple rupture fracture mode along prior austenite grain boundaries. This was attributed to a combination of a near-continuous network of grain boundary carbides and segregation of embrittling elements, especially phosphorous, to these boundaries. The results of the hydrogen-charged tensile tests and the tendency for the uncharged tensile specimens to fail along prior austenite boundaries both indicate that the material tested is prone to hydrogen embrittlement.

Grain boundary segregation is known to be affected by heat treatment during austenitization and tempering.[2,3] Therefore, it was decided to study the influence of cooling rate variations from both the austenitization temperature (1050°C) and the tempering temperature (750°C) on the uncharged tensile ductility. Auger analysis was also performed to determine the effect of cooling rate on segregation levels, particularly of phosphorous.

7.10.4.2 Experimental Procedure

The 12Cr-1Mo material used was from the electroslag remelted (ESR) National Fusion Heat. The stock was obtained from GA Technologies as 1.59 cm thick plate. Tensile specimen blanks were austenitized at 1050°C for 1/2 hour and tempered at 750°C for 1 hour. After both austenitizing and tempering, three cooling methods were employed: rapid quench in oil or ice brine, static air cool, and aslow cool in diatomaceous earth. The blanks were quenched in oil from the austenitization temperature and in ice brine after tempering. The slow cooled specimens took approximately one day to reach room temperature. This matrix of conditions resulted in nine different experimental heat treatments; two specimens were tensile tested in the uncharged condition for each.

Tensile tests were performed at a crosshead rate of 0.05 cm/min. Tensile ductility was measured by reduction-in-area. The 0.2% yield strength and the ultimate tensile strength were also determined.

7.10.4.3 Experiment Results

The tensile results are shown in Table 1 and the average of the two ductility values are presented in Figure 1 as a function of cooling rate. The tensile ductility decreased with decreasing cooling rate after both austenitizing and tempering. The yield and ultimate strengths were not affected by cooling rate after austenitization, but both generally increased as the cooling rate after tempering decreased.

TABLE 1

Tensile Properties

	RA%	0.2% Y.S.(MPa)	UTS (MPa)
Oil Quench From Austenitization			
Quench from Temper	61.2	707	887
	59.0		
Air Cool from Temper	60.5	695	870
	59.5		
Slow Cool from Temper	57.9	754	907
	57.8		
Air Cool From Austenitization			
Quench from Temper	58.3	716	912
	60.6		
Air Cool from Temper	56.8	764	937
	53.7		
Slow Cool from Temper	52.3	788	941
	55.9		
Slow Cool from Austenitization			
Quench from Temper	51.4	696	902
	54.4		
Air Cool from Temper	52.0	709	904
	51.8		
Slow Cool from Temper	48.0	729	911
	48.5		

Examination of the tensile fracture surfaces in the scanning electron microscope (SEM) showed a corresponding change in fracture appearance with the changes in cooling rate. All specimens exhibited a dimpled rupture fracture mode. However, the specimens with least ductility (slow cooled samples) had a greater tendency to fracture along prior austenite grain boundaries; fracture by void nucleation and growth (dimpled rupture) along grain boundaries is termed intergranular rupture. Examples of this are shown in Figure 2 for a quenched specimen (oil quench from austenization and ice brine quenched after tempering, O.Q./I.B.Q.) and a slow cooled specimen (slow cooled from both austenization and tempering, S.C./S.C.). These specimens had average tensile ductilities of 60% and 48%, respectively. The slow-cooled specimens showed considerably more secondary cracking which is a result of the intergranular rupture process.

Auger analysis was performed on samples from these same two heat treatments, O.Q./I.B.Q. and S.C./S.C. Specimens were machined from the heat treated blanks and were then charged with hydrogen prior to fracture in vacuum in the Auger chamber. The reason for hydrogen charging was to insure brittle fracture at the prior austenite boundaries, the area of primary interest. The surface measurements showed consistently higher levels of phosphorous, chromium and molybdenum on the brittle intergranular facets compared to the ductile fracture regions. Although additional testing and analyses are required to determine the interaction of the elements, the data presently suggest that chromium and molybdenum cosegregate in discrete regions along the boundary while phosphorous is present uniformly on the intergranular facet. Since chromium and molybdenum are carbide formers, their increased concentration at the grain boundaries is probably due to the presence of the large carbide precipitates there.

The phosphorous composition was profiled as a function of depth below the intergranular facet for both the O.Q,/I.B.Q. and S.C./S.C. samples. The specimens slow cooled from both the austenitization and tempering temperature had a surface phosphorus concentration on the intergranular facet of approximately 1.5 at.% which is almost two orders of magnitude greater than the average heat concentration of 0.028 at.%. The phosphorous concentration decayed exponentially to the bulk value at a depth of approximately 60 nm below the surface. The water-quenched specimen had a surface phosphorous concentration on the intergranular facets of approximately 1.0 at.%, and this concentration decayed to the bulk value in only 25 nm.

7.10.4.4 Discussion

The results of the tensile tests have shown a strong correlation between tensile ductility, tensile fracture, and cooling rate. The faster the cooling rate, the greater was the ductility as evidenced by less intergranular rupture on the fracture surfaces. The Auger analyses have also established that the phosphorous segregation at the prior austenite grain boundaries increases with decreasing cooling rates after austenitizing and tempering.

The effect of heat treatment on grain boundary segregation agrees with other studies which have measured phosphorous segregation at prior austenite grain boundaries during austenitization[4] and tempering.[5] In both studies the synergistic effects of chromium and molybdenum on phosphorous segregation

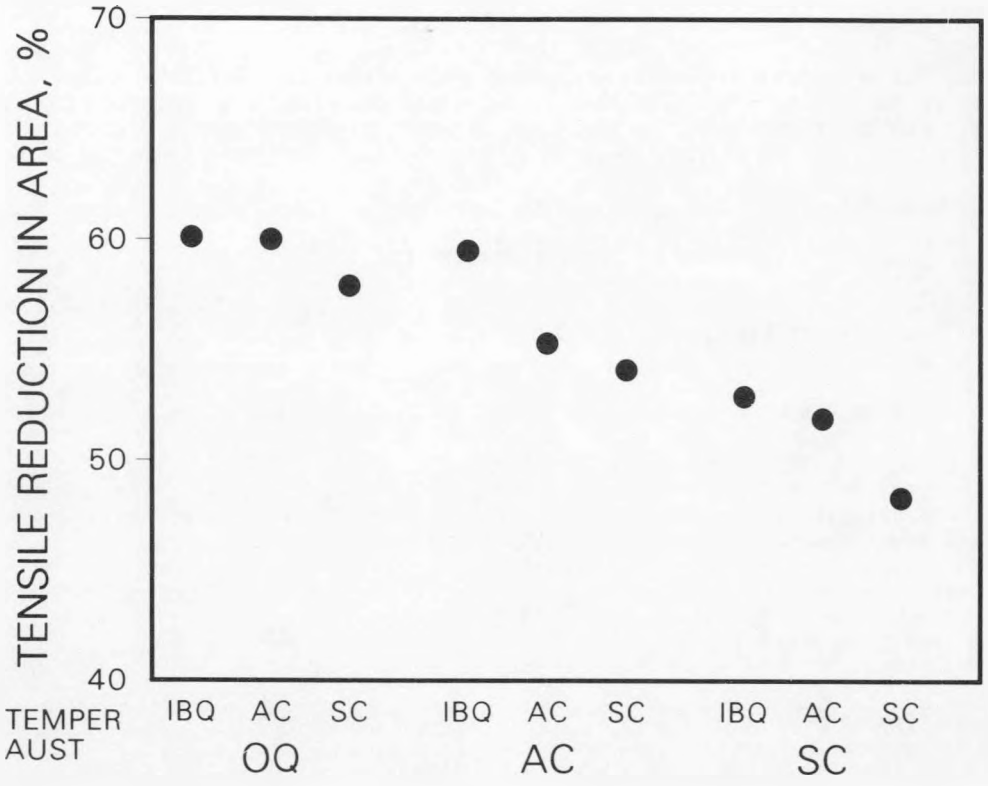

Figure 1. Tensile ductility as a function of cooling rate from both the austenitization and tempering temperatures.

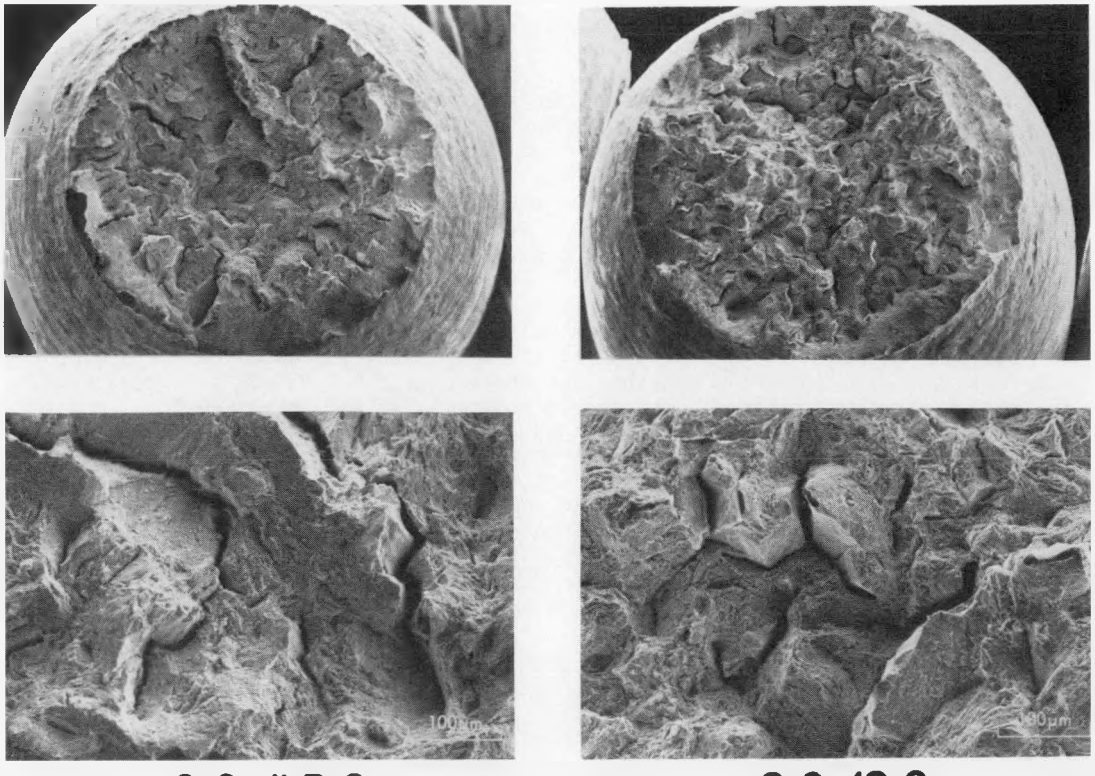

Figure 2. Tensile fracture appearance of quenched (O.Q./I.B.Q.) and slow cooled (S.C./S.C.) specimens.

were also noted. More detailed STEM (scanning-transmission electron microscopy) studies are planned to better understand the partitioning of elements at the grain boundaries in this alloy.

The reduced ductility and more extensive intergranular rupture observed in the S.C./S.C. samples might not be totally due to an increase in grain boundary phosphorous concentration. The yield strength also increased as the cooling rate after tempering decreased. This change in strength indicates that a microstructural change, probably in carbide morphology, is also occurring as a result of the slower cooling rates. Additional research is needed to clearly define the effects of segregation and microstructure on intergranular cracking. The present work has established, however, that even with rapid cooling from both the austenitization and tempering temperatures, this 12Cr-1Mo alloy still exhibits grain boundary embrittlement.

Although the hydrogen-charged ductilities have not been measured in this study, it has been found that phosphorous segregation[2,3] and an intergranular rupture fracture mode in the uncharged condition[1] are both indications of potentially poor hydrogen compatibility. Our experiments on uncharged samples therefore add to our concern that this alloy is prone to grain boundary embrittlement when uncharged and considerably more so when exposed to hydrogen. Efforts are continuing to obtain a different heat of this same alloy with an unusually low phosphorous level and to directly test the hydrogen compatibility of the alloy.

7.10.5 Conclusions

1. The uncharged tensile ductility and fracture mode of this 12Cr-1Mo steel is sensitive to variations in cooling rate from the austenitization and tempering temperatures. The tensile ductility increased and the occurrence of intergranular rupture decreased as the cooling rates were increased.
2. Phosphorous segregation at the prior austenite grain boundaries also decreased as the cooling rates were increased.
3. Even when quenched from the austenization and tempering temperatures, the alloy exhibited some intergranular cracking in the uncharged condition. This grain boundary weakness indicates a potential susceptibility to hydrogen embrittlement.

7.10.6 References

1. J. M. Hyzak and W. M. Garrison, "Hydrogen Embrittlement of ESR Processed 12Cr-1Mo Steel," Alloy Development for Irradiation Performance Report, Dept. Energy, DOE/ER-0045/8, March, 1982, pp. 401-13.
2. C. J. McMahon, Jr., V. Vitek and J. Kameda, "Mechanics and Mechanisms of Intergranular Fracture," Developments in Fracture Mechanics-2 The Mechanics and Mechanisms of Fracture in Metals, G. G. Chell, ed., pp. 193-246, Applied Science Publishers, London, 1981.
3. C. L. Briant and S. K. Banerji, "Intergranular Failure in Steels: The Role of Grain Boundary Composition," Int'l Metals Rev., 4 (1978) pp. 164-199.
4. J. Q. Clayton and J. F. Knott, "Phosphorous Segregation in Austenite in Ni-Cr and Ni-Cr-Mn Steels", Metal Science, 16, (1982), pp. 145-151.
5. Ph. Lemble, A. Pineau, J. L. Castagne, Ph. Dumoulin, and M. Guttmann, "Temper Embrittlement of 12%Cr Martensitic Steel", Metal Science, 13, (1979), pp. 496-502.

7.11 AN ASSESSMENT OF THE WELDABILITY OF HT-9 USING A Y-GROOVE TEST. - J. F. Hilderbrand, J. R. Foulds a T. A. Lechtenberg (GA Technologies)

7.11.1 ADIP Task

The Department of Energy/Office of Fusion Energy has cited the need to investigate ferritic/matensitic alloys under the ADIP program task, Ferritic Steels Development (Path E).

7.11.2 Objective

The weldability of martensitic steels, an important issue, needs to be assessed for proper component design. Weld process variables, such as preheat temperature, may be adjusted to minimize cracking. This study assesses the weldability of 12Cr-1Mo HT-9 with respect to cracking as a result of restraint and notch sensitivity and also as a result of post-weld thermal shock.

7.11.3 Summary

A minimum preheat temperature of 200°C (392°F) was found necessary for gas tungsten-arc (GTA) welding HT-9 plate of thickness 9.5mm (3/8 in.) and 16mm (5/8 in.). Thermal shock treatments produced no cracking in welded test specimens.

7.11.4 Progress and Status

7.11.4.1 Introduction

Several methods have been published for weldability testing, depending on the type of cracking to which sensitivity is being assessed, e.g. hot-cracking, hydrogen-induced cracking, underbead or root-cracking. With high strength martensitic steels cracking is often observed to initiate in the heat-affected zone (HAZ) and propagate into weld metal.[2] The Y-groove weldability test[2], similar to the Tekken restraint test, was primarily designed to study crack sensitivity of the HAZ.[3] In a Y-groove test both weld metal and HAZ exist at the notch created as a result of bead deposition. Thus, susceptibility to cracking in both weld and HAZ regions is enhanced through a stress intensity factor.

7.11.4.2 Experimental

Plates of the AOD heat of HT-9[4], 9.5mm (3/8 in.) and 16 mm (5/8 in.) thick were used for this experiment. Figure 7.11.1 is a schematic of the Y-groove butt joint design and test set-up. The end support welds were multipass shielded metal arc (SMA) using MTS-4 filler wire and no preheat temperature. A single bead was deposited in the root of the Y-groove using the gas tungsten-arc (GTA) process with helium, 2.5 mm (3/32 in.) MTS-4 filler wire, 180-190 Ampere at 21 volts and a travel speed of 3 in. per minute. The preheat temperatures were room temperature, 100°C (212°F) and 200°C (392°F), provided by touch heating and the temperature was measured by a contact pyrometer.

The as-welded plates were then radiographed in accordance with ASME Code Section VIII in addition to visual examination.

Weldments exhibiting radiographic indications of defects were sectioned and metallographically examined. Surviving weldments (no defects visible) were then subjected to thermal cycling in a resistance furnace with temperatures measured on the plate surface near the weld. Thermal cycles used are described in Table 7.11.1.

Table 7.11.1
Thermal cycles shock testing of Y-groove weldments

Type	Max. Temperature	Heating Rate (°C/Min.)	Cooling Rate (°C/Min.)
A	760°C (1400°F)	4.2	0.4
B	760°C (1400°F)	18.5	6.7
C	815°C (1500°F)	102	25.9

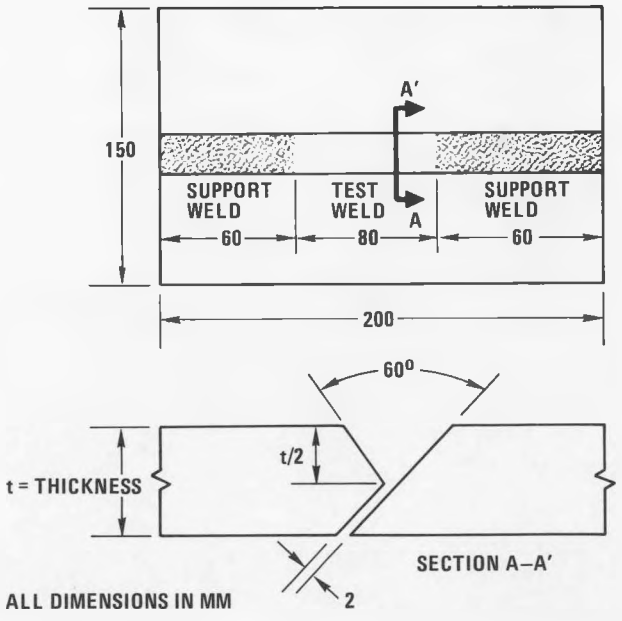

Fig. 7.11.1 Schematic of Y-groove butt joint design and test set-up

Type C represents the most severe cycling. Times at peak temperature were less than 5 minutes. The test specimens were again radiographed for defects and metallographically analyzed where necessary.

7.11.4.3 Results and Discussion

Table 7.11.2 summarizes the results obtained on a set of Y-groove heat welds.

Table 7.11.2
Y-Groove test results

Spec. #	Plate Thickness in. (mm)	Preheat Temp. °C (°F)	Cracking[a]
1	3/8 (9.5)	25 (78)	Yes
2	3/8 (9.5)	100 (212)	Yes
3	3/8 (9.5)	200 (392)	No[b]
4	5/8 (16)	25 (78)	Yes
5	5/8 (16)	100 (212)	Yes
6	5/8 (16)	200 (392)	No[c]

(a) Visible cracks through radiography and metallographic inspection.
(b) Weld defects through radiography; shrinkage, gas porosity and lack of fusion observed metallographically.
(c) Weld defect through radiography; interdendritic, porosity observed metallographically.

Figure 7.11.2 shows a typical Y-groove test weld and part of the adjacent support welds. The single pass bead lay well below the upper plate surfaces and the narrow gap made bead deposition difficult.

Macroscopically visible cracking was observed in all test welds prepared with preheats of room temperature and 100°C. Figure 7.11.3 is a macroetched transverse section view of a weld crack in the 5/8" thick room temperature preheat Y-groove weldment. The crack appears to originate at the fusion boundary at the notch formed by the bottom of the weld bead and the straight-edged base metal plate. Propagation of the crack proceeded into the weld metal in all cases.

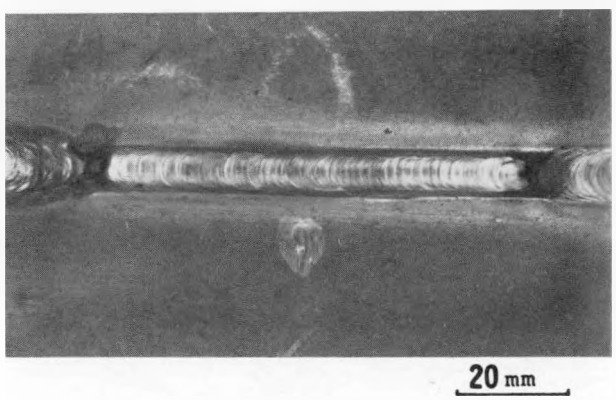

Fig. 7.11.2 Typical Y-groove test weld with part of adjacent support welds

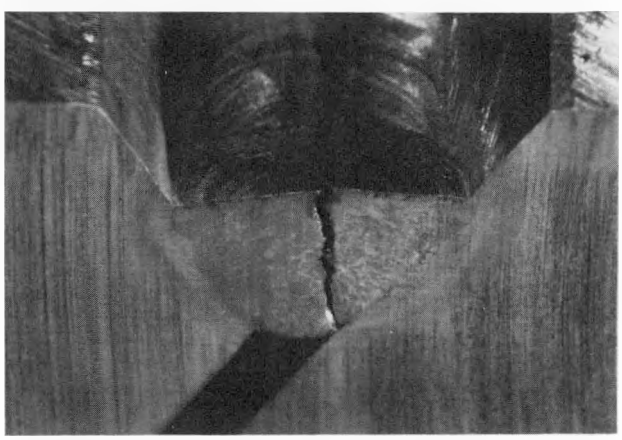

Fig. 7.11.3 Macroetched transverse section of weld crack in 5/8" thick, room temperature preheat HT-9 weldment

Test welds prepared with a 200°C preheat indicated weld defects through X-ray radiography. The test welds were sectioned at locations where radiography indicated defects and the sections metallographically polished, etched and examined. In all cases, the radiographic indications proved to be as a result of the weld-process (shrinkage, lack of fusion defects, etc.) and not Y-groove cracking. Figures 7.11.4 through 6 are examples of interdendritic shrinkage porosity in the 3/8", 200° C preheat (#3), 5/8", 200°C preheat (#6) and lack of fusion with gas porosity in the 3/8", 200°C preheat (#3) test welds respectively.

A set of 3 Y-groove test welds prepared each from 3/8" and 5/8" thick plate with a preheat temperature of 200°C was prepared for thermal cycling. These were examined visually and radiographically. No weld cracks were observed. Thermal cycling conducted as per Table 7.11.1 did not result in Y-groove cracking on

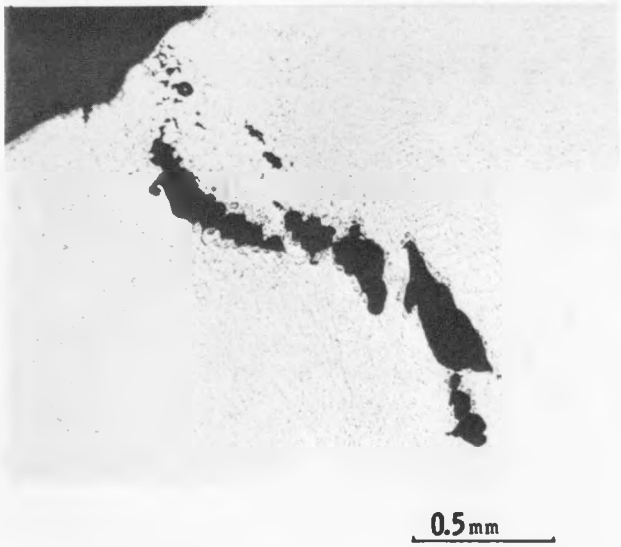

Fig. 7.11.4 Interdendritic shrinkage porosity in 3/81" thick, 200°C preheat Y-groove test weld

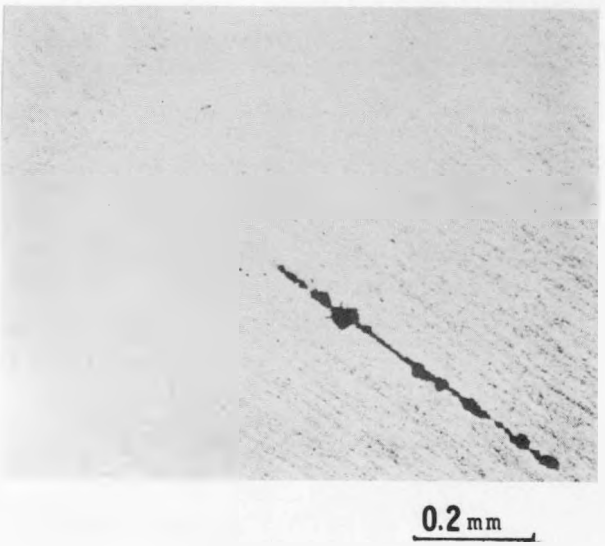

Fig. 7.11.5 Interdendritic shrinkage porosity in 5/8" thick, 200°C preheat Y-groove test weld

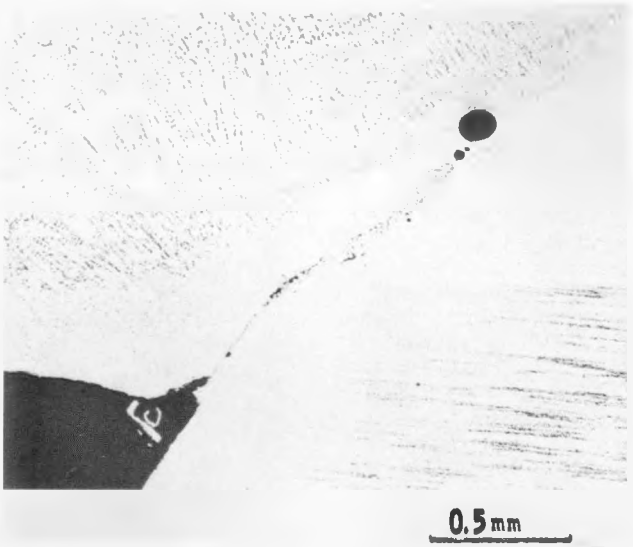

Fig. 7.11.6 Lack of fusion and gas porosity in 3/8" thck, 200°C preheat Y-groove test weld

post-thermal cycling examination (radiography and metallography). The structural integrity of Y-groove test welds GTA prepared with a 200°C preheat on 3/8" and 5/8" thick plate was maintained even with severest notch and thermal cycling conditions.

7.11.5 Conclusions

Y-groove and thermal shock tests on HT-9 plate indicate that a minimum preheat temperature of 200°C is recommended for GTA welding of plate thicknesses 3/8" and 5/8" to eliminate weld crack susceptibility.

7.11.6 References

1. Welding Handbook, vol. 1, Ed. C. Weisman, American Welding Society, Florida, pp 143-148 (1976).
2. H. Kihara: 1968 Int. Inst. of Welding Houdremont Lecture, Welding in the Construction Maintenance of Equipment for the Chemical Industry, Oct. 1968, pp 2-21
3. M. Inagaki and H. Nakamura, High Pressure, v. 3, No. 6 (1965) p. 592.
4. T. A. Lechtenberg et al., ADIP March 1980, DOE/ER-0045/2, pp 109-131.

7.12 TIME-TEMPERATURE CHARACTERISTICS OF THE VARIOUS HEAT-AFFECTED ZONES IN HT-9 WELDMENTS - J.. R. Foulds (GA Technologies Inc.)

7.12.1 ADIP Task

The Department of Energy/Office of Fusion Energy has cited the need to investigate ferritic/martensitic alloys under the ADIP program task, Ferritic Steels Development (Path E).

7.12.2 Objective

The objective of this study is to measure the peak temperatures and the thermal histories of the various heat-affected regions during gas tungsten-arc (GTA) welding of HT-9.

7.12.3 Summary

Temperatures at different distances from the fusion boundary were measured during GTA weld depositing MTS-4 filler wire on 9.52-mm (3/8") thick HT-9 plate. Peak temperature measurements indicate each of the heat-affected regions to be austenitized. An exponential expression has been used to describe the cooling curves as a function of peak temperature (or distance) from the fusion boundary.

7.12.4 Progress & Status

7.12.4.1 Introduction

The heat-affected zone in HT-9 weldments has been observed to consist of several microstructurally different regions dependent on the peak temperatures experienced. Lippold[1] has described four different regions relating their microstructures to a pseudo binary Fe-C (12%Cr) phase diagram - Figure 7.12.1.

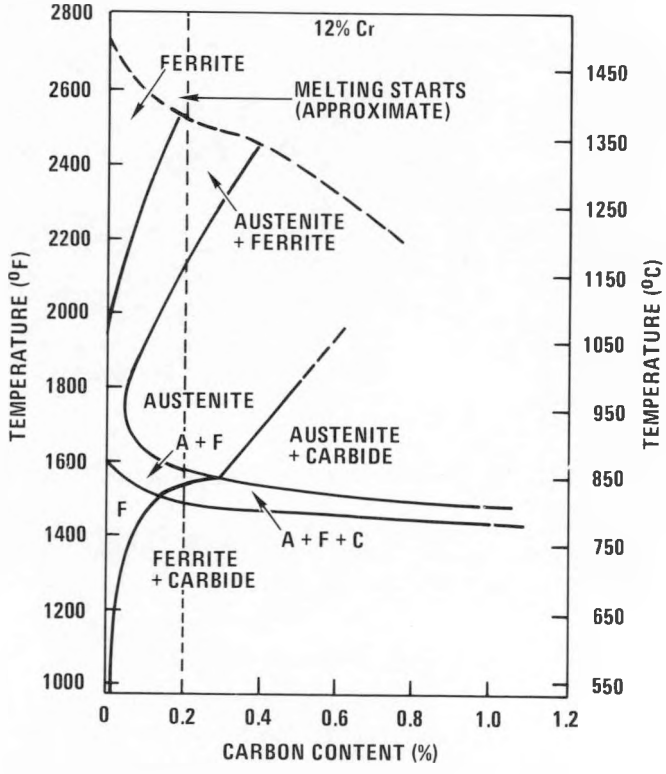

Fig. 7.12.1. Pseudo-binary Fe-C (12% Cr) phase diagram with dashed line representing the 0.2%C HT-9

An earlier study[2] indicated that, at least for HT-9 weld metal, weld preheat temperature or cooling rate can significantly affect the post-weld heat treated (PWHT'ed) dynamic fracture behavior with no evident room temperature strength (microhardness) differences. Faster weld metal cooling rates result in a post-weld heat treated higher upper shelf energy and lower ductile-brittle transition temperature (DBTT). It is highly probable that both visible microstructure differences (strong function of peak temperature) and less

visible cooling rate effects can influence the fracture behavior of the various HT-9 weldment heat-affected regions. This study characterizes in detail the temperature histories of the different heat-affected regions under typical welding conditions. It is the first in a series of experiments designed to precisely simulate heat-affected HT-9 weldment regions for the purpose of dynamic and static fracture toughness evaluations as a function of microstructure and process parameters.

7.12.4.2 Experimental

A plate of the HT-9 AOD heat[3], 102 x 203 x 9.5 mm (4 x 8 x 3/8 in.) was V-grooved and undergroove bored for thermocouples as shown in Figure 7.12.2.

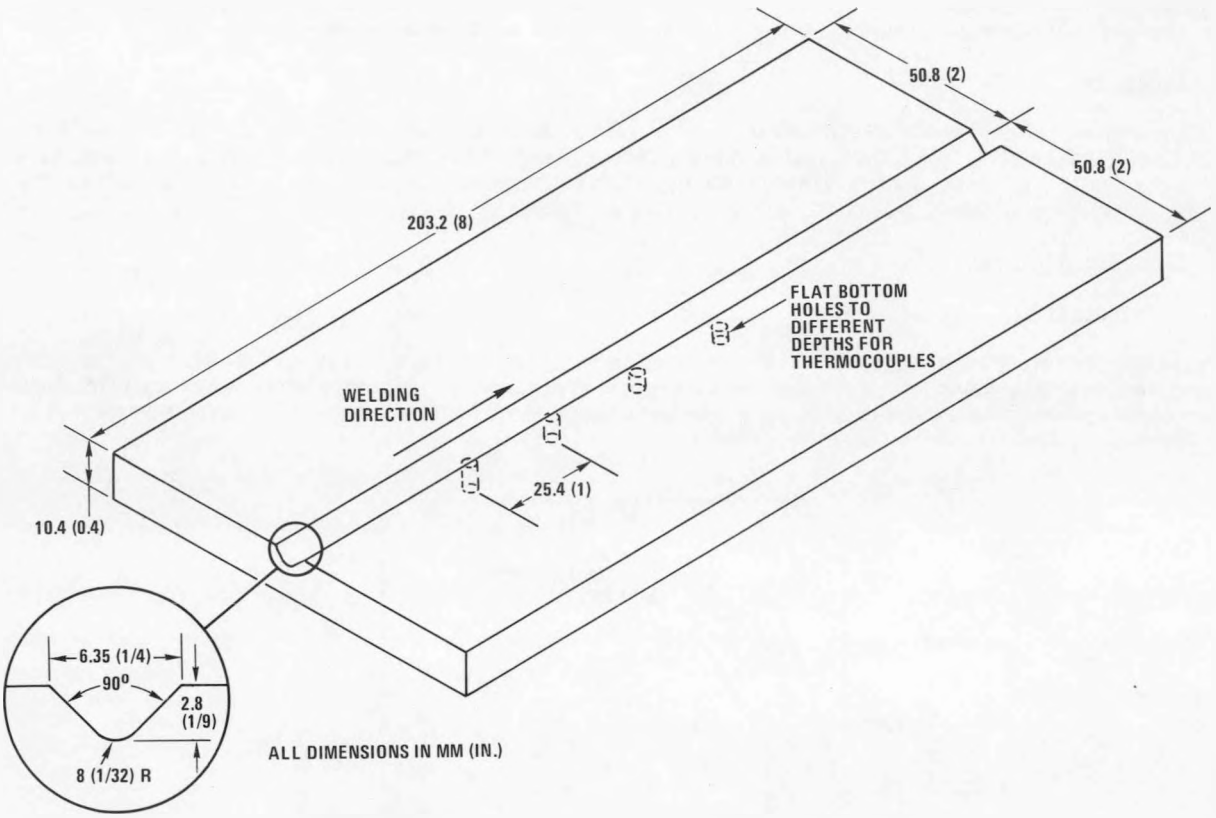

Fig. 7.12.2. Experimental test set-up: V-grooved HT-9 plae with undergroove-bored holes for heat-affected zone temperature measurement during welding

Four flat-bottom holes, 1/8 in. in diameter were spaced 25.4 mm (1 in.) apart and drilled to depths (measured from bottom surface of plate) of 6.4 mm (0.25 in.), 5 mm (0.20 in.), 3.8 mm (0.15 in.), 2.5 mm (0.10 in.) in that order. Chromel-Alumel thermocouples were spot-welded to the hole bottoms and held in plate by the holes with a thermosetting resin. A GTA weld was deposited in the V-groove using MTS-4 filler wire in a direction toward decreasing hole depth (larger underbead distance). Table 7.12.1 details the welding parameters used.

Table 7.12.1. Welding Parameters

Filler Wire	MTS 4, dia = 1.14 mm (0.045 in.) 0.26C 0.26Si 0.5 Mn 11.6 Cr 0.95Mo 0.62 NI 0.29V 0.49W 0.011 P 0.005S 0.04 Cu
Base metal	HT-9 (AOD)
Wire feed	0.18 mm/sec (0.43 in./min)
Current (A)	205
Voltage (V)	11
Travel speed	2.2 mm/sec (5.1 in./min)
Heat input rate	1.33 kJ/mm (32 BTU/in.)
Preheat temperature	21°C
Electrode	3.2 mm (1/8 in.), 2% Thoriated Tungsten
Inert gas	100% Ar

Temperatures at each location were monitored as a function of time using a strip-chart recorder. Subsequent to welding, transverse sections were cut at each thermocouple location, polished, etched and optically examined for measurement of thermocouple bead distance from the fusion boundary as well as bead location with respect to the various heat-affected regions.

7.12.4.3 Results and Discussion

Peak Temperature Measurement

Table 7.12.2 shows the peak temperatures measured at the four thermocouple locations along with the measured distances of the thermocouple beads from the fusion boundary.

Table 7.12.2. Peak Temperatures and Thermocouple Bead Locations

Bead #	Peak Temp (°C), Tp	d(a) (mm)
1	>1400(b)	0.000
2	1117	1.986
3	838	3.480
4	722	4.496

(a) Dist. of thermocouple bead from fusion boundary
(b) Peak temperature not measured accurately due to Chromel-Alumel bead breakdown

Macroetching of the transverse weldment section revealed two clearly visible heat-affected regions - a dark grey appearing zone adjacent to weld metal followed by a white zone. The zones have been reported earlier.[2] Figure 7.12.3 is a macroscopic view of a transverse section taken at the location of thermocouple bead #2. The macrograph indicates good contact between thermocouple bead and plate. Also, there appears little or no influence of the drilled hole on the overall heat flow conditions as evidenced by the undistorted outlines of the heat-affected regions. Note two distinct heat-affected regions - 1 (dark grey) and 2 (white).

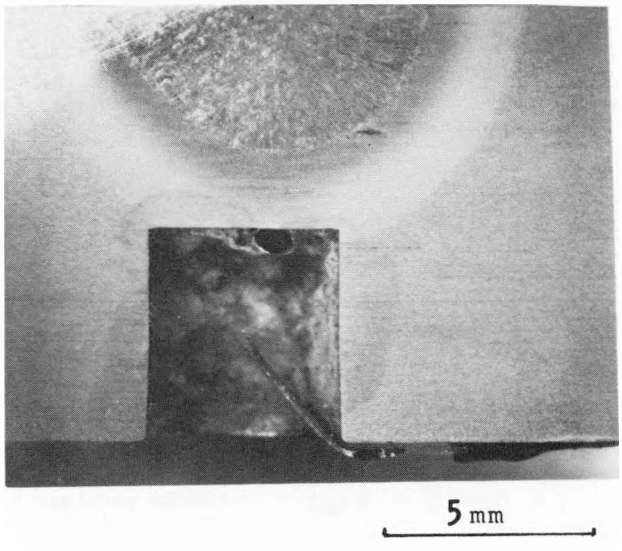

Fig. 7.12.3. Macroetched transverse section at location of thermocouple bead #2

Figure 7.12.4 is a plot of peak temperature as a function of distance from the fusion boundary. Superimposed on this plot is a room-temperature microhardness traverse. The important observations to be made from Figures 7.12.3 and 7.12.4 are:

(1) Only two heat-affected regions are clearly visible. Zone 1 (dark grey) is as a result of the zone being heated to a two-phase austenite (γ) + delta-ferrite (δ) region. Zone 2 (white) is as a result of the zone being heated up to temperatures in the single phase austenite region.

(2) The hardness traverse indicates the absence of an overtempered region sometimes observed immediately adjacent to the unaffected base metal.

(3) Fine and coarse prior austenite grain structures anticipated within Zone 2[1] were not distinguishable through macroetching or microhardness. Microstructure observations[4] indicate little austenite grain coarsening even immediately adjacent to the fusion boundary (grain size $\sim 10\,\mu m$). Cooling curves obtained indicate an austenitizing time of less than 10 seconds.

(4) Peak temperatures measured were 1450°C (2642°F) estimated at the fusion boundary, 1300°C (2372°F) at the $\gamma+\delta/\gamma$ (HAZ1/HAZ2) interface, 1050°C (1922°F) at the HAZ2/base metal interface. The schematic of Figure 7.12.5 summarizes the peak temperature observations. These temperatures are higher than predicted from Figure 7.12.1, but in closer agreement with an early Fe-Cr-C equilibrium phase diagram published by Bungardt et al.[5] and reproduced in Figure 7.12.6.

Thermal Histories

As mentioned earlier, cooling rates in addition to peak temperatures may be significant in influencing fracture behavior. Figure 7.12.7 is the measured time-temperature behavior at location of thermocouple bead #2. Time t = 0 represents the time at which the arc is directly above the thermocouple bead. In all cases, heating rates were between 85-175°C/second.

An attempt was made to empirically model the temperature as function of time. The function chosen was

$$T = T_\infty + (T_o - T_\infty)e^{-kt^{0.4}} \qquad (1)$$

where T is temperature in ^oC, T_o is the temperature at time t = 0 seconds T_∞ = temperature at time infinity or at relatively very long times (this has been taken as room temperature, 25^oC here), t is the time in

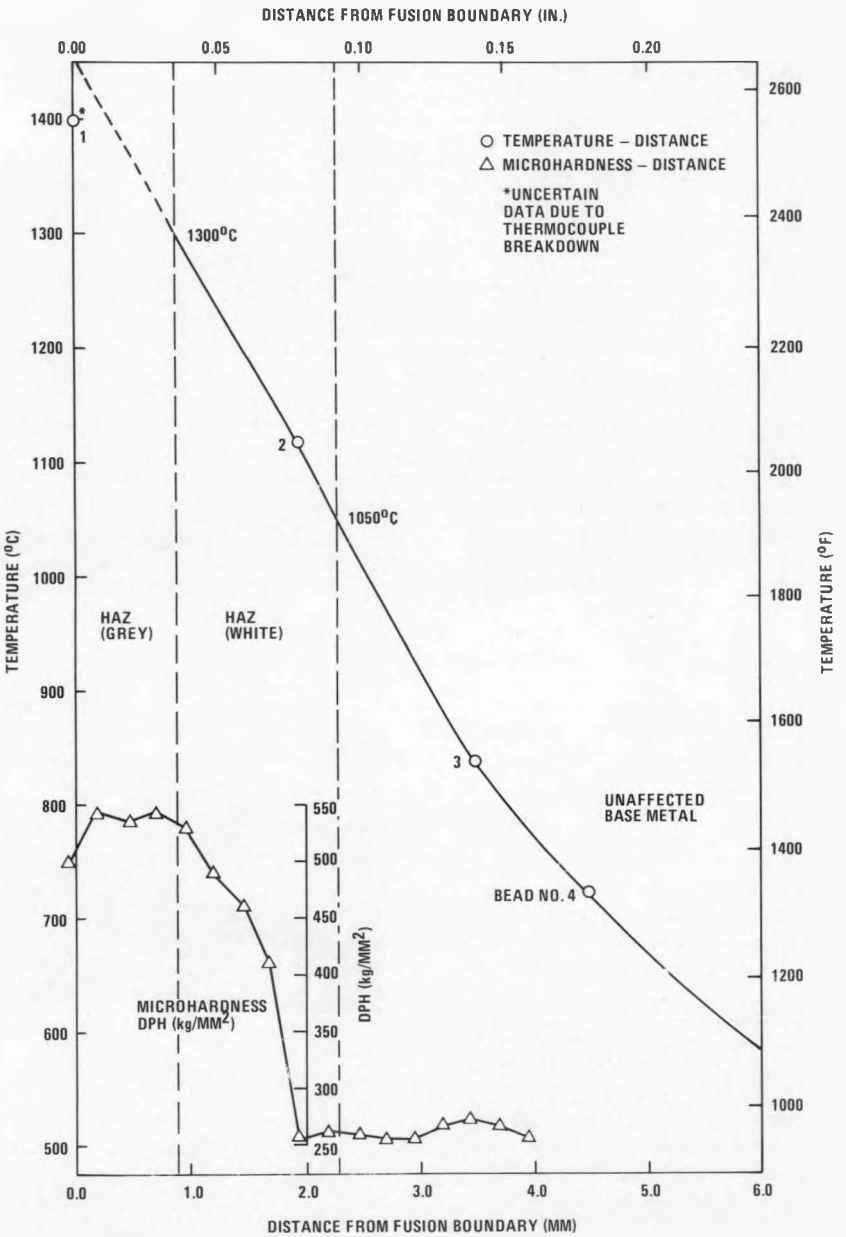

Fig. 7.12.4. Heat-affected zone peak temperature and microhardness as a function of distance from the fusion boundary.

seconds and k is an empirical constant. The form of equation (1) is similar to Rosenthal's heat flow equations[6], except the pre-exponent ($T_o - T_\infty$) used here was independent of power input and material thermal conductivity. Table 7.12.3 summarizes the results of least squares fits to the data from each thermocouple using the measured T_o, T_∞ values for boundary conditions.

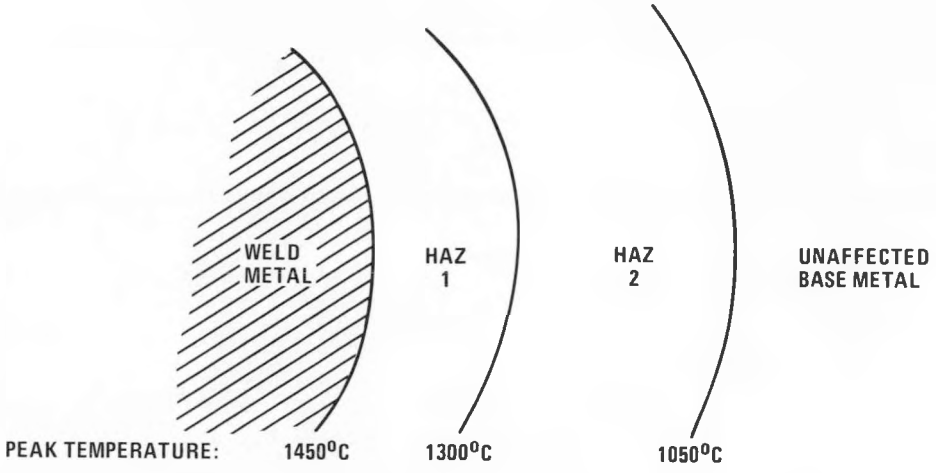

Fig. 7.12.5. Peak temperatures at macroscopically visible interfaces in the HT-9 weldment

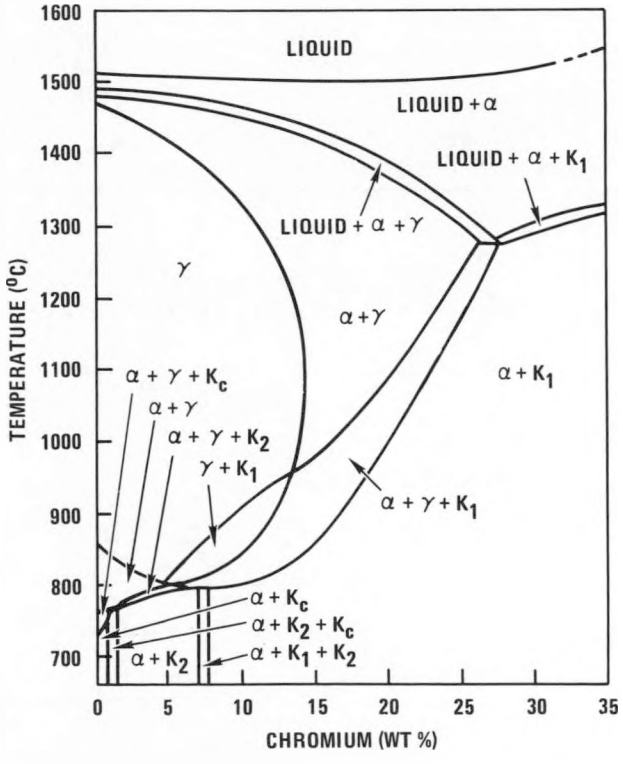

Fig. 7.12.6. Fe-Cr-C equilibrium phase diagram[5]; $K_1 \equiv (Fe,Cr)_{23}C_6$, $K_2 \equiv (Fe,Cr)_7C_3$, $K_c \equiv Fe_3C$

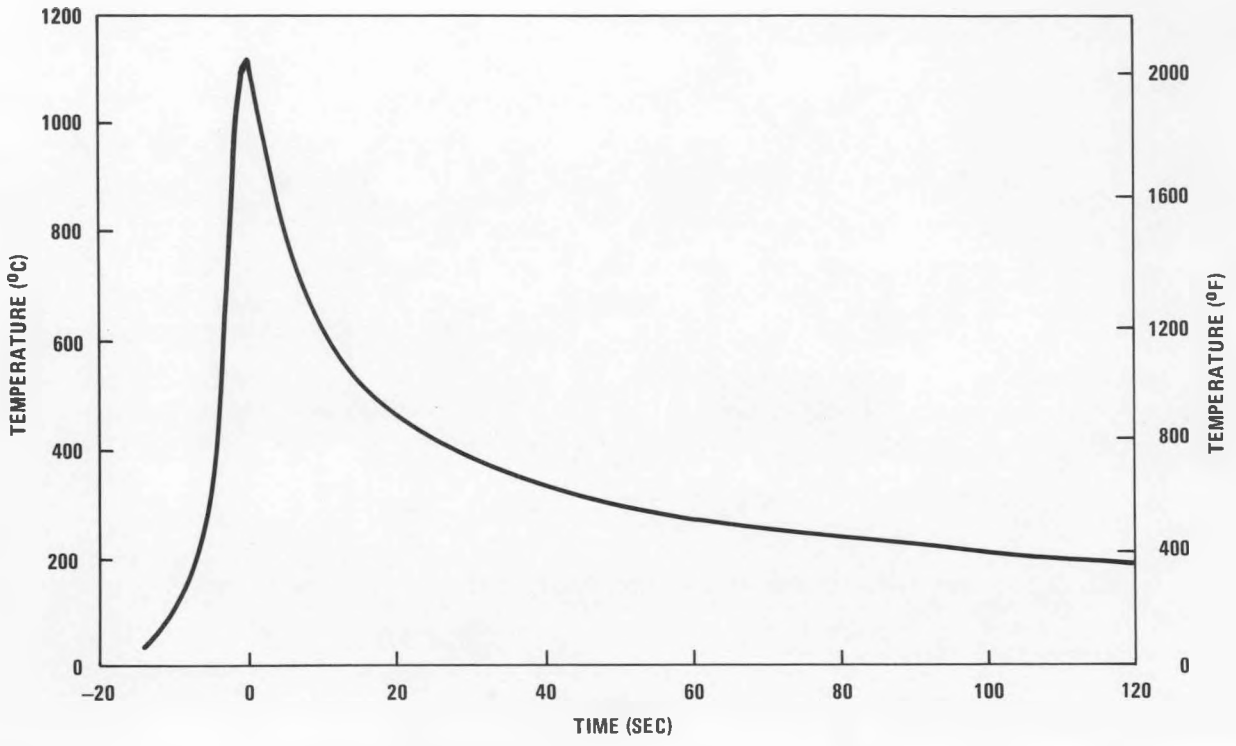

Fig. 7.12.7. Measured thermal history at location of thermocouple bead #2

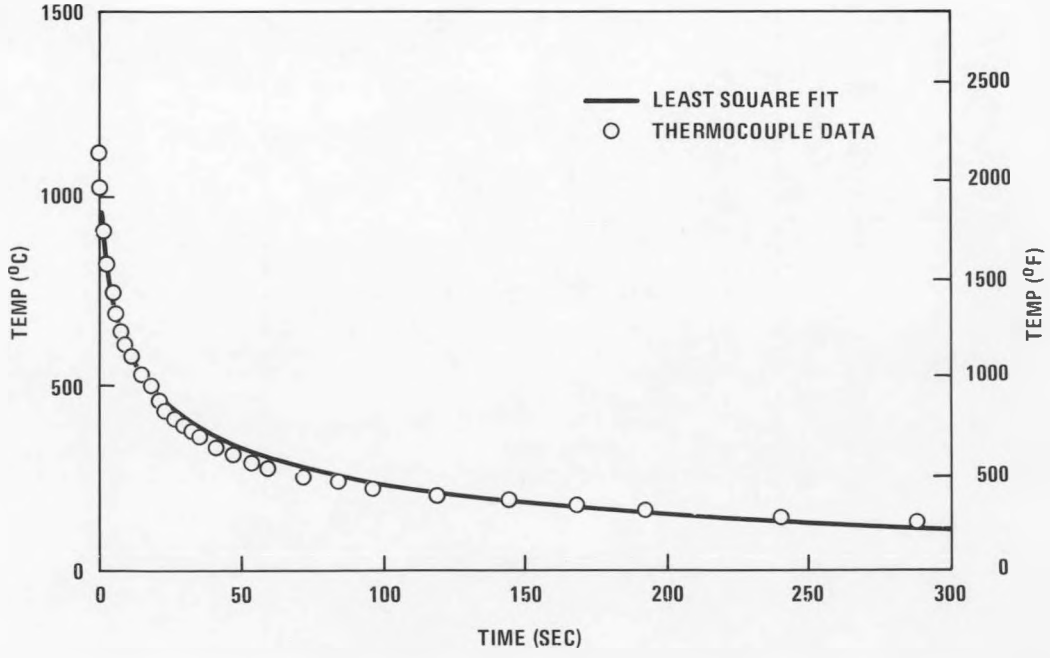

Fig. 7.12.8 A least-square fit to measured thermal history data at location of thermocouple bead #2

Table 7.12.3

Bead*	T_∞ (°C)	T_o(°C)	k
1	25	1405	0.347
2	25	1117	0.263
3	25	838	0.211
4	25	722	0.167

Figure 7.12.8 is a typical fit compared with actual data taken from bead #2 for the cooling cycle. The parameter K was found to be an approximately linear function of the peak temperature T_o. A least squares fit yielded:

$$k = (-1.0133 \times 10^{-2}) + (2.5197 \times 10^{-4})\ T_o \qquad (2)$$

where k is in $(sec)^{-0.4}$, and T_o is the peak temperature in °C, the regression coefficient obtained was 0.995.

From Figure 7.12.4, peak temperatures corresponding to "average" microsructures for zones 1 and 2 were chosen as $T_o \sim 1375$°C, $T_o \sim 1175$°C respectively. Thus, determining k using T_o in equation (2), for zone 1:

$$T = 25 + (1375-25)e^{-0.336t^{0.4}} \qquad (3)$$

and for zone 2:

$$T = 25 + (1175-25)e^{-0.286t^{0.4}} \qquad (4)$$

with T in °C and t in seconds.

Equations (3) and (4) and similar equations derived for various locations within each zone may be used to simulate heat-affected zone microstructures on larger quantities of material for structure and mechanical property (e.g. fracture resistance) characterizations.

7.12.5 Conclusions

For the GTA-welded HT-9 plate studies:

1. Only two heat affected regions were discernible through macroetching and/or microhardness.
2. Both regions experienced peak temperatures above published values of austenitizing temperature.
3. The zones (regions) were defined as resulting from heating to an austenite + delta ferrite ($\gamma + \delta$) phase region (zone 1 dark grey adjacent to weld metal) and a single phase austenite (γ) phase region (zone 2 adjacent to zone 1).
4. The definition became apparent since peak temperatures measured and estimated at the fusion boundary ($\gtrsim$1400°C), zone 1/zone 2 interface ($\sim$1300°C) and zone 2/unaffected base metal interface ($\sim$1050°C) were in fair agreement with phase boundary values predicted from the phase equilibrium diagram of Bungardt et al.
5. Measured thermal histories and a mathematical description of these permit a fairly precise simulation of heat-affected zone microstructures on bulk material. This will enable microstructure and mechanical property characterizations essential for determining a 'weak link' microstructure and consequent alloy development.

7.12.6 References

1. J. C. Lippold, ADIP Quarterly - June 1980, DOE/ER-0045/2, pp 98-108.
2. T. A. Lechtenberg and J. R. Foulds, ADIP Semiannual - March 1983, DOE/ER-0045/10, pp 155-162.
3. T. A. Lechtenberg et al., ADIP Quarterly - March 1980, DOE/ER-0045/2, pp 109-131.
4. J. R. Foulds and T. A. Lechtenberg, This ADIP report - 7.14, 1983.
5. K. E. Bungardt, E. Kunze and E. Horne, Archiv fur das Eisenhuttenweser, v. 29, March 1958, pp 193-203.
6. D. Rosenthal, Trans. ASME, v. 68, 1946, p. 849.

7.13 Fractographic Examination of Cracking in Multipass Welds in HT-9 — Sandia National Laboratories)
No contribution.

7.14 TEM OBSERVATIONS OF HT-9 AS-WELDED WELDMENT MICROSTRUCTURES - J. R. Foulds and T. A. Lechtenberg (G. A. Technologies)

7.14.1 ADIP Task

The Department of Energy/Office of Fusion Energy has cited the need to investigate ferritic/martensitic alloys under the ADIP program task, Ferritic Steels Development (Path E).

7.14.2 Objective

The objective of this study is to characterize the various weld metal, heat-affected zone and base metal microstructures in an as-welded HT-9 weldment through transmission electron microscopy (TEM).

7.14.3 Summary

TEM studies of different locations in an HT-9 weldment indicated delta-ferrite (δ) occurrence, $M_{23}C_6$ precipitation at δ-martensite interfaces, fine carbide precipitation at prior austerite grain boundaries, and martensite lath and lath packet size to be the distinguishable microstructure features observed. Furthermore, retained austenite films were observed in the weld metal and the HAZ adjacent to the weld metal that reached the highest temperature during joining. The microstructures correlate well with the observed room temperature microhardness except for the fusion boundary in weld metal which exhibited a hardness drop and an unexpected minimum amount of delta-ferrite.

7.14.4 Progress and Status

7.14.4.1 Introduction

Microstructures, both weld metal and heat-affected zones, generated during welding of HT-9 play an important role on weldment properties. Little et al[1] have described the effect of prior austenite grain size on the ductile-brittle transition temperature (DBTT). More recently[2], increased cooling rates in HT-9 weld metal have resulted in a lower DBTT and also a higher upper shelf energy (USE) with no observable differences in post-weld heat treated weld metal microhardness. Odette et al[3], on the basis of a Ritchie-Knott-Rice[4] cleavage fracture model, have determined the critical distance over which the critical fracture stress is exceeded to be approximately twice the prior austenite grain size. These observations point to the important role of microstructure in influencing fracture behavior. The thermal histories responsible for the various microstructures in an HT-9 weldment have been described in another progress report in this volume. This study attempts a description of the microstructures as related to these thermal histories. This is part of an on-going program to quantify the effect of welding on the use of the ferritic/martensitic steels in various fusion components.

7.14.4.2 Experimental

HT-9 plate 7/16 in. (11.1 mm) thick was GTA-welded using MTS-4 filler wire and a 400°C preheat temperature as described earlier.[2] Figure 7.14.1 is a macroview and schematic showing the various beads and the region chosen for microstructure evaluation. The last-deposited bead region was chosen to avoid any tempering effects of successive beads.

A 0.25" (6mm) deep transverse section of as-welded plate was sectioned with 10 mil thick saw-cuts made parallel to A-A. The TEM blanks were punched out of these thin sections. Both, the saw cuts and blanks were obtained with enough precision to ensure the TEM blanks were from locations pin-pointed to within 0.1 mm and this was corroborated by lightly chemically etching the slabs and comparing the colour of the various areas with known HAZ's. The thin foils lay in planes perpendicular to the transverse section. Microstructure variations were studied along B-B' using a 100kV Philips EM300 transmission electron microscope equipped with a tilt goniometer and rotation stage. The room temperature microhardness variation along B-B' was also obtained using a Vickers 136° diamond pyramid indenter and 500g load.

7.14.4.3 Results and Discussion

Figure 7.14.2 is the as-welded microhardness profile with delineated heat-affected regions 1 and 2 (HAZ 1 & HAZ 2).

The locations marked A, B, C, D, E, and F represent the areas examined on the TEM. A and B are from weld metal with B at the fusion boundary; C and D are from the grey HAZ (HAZ 1) with C nearer the fusion boundary and having the lower hardness; E is a location in the center of the white heat-affected region (HAZ 2) and F is from the unaffected base metal region.

Peak temperature measurements[5] at the HAZ 1/HAZ 2 and HAZ 2/unaffected base metal interfaces 1300°C (2372°F) and 1050°C (1922°F), respectively, indicate the dark grey heat-affected zone (HAZ 1) had experienced a peak temperature in the austenite (γ) + delta ferrite (δ) region and the white zone (HAZ 2) a peak temperature in the single phase γ region. This was deduced from the phase boundary temperatures published for a 12Cr, 0.2C steel by Bungardt et al[7]. (See Figure 7.12.6 in this report).

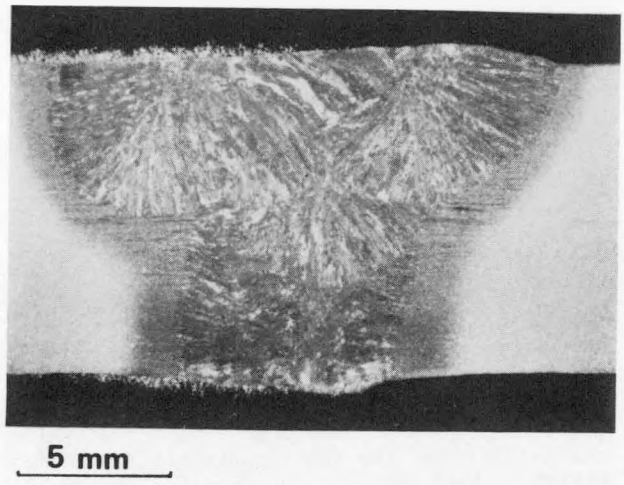

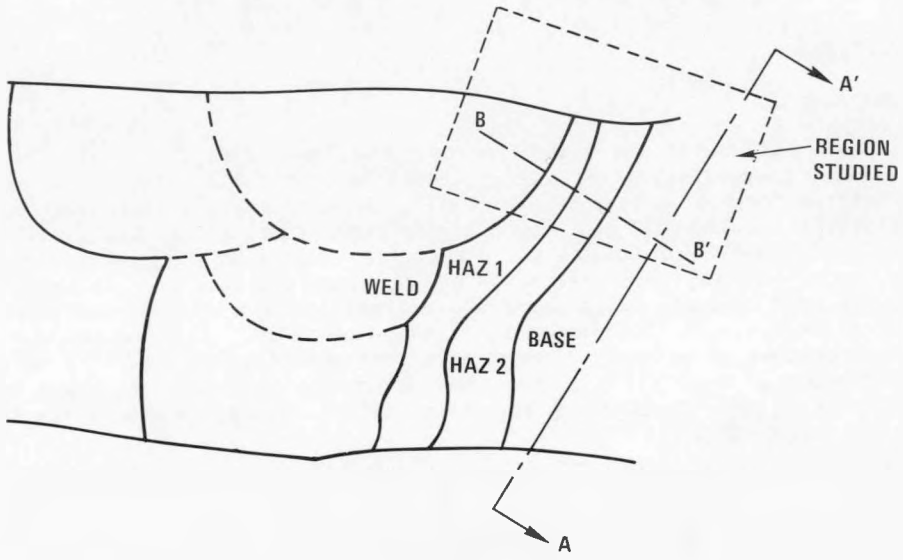

Fig. 7.14.1 Optical photomicrograph (a) and schematic (b) of the weldment used for the TEM observations, and the details of the location of the specimens used.

Figure 7.14.3 shows typical optical micrographs of weld, HAZ 1, and unaffected base metal. Prior austenite grain size measurement in weld metal and HAZones was very difficult. It appears that the prior austenite grain size in HAZ 1 was 10-20 μm compared with a base metal size of approximately 50-70 μm variations in the prior austenite grain size in HAZ 2 were not observed due to the difficulty in distinguishing the boundaries.

The optical micrographs provide little information on fine carbide precipitation, lath spacings and δ-ferrite morphology. Below is described the TEM observations made at the various locations specified in figure 7.14.2.

Location 'A': The microstructure observed in this weld metal region was as-quenched lath martensitic with a significant amount of δ-ferrite at prior austenite grain boundaries. δ was qualitatively estimated at about 4-6 volume percent with a globular, almost vermicular morphology. This has been observed earlier on the scanning electron microscope (SEM)[2], although in that study no precipitation associated with this phase was seen. Also, these earlier SEM observations suggested a predominance of interdendritic ferrite, whereas these TEM observations showed the phase to be more intergranular than interdendritic. Interdendritic ferrite content, however, was observed to increase further into the weld metal away from the fusion boundary. TEM observation indicated blocky discontinuous $M_{23}C_6$ precipitation at the δ/martensite interface (see Figure 7.14.4). The δ-ferrite and matrix in the carbide vicinity experienced preferential polishing during specimen electro-chemical thinning. δ in HT-9 weld metal has been shown[2] related to segregation during solidification of "ferritizers" (Cr,Mo,Si). This carbide-phase was observed in the SEM previously.[2]

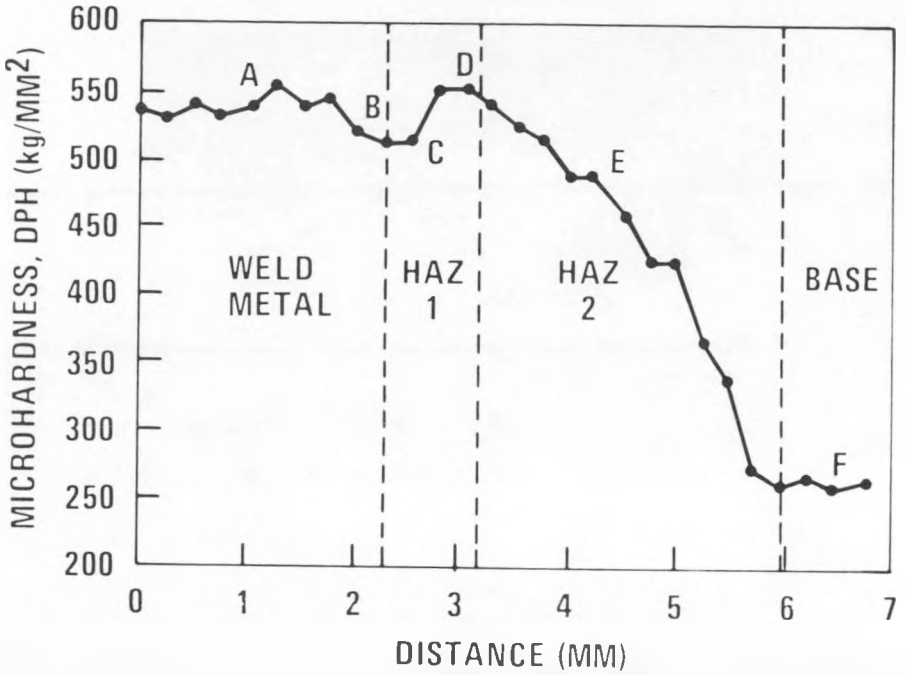

Fig. 7.14.2 Microhardness measurements traversing the as-welded HT-9 weldment.

The interfacial $M_{23}C_6$ precipitated here was blocky, discontinuous and apparently less homogeneously nucleated compared with a fine continuous homogeneously nucleated precipitate which has been seen in 316 stainless steel weld metal containing δ-ferrite.[8] It is noted that δ-ferrite interfacial $M_{23}C_6$ precipitation was visible wherever δ-ferrite occurred for every location in the HT-9 weldment and HAZ's studied here. A possible orientation relationship (δ-$M_{23}C_6$, Martensite-$M_{23}C_6$) is being investigated. Figure 7.14.5 shows δ surrounded by $M_{23}C_6$ in both bright and dark field.

The matrix structure was typically as-quenched lath martensitic. Variability in interlath spacing and lath packet size did not warrant any quantification of these demensions. Figure 7.14.6 shows a typical martensite lath structure at location 'A'. Retained austenite at interlath areas was identified but could not be quantified - Figure 7.14.7.

Fine precipitates (~0.1μm size) were observed at prior austenite grain boundaries, but were not identifiable. Figure 7.14.8 is an example of this form of precipitation.

Occasional unidentified globular precipitates (~0.2-0.3 μm) were also observed. These were not seen in base metal and are believed to be inclusions from the filler wire.

Location 'B': On approaching the fusion boundary, a few changes in HT-9 weld metal microstructure were observed. δ-ferrite decreased to below ~2 volume percent at the fusion boundary (location 'B'). Also, the average δ-ferrite globule size decreased considerably. The accompanying $M_{23}C_6$ δ-ferrite/martensite interface precipitate also decreased in size and content. Figure 7.14.9 shows globular δ-ferrite at a prior austenite grain triple point with accompanying $M_{23}C_6$ precipitation.

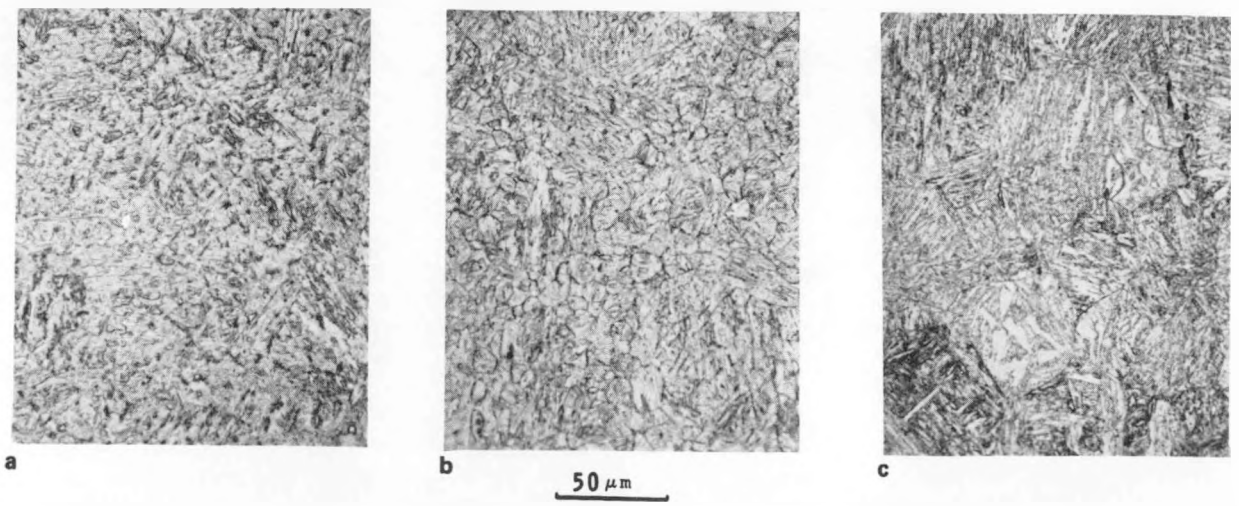

Fig. 7.14.3 Optical micrographs of the as-welded HT-9 - a) weld, b) HAZ, c) Base Metal.

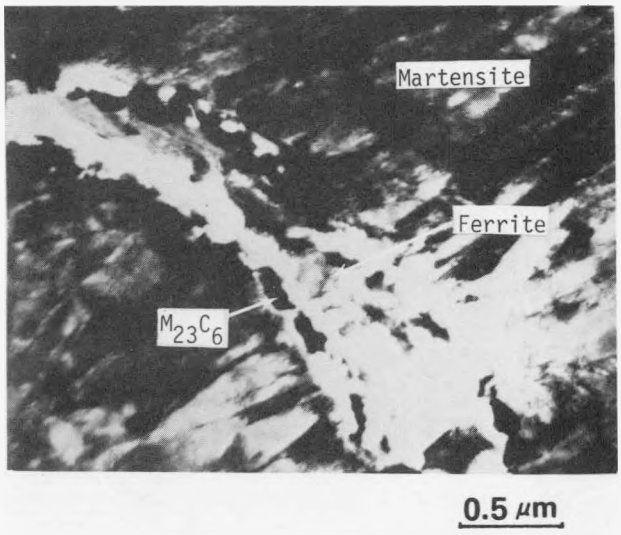

Fig. 7.14.4 TEM micrograph of the $M_{23}C_6$ precipitate at the delta-ferrite/martensite interface.

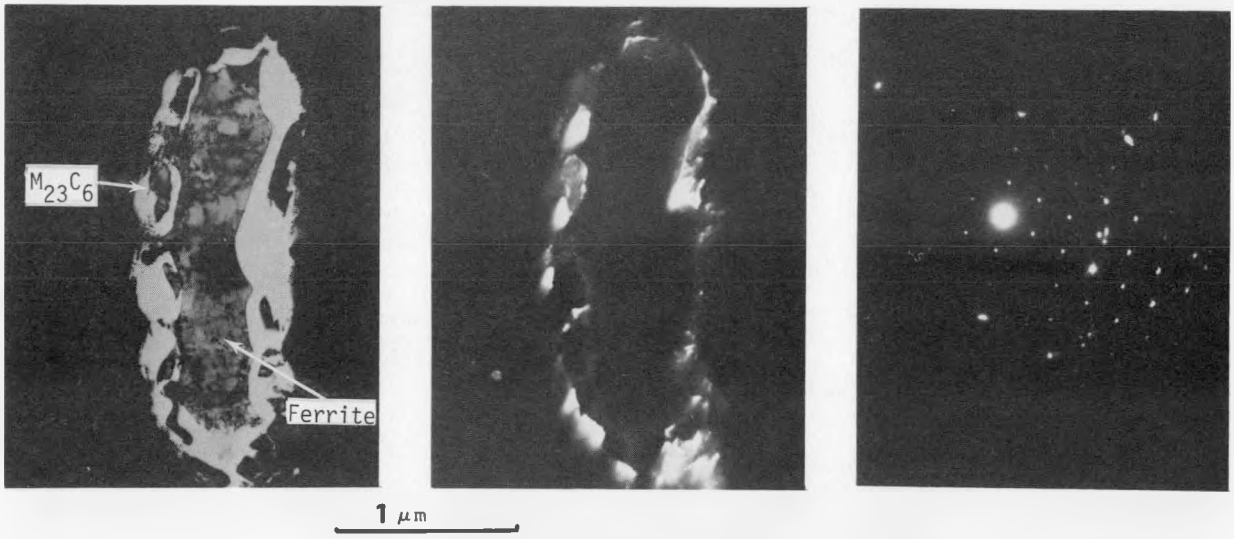

Fig. 7.14.5 TEM micrograph of the blocky, discontinuous $M_{23}C_6$ carbide at the delta-ferrite boundaries.

Fig. 7.14.6 TEM micgrograph of the typical, dislocated lath martensite matrix.

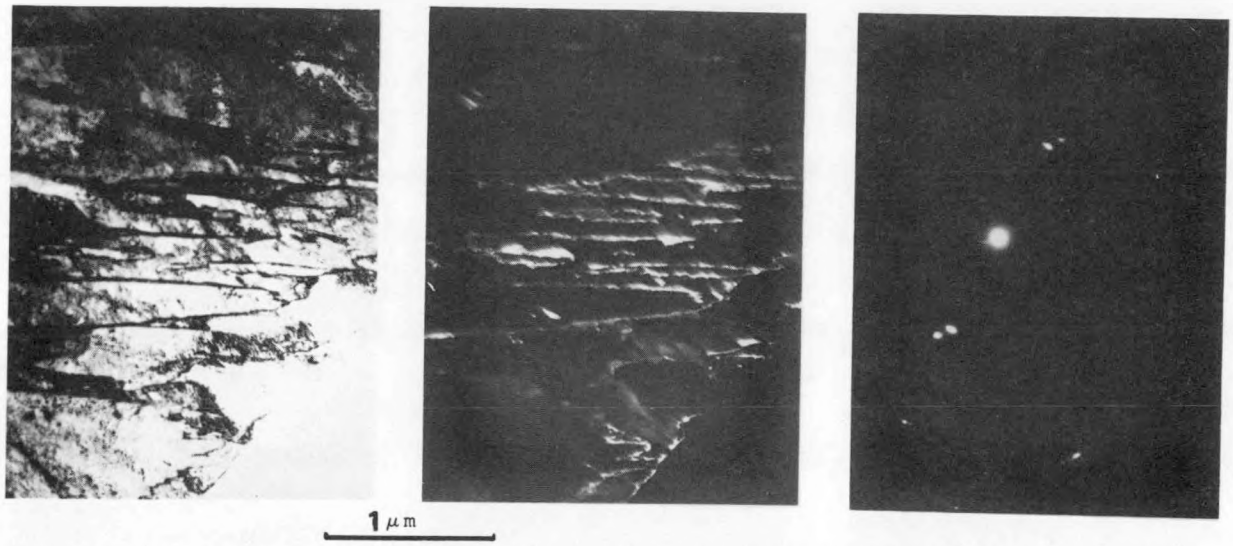

Fig. 7.14.7 TEM BF/DF micrographs of thin films of austenite retained at lath boundaries in the as-welded weld material.

The matrix structure was lath martensite. The lath packet size appeared finer than for location 'A' further away from the fusion boundary, although this could not be quantified. Fig. 7.14.10 is the typical martensitic structure observed. Again, retained austenite at interlath areas was visible and appeared to decrease slightly, but was not quantified. The fine prior austenite grain boundary precipitation reduced to almost zero at this location near the fusion boundary.

Qualitatively, the δ-ferrite, interfacial $M_{23}C_6$ precipitation and fine prior austenite grain boundary precipitation decrease in HT-9 weld metal closer to the fusion boundary and the martensitic lath packet structure also appears finer closer to the fusion boundary. Furthermore, the hardness also decreases in this HAZ region. The microstructural effects may be attributed to faster cooling rates nearer the fusion boundary because this implies a shorter time in the $M_{23}C_6$ forming temperature range and thus a lower $M_{23}C_6$ growth. A reduction in the fine prior austenite grain boundary precipitation may also be similarly related to the cooling rate. Possible dilution effects are considered minimal here since the MTS-4 filler wire and base metal HT-9 compositions are very similar. Variations in prior austenite grain size were not observed.

Location 'C': This is a location in HAZ 1 approximately 0.55 mm from the fusion boundary. The peak temperature estimated[5] at this location during welding was approximately 1370°C (2500°F), well within the $\gamma+\delta$ phase region. In fact, this δ-ferrite was estimated at approximately 3-5 volume percent. It occurred in a discontinuous globular manner at prior austenite grain boundaries which could be the result of solid-state transformations. The accompanying $M_{23}C_6$ at the ferrite-martensite interface was also observed with a morphology similar to that seen for location 'A' in the weld metal. The lower hardness at this location may be attributed to an increased , although this argument cannot be extended to location 'B' in the weld metal across the fusion boundary where δ is a minimum and so is the hardness.

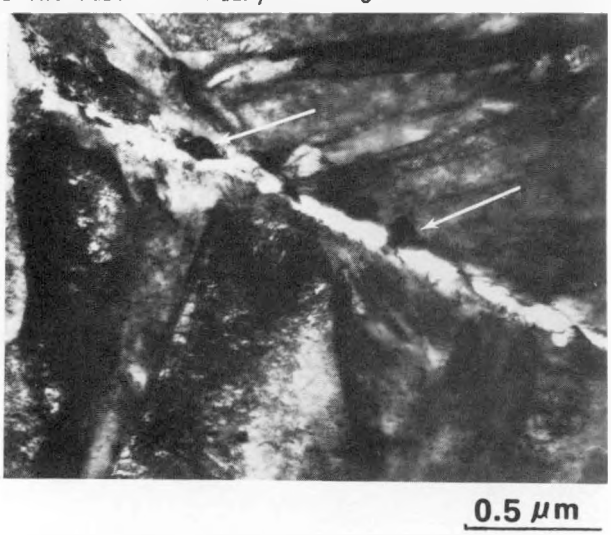

Fig. 7.14.8 TEM micrograph of unidentified precipitates in prior-austenite grain boundaries.

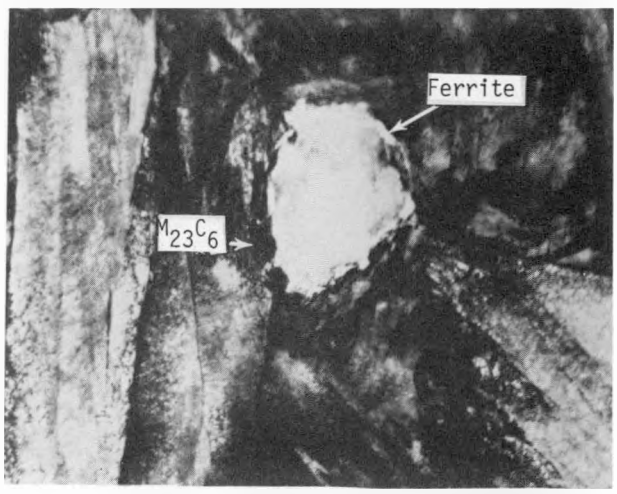

Fig. 7.14.9 TEM micrograph of globular delta-ferrite at prior-austenite grain boundaries in the weld metal with $M_{23}C_6$ precipitates at the delta-ferrite boundaries.

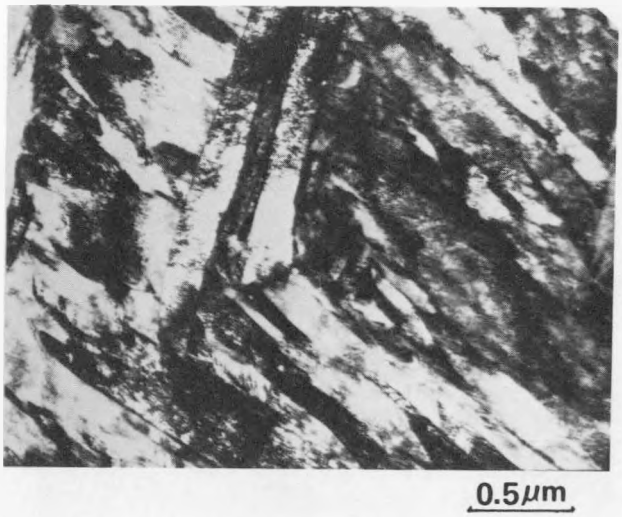

Fig. 7.14.10 TEM micrograph of typical HAZ lath martensitic matrix.

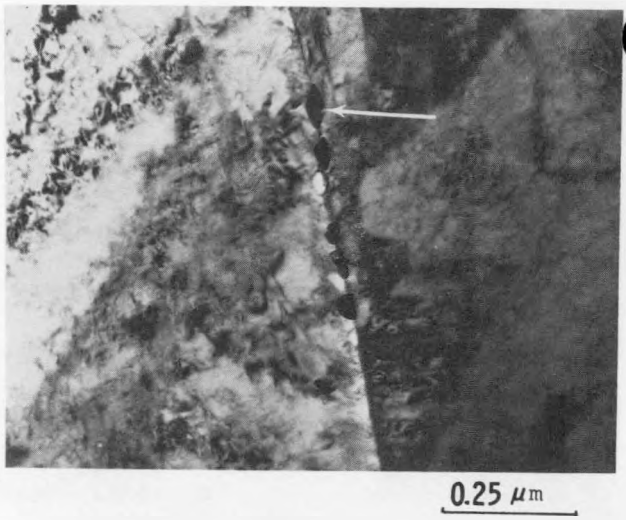

Fig. 7.14.11 TEM micrograph of unidentified HAZ precipitate at prior-austenite grain boundaries at location "C".

The matrix structure at location 'C' is typically as-quenched lath martensite. The lath packet size appeared to be similar to that observed for location 'B' in the weld metal at the fusion boundary. Retained austenite at interlath regions was visible but not quantified. Fine precipitation at prior austenite grain boundaries reappeared, but was significantly less than observed for location 'A' in weld metal. Figure 7.14.11 is an example of the fine grain boundary precipate observed.

Location 'D': This is a region in the HAZ1 near the HAZ1/HAZ2 interface that exhibits a peak hardness. TEM observations revealed very little ferrite (<1 volume percent) and accompanying $M_{23}C_6$ precipitation. The fine prior austenite grain boundary precipitate increased in size and content from location 'C'. The matrix structure was typically as-quenched lath martensitic. Figure 7.14.12 is a typical TEM micrograph showing the fine prior austenite grain boundary precipitation and matrix lath structure. The peak temperature estimated at this location is approximately 1325°C (2417°F)[5] barely into the $\gamma+\delta$ two phase region.[6] The observations on δ are in agreement with this. The peak hardness may be related to the lowest δ-ferrite in HAZ 1.

Location 'E': This represents an area approximately in the center of HAZ 2. As reported earlier[5], both HAZ 1 and 2 were completely 'austenitized'. The peak temperature at location 'E' was measured at approximately 1175°C (2147°F). In going toward unaffected base metal through HAZ 2, the hardness continually decreases. The anticipated variation in prior austenite grain size (coarser nearer the weld) probably results in the variation in as-quenched martensite hardness observed. The coarser prior austenite grain may result in a higher as-quenched martensite hardness. The structure observed at 'E' was typically as-quenched lath martensite. The lath packet size was not measured. Surprisingly, the ferrite content here was greater

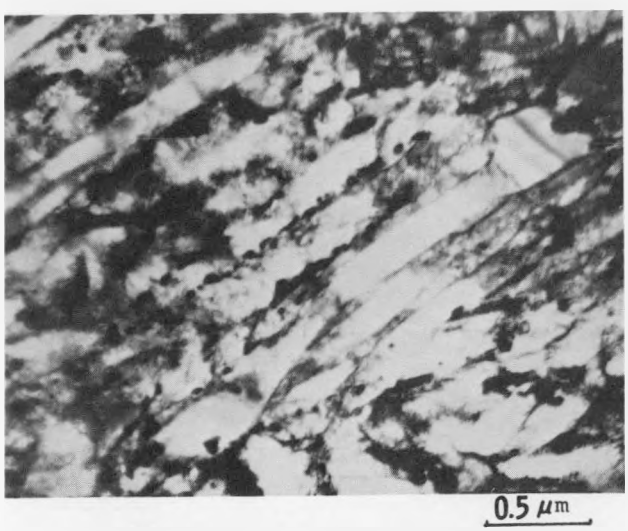

Fig. 7.14.13 TEM micrograph of typical base metal tempered lath martensite.

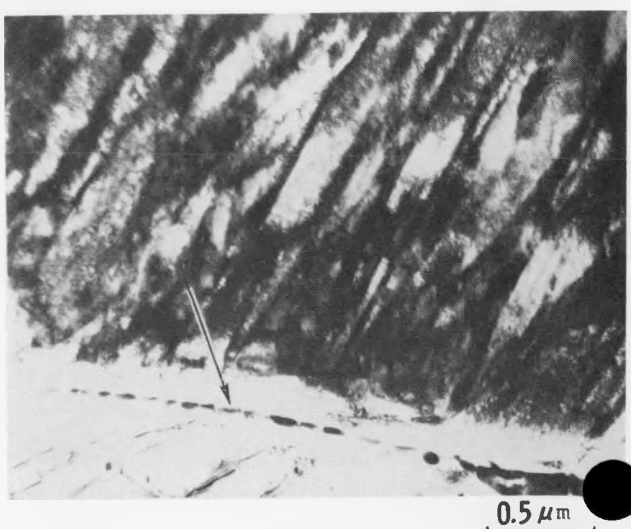

Fig. 7.14.12 TEM micrograph of unidentified HAZ precipitation at prior-austenite grain boundaries at location "D".

than observed at 'D'. In fact, it was estimated at about 2-4 volume percent. Ferrite occurred at prior austenite grain boundaries with the accompanying blocky interfacial $M_{23}C_6$. The origin of the ferrite is not clear, although its morphology is reminiscent of the δ observed in the regions experiencing peak temperatures at or above the $\gamma+\delta$ two-phase regions ('A', 'B' and 'C'). The prior austenite grain boundary precipitate was not visible at this location.

Location 'F': This represents unaffected base metal. No overtempering was visible from a hardness measurement. The structure was tempered lath martensite with carbide ($M_{23}C_6$ predominantly) precipitation at interlath regions as seen in Figure 7.14.13. Blocky carbide precipitation was also observed at prior austenite grain boundaries with some occurring within martensitic laths. Ferrite was conspicuously absent, although it is noted that occasional ferrite stringers were visible optically.

7.14.5 Conclusions

Only two heat-affected zones were observed in the as-welded HT-9 weldment. HAZ 1 represents a zone experiencing a peak temperature in the 2-phase $\gamma+\delta$ region and HAZ 2, a zone entirely 'austenitized' having a varying prior austenite grain size depending on peak temperature. Within HAZ 2, specific zones based on grain size[6] were not distinguishable. Also, no overtempered region near unaffected base metal[6] was observed.

The variation in microhardness and microstructure in an as-welded HT-9 weldment is summarized qualitatively in Figure 7.14.14.

The microhardness decrease in weld metal on approaching the fusion boundary is not understood. The hardness variation in HAZ 1 may be due to an increased ferrite content. The HAZ 2 microhardness variation may be attributed to a varying prior austenite grain size or the, as yet unexplained, ferritic content, although the grain size variation is only from approximately 5 μm near base metal to about 10 μm at the HAZ 2/HAZ 1 interface.

In the weld and heat-affected zones, $M_{23}C_6$ precipitation is related to the δ-ferrite content, increasing with increasing δ. In unaffected tempered base metal the precipitation is characteristic of the materials tempering response.

The ferrite observed in HAZ 2 having a δ morphology was not expected.

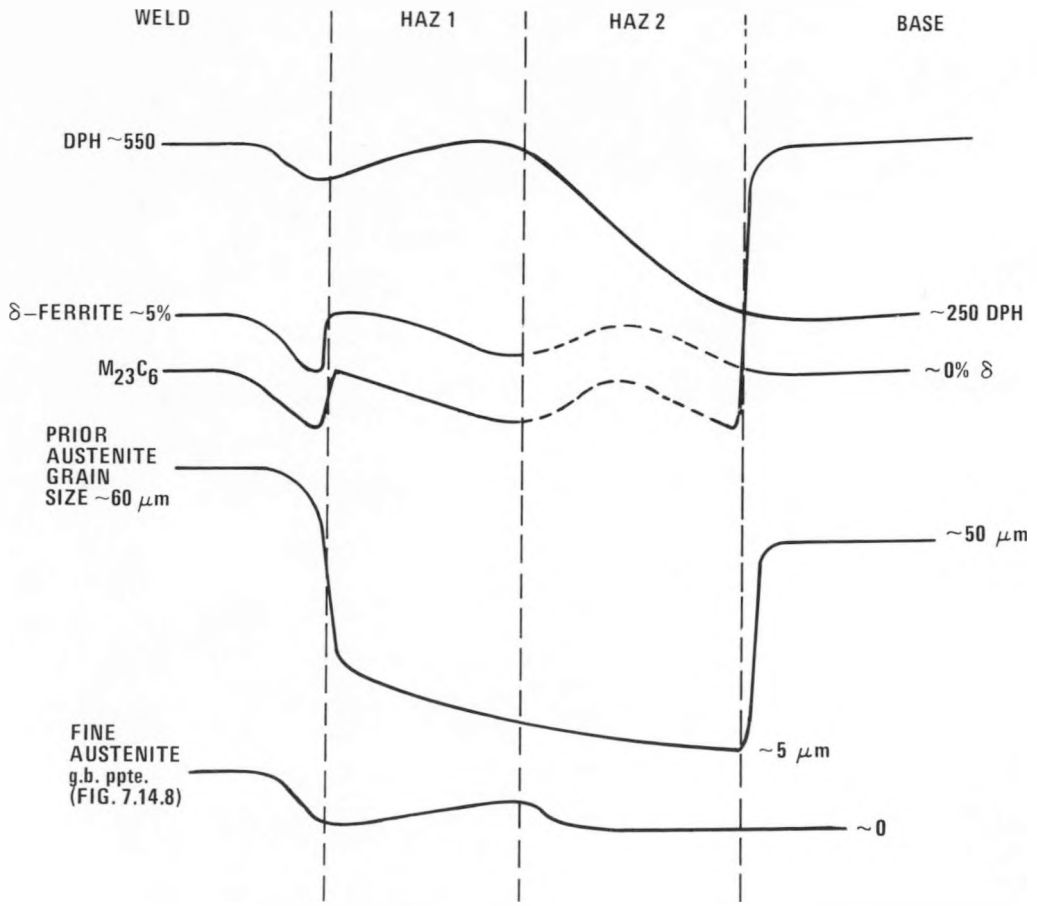

Fig. 7.14.14 Schematic depicting the phases observed in the weld/HAZ/Base metal survey and the relative amounts in each area studied.

7.14.6 Future Work

Work is in progress to:

(1) determine reason for low δ-ferrite in weld metal at the fusion boundary;
(2) determine the cause of the low hardness at fusion line;
(3) identify fine prior austenite grain boundary precipitate (possibly of a high temperature variety);
(4) determine cooling rate effects on visible aspects of HT-9 weldment microstructure; and
(5) determine origin of ferrite formation in HAZ 2 and base metal.

7.14.7 References

1. E. A. Little et al., Metals Technology, April 1977, pp 205-217.
2. T. A. Lechtenberg and J. R. Foulds, ADIP Semiannual, March 1983, DOE/ER-0045/10, pp 155-162.
3. G. R. Odette et al., presented at the Third Topical Meeting on Fusion Reactor Materials, Albuquerque, NM, September 1983.
4. R. O. Ritchie, J. F. Knott and J. R. Rice, J. Mech. Phys. Solids, v. 21, 1973, p 395.
5. J. R. Foulds, This ADIP Report - 7.12, 1983.
6. J. C. Lippold, ADIP Quarterly, June 1980, DOE/ER-0045/2, pp 98-108.
7. K. E. Bungardt, E. Kunze and E. Horne, Archiv fur das Eisenhuttenweser, v. 29, March 1958, pp 193-203.
8. J. R. Foulds and J. Moteff, Met-Trans. 13A(1), 1982, pp 173-174.

15 An Assessment of the Applicability of Critical-Stress-Critical-Distance Models of Cleavage Fracture in Martensitic Steels — GA Technologies

No contribution.

7.16 THE J_{1c} FRACTURE TOUGHNESS TRANSITION BEHAVIOR OF HT-9 - F. H. Huang (Westinghouse Hanford Company)

7.16.1 ADIP Task

The Department of Energy/Office of Fusion Energy (DOE/OFE) has cited the need to investigate ferritic alloys under the ADIP program task Ferritic Steels Development (Path E).

7.16.2 Objective

The objective of this work is to evaluate the transition and lower shelf toughness of HT-9. The goal is to characterize the fracture behavior of fusion first wall ferritic materials.

7.16.3 Summary

Small compact tension specimens of two heats of HT-9 were tested at temperatures ranging from room temperature to -192°C. The ductile-brittle transition toughness of HT-9 was evaluated using the J-integral approach. There were two loading rates of 2.1×10^{-5} m/s and 3.2×10^{-2} m/s. The ductile-brittle transition temperatures of HT-9 (#1 heat) tested at 2.1×10^{-5} m/s and HT-9 (#2 heat) tested at 3.2×10^{-2} m/s were found to be -60 and -10°C, respectively. Results showed the fracture toughness of the former was not sensitive to loading rate and the lower shelf toughness decreased with temperature to a J_{1c} value of 5 kJ/m^2 at -190°C. Furthermore, the values of J_{1c} were valid since the thickness of the test specimens was well above the thickness criterion.

7.16.4 Introduction

The ductile-brittle transition behavior of ferritic alloys historically has been studied by performing impact Charpy tests. The primary results provided by this rapid, inexpensive test technique are ductile-brittle transition temperature (DBTT) data obtained under impact loading conditions. With the development of elastic-plastic fracture mechanics, transition temperature data can be obtained by conducting J-integral fracture toughness tests at any loading rate between that of impact tests and conventional rates used in static toughness tests. More importantly, it has become possible to evaluate, quantitatively, fracture toughness in the upper shelf, transition and lower shelf regions using relatively small specimens. The purpose of the work described in this report was to determine the fracture toughness of HT-9 as a function of temperature and to study the effect of loading rate on the transition temperature behavior of HT-9 in two different thermomechanical treatments.

7.16.5 Progress and Status

7.16.5.1 Experimental Procedure

Circular compact tension specimens (Fig. 7.16.1a) were fabricated from HT-9 manufactured by Carpenter Technology Corporation. The 178 mm diameter, #1 heat, bar stock was machined down to a 50 mm strip. It was successively cold rolled to thicknesses of 10.7, 6.4 and 3.8 mm. Following each rolling operation, the material was given a heat treatment of 1038°C/5 min/AC + 760°C/30 min/AC. 2.54 mm thick specimens were fabricated from the 3.8 mm sheet with a notch in the specimen parallel to the rolling direction of the sheet (Fig. 7.16.1b). HT-9 (#2 heat) bar stock had a diameter of 33.3 mm. This bar stock was hot worked after soaking at 1149°C for a minimum of over one hour, tempered at 750°C for one hour, followed by an air cool. Circular compact tension specimens were fabricated from the slices of the bar stock (Fig. 7.16.1c).

Prior to the test, a 1.3 mm long precrack was produced in each specimen by tension-tension fatigue loading. Fracture toughness tests on unirradiated specimens were performed using an MTS hydraulic system controlled by a DEC PDP 11 computer. The crosshead speeds for the tests were either 2.1×10^{-5} m/s or 3.2×10^{-2} m/s. Load and displacement were recorded with the computer data acquisition system using a data interrupt time of 1 millisecond. Because the specimens were small, load-line displacements were determined directly from loading time by correcting for the load-train compliance.[1]

A Flexi-Cooling System from FTS System, Inc. was used for testing over the temperature range of -6 to -80°C (Fig. 7.16.2). The specimen was immersed in a bath of ethylene glycol contained in an insulated beaker. Low temperatures in the bath were produced by a freon-cooled coil which wound around a heater, a sensor, a thermocouple and a stirrer. For tests below -80°C, liquid nitrogen was used to obtain the desired temperature.

Test results in the region above the transition temperature were analyzed using the multiple specimen R-curve method, whereas the fracture toughness data in the transition and lower shelf region were determined as the values of J at maximum load. Details of the test procedure were given in References 1 and 2. During the test, the specimen was loaded to the desired displacement level or until fast fracture occurred. The specimen was unloaded and heated to 500°C for one hour to heat tint the crack area for crack extension measurements.

The values of J for the compact tension specimen were calculated from load versus load-line displacement curves in the form[3] as follows:

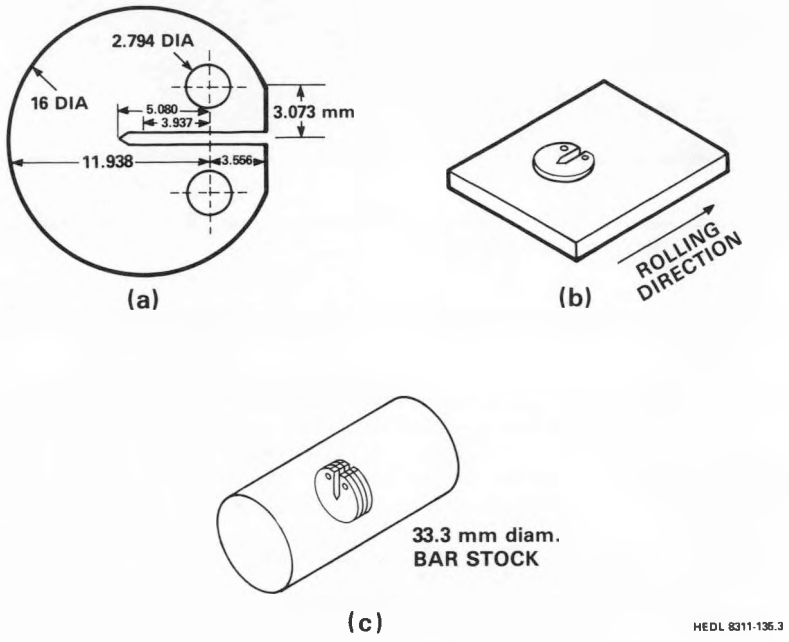

Fig. 7.16.1. (a) Compact tension specimen dimensions. (b) Orientation of fracture toughness specimen with respect to the rolling direction of HT-9 (#1 heat) stock material. (c) Processing of HT-9 (#2 heat) specimens from alloy stock.

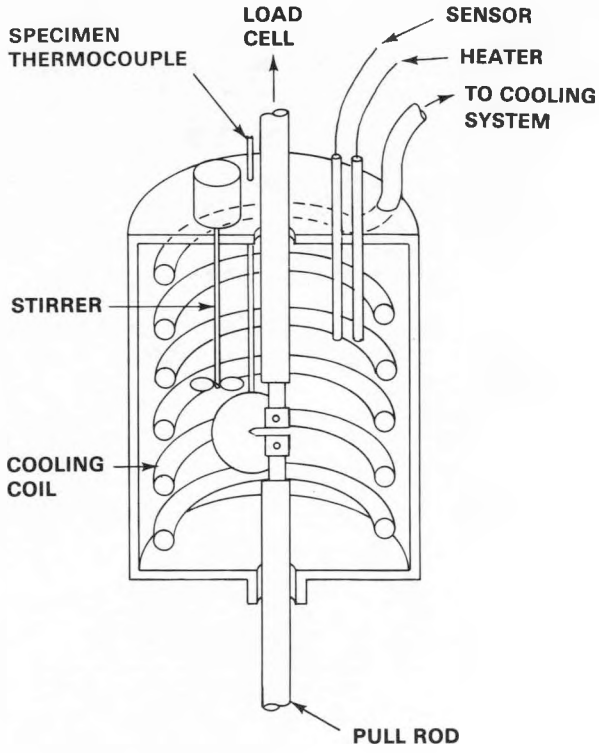

Fig. 7.16.2. Low temperature test apparatus.

$$J = \frac{1 + \alpha}{1 + \alpha^2} \frac{2A}{Bb} \quad (1)$$

$$\alpha = 2\left[\left(\frac{a}{b}\right)^2 + \left(\frac{a}{b}\right) + \frac{1}{2}\right]^{\frac{1}{2}} - \left(\frac{2a}{b} + 1\right) \quad (2)$$

where A is the area under load versus load-line displacement curve, B is the specimen thickness, b is unbroken ligament size and a is the crack length.

7.16.5.2 Results

HT-9 (#1 Heat)

The specimens tested at -42°C exhibited some stable crack extension. As the test temperature was decreased to -74°C and below, fast fracture was observed. The critical J value, J_{1c}, for the -42°C test was determined as the value at the intersection between J-R curve and the blunting curve. For the lower temperature tests, which demonstrated plastic instabilities, Equation (1) was used to calculate the values of J_{1c} up to the maximum load. Fig. 7.16.3 shows the J-R curve tested at -42°C from which the static fracture toughness was determined to be 77.4 kJ/m^2. The effect of loading rate on fracture toughness was studied by testing one specimen at a high rate of 3.2×10^{-2} m/s. The load records and the J values were plotted in Fig. 7.16.4 as a function of displacement. No plastic instability was observed indicating that the fracture toughness of the material is insensitive to loading rate at -42°C.

Low temperature yield strength data for ferritic steels are not available. To estimate the yield strength of HT-9, the test temperature and loading time of the fracture toughness test were used in the following equation:[4]

$$\sigma_y = \sigma_{ys} + 75°F,\ t_o + \frac{174000}{[(T + 459)\log\ (2 \times 10^{10} t)} - 2.74 \quad (3)$$

where

t = loading time to maximum loads, s;
t_o = time of load application for a static test, 50 s;
T = testing temperature, °F;
σ_{ys} = yield strength at room temperature static test; and
σ_y = value of σ_{ys} adjusted for temperature and strain rate.

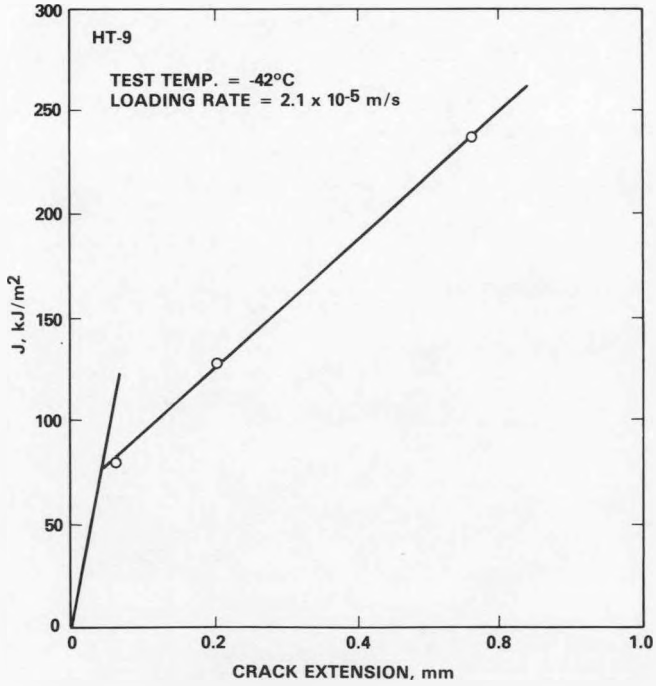

Fig. 7.16.3. J versus Δa for HT-9 (#1 heat) specimens tested at -42°C and 2.1×10^{-5} m/s.

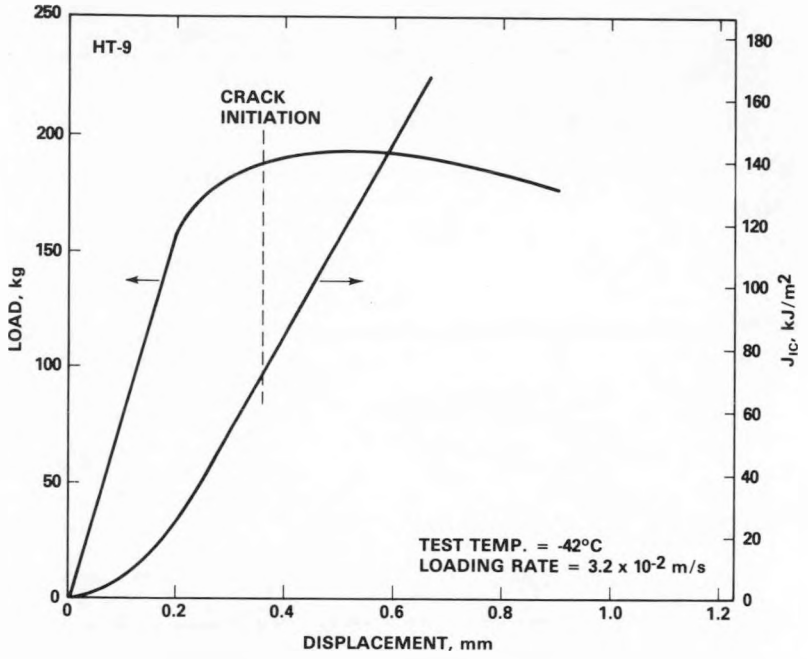

Fig. 7.16.4. Load and J versus displacement for HT-9 (#1 heat) specimens tested at -42°C and 3.2×10^{-2} m/s.

Both loading rate and temperature dependence of yield stress are included in Equation (3). Unlike face-centered-cubic (fcc) metals, body-centered-cubic (bcc) metals exhibit a rate and temperature-sensitive yield behavior. The influences of these two variables on the yield behavior of bcc metals have been studied based on rate theory.[5]

As shown in Figs. 7.16.5 and 7.16.6, the specimens had rapid crack extension when tested at -58°C and below. The values of J in these transition and lower shelf regions were calculated from Equation (1) at maximum load.

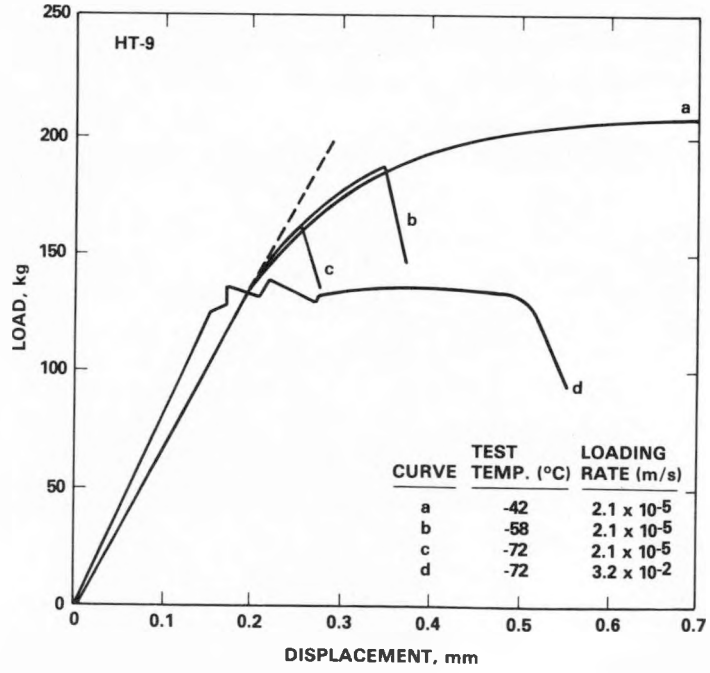

Fig. 7.16.5. Load versus displacement for HT-9 (#1 heat) specimens tested at various temperatures and loading rates in the transition region.

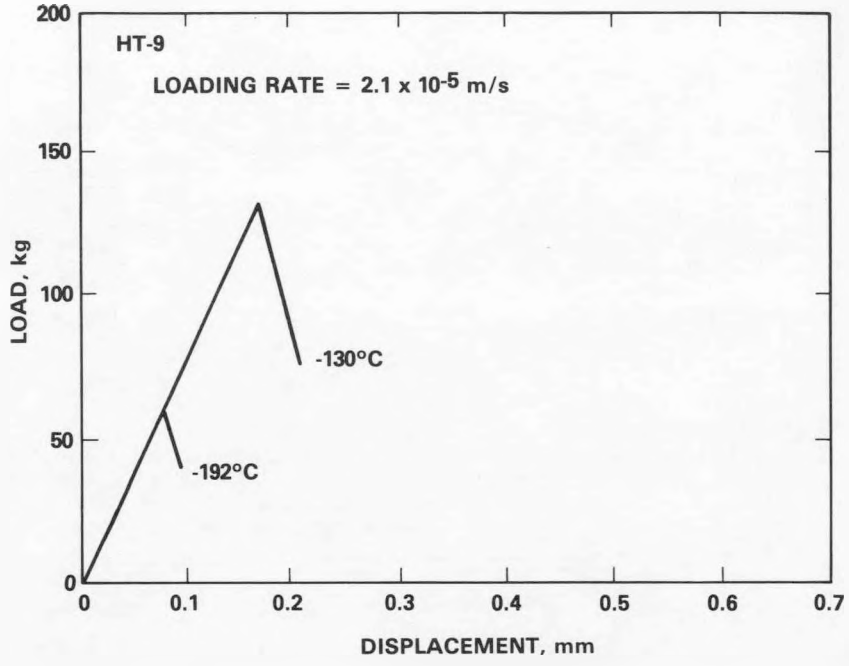

Fig. 7.16.6. Load versus displacement for HT-9 (#1 heat) specimens tested at -130°C and -192°C.

The temperature dependence of elastic/plastic fracture toughness, J_{1C}, is presented in Fig. 7.16.7. The DBTT was determined to be -60°C, calculated as the average of the upper shelf toughness and the fracture toughness at the liquid nitrogen test temperature of -192°C. Compared to the DBTT obtained from HT-9 Charpy V-notch specimens,[6] 0°C, this DBTT of the static J_{1C} test is lower. The difference in DBTT might be due to the difference in loading rate of six orders of magnitude.

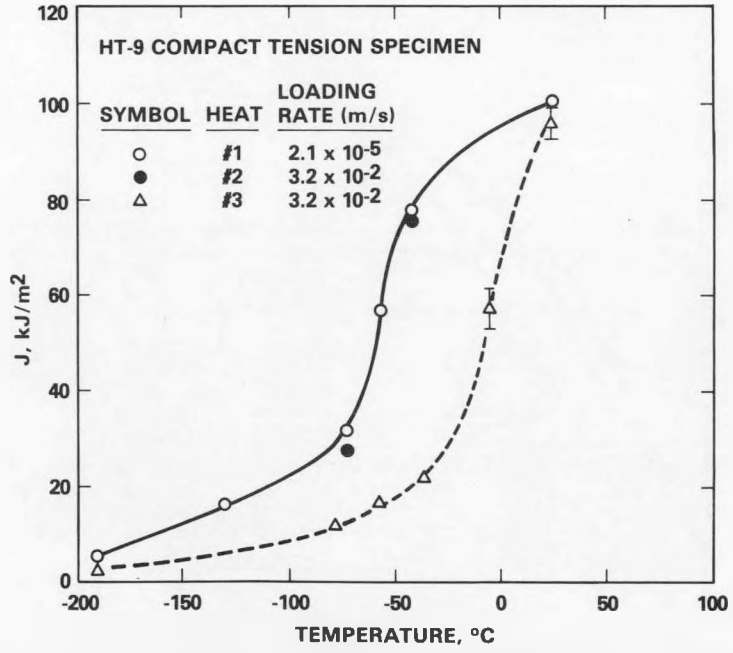

Fig. 7.16.7. The temperature dependence of J_{1C} fracture toughness.

HT-9 (#2 Heat)

Fracture toughness tests on compact tension specimens of HT-9 (#2 heat) were performed at -6 to -191°C, with a loading rate of 3.2×10^{-2} m/s. All specimens except the one tested at -6°C exhibit rapid crack extension. The values of J_{1c} were calculated from Equation (1) at maximum load for the -36°C or lower temperature tests. As there was no sudden load drop observed for the only one specimen tested at -6°C, the J_{1c} value at this temperature was estimated assuming the crack was initiated beyond the yield point and before the maximum load was reached. Tests were also conducted at room temperature at loading rates of 4.3×10^{-3} m/s and 2.1×10^{-2} m/s. The effect of loading rate on the upper shelf fracture toughness was found to be minimal. The variation of the fracture toughness versus temperature is shown in Fig. 7.16.7. As shown in Fig. 7.16.7 the DBTT for this heat of HT-9 tested at a high loading rate was determined to be -10°C, 50°C higher than that of HT-9 (#1 heat).

7.16.5.3 Discussion

The yield strength of bcc materials such as ferritic alloys is sensitive to the loading rate and test temperature. At low temperatures, the yield stress of the material is rapidly raised by increasing the loading rate and when the rate exceeds a critical value brittle fracture occurs with loss of energy-absorbing capacity. Other factors such as irradiation and plastic constraint due to the presence of a notch, also contribute to the elevation in yield stress and the corresponding ductile-brittle transition behavior exhibited by HT-9. However, the extreme rate sensitivity may vary among different materials and thermomechanical conditions.

At -42°C, HT-9 (#1 heat) exhibited stable crack growth at either a slow rate of 2.1×10^{-5} m/s or a fast rate of 3.2×10^{-2} m/s as evidenced in Fig. 7.16.5 where a smooth loading curve was shown. Figs. 7.16.8a and 7.16.8b illustrate the stable crack extensions at two different rates. The material did not exhibit fast fracture until the temperature decreased to -58°C and below (Figs. 7.16.8c and 7.16.8d). At -74°C, the difference in fracture toughness at the low and high rate is insignificant (Figs. 7.16.5c, 7.16.5d and 7.16.7). For HT-9 (#2 heat), however, a sudden load drop and a fast fracture were observed at -36°C (Fig. 7.16.9). In contrast to the specimen tested at -6°C, there is no lateral contraction near the crack tip in the specimen tested at -36°C as shown in Fig. 7.16.10. This provides evidence that the

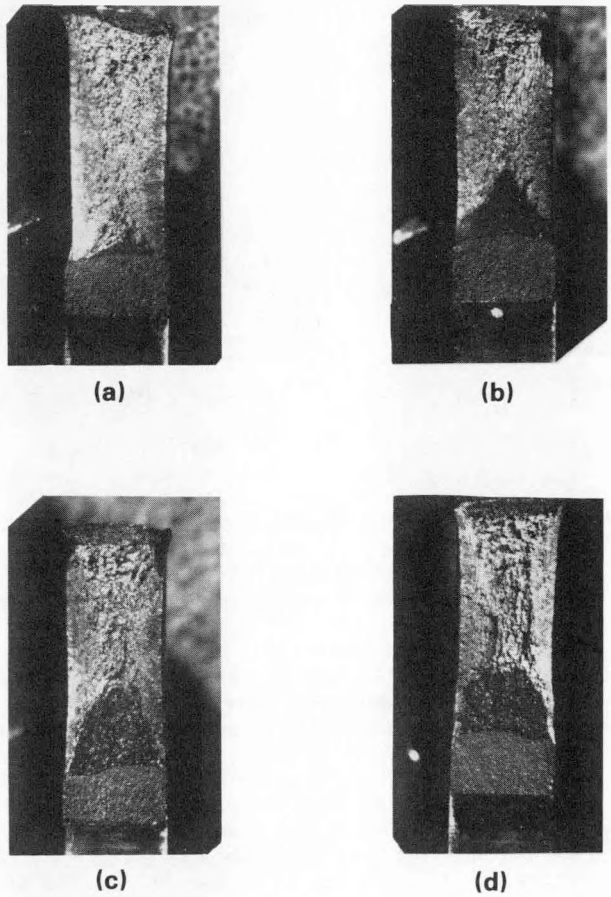

Fig. 7.16.8. Crack extension as revealed by heat tinting for HT-9 (#1 heat) specimens tested at: (a) -42°C, 2.1×10^{-5} m/s, (b) -42°C, 3.2×10^{-2} m/s, (c) -58°C, 2.1×10^{-5} and (d) -74°C, 2.1×10^{-5} m/s.

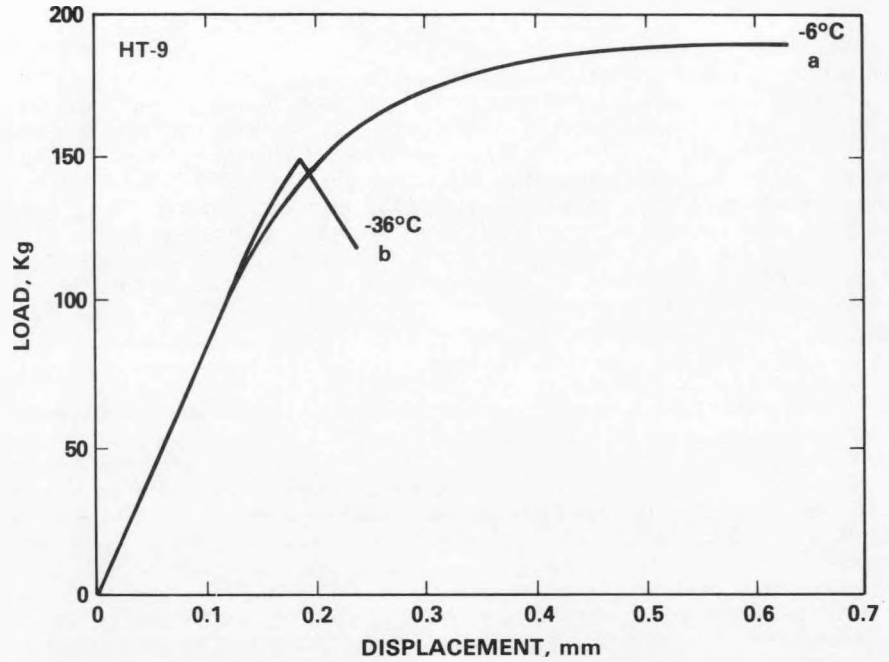

Fig. 7.16.9. Load versus displacement for HT-9 (#2 heat) specimens tested at -6°C and -36°C.

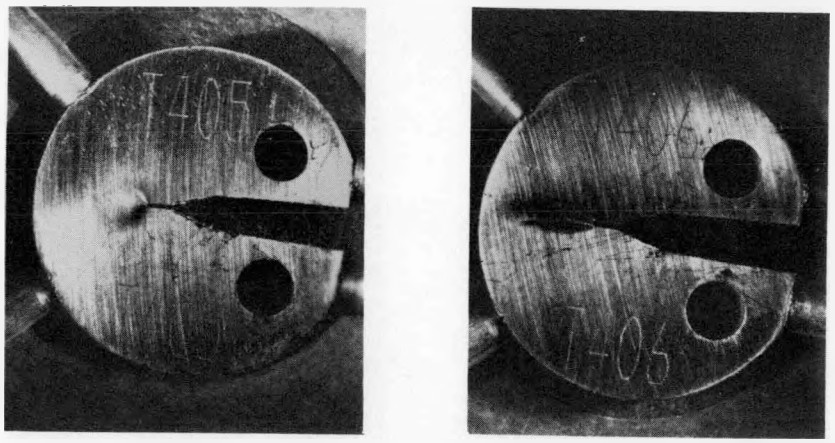

Fig. 7.16.10. Crack tip deformation profiles for HT-9 (#2 heat) tested at: (a) -6°C and (b) -36°C.

material exhibits little plasticity at -36°C compared to the deformation near the crack tip at -6°C. It is unclear whether the difference in DBTT between these two heats of HT-9, 50°C, results from the difference in loading rate or thermomechanical treatment (TMT). The insensitivity of fracture toughness to loading rate at -42 and -74°C displayed by HT-9 (#1 heat) indicates that TMT may be more influential than loading rate in affecting the cleavage fracture responses of HT-9.

The transition toughness characterization of the material is illustrated in Fig. 7.16.7. In the upper shelf region the fracture toughness decreases with decreasing temperature. As the temperature decreases further, the material exhibits a ductile-brittle transition behavior, and a sharp drop in toughness occurs. In the lower shelf region, the fracture toughness continues to decrease with temperature. At -190°C, the value of J_{1c} was found to be 5 kJ/m^2. The trend indicates that there is no minimum value of fracture resistance for HT-9. Results obtained from Charpy impact tests also show the similar trend.[7] The transition behavior of the material can also be easily identified from the non-linear load-displacement curve with a sudden load drop at the maximum load. Curve b in Fig. 7.16.5 shows that, at -58°C, HT-9 (#1 heat) exhibited a limited amount of plastic deformation beyond yielding and then a rapid crack extension at a maximum load of 185 kg. Interestingly, the load-displacement curve for this specimen tested at -58°C is similar to that of a specimen tested at -42°C (Fig. 7.16.5, curve a). The -42°C sample did not exhibit fast fracture. The similarity in the loading curves is an indication that the tearing modulus[8] for the unstable specimen is equal to that for the stable specimen from crack initiation to the point of instability. This suggests that the temperature induced instability is a material property as discussed by Joyce and Hasson.[9]

The transition behavior of HT-9 (#2 heat) is expected to be similar to that of HT-9 (#1 heat) except that the transition occurs at a higher temperature.

The fracture surfaces of the tested specimens were examined using a scanning electron microscope. Fractographic analyses is given in a separate report in this ADIP semiannual progress report.[10]

7.16.6 Conclusions

The ductile-brittle transition behavior of HT-9 was investigated using J_{1c} tests over the temperature region of 25 to -192°C. The DBTT determined from the J_{1c} tests was lower than that determined by Charpy tests. In addition, quantitative fracture toughness data in the transition and lower shelf regions were obtained.

At low temperatures, the yield stress of HT-9 increases while the fracture toughness decreases, the minimum specimen thickness required for valid J_{1c} tests is thus reduced, which was well below the thickness (2.54 mm) of the specimens used in this work. The low-shelf toughness was found to be less than 5 kJ/m^2 at -190°C, which is smaller than that estimated from Charpy impact tests.

The influence of loading rate on the low temperature fracture toughness of HT-9 (#1 heat) was not significant. However, results showed that the transition fracture toughness of HT-9 (#2 heat) tested at a higher loading rate was much lower than that of HT-9 (#1 heat).

7.16.7 References

1. F. H. Huang and G. L. Wire, "Techniques Developed for Elevated Temperature Fracture Toughness Testing of Irradiated Materials in Thin Sections," *J. Engng. Mater. Technol.* 101(4), 403-406 (1978).

2. F. H. Huang and G. L. Wire, "Fracture Toughness Testing on Ferritic Alloys Using Electropotential Techniques," *J. Nucl. Mater.* 104, 1511-1516 (1981).

3. G. A. Clarke and J. D. Landes, "Evaluation of the J-Integral for the Compact Specimen," *J. Test. Eval.* 7, 264-269 (1983).

4. A. K. Shoemaker and R. R. Seeley, "Summary Report of Round Robin Testing by the ASTM Task Group E24.01.06 on Rapid Loading Plane-Strain Fracture Toughness K_{1c} Testing," *J. Test. Eval.* 11(4), 261-272 (1983).

5. R. E. Bennet and G. M. Sinclair, "Parameter Representation of Low Temperature Yield Behavior of Body-Centered-Cubic Transition Metals," *J. Basic Engng.*, Trans. of ASME, Series D, 88(2), 518-524 (1966).

6. J. R. Hawthorne and F. A. Smidt, Jr., "Evaluation of Fracture Resistance of Ferritic Stainless Steels for First Wall and Blanket Applications," *J. Nucl. Mater.* 104, 883-886 (1981).

7. W. L. Hu and D. S. Gelles, "Miniature Charpy Impact Test Results for the Irradiated Ferritic Alloys HT-9 and Modified 9Cr-1Mo," Proceedings of Topical Conference on Ferritic Alloys for Use in Nuclear Energy Technologies, Snowbird, Utah, 1983.

8. P. C. Paris, H. Tada, A. Zahoor and H. Ernst, "The Theory of Instability of the Tearing Mode of Elastic-Plastic Crack Growth," *Elastic-Plastic Fracture*, ASTM STP 668, 5-36 (1979).

9. J. A. Joyce and D. F. Hasson, "Characterization of Transition Temperature Behavior of HY130 Steel by the J_{1c} Fracture Toughness Parameter," *Engng. Fract. Mech.* 13(3), 417-430 (1980).

10. D. S. Gelles and F. H. Huang, "Fractographic Examination of HT-9 Miniature Compact Tension Specimens Tested at Low Temperatures," ADIP Section 7.7 this document.

7.17 THE FRACTURE TOUGHNESS OF FERRITIC ALLOYS IRRADIATED IN HFIR - F. H. Huang (Westinghouse Hanford Company)

7.17.1 ADIP Task

The Department of Engery/Office of Fusion Energy (DOE/OFE) has cited the need to investigate ferritic alloys under the ADIP program task Ferritic Steels Development (Path E).

7.17.2 Objective

The objective of this work is to evaluate the fracture toughness of ferritic alloys irradiated in the High Flux Isotope Reactor (HFIR). The goal is to characterize the fracture behavior of the fusion candidate materials influenced by both displacement damage and transmutation produced helium at levels relevant to fusion reactor irradiation conditions.

7.17.3 Summary

The fracture toughness of HT-9 and 9Cr-1Mo irradiated in HFIR to 10 dpa at 50°C was evaluated using electropotential single specimen techniques. Circular compact tension specimens were tested at temperatures ranging from room temperature to 450°C. The test results were analyzed using the J-Integral approach. Analyses showed that the fracture toughness of both alloys was reduced as a result of HFIR irradiation. The degradation of irradiation toughness resistance was more severe for 9Cr-1Mo than HT-9. The thickness criterion for valid J_{1C} values was satisfied by the thickness of the test specimens.

7.17.4 Introduction

Knowledge of irradiation damage in fusion reactors is relatively limited compared to that in fission reactors. The large amount of helium produced by (n, α) transmutations and the radiation damage induced by the high energy neutrons (14.1 MeV) undoubtedly will degrade the mechanical properties of the fusion structures. To develop materials for fusion reactors, the candidate alloys such as HT-9 and 9Cr-1Mo have been irradiated in a simulated environment with atom displacement damage and helium levels equivalent to that in fusion reactors. Fracture toughness specimens have been irradiated in EBR-II to study the post-irradiation toughness responses of ferritic alloys, however, irradiation in EBR-II produces little helium concentration.[1] HFIR provides a mixed-spectrum irradiation environment with transmutation helium from the thermal spectrum and displacement damage from the fast spectrum. It is known that the amount of the helium produced depends upon the nickel content in the alloy, HT-9 contains only 0.5% Ni and 9Cr-1Mo 0.1% Ni. Although these amounts were not adequate for simulating fusion helium production, it still is useful to assess the effects of the high displacement damage acting synergistically with helium during HFIR irradiation on the mechanical properties of these materials.

The purpose of this work was to determine the upper shelf fracture toughness of HT-9 and 9Cr-1Mo irradiated in HFIR. Comparison of the results with those obtained from the unirradiated materials permits an evaluation of the effect of HFIR irradiation on the fracture properties of ferritic alloys.

7.17.5 Progress and Status

7.17.5.1 Experimental Procedure

Compact tension specimens of HT-9 (heat number 91535) and 9Cr-1Mo (heat number 30176) produced by Carpenter Technology Corporation were fabricated from the 33.3 mm diameter bar stock of HT-9 and 25 mm plate of 9Cr-1Mo. The material stock of HT-9 was hot forged and rolled at 1038°C, and annealed at 760°C for 2.5 hours. The final heat treatment for the 3.18 mm plate stock was 1038°C/10 min/AC plus 760°C/30 min/AC. 9Cr-1Mo specimens received a heat treatment of 1038°C/30 min/AC plus 760°C/30 min/AC. Details of the specimen configurations were shown in Reference 2. The specimens were irradiated in the beryllium reflector of HFIR at the reactor coolant temperature of 50°C, to a displacement damage level of 10 dpa.

The specimens were tested at temperatures of 25, 93 and 205°C for HT-9 and 93, 205 and 450°C for 9Cr-1Mo using electropotential single specimen techniques.[3] Four copper electrodes were welded at the lead positions of each specimen described in Reference 2 for power input and potential output. Prior to the test, all specimens were fatigue precracked to a predetermined crack length measured by the electropotential technique. During the test, load and potential output were simultaneously recorded for J calculation and continuous crack extension measurements. After the test was completed, the total crack extension was measured from the heat tinted area on the fracture surface of the tested specimen.

7.17.5.2 Results and Discussions

Load and potential output versus displacement curves of HT-9 and 9Cr-1Mo tested at 205°C are shown in Fig. 7.17.1. The loading curves level off beyond the yield indicating little resistance to crack propagat in the material after the crack was initiated. As shown in Fig. 7.17.1 there is a trough in the potential curves. The initial increase in potential output upon loading due to the blunting of the notch was offset by the initial decrease in resistance during elastic loading. After the specimen has yielded and the crack has been initiated, the potential output reverses its down-trend. The calculated J values are plotted against crack extension in Fig. 7.17.2 for both alloys tested at 205°C. The critical fracture toughness, J_{1C},

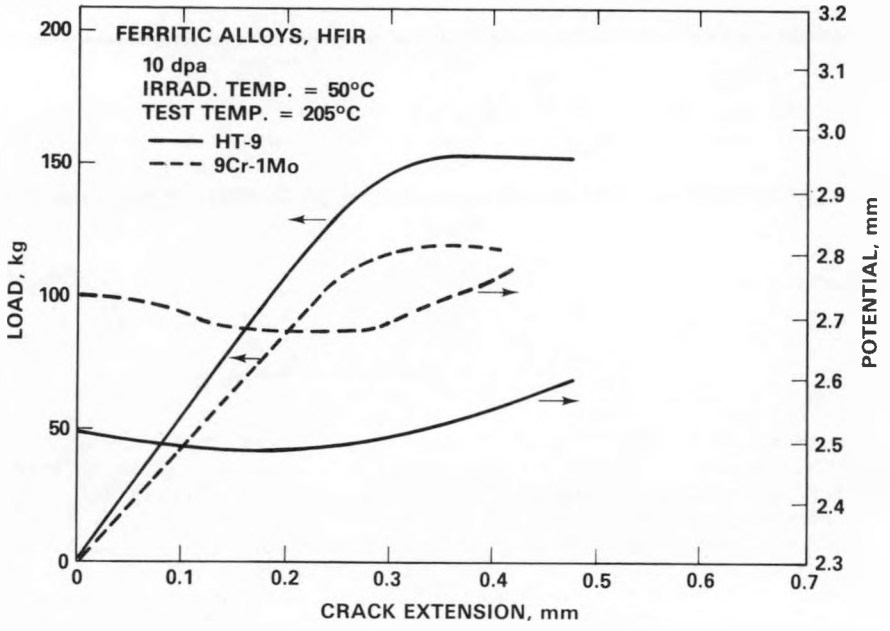

Fig. 7.17.1. Potential output and load versus displacement for irradiated HT-9 and 9Cr-1Mo tested at 205°C.

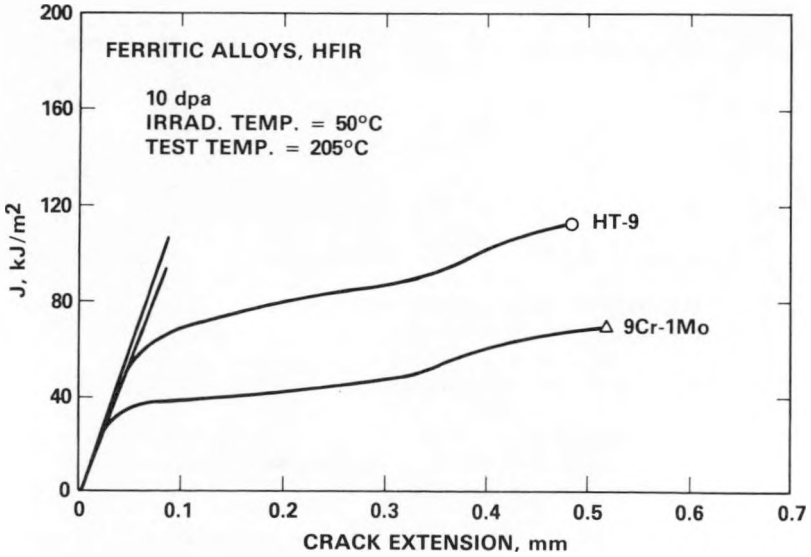

Fig. 7.17.2. J versus Δa curves obtained via an electropotential calibration curve for irradiated HT-9 and 9Cr-1Mo tested at 205°C.

was determined from these J versus Δa curves and the blunting lines. Table 7.17.1 compiles the values of J_{1c} and tearing modulus (T) in terms of test temperature. T is defined in Reference 4.

Table 7.17.1. Fracture toughness of ferritic alloys irradiated in HFIR

Alloy	Test Temp. (°C)	J_{1c} (kJ/m^2)	T
HT-9	25	63.3	-
HT-9	93	52.0	33
HT-9	205	56.7	28
9Cr-1Mo	93	32.9	23
9Cr-1Mo	205	35.2	16
9Cr-1Mo	450	30.8	59

The temperature dependence of J_{1c} and T for HT-9 and 9Cr-1Mo irradiated in HFIR are shown in Figs. 7.17.3 and 7.17.4, respectively. Also plotted in Fig. 7.17.3 are the preirradiation fracture toughness data of both alloys for comparisons. As can be seen in Fig. 7.17.3, the post-irradiation fracture toughness decreased slightly with increasing temperature. Evidently, the fracture toughness degradation due to HFIR irradiation to 10 dpa at 50°C is much more severe for 9Cr-1Mo than for HT-9. Results in Fig. 7.17.4 indicate that the tearing modulus of 9Cr-1Mo was lower than that of HT-9. The toughness degradation and irradiation hardening resulting from HFIR irradiation reduced the minimum thickness (25 $J_{1c}/\sigma_y)^5$ required for valid J_{1c} values to 1.0-1.6 mm, which is less than the thickness of (2.54 mm) of the specimens tested in this work.

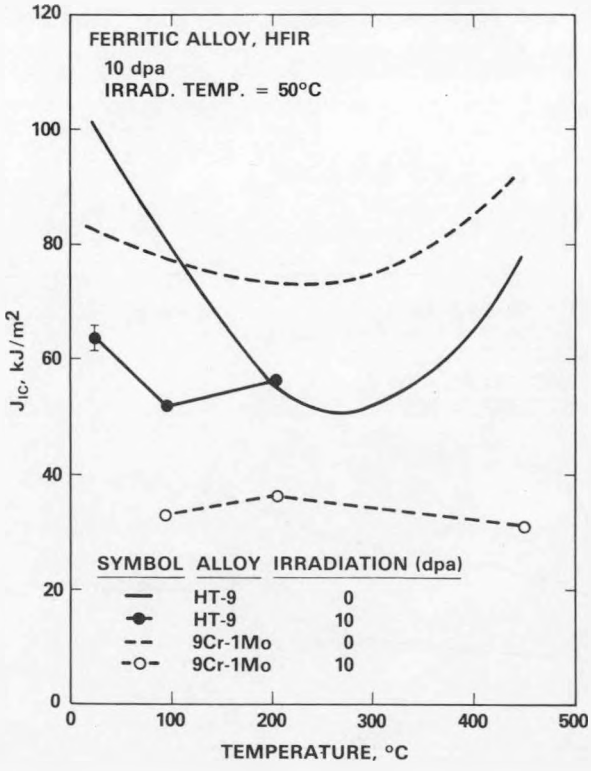

Fig. 7.17.3. Temperature dependence of fracture toughness for irradiated HT-9 and 9Cr-1Mo.

Compared to the EBR-II irradiation,[2] HFIR irradiation has a greater negative impact on the fracture properties of ferritic alloys. This is consistent with tensile data that showed a much more severe ductility loss suffered by HT-9 irradiated in HFIR[1,6] than in EBR-II.[7] The major differences in the HFIR irradiation as compared to the EBR-II irradiation are the higher production rate of helium and the lower irradiation temperature of 50°C. Because of the low nickel content in the materials, the quantity of helium produced in HFIR is small (about 20 at.ppm). However, at present the available data are not sufficient

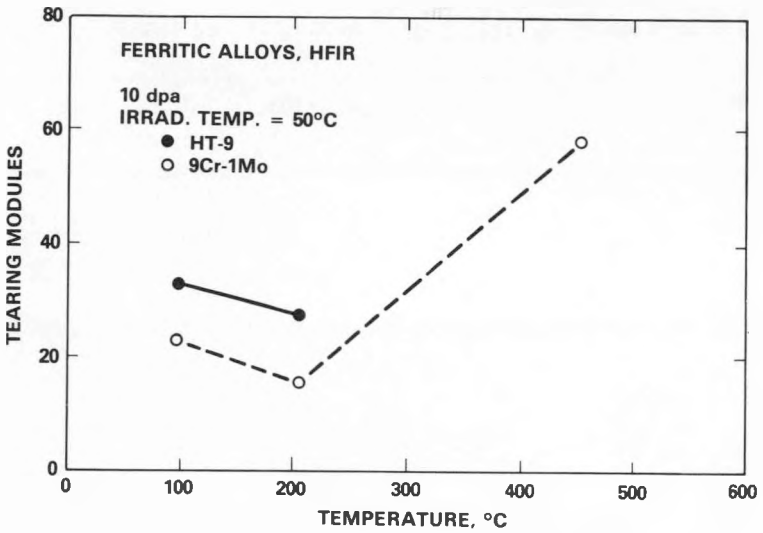

Fig. 7.17.4 Temperature dependence of tearing modulus for irradiated HT-9 and 9Cr-1Mo.

enough to single out the influence of helium on the drastic reduction in elongation due to HFIR irradiation for ferritic alloys. The unusual high strength accompanied by poor fracture toughness exhibited by these materials is a consequence of flow localization around the crack tip in the materials.[8,9] In addition to flow being localized within very narrow bands, the helium may participate in reducing the fracture surface energy and providing weak paths for crack propagation. The problems of embrittlement associated with the extremely low ductility displayed by high strength materials such as precipitation-hardening alloys or irradiated materials are more easily understood from the concept of fracture energy than fracture strain or stress, as these materials mostly still retain satisfactory toughness.

On the other hand, irradiation at low temperatures results in a large amount of hardening, since annealing cannot occur. This low irradiation temperature in HFIR may be responsible for the significant reduction in fracture toughness. As irradiations in EBR-II are limited to a minimum of 370°C further studies on HFIR irradiation effects are needed to clarify the uncertainty.

7.17.6 Conclusion

The first fracture toughness data of HT-9 and 9Cr-1Mo irradiated in HFIR to 10 dpa at 50°C were obtained. Results showed that the post-irradiation fracture toughness decreased slightly with increasing temperature. The thickness of the specimens satisfied the thickness criterion for a valid J_{1C} test.

Test results also showed that the reduction in fracture toughness for both alloys due to HFIR irradiation appeared to be more significant than EBR-II irradiation. Among other factors influencing the fracture properties, the effects of low irradiation temperature and helium need further studies.

7.17.7 References

1. R. L. Klueh, J. M. Vitek and M. L. Grossbeck, "Effect of Low Temperature Irradiation with (n, α) Helium Production on Tensile Properties of 12Cr-1MoVW-Type Steels," *J. Nucl. Mater.* 104, 887-892 (1981).

2. F. H. Huang and D. S. Gelles, "Fracture Toughness of Irradiated HT-9 Weld Metal," pp. 125-130 in *ADIP Semiannu. Prog. Rep. Mar. 31, 1983,* DOE/ER-0045/10, U.S. DOE, Office of Fusion Energy.

3. F. H. Huang and G. L. Wire, "Analysis of Single Specimen Tests on HT-9 for J_{1C} Determination," pp. 236-254 in *ADIP Quart. Prog. Rep. Sept. 30, 1980,* DOE/ER-0045/3, U.S. DOE, Office of Fusion Energy.

4. P. C. Paris, H. Tada, A. Zahoor and H. Ernst, "The Theory of Instability of the Tearing Mode of Elastic-Plastic Crack Growth," pp. 5-36 in *Elastic-Plastic Fracture,* ASTM STP 668, American Society for Testing and Materials, Philadelphia, 1979.

5. ASTM Standard E813, "Standard Test Method for J_{1C}, A Measure of Fracture Toughness".

6. R. L. Klueh, J. M. Vitek and M. L. Grossbeck, "Nickel-Doped Ferritic (Martensitic) Steels for Fusion Reactor Irradiation Studies: Tempering Behavior and Unirradiated and Irradiated Tensile Properties," pp. 648-664 in *Effects of Radiation on Materials,* ASTM STP 782, American Society for Testing and Materials, Philadelphia, 1982.

7. F. A. Smidt, Jr., H. R. Hawthorne and V. Provenzano, "The Fracture Resistance of HT-9 After Irradiation at Elevated Temperatures," pp. 269-284 in *Effects of Irradiation on Materials,* ASTM STP 725, American Society for Testing and Materials, Philadelphia, 1981.

8. G. T. Hahn and A. R. Rosenfield, *Metall. Trans.* A(9A) 653-668 (1975).

9. F. H. Huang, "The Fracture Characterization of Highly Irradiated Type 316 Stainless Steel," HEDL-SA-2967, Accepted for Publication in *Int. J. Fracture*, 1983.

8. STATUS OF IRRADIATION EXPERIMENTS AND MATERIALS INVENTORY

8.1 IRRADIATION EXPERIMENT STATUS AND SCHEDULE — M. L. Grossbeck (Oak Ridge National Laboratory)

A large number of planned, in-progress, and completed reactor irradiation experiments support the ADIP program. Table 8.1.1 summarizes the parameters that describe completed experiments. Experiments that have been removed from the reactor only recently, are currently undergoing irradiation, or are planned for future irradiation are included in the schedule bar charts of Table 8.1.2.

Experiments were under way during the reporting period in the Oak Ridge Research Reactor (ORR) and the High Flux Isotope Reactor (HFIR), which are mixed-spectrum reactors, and in the Experimental Breeder Reactor (EBR-II), which is a fast reactor.

During the reporting period experiments HFIR-CTR-42, -43, -44, -45, -46, and HFIR-MFE-RB2 were removed from the HFIR. The first two, HFIR-CTR-42 and -43 contain the first tensile specimens of the Path A PCA. The second two, HFIR-CTR-44 and -45 are cooperative experiments with the European Community and Japan on austenitic stainless steels. The last two, HFIR-CTR-46 and HFIR-MFE-RB2, contained specimens of ferritic steels. Experiment AD-2, also a ferritic steel experiment, was removed from EBR-II. Two irradiation capsules were loaded into the HFIR, HFIR-CTR-47 and -48. These experiments were designed to study the effect of HFIR irradiation on impact properties of ferritic alloys.

The higher temperature capsule of the spectral tailoring experiment, ORR-MFE-4B, was successfully repaired and reloaded in the ORR following a containment failure. The pressurized tubes were measured and found to yield useful irradiation creep data.

The initial scheduling of a new series of experiments for the HFIR, the HFIR-JP series, is shown on the final page of Table 8.1.2. The experiments are part of a joint program between the United States and Japan. They will contain specimens from both national programs, with the first eight experiments devoted to Path A alloys. Irradiation will be in the outer target rod positions in the flux trap region of HFIR.

Table 8.1.1. Descriptive parameters for completed ADIP program fission reactor irradiation experiments

Experiment	Major objective	Alloy	Temperature (°C)	Displacement damage (dpa)	Helium (at. ppm)	Duration (months)	Date completed
			Experiments in ORR				
ORR-MFE-1	Scope the effects of composition and microstructure on tensile, fatigue, and irradiation creep	Paths A, B, C	250–600	2	≤10	4	6/78
ORR-MFE-2	Scope the effects of composition and microstructure on tensile, fatigue, and irradiation creep	Paths A, B, C	300–600	6	≤60	15	4/80
ORR-MFE-5	In-reactor fatigue crack growth	Path A	325–460	1	<10	2	2/81
			Experiments in EBR-II				
Subassembly X-264	Effect of preinjected helium on microstructure, tensile properties, and irradiation creep	316, PE-16, V–20% Ti, V–15% Cr–5% Ti, Nb–1% Zr	500–825	8	2–200	4	1/77
AA-X Subassembly X-287	Effect of preinjected helium on microstructure, tensile properties, and irradiation creep	316, PE-16, V–20% Ti, V–15% Cr–5% Ti, Nb–1% Zr	400–700	20	2–200	23	12/78
Subassembly X-217D	Stress relaxation	Titanium alloys	450	2		1	1/78
Pins B285, B286, and B284	Swelling, fatigue crack growth, and tensile properties	Titanium alloys	370–550	25		14	9/79
			Experiments in HFIR				
HFIR-CTR-3	Swelling and tensile properties	PE-16, Inconel 600	300–700	4.3–9	350–1800	3	2/75
HFIR-CTR-4	Swelling and tensile properties	PE-16	300–700	2.2–4.5	100–350	2	3/77

Table 8.1.1. (Continued)

Experiment	Major objective	Alloy	Temperature (°C)	Displacement damage (dpa)	Helium (at. ppm)	Duration (months)	Date completed
HFIR-CTR-5	Swelling and tensile properties	PE-16, Inconel 600	300–700	4.3–9	350–1800	3	4/75
HFIR-CTR-6	Swelling and tensile properties	PE-16, Inconel 600	300–700	4.3–9	350–1800	3	4/75
HFIR-CTR-7	Swelling and tensile properties	PE-16	300–700	9–18	1250–3000	7	8/77
HFIR-CTR-8	Swelling and tensile properties	PE-16	300–700	9–18	1250–3000	7	8/77
HFIR-CTR-9	Swelling and tensile properties	316, 316 + Ti	280–680	10–16	400–1000	6	5/77
HFIR-CTR-10	Swelling and tensile properties	316, 316 + Ti	280–680	10–16	400–1000	6	5/77
HFIR-CTR-11	Swelling and tensile properties	316, 316 + Ti	280–680	10–16	400–1000	6	5/77
HFIR-CTR-12	Swelling and tensile properties	316, 316 + Ti	280–680	7–10	200–500	4	2/77
HFIR-CTR-13	Swelling and tensile properties	316, 316 + Ti	280–680	7–10	200–500	4	2/77
HFIR-CTR-14	Fatigue	316	430	9–15	400–1000	7	12/77
HFIR-CTR-15	Fatigue	316	550	6–9	200–400	4	10/78
HFIR-CTR-16	Weld characterization, swelling, and tensile properties	316, PE-16, Inconel 600	55	6–9	150–2700	4	8/77
HFIR-CTR-17	Weld characterization	316	280–620	7–13	180–460	5.5	10/77
HFIR-CTR-18	Swelling and tensile properties	316, PE-16	280–700	17–27	1600–5600	12	6/78
HFIR-CTR-19	Weld characterization	316	280–620	7–10	200–500	4	12/77
HFIR-CTR-20	Fatigue	316	430	6–9	200–400	4	1/78
HFIR-CTR-21	Fatigue	316	550	9–15	400–1000	7	7/78
HFIR-CTR-22	Fatigue	316	430	6–9	200–400	4	3/78
HFIR-CTR-23	Fatigue	PE-16	430	6–9	370–1000	3.5	2/79
HFIR-CTR-24	Temperature calibration and tensile properties	316	300–620	2.2	30	1	12/78
HFIR-CTR-26	Swelling and tensile properties	316	284–620	30	1900	10	4/80
HFIR-CTR-27	Swelling and tensile properties	316	284–620	56	3500	18	1/81
HFIR-CTR-28	Swelling and tensile properties	316	370–560	30	1900	10	12/80
HFIR-CTR-29	Swelling and tensile properties	316	370–560	56	3500	18	8/81
HFIR-CTR-30	Swelling, microstructure, and ductility	Paths A, B, C, D, E	300–600	40	$\leq$15,000	14	11/8/81
HFIR-CTR-31	Swelling, microstructure, and ductility	Paths A, B, C, D, E	300–600	20	$\leq$7500	8	5/28/81
HFIR-CTR-32	Swelling, microstructure, and ductility	Paths A, B, C, D, E	300–600	10	$\leq$3000	4	12/81
HFIR-CTR-33	Swelling, tensile properties, weld characterization	Paths A and E	55	10	$\leq$510	4	10/80
HFIR-MFE-T1	Swelling, tensile fatigue	Path E	55	30	$\leq$300	12	8/10/82
HFIR-MFE-T2	Swelling, tensile fatigue	Path E	55	9	$\leq$75	3	5/3/81
HFIR-MFE-T3	Impact properties	Path E	55	10	$\leq$85	4	12/24/81

Table 8.1.2. Objectives and schedule for current and planned ADIP program reactor irradiation experiments

Experiment designation	Major objective
A. Oak Ridge Research Reactor	
ORR-MFE-4	Effect of irradiation on tensile, fatigue, and irradiation creep of path A PCA (Prime Candidate Alloy) and path B base research alloys. Spectral tailoring to maintain correct He/dpa ratio. Irradiation on continuing basis. 330–600°C①
B. Experimental Breeder Reactor (EBR-II)	
Experiment plan depends on alloy availability. EBR-II space not yet identified.	Effect of irradiation on swelling, tensile, fatigue, and crack growth properties of V and Nb scoping alloys. 370, 450, 550, and 650°C. Position in reactor not finalized, therefore no fluence estimate.③
AD-2 (6 pins in separate subassemblies of row 4)	To supplement present EBR-II data on ferritic alloys with data on crack growth, fatigue, and fatigue toughness. Temperature 390, 450, 500, and 550°C. 15 and 30 dpa.
C. Fast Flux Test Facility (FFTF)	
FFTF MOTA Fusion Experiment	Microstructural and mechanical properties of Path A, C, and E alloys. 15, 45, 75, 105 dpa; 420, 500, 600°C.

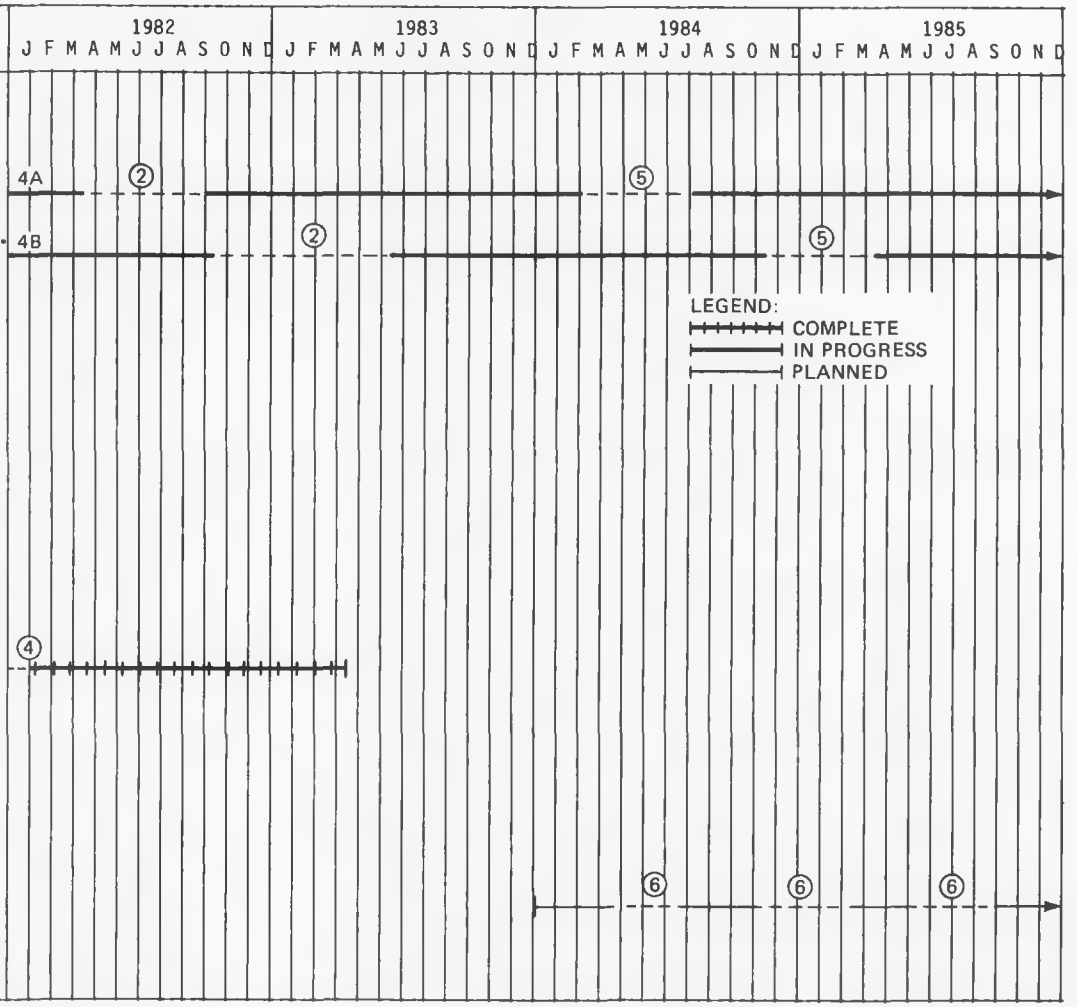

①MFE-4A operates at 330 and 400°C. MFE-4B will operate at 500 and 600°C.

②Removed from reactor for reencapsulation.

③Delayed for undetermined period.

④Interim examination. Experiment out of reactor. Reencapsulated in subassembly X-344B.

⑤Remove from reactor for 10 dpa specimen discharge.

⑥Remove for specimen discharge.

Table 8.1.2. (Continued)

Experiment designation	Major objective
D. High Flux Isotope Reactor (HFIR)	
HFIR-MFE-RB1	Swelling, microstructure, crack growth, fracture toughness, impact, tensile, and fatigue properties of path E alloys. 10 dpa, 90 ppm He, 55°C.
HFIR-MFE-RB2	Similar to HFIR-MFE-RB1, to 20 dpa, 200 ppm He.
HFIR-MFE-RB3	Similar to HFIR-MFE-RB1, to 10 dpa, 90 ppm He.
HFIR-CTR-34	Impact properties of path E alloys. 10 dpa, 0 to 75 ppm He, 300, 400°C.
HFIR-CTR-35	Impact properties of path E alloys. 10 dpa, 0 to 75 ppm He, 300, 400°C.
HFIR-CTR-36	Fatigue properties of path A alloys. 30 dpa, 2000 ppm He.
HFIR-CTR-39	Swelling, tensile properties of path E alloys. 12 dpa, up to 90 ppm He, 300 to 500°C.
HFIR-CTR-40	Swelling, tensile properties of path E alloys. 12 dpa, up to 90 ppm He, 300 to 500°C.
HFIR-CTR-41	Swelling, tensile properties of path E alloys. 12 dpa, up to 90 ppm He, 300 to 500°C.
HFIR-CTR-42	Swelling, tensile properties of path A alloys. 20 dpa, 1100 ppm He, 300 to 600°C.

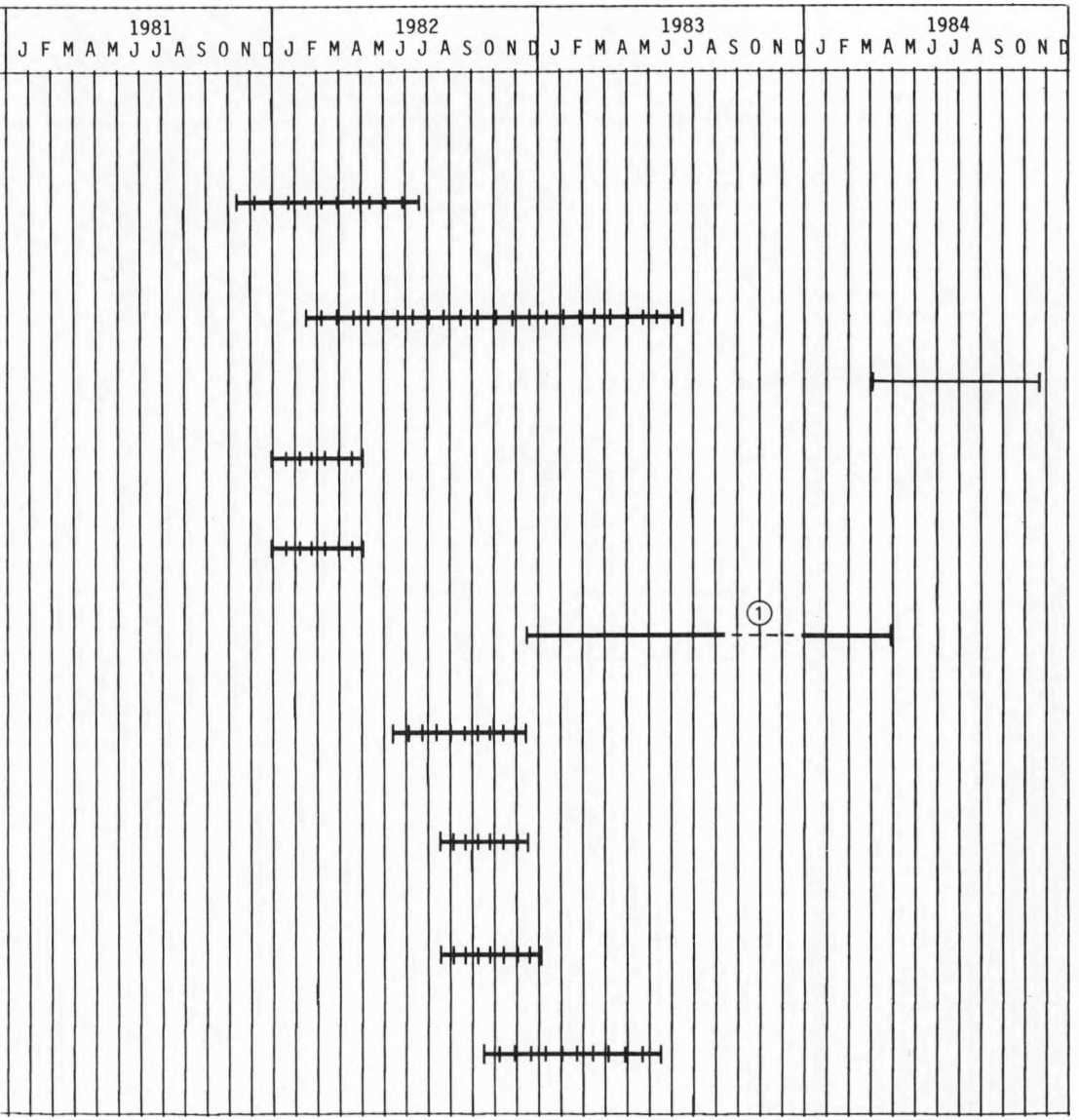

① HFIR shut down for reflector replacement.

Table 8.1.2. (Continued)

Experiment designation	Major objective
HFIR-CTR-43	Swelling, tensile properties of path A alloys. 20 dpa, 1100 ppm He, 300 to 600°C.
HFIR-CTR-44	Swelling, tensile properties of path A alloys. 10 dpa, 500 ppm He, 250–400°C. Joint experiment of U.S., European Community, and Japan.
HFIR-CTR-45	Similar to HFIR-CTR-44.
HFIR-CTR-46	Impact properties of path E alloys. 10 dpa, 75 ppm He, 300 and 400°C.
HFIR-CTR-47	Impact properties of path E alloys. 40 dpa, 400 ppm He, 300 and 400°C.
HFIR-CTR-48	Similar to HFIR-CTR-47.
HFIR-CTR-49	Tensile properties of path E alloys. 40 dpa, 400 ppm He, 300 to 500°C.
HFIR-CTR-50	Similar to HFIR-CTR-49.
HFIR-CTR-51	Swelling, tensile properties of low-activation alloys. 20 dpa, 300–600°C
HFIR-CTR-52	Fatigue properties of 316 SS 10 dpa, 500 ppm He 430°C. Joint experiment with European community and Japan.
HFIR-MFE-100	Swelling, tensile properties of Paths A, C, E alloys. 100 dpa, 300–600°C

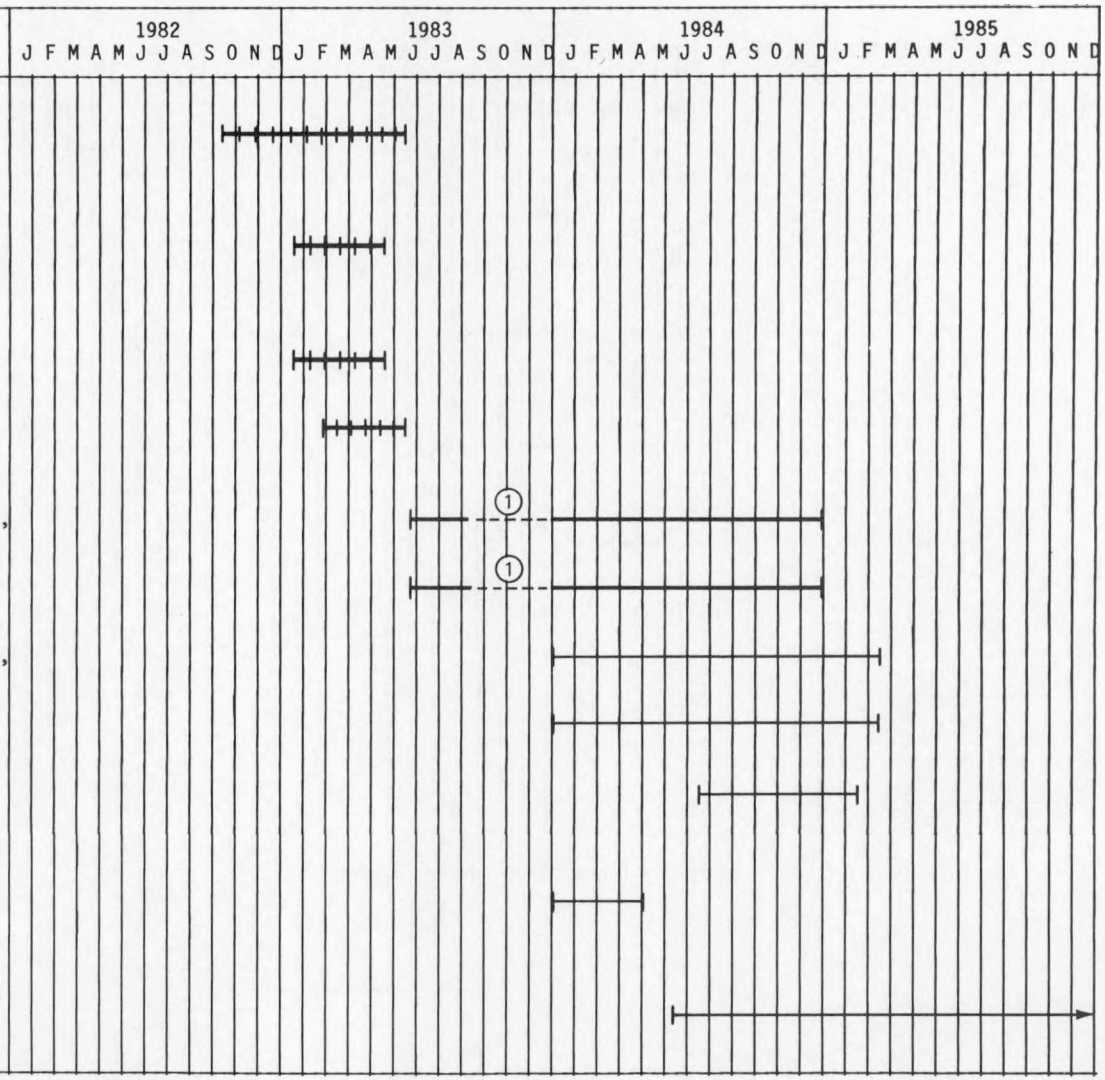

①HFIR shut down for reflector replacement.

Table 8.1.2. (Continued)

Experiment designation	Major objective
HFIR-JP-1①	Swelling, tensile and fatigue properties, and microstructure of path A alloys. 300–600°C, 30 dpa, 2000 ppm He.
HFIR-JP-2	Similar to HFIR-JP-1 but to 50 dpa, 3500 ppm He.
HFIR-JP-3	Similar to HFIR-JP-1.
HFIR-JP-4	Swelling, tensile properties, and microstructure of path A alloys. 55°C, 50 dpa, 2000 ppm He.
HFIR-JP-5	Similar to HFIR-JP-2.
HFIR-JP-6	Similar to HFIR-JP-1.
HFIR-JP-7	Similar to HFIR-JP-1.
HFIR-JP-8	Similar to HFIR-JP-2.

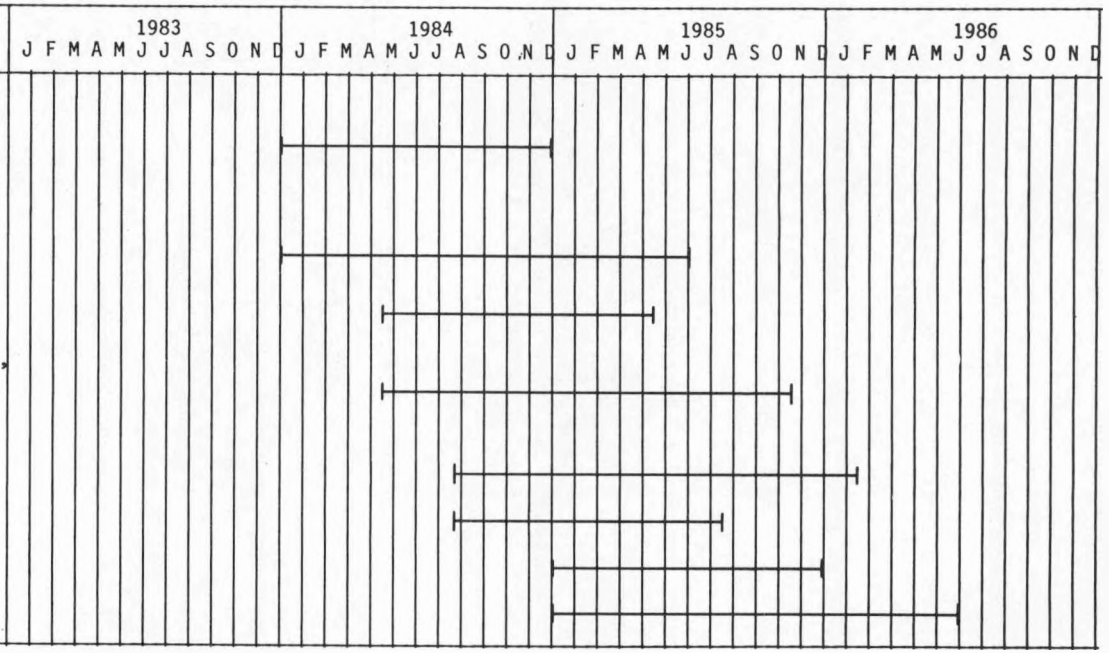

①The HFIR-JP experiment series is a joint program shared by the U.S. and Japan Fusion Reactor Materials activities.

8.2 FUSION PROGRAM RESEARCH MATERIALS INVENTORY — T. K. Roche, F. W. Wiffen (Oak Ridge National Laboratory), J. W. Davis (McDonnell Douglas Company), and T. A. Lechtenberg (GA Technologies)

8.2.1 ADIP Tasks

ADIP Task I.D.1, Materials Stockpile for MFE Programs.

8.2.2 Objective

Oak Ridge National Laboratory maintains a central inventory of research materials to provide a common supply of materials for the Fusion Reactor Materials Program. This will minimize unintended material variations and provide for economy in procurement and for centralized record keeping. Initially this inventory is to focus on materials related to first-wall and structural applications and related research, but various special purpose materials may be added in the future.

The use of materials from this inventory for research that is coordinated with or otherwise related technically to the Fusion Reactor Materials Program of DOE is encouraged.

8.2.3 Materials Requests and Release

Materials requests shall be directed to the Fusion Program Research Materials Inventory at ORNL (Attention: F. W. Wiffen). Materials will be released directly if

(a) the material is to be used for programs funded by the Office of Fusion Energy, with goals consistent with the approved Materials Program Plans of the Materials and Radiation Effects Branch.

(b) the requested amount of material is available without compromising other intended uses.

Materials requests that do not satisfy both (a) and (b) will be discussed with the staff of the Reactor Technologies Branch, Office of Fusion Energy, for agreement on action.

8.2.4 Records

Chemistry and materials preparation records are maintained for all inventory material. All materials supplied to program users will be accompanied by summary characterization information.

8.2.5 Summary of Current Inventory and Material Movement During Period April through September, 1983

A condensed, qualitative description of the content of materials in the Fusion Program Research Materials Inventory is given in Table 8.2.1. This table indicates the nominal diameter of rod or thickness of sheet for product forms of each alloy and also indicates by weight the amount of each alloy in larger sizes available for fabrication to produce other product forms as needed by the program. There was no material added to the inventory during this reporting period. Table 8.2.2 gives the materials distributed from the inventory.

Alloy compositions and more detail on the alloys and their procurement and/or fabrication are given in this and earlier ADIP progress reports.

Table 8.2.1 Summary status of materials available in the fusion program research materials inventory

Alloy	Product form			
	Ingot or bar[a] weight (kg)	Rod diameter (mm)	Sheet thickness (mm)	Thin-wall tubing wall thickness (mm)
	Path A alloys			
Type 316 SS	900	16 and 7.2	13 and 7.9	0.25
Path A PCA[b]	490	12	13	0.25
USSR Cr-Mn Steel[c]		10.5	2.6	
NONMAGNE 30[d]		18.5	10	
	Path B alloys			
PE-16	140	16 and 7.1	13 and 1.6	0.25
B-1	180			
B-2	180			
B-3	180			
B-4	180			
B-6	180			

Table 8.2.1 (continued)

Alloy	Product form			
	Ingot or bar[a] weight (kg)	Rod diameter (mm)	Sheet thickness (mm)	Thin-wall tubing, wall thickness (mm)
Path C alloys				
Ti-64			2.5 and 0.76	
Ti-6242S		63	6.3, 3.2, and 0.76	
Ti-5621S			2.5 and 0.76	
Ti-38644			0.76 and 0.25	
Nb—1% Zr		6.3	2.5, 1.5, and 0.76	
Nb—5% Mo—1% Zr		6.3	2.5, 1.5, and 0.76	
V—20% Ti		6.3	2.5, 1.5, and 0.76	
V—15% Cr—5% Ti		6.3	2.5, 1.5, and 0.76	
VANSTAR-7		6.3	2.5, 1.5, and 0.76	
Path D alloy				
LRO-37[e]			3.3, 1.6, and 0.8	
Path E alloys				
HT9 (AOD fusion heat)[f]	3400		28.5, 15.8, 9.5, and 3.1	
HT9 (AOD/ESR fusion heat)	7000	25, 50, and 75	28.5, 15.8, 9.5, and 3.1	
HT9			4.5 and 18	
HT9 + 1% Ni			4.5 and 18	
HT9 + 2% Ni			4.5 and 18	
HT9 + 2% Ni + Cr adjusted			4.5 and 18	
T-9 modified[g]			4.5 and 18	
T-9 modified + 2% Ni			4.5 and 18	
T-9 modified + 2% Ni + Cr adjusted			4.5 and 18	
2 1/4 Cr-1 Mo			*h*	

[a]Greater than 25 mm, minimum dimension.

[b]Prime candidate alloy.

[c]Rod and sheet of a USSR stainless steel supplied under the U.S.-USSR Fusion Reactor Materials Exchange Program.

[d]NONMAGNE 30 is an austenitic steel with base composition Fe—14% Mn—2% Ni—2% Cr. It was supplied to the inventory by the Japanese Atomic Energy Research Institute.

[e]LRO-37 is the ordered alloy $(Fe,Ni)_3(V,Ti)$ with composition Fe—39.4% Ni—22.4% V—0.43% Ti.

[f]Alloy 12 Cr-1 MoVW, with composition equivalent to Sandvik alloy HT9.

[g]T-9 modified is the alloy 9 Cr-1 MoVNb.

[h]Material is thick-wall pipe, rerolled as necessary to produce sheet or rod.

Table 8.2.2. Fusion program research materials inventory disbursements
April 1, 1983 to September 30, 1983

Alloy	Heat	Product form	Dimension[a] (mm)	Quantity (m)	Quantity (m^2)	Sent to
Path A alloys — austenitic stainless steels						
316 SS Ref. heat	X-15893	Rod	13.31	1.84		Radiation Effects Group, M&C Division, ORNL
		Rod	9.14	3.68		Petten, Netherlands, for IEA Annex II Program
Path A PCA[b]	K-280	Bar	33.35	0.61		GA Technologies
		Rod	9.14	2.75		Petten, Netherlands, for IEA Annex II Program
		Rod	4.17	9.75		Radiation Effects Group, M&C Division, ORNL
		Plate	4.01		0.13	HEDL
		Sheet	0.76		0.068	Radiation Effects Group, M&C Division, ORNL
		Sheet	0.61		0.041	HEDL
		Sheet	0.61		0.014	Argonne National Laboratory
		Sheet	0.25		0.033	Radiation Effects Group, M&C Division, ORNL
EP-838[c]		Sheet	0.71		0.031	Radiation Effects Group, M&C Division, ORNL
		Sheet	0.25		0.029	Radiation Effects Group, M&C Division, ORNL
NONMAGNE-30[d]		Plate	9.40		0.015	HEDL
Path C alloys — reactive and refractory alloys						
V—20% Ti	CAM 832 Bot-3	Sheet	0.84		0.012	EG&G Idaho, Inc.
	CAM 833-7	Sheet	0.84		0.016	Radiation Effects Group, M&C Division, ORNL
	CAM 832 Bot-4	Sheet	0.28		0.04	Radiation Effects Group, M&C Division, ORNL
V—15% Cr—5% Ti	CAM 835B-4	Rod	6.35	1.22		Argonne National Laboratory
	CAM 834-6	Sheet	0.84		0.019	Argonne National Laboratory
	CAM 835A-3	Sheet	0.84		0.005	Grumman Aerospace Corp.
	CAM 834-6	Sheet	0.84		0.007	Grumman Aerospace Corp.
	CAM 834-6	Sheet	0.84		0.003	EG&G Idaho, Inc.
	CAM 835A-3	Sheet	0.84		0.042	EG&G Idaho, Inc.
	CAM 834-3	Sheet	0.84		0.041	Radiation Effects Group, M&C Division, ORNL
	CAM 834-2	Sheet	0.28		0.086	Radiation Effects Group, M&C Division, ORNL
Vanstar-7	CAM 837-7	Sheet	0.84		0.016	Radiation Effects Group, M&C Division, ORNL
	CAM 836 Bot-3	Sheet	0.25		0.067	Radiation Effects Group, M&C Division, ORNL
Path D alloys — innovative material concepts						
LRO-37-HP[e]	EB 11581-2-1630	Sheet	0.76		0.046	Alloy Design Group, M&C Division, ORNL
LRO-37-CG	EB 11681-2-0735	Sheet	0.76		0.064	Alloy Design Group, M&C Division, ORNL

Table 8.2.2. (continued).

Alloy	Heat	Product form	Dimension[a] (mm)	Quantity (m)	Quantity (m^2)	Sent to
		Path E alloys — ferritic steels				
T-9	30176	Sheet	0.76		0.068	Radiation Effects Group, M&C Division, ORNL
		Sheet	0.25		0.045	Radiation Effects Group, M&C Division, ORNL
HT-9	AOD/ESR-9607R2	Tubing	4.57	0.91		HEDL
		Plate	28.58		0.35	Univ. of California, Santa Barbara
		Plate	15.88		0.31	Sandia National Laboratories, Livermore
		Sheet	0.76		0.17	Radiation Effects Group, M&C Division, ORNL
		Sheet	0.25		0.085	Radiation Effects Group, M&C Division, ORNL

[a]Characteristic dimension: thickness for plate and sheet, diameter for rod and tubing.

[b]Prime candidate alloy.

[c]A USSR Cr-Mn stainless steel supplied under the U.S.–USSR Fusion Reactor Materials Exchange Program.

[d]An austenitic steel with base composition Fe–14% Mn–2% Ni–2% Cr supplied to the inventory by the Japanese Atomic Energy Research Institute.

[e]LRO-37 is the ordered alloy $(Fe,Ni)_3(V,Ti)$ with composition Fe–39.4% Ni–22.4 % V–0.43% Ti.

9. MATERIALS COMPATIBILITY AND HYDROGEN PERMEATION STUDIES

9.1 CORROSION OF PATH A PCA AND 12 Cr-1 MoVW STEEL IN THERMALLY CONVECTIVE LITHIUM — P. F. Tortorelli and J. H. DeVan (ORNL)

9.1.1 ADIP Task

ADIP Task I.A.3, Perform Chemical and Metallurgical Compatibility Analyses.

9.1.2 Objective

The purpose of this task is to determine the corrosion resistance of candidate first-wall materials to slowly flowing lithium in the presence of a temperature gradient. Corrosion and deposition rates are measured as functions of time, temperature, additions to the lithium, and flow conditions. These measurements are combined with chemical and metallographic examinations of specimen surfaces to establish the mechanisms and rate-controlling processes for dissolution and deposition reactions.

9.1.3 Summary

Exposure of path A PCA alloys to thermally convective lithium for 6700 h at 600 and 570°C resulted in corrosion reactions that were similar to what is observed for other austenitic alloys exposed under similar conditions. It corroded more rapidly than type 316 stainless steel, and the presence of nitride stringers in PCA did not affect the measured weight losses. Consideration of the weight change and surface analysis data for 12 Cr-1 MoVW steel exposed to thermally convective lithium between 500 and 350°C for 10,088 h revealed that reactions with carbon and nitrogen were probably the principal corrosion processes for this alloy in this temperature range. Corrosion was not severe.

9.1.4 Progress and Status

We have continued our mass transfer studies of candidate first-wall materials in flowing lithium by use of previously described[1] thermal convection loops (TCLs) with accessible specimens. These loops are designed so that lithium samples can be taken and corrosion coupons can be withdrawn and inserted without interrupting the lithium flow. One such lithium–type 316 stainless steel TCL is being used to observe the dissolution behavior of path A PCA specimens with different thermomechanical treatments. Our purpose is to study the effects of microstructure on corrosion of austenitic stainless steel by lithium as well as to determine the dissolution rate of PCA relative to that of standard type 316 stainless steel. In the first experiment, coupons of path A PCA alloys A1 and A3 were placed at the 600 and 570°C positions in a type 316 stainless steel TCL that had previously circulated lithium for greater than 10,000 h. The second experiment, which is currently in progress, uses specimens of PCA alloys A3 and A3A in these loop positions. While A1 (annealed), A3 (cold worked) and A3A (cold worked, nitride stringers) differed microstructurally, they all had the same composition:

Element	Content (wt %)	Element	Content (wt %)	Element	Content (wt %)
Ni	15.9	Mn	1.9	Al	0.05
Cr	14.0	Si	0.4	C	0.05
Mo	1.9	Ti	0.3	N	<0.01
Fe	65.0				

Because of prior operation with lithium, the hot-leg surfaces of the loop were known to have a considerably higher iron concentration than the as-received PCA alloys. However, the cold leg of the loop had been replaced before operation with the PCA specimens.

The preceding progress report included weight loss versus exposure time results for A1 and A3 specimens over the 6700-h duration of the first experiment. Since then a second set of specimens (alloys PCA-A3 and -A3A) has been exposed at 600 and 570°C to lithium in the same TCL for about 5000 h. The weight loss results from these specimens are shown in Fig. 9.1.1, which also contains the data from the previous PCA experiment. It is apparent that there is no difference in the weight loss behavior of A3 compared with A3A. Despite the known influence of nitrogen on the corrosion of ferrous alloys by lithium,[2] the presence of the nitrides in A3A did not lead to accelerated dissolution. However, it remains to be seen (by metallographic examination after a cumulative exposure of about 7000 h) whether the nitrides have an effect on the type of corrosive attack. The data in Fig. 9.1.1 also revealed that the total weight losses for the A3 specimens in the first and second experiments were similar and that the weight losses of A3 and A3A are less than that of A1 but still greater than those measured for type 316 stainless steel exposed under similar conditions.

The PCA-A1 and -A3 specimens exposed for 6700 h in the first TCL experiment have now been analyzed by optical and scanning electron microscopy. Metallographic examination of polished cross sections of these PCA specimens revealed corrosive attack consistent with the previously reported[3] dissolution rate measurements. As shown by the optical micrographs in Fig. 9.1.2 and the data in Table 9.1.1, the PCA-A1 specimen exposed at 600°C was attacked (as revealed by the depth of porosity) to a greater extent than the PCA-A3 material exposed at the same temperature. At 570°C, both A1 and A3 had similar depths of porosity. The depths of the porous layers on the PCA specimens were greater than those for similarly exposed type 316 stainless steel.

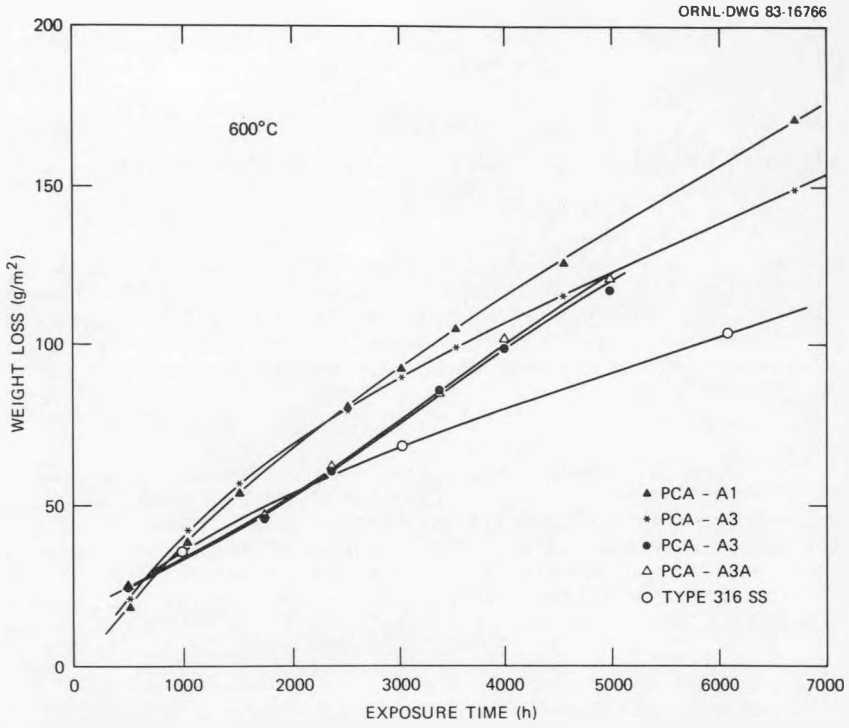

Fig. 9.1.1. Weight loss versus exposure time for austenitic alloys exposed to thermally convective lithium at 600°C.

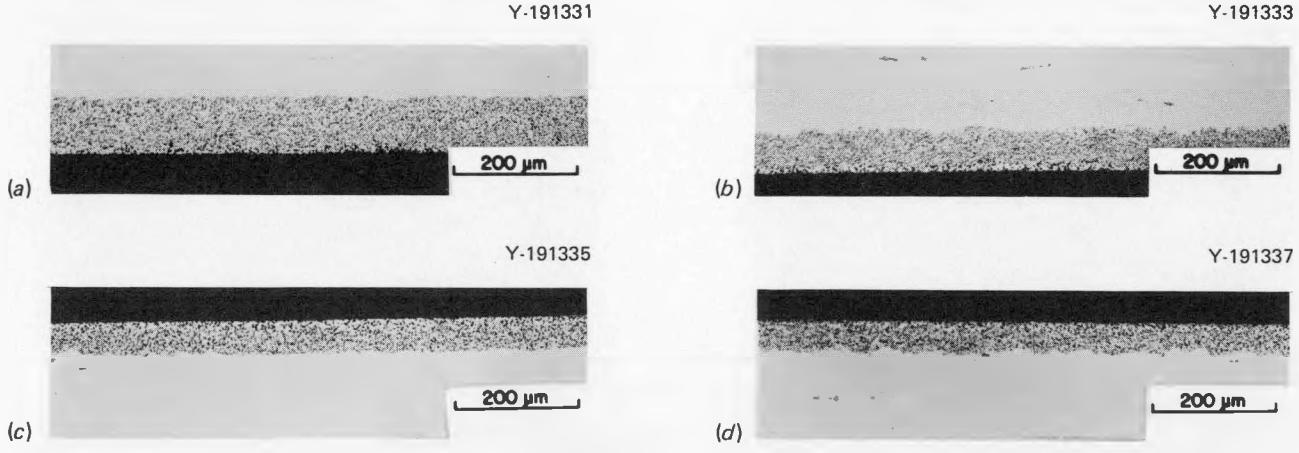

Fig. 9.1.2. Polished cross sections of PCA exposed to thermally convective lithium for 6700 h (*a*) A1, 600°C. (*b*) A3, 600°C. (*c*) A1, 570°C. (*d*) A3, 570°C.

le 9.1.1. Average depth of corrosive tack of PCA and type 316 stainless steel exposed to thermally convected lithium

T_{max} (°C)	Depth of porosity[a] (μm)		
	PCA-A1[b]	PCA-A3[b]	Type 316 SS[c]
600[d]	91 ± 3	68 ± 6	52 ± 4
570	54 ± 4	51 ± 2	41 ± 4

[a]Average of 20 measurements across both sides of specimen coupons.

[b]6700 h of lithium exposure.

[c]7500 h of lithium exposure.

[d]Maximum loop temperature.

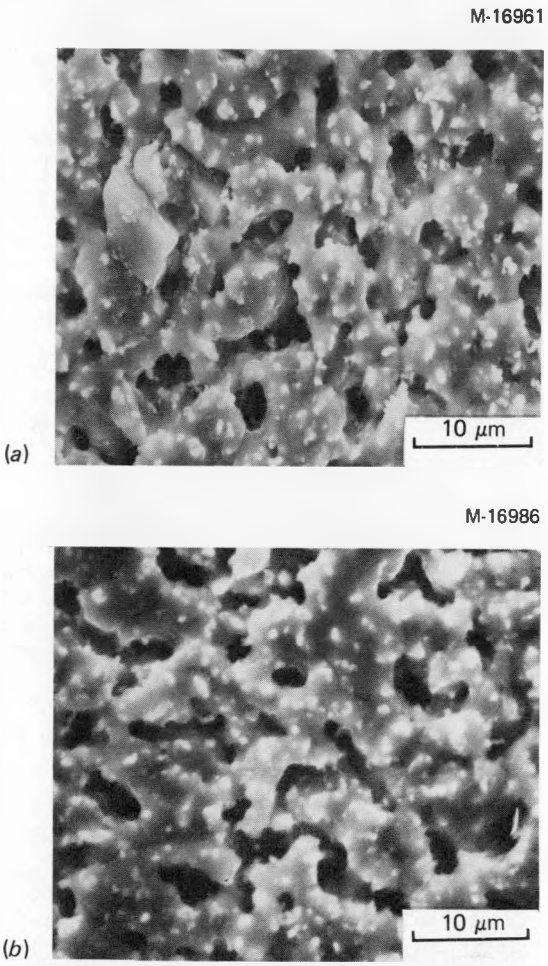

Fig. 9.1.3. Scanning electron micrographs of PCA exposed to thermally convective lithium for 6700 h at 600°C (*a*) A1. (*b*) A3.

Scanning electron microscopy and associated energy-dispersive x-ray analysis of the PCA specimens exposed at 600°C showed that A1 and A3 had similar porous surface layers (see Fig. 9.1.3). Energy-dispersive x-ray spectra taken from these surfaces revealed significant depletion in nickel and chromium. Analyses of a selected number of the nodules observed on these surfaces showed them to be enriched in molybdenum or titanium relative to the surrounding matrix.

The development of porosity and the preferential leaching of nickel and chromium from PCA were not unexpected. Such observations have also been reported for type 316 stainless steel and higher nickel alloys exposed to flowing lithium.[4-7] However, while the corrosion reactions between flowing lithium and PCA are the same as those that occur in other lithium–nickel-bearing-alloy systems, the extent of these reactions is not necessarily similar. For example, as measured by weight losses and depth of attack, the corrosion of PCA is greater than that of type 316 stainless steel. Because of the role of nickel in the dissolution process, this greater susceptibility of PCA relative to type 316 stainless steel can be attributed to the higher nickel content of PCA. Indeed, prior work has shown that the mass transfer of Fe-Ni-Cr alloys in thermally convective lithium increased as the concentration of nickel was increased from 11 to 32 wt. % (ref. 6). Furthermore, a recent study of PCA exposed in a lithium forced-convection loop system yielded similar results on the accelerated corrosion of this alloy with respect to typical austenitic stainless steel.[7] It is interesting to note that this compositional dependence is also observed in another liquid metal system: PCA suffered greater corrosion than type 316 stainless steel in Pb–17 at. % Li (ref. 8).

The above data show that for long exposures the corrosion of the annealed PCA specimen at 600°C was greater than that of the cold-worked specimen exposed at this temperature, while, at 570°C, no difference was observed. The reason for the greater corrosion of the annealed material at 600°C is not apparent, particularly since other work has shown the opposite effect.[7] However, these other experiments were not only conducted at lower temperatures but were also for shorter exposure times than the present study, which for short times showed slightly greater weight losses for the cold-worked specimens. A possible explanation for the greater corrosion of the annealed material in this study may have to do with the respective starting grain sizes of A1 (1175°C, 15 min, cold worked 25%, 1100°C, 30 min) and A3 (1175°C, 15 min, cold worked 20%). If the corrosion process is initiated by localized reactions at grain boundaries,[5] the smaller grain size of A1 can lead to greater attack due to the higher density of grain boundaries exposed to the lithium. At lower temperatures (like those of the work reported in ref. 7), another reaction may control the overall corrosion process such that the cold worked material is corroded more rapidly. In this regard, it is interesting to note that the present results show an effect at 600°C but not at 570°C.

The observation of molybdenum-enriched nodules on lithium-dissolved surfaces has also been reported previously for type 316 stainless steel.[5] These features are thought to result from the resistance of molybdenum to dissolution in lithium such that the nodules are areas of molybdenum precipitates (or residual molybdenum since its carbide is unstable in lithium) that recede more slowly than the surrounding matrix. This same type of behavior probably explains the new observation of a titanium-enriched feature. Titanium is used in PCA as a carbide former, and such titanium-containing nodules probably represent sites of this carbide (which is stable in lithium).

In the preceeding progress report,[3] we reported on the weight change behavior with time for specimens of 12 Cr-1 MoVW steel exposed to lithium between 500 and 350°C for 10,088 h in a TCL mode of the same alloy. The results showed that the dissolution process was sluggish. Small weight losses were measured at every loop position in both the hot and cold legs. However, the only monotonic weight losses with time were for the hottest and coldest specimens. Such a pattern of weight changes around the lithium loop suggested a change in corrosion mechanism as temperatures decreased below 500°C. Since the last progress report, surface analysis of the 12 Cr-1 MoVW steel loop coupons was completed to complement the weight change data. Metallographic examination of polished and etched cross sections revealed a complex microstructure consisting of a dark surface layer above a carbide-free zone. Figure 9.1.4 compares the cross sections of the loop specimens at the maximum and minimum temperature positions and at two intermediate locations. Note that the dark-etching surface layer is much thicker and more continuous at the position of minimum temperature.

The distributions of iron, chromium, molybdenum, and carbon across the cross-sectional areas shown in Fig. 9.1.4 for the 10,088 h exposures were determined by wavelength dispersive x-ray analysis using an electron microprobe. The data appeared to be consistent with the presence of carbide-free zones as observed by optical metallography; in each of the four cases, relative chromium depletion to about 6 wt. % was detected at approximately 10 to 20 μm below the surface. Some concentration of chromium between this zone and the surface was noted for the four specimens, but the validity of these results is uncertain because of inaccuracy in determining the exact electron beam position with respect to the edges of the specimens as a result of the somewhat open nature of the dark layer and the presence of the mounting epoxy. Furthermore, higher chromium concentrations in these areas may be an artifact of the polishing process; chromium enrichment at such surfaces has sometimes occurred during specimen preparation. Data for iron reflected only relative changes in the chromium concentration, while little change in molybdenum levels was noted.

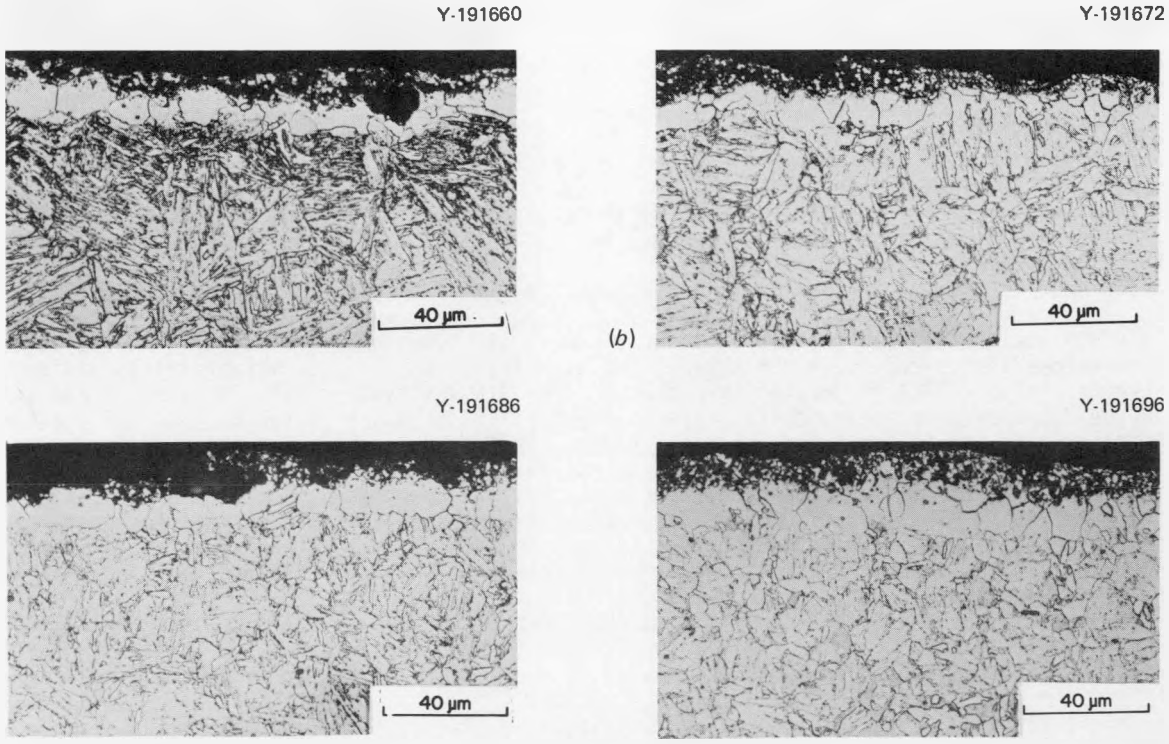

Fig. 9.1.4. Polished and etched cross sections of 12 Cr-1 MoVW steel exposed to thermally convective lithium for 10,088 h. (*a*) 500°C (maximum temperature). (*b*) 440°C. (*c*) 415°C. (*d*) 350°C (minimum temperature).

Energy dispersive x-ray data taken with the electron beam normal to the lithium-corroded surfaces in a scanning electron microscope revealed depletion of chromium from the 500°C specimen (relative to unexposed 12 Cr-1 MoVW steel). This is shown qualitatively by the data in Table 9.1.2, which lists ratios of $K\alpha$ transition peak intensities for 12 Cr-1 MoVW steel in the unexposed and lithium-exposed (500, 440, 415, 350°C; 10,088 h) conditions. Such analysis of the specimens exposed at the lower temperatures showed surface enrichment in chromium and nickel. However, the scanning electron micrographs revealed that relatively little change in surface structure was induced by the lithium exposure.

Table 9.1.2. The $K\alpha$ peak ratios for specimens of 12 Cr-1 Mo steel exposed to thermally convective lithium for 10,088 h

Temperature (°C)	Position	$K\alpha$ peak ratios		
		Cr/Fe	Si/Fe	Ni/Fe
Unexposed		0.150	0.021	0.000
500	Hot leg	0.093	0.003	0.000
440	Hot leg	0.356	0.004	0.006
415	Cold leg	0.362	0.004	0.009
350	Cold leg	0.248	0.004	0.010

Although movement of steel components from hotter to cooler regions was not apparent in the weight change data,[3,9] the results from the energy dispersive x-ray analysis of selected surfaces does suggest that a net transport of certain alloy components did result from the temperature gradient. This is most apparent from a consideration of the Cr:Fe $K\alpha$ peak ratios in Table 9.1.2, which indicate that surface chromium was depleted at 500°C and enriched at lower temperatures. In addition, there is some evidence that there was movement of nickel to the loop's colder region since measurable surface concentrations of nickel were detected only on the cooler loop specimens. (The relatively small amount of nickel in the starting material precludes any measurement of nickel depletion.) Therefore, with respect to mass transfer of these two elements, the behavior of the 12 Cr-1 MoVW steel is similar to that of type 316 stainless steel, which undergoes nickel, and to a lesser extent, chromium transfer from hotter to cooler loop surfaces in molten lithium.[4] However, the magnitude of such transfer in the former system is obviously not sufficient to control the overall corrosion process.

The depth of the observed carbide-free zones (Fig. 9.1.4) correlated well with the locations of reduced chromium concentration noted by microprobe examination of polished cross sections. The lack of carbides in these zones is consistent with reduced chromium concentrations. Thus, there is evidence for the movement of chromium to the lithium-exposed surfaces in both the hotter and cooler loop regions. However, the energy-dispersive data in Table 9.1.2 suggest that this movement of chromium was accompanied by dissolution of chromium in the hottest region and possible deposition of this chromium in the cooler areas of the loop. The migration of chromium to lithium-steel interfaces can indicate a tendency for impurity reactions at these surfaces. Indeed, a Li_9CrN_5 product has been identified and observed on exposed stainless steel.[2] In addition, a dark surface layer very similar in appearance to those shown in Fig. 9.1.4 has been observed on type 316 stainless steel at 500°C in nitrogen-contaminated lithium.[10] Accordingly, a plausible explanation for the unusual weight change profile (maximum loss at the coldest point) (refs. 3 and 9) is that a corrosion reaction involving nitrogen (or carbon) impurities predominates at the 350°C temperature position, such that the reaction products that form in this temperature range are more soluble than those forming elsewhere in the loop (for example, there is a definite temperature range of stability of the nitride in the chromium-lithium system[11]). At 500°C, the expected dissolution process may be more dominant than the impurity reactions but still not contribute as much to weight loss. Such impurity-controlled corrosion reactions would indicate that impurities such as carbon and nitrogen in the steel and lithium will play a key role in the corrosion of 12 Cr-1 MoVW steel at 500°C and below. Such reactions may occur despite the low impurity levels in the lithium; the steel can act as a source of both carbon and nitrogen. (The stability of lithium oxide precludes any effect of oxygen on the corrosion of steel.) At temperatures significantly greater than 500°C, conventional mass transfer may become much more important in nonisothermal 12 Cr-1 MoVW steel-lithium systems. A loop experiment with a maximum temperature of 600°C is currently under way to determine if this is the case.

Despite the observed corrosion processes described above, the corrosion of the 12 Cr-1 MoVW steel in thermally convective lithium between 500 and 350°C was not excessive after 10,088 h. The weight losses and corrosion rates were small,[3,9] and the microstructure was not altered by the corrosion process to any great depth (Fig. 9.1.4). The reactions were sluggish; most loop specimens did not exhibit much change in weight or surface structure, particularly after the first few thousand hours of exposure. Severe corrosion under such conditions should not be expected unless there is an abnormally high nitrogen activity in the lithium or the steel.

9.1.5 Conclusions

1. The exposure of path A PCA alloys to thermally convective lithium for 6700 h at 600 and 570°C resulted in corrosion reactions that were similar to what is observed for other austenitic alloys exposed under similar conditions: preferential depletion of nickel and chromium, porosity development, and surface ridges. However, when compared with baseline data of type 316 stainless steel, PCA was corroded more readily because of its higher concentration of nickel.

2. The solution-annealed PCA corroded more than did cold-worked PCA at 600°C, but both forms of this alloy showed similar corrosion rates at 570°C. Such an observation may indicate an influence of grain boundary density on the rate-controlling step for the corrosion process at higher temperatures. The presence of nitride stringers in the cold-worked PCA did not influence the cumulative weight loss of this material after 5000 h at 600 and 570°C.

3. Some mass transfer of chromium and nickel was detected in a 12 Cr-1 Mo steel — lithium thermal convection system that operated between 500 and 350°C for 10,088 h. However, from a consideration of the weight change data, surface analysis, and prior results for austenitic alloys, reactions with carbon and nitrogen were deduced to be the principal corrosion processes. The reactions in the temperature range of this experiment were relatively sluggish and corrosion was not severe.

9.1.6 References

1. J. H. DeVan and J. R. DiStefano, "Thermal-Convection Loop Tests of Type 316 Stainless Steel in Lithium," pp. 200–208 in *ADIP Quart. Prog. Rep. Mar. 31, 1978*, DOE/ET-0058/1, U.S. DOE, Office of Fusion Energy.

2. M. G. Barker et al., "The Interaction of Chromium with Nitrogen Dissolved in Liquid Lithium," *J. Nucl. Mater.* 114, 149–49 (1983).

3. P. F. Tortorelli and J. H. DeVan, "Corrosion of Path A PCA, Type 316 Stainless Steel, and 12 Cr-01 MoVW Steel in Flowing Lithium," pp. 186–190 in *ADIP Semiannu. Prog. Rep. March 31, 1983*, DOE/ER-0045/10, U.S. DOE, Office of Fusion Energy.

4. P. F. Tortorelli and J. H. DeVan, "Thermal Gradient Mass Transfer in Lithium-Stainless Steel Systems," *J. Nucl. Mater.* **85&86** (1979) 289–93.

5. P. F. Tortorelli and J. H. DeVan, "Effects of a Flowing Lithium Environment on the Surface Morphology and Composition of Austenitic Stainless Steel," submitted for publication in *Microstructural Science*, 1983.

6. P. F. Tortorelli and J. H. DeVan, "Effect of Nickel Concentration on the Mass Transfer of Fe-Ni-Cr Alloys in Lithium," *J. Nucl. Mater.* 103&104, 633–38 (1981).

7. O. K. Chopra and D. L. Smith, "Environmental Effects on Properties of Structural Alloys," pp. 195–200 in *Adip Semiannu. Prog. Rep. March 31, 1983*, DOE/ER-0045/10, U.S. DOE, Office of Fusion Energy.

8. O. K. Chopra and D. L. Smith, "Corrosion of Ferrous Alloys in Eutectic Lead-Lithium Environment," to be published in the proceedings of the Third Topical Meeting on Fusion Reactor Materials, September, 1983.

9. P. F. Tortorelli and J. H. DeVan, "Corrosion of an Fe–12 Cr-1 MoVW Steel in Thermally-Convective Lithium," to be published in the proceedings of Topical Conf. on Ferritic Alloys for Use in Nuclear Energy Technologies, Snowbird, Utah, June, 1983.

10. P. F. Tortorelli, J. H. DeVan, and J. E. Selle, "Effects of Nitrogen and Nitrogen Getters in Lithium on the Corrosion of Type 316 Stainless Steel," preprint 115, *NACE Corrosion/79*, March 1979.

11. W. F. Calaway, "The Reaction of Chromium with Lithium Nitride in Liquid Lithium," pp. 18-18–26 in *Proceedings of Second International Conference on Liquid Metal Technology in Energy Production*, CONF-800401, U.S. DOE, 1980.

9.2 CORROSION OF TYPE 316 STAINLESS STEEL IN FLOWING Pb–17 at. % Li –

P. F. Tortorelli and J. H. DeVan (ORNL)

9.2.1 ADIP Task

ADIP Task I.A.3, Perform chemical and metallurgical compatibility analyses.

9.2.2 Objective

The purpose of this task is to determine the corrosion resistance of candidate first-wall materials to slowly flowing Pb–17 at. % Li in the presence of a temperature gradient. Dissolution and deposition rates are measured as functions of time, temperature, and additions to the lead-lithium. These measurements are combined with chemical and metallographic examinations of specimen surfaces to establish the mechanisms and rate-controlling processes for the dissolution and deposition reactions.

9.2.3 Summary

The corrosion of type 316 stainless steel exposed to thermally convective Pb–17 at. % Li was severe. Plugging started to occur after just several hundred hours. At 500°C, the weight loss of type 316 stainless steel exposed to Pb–17 at. % Li was more than an order of magnitude greater than that of this alloy exposed to thermally convective lithium at 600°C.

9.2.4 Progress and Status

Results from previous experiments in static Pb–17 at. % Li revealed that the weight losses of type 316 stainless steel and 12 Cr-1 Mo steel were much greater than the negligible weight changes that had been measured when these alloys were exposed to pure, static lithium under similar conditions. Subsequently, an experiment was initiated to study the dissolution and deposition reactions in a type 316 stainless steel – Pb–17 at. % Li thermal convection loop (TCL) with accessible specimens. Such loops have been described previously[2] and are designed so that corrosion coupons can be withdrawn and inserted without interrupting the lead-lithium flow. The TCL used for the present experiment was one of type 316 stainless steel that had previously circulated lithium for over 10,000 h. The interior surface of its hot leg was therefore depleted in nickel. While the presence of the resultant ferritic surface may affect dissolution of the fresh austenitic loop coupons, this effect has been measured for lithium, was found to be not large, and has been taken into account when we compared the present dissolution data with prior results for type 316 stainless steel in lithium by using only data typical of such loop conditions.

The Pb–17 at. % Li was prepared by first purging the molten lead with hydrogen, adding the appropriate amount of lithium in molten form, and then holding the mixture at 730°C for 3 to 4 h in a molybdenum-lined pot. The lead-lithium was then transferred into the cleaned TCL, and the specimens of type 316 stainless steel were inserted into the hot and cold legs of the loop. The maximum loop temperature was 500°C, and initially a temperature difference of 150°C was maintained. However, after a few hundred hours of exposure, sufficient mass transfer had occurred to initiate some plugging in the cold leg. It was, therefore, necessary to raise the minimum temperature to about 430°C to prevent severe flow restrictions by mass transfer deposits.

Prior work with Pb–17 at. % Li in capsule tests showed that exposure of corroded specimens to low-temperature molten lithium was the most effective way to remove residual lead.[1] Consequently, after each exposure period in the TCL, all 16 coupons were inserted in molten lithium (at about 250°C) for about 6 h. The specimens were then rinsed in water to remove the lithium and weighed. The lithium soak procedure was then repeated until the weights became constant. In the present case, this required only two soaks per exposure period.

The loop specimens have now accumulated 2018 h of exposure time, and the resulting weight loss data as a function of time are shown for the 500°C specimen in Fig. 9.2.1, which also contains data for type 316 stainless steel exposed to thermally convective lithium at 600°C. Note that, despite its lower temperature, the specimen exposed to the Pb–17 at. % Li suffered weight losses that were, after about 1500 h, greater than those for the lithium-exposed coupon by more than an order of magnitude. This finding is in qualitative agreement with results from a forced convection loop experiment with Pb–17 at. % Li (ref. 3) and is to be expected from a review of earlier work with lead.[4] The reason for the rather unusual shape of the weight loss curve for Pb–17 at. % Li (relative to what is normally observed – see the lithium curve and refs. 3 and 4 – may be related to unintentional descaling of the ferrite (nickel-depleted) layer during specimen cleaning. Some loose magnetic material has been found during cleanup, and a similar observation was made during cleaning of PCA exposed to Pb–17 at. % Li (ref. 3).

Weight change measurements will continue for several thousand more hours to complete a characterization of the weight change behavior with time, and then the specimens will be examined metallographically. In addition, a 9 Cr-1 Mo TCL is presently being constructed in order to study the corrosion of Fe-Cr-Mo steels in thermally convective Pb–17 at. % Li.

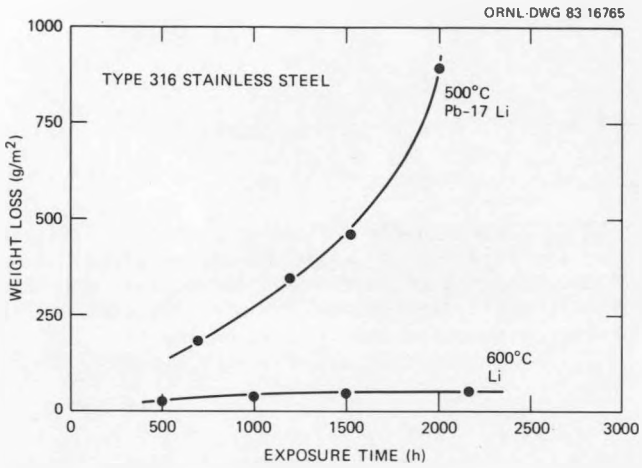

Fig. 9.2.1. Weight loss versus exposure time for type 316 stainless steel exposed to thermally convective Pb–17 at. % Li and Li at 500°C and 600°C, respectively. In both cases, these temperatures were the maximum loop temperatures.

9.2.5 Conclusion

The corrosion of type 316 stainless steel exposed to thermally convective Pb–17 at. % Li was severe. The weight loss of type 316 stainless steel exposed to Pb–17 at. % Li at 500°C was greater by more than an order of magnitude than that of this alloy when exposed to thermally convective lithium at 600°C.

9.2.6 References

1. P. F. Tortorelli and J. H. DeVan, "Compatibility of Stainless Steel with Pb–17 at. % Li," *J. Mater. Energy Syst.* 4, 78–83 (1982).

2. J. H. DeVan and J. R. DiStefano, "Thermal-Convection Loop Tests of Type 316 Stainless Steel in Lithium," pp. 200–208 in *ADIP Quart. Prog. Rep. Mar. 31, 1978*, DOE/ET-0058/1, U.S. DOE, Office of Fusion Energy.

3. O. K. Chopra and D. L. Smith, "Corrosion of Ferrous Alloys in Eutectic Lead-Lithium Environment," to be published in the proceedings of the Third Topical Meeting on Fusion Reactor Materials, September 1983.

4. P. F. Tortorelli and O. K. Chopra, "Corrosion and Compatibility Considerations of Liquid Metals for Fusion Reactor Applications," *J. Nucl. Mater.* 103&104, 621–32 (1981).

9.3 COMPATIBILITY STUDIES OF STRUCTURAL ALLOYS WITH SOLID BREEDER MATERIALS - O. K. Chopra and D. L. Smith (Argonne National Laboratory)

9.3.1 ADIP Task

ADIP Task I.A.3, Perform Chemical and Metallurgical Compatibility Analyses.

9.3.2 Objective

The objective of this task is to evaluate the compatibility of solid breeder materials with structural alloys. The interactions between breeder materials and alloys are investigated as a function of temperature, time, and environmental parameters (i.e., flowing helium environments with different moisture contents). Reaction rates are determined by measurinig the weight change, depth of internal penetration, and thickness of corrosion scales. These measurements, coupled with metallographic evaluation of the alloy surfaces, are used to establish the mechanisms and rate-controlling processes for the corrosion reactions.

9.3.3 Summary

Compatibility tests between Li_2O pellets and austenitic Type 316 stainless steel or ferritic HT-9 alloy and Fe-9Cr-1Mo steel in a flowing-helium environment indicate that the reaction rates in helium containing 93 ppm H_2O are greater than in helium with 1 ppm H_2O. The corrosion behavior of Type 316 stainless steel is similar to that of the ferritic steels. The Li_2O pellets, exposed both with and without the alloy specimens, lose weight in flowing helium.

9.3.4 Progress and Status

Compatibility tests conducted at 973 and 773 K (700 and 500°C) with sealed capsules of HT-9 alloy and Type 316 stainless steel packed with solid tritium-breeding material such as Li_2O, $LiAlO_2$, and Li_2SiO_3 indicate that Li_2O is the most reactive of the three breeder materials.[1,2] Alloy specimens packed with Li_2O developed an adherent reaction scale consisting of the ceramic material embedded with iron-rich reaction products. However, for both HT-9 alloy and Type 316 stainless steel, the thickness of the reaction scale or the depth of internal penetration was the same after 1000 and 2000 h.

The corrosive interactions between structural alloys and Li_2O pellets were also investigated in a flowing helium environment with controlled partial pressures of oxygen and hydrogen.[2] Such experiments simulate the conditions projected for blanket structures during reactor operation. Tests were conducted at 823 K (550°C) for 500, 1000, and 2000 h in flowing helium with 93 ppm H_2O and 1 ppm H_2 and for 1000, 2500, and 4000 h in flowing helium with 1 ppm each of H_2O and H_2. Four reaction couples consisting of ~10 x 10 x 0.4-mm specimens of HT-9 alloy, Fe-9Cr-1Mo steel, 20% cold-worked Type 316 stainless steel, and either pure nickel or annealed Type 316 stainless steel, were sandwiched between two Li_2O pellets and were included in each compatibility test. During testing, the flow rate of the gas mixture was ~0.45 cm^3/s, i.e., a velocity of ~1.6 mm/s across the reaction couples.

Data on the reaction kinetics and a metallographic evaluation of the alloy specimens have been presented in earlier reports.[3,4] After exposure, all alloy specimens gained weight, whereas the Li_2O pellets lost weight. There was a net loss in weight for the total reaction couple. The ferritic steels exposed in helium with either 93 or 1 ppm H_2O developed a dense iron-rich scale and a porous chromium-rich subscale. Similar features were observed for the reaction scales formed on Type 316 stainless steel exposed in helium containing 93 ppm H_2O. However, the dense outer scale consisted of three distinct regions: a thin manganese-rich surface layer, a wide iron-rich region, and a nickel-rich inner layer. The reaction scales also showed some differences in thickness and morphology depending on the location. For example, the nickel-rich layer was continuous near the edge of the specimen and became irregular towards the center. Furthermore, the total scale thickness was smaller towards the specimen edge.

The results for ferritic HT-9 alloy and Fe-9Cr-1Mo steel indicate that the reaction rates in helium containing 93 ppm H_2O are greater than in helium with 1 ppm H_2O.[4,5] The depth of internal penetration for specimens exposed in helium containing 1 ppm H_2O reaches a constant value after ~1000 h, while the specimens exposed in helium with 93 ppm H_2O show a gradual increase in penetration up to 2000 h. For both moisture contents, the thickness of the total reaction scale follows a power law and the rates decrease with time. The weight loss for Li_2O pellets follows a linear law with time and yields weight loss values of 12.2 and 3.8%/yr in helium with 93 and 1 ppm H_2O, respectively.

During the current reporting period, metallographic examinations were performed on Type 316 stainless steel specimens exposed at 823 K in flowing helium containing 1 ppm each of H_2O and H_2. Compatibility tests were also performed with Li_2O pellets (without the alloy specimens) in flowing helium containing 1 ppm each of H_2O and H_2 to determine the weight loss for Li_2O in a flowing-gas environment.

The average values for the depth of internal penetration and total scale thickness on austenitic and ferritic steels exposed with Li_2O in flowing helium are plotted as a function of time in Fig. 9.3.1. The depth of internal penetration represents the actual metal loss and was obtained from the difference between the initial specimen thickness and that of the unreacted metal after the test. In some instances, the reaction scales on the alloy specimens broke off when the reaction couples were removed from the holder; consequently, the total scale thickness was determined from measurements of the thickness of the spalled

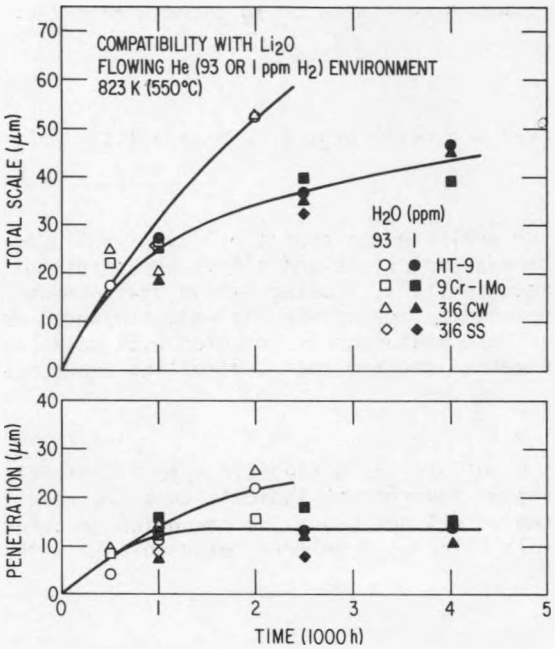

Fig. 9.3.1. Internal penetration and total scale thickness for austenitic and ferritic steels exposed with Li_2O pellets at 823 K in flowing helium containing 93 or 1 ppm H_2O and 1 ppm H_2.

scale and the corrosion scale remaining on the specimens. The results indicate that the corrosion behaviors of austenitic and ferritic steels are similar. Internal peneteration and total scale thickness under various test conditions are approximately the same for Type 316 stainless steel and the ferritic steels.

The depth of internal penetration of the various specimens exposed in helium containing 1 ppm H_2O reaches a constant value (~15 μm) after an initial period of 1000 h. The specimens exposed in helium containing 93 ppm H_2O may exhibit similar behavior. However, the longest duration of the tests with 93 ppm H_2O was 2000 h and the penetration depth increased with time. The thickness of the reaction scale for the specimens exposed in helium with either 93 or 1 ppm H_2O increases with time. The data may be expressed by a power law relationship with time. It is probable that the total scale thickness also reaches a saturation value after longer exposure times.

Micrographs of the reaction scales on 20% cold-worked Type 316 stainless steel exposed in flowing helium containing 1 ppm H_2O and H_2 are shown in Fig. 9.3.2. The scale morphology is basically similar to that observed for the ferritic steels; the specimens show a uniform and dense outer scale, a porous subscale, and corrosive penetration in the bulk material. Energy dispersive x-ray analyses of the reaction scales on austenitic and ferritic steels indicate that the dense outer scale is rich in iron while the subscale contains significant amounts of chromium, i.e., ~18% for ferritic steels and ~48% for Type 316 stainless steel. In addition, the iron-rich outer scale on Type 316 stainless steel consists of a manganese-rich surface layer and a white inner band that is rich in nickel. Similar behavior was observed for Type 316 stainless steel specimens exposed in helium containing 93 ppm H_2O and 1 ppm H_2. X-ray diffraction analyses of the reaction scales are in progress to identify the various reaction products.

The reaction scale on the edge of the Type 316 stainless steel specimen exposed for 2500 h at 823 K in flowing helium containing 1 ppm H_2O and H_2 is shown in Fig. 9.3.3. The specimen edge was not in contact with the Li_2O pellets and thus was exposed to the gas environment alone. The reaction scale is identical to that observed on the surfaces exposed in contact with Li_2O pellets. These results indicate that lithium is transferred via the vapor phase or by surface diffusion to react with surfaces that are not in contact with Li_2O.

The Li_2O pellets from the various reaction couples lost weight after exposure and the rates of weight loss were 12.2 and 3.8%/yr in flowing helium containing 93 and 1 ppm H_2O, respectively. These values are two to three orders of magnitude greater than those predicted from equilibrium reaction kinetics. However, two separate interactions, viz., gas- and alloy-pellet interactions, contribute to the measured weight loss for the Li_2O pellets. A compatibility test was conducted with Li_2O pellets, without the alloy specimens, at 823 K in flowing helium containing 1 ppm each of H_2O and H_2 to determine the weight loss due to gas-pellet interactions. The results are shown in Fig. 9.3.4. Two specimens, shown by circles in Fig. 9.3.4, were baked for ~2 h at 823 K under dynamic vacuum before exposure to the flowing-gas environment. These specimens show substantial weight loss (~0.5%) after baking. However, the weight losses of all the

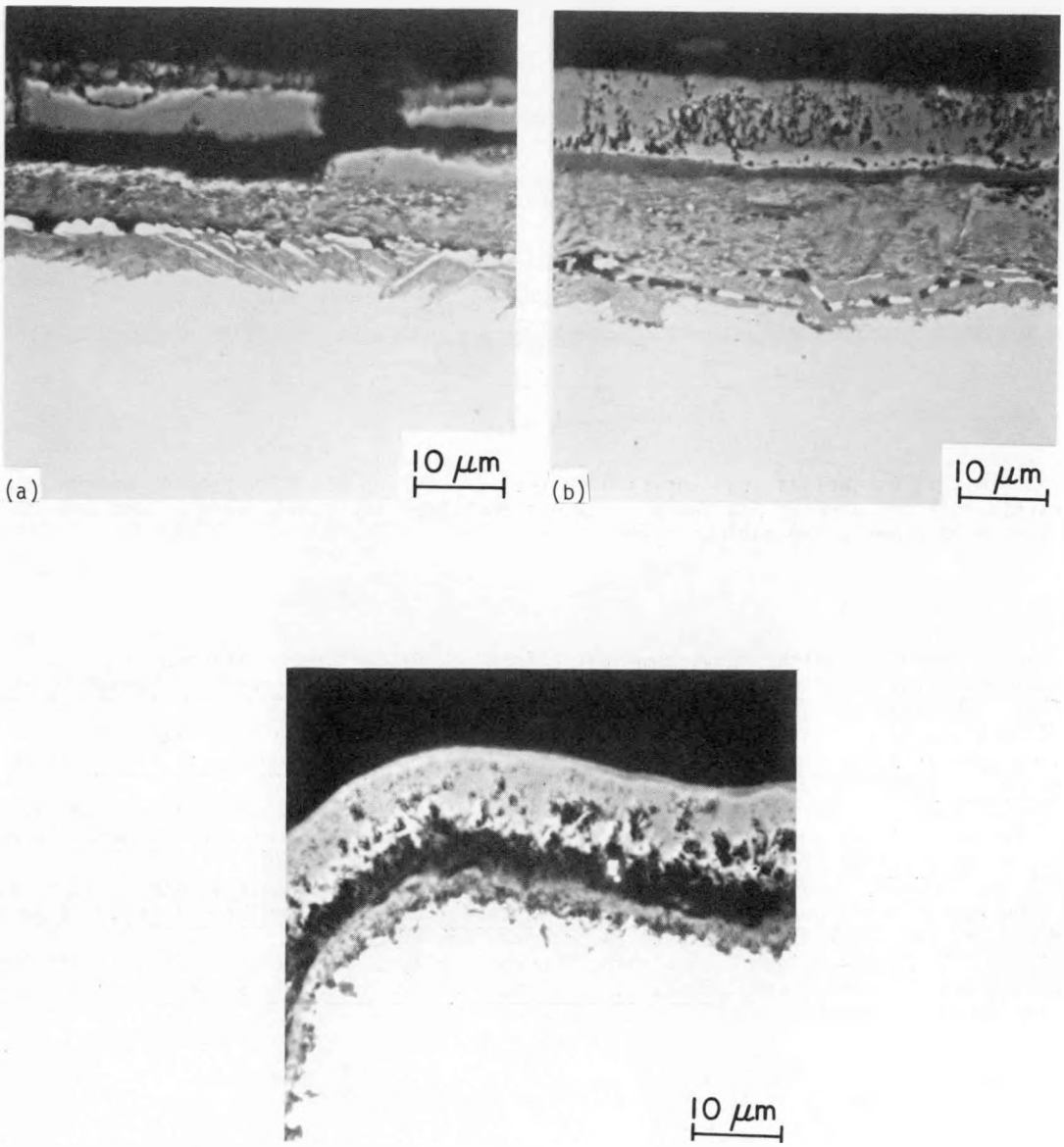

Fig. 9.3.3. Reaction scale on the edge of Type 316 stainless steel specimen exposed for 2500 h at 823 K in flowing helium containing 1 ppm H_2O and H_2.

specimens, with or without prior baking, are comparable after exposure to the flowing gas environment. The results yield a weight loss of 3.2%/yr for Li_2O pellets exposed to the flowing-gas environment. This value is similar to that observed for Li_2O pellets exposed with alloy specimens.

9.3.5 Conclusions

Data from the compatibility tests in a flowing-helium environment indicate that the corrosion behavior of Type 316 stainless steel is similar to that of the ferritic HT-9 alloy or Fe-9Cr-1Mo steel. All alloy specimens develop a dense iron-rich outer scale and a porous subscale. The dense outer scale on Type 316 stainless steel consists of a thin manganese-rich surface layer and an inner band rich in nickel. For austenitic and ferritic steels, the reaction rates in helium containing 93 ppm H_2O are greater than in helium with 1 ppm H_2O.

The Li_2O pellets exposed to flowing helium containing 1 ppm each of H_2O and H_2 show weight loss of ~3.2%/yr. This value is comparable with the rate observed earlier for Li_2O pellets that were exposed with alloy specimens.

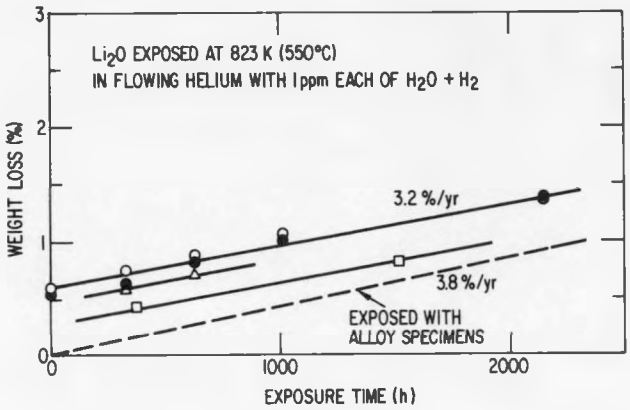

Fig. 9.3.4. Weight loss for Li_2O pellets exposed at 823 K in flowing helium containing 1 ppm each of H_2O and H_2. Each symbol type represents weight loss for a single specimen after various times.

9.3.6 References

1. O. K. Chopra and D. L. Smith, "Environmental Effects on Properties of Structural Alloys," pp. 321-327 in Alloy Development for Irradiation Performance: Semiannual Progress Report for Period Ending September 30, 1981, Oak Ridge National Laboratory, DOE/ER-004577.

2. O. K. Chopra and D. L. Smith, "Compatibility Studies of Structural Alloys with Solid Breeder Materials," pp. 507-513 in Alloy Development for Irradiation Performance: Semiannual Progress Report for Period Ending March 31, 1982, Oak Ridge National Laboratory, DOE/ER-0045/8.

3. O. K. Chopra and D. L. Smith, "Compatibility Studies of Structural Alloys with Solid Breeder Materials," pp. 323-338 in Alloy Development for Irradiation Performance: Semiannual Progress Report for Period Ending September 30, 1982, Oak Ridge National Laboratory, DOE/ER-0045/9.

4. O. K. Chopra and D. L. Smith, "Compatibility Studies of Structural Alloys with Solid Breeder Materials," pp. 204-208 in Alloy Development for Irradiation Performance: Semiannual Progress Report for Period Ending March 31, 1983, Oak Ridge National Laboratory, DOE/ER-0045/10.

5. O. K. Chopra, T. Kurasawa, and D. L. Smith, "Compatibility of Ferritic Steels with Sintered Li_2O Pellets in a Flowing Helium Environment," Proc. Topical Conf. on Ferritic Alloys for Use in Nuclear Energy Technologies, AIME (1983) in press.

9.4 CORROSION AND OXIDATION OF VANADIUM-BASE ALLOYS IN HELIUM ENVIRONMENTS - B. A. Loomis and D. L. Smith - (Argonne National Laboratory)

9.4.1 ADIP Task

I.A.3 Perform Chemical and Metallurgical Compatibility Analyses.

9.4.2 Objective

The objective of this task is to determine the increase in weight of vanadium-base alloys at elevated temperatures on exposure to helium environments containing oxygen, hydrogen and water vapor impurities. These determinations when combined with analyses of the distribution of oxygen and redistribution of alloying elements in the exposed vanadium alloys will allow the selection of a vanadium-base alloy with maximum corrosion and oxidation resistance.

9.4.3 Summary

The increase in weight of unalloyed V and V-5Ti, V-15Cr and V-15Cr-5Ti alloys at 725, 825 and 925 K was determined for exposure times ranging up to 1000 hours in He containing H_2 and/or H_2O impurity. The microhardness of the specimens in a transverse section was also determined after exposure for 1000 hours. These results were utilized to discuss the consequences of the selection of certain radiation-damage resistant, V-base alloys for structural materials applications in a fusion reactor.

9.4.4 Progress and Status

9.4.4.1 Introduction

A major concern regarding the use of V alloys for structural materials applications in fusion reactors is the chemical reactivity of the alloys at elevated temperatures with the constituents in air during an accidental exposure. The chemical reactivity of these alloys might result in unacceptable corrosion, oxidation, and embrittlement effects when exposed to even fairly low partial pressures of either oxygen, nitrogen, hydrogen or water vapor.

In this report, the corrosion and the increase in weight of several V-base alloys on exposure at elevated temperatures to helium environments containing hydrogen and/or water vapor are presented. The increase in weight data for the V-base alloys are compared with the data determined for Path A-PCA austenitic and HT-9 ferritic steels in the same environments.

9.4.4.2 Materials and Procedure

The materials for this investigation were unalloyed V, V-5 Ti, V-15Cr, V-15Cr-5Ti, Path A-PCA (nominal Fe-16Ni-13Cr-2 Mo, Mn-0.5 Ti, Si composition) steel, and HT-9 (nominal Fe-12Cr-1 Mo-0.5Ni, Mn, W-0.3V composition) steel.[+] Specimens of unalloyed V, V-5Ti and V-15Cr were prepared from V stock that contained ~150 ppm oxygen. Rolled sheets of these materials were annealed for one hour at 1475 K in a vacuum of $\sim 10^{-6}$ Pa to produce a recrystallized structure with an average grain diameter of ~0.02 cm. The V-15Cr-5Ti alloy was obtained from the Fusion Materials Program Inventory (MFE Heat No. CAM 834-6) at Oak Ridge National Laboratory. Specimens of this material were also annealed for one hour at 1475 K. The Path A-PCA and HT-9 materials were supplied by the Fusion Materials Program Inventory from MFE Heats No. K-280 and No. XAA-3587, respectively. The Path A-PCA material was aged for 8 hours at 1075 K in argon, 23%-cold worked, and aged for 2 hours at 1025 K in argon. The HT-9 alloy was normalized for one hour at 1325 K in argon, air cooled from 1325 K, tempered for 2.5 hours at 1025 K, and air cooled from 1025 K.

Specimens of each of the materials with dimensions of 1 cm x 1 cm x 0.05-1.5 cm and a 0.003-cm surface finish were inserted in furnaces at temperatures of 725, 825 and 925 K. The specimens were exposed to flowing helium that contained either 10 ppm by volume of water or 1 ppm hydrogen and 1 ppm water for increasing periods of time ranging up to 1000 hours. The flow rate of the gas was 3×10^3 cm^3/hour. The increase in weight of the specimens was determined with an accuracy of 2×10^{-6} g at time intervals of ~140 hours. The Knoop hardness values of the materials were determined on cross sections of the specimens after exposure for 1000 hr.

[+]The nominal compositions of the materials are expressed in weight percent of solute.

9.4.4.3 Experimental Results

The increase-in-weight values for the unalloyed V, V-base alloys, PCA S.S. and HT-9 alloys that were determined on exposure of the materials at 725, 825 and 925 K to flowing He containing He and/or H_2O are shown in Fig. 9.4.1.

The increase in weight of a specimen on exposure to the He environments utilized in this study was described (R^2 correlation coefficient > 0.9) by the equation

$$W = \hat{K}(E)^n. \qquad (1)$$

In Eq. (1), W is the increase in weight per unit of surface area ($\mu g/cm^2$); E is the cumulative exposure time (hours); $\hat{K}$ and n are constants for a material and a set of experimental parameters. The values of the $\hat{K}$ and n for each of the materials and exposure conditions utilized in this study are listed in Table 9.4.1.

The observation of the microstructure in cross-sections of the specimens after 1000-hour exposure to the He environments revealed, in general, contiguous surface and near-surface layers (Fig. 9.4.2). We shall denote the outermost layer as the "corrosion" layer and the near-surface layer as the "internal oxidation" layer. The near surface, internal oxidation layer was readily distinguishable in the microstructure of the V-5Ti and V-15Cr-5Ti specimens and generally less apparent in the microstructure of the V and V-15Cr specimens. The thickness of these layers in the specimens is listed in Table 9.4.1. The thickness of the corrosion layer on the V-15Cr, V-15Cr-5Ti and the PCA materials approached a limiting value for temperatures above 725 K (Table 9.4.1). However in the case of the V and V-5Ti materials, the corrosion layer thickness attained a maximum value at 825 K. In the case of the V and V-5Ti specimens, the corrosion layer showed a tendency to partially separate from the underlying material with a maximum tendency at 825 K. In contrast, the corrosion layer on the V-15Cr-5Ti materials did not show a tendency to separate for these experimental conditions. The thickness of the internal oxidation layer in the V and V-base mateials increased substantially with an increase of temperature. The approximately linear rate of weight change (400 to 1000 hours) for the unalloyed V, V-base alloys and Fe-base alloys is presented in Table 9.4.1. However, these rate of weight change data may not be applicable for exposure times of 10^4 to 10^5 hours.

The profiles of the microhardness of the specimens in the section transverse to the specimen surfaces after exposure for 1000 h to the He + 10 ppm H_2O environment are shown in Fig. 9.4.3. The presence of the Ti solute in the V-base alloys resulted in a substantial increase in hardness of the near-surface layers of the specimens and essentially no increase in hardness of the specimen core (Figs. 9.4.3 b and d). In the case of the unalloyed V (Fig. 9.4.3 a) and the V-15Cr alloy (Fig. 9.4.3. c), the hardness of the near-surface layers was moderately increased. However in contrast to the alloys containing Ti solute, the hardness of the specimen core increased especially at 925 K.

9.4.5 Discussion of Results

The increase in weight of the unalloyed V, V-base alloys, PCA S.S. and HT-9 alloy was approximately described by $w = K(E)^n$ on exposure at 725, 825 and 925 K to He environments for periods ranging up to 1000 hours. However, the curves for the V-5Ti alloy at 825 K and V-base alloys at 925 K showed a significant increase in weight at approximately 600 hours of exposure. These results could not be attributed to a change in the experimental parameters. The presence of Ti solute in the V-base alloys resulted in a substantial increase in hardness of the near-surface layers of the specimens. If the increase in hardness was due to internal oxidation, we may assume that ingress of O_2 was limited to the near-surface layers. In the case of the unalloyed V and V-15Cr alloy, the ingress of O_2 was

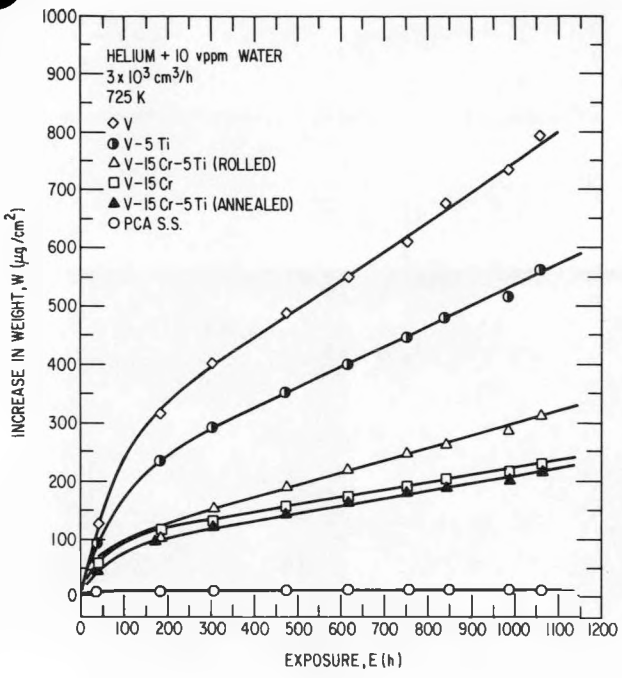

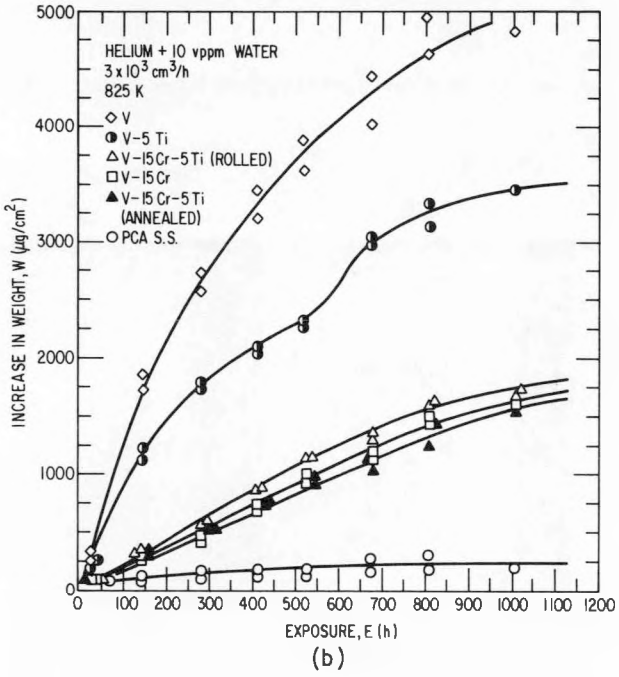

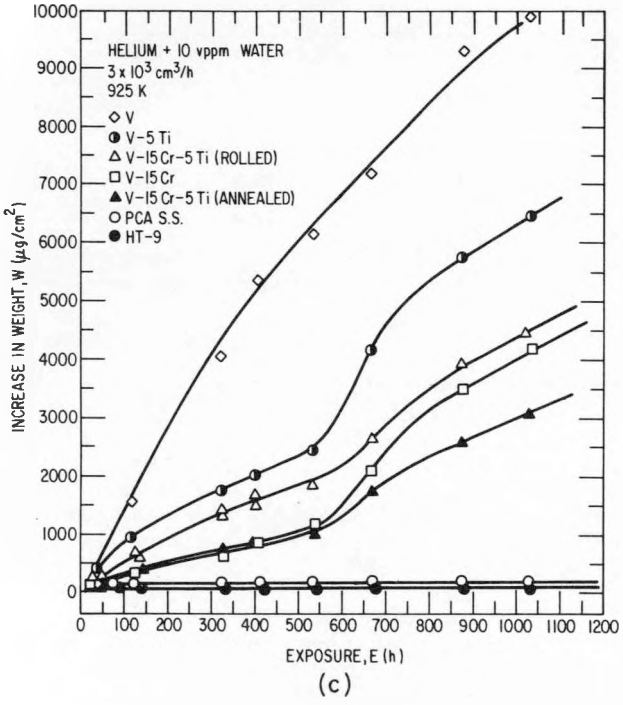

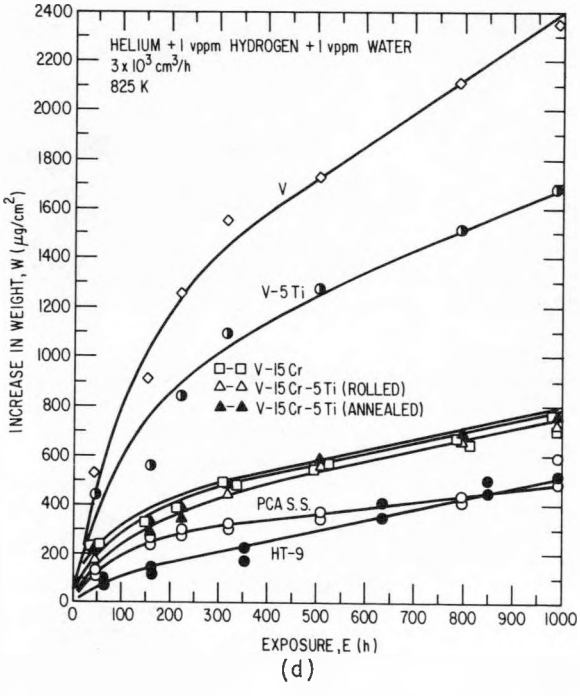

Fig. 9.4.1. Increase in weight of unalloyed V, V-5Ti, V-15Cr, V-15Cr-5Ti, PCA S.S. and HT-9 materials on exposure at 725 K (a), 825 K (b) and 925 K (c) to He + 10 ppm H_2O and at 825 K (d) to He + 1 ppm H_2 + 1 ppm H_2O.

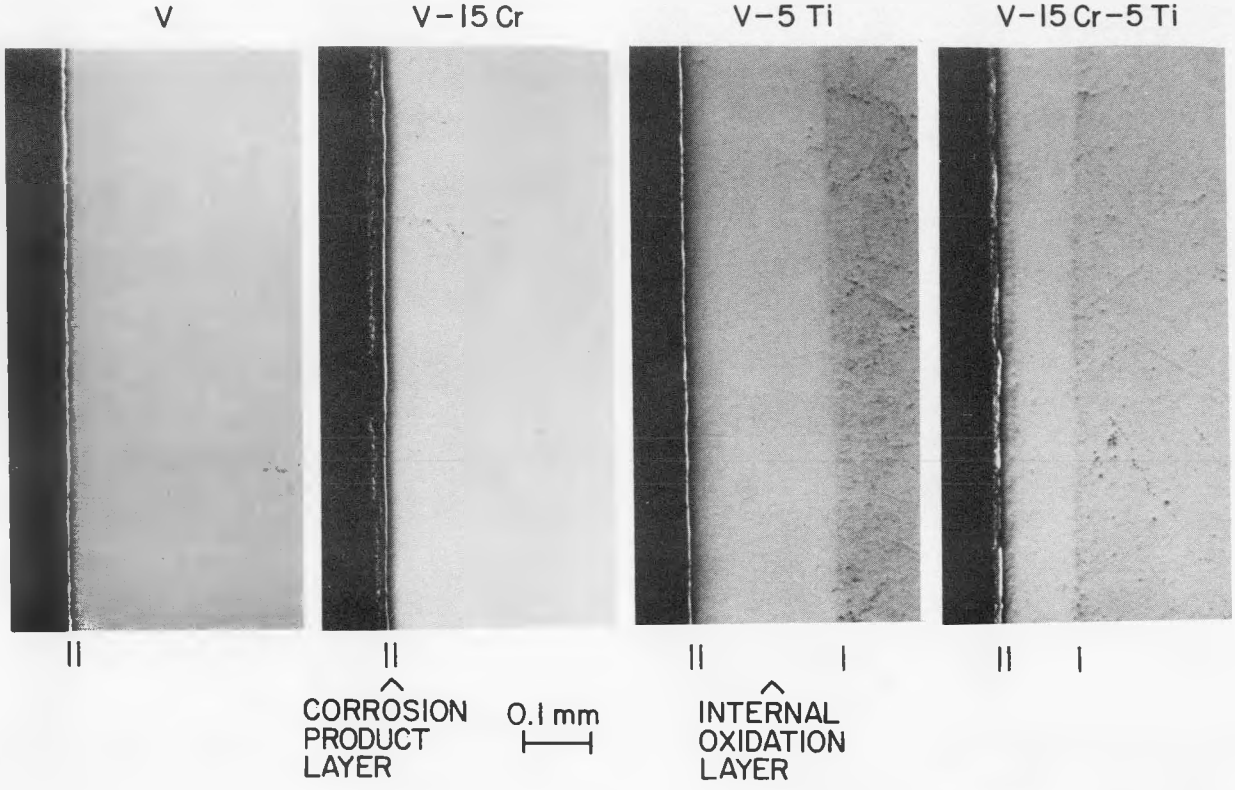

Fig. 9.4.2. Corrosion and internal oxidation layers in the unalloyed V and V-base alloys after 1000-hour exposure at 925 K to He + 10 ppm H_2O.

apparently not limited to the near-surface layers. Swelling studies on unalloyed V[1-3] and V-base alloys[2,4,5] have shown that the addition of 15 w/o Cr to V causes a substantial increase of the V swelling.[5] However, the results of the present study show that Cr is a beneficial solute for improving the corrosion resistance of V in He containing low (< 10 ppm) concentrations of water vapor. The swelling studies have also shown that the addition of 1 w/o Ti to V or 5 w/o Ti to a V-15Cr alloy effectively suppresses void formation and growth.[1,4] The present study has shown that the addition of 5 w/o Ti to a V-15Cr alloy does not significantly alter the corrosion resistance of the V-15Cr alloy. Moreover, the presence of the Ti solute in unalloyed V or a V-15Cr alloy causes the formation of an internal oxidation layer. This layer may result in embrittlement of the material. Loomis and Gerber[6] have investigated the effects of substitutional-atom solutes on the void swelling of Nb. These studies revealed that Ti solute was effective in minimizing void swelling. However, the most effective solutes for suppression of void swelling in Nb were solutes that diffuse relatively slowly in Nb. These results suggest that slowly diffusing solutes in V might be equally effective for the suppression of void swelling, and thus the deleterious internal oxidation effects of the Ti solute might be avoided. The slowly diffusing solutes which might be effective in the suppression of swelling of V are Nb, Ta, Mo and W.[7] However, consideration of the impact of these solutes on the induced radioactivity of V-base alloys in a fusion reactor suggests that W should receive preferential consideration.[8]

Table 9.4.1 Parameters for the increase in weight of V-base alloys, PCA stainless steel and HT-9 alloy at 725, 825, and 925 K in He.

Material	Gas (vppm)[a]	Temperature (K)	Eq.(1) Parameters		Layer Thickness at 1000 Hours		Experimental Weight Gain at 400 hr	Rate of Weight Change[b]
			$\mathring{K}$	n	Corrosion (10^{-4}cm)	Oxidation (10^{-4}cm)	($\mu g/cm^2$)	($\mu g/cm^2 \cdot hr$)
V	He+10H_2O	725	17.24	0.54	11[c]	180	445	0.504
V-5Ti	"	"	13.07	0.54	13[c]	35	320	0.344
V-15Cr	"	"	10.80	0.44	6	~10	146	0.106
V-15Cr-5Ti[d]	"	"	5.28	0.58	6	20	168	0.186
V-15Cr-5Ti[e]	"	"	7.54	0.48	6	20	130	0.131
PCA	"	"	0.13	0.55	3	n.v.[f]	3	0.004
V	He+10H_2O	825	32.90	0.76	64[c]	280	3250	2.917
V-5Ti	"	"	22.42	0.75	31[c]	75	2050	2.583
V-15Cr	"	"	4.94	0.83	14	~20	705	1.374
V-15Cr-5Ti[d]	"	"	6.65	0.81	18	28	853	1.549
V-15Cr-5Ti[e]	"	"	8.40	0.75	16	36	737	1.227
PCA	"	"	31.36	0.28	8	n.v.	164	0.082
V	He+10H_2O	925	96.90	0.67	16[c]	> 400	5415	8.475
V-5Ti	"	"	24.29	0.77	9[c]	220	2050	7.416
V-15Cr	"	"	18.17	0.72	17	~15	850	5.250
V-15Cr-5Ti[d]	"	"	10.15	0.84	29	110	1600	4.833
V-15Cr-5Ti[e]	"	"	12.92	0.75	18	128	870	3.550
PCA	"	"	18.32	0.37	9	n.v.	172	0.118
HT-9	"	"	11.20	0.26	5	n.v.	52	0.024
V	He+1H_2+1H_2O	825	76.67	0.50	25[c]	200	1575	1.375
V-5Ti	"	"	66.12	0.47	27[c]	60	1150	0.971
V-15Cr	"	"	51.23	0.38	10	~15	502	0.349
V-15Cr-5Ti[d]	"	"	42.20	0.42	11	60	527	0.397
V-15Cr-5Ti[e]	"	"	29.21	0.47	12	50	499	0.426
PCA	"	"	24.47	0.43	11	n.v.	318	0.267
HT-9	"	"	4.65	0.68	10	n.v.	319	0.319

(a) Volume parts per million of H_2 or H_2O in He.
(b) 400 to 1000 hours exposure.
(c) Layer tends to spall.
(d) As-received, rolled material.
(e) Annealed material.
(f) Not visible.

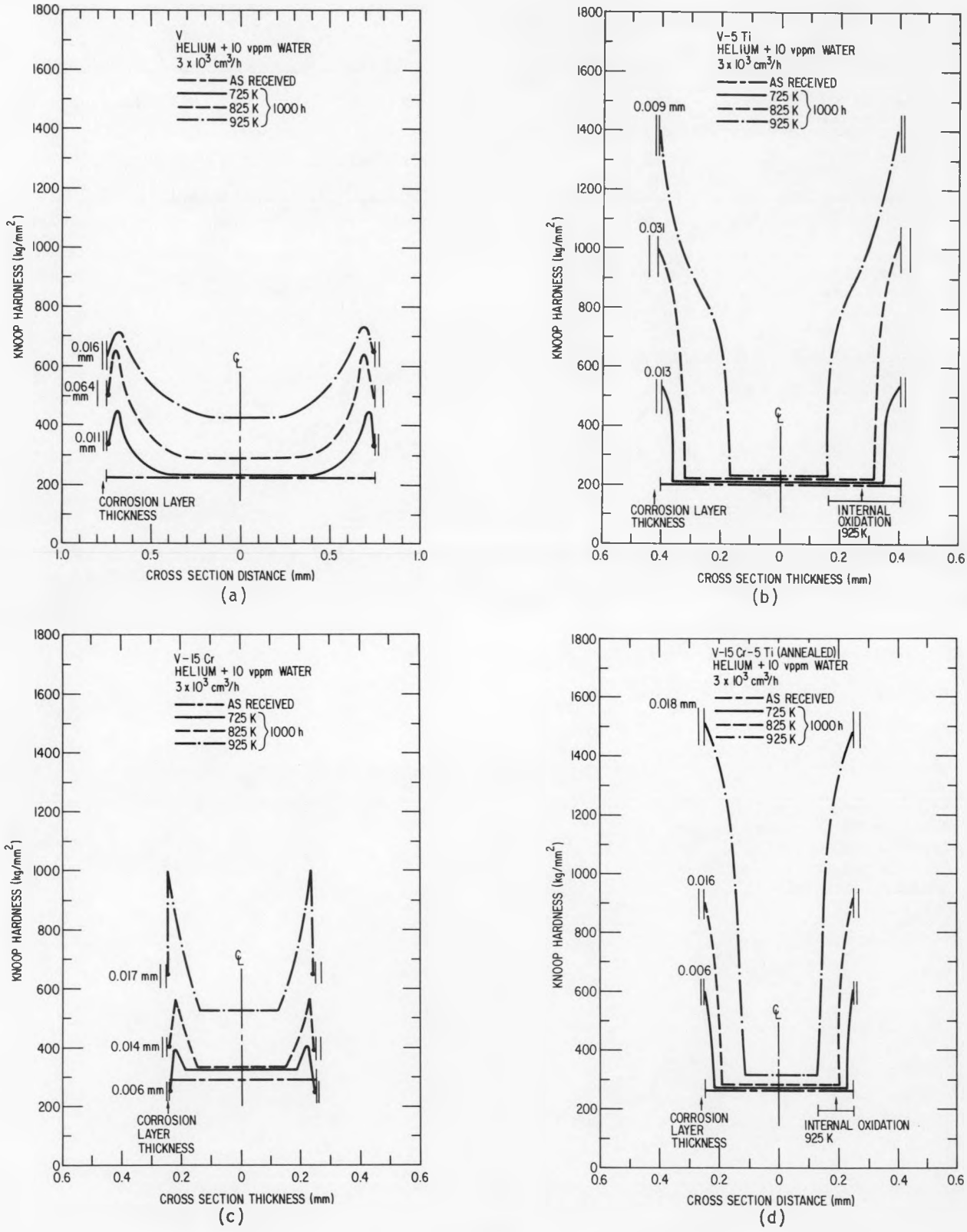

Fig. 9.4.3. Microhardness profile for unalloyed V (a), V-5Ti (b), V-15Cr (c), and V-15Cr-5Ti (d) after 1000 h exposure to He + 10 ppm H_2O.

9.4.6 Conclusions

The data obtained in this experimental study on the increase in weight of unalloyed V, V-base alloys and Fe-base alloys during exposure at temperatures ranging from 725 to 925 K in He environments containing hydrogen (1 ppm) and/or water (1-10 ppm) suggest the following conclusions.

1. The presence of Cr in a V alloy is beneficial for a minimum increase in weight.
2. The presence of Ti in a V alloy does not minimize the increase in weight and may result in unacceptable mechanical properties due to embrittlement.
3. The rate of increase in weight (400 to 1000 hours) for the V-base alloys is substantially greater than the rate for the Fe-base alloys on exposure to He environments containing 10 ppm water.
4. The rate of increase in weight for the V-base alloys is comparable to the rate for Fe-base alloys on exposure to He environments containing 1 ppm hydrogen and 1 ppm water.
5. The presence of Ti solute in V-base alloys limits the ingress of O_2 to the near-surface layers.
6. The replacement of the Ti in the V-15Cr-5Ti alloy with W may result in a material that is less susceptible to potential embrittlement without impairment of the corrosion resistance on exposure in He environments containing water vapor.

9.4.7 References

1. A. T. Santhanam, A. Taylor, B. J. Kestel and C. Steves, J. Vac. Sci. Technol., 12 (1975) 528.

2. S. C. Agarwal, D. I. Potter and A. Taylor, in: Irradiation Effects on the Microstructure and Properties of Metals, ASTM STP 611, American Society for Testing and Materials (1976) p. 298.

3. A. T. Santhanam, A. Taylor and S. D. Harkness, in: Proceedings of the 1973 International Conference on Defects and Defect Clusters in B.C.C. Metals and Their Alloys, R. J. Arsenault, Ed., Vol. 18 (1973) p. 302.

4. B. A. Loomis and G. Ayrault, in: Damage Analysis and Fundamental Studies (Quarterly Progress Report for October-December, 1982) DOE/ER-0046/12, February, 1983, p. 194.

5. S. C. Agarwal, L. E. Rehn and F. V. Nolfi, Jr., J. Nucl. Mater. 78 (1978) 336.

6. B. A. Loomis and S. B. Gerber, J. Nucl. Mater. 117 (1983) 224.

7. D. Ablitzer and A. Vignes, in Proc. of the Int. Conf. on The Properties of Atomic Defects in Metals, eds., N. L. Peterson and R. W. Siegel (Argonne National Laboratory, Oct., 1976) p. 97.

8. F. W. Mann, in: Damage analysis and Fundamental Studies (Quarterly Progress Report for January-March 1983) DOE/ER-0046/13, Vol. 1, May, 1983, p. 63.

9.5 ENVIRONMENTAL EFFECTS ON PROPERTIES OF STRUCTURAL ALLOYS - O. K. Chopra and D. L. Smith (Argonne National Laboratory)

9.5.1 ADIP Task

ADIP task I.A.3, Perform Chemical and Metallurgical Compatibility Analyses.

9.5.2 Objective

The objective of this program is to investigate the influence of chemical environment on the corrosion and mechanical properties of structural alloys under conditions of interest for fusion reactors. Test environments to be investigated include lithium, lead-lithium, helium, and water. Emphasis will be placed on the combined effects of stress and chemical environment on corrosion and mechanical behavior of materials. Initial investigations are focused on the influence of flowing lithium and lead-lithium environments on corrosion and mechanical properties of structural materials.

9.5.3 Summary

Corrosion data are presented for several austenitic and ferritic steels exposed at temperatures between 700 and 755 K in flowing lithium and Pb-17Li environments. The results indicate that dissolution rates for both steels are an order of magnitude greater in Pb-Li than in lithium. Tensile data for cold-worked Type 316 stainless steel show that a flowing environment has no effect on the tensile properties of Type 316 stainless steel at temperatures between 473 and 773 K.

9.5.4 Progress and Status

9.5.4.1 Lithium Environment

The effects of a flowing lithium environment on the corrosion behavior and tensile properties of ferritic and austenitic steels are being investigated. Tests are conducted in a forced-circulation lithium loop equipped with a cold-trap purification system. The cold-trap temperature is maintained at 498 K (225°C). The corrosion behavior is evaluated from measurements of weight loss and depth of internal penetration for various specimens exposed for different times. Flat specimens, 5.59 x 1.22 mm in cross section and 22.23 mm in gauge length, are used for the tensile tests. During the tests, the concentration of carbon and hydrogen in lithium was ~8 and 120 wppm, respectively, and the nitrogen content was between 50 and 250 wppm.

The corrosion data in flowing lithium at 700 and 755 K (427 and 482°C) indicate that weight losses for austenitic stainless steels follow a power law relationship with time, whereas weight losses of ferritic steels follow a linear law.[1] For identical exposure conditions, weight losses for the different austenitic stainless steels increase in the following order: annealed Type 304L, annealed Type 316, 20% cold-worked Type 316, and 25% cold-worked PCA. The corrosion rate of Type 316 stainless steel in cold-trapped circulating lithium is an order of magnitude greater than that observed in the thermal convection loop.[2] The dissolution rates of the ferritic HT-9 alloy and Fe-9Cr-1Mo steel are an order of magnitude lower. The austenitic stainless steels develop a porous ferrite scale after exposure to lithium and the thickness of the ferrite layer increases linearly with time. The ferritic steels show little or no internal corrosion. The concentration of nitrogen in lithium has a strong effect on the corrosion behavior. For both austenitic and ferritic steels, the dissolution rates in lithium containing ~200 wppm nitrogen are a factor of 2 to 4 greater than in low-nitrogen (i.e., 50 wppm) lithium.

Tensile data for cold-worked Type 316 stainless steel indicate that at temperatures between 480 and 755 K (233 and 482°C), a flowing lithium environment has no effect on the tensile strength or total elongation of the steel. The tensile properties in flowing lithium and in vacuum are comparable.

During the current reporting period, corrosion tests were continued at 700 and 755 K with several austenitic and ferritic steels to study the time and temperature dependence of corrosion in lithium. Tensile tests were performed on 20% cold-worked Type 316 stainless steel in flowing lithium at 507 and 755 K (234 and 482°C) and strain rates of 4×10^{-2} and 4×10^{-6} s^{-1} to determine the influence of strain rate on tensile properties.

The weight losses for Type 316 stainless steel, PCA, and the ferritic HT-9 alloy and Fe-9Cr-1Mo steel exposed at 700 and 755 K in flowing lithium are shown in Figs. 9.5.1-9.5.3. Each symbol type shown in the figures represents weight loss for a single specimen after various exposure times. The results show that the dissolution rates for Type 316 stainless steel and PCA reach a steady-state value after an initial transition period of ~1500 h characterized by rapidly changing rates. For austenitic stainless steels, the steady-state dissolution rates at 700 K are similar to that at 755 K. The weight loss of 20% cold-worked Type 316 stainless steel is greater than for the annealed steel; however, the steady-state dissolution rates are comparable for the annealed and cold-worked material. At both temperatures, the dissolution rates of PCA are a factor of ~2 greater than that of Type 316 stainless steel.

The weight loss for the ferritic steels increases linearly with exposure time. All specimens showed significant weight loss after the initial exposure to lithium. The dissolution rates of both HT-9 alloy and Fe-9Cr-1Mo steel are an order of magnitude lower than those for Type 316 stainless steel. Dissolution rates at 700 K are lower than at 755 K.

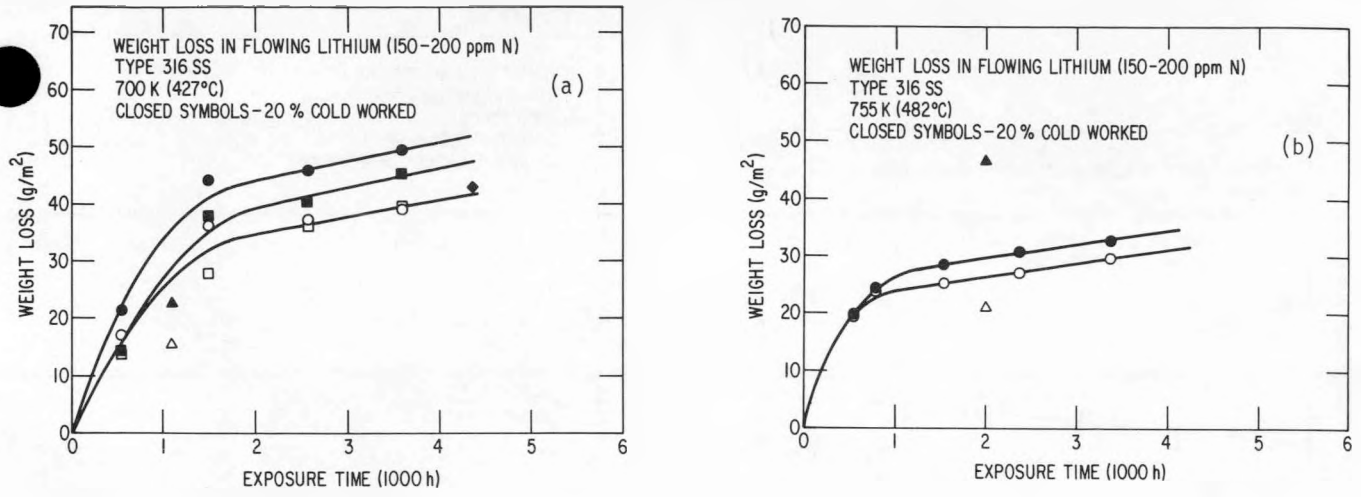

Fig. 9.5.1. Weight loss versus exposure time for annealed and 20% cold-worked Type 316 stainless steel exposed at (a) 700 K and (b) 755 K to flowing lithium containing 150-200 wppm nitrogen. Each symbol type represents weight loss for a single specimen after various exposure times.

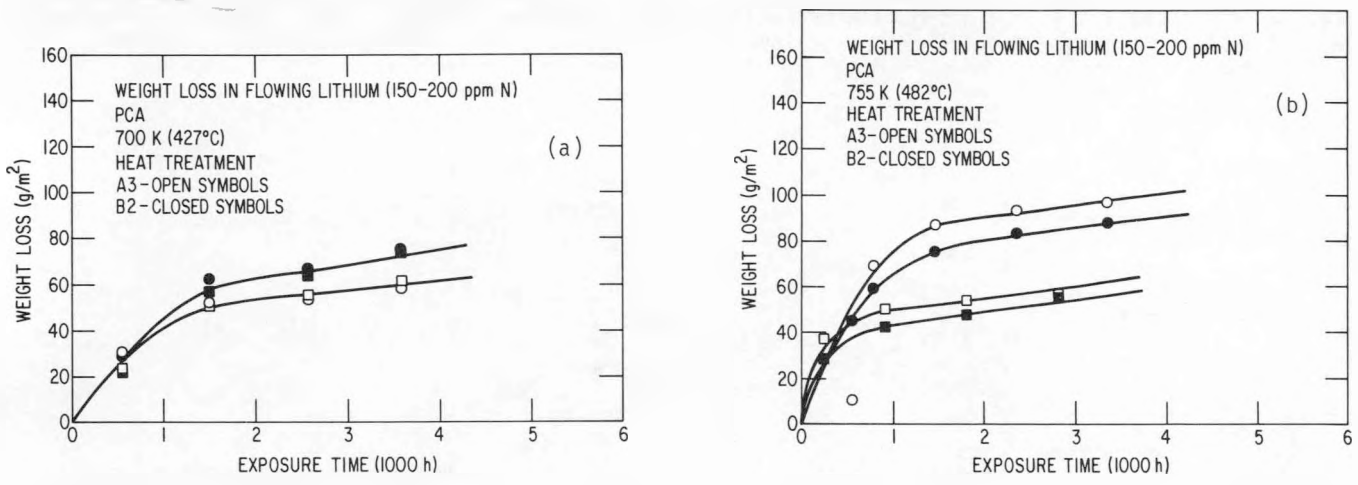

Fig. 9.5.2. Weight loss versus exposure time for PCA exposed at (a) 700 K and (b) 755 K to flowing lithium containing 150-200 wppm nitrogen. Each symbol type represents weight loss for a single specimen after various exposure times.

Duplicate specimens of the various alloys were exposed to lithium at 700 K. For all exposure times, the weight losses of both specimens are comparable. However, alloy specimens that were exposed separately at different periods show significant differences in weight loss. For example, two sets of PCA specimens (heat treatment A3 and B2) exposed to lithium at 755 K show a factor of two difference in weight loss, Fig. 9.5.2(b). The specimens shown by square symbols were exposed ~500 h after the specimens represented by circles. Differences in weight loss are also observed for Type 316 stainless steel and ferritic steel specimens that were exposed in the lithium loop at different periods. The differences in weight loss may result from variations in the impurity content in lithium, particularly the concentration of nitrogen in lithium. During the corrosion tests, the nitrogen content in lithium varied between 200 and 50 wppm.

The influence of a lithium environment on the tensile properties of 20% cold-worked Type 316 stainless steel was investigated by conducting tests in flowing lithium and in vacuum at temperatures between 473 and 773 K and at strain rates of 4×10^{-2}, 4×10^{-4}, and 4×10^{-6} s^{-1}. The tensile strength and total elongation of the material in lithium and vacuum are shown in Fig. 9.5.4. The results show that at all strain rates, a lithium environment has no effect on the tensile properties of the steel.

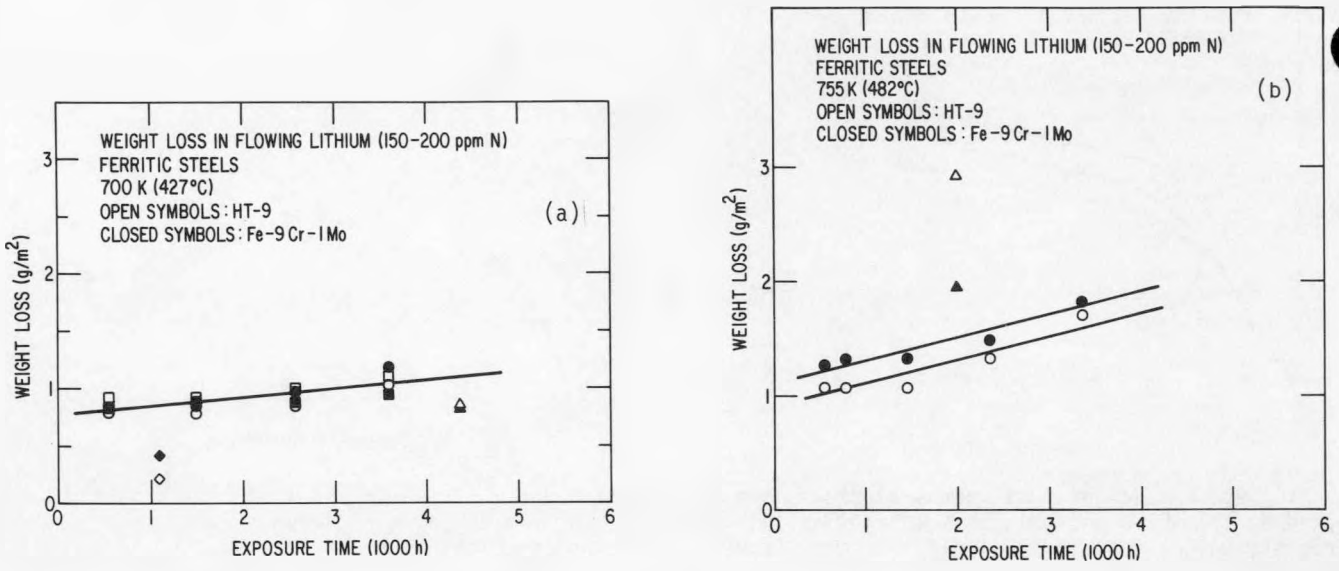

Fig. 9.5.3. Weight loss versus exposure time for the HT-9 alloy and Fe-9Cr-1Mo steel exposed at (a) 700 K and (b) 755 K to flowing lithium containing 150-200 wppm nitrogen. Each symbol type represents weight loss for a single specimen after various exposure times.

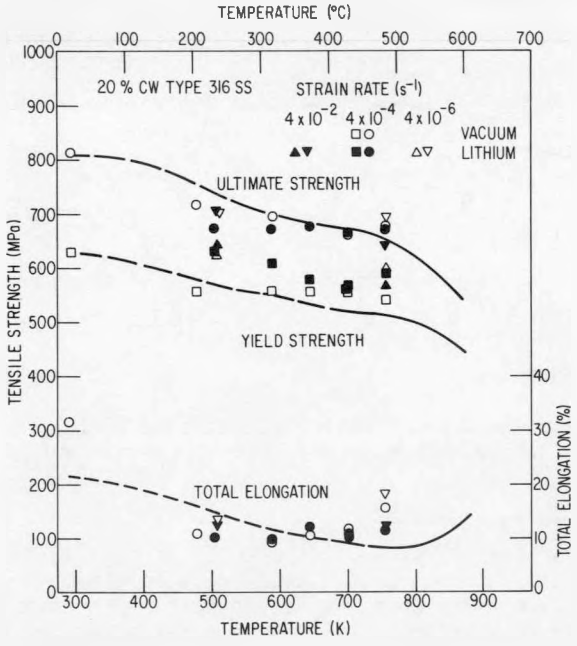

Fig. 9.5.4. Tensile strength and total elongation for 20% cold-worked Type 316 stainless steel tested in flowing lithium or vacuum. The curve represents the average values in air.

9.5.4.2 Pb-17Li Environment

The effects of a flowing Pb-17Li environment on the corrosion behavior and mechanical properties of austenitic and ferritic steels are being investigated. Tests are conducted in a forced-circulation Pb-17Li loop operating at temperatures between 727 and 573 K (454 and 300°C). Corrosion data for annealed and cold-worked Type 316 stainless steel and ferritic HT-9 and Fe-9Cr-1Mo steels in flowing Pb-17Li at 700 and 727 K were presented earlier.[1] The results showed that the dissolution rates of both austenitic and ferritic steels in flowing Pb-17Li are an order of magnitude greater than in flowing lithium. The overall corrosion behavior of the various alloys in Pb-17Li is similar to that in lithium. The weight losses for the austenitic stainless steels follow a parabolic law with time, whereas the weight losses for ferritic steels

are linear. The dissolution rates of the austenitic steels are an order of magnitude greater than for the ferritic steels. The weight loss for cold-worked Type 316 stainless steel is higher than of the annealed steel.

The corrosion tests have continued during the current reporting period. The weight loss for Type 316 stainless steel and ferritic steels in Pb-17Li at 700 and 727 K is shown in Fig. 9.5.5. The dissolution rates for Type 316 stainless steel reached a steady-state value (shown by the dashed lines) after an initial period of high dissolution rates. The weight losses with time may also be expressed by a parabolic law; these predictions are shown by the solid curves in Fig. 9.5.5a. The dissolution rates for the ferritic steels are constant and an order of magnitude lower than the steady-state rates for Type 316 stainless steel. For all alloys, the weight loss at 727 K is about a factor of two greater than at 700 K.

The Arrhenius plot of the dissolution rates for Type 316 stainless steel and the ferritic steels in flowing Pb-17Li is shown in Fig. 9.5.6. The dissolution rate for Type 316 stainless steel at 773 K in a Pb-17Li thermal convection loop is also included in the figure. The combined data for Type 316 stainless steel yield an activation energy of ~38 kcal/mole. This value is identical to that obtained in the lithium thermal convection loop at temperatures between 773 and 873 K.[3]

9.5.5 Conclusions

The corrosion data for austenitic and ferritic steels in flowing lithium at 700 and 755 K indicate that the dissolution rates for austenitic stainless steels reach a steady-state value after an initial period of high rates. The weight losses of ferritic steels follow a linear law with time. Data also indicate that the dissolution behavior of both austenitic and ferritic steels is strongly affected by the impurity content of the lithium, particularly the concentration of nitrogen in lithium. Variations in the lithium purity during the tests lead to significant variations in the values of weight loss.

Tensile data for cold-worked Type 316 stainless steel at temperatures between 473 and 755 K and strain rates in the range of 4×10^{-2} to 4×10^{-6} s^{-1} indicate that a flowing lithium environment has no effect on the tensile strength or total elongation of the steel. Tensile tests are being conducted on the HT-9 alloy to study the possible embrittlement of the material in lithium.

Corrosion tests in a flowing Pb-17Li environment indicate that the dissolution rates for both austenitic and ferritic steels in Pb-17Li are an order of magnitude greater than in flowing lithium. The influence of time, temperature, or alloy composition on the corrosion behavior in Pb-17Li is similar to that in lithium. Dissolution rate data for Type 316 stainless steel exposed to Pb-17Li yield an activation energy of 38 kcal/mole.

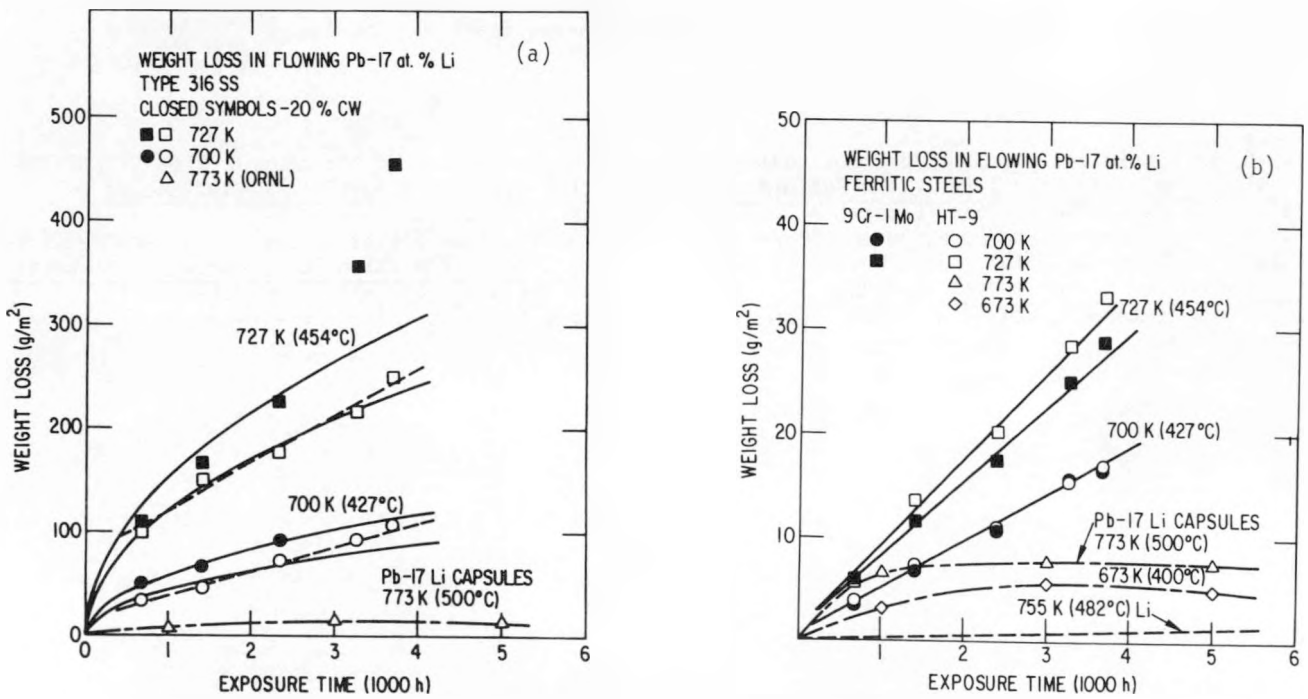

Fig. 9.5.5. Weight loss versus exposure time for (a) Type 316 stainless steel and (b) ferritic HT-9 and Fe-9Cr-1Mo steels in flowing Pb-17Li at 700 and 727 K.

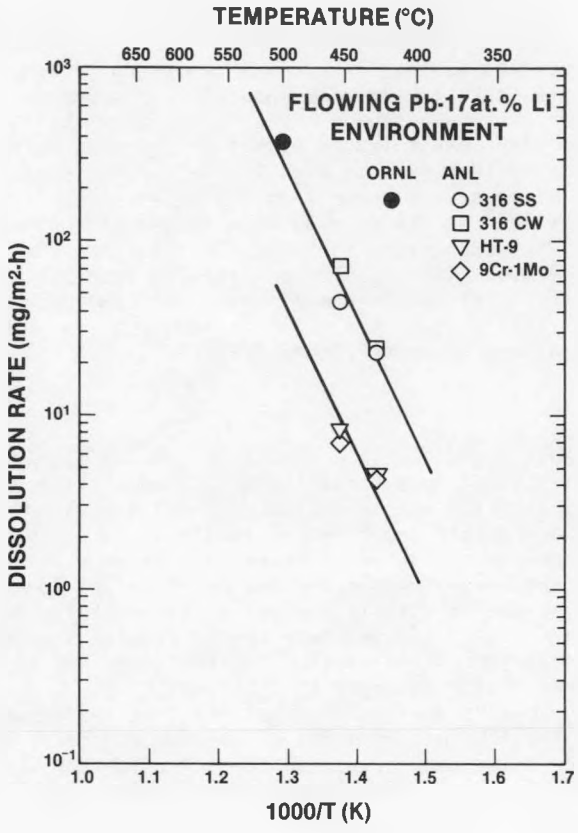

Fig. 9.5.6. Arrhenius plot of dissolution rate data for austenitic and ferritic steels exposed to flowing Pb-17Li.

9.5.6 References

1. O. K. Chopra and D. L. Smith, "Environmental Effects on Properties of Structural Alloys," pp. 195-200 in Alloy Development for Irradiation Performance: Semiannual Progress Report for Period Ending March 31, 1983, Oak Ridge National Laboratory, DOE/ER-0045/10.

2. P. F. Tortorelli and J. H. Devan, "Corrosion of Path A PCA, Type 316 Stainless Steel, and Fe-12Cr-1MoVW Steel in Flowing Lithium," pp. 290-303 in Alloy Development for Irradiation Performance: Semiannual Progress Report for Period Ending September 30, 1981, Oak Ridge National Laboratory, DOE/ER-0045/9.

3. P. F. Tortorelli and J. H. Devan, "Corrosion of Type 316 Stainless Steel in Flowing Pb-17 at. % Li," this report.

DOE/ER-0045/11
Distribution
Category
UC-20, 20c

DISTRIBUTION

1–6. Argonne National Laboratory, 9700 South Cass Avenue, Argonne, IL 60439

L. Greenwood
V. Maroni
R. F. Mattas
R. E. Nygren
D. L. Smith
H. Wiedersich

7–8. Battelle-Pacific Northwest Laboratory, P.O. Box 999, Richland, WA 99352

J. L. Brimhall
D. Dingee

9. Brookhaven National Laboratory, Upton, NY 11973

C. L. Snead, Jr.

10. Colorado School of Miners, Golden, CO 80401

G. R. Edwards

11–194. Department of Energy, Technical Information Center, Office of Information Services, P.O. Box 62, Oak Ridge, TN 37830

For distribution as shown in TID-4500 Distribution Category, UC-20 (Magnetic Fusion Energy), and UC-20c (Reactor Materials)

195–201. Department of Energy, Office of Fusion Energy, Washington, DC 20545

M. M. Cohen
G. M. Haas
T. C. Reuther, Jr. (5 copies)

202. Department of Energy, Oak Ridge Operations Office, P.O. Box E, Oak Ridge, TN 37830

Office of Assistant Manager for Energy Research and Development

203. Energy Technology Engineering Center, P.O. Box 1449, Canoga Park, CA 91304

ETEC Library

204–205. GA Technologies, Inc., P.O. Box 81608, San Diego, CA 92138

T. A. Lechtenberg

D. I. Roberts

206–208. Lawrence Livermore National Laboratory, P.O. Box 808, Livermore, CA 94550

E.N.C. Dalder
M. Guinan
C. M. Logan

209. Los Alamos National Laboratory, Mail Stop H809, Los Alamos, NM 87545

M. S. Wechsler

210. Massachusetts Institute of Technology, 138 Albany Street, Cambridge, MA 02139

O. K. Harling

211–212. Massachusetts Institute of Technology, 77 Massachusetts Ave., Cambridge, MA 02139

N. J. Grant
V. B. Vander Sande

213–214. McDonnell Douglas Astronautics Company, East, P.O. Box 516, St. Louis, MO 63166

J. W. Davis
D. L. Kummer

215. Mellon Institute, Schenley Park, Pittsburgh, PA 15213

J. C. Williams

216. National Materials Advisory Board, 2101 Constitution Ave., Washington, DC 20418

K. M. Zwilsky

217–218. Naval Research Laboratory, Washington, DC 20375

Superintendent, Materials Science and Technology Division
J. A. Sprague

219–257. Oak Ridge National Laboratory, P.O. Box X, Oak Ridge, TN 37830

Central Research Library (2 copies)
Document Reference Section
Laboratory Records Department (2 copies)
Laboratory Records Department, RC
ORNL Patent Section
E. E. Bloom (10 copies)
D. N. Braski
F. R. Cox (3 copies)
J. H. DeVan
I. T. Dudley
M. L. Grossbeck
R. L. Klueh
R. A. Lillie
C. T. Liu
K. C. Liu
L. K. Mansur
P. J. Maziasz
C. J. McHargue
T. K. Roche
A. F. Rowcliffe
M. J. Saltmarsh
J. L. Scott
P. F. Tortorelli
J. M. Vitek
F. W. Wiffen

258–259. Rensselaer Polytechnic Institute, Troy, NY 12181

D. Steiner
N. Stoloff

260–261. Sandia National Laboratories, Livermore Division 8316, Livermore, CA 94550

W. Bauer
J. C. Lippold

262. Science Applications, Inc., 1200 Prospect, La Jolla, CA 92037

H. Gurol

263–264. University of California, Department of Chemical, Nuclear, and Thermal Engineering, Los Angeles, CA 90024

M. A. Abdou
R. W. Conn
N. M. Ghoniem

265. University of California, Santa Barbara, CA 93106

G. R. Odette

266. University of Missouri, Department of Mechanical and Aerospace Engineering, Columbia, MO 65211

M. Jolles

267. University of Virginia, Department of Materials Science, Charlottesville, VA 22901

W. A. Jesser

268. University of Wisconsin, 1500 Johnson Drive, Madison, WI 53706

W. G. Wolfer

269. Westinghouse Electric Company, Advanced Energy Systems Division, P.O. Box 10864, Pittsburgh, PA 15236

R. Bajaj
W. A. Boltax

270–277. Westinghouse Hanford Company, P.O. Box 1970, Richland, WA 99352

H. R. Brager
D. G. Doran
A. M. Ermi
F. A. Garner
D. S. Gelles
E. C. Opperman
R. W. Powell
J. L. Straalsund